Proceedings of the 32nd Symposium on Celestial Mechanics

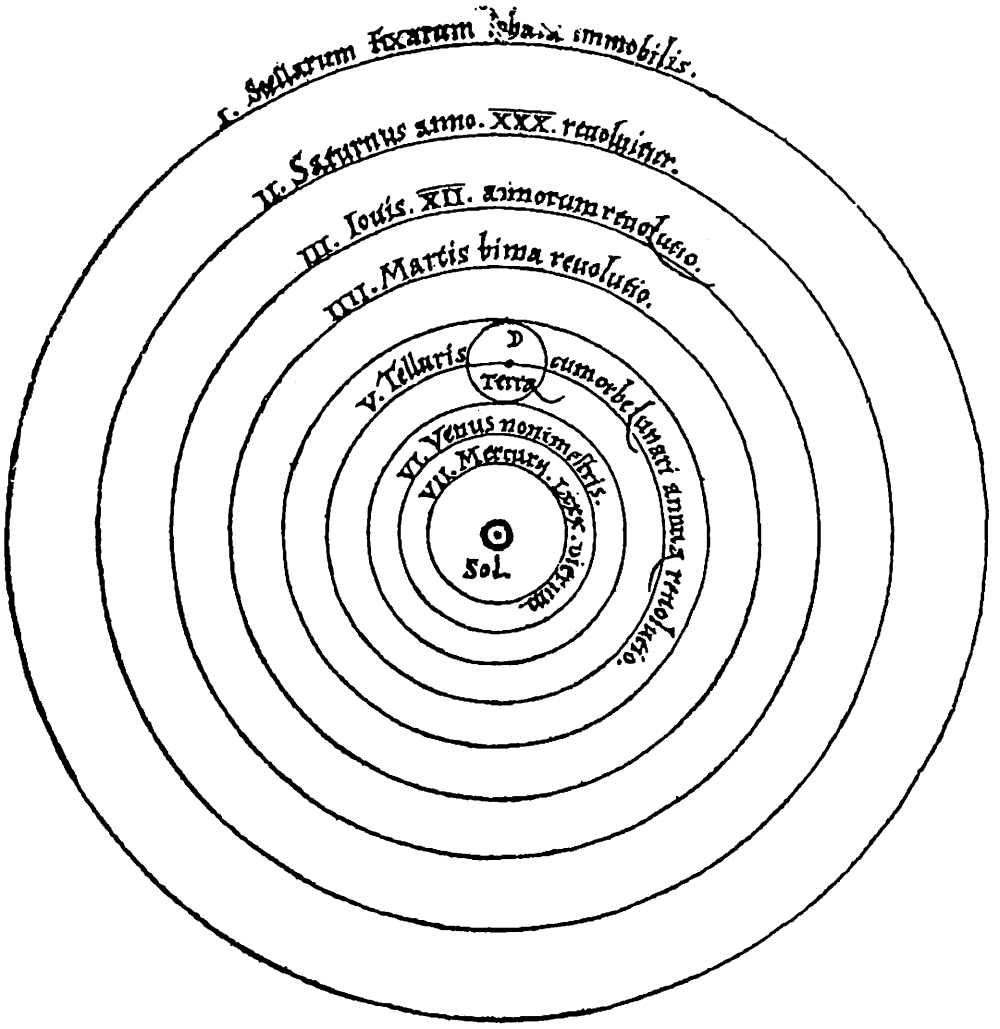

The Graduate University for Advanced Studies
Hayama, Kanagawa, JAPAN
15-17, March, 2000

Editors : H. Arakida, Y. Masaki, H. Umehara

Proceedings of the 32nd Symposium on Celestial Mechanics
天体力学N体力学研究会集録

The Graduate University for Advanced Studies
Hayama, Kanagawa, JAPAN
15-17, March, 2000

Editors : H. Arakida, Y. Masaki, H. Umehara

Preface

天体力学N体力学研究会 (The 32nd Symposium on Celestial Mechanics) は、昨年度の天体力学・N体力学研究会 (通信総合研究所鹿嶋)、一昨年度までの第n回天体力学研究会を引き継ぐ研究会として、2000年3月15日～17日の3日間、神奈川県葉山町にある総合研究大学院大学本部にて開催されました。口頭12編、ポスター25編の発表があり、シニア研究者はもとより多くの若手研究者まで、合わせて約50人の参加を頂く事が出来ました。

本研究会では、ポスター発表を例年以上に重視しそれに見合った時間とスペースを割り当て、充分な議論、討論ができるように配慮しました。宿舎が総研大本部であったこともあり、夜遅くまでポスターを囲んだ議論が行われるなど昼夜を問わず活発な議論が交わされました。

また、本研究会では昨年度の天体力学・N体力学研究会からの流れを踏襲し、複数分野の研究交流によって、新たな問題解決や問題提起を生む研究会を目指しました。そこで、研究会で取り扱うテーマとして従来の天体力学に関わる話題だけではなく、物性、生物、惑星科学、宇宙論といった多くの分野にみられる多粒子系の集団運動やハミルトン系の力学、非線形力学系の問題などが議論されました。

最後になりますが、座長を引き受けてくださった方々をはじめ参加者の皆様の御協力を得て、不慣れな世話人にも関わらず研究会を盛況のうちに終了することが出来ました事を心から感謝致します。

平成12年3月17日
天体力学N体力学研究会世話人代表
荒木田英禎

表紙

コペルニクスが描いた太陽系の図。地球をはじめとする惑星は太陽のまわりを公転し、月だけが地球のまわりを公転している。
出典:Nucolaus Copernicus, *DE REVOLUTIONIBIU ORBIUM COELESTIUM*, Johnson Reprint Corporation, 1965

Editors

荒木田英禎 (Hideyoshi Arakida)
総合研究大学院大学/国立天文台天文情報公開センター
The Graduate University for Advanced Studies/
Public Relation Center, National Astronomical Observatory
E-Mail : h.arakida@nao.ac.jp

眞崎良光 (Yoshimitsu Masaki)
総合研究大学院大学/国立天文台位置天文天体力学研究系
The Graduate University for Advanced Studies/
Division of Celestial Mechanics, National Astronomical Observatory
E-Mail : masakiys@cc.nao.ac.jp

梅原広明 (Hiroaki Umehara)
郵政省通信総合研究所関東支所鹿嶋宇宙通信センター宇宙制御技術研究室
Kashima Space Research Center, Communications Research Laboratory
E-Mail : ume@crl.go.jp

Table of Contents

Formation of Planetary System

Dynamics in our Solar System

Extra-Solar Planets

Dynamics of Artificial Satellites

Observation in Celestial Mechanics

Many Body System in the Universe

Chaotic Dynamics

Many Body Chaos in Physics

Few Body Problem

Theory of Dymamical System

Numerical Techniques

The Formation of Planetesimals through the Fragmentation of a Dust Layer

Izumi Furuya
Graduate School of Science and Technology, Kobe University
Rokkodai-cho, Nada, Kobe, 657-8501, Japan
E-mail: furuya@jet.planet.sci.kobe-u.ac.jp

Yoshitsugu Nakagawa
Faculty of Science, Kobe University
Rokkodai-cho, Nada, Kobe, 657-8501, Japan
E-mail: yoshi@whynot.phys.kobe-u.ac.jp

Abstract

Gravitational fragmentation of a dust layer is considered to be a prevailing process of planetesimal formation. The mass of a planetesimal formed by gravitational fragmentation has been estimated only by the linear perturbation theory for axisymmetric mode and has not been evaluated by any numerical simulations. In this study, we reproduce the gravitational fragmentation by local N-body numerical simulations and compare the obtained mass of a fragment with the analytic estimate. According to our results obtained until now, stable particle aggregates are formed when Hill radius $r_{\rm H}$, i.e., the radius of the sphere of gravitational influence of a particle, is larger than the sum of two particle radii $2r_{\rm p}$, especially when $r_{\rm H}/2r_{\rm p} \simeq 2$. The mass of a particle aggregate is found to be almost same as that of the analytic estimate. On the other hand, when $r_{\rm H}$ is smaller than $2r_{\rm p}$, only non-axisymmetric wake-like structures appear.

1 Introduction

The solar nebula is considered to be turbulent more or less at early stages. After such turbulent motion has decayed, dust particles settle toward the central plane of the nebula and accumulate into a thin layer around the central plane — a dust layer (Weidenschilling 1980, Nakagawa et al. 1981). When the density in the dust layer exceeds the Roche density, the layer becomes gravitationally unstable to fragment into a number of planetesimals (Hayashi 1972, Goldreich and Ward 1973). The sizes of the resulting fragments are estimated in terms of the linear perturbation theory for axisymmetric mode (e.g., Toomre 1964) as the critical wavelength given by

$$\lambda_{\rm crit} = \frac{4\pi^2 G\Sigma}{\kappa^2}, \tag{1}$$

where κ is the epicyclic frequency and Σ is the surface density of the layer. The condition for gravitational instability of the layer is given by Toomre's parameter Q as

$$Q \equiv \frac{\sigma_r \kappa}{3.36 G\Sigma} < 1, \tag{2}$$

where σ_r is the radial velocity dispersion. If the above condition is met, the dust layer is unstable to perturbations of wavelengths around the critical wavelength $\lambda_{\rm crit}$. The mass of a planetesimal is estimated as $\pi\Sigma\lambda_{\rm crit}^2$ by assuming that ring-shaped fragments are broken into sub-fragments having the same size both in the azimuthal and radial directions. The mass has not been evaluated by numerical simulations. In the present study, we reproduce the gravitational fragmentation by local N-body numerical simulation and compare the obtained mass of a fragment with the analytic estimate.

2 Simulation Method

We follow the motions of dust particles in a cell present in a narrow ring which is a part of the dust layer. We then apply a local N-body method which was first applied to the study of a dense ring system by Wisdom and Tremaine (1988) and then used by Salo (1991, 1992a, 1992b, 1995), Richardson (1993, 1994) and Daisaka and Ida (1999). In this study, we assume that all particles have the same radius $r_{\rm p}$ and mass m. We take only the mutual forces and inelastic collisions of the particles into account, but we leave the disruption and sticking of the particles out of consideration.

To use GRAPE-3A effectively we adopt the following 'subregion method' which is introduced by Daisaka and Ida (1999). We then apply periodic shearing boundary conditions and use a unit cell having a rectangular cross section with area $L_x \times L_y$ (L_x and L_y are a few times as large as λ_{cr}) and extending infinitely in the z direction (in Fig.1, a cell with thick line). In order to provide a realistic gravitational perturbation on the unit cell, it is necessary to include contributions from the eight surrounding cells. The equations of motion used in this study (see Eq.(4) below) are invariant under the transformation

$$(x, y, z) \rightarrow (x + nL_x, y - \frac{3}{2}nL_x\Omega t + mL_y, z), \tag{3}$$

where m and n are integers. The particle distribution in these cells is identical to the distribution in the central cell at all times. Cells $n = \pm 1$ slide upward and downward with the shear velocity $(3/2)\Omega L_x$. The particle number in each cell is maintained by entrance of their corresponding images from a surrounding cell. We divide the simulation region into nine subregions (with broken line in Fig. 1) and assign to each subregion a virtual region (having the same size as the original) in which the subregion is centered. The subregion and the virtual region are represented by dark and light shaded regions respectively in Fig. 1. For particles in the subregion, we take the gravitational forces of all particles in the virtual region into account.

In simulating such a situation described above, we erect the Hill coordinate system with origin at a reference point moving on a circular orbit with semimajor axis a_0 at the Keplerian angular velocity Ω_0 $(= (GM_\odot/a_0^3)^{1/2})$(Hill 1878, Nakazawa 1988). The x axis pointing radially outward, the y axis pointing in the direction of the orbital motion, and the z axis normal to the equatorial plane. In this study, the equations of motion for particle i are

$$\begin{aligned}
\ddot{x}_i - 2\Omega_0\dot{y}_i &= 3\Omega_0^2 x_i + \sum_{j=1, i\neq j}^{N} \frac{Gm_j}{r_{ij}^3}(x_j - x_i), \\
\ddot{y}_i + 2\Omega_0\dot{x}_i &= + \sum_{j=1, i\neq j}^{N} \frac{Gm_j}{r_{ij}^3}(y_j - y_i), \\
\ddot{z}_i &= -\Omega_0^2 z_i + \sum_{j=1, i\neq j}^{N} \frac{Gm_j}{r_{ij}^3}(z_j - z_i),
\end{aligned} \tag{4}$$

where N is the number of particles, m_j is the mass of particles j and r_{ij} is the distance between particle i and j.

We assume that all particles have same radius r_p and mass m for simplification. The equations are written in non-dimensional forms independent of mass and the heliocentric distance a_0, if we scale the time by Ω_0^{-1}, the length by $ha_0 = r_{\rm H}$ and the mass by $h^3 M_\odot$:

$$\begin{aligned} \tilde{t} &= \Omega_0 t, \\ \tilde{r} &= (\tilde{x}, \tilde{y}, \tilde{z}) = \frac{(x, y, z)}{h a_0}, \\ \tilde{m} &= \frac{m}{h^3 M_\odot} = \frac{3}{2}, \end{aligned} \tag{5}$$

where h is the reduced Hill radius defined by

$$h = (\frac{2m}{3M_\odot})^{\frac{1}{3}}. \tag{6}$$

With the above scaling, Eq. (4) can be expressed as

$$\begin{aligned} \ddot{\tilde{x}}_i - 2\dot{\tilde{y}}_i &= 3\tilde{x}_i + \frac{3}{2}\sum_{j=1, i\neq j}^{N} \frac{1}{\tilde{r_{ij}}^3}(\tilde{x_j} - \tilde{x_i}), \\ \ddot{\tilde{y}}_i + 2\dot{\tilde{x}}_i &= +\frac{3}{2}\sum_{j=1, i\neq j}^{N} \frac{1}{\tilde{r_{ij}}^3}(\tilde{y_j} - \tilde{y_i}), \\ \ddot{\tilde{z}}_i &= -\tilde{x_i} + \frac{3}{2}\sum_{j=1, i\neq j}^{N} \frac{\tilde{1}}{\tilde{r_{ij}}^3}(\tilde{z_j} - \tilde{z_i}). \end{aligned} \tag{7}$$

We apply the initial conditions that the x and y coordinates of particles are chosen at random, avoiding overlapping of particles, and uniformly distributed across the unit cell. The vertical distribution is also taken to be uniform up to a distance of h above and below the equatorial plane. The position of pairs of particles are chosen symmetrically so that the center of mass will lie at the center of the unit cell. The velocities except for the shear velocity of individual particles $3\tilde{x}_i/2$ are chosen randomly so that the initial random velocity becomes large enough to achieve $Q > 2$, since Salo (1995) and Daisaka (1999) showed that $Q \simeq 2$ in the equilibrium state.

The calculated system is characterized by two non-dimensional parameters ; dynamical optical depth τ and the ratio $r_h/2r_p$. Having scaled the time by Ω_0^{-1} and the length by r_h, if we obtain one solution, we can use it as solutions for any arbitrary m and a_0. The number of particles whose centers lie in the unit cell is constant and is denoted by N. Thus dynamical optical depth is given by

$$\tau \equiv \frac{N\pi r_p^2}{L_x L_y}. \tag{8}$$

The other parameter, the ratio $r_{\rm H}/2r_{\rm p}$, is

$$\frac{r_h}{2r_p} = 105.6\,(\frac{\rho}{2{\rm g/cm}^3})^{1/3}(\frac{a_0}{1{\rm AU}}), \tag{9}$$

where Sun's mass $M_\odot = 2.0 \times 10^{33}$g, and ρ is the material density of particles. According to Ohtsuki (1993), which carried out three-body trajectory integration, the possibility of accretion is determined by the ratio $r_{\rm H}/2r_{\rm p}$. Accretion is possible even inside the Roche limit. The capture probability decreases abruptly for $r_{\rm H}/2r_{\rm p} \leq \frac{3}{2}$, where the target body protrudes out of the Hill sphere.

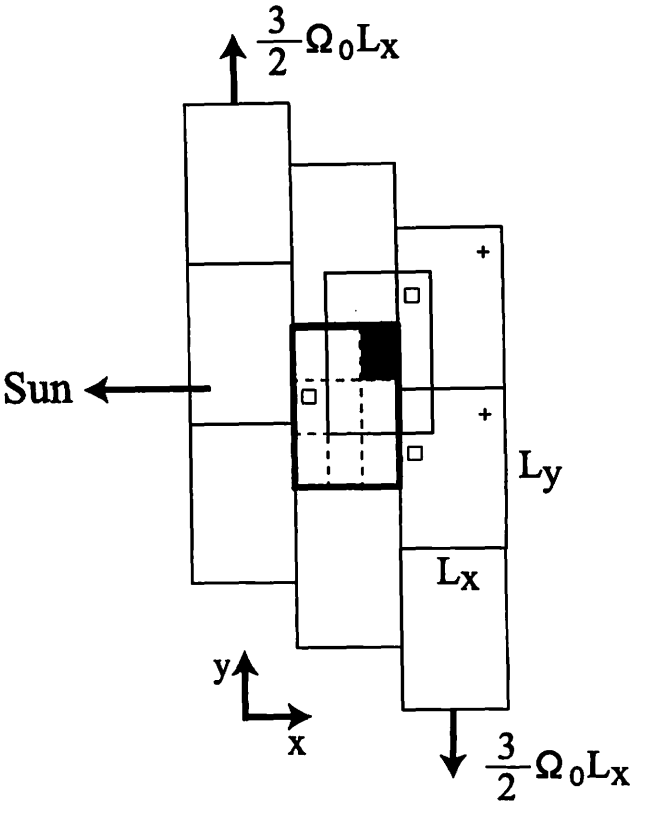

Figure 1: Schematic illustration of a simulation cell (thick lines) and its eight surrounding copies (thin lines). Gravitational forces exerted on a given target particle (denoted by the cross) in the subregion (light shaded) are calculated from all the other particles in the virtual region (dark shaded).

In our simulations, we adopt a smooth inelastic hard sphere collision model that has been commonly used in previous simulations (Wisdom and Tremaine 1988, Salo 1991, 1992a, 1992b, 1995, Richardson 1994, Daisaka and Ida 1999). A collision changes only the impact velocity in normal direction depending on restitution coefficient $\epsilon_n (0 \leq \epsilon_n \leq 1)$. The change of tangential component is neglected, by assuming tangential restitution coefficient $\epsilon_t = 1$, in order to exclude the effects of spins of particles. Hereinbelow ϵ denotes ϵ_n for simplicity. The relative velocity $\boldsymbol{v}'_{ij}$ after collision is given by

$$\boldsymbol{v}'_{ij} = \boldsymbol{v}_{ij} - (1+\epsilon)\frac{\boldsymbol{r}_{ij}\cdot\boldsymbol{v}_{ij}}{r_{ij}}\frac{\boldsymbol{r}_{ij}}{r_{ij}}, \tag{10}$$

where $\boldsymbol{v}_{ij}$ and $\boldsymbol{r}_{ij}$ are the relative velocity and the relative position of two colliding particles i and j. We treat ϵ as a parameter.

Ideally, a collision should be detected the instant it occurs. However, such operation is impractical, and hence a certain amount of penetration or temporary overlap is unavoidable. When two or more particles are approaching and overlapping each other, we consider that they collide.

3 Results

We have numerically solved N-body problem for Keplerian particles with gravity, taking into account inelastic collisions as well as gravitational scattering between them, in order to see how structure of the spatial distribution of the particles appears and evolves. At the initial state the particles were distributed uniformly in the local computation area of a square $L \times L$ and we pursued the orbits of those particles in the area under some appropriate periodic boundary conditions. We examined 8 cases of the total particle number $100 \leq N \leq 9248$. In each case, we made computations for several different heliocentric distances, which correspond to the cases of the ratios $r_{\rm H}/2r_{\rm p} = 0.82.$ 1.18, 1.60, and 2.05. In all cases we assumed that the restitution coefficient $\epsilon = 0.01$.

We found that in the case of $r_{\rm H}/2r_{\rm p} = 0.82\ (< 1)$ only non-axisymmetric wake-like structures appear and, on the other hand, in the cases of $r_{\rm H}/2r_{\rm p} = 1.183$, 1.6, and 2.05 (> 1), ellipsoidal aggregates are formed. Especially, in the case of $r_{\rm H}/2r_{\rm p} = 2.05$, quite stable aggregates are formed, while in the cases of $r_{\rm H}/2r_{\rm p} = 1.183$ and 1.6, ellipsoidal aggregates are formed and dissolved repeatedly. Further, in the case of $r_{\rm H}/2r_{\rm p} = 2.05$, as illustrated in Figs.2, the number of stable aggregates depends on the size of computation area L; in the case of $L/\lambda_{\rm crit} = 1.22$, a single aggregate is formed, while in the cases of $L/\lambda_{\rm crit} = 2.44$ and 4.15, two aggregates are formed.

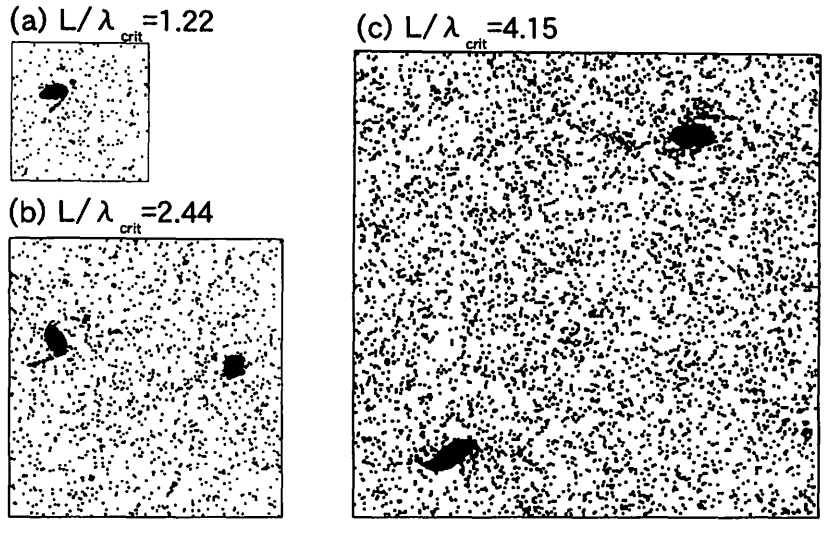

Figure 2: Examples of stable aggregates with various $L/\lambda_{\rm crit}$. (a) and (b) : Examples of aggregates at 12.03 Kepler time. (N = 800 and 3200) (c) : Aggregates after 34.18 Kepler time. (N = 9248) The size of calculation region L of (a), (b) and (c) are $38.5r_{\rm H}$, $77.1r_{\rm H}$ and $131.1r_{\rm H}$, respectively.

The properties of those aggregates are summarized in Table 1. The Q-values inside the aggregates are apparently smaller than unity as is expected from the linear theory. As the size of computation area becomes large, the number of particles within the aggregates $N_1 + N_2$ increases but the ratio of their number to the total $(N_1 + N_2)/N$ decreases. The velocity dispersion inside the aggregates is smaller than outside. The fluctuation of velocity dispersion for the case of $r_{\rm H}/2r_{\rm p} = 2.05$ is smaller than that for $r_{\rm H}/2r_{\rm p}$ =1.6, this may be due to the repeated formation and disappearance of aggregates in the case of $r_{\rm H}/2r_{\rm p}$ =1.6 (see Fig.3).

Finally we compare the mass of our aggregate m_{comp} with the theoretical mass m_{theor}

estimated by the linear theory as

$$m_{theor} = \pi\Sigma\lambda_{\rm crit}^2 = (4\pi)^2 \left(\frac{\Sigma\pi a_0^2}{M_\odot}\right)^3 M_\odot. \tag{11}$$

We adopt the result of the case of $r_{\rm H}/2r_{\rm p} = 2.05$ and $L/\lambda_{\rm crit} = 4.15$, where the largest aggregates are formed. If we put $r_{\rm p} = 100$cm, the material density $\rho = 2\ {\rm g\,cm^{-3}}$, and the surface density Σ=26.6 $\rm g\,cm^{-2}$, then we have the heliocentric distance $a_0 = 0.0194$ AU (2.91×10^{11} cm) and $m_{theor} \simeq 1.4 \times 10^{10}$ g, while $m_{comp} \simeq 1.6 \times 10^{10}$ g. Therefore, the agreement is quite well. However, our results of computation seem depend on the size of computation area L; hence, numerical computations in larger area are still necessary.

Table 1: Properties of stable aggregates in Fig.2. The subscript 1 and 2 denote the aggregate on the left and right side, respectively. (For example, σ_{x1} denotes the x-component of velocity dispersion inside the aggregate on the left side.) $\sigma_{x-\rm outer}$ denotes the x-component of velocity dispersion outside the aggregates.

L/λ_{crit}	$\sigma_{x1}/r_{\rm H}\Omega$	$\sigma_{x2}/r_{\rm H}\Omega$	$\sigma_{x-\rm outer}/r_{\rm H}\Omega$	Q_1	Q_2	N_1	N_2	$\frac{N_1+N_2}{N}$
1.22	4.777	–	16.43	0.072	–	500	–	0.625
2.44	7.128	6.381	18.58	0.073	0.072	1033	652	0.526
4.15	5.307	7.730	21.65	0.076	0.071	1858	1823	0.398

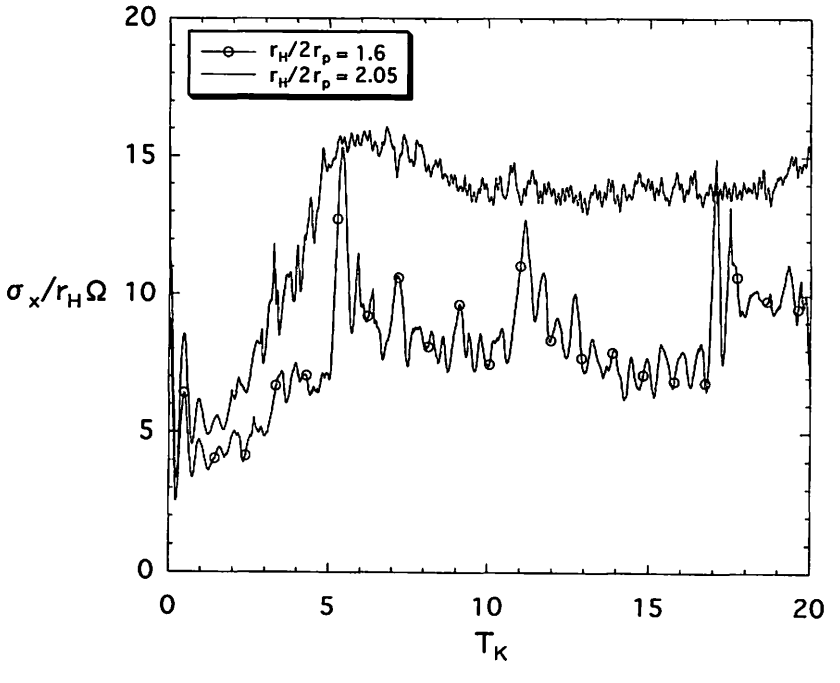

Figure 3: The evolution of velocity dispersion for $r_{\rm H}/2r_{\rm p} = 1.6$ and 2.05. σ_x denotes the velocity dispersion of all particles in the calculation region. In both cases, $L/\lambda_{\rm crit} = 2.44$ and $\tau = 0.1$.

References

[1] Daisaka, H., and S. Ida, 1999. Spatial structure and coherent motion in dense planetary ring induced by self-gravitating instability. *Earth , Planet and Space*, **51**, 1195-1213.

[2] Goldreich, P., and W. R. Ward, 1973. The formation of planetesimals. *Astrophys. J.*, **183**, 1051-1061.

[3] Hayashi, C. 1972. Origin of the solar system. *In Proc. 5th Lunar Planetary Symposium, eds. K. Takayanagi and M. Shimizu (Tokyo:Inst. Space Aeronautical Sci.)*, pp.13-18.

[4] Hayashi, C., K. Nakazawa, and Y. Nakagawa, 1985. Formation of the solar system. In *Protostars and Planets II*(D. C. Black and M. S. Matthews. Eds.), pp. 1100-1153. Univ. of Arizona Press, Tucson.

[5] Hill, G. W., 1878. Researches in the lunar theory. *Amer. J. Math.*, **1**, 5-26, 129-147, 245-260.

[6] Nakagawa, Y. , Nakazawa, K. , and Hayashi, C., 1981. Growth and sedimentation of dust grains in the primordial solar nebula. *Icarus* **45**, 517-528.

[7] Nakazawa, K. and S. Ida, 1988. Hill's approximation in the tree-body problem. *Prog. Theor. Phys. Suppl.*, **96**, 167-174.

[8] Ohtsuki, K. 1993. Capture probability of colliding planetesimals : Dynamical constraints in accretion of planets, satellites, and ring particles. *Icarus*, **106**, 228-246.

[9] Richardson, D. C., 1993. A new tree code method for simulation of planetesimal dynamics. *Mon. Not. R. Astron. Soc.*, **261**, 396-414.

[10] Richardson, D. C., 1994. Tree code simulations of planetary rings. *Mon. Not. R. Astron. Soc.*, **269**, 493-511.

[11] Salo, H. 1991. Numerical simulations of dense collisional systems. *Icarus*, **90**, 254-270.

[12] Salo, H. 1992a. Numerical simulations of dense collisional systems. II. Extended distribution of particle sizes. *Icarus*, **96**, 85-106.

[13] Salo, H. 1992b. Gravitational wakes in saturn's rings. *Nature*, **395**, 619-621.

[14] Salo, H. 1995. Simulation if dense planetary rings III. Self-gravitating identical particles. *Icarus*, **117**, 287-312.

[15] Toomre, A. 1964. On the gravitational stability of a disk of stars. *Astrophys. J.*, **139**, 1217-1238.

[16] Weidenschilling, S. J. 1980. Dust to planetesimals: Settling and coagulation in the solar nebula. *Icarus*, **44**, 172-189.

[17] Wisdom, J. and S. Tremaine, 1988. Local simulations of planetary rings. *Astron. J.*, **95**, 925-940.

Co-accretional evolution of the Earth-Moon system after the giant impact; reduction of the angular momentum by escaping of Lunar impact ejecta

Ryuji Morishima and Sei-ichiro Watanabe
Department of Earth and Planetary Sciences, Nagoya University

Abstract

Recently, the Moon-forming giant impact is considered to have occurred in the course of the Earth's accretion. In co-accretional stage after that, much of lunar impact ejecta would be ejected to circumterrestrial orbit due to high velocity impacts of residual planetesimals. We performed orbital calculations of the escaped particles from the satellite with various mass ratio and semi-major axis. For the lunar sized satellite, most of the particles escape from the Hill sphere of the planet, which take away a great quantity of the angular momentum. Simulating co-accretional evolution including re-distribution of lunar impact ejecta and tidal interaction, we estimated the angular momentum of the Earth-Moon system at $0.7-0.8$ Earth's mass as about $1.2-1.4$ times larger than that of the present Earth-Moon system. It is great advantage for making large Moon by the giant impact.

1 Introduction

惑星集積の最終段階において惑星サイズの天体が原始地球に衝突するいわゆるジャイアントインパクトにより、月は形成されたと考えられている。この説は地球月系の力学的、地球化学的特徴を説明するのに都合がいいと考えられている。巨大衝突が起こると、ロッシュ半径付近に分布する、周地球ディスクが形成され [1,2]、それが集積して1つの月が形成される [3] ことがシミュレーションによって示された。それらのシミュレーションの詳しい解析によると、質量和が $1M_{\rm E}$(地球質量) で角運動量が $1L_{\rm EM}$(地球月系の総角運動量) の衝突では一般に月より小さい衛星が形成されることが分かった (ただしパラメターによっては月質量程度になりそうな場合もある)。それに対し、質量和が $0.6-0.7M_{\rm E}$ で角運動量は $1.0-1.25L_{\rm EM}$ の巨大衝突によって、その時点で、ほぼ月質量を持った衛星が形成される場合もあることが示された [4,5]。

巨大衝突による月形成が地球の集積の途中段階において起こった場合、地球と月はその後の微惑星集積により共成長進化すると考えられる。共成長段階において、微惑星の月への衝突速度は、月の脱出速度を大きく越えるため、月から大量の ejecta が周地球軌道に飛び出ると考えられる。そこで我々は、様々な (惑星に対する) 質量比と、軌道半径の衛星から発射される ejecta の軌道を数値計算することにより、Ejecta の質量と角運動量の再分配率をもとめた。その結果をもとに、微惑星集積、ejecta による再分配、潮汐相互作用を含んだ地球月系の質量と角運動量の進化を行った。

2 Methods

衛星表面から脱出速度を越えて発射された ejecta がどのように分配されるかをもとめるために、太陽、惑星、衛星、a massless particle の4体問題の軌道計算を行う。計算において、衛星の軌道は円とし、軌道面は惑星の軌道面と同じとする。様々な衛星表面の points、発射方向、速度を初期条件として与え軌道計算し、各初期条件ごとに重みをつけて足し合わせることによって、ejecta の分配率がもとまる。

Ejecta がどのような分布で飛び出るかは、微惑星の衛星への衝突速度とフラックスの分布に依存し、その分布に Harris and Kaula (1975)[6] のモデルを用いる。彼らのモデルによると、衛星

が公転しているために、衛星の前方により速い速度の微惑星が多く衝突し、衛星の側面では斜め衝突になる。

衛星表面から飛び出す ejecta の速度分布および総量は、以下のスケーリング則で与えられる。

$$dm_{\rm ej} \propto v_{\rm ej}^{-c_1-1} dv_{\rm ej}, \tag{1}$$

$$\frac{m_{\rm esc}}{m} = \int_{v_{\rm esc}}^{v_{\rm imp}} \frac{dm_{\rm ej}}{m} = c_2 \left[\left(\frac{v_{\rm imp}}{v_{\rm esc}} \right)^{c_1} - 1 \right], \tag{2}$$

ここで、$m_{\rm ej}$ は衛星表面からの発射速度が $v_{\rm ej}$ より速い ejecta の総質量を表し、$m_{\rm esc}, m$ はそれぞれ衛星から脱出する ejecta の総質量と衝突する微惑星質量を表す。$v_{\rm esc}, v_{\rm imp}$ は、衛星の脱出速度と微惑星の衝突速度を表す。また、c_1, c_2 は衝突の室内実験や、シミュレーションにより得られ、今回 Table 1 の 6 種類のモデルを用い比較を行う。

Ejecta の発射位置は、衛星表面の 40 ポイントを選び、各ポイントから衛星表面に対して 45° で等角度間隔で 20 方向に発射させる。その際重みをつけた平均の射出方向は、上で述べたモデルの角度とする。また、各ポイントから飛び出るフラックスは式 (2) で重みつけられる。射出速度は衛星脱出速度よりも速い 10 通りの速度とし、式 (1) で重みつけられる。

3 Results

今回扱った衛星質量比 (≥ 0.003) の範囲内では、最も長く惑星のヒル圏内に存在しつづけた test particles で数百年程度で (惑星の軌道長半径は 1AU として)、それまでの間に衛星、惑星、脱出の 3 通りの結果に振り分けられることが分かった。

発射速度に関して足し合わせた test particles の分配率の結果を見る前に、各発射速度ごとで、どのように particles の分配が行われるかを見てみる。Figure 1 は、$a_{\rm s}/r_{\rm p} = 10, m_{\rm s}/m_{\rm p} = 0.0125$ ($a_{\rm s}/r_{\rm p}$ は、衛星軌道半径/惑星半径を、$m_{\rm s}/m_{\rm p}$ は、衛星質量/惑星質量をそれぞれ表す) の場合の、質量分配率とそれぞれに分配される平均角運動量を $v_{\rm ej}/v_{\rm esc,s}$ の関数として表したものである。2 つの速度領域で結果を説明する。

$v_{\rm ej} \simeq v_{\rm esc}$ の場合、particles は衛星のヒル圏から飛び出るまでに衛星との相対速度をほとんど失ってしまうので、最初は惑星の周りをほぼ衛星と同じ円運動を行おうとする。衛星との相対速度が小さいので、衛星の重力 Focusing が大きく、衛星への再集積率 $P_{\rm s}$ は非常に高い。再集積しない残りの particles は、衛星の重力散乱により、惑星周りでの軌道離心率、軌道傾斜角が増加する。重力散乱による particles の軌道離心率の典型的大きさは、$v_{\rm esc}/v_{\rm k}$ ($v_{\rm k}$ は惑星周りのケプラー速度を表す) 程度の大きさになるので、$v_{\rm esc} > v_{\rm k}$ の場合には、the particles の惑星への衝突や、惑星重力圏からの脱出が可能になる。したがって、軌道半径が小さく、質量比が小さい衛星ほど particles を惑星周りの軌道から排除する効力が弱いので、衛星への再集積率は高くなる。また、脱出する particles の軌道は衛星軌道に接する放物線でほぼ表され、その specific 角運動量は衛星の specific 角運動量のだいたい $\sqrt{2}$ 倍になっていると考えられる。

次に、$v_{\rm ej} \gtrsim (v_{\rm esc}^2 + v_{\rm k}^2)^{1/2}$ ($\simeq 1.45 v_{\rm esc}$, Fig. 1 のパラメーターの場合) の場合、衛星ヒル圏から飛び出た後の particles の衛星に対する相対速度が衛星の軌道速度よりも大きく、particles は、即座の脱出、惑星への直接落下、惑星周りの軌道、の 3 つに分類される。衛星の前面から飛び出た particles は、衛星の公転速度にさらに速度が加わることにより、容易に惑星の重力圏から飛び出してしまう。一方、衛星の後面から飛び出た particles は、衛星の公転速度と衛星ヒル圏から飛び出た後の残りの速度が打消し合うために惑星に向かって自由落下をする。そのために、Fig. 1 において $v_{\rm ej} \simeq 1.45 v_{\rm esc,s}$ で惑星への分配率は極大値をとると考えられる。

Figure 1 の結果を v_{ej} に関して重みをつけてたし合わせたものが Figure 2a-c である。衛星への分配率と脱出への分配率 P_e が逆相関を示し、$a_s/r_p, m_s/m_p$ が小さいほど P_s が大きく P_e は小さくなることが分かる。これは、Fig. 1 で説明したように、$a_s/r_p, m_s/m_p$ が小さい衛星ほど、particles を排除する能力が低いためである。また月質量比 (= 0.0123) 程度の場合、半分以上の ejecta が脱出してしまい、それらの specific 平均角運動量は衛星の specific 角運動量よりも常に大きいことが分かる。

以上の Ejecta の軌道計算の結果を補間して用い、巨大衝突の後の、地球-月系の質量と角運動量がどのような進化をたどるかを計算する。共成長モデルは Haris and Kaula(1975) のモデルを改良した、Morishima and Watanabe[7] のモデルを用いる。

Fig.3 は table 1 の 6 通りの c_1, c_2 の組合わせでの、月質量と地球月系の角運動量の進化を地球の質量の関数として表したものである。横軸は時間軸の代わりで、地球の質量が倍になるのに約 1 億年かかっている。計算の初期値は、それぞれ最終的に現在の値となるように設定してある (角運動量のずれは 46 億年間の太陽潮汐の影響を考慮しているため)。Fig. 3a の破線は、地球月系の総角運動量を地球の自転に押し付けた場合に回転不安定を起す境界線を表している。したがって共成長は、破線より右側の領域で起こると考えられる。Fig. 3 を見ると c_1, c_2 が大きく、より多く Ejecta を放出するほど、衛星の成長率は小さく角運動量の減少が大きくなることが分かる。完全合体する場合 (Model 1) でも、微惑星の衛星への衝突の非対称性により、角運動量を失う。Model 5 のように衛星がほとんど成長しない場合、角運動量の損失は大きく、地球質量が現在の 0.7 倍のとき、角運動量は現在の約 1.4 倍である。

この計算の重要な点は、巨大衝突で形成された惑星衛星系は、衛星質量と角運動量両方が Fig. 3 で示した組み合わせに乗らなければ最終的に現在の地球月系にはなり得ないということである。Cameron and Canup(1998)[5] の結果の一例を挙げると、質量和が $0.65M_E$ で角運動量が $1.1L_E$ の巨大衝突で、現在の月の大きさの衛星ができる。最終的に月質量を満たそうとすると、月は全く成長できないことになり、月から飛び出る大量の ejecta のために最終的な角運動量は現在の値よりも遥かに小さくなってしまう。したがって、上で述べた条件の巨大衝突では地球月系は形成されないことが分かる。現在はまだ巨大衝突のシミュレーションのデータが少ないが、今後、本研究の結果と組み合わせて議論することにより、巨大衝突が起こった時の地球質量を制約することができると考えられる。

参考文献

[1] Benz, W., A. G. W. Cameron, and H. J. Melosh, *Icarus*, **81**, 113-131, 1989.

[2] Cameron, A. G. W. and W. Benz, *Icarus*, **92**, 204-216, 1991.

[3] Ida, S., R. M. Canup, and G. R. Stewart, *Nature*, **389**, 353-357, 1997.

[4] Cameron, A. G. W. and R. M. Canup, *Lunar and Planet. Sci 29th*, abstract 1062, 1998.

[5] Cameron, A. G. W. and R. M. Canup, *Origin of the Earth and Moon*, abstract 3, 1998.

[6] Harris, A. W. and W. M. Kaula, *Icarus*, **24**, 516-524, 1975.

[7] Morishima, R. and S. Watanabe, in preparation.

Model	1	2	3	4	5	6
C_1	—	1.36	1.23	1.50	1.13	2.0
C_2	0	0.085	0.12	0.19	0.55	0.50

Table 1 Ejectaの射出に関するスケーリング則の冪数と係数

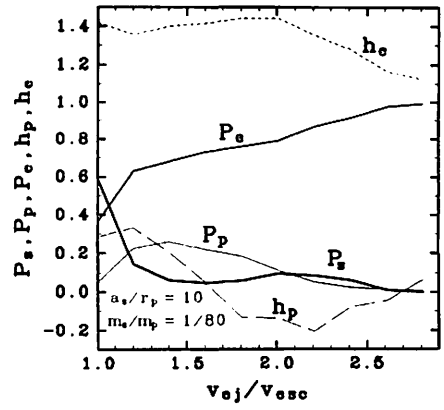

Fig. 1 Ejectaの分配率と角運動量を射出速度の関数としてあらわした図。P_s, P_p, P_e はそれぞれ衛星への衝突、惑星への衝突、惑星ヒル圏脱出への分配率を表し、h_p, h_e はそれぞれ惑星に衝突と脱出するejectaの単位質量当りの平均角運動量を表している。角運動量は衛星のケプラー角運動量で規格化されている。

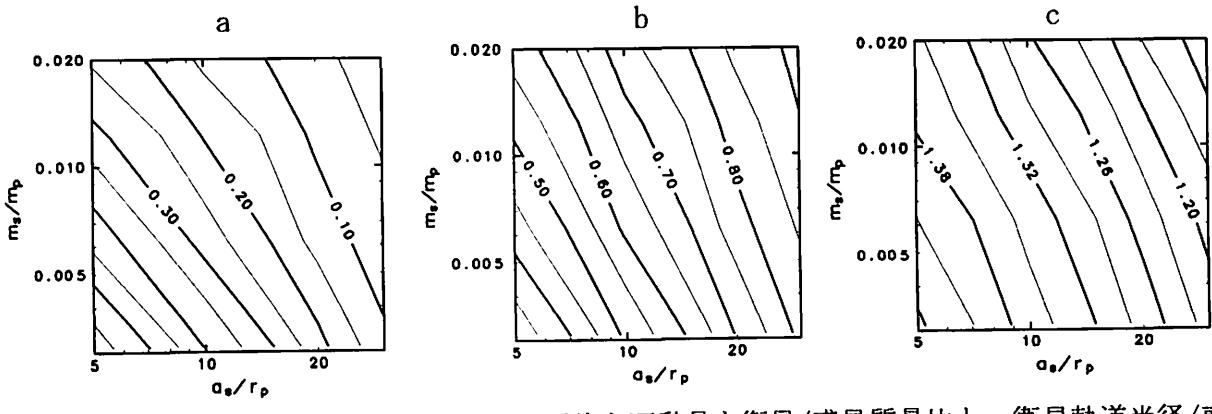

Fig. 2 Ejectaの分配率と脱出するejectaの平均角運動量を衛星/惑星質量比と、衛星軌道半径/惑星半径の関数として示したコンターマップ。a, b, cはそれぞれ P_s, P_e, h_e を表す。

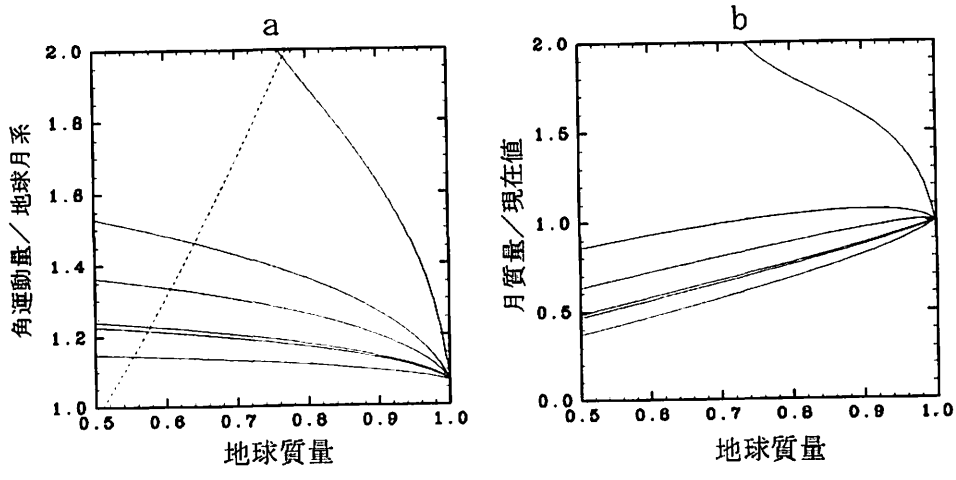

Fig. 3 月の質量と、地球月系の総角運動量の進化を地球の質量の関数として表した図。6つのカーブはTable 1 の6つに対応し、a, b共に一番下からモデル1で一番上のカーブがモデル6である。Fig. 9aの点線は、惑星の自転不安定の境界線を表している。

The gas drag effect on the stability of the protoplanet system

KAZUNORI IWASAKI

Department of Earth and Planetary Sciences, Faculty of Science
Tokyo Institute of Technology, Tokyo 152-8551, Japan
E-mail: kiwasaki@geo.titech.ac.jp

Abstract

According to the recent works on the planetary formation, at the late stage several tens of protoplanet($1 \times 10^{-7} M_{\odot}$) are formed in the terrestrial planet region(about 1AU) with equal separation distance about 10. The present terrestrial planets are thought to be formed from these protoplanets through their orbital crossings and collisions for a long term. Chambers et al.(1996) investigated the timescale of the orbital instability(which corresponds to orbital crossing), T_{inst}, of such a protoplanet system($1 \times 10^{-7} M_{\odot}$, equally spaced) in a vacuum space and found that the logarithmic of the timescale, is approximately proportional to the initial orbital separation distance, $\Delta \tilde{a}_{ini}$. In this paper, we pursued numerically the orbital evolution of five-protoplanets($1 \times 10^{-7} M_{\odot}$) system, suffering from the gas drag force of the solar nebula, in order to investigate the influence of the gas drag force by solar nebula on the above timescale. From our results, we found that T_{inst}^{gas} suddenly becomes large as compared with T_{inst}, when the initial orbital separation, $\Delta \tilde{a}_{ini}$, crosses the critical value, $(\Delta \tilde{a}_{ini})_{crit}$. When we applies our results to the realistic protoplanet system, the critical orbital separation, $(\Delta \tilde{a}_{ini})_{crit}$ are estimated about 10 in this case. Thus it is difficult for the protoplanet system to become unstable in the solar nebula.

1 INTRODUCTION

The recent works on the planetary formation show that at the final stage of the planetary accretion, several tens of the massive protoplanets whose masses are equally about $1 \times 10^{-7} M_{\odot}$ are formed through a succesive accretion of planetsimals in the terrestrial planet region (Wetherill and Stewart 1989, Kokubo and Ida 1998). In this stage, the massive protoplanets move along nearly coplanar and circular orbits owing to the interaction with planetesimals (of which effect is called the dynamical friction) and/or the gas drag effect due to the nebula gas. However, the protoplanets would interact with their neighbors through the mutual gravity and, for a long term, they would happen to be transformed to the quitely different orbits or to collide each other. Through this process, the present terrestrial planets would be formed on widely separated orbits as we observe. Unfortunately, we have no precise knowledge, until now, about a long term behavior of orbits of the massive protoplanets mentioned above. In order to understand the late stage coagulation of the planetary system we should be able to answer clearly the following questions on the orbital stability of a system composed of multi-protoplanets.

(1) Is the multi-protoplanet system visited by the catastrophic events such as the orbital crossings and the mutual collisions?

(2) If so, when do the protoplanets suffer such events?

Recently, Chambers et al.(1996) studied the stability of the multi-protoplanet system, in which the protoplnets ($1 \times 10^{-7} M_{\odot}$) are equally spaced in units of the Hill radius, r_H, and their initial orbits are circular and coplanar($e, i = 0$). In the above, the Hill radius, r_H, is given by

$$r_H = \frac{(a_1)_{ini} + (a_2)_{ini}}{2} \left[\frac{m_1 + m_2}{3 M_{\odot}} \right]^{\frac{1}{3}} , \tag{1}$$

where $(a_1)_{ini}$, $(a_2)_{ini}$, m_1 and m_2 are the initial semimajor axes and the masses of the two protoplanets, respectively. They pursued numerically the orbital evolution of multi-protoplanet systems "in a vacuum space"

changing the initial values of the orbital separation measured in units of the Hill radius, $\Delta\tilde{a}_{ini}$. The integrations were continued until two of them approaches within a sphere with one Hill radius (in this sphere the motion of particle is ruled by the gravity of the protoplanet) or until the evolutionary time reaches to 1×10^7 year. They found that the time of occurrence of the first close encounter between adjacent two protoplanets, T_{inst}, is given by a function of $\Delta\tilde{a}_{ini}$, i.e.,

$$\log_{10} T_{inst} = b\Delta\tilde{a}_{ini} + c \tag{2}$$

where b and c are numerical constants. These coefficients are almost independent of n, the number of the protoplanets, as long as $n \geq 5$ and are given by

$$b = 0.760 \text{ and } c = -0.1\,. \tag{3}$$

In the actual system of the planetary accretion process, the protoplanets have to experience other kinds of the energy dissipation processes besides the collisional dissipation such as the dynamical friction due to a swarm of planetesimals and gaseous drag due to the solar nebula. Generally, any kind of the energy dissipation leads to a decrease in the eccentricities and inclinations of the protoplanets. By the decrease in the eccentricities and inclinations, however, the protoplanets must be prevented from the onset of the orbital instability. Namely, if the dissipation effects are too intense, the protoplanets will not be able to collide with each other since there hardly occur the orbital crossings and, as a result, the terrestrial which we observe now will not be formed. Thus, it is very important to investigate the influence of the energy dissipation on the instability time of the multi-protoplanet system.

The aim of our study is to see the influence extensively of the effect of the gas drag on the orbital instability of the multi-protoplanet system and to obtain the onset time of the orbital instability of the system suffering gas drag force. To achieve our purpose, we calculate numerically the orbital evolution of the protoplanet system taking the gas drag effect of the solar nebula into consideration. Basic equations governing the orbital motions of the protoplanets will be presented in the next section as well as the numerical procedures we use. In section 3, we will show briefly the results of the special cases without the gaseous drag to compare with those of Chambers et al.(1996). We place five protoplanets equally spaced in the terrestrial planets region; their masses are put to be $1 \times 10^{-7} M_\odot$ and the eccentricities and inclinations are taken to be zero initially as Chambers et al.(1996) did.

In section 4, we include the effect of the gas drag, which is characterized by the dissipation time, τ_0, of the kinetic energy due to the gaseous drag. The instability time of the protoplanet system, T_{inst}^{gas}, is defined as the time at which two of the five-protoplanets approach within their mutual Hill radius for the first time (this definition is the same as T_{inst} in Chambers et al.(1996)). On the basis of our orbital calculations, we find T_{inst}^{gas} as a function of $\Delta\tilde{a}_{ini}$ and τ_0. We will see that, when the orbital separation is large, gravitational interaction between the protoplanets is weak compared with the gas drag force by which the eccentricities of the protoplanets are dumped and, as a result, the instability time, T_{inst}^{gas}, becomes large compared with T_{inst}, which is the instability time for the case without the gas drag effect. Furthermore, the gas density is large, as expected readily, T_{inst}^{gas} increases because the gas drag effect suppresses strongly the increment of the eccentricities of the protoplanets. In section 5, we summarize the results obtained by our present study in short.

2 METHODS OF ORBITAL CALCULATIONS

2.1 Basic equations

Suppose that n-protoplanets are rotating around the sun under the influence of the mutual gravity. In a coordinate system where the sun is at the origin, the equation of motion of the i-th protoplanet is given by

$$\ddot{\mathbf{x}}_i = -\,G\,M_\odot\,\frac{\mathbf{x}_i}{|\mathbf{x}_i|^3} - \sum_{j\neq i}^{n}\left(G\,m_j\,\frac{\mathbf{x}_i-\mathbf{x}_j}{|\mathbf{x}_i-\mathbf{x}_j|^3}\right) - \sum_{j}^{n}\left(G\,m_j\,\frac{\mathbf{x}_j}{|\mathbf{x}_j|^3}\right)\,, \tag{4}$$

where $M_\odot$ and m_i are the masses of the sun and the i-th protoplanet, respectively, $\mathbf{x}_i$ is the position vector of the i-th protoplanet, and G is the gravitational constant. In the above equation, we only take account of the gravitational interactions. The protoplanets orbiting within the solar nebula suffer from a drag force due to the nebular gas and, hence, we must include the gas drag term in Eq.(4).

The gas drag force per unit mass acting on a spherical body is expressed by the following form (Adachi et al. 1976):

$$f_d = C_d \frac{\pi r_p^2}{m_p} \rho u^2 , \tag{5}$$

where r_p and m_p are the radius and the mass of a protoplanet, respectively, and u is the relative velocity between the protoplanet and the nebular gas. Furthermore, ρ is the density of the nebular gas and C_d is a nondimensional drag coefficient. For a massive bodies ($\geq 10^{15}g$) with relative velocity less than the sound velocity, C_d is approximately given by 0.5 (Adachi et al. 1976). Thus, we put simply $C_D = 0.5$ from now on. We assume that the nebular gas moves àround the sun circularly with Keplerian verocity, Ω_k. Furthermore, we adopt the Hayashi model as a model of the gas nebula (Hayashi et al. 1985). Namely, we suppose that the distributions of the density, ρ, and the temperature, T, of the solar nebula are given by

$$\rho = \rho_0 \left(\frac{r}{1\mathrm{AU}}\right)^{-11/4} \tag{6}$$

and

$$T = T_0 \left(\frac{r}{1\mathrm{AU}}\right)^{-1/2} , \tag{7}$$

where r is the radial distance from the sun and ρ_0 and T_0 are the density and the temperature, respectively, at 1AU.

2.2 Procedure of Integration

When we consider a gravitational system consisting of three or more celestial bodies, we cannot obtain any analytical solution as verified by Poincaré (1892). Thus, in order to investigate the orbital evolution of the n-protoplanet system, we are obliged to manage by the numerical manners. In the present study, we pursue the orbits of the protoplanets with the help of the 4th-order $P(EC)^n$ Hermite scheme (Makino and Aarseth 1992, Kokubo et al. 1998, Kokubo and Makino 1998). This scheme is very powerful for a long term integration of planetary orbits because this integrator has no secular errors in semimajor axes, eccentricities, and inclinations owing to the time symmetric property. Furthermore, as will be seen later, by adopting suitably a parameter α in the difference formula ($\alpha = 7/6$), we can reduce the secular error drastically in the arguments of perihelion which determine the relative positions between the protoplanets during encounters (Kokubo and Makino 1998). Since we consider the case where the protoplanets are almost in Keplerian motion except the period of their conjunctions, the Hermite scheme is a suitable method for calculating a long term orbital evolution of the n-protoplanet system.

3 THE CASE WITHOUT THE GAS DRAG EFFECT

3.1 Initial conditions

In order, partly, to check the validity of our numerical code for the long term orbital calculations and, partly, to confirm the results obtained by Chambers et al.(1996), we first study the orbital evolution of a system composed of five protoplanets under the gas-free condition. For the initial conditions, we adopt almost the same ones as Chambers et al; that is,

(a) The protoplanets have the same mass, $m = 1 \times 10^{-7} M_\odot$($m$ being of the order of Martian mass).

(b) The orbits of the five protoplanets are circular and coplanar, i.e., the eccentricities and inclinations are zero.

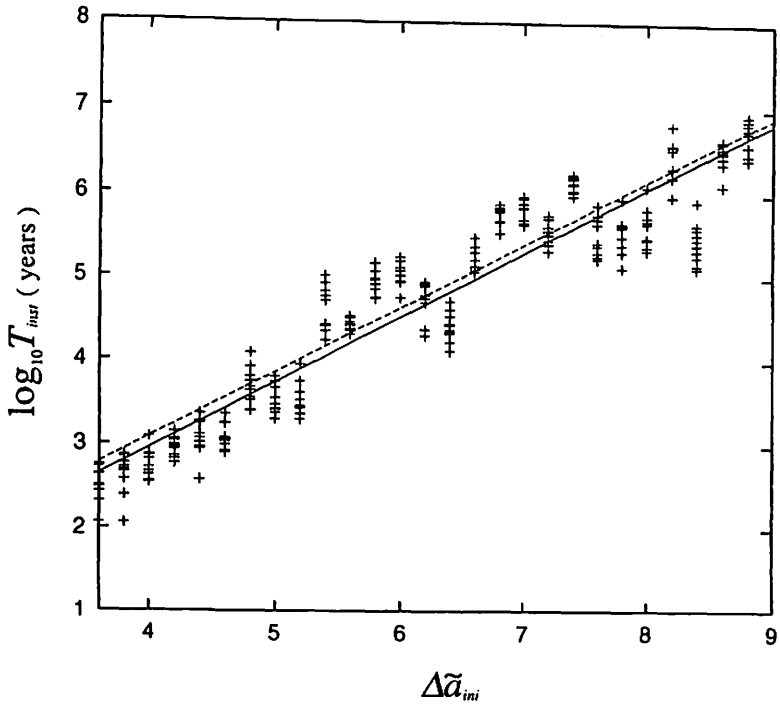

Figure 1: Instability time T_{inst} as a function of $\Delta\tilde{a}_{ini}$ for the case without the gaseous drag. Ten computational runs are made for every $\Delta\tilde{a}_{ini}$. The solid line shows the least-squares fit given by Eqs.(10) to (12). The empirical formula found by Chambers et al.(1996) is also shown by the dotted line.

(c) The innermost protoplanet is put at the heliocentric distance, a_0, of 1AU.

(d) The semimajor axes of the five protoplanets distribute with an equal separation distance, $\Delta\tilde{a}_{ini}$.

(e) The argument of perihelion of each protoplanet is assigned by the random number such that the difference between the arguments of the adjacent protoplanets is never less than 20 degree.

According to assumption (a), the Hill radius, r_H, defined by Eq.(1), is given by

$$r_H = 4.05 \times 10^{-3}\mathrm{AU}\,. \tag{8}$$

In our present study, we have only one variable parameter, i.e., the separation distance between adjacent protoplanets, Δa_{ini} (or the normalized separation distance, $\Delta\tilde{a}_{ini}$). As for $\Delta\tilde{a}_{ini}$, we choose 27 cases, i.e.,

$$\Delta\tilde{a}_{ini} = 3.6 - 8.8 \qquad \text{(with interval 0.2)}\,. \tag{9}$$

For each $\Delta\tilde{a}_{ini}$, we pursue the orbital calculations for 10 cases with different configuration of the arguments of perihelia of the five protoplanets. Chambers et al. took $\Delta\tilde{a}_{ini}$ from 2.0 to 8.8 with interval 0.2 and made three simulations for every $\Delta\tilde{a}_{ini}$.

3.2 Time of onset of the orbital instability

We pursue numerically the orbital evolution of the five-protoplanets system changing $\Delta\tilde{a}_{ini}$ as well as the geometrical configuration of the five protoplanets, as mentioned in the previous subsection. The method of numerical calculations is already described in subsection 2.2. Orbital calculation is stopped when the distance between any two of the five protoplanets become less than the Hill radius or when the evolutionary time exceeds the admissible time, 1×10^7years, set to save the computational time. The former case is recognized as one that there occurs the orbital instability and the evolutionary time, at which the minimum distance between any two

protoplanets becomes first less than the Hill radius, is regarded as the instability time, T_{inst} (such a definition of T_{inst} is quite the same as in Chambers et al. (1986)).

In Fig.1, we show the instability time, T_{inst}, as a function of $\Delta\tilde{a}_{ini}$. On the general trend, we can say that $\log_{10} T_{inst}$ is approximately proportional to $\Delta\tilde{a}_{ini}$ as pointed out by Chambers et al.(1996). The solid line in Fig.1 is the least-square fit of all the points, given by

$$\log_{10} T_{inst} = b\,\Delta\tilde{a}_{ini} + c\,, \tag{10}$$

where

$$b = 0.777 \pm 0.0114 \tag{11}$$

and

$$c = -0.154 \pm 0.0643\,. \tag{12}$$

In this figure, the empirical formula found by Chambers et al.(1996) is also shown by the dotted line. In their formula, b and c are given, respectively, by

$$b = 0.765 \pm 0.030 \tag{13}$$

and

$$c = -0.030 \pm 0.192\,. \tag{14}$$

The values of b and c found by our present calculations are in good agreement with those of Chambers et al. within the uncertainties. Thus, we can say that the numerical code, developed by us, can simulate precisely a long term orbital evolution of the multi-protoplanet system and that the stability (or the instability) of the multi-protoplanet system is really characterized by the empirical relation (10) between T_{inst} and $\Delta\tilde{a}_{ini}$, first found by Chambers et al.

4 GAS DRAG EFFECT ON THE ORBITAL STABILITY

4.1 The gas drag effect

Before we present the results of the orbital evolution of the five-protoplanets sysytem suffering from gas drag force, we mention briefly the principal property of gas drag force. Adachi et al.(1976) investigated the gas drag effect on the motion of a planetesimal orbiting around the sun. Acoording to them, the characteristic time for the drag dissipation, τ_0, is given by

$$\tau_0 = \frac{2m_p}{\pi C_D r_p^2 \rho a \Omega_k}\,, \tag{15}$$

where r_p and m_p are the radius and the mass of a protoplanet, respectively. Furthermore, ρ is the gas density of the solar nebula and Ω_k is the Keplerian angular velocity of the circular orbit with the semimajor axis, a. As mentioned in section 2.1, we adopt the Hayashi model (Hayashi 1981) as the nebular model and the gas density, ρ, is given by Eq.(6). Thus, we have for τ_0 numerically

$$\tau_0 = 2.18 \times 10^4 \frac{1}{C_D} \left(\frac{m_p}{1\times 10^{-7} M_\odot}\right)^{\frac{1}{3}} \left(\frac{a}{1\ \mathrm{AU}}\right)^{1.75} \left(\frac{\rho_0}{1\times 10^{-9}\ \mathrm{g/cm^3}}\right)^{-1} T_k\,, \tag{16}$$

where ρ_0 represents the gas density at 1AU and T_k is the Keplerian period, $2\pi/\Omega_k$. In the above, we take 3 g/cm^3 as the material density of a protoplanet. As will be seen later, a and m_p are fixed to be definite values and, hence, τ_0 depends on only ρ_0. Thus, we use τ_0 in place of ρ_0 as a prameter indicating the intensity of the gas drag force.

When the eccentricity, e is not zero, the eccentricity decrease with time owing to gas drag effect. From the approxmate fomulae of eccentricities in Adachi et al.(1976), the characteristic time of the dumping of the eccentricity is found to be

$$T_{dump} \simeq \left| e \Big/ \left(\frac{de}{dt}\right)\right| = \frac{\tau_0}{0.77e}\,. \tag{17}$$

This is refered to in the later sections.

4.2 Initial conditions

We investigate the effect of the gas drag force on the orbital instability time of the protoplanet system. As in the previous section, we consider the system composed of the five protoplanets with mass of $1 \times 10^{-7} M_\odot$, which revolve around the sun within the solar nebula. As for the parameter, τ_0, indicating the intensity of gas drag force, we consider four cases where

$$\tau_0 = 5.0,\ 15,\ 50,\ \text{and}\ 150 T_k\ . \tag{18}$$

The above values of τ_0 correspond to the following nebular densities, ρ_0, at 1AU:

$$\rho_0 = 8.7 \times 10^{-6},\ 2.9 \times 10^{-6},\ 8.7 \times 10^{-7},\ \text{and}\ 2.9 \times 10^{-7}\ \text{g/cm}^3\ , \tag{19}$$

where we use $C_D = 0.5$. Recent observations of the young stellar objects reveal that they are surrounded by the relatively dense nebulae, of which masses are in the range from $0.001 M_\odot$ to $0.2 M_\odot$. Even if we suppose the most massive solar nebula with mass of $0.2 M_\odot$, nebular densities given by Eq.(19) are too large. Such a choice of artificially small τ_0 (or, artificially large ρ_0) is to save the computational time of orbital calculations; if we put τ_0 to be, for example, $1 \times 10^4 T_k$, we have to pursue orbits for a very long period of 1×10^9 year or more. It is practically difficult at present to calculate orbits with a sufficient accuracy for such a long period. In applying our results to the study of the late stage planetary accretion, we will utilize the scaling law found from our orbital calculations.

The other initial orbital conditions are almost the same as those mentioned in section 3.1 where we are interested in the orbital evolution of the protoplanet system without gaseous drag; all protoplanets have the null eccentricity and inclination at the initial stage. Furthermore the separation distances between adjacent protoplanets are all the same and the semimajor axis of the innermost protoplanet is 1AU; the separation distance, $\Delta \tilde{a}_{ini}$, is put to be

$$\Delta \tilde{a}_{ini} = 3.6 - 8.6\ \text{(with interval 0.2)}, \tag{20}$$

which is quite the same as in the gas-free case (see Eq.(9)). For every $\Delta \tilde{a}_{ini}$, we make simulations for 4 cases with different initial configuration of the protoplanets.

We will add a comment on the admissible computational time. Let T_{inst}^{gas} be the instability time for the case with the gaseous drag. Generally, T_{inst}^{gas} is expected to become larger than, T_{inst}, which is the orbital instability time in the cases of the gas free condition, because the gas drag effect stabilize the protoplanet system through the dumping of the eccentricities of the protoplanets. Thus we stop to calculate when the evolutionary time t exceeds

$$T_{stop} = 200 \times T_{inst}\ , \tag{21}$$

where T_{inst} is given by Eq.(10). Hereafter, T_{stop} will be called the cut-off time of calculations.

4.3 Instability time for the case with gas

Now, we will investigate the effect of the gas drag on the orbital instability time, T_{inst}^{gas}. From Fig.2, where T_{inst}^{gas} is shown as a function of $\Delta \tilde{a}_{ini}$, we first see that T_{inst}^{gas} is nearly equal to T_{inst} when $\Delta \tilde{a}_{ini} < 5.4$. For the ranges where $\Delta \tilde{a}_{ini} \geq 5.8$, there occurs no orbital instability within a period of T_{stop}. In the intermediate region where $5.4 \leq \Delta \tilde{a}_{ini} \leq 5.8$, we observe the orbital instability in some cases of the initial configuration but not in other cases (note that 4 cases are calculated for every $\Delta \tilde{a}_{ini}$); even for the case where we observe the orbital instability, the instability time, T_{inst}^{gas}, becomes large compared with that for the gas-free case. Such a region is bounded by the two vertical dotted-lines in Fig.2.

In an analogy of the phase transition in, for example, the ionization process, the intermediate region mentioned above may be called "the transition zone". In order to describe properly the location of the transition zone, we will introduce two kinds of the critical separation distance; $(\Delta \tilde{a}_{ini})_0$ and $(\Delta \tilde{a}_{ini})_1$. The former, $(\Delta \tilde{a}_{ini})_0$ is defined as the minimum value of $\Delta \tilde{a}_{ini}$, in the case of which four computational runs include, at least, one case without the onset of the orbital instability. The latter, $(\Delta \tilde{a}_{ini})_1$ is defined as the minimum value of $\Delta \tilde{a}_{ini}$, in the case of which "all of the cases" reach the cut-off time of calculations, or in other words, we observe no

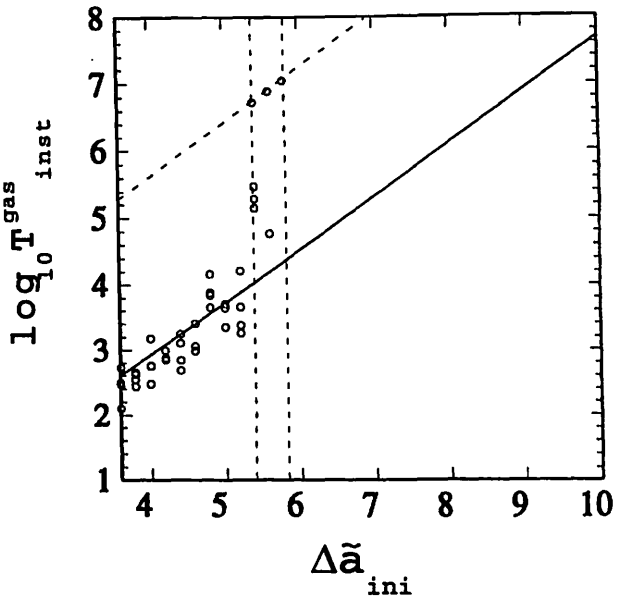

Figure 2: The instability time T^{gas}_{inst} as a function of $\Delta\tilde{a}_{ini}$ for the case of $\tau_0 = 15T_k$. The solid line shows T_{inst}, given by Eq.(10), and the upper dotted line denotes the cut-off time of calculation, $T_{stop}(= 200 \times T_{inst})$. The region bounded by two vertical dotted lines shows the transition zone.

orbital instability in all computational runs. For the case of $\tau_0 = 15T_k$, the values of $(\Delta\tilde{a}_{ini})_0$ and $(\Delta\tilde{a}_{ini})_1$ are 5.4 and 5.8, respectively.

The behavior of T^{gas}_{inst} for the cases other than $\tau_0 = 15T_k$ is similar as in the case of $\tau_0 = 15T_k$; they are shown in Fig.3 (note that we calculated only two cases for the different initial configuration when $\tau_0 = 150T_k$ and $\Delta\tilde{a}_{ini} = 7.0$, because of the very long calculation time). As seen from three figures, T^{gas}_{inst} behaves quite similarly as long as we are concerned with the qualitative behaviors; The $T^{gas}_{inst} - \Delta\tilde{a}_{ini}$ diagram is commonly divided into three zone, i.e., the unstable zone where T^{gas}_{inst} can be described approximately by that in the gas-free case, the stable zone where we cannot observe the orbital instability, and the transition zone mentioned above. The three zones are bounded by the two critical values of $\Delta\tilde{a}_{ini}$, introduced in the last paragraph. It is interesting to point out that the widths of the transition zone (i.e., $(\Delta\tilde{a}_{ini})_1 - (\Delta\tilde{a}_{ini})_0$) are almost the same ($\simeq 0.06$) irrelevant to the adopted value of τ_0, although we cannot say definitely in the case of $\tau_0 = 150T_k$ because of the lack of the computational runs. The detailed behaviors of "the phase transition" are illustrated in Fig.4, where we show the number, N, of runs which reach the cut-off time of calculations, T_{stop}, without the onset of the orbital instability. We can see that the number, N, of the "stable" cases, increases suddenly in the narrow range of $\Delta\tilde{a}_{ini}$. The values of $(\Delta\tilde{a}_{ini})_0$ and $(\Delta\tilde{a}_{ini})_1$ are tabulated in Table 1. The two critical values increase with an increase in τ_0 (or with a decrease in the gas drag effect). This means that, for the cases where the gaseous drag is strong, the protoplanet system is forcedly stabilized even when the separation distance between adjacent protoplanets, $\Delta\tilde{a}_{ini}$, is small.

Table 1: Critical values of $(\Delta\tilde{a}_{ini})_0$ and $(\Delta\tilde{a}_{ini})_1$. The value of $(\Delta\tilde{a}_{ini})_1$ is less definite for the case of $\tau_0 = 150T_k$ because of the lack of computational runs.

τ_0/T_k	5.0	15	50	150
$(\Delta\tilde{a}_{ini})_0$	4.6	5.4	6.0	6.6
$(\Delta\tilde{a}_{ini})_1$	5.2	5.8	6.6	~ 7.0

In Figs.5 and 6, we show the typical examples of the time evolution of the eccentricities of the protoplanets for the cases of $\tau_0 = 15T_k$ in the unstable zone and stable zone. From these figures, we can readily reach the

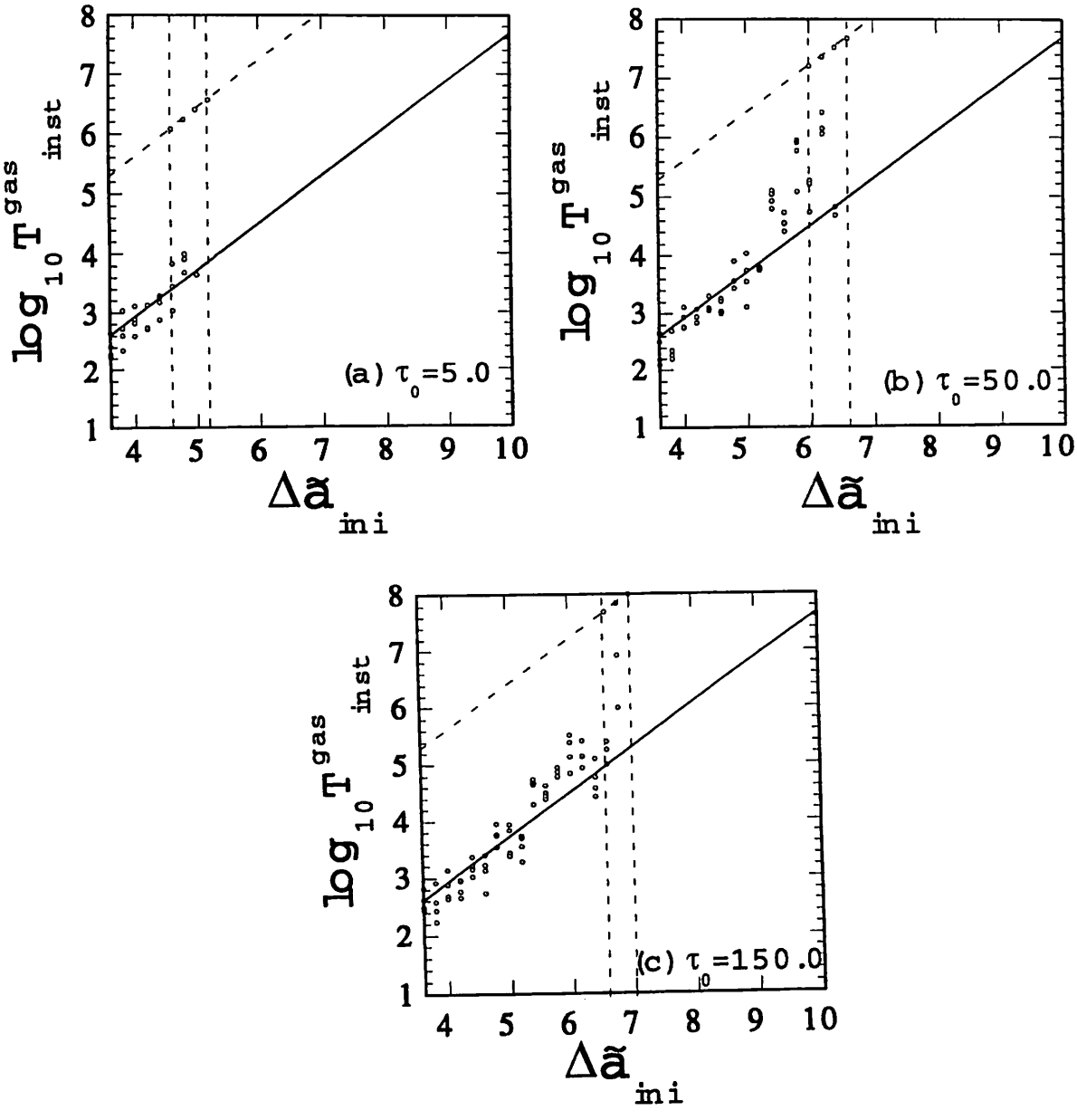

Figure 3: The same as Fig.2, but for the cases of (a)$\tau_0 = 5.0T_k$, (b)$\tau_0 = 50.0T_k$, and (c)$\tau_0 = 150.0T_k$.

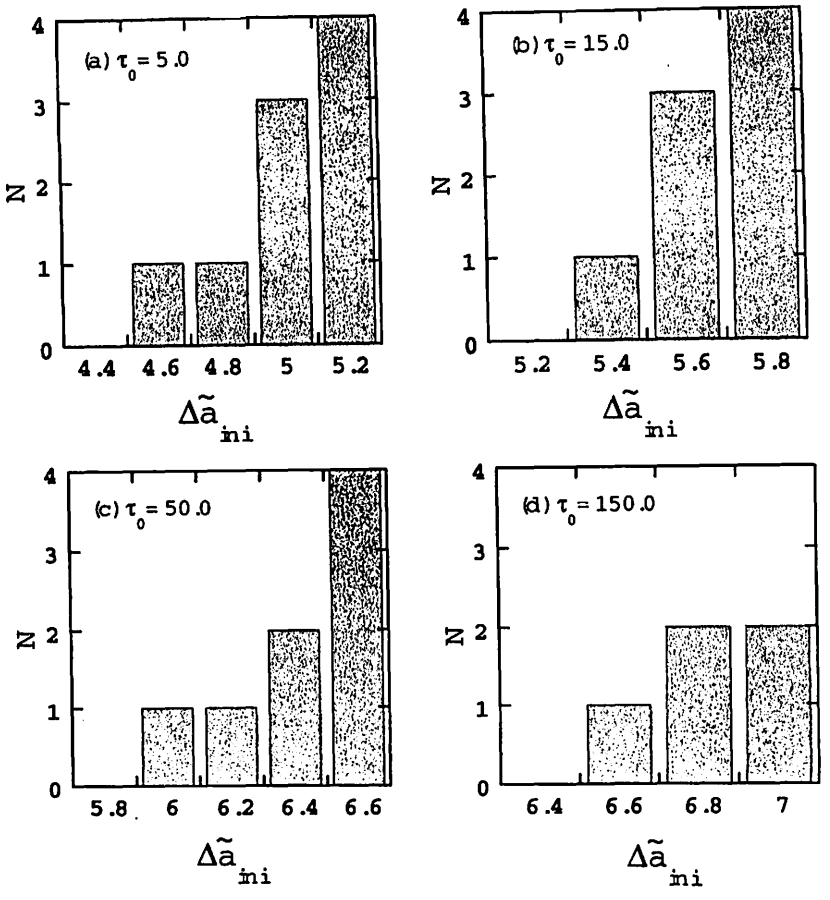

Figure 4: The number of runs, N, which reach the cut-off time of calculations, T_{stop}, without the onset of the orbital instability. Panels (a), (b), (c), and (d) are of the cases of $\tau_0 = 5.0T_k$, $15T_k$, $50T_k$, and $150T_k$, respectively.

following conjecture. In the unstable zone where $\Delta\tilde{a}_{ini} < (\Delta\tilde{a}_{ini})_0$, the orbital instability occurs before the eccentricities of the protoplanets are dumped by the gas drag effect (see Fig.5). Hence, we should have the relation of

$$T_{inst} < T_{dump} , \tag{22}$$

where T_{inst} is the orbital instability time in the case without the gas and T_{dump} is the characteristic dumping time of eccentricities, defined in Eq. (17). On the other hand, in the stable zone where $(\Delta\tilde{a}_{ini})_1 < \Delta\tilde{a}_{ini}$, the eccentricities are dumped, as an average, by the gas drag force and there occurs no orbital instability(see Fig.6); the relation

$$T_{dump} < T_{inst} \tag{23}$$

should be realized. In the transition zone where $(\Delta\tilde{a}_{ini})_0 < \Delta\tilde{a}_{ini} < (\Delta\tilde{a}_{ini})_1$, the situation is complicated as seen above. Even if we consider the cases with a fixed $\Delta\tilde{a}_{ini}$, in some cases Eq.(22) holds and in other cases Eq.(23) holds. Inversely speaking, however, we have the relation

$$T_{inst} = C_r T_{dump} . \tag{24}$$

where C_r is a constant whose value is about 1. Since T_{dump} is a function of the eccentricity (see Eq.(17)), we must know the typical value of the eccentricities of the protoplanets in order to write down Eq.(24) in an explicit form. For the cases without the gas, the eccentricities of the prtotoplanets are kept to be small during a period of the first 90 percent of the instability time, T_{inst}, and increase rapidly during the rest of about 10 percent of T_{inst}. Such a behavior is illustrated in Fig.7, where we show the time evolution of the root mean

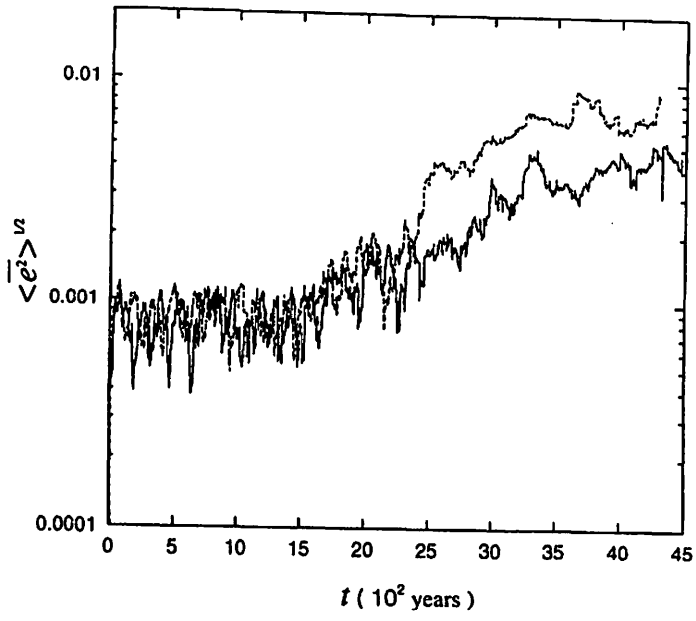

Figure 5: Time variation of the root mean square of the eccentricities of the five protoplanets for the case $(\tau_0\ ,\ \Delta a_{ini}) = (15T_k,\ 4.8)$ (in the unstable zone). The solid line shows the case with the gas in which the orbital instability occurs at $t \simeq 4.5 \times 10^3$year, whereas the dotted-line denotes the case without the gas, in which the instability occurs at $t \simeq 4.3 \times 10^3$year.

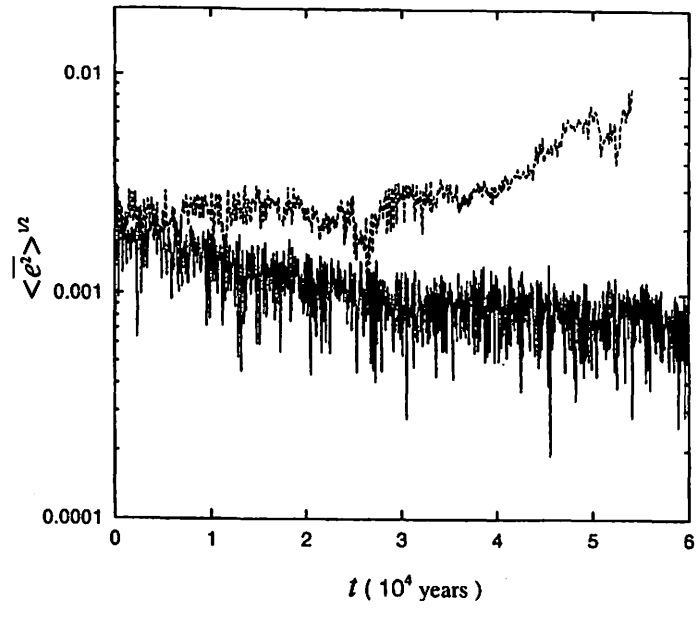

Figure 6: Time variation of the root mean square of the eccentricities of the five protoplanets for the cases of $\Delta\tilde{a}_{ini} = 6.2$ (in the stable zone). The solid line shows the case with the gas ($\tau_0 = 15T_k$). The dotted line denotes the case without the gas condition, in which the instability occurs at 5.4×10^4year.

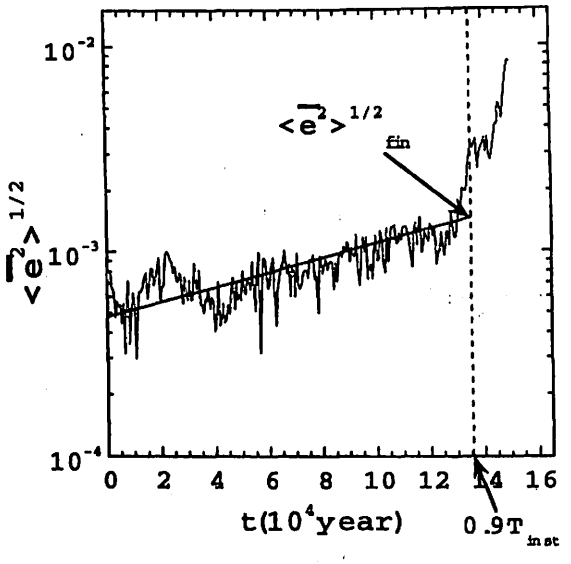

Figure 7: Time evolution of the root mean square of the eccentricities of all the protoplanets for the case of $\Delta\tilde{a}_{ini} = 6.6$ without the gas. The solid line shows the least square fit obtained from the data of the period of the first 90 percent of T_{inst}. The vertical dotted line indicates $t = 0.9T_{inst}$. The intersecting point between the solid line and the vertical dotted line corresponds to $< \overline{e^2} >_{fin}^{1/2}$.

square of the eccentricities of all the five protoplanets for the case without the gas ($\Delta\tilde{a}_{ini} = 6.6$). For the cases with other $\Delta\tilde{a}_{ini}$, $< \overline{e^2} >^{1/2}$ behaves similarily as in Fig.7. We can see from this figure that $\log_{10}< \overline{e^2} >^{1/2}$ is approximately proportional to the evolutionary time t during the first 90 percent of T_{inst} and, thus, we have

$$\log_{10}< \overline{e^2} >^{\frac{1}{2}} = pt + q, \quad \text{for } t \leq 0.9T_{inst} \, . \tag{25}$$

Constants p and q are obtained by the least square fit for all available data of the orbital calculations. In Fig.8, the values of p and q are shown as a function of $\Delta\tilde{a}_{ini}$. In this figure, we can readily see that the values of p decrease as a whole as the separation distance, $\Delta\tilde{a}_{ini}$, increases. This is probably because the increase of the separation distance weakens the gravitational interaction between the protoplanets. Also, the values of q vary widely for all of $\Delta\tilde{a}_{ini}$. However, the tendency of decreasing as seen in the value of p is not found out in the values of q. By the use of Eq.(25), we estimate the typical value of the root mean square of the eccentricities at the onset of the orbital instability, which is given by

$$\log_{10}< \overline{e^2} >_{fin}^{\frac{1}{2}} = 0.9pT_{inst} + q \, . \tag{26}$$

the values of p In Fig.9, we show $< \overline{e^2} >_{fin}^{1/2}$ as a function of $\Delta\tilde{a}_{ini}$. From this figure, we find that $< \overline{e^2} >_{fin}^{1/2}$ is confined within the range between 0.001 and 0.02 for the case of $\Delta\tilde{a}_{ini} = 3.8 \sim 8.6$ though $< \overline{e^2} >_{fin}^{1/2}$ scatters widely for all of $\Delta\tilde{a}_{ini}$. For the convenience, we pressume that $\log_{10}< \overline{e^2} >_{fin}^{1/2}$ is given by the mean value:

$$\begin{aligned} \log_{10}< \overline{e^2} >_{fin}^{\frac{1}{2}} &= \frac{\log_{10}(0.001) + \log_{10}(0.02)}{2} \\ &\simeq -2.35 \, . \end{aligned} \tag{27}$$

From Eq.(17), the dumping time of the eccentricities is given by

$$T_{dump} \simeq \frac{\tau_0}{0.77< \overline{e^2} >_{fin}^{\frac{1}{2}}} \, . \tag{28}$$

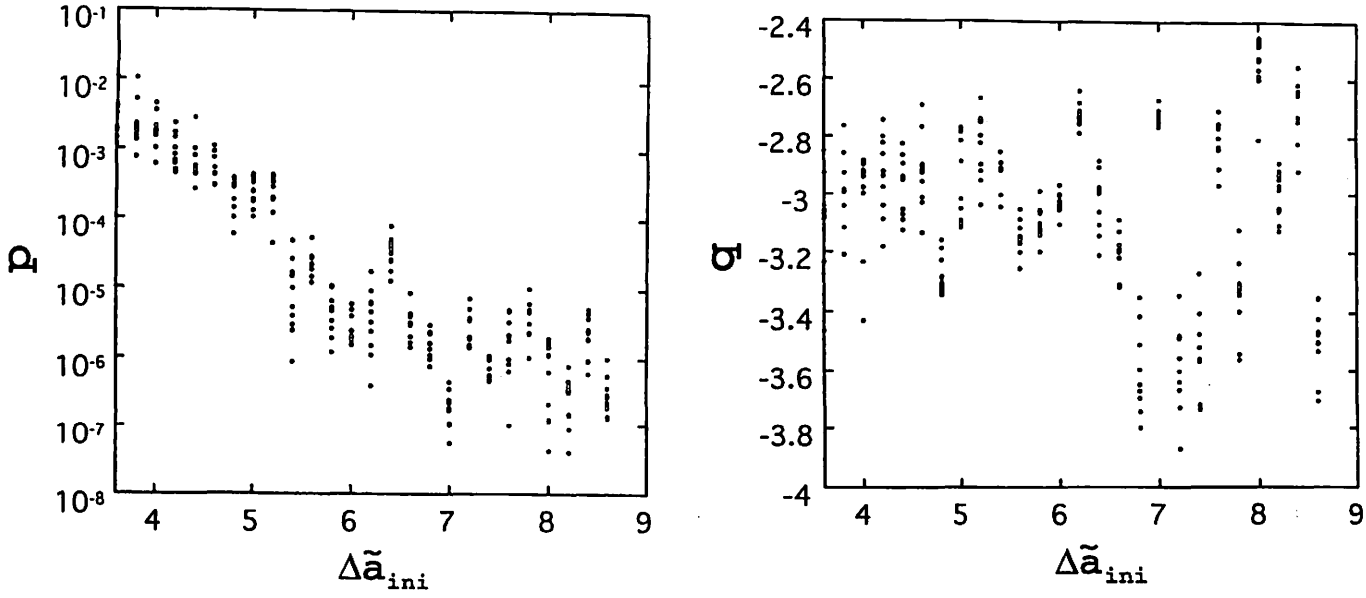

Figure 8: The values of p (the left panel) and q (the right panel) evaluated by the least squares fit in the relation (25).

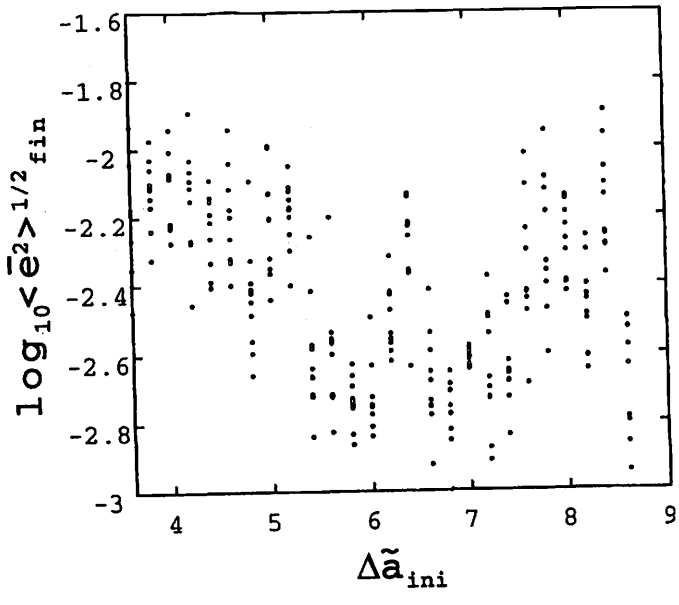

Figure 9: The root mean square of the eccentricities of the protoplanets, $<\overline{e^2}>_{fin}^{1/2}$, at $t = 0.9T_{inst}$.

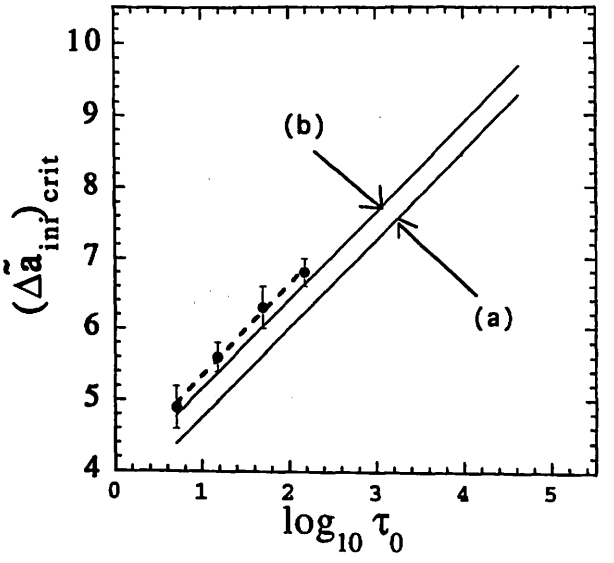

Figure 10: The critical initial orbital separation, $(\Delta\tilde{a}_{ini})_{crit}$, vs. τ_0 which is evaluated by the semi-emprical formula, (29), in the case of (a) $C_r = 1.0$ and (b) $C_r = 2.0$. The critical values found from our numerical simulations are also shown by dots(Vertical error bars represent the range of $(\Delta\tilde{a}_{ini})_0 < \Delta\tilde{a}_{ini} < (\Delta\tilde{a}_{ini})_1$).

Therefore, substituting Eqs.(28) and (10) into Eq.(24), we find a semi-emprical expression of $(\Delta\tilde{a}_{ini})_{crit}$ $((\Delta\tilde{a}_{ini})_0 < (\Delta\tilde{a}_{ini})_{crit} < (\Delta\tilde{a}_{ini})_1)$ as

$$(\Delta\tilde{a}_{ini})_{crit} = 1.2\log\left(\frac{C_r\tau_0}{<\overline{e^2}>_{fin}^{\frac{1}{2}}}\right) + 0.44\,. \tag{29}$$

In Fig.10, we show the above estimated relation (29) and the relation of $(\Delta\tilde{a}_{ini})_{crit}$ and τ_0 obtained by our numerical simulations where $(\Delta\tilde{a}_{ini})_{crit}$ evaluated in our numerical simulations is precisely defined as

$$(\Delta\tilde{a}_{ini})_{crit} = \frac{(\Delta\tilde{a}_{ini})_0 + (\Delta\tilde{a}_{ini})_1}{2}\,. \tag{30}$$

In this figure, when we adopt 2.0 as the value of C_r, the estimated relation (29) is in good agreement with the relation in our numerical simulations. Actually, the value of $(\Delta\tilde{a}_{ini})_{crit}$ in the relation (29) has an uncertainty about ± 0.8 owing to scattering of $<\overline{e^2}>_{fin}^{1/2}$ between 0.001 and 0.02. However, since this uncertainty($\simeq 0.8$) is small(about 10 percent) in comparison with the typical value of $(\Delta\tilde{a}_{ini})_{crit}$ which is about 7.0, these results are not affected seriously.

By the way, we adopt 5.0 to 150.0 as the values of τ_0 in our simulations because in our calculation range ($3.6 \leq \Delta\tilde{a}_{ini} \leq 7.0$) for the larger values of τ_0 the appreciable change of the orbital instability time by the gas drag effect can not be seen. However these values of τ_0 correspond to 2.9×10^{-7} to 8.7×10^{-6} g/cm^3 of the values of the gas nebular density at 1AU, ρ_0, and these values of the density are very larger than the values given by the standard gas nebular model which is about 1×10^{-9} g/cm^3. Thus we extrapolate the relation (29) to $\tau_0 = 4.3 \times 10^4$ which corresponds to $\rho_0 = 1.0 \times 10^{-9}$ g/cm^3. In Fig.10, we find that the value of $(\Delta\tilde{a}_{ini})_{crit}$ for the case of $\tau_0 = 4.3 \times 10^4$ are about 10. We readily understand that for the case of $\Delta\tilde{a}_{ini} > 10$ the orbital instability never occurs under the standard gas nebular.

5 Summary and Conclusion

In the present study, of which principle aim is to investigate the gas drag effect on the orbital instability of the protoplanet system, we have pursued numerically a long term evolution of orbits of five protoplanets

considering the gas drag force. We have supposed that, initially, the protoplanets distribute uniformly in the radial direction with the same mutual separation distance, $\Delta\tilde{a}_{ini}$, and their initial orbits are co-planar and circular. In our orbital calculations, the density of the nebular gas is increased artificially by a factor of 1×10^2 to 1×10^4 compared to that of the standard nebula model (in order to save CPU time of computations).

First, we have obtained the time of onset of the orbital instability, T_{inst}, under the gas free condition and confirmed the result of Chambers et al. (1996) that T_{inst} is written empirically as a simple function of the initial separation distance, $\Delta\tilde{a}_{ini}$. Next, we have investigated the orbital instability time, T_{inst}^{gas}, of the protoplanet system suffering the gaseous drag. Obtained results are summarized as follows.

(1) Roughly speaking, the gaseous drag suppresses, more or less, the occurrence of the orbital instability of the protoplanet system through dumping of the eccentricities of the protoplanets.

(2) The degree of the stabilization depends on the gaseous density as well as the initial separation distance, $\Delta\tilde{a}_{ini}$:

   (a) For the case where $\Delta\tilde{a}_{ini} < (\Delta\tilde{a}_{ini})_{crit}$, then T_{inst}^{gas} is almost equal to T_{inst} and the gas does not play important role or the orbital stability of the orbital stability of the protoplanet system.

   (b) for the opposite case where $\Delta\tilde{a}_{ini} > (\Delta\tilde{a}_{ini})_{crit}$, T_{inst}^{gas} is increased, at least, 200 times as long as T_{inst}. In this case the protoplanet system is not visited practically (within an age of the planetary formation) by catastrophic orbital instability.

(3) The critical separation distance, $(\Delta\tilde{a}_{ini})_{crit}$, mentioned above, is a function of a gaseous density.

Furthermore, we have written $\Delta\tilde{a}_{inicrit}$ in analytical (but empirical) form as a formation of the gaseous density. Using this expression, the critical orbital separation, $(\Delta\tilde{a}_{ini})_{crit}$, is evaluated to be about 10, when we adopt $1g/cm^3$ as the density of the nebula at 1AU in accordance with the standard model. Thus, for the case of $(\Delta\tilde{a})_{ini} > 10$, the orbital instability never occurs. According to Kokubo and Ida (1998), the typical orbital separation of the formed protoplanets is about 10. So, it is difficult to judge whether such a protoplanet system is stable or not. However, if the protoplanet system becomes unstable and the protoplanets collide each other, the mean orbital separation of the protoplanets increases inevitably after the collisions (say, $12 \sim 15$; note that the orbital separation of the terrestrial is 30). When the orbital separation exceeds 10, the coagulation process of the terrestrial planets stops on the way since the orbital instability never occurs. Thus, it is natural to think that the gas nebula are already dissipated at the final stage of the terrestrial planet formation. The cause of decreasing the eccentricities of the terrestrial planets formed through the collisions are thought not to be the gas drag effect of the solar nebula.

REFERENCES

ADACHI, I., C. HAYASHI AND K. NAKAZAWA 1976. The gas drag on the elliptic motion of a solid body in the primordial solar nebula. *Prog. Theor. Phys.* **56**, 1756-1771.

BROUWER, D. AND G. M. CLEMENCE 1961. Methods of Celestical Mechanics. *Academic Press, New York.*

CHAMBERS, J. E. AND G. W. WETHERILL 1998. Making the terrestrial planets: N-body integrations of planetery embryos in three dimensions. *Icarus* **136**, 304-327.

CHAMBERS, J. E., G. W. WETHERILL, AND A. P. BOSS 1996. The stability of multi-planet systems. *Icarus* **119**, 261-268.

GLADMAN, B. 1993. Dynamics of systems of two close planets. *Icarus* **106**, 247-263.

GOLDREICH, P. AND W. R. WARD 1973. The formation of planetsimals. *Astrophys. J.* **183**, 1051-1061.

GREENBERG, R., J. WACKER, C. R. CHAPMAN, AND W. K. HARTMANN 1978. Planetesimals to planets: Numerical simulation of collisional evolution. *Icarus* **35**, 1-26.

GREENZWEIG, Y. AND J. J. LISSAUER 1990. Accretion rates of protoplanets. *Icarus* **87**, 40-77.

GREENZWEIG, Y. AND J. J. LISSAUER 1992. Accretion rates of protoplanets II. Gaussian distributions of planetesimal velocities. *Icarus* **100**, 440-463.

HASEGAWA, M. AND K. NAKAZAWA 1990. Distant encounter between Keplerian particles. *Astron. Astrophys.*, **227**, 619-627.

HAYASHI, C. 1972. Origin of the solar system. In *Proc. 5th Lunar Planetary Symposium.* eds. Takayanagi, K. and Simizu, M. (Tokyo: Inst. Space Aeronautical Sci.), pp. 13-18.

HAYASHI, C. 1981. Structure of the solar nebula, growth and decay of magnetic fields and effects of magnetic and turbulent viscosities on the nebula, *Theor. Phys. Suppl.*, **70**, 163-196.

HAYASHI, C., K. NAKAZAWA, AND I. ADACHI 1977. *Publ. Astron. Soc. Japan*, **29**, 163.

HAYASHI, C., K. NAKAZAWA, AND Y. NAKAGAWA 1985. Formation of the Solar System, In *Protostars and Planets II (Eds. D. C. Black and M. S. Matthews, Univ. of Arizona Press, Tucson)*, pp. 1100-1153.

HÉNON, M. AND J. M. PETIT 1986. *Celest. Mech.***38**, 67.

HILL, G. W. 1878. Researches on the lunar theory. *AM. J .Math.* **1**,5-26; 129-147; 245-260.

HUT, P., J. MAKINO, AND S. MCMILLAN 1995. Building a better leapflog. *Astrophs. J. Lett.* **443**, 93-96.

IDA, S. 1990. Stirring and dynamical friction of planetesimals in the solar gravitational field. *Icarus* **88**, 129-145.

IDA, S. AND J. MAKINO 1992. *N*-body simulation of gravitational interaction between platesimals and a protoplanet. I. Velocity distribution of planetesimals *Icarus* **96**, 107-120.

ITO, T. AND K. TANIKAWA 1998. Stability and instability of the terrestrial protoplanet system and their possible roles in the final stage of planet formation. *Icarus* **139**, 336-349.

KARY, D. M., J. J. LISSAUER, AND Y. GREENZWEIG 1993. Nebular Gas Drag and Planetary Accretion. *Icarus* **106**, 288-307.

KOKUBO, E. AND S. IDA 1996. On runaway growth of planetesimals. *Icarus* **123**, 180-191.

KOKUBO, E. AND S. IDA 1998. Oligarchic Growth of Protoplanets. *Icarus* **131**, 171-178.

KOKUBO, E. AND J. MAKINO 1998. New time-symmetric integrators for planetary dynamics. In *Proceedings of the 30th symposium on celestical mechanics(Eds. T. Fukushima, T. ito, T. Fuse, and H. umehara)*, p.248.

KOKUBO, E., K. YOSHINAGA, AND J. MAKINO 1998. On a time-symmetric Hermite integrator for planetary N-body simulation. *Mon. Not. R. Astron. Soc.* **297**, 1067-1072.

LECAR, M. AND S. J. AARSETH 1986. A numerical simulation of the formation of the terrestrial planets. *Astrophys. J.* **305**, 564-579.

MAKINO, J. AND S. J. AARSETH 1992. On an Hermite integrator with Ahmad-Cohen scheme for gravitational Many-body problems. *Publ. Astron. Soc. Jpn.* **44**, 141-151.

NAKAZAWA, K., S. IDA, AND Y. NAKAGAWA 1989a. Collisional probability of planetesimals revolving in the solar gravitational field I. Basic formulation *Astron. Astrophys.* **220**, 293-300.

NAKAZAWA, K., S. IDA, AND Y. NAKAGAWA 1989b. Collisional probability of planetesimals revolving in the solar gravitational field II. The validity of the two-body approximation *Astron. Astrophys.* **221**, 342-347.

OHTSUKI K., S. IDA, Y. NAKAGAWA, AND K. NAKAZAWA 1993. Planetary accretion in the solar gravitational field. In *Protostars and Planets III* (E. H. Levy and J. I. Lunine, Eds.), pp.1061-1088. Univ. of Arizona Press, Tucson.

POINCARÉ, H. 1892. New methods of celestial mechanics. *History of Modern Physics and Astronomy, New York: Amer. Inst. of Phys.* I17-I41.

SAFRONOV, V. S. 1969. *Evolution of the Protoplanetary Cloud and Formation of the Earth and Planets.* NASA TTF-677.

TAKEDA, H. 1988. Drag on a gravitaing body. *Theor. Phys. Suppl.* **96** 196-210.

TANAKA, H. AND S. IDA 1996. Distribution of planetesimals around a protoplanet in the nebula gas I. The semi-analytic calculation of the gravitational scattering by a protoplanet *Icarus* **120**, 371-386.

WEIDENSCHILLING, S. J., SPAUTE, D., DAVIS D. R., MARZARI F., AND K. OHTSUKI 1997. Accretional evolution of a planetesimal swarm 2. the terrestrial zone. *Icarus* **128**, 429-455.

WETHERILL, G. W. AND G. R. STEWART 1989. Accumulation of a swarm of small planetesimals. *Icarus* **77**, 330-357.

WETHERILL, G. W. AND G. R. STEWART 1993. Formation of planetary embryos: Effects of fragmentation, low relative velocity, and independent variation of eccentricity and inclination. *Icarus* **106**, 190-209.

YOSHINAGA, K., E. KOKUBO, AND J. MAKINO 1998. The stability of protoplanet systems. *Icarus* **139**, 328-335.

The Evolution of the Protolunar Disk after Giant Impact

Takaaki Takeda, Shigeru Ida
Earth and Planetary Science, Faculty of Science
Tokyo Institute of Technology, Ookayama, Meguro-ku, Tokyo 152-8551, Japan
Telephone: 03-5734-2243
Fax: 03-5734-3538
E-mail:ttakeda@geo.titech.ac.jp,ida@geo.titech.ac.jp

Introduction

In past decades, 'Giant Impact Hypothesis' (Hartmann and Davis 1975; Cameron and Ward 1976) has become the most favored scenario of the origin of the Moon. It proposes that a collision between a Mars-sized protoplanet and the early Earth ejected mantle materials into Earth's orbit, and that the Moon was accreted from these materials.

Several researchers simulated the evolution of a protolunar disk by direct N-body simulations (Ida, Canup and Stewart 1997; Kokubo, Canup, and Ida 1999) Their important results are that the a single large aggregate is formed just outside the Roche limit, and the time scale of the accretion is about a month to a year. The result that a single moon forms comes from that accretion of disk material is inhibited inside Roche limit by the tidal effect of the Earth. Within Roche limit, aggregates are sheared apart constantly and spiral patterns develop. Outside Roche limit, tidal effect is not important and aggregates can grow. Once a moonlet is formed outside Roche limit, that moonlet grows exclusively sweeping the materials diffused out from inside Roche limit. Thus, the time scale of the moon accretion is determined by the timescale of diffusion of protolunar disk. The result that the time scale of moon accretion is very short comes from the very short diffusion time of the protolunar disk.

However, particle number of N body simulation is limited, and size of the particle is determined by the particle number. If the typical particle number 10,000 is used to represent the protolunar disk of 3 lunar mass, the size of each particles becomes the order of 100 km, while appropriate particle size is unknown. Since collision between two particle with different semimajor axes exchange angular momentum, the size of particles effect the evolution of the particle disk. Thus, we should know the effect of size of particle on the diffusion process of plotolunar disk, to know the validity of the result of N body simulation that the moon formation is very fast. We analyse the diffusion process in details and see the effect of particle size on the diffusion. We conclude that only small effect exists on diffusion, so that the time scale of lunar formation is about a month, with any size of constituent particles.

This result is inevitable one as long as considering pure particle disk considering only collisions and gravitational interaction. However, such a fast evolution of protolunar disk release enormous heat, enough to vaporize the half of the entire disk. This may undermine the assumption that the protolunar disk can be represent by a particle disk. We should investigate the evolution of the protolunar disk with the effect of the heat.

Basic Equation

The outward flux of material F, through radius r, is expressed as following (Lynden-Bell and Pringle 1974).

$$F\frac{dh}{dr} = -\frac{\partial F_{\rm AM}}{\partial r} = -\frac{\partial}{\partial r}\left(-2\pi\nu\Sigma r^3\frac{d\Omega}{dr}\right) \tag{1}$$

where, $F_{\rm AM}$ is a couple exerted on the stuff outside r by stuff inside r, or outward angular momentum flow though radius r, and $h(r)$ is specific angular momentum, which is $\sqrt{GM_\oplus r}$ for Keplerian disk.

With positive $\partial F_{\rm AM}/\partial r$ at given r, the outflow of angular momentum from the cylinder of radius r exceeds inflow to there, so that the material at radius r migrate inward losing its angular momentum. On the contrary, the material flows outward with negative $\partial F_{\rm AM}/\partial r$. Thus with a peak of $F_{\rm AM}(r)$, the inner material migrate inward and outer material outward, i.e. the disk diffuses.

The angular momentum transferring can be categorized by its mechanism. Mutual gravity of particles deals torque each other directly, and transfers angular momentum from particles to other particles. Collisions also transfer angular momentum directly as we mentioned above. Also, random motion of particles transfer angular momentum, since the particles with eccentricity can deposit its angular momentum to other particles with different semimajor axis by collisions or gravitational interaction.

Thus, $F_{\rm AM}$ can be categorized for three terms.

$$F_{\rm AM} = F_{\rm grav} + F_{\rm col} + F_{\rm trans} \tag{2}$$

This experssion is a expansion of the formulation in Wisdom and Tremaine (1988), which is considering the angular momentum flux in particle disk without self gravity.

Gravitational angular momentum flow $F_{\rm grav}$ is angular momentum flow by gravitational torque. This term is given as,

$$F_{\rm grav} = -\sum_{r_i<r} N_i^{\rm grav} \tag{3}$$

where summation is taken over all particles inside r, and $N_i^{\rm grav}$ is gravitational torque exerted on particle i. Since same amount of torque is exerted on the particles outside r as counter part, this is apparently angular momentum flow through radius r.

Collisional angular momentum flow $F_{\rm col}$ is angular momentum flow by collisions. This term is given as,

$$F_{\rm col} = -\sum_{\rm col} \Delta l \tag{4}$$

where summation is taken over collisions which straddle the surface of given r over unit time, and Δl is the angular momentum that are transfered by each collision from inner particle to outer particle.

Translational angular momentum flow $F_{\rm trans}$ means the angular momentum flow due to the movement of particles, and given as the integration of pressure tensor.

$$F_{\rm trans} = \int r d\theta \int dz \int dv (v_r - u_r) r (v_\theta - u_\theta) f, \tag{5}$$

where $\boldsymbol{u}$ is average velocity and f is distribution function of mass in phase space. This term becomes as following in particle image.

$$F_{\rm trans} = \frac{1}{r_0} \sum_i m_i (v_{ri} - u_r(r_i)) r_i (v_{\theta i} - u_\theta(r_i)), \tag{6}$$

where r_0 is the width of averaging range, which must be taken to discuss statistically. Summation is taken over the particles within the range $[r - \frac{1}{2}r_0, r + \frac{1}{2}r_0]$

Inside Roche limit, spiral patterns develops and particles moves coherently as a group in a spiral arm. To discuss the translational angular momentum flow, we separate the velocity of particle to the bulk velocity and local velocity, adopting the concept used in Salo (1995). Bulk velocity $\boldsymbol{v}_{\rm bulk}$ is average velocity of nearby particles and shows coherent motion of patterns. Local velocity $\boldsymbol{v}_{\rm local}$ is velocity relative to the bulk velocity and shows the random motion. The velocity of each particle is expressed as $\boldsymbol{v} = \boldsymbol{v}_{\rm bulk} + \boldsymbol{v}_{\rm local}$. Introducing these two velocities, $F_{\rm trans}$ is expressed as the sum of two terms.

$$F_{\rm trans} = F_{\rm bulk} + F_{\rm local}, \tag{7}$$

where $F_{\rm bulk}$ is angular momentum flow due to the motion of spiral pattern, i.e. motion of particles as a group, while $F_{\rm local}$ comes from the particles' random motion relative to the nearby particles. $F_{\rm bulk}$ and $F_{\rm local}$ are given as following.

$$F_{\rm bulk} = \frac{1}{r_0}\sum_i m_i(v_{ri,\rm bulk} - u_r(r_i))r_i(v_{\theta i,\rm bulk} - u_\theta(r_i)), \tag{8}$$

$$F_{\rm local} = \frac{1}{r_0}\sum_i m_i v_{ri,\rm local} r_i v_{\theta i,\rm local}, \tag{9}$$

where summations are also taken over the particles within the range $[r - \frac{1}{2}r_0, r + \frac{1}{2}r_0]$.

Calculation Method

We follows the evolution of protolunar disk by N-body simulation, integrating the orbit of particle by 4th ordered predictor-corrector method. As for the effect of collision, we calculate new velocities with normal restitution coefficient 0.1, whenever any particles overlap in any time step. We assume perfectly smooth sphere and put tangential restitution coefficient 1, so that there is no exchange between orbital and spin angular momentum. We follows the collisions and gravitational interaction for each step and calculated $F_{\rm col}$ and $F_{\rm grav}$. Also, we calculate $F_{\rm bulk}$ and $F_{\rm local}$ from $\boldsymbol{r}$ and $\boldsymbol{v}$ periodically, and averaged them over 2 Kepler time. Sampling time is about $100^{-1}\mathrm{T}_{\rm Kepler}$ Kepler time here means the Kepler time at $R = R_{\rm Roche}$.

We simulated two sets of runs with different initial surface density. In both cases, we initially put the particles to follow $\Sigma(a) \propto a^{-3}$ distribution, where a is semimajor axis, between $0, 4R_{\rm Roche}$ and $1.1R_{\rm Roche}$. Total initial disk mass in RUN1 and RUN 2 are 3 lunar mass and 4 lunar mass. In each case we simulated with different initial particles number $N = 3000, 10000, 30000, 100000$, and see the angular momentum process in each run.

As we follow dynamical evolution, we also follow the heat generation of the disk using a simple model. For each inelastic collisions, the particles lose their kinetic energy, and that energy would be heat energy eventually. We define the internal heat energy for each particles and summed lost kinetic energy to them for every collisions. We neglect the cooling by radiation, since the time scale of radiative cooling is much longer than the dynamical evolution time of the disk.

Results

Figs.1 show the snapshots of RUN1, when spiral structure develop, for two case of N=100,000 and N=10,000. The small circles show each particle and the large circular region without particles is the Earth. The large circles around the Earth is $r = 0.5R_{\rm Roche}$ and $r = R_{\rm Roche}$. We can see clear spiral structures develop in both case, though it becomes rather unclear if we reduce N to small as 3,000.

The surface density distribution for each run is in Fig.2, at the same time as Fig. Figs.1. We can see that the disk diffuse faster with smaller N, i.e. larger particle size, which indicate that the effect of particle size on diffusion time actually exist.

We show the detail of angular momentum transfer in Figs.3. We can see that in inner region $r < 0.5$, $F_{\rm grav}$ and $F_{\rm trans}$ are small and $F_{\rm col}$ dominate. Especially $F_{\rm grav}$ is neally 0. This comes from the fact that in inner regeion, spiral pattern is unclear and density profile is uniform, as seen in Figs.1. This is because that the tidal effect is stronger near the surface of the Earth,and prevent the particles from aggregating, Since $F_{\rm col}$ depend on the particle size, the diffusion is faster in smaller N case. However, in outer region, the $F_{\rm col}$ becomes less dominative, and $F_{\rm grav}$ and $F_{\rm trans}$ becomes important.

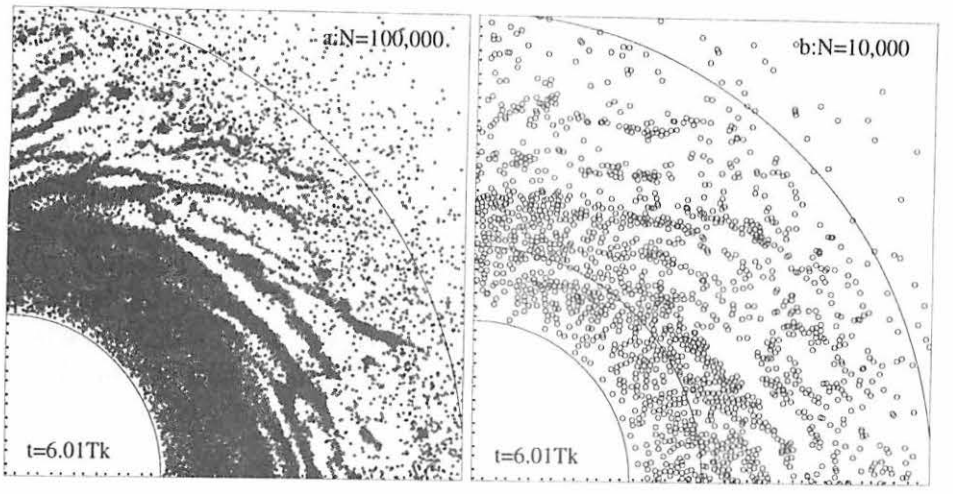

Figure 1: Snapshots of RUN1 after spiral structure develop, but lunar seed is not formed outside Roche limit. (a) N=100,000 (c) N=10,000

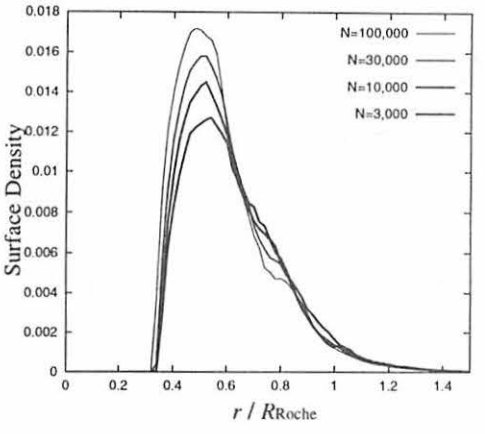

Figure 2: Surface density distribution at $t = 6$ Tk. The unit of surface density is $M_\oplus / R_{\rm Rohe}^2$.

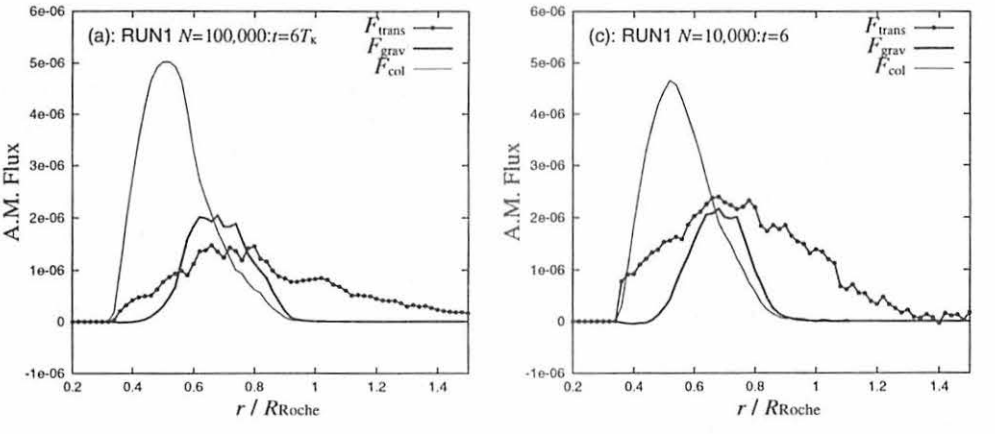

Figure 3: (a) the three angular momentum flow $F_{\rm col}$, $F_{\rm grav}$ and $F_{\rm trans}$ as function of r, at $t = 6T_{\rm K}$ in the case of RUN1, N=100,000.

In outer region, we found that $F_{\rm grav}$ is proportional to Σ^3, which is analytical estimation in linear theory. Since $F_{\rm grav}$ depend only in surface density, the diffusion in this region is rather insensitive to particle size.

We found that the translational angular moneutm transfer $F_{\rm trans}$ is the same order to $F_{\rm grav}$ in the region where spiral structure develops. However, it tends to be smaller in the case of smaller N, as seen in Fkg.3. We separate $F_{\rm trans}$ to the angular momentum flow due to the movement of the particle as a groupe $F_{\rm bulk}$, and the flow due to random motion of each particles $F_{\rm local}$. We show $F_{\rm bulk}$ and $F_{\rm local}$ on varoius N in Figs.4. There is no clear dependency on N in $F_{\rm bulk}$, while $F_{\rm local}$ is larger in the case of smaller N. Also we can see that $F_{\rm bulk}$ is nearly 0 at $r < 0,5R_{\rm Roche}$, the same tendency for $F_{\rm grav}$. This indicates that the bulk motion as a group is excited by the collective gravitational effect, and in depend on Σ as $F_{\rm grav}$ does, while random motion is excited by collisions, so that the size of particles is important for $F_{\rm local}$.

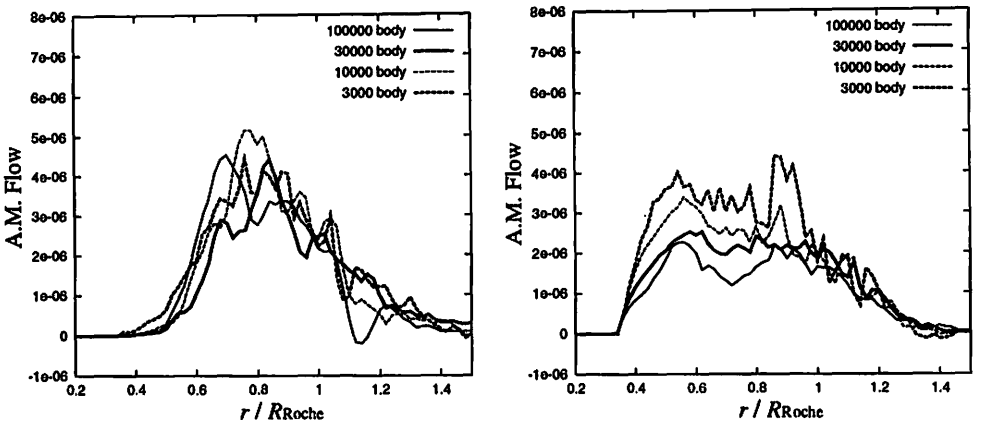

Figure 4: The left graph shows $F_{\rm bulk}$ and right shows $F_{\rm local}$, averaged from $t = 4T_k$ to $T = 6T_k$. $F_{\rm bulk}$ has no clear tendency on N. $F_{\rm local}$ is greater in the case with samller N.

Conclusion and Discussion

We found that the angular momentum transfer in the particle disk has two patterns. In the region $r < 0,5R_{\rm Roche}$, the spiral structure does not develop since tidal effect from the Earth is strong. In this region, angular momentum transfer is like the model without self gravity of particles, which is studied in Goldreich and Tremain (1978) and Araki and Tremain (1986). If optical depth is greater than 1, the collisons of particles dominates the angular momentum transfer process, and this transfer is greater if constituent particles are larger. Thus, we can conclude that N-body simulations with limited number is overestimationg the diffusion rate in the inner regeion near the Earth.

In outer region, where the spiral structure develop, the existence of non axisymmetric structure becomes important, and $F_{\rm col}$ and $F_{\rm trans}$ and $F_{\rm grav}$ becomes comparable. Since gravitational torque depends on the mass distribution only, $F_{\rm grav}$ depends on the surface density only and proportional to Σ^3. Also the constant forming and shearing of arms generate the movement of particles as a group, and the angular momenutm trnsfer due to this movement $F_{\rm bulk}$ is also depend on surface density. In N body simulation of limited number, $F_{\rm trans}$ is also overestimated to some extent, since angular momentum due to local random motion $F_{\rm looal}$ has dependency on particle size.

We found that the amount of components of angular momentum transfer that depend on particle size is just comparable to the components independant to particle size, with typical N which is in order of 10000. This indicate that the limited numbered N body simulation is overestimating the

diffusion rate only about two times at most, if disk mass is about [2-3] lunar mass. Since $F_{\rm grav}$ and $F_{\rm bulk}$ is proportinal to Σ^3, the ratio of components independant of particle size to the total angular momentum transfer becomes smaller if we consider less massive disk. We would need much more particles in simulating the evolution of less massive particle disk by global N body method.

Thus we conclude that the rapid lunar fomation is inevitable result from the protolunar disk with total mass about 2-3 lunar mass, as long as dynamical evolution is concerned. However, rapid evolution of the disk release large amount of heat (Thompson and Stevenson 1988). We show the temperature of disk in Fig.5. This figure shows the temperature of particles if all energies released by inelastic

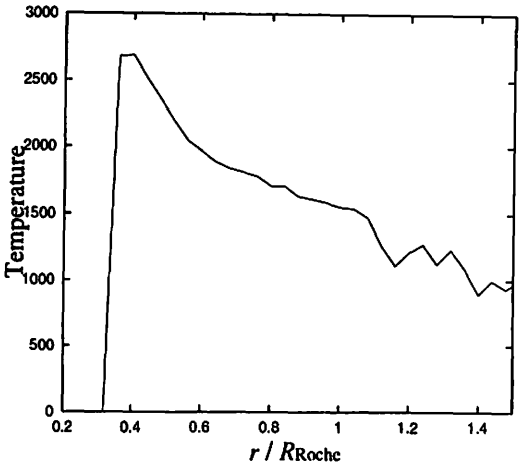

Figure 5: Average temperature of particles after 16 T_k as a function of r. Latent heat of fusion is included, though vaporization is not considered. Initial temperature is set to 0 K.

collisions are used to heaten the particles. We set the particles' temperature 0 K at $t = 0$. After 16 Kepler time, a time by which a lunar seed of about 1/3-1/4 appears, the disk is nearly 2000-3000 K. With these high temperature, particles must be partially vaporized, even though we set the initial temperature 0. In such high temperature, gravitational instability may not develop (Thompson and Stevenson 1988). And in this case, the time scale of lunar formation would be much elonged. Thus, we shoud investigate the evolution of protolunar disk with the effect of heat in future.

References

Araki, S. , and S. Tremaine 1986. The Dynamics of Dense Particle Disks. *Icarus* **65**, 83-109

Cameron, A.G.W. , and W.R. Ward 1976. *The Origin of the Moon. Proc. Lunar Planet. Sci. Conf. 7th*, 120-122

Goldreich P. , and, S. Tremaine 1978. The Velocity Dispersion in Saturn's Rings *Icarus* **20**,227-239

Hartmann,W.K., and D.R.Davis 1975. Satellite-Sized Planetesimals and Lunar Origin. *Icarus* **24**, 504-515.

Ida S., Canup R.M. and Stewart G.R. 1997. Lunar accretion from an impact-generated disk. *Nature* **389**, 353-357.

Kokubo, E. , Makino, J. ,and, Ida, S. Evolution of a Circumterrestrial Disk and Formation of a Single Moon.

Kokubo E., R.M. Canup, and S. Ida 1999. Lunar accretion from an impact-generated disk. In *Origin of the Earth and Moon*, eds. R.M. Canup and K. Righter, Univ. of Arizona Press, in press.

Salo H. 1995. Simulations of Dense Planetary Rings III. Self-Gravitating Identical Particles. *Icarus* **117**, 287-312

Thompson C, and, D.J. Stevenson 1988. Gravitational Instability in Two-Phase Disks and the Origin of the Moon *Astrophysical Journal* **333**, 452-481

Lynden-Bell, D. and J.E. Pringle 1974. The evolution of viscous discs and the origin of the nebular variables. *Mon . Not. Roy. Astron. Soc.* **168**, 603-637.

Wisdom J., and, S. Tremaine 1988. Local Simulations of Planetary Rings. *Astronomical Journal* **95**,925-940

Viscosity in Dense, Self-Gravitating Particle Systems Induced by Gravitational Instability

Hiroshi Daisaka
Department of Earth and Planetary Sciences, Faculty of Science, Tokyo Institute of Technology
Tokyo 152-8551, Japan
Telephone: +81-3-5734-2243, Fax: +81-3-5734-3538
E-mail: hdaisaka@geo.titech.ac.jp

ABSTRACT

We have investigated the viscosity (angular momentum transfer rate) in optically thick planetary ring such as the Saturn's main ring by performing local N-body simulations. In ring systems, visous steress comes from momentum transport processes which classified into three types: movement particle itsself, collisions due to finite size of collisions, and gravitational torque.

Local N-body simulations of Salo (1995) and Daisaka and Ida (1999) already showed the formation of wake structure by gravitational instabilty induced by self-gravity and collisional damping, but the viscosity in such system did not considered. Such wake formation may influence source of the viscosity. We calculated the ring's viscosity directly from our simulations. Our simulations show that the viscosity becomes more than 10 times larger than previous study in which the wake formation was not considered. In the ring where wake develops, self-gravity plays an important roll on the determination of the viscosity.

1 INTRODUCTION

Viscosity (angular momentum transfer rate) is one of the important physical properties in disk systems, since the evolution and the stability of the systems are governed by the property of viscosity. That is the key to explain the origin of the ringlet structure with width 10km in the Saturn's main ring, which was discovered by Voyager but was not yet clearly understood. Several models were proposed for explanation of the ringlet, for example, viscous instability (Lin and Bodneheimer, 1980; Lukkari, 1980; Ward, 1980) and moonlet hypothesis (Henon, 1981), but their availability depends on the property of the ring's viscosity. Nevertheless, understanding of the ring's viscosity is still lacking.

The ring's viscosity were studied by both theoretical and numerical approaches. In previous studies, the effect of collisions between particles were mainly considered in momentum transport process, since Saturn's main ring is a highly packed particle system, in other word, spatial volume is almost occupied by ring particles. In theoretical study, Boltzmann transport equation with suitable collision integral was used to yield an effective viscosity. (e.g., Goldreich and Tremaine, 1978; Araki and Tremaine, 1986). In numerical study, local simulation was performed and viscosity was calculated directly from movement and interactions of particles (Wisdom and Tremaine, 1988; Salo ,1991; Richardson, 1994). Results of both theoretical and numerical studies were consistent with each other.

In these studies, spatial uniformity was not considered. Theorical studies assumed spatial uniformity in particle distribution and numerical simulation used small computational area. However, Salo (1995) and Daisaka and Ida (1999) performed local N-body simulations with large number of self-gravitating, inelastic particles in large computational area. Their simulations showed the formation of spatial inhomogeneous structure such as gravitational wake (Julian and Toomre, 1966) and clump induced by self-gravity and collisional damping of particles. There is a possibility that such spatial uniformity changes picture of viscosity source obtained in previous studies. Wake structure is non-axisymmetrical one and its shape changes with time, being created and destroyed continiously on the time scale of an order of Keplerian

period like turbulence in fluid. Therefore, we expect that it could yield rather strong effective gravitational torque which leads to momentum transfer. Another effect could be expected that momentum transport similar to in turbulent occurs in system Thus, we should consider that the wake formation may affect momentum transport, that is, viscosity mechanism. In this study, we performed local N-body simulations and obtain ring's viscosity where wake develops directly and numericaly from our simulations.

2 NUMERICAL METHOD

We will briefly explain method of numerical simulation used in this study. The detail is described in Daisaka and Ida (1999) and also in Daisaka et al. (2000).

In the present study, we obtain the ring's viscosity (angular momentum transfer rate) by performing local N-body simulations. We adopt local simulation method which was first applied for the study of a dense ring system by Wisdom and Tremaine (1988). The "local" means that we consider a box with width L_x and height L_y at a semimajor axis a_0 in the ring, which revolves in a circular orbit with the Kepler angular velocity Ω_0 at the reference point a_0 and is small compared to the width of the whole ring. Motion of particles is pursued only in this box with the periodic boundary conditions taking into account shearing motion. This method would be valid because we are considering the structure with much smaller scale than the width of the B-ring and the orbits of ring particles are nearly circular in the coplanar plane. In the original method, self-gravitational force of particles was not included, but we take into account self-gravity as well as direct (inelastic) collision between particles in our simulations as Salo (1992b, 1995), Richardson (1994), and Daisaka and Ida (1999) did. We use HARP-2 in gravitational calculations.

The following is the calculation conditions: in this study, we limit simulations with identical, smooth particles. We use constant restitution coefficient ϵ as to be 0.5. According to Salo (1995) and Daisaka and Ida (1999), large computational area is required for wake formation. So we use computational area with width and height larger than $3\lambda_{cr}$ in simulations, where $\lambda_{cr} = 4\pi^2 G\Sigma/\Omega^2$ is the longest unstable wavelength against gravitational perturbation in linear theory (Julian and Toomre 1966).

The particle system is characterized by by two non-dimensional parameters. One is the dynamical optical depth and is defined as

$$\tau = \frac{N\pi r_p^2}{L_x L_y} \tag{1}$$

where $L_x \times L_y$ and N are the domain area and total number of particles in the domain, and r_p is particle radius. The optical depth can be reduced to $\tau \sim t_K/t_c$ (e.g., Goldreich and Tremaine 1982), where t_K and t_c are the Keplerian time and the mean collision time. This expression shows that the optical depth controls the strength of tidal force. In the situation for large τ, tidal force becomes rather weak because of shorter mean collision time.

The other parameter is the ratio $r_h/2r_p$, where r_h is Hill's radius. This parameter can be expressed as

$$\frac{r_h}{2r_p} \simeq 0.82\left(\frac{\rho}{900\mathrm{kg/m}^3}\right)^{1/3}\left(\frac{a_0}{10^8\mathrm{m}}\right). \tag{2}$$

where Saturn's mass $M_s = 5.69 \times 10^{26}$kg is assumed and ρ represents material density of a ring particle. This parameter regulates the effect of self-gravity, since $\pi(2r_p)^2$ and πr_h^2 express geometrical and characteristic gravitational cross sections for small random velocity. In large $r_h/2r_p \gtrsim 1$ case, self-gravity become rather strong. According to Salo (1995) and Daisaka and Ida (1999), simulations with a wider range of the parameters showed that the wake could be formed more easily in large τ and large $r_h/2r_p$ cases. Simulations with parameters for the Saturn's B-ring ($\tau \sim 1, r_h/2r_p \sim 1$) also showed the wake formation, and this leads us to expect that there exists wake structure in real ring system. So we should consider the viscosity in particle systems where the wake develops. We performed simulations with various value of τ and $r_h/2r_p$ but we will mainly introduce the results of simulations with fixed τ in this proceeding.

We briefly explain the calculation method of the viscosity used in our simulations. The viscosity is calculated directly by motion and interactions such as self-gravitational interactions and direct collisions of all particles. We separate the viscosity into three types: translational, collisional, and gravitational viscosity. The translational viscosity comes from momentum transport due to movement of particles across a surface. In simulations, we evaluate momentum flux of particles by time and spatial averaging. The collisional viscosity comes from collisions due to finite size of particles. This viscosity becomes rather effective in the case where mean free path is the same as particle physical radius. In simulations, we directly count collisions during time interval for evaluation of the collisional viscosity. The gravitational viscosity comes from self-gravitational torque of particles and we compute torque from particle distribution obtained by our simulations.

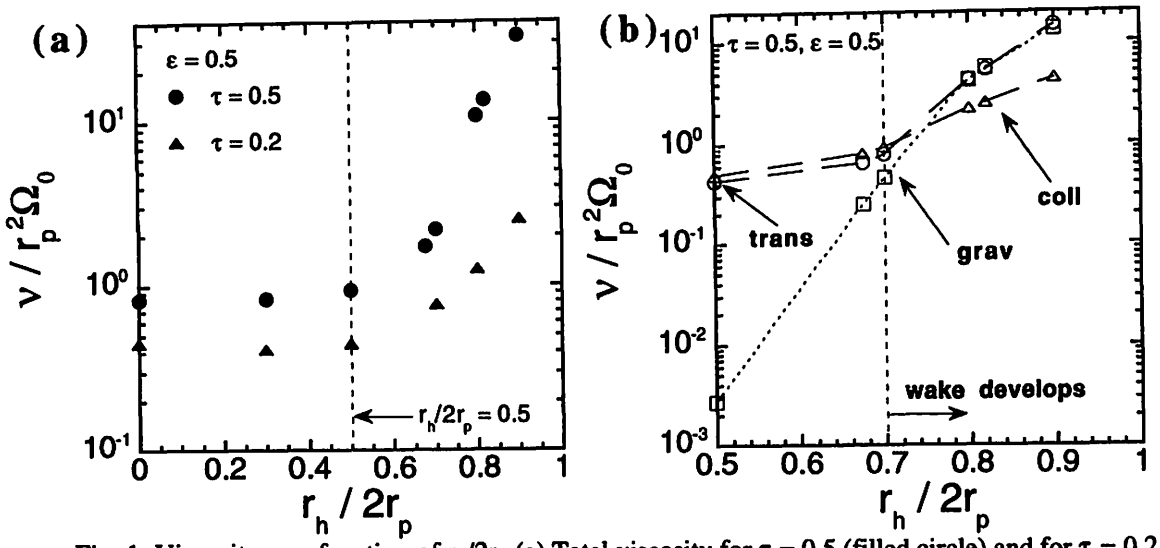

Fig. 1 Viscosity as a function of $r_h/2r_p$.(a) Total viscosity for $\tau = 0.5$ (filled circle) and for $\tau = 0.2$ (filled triangle). In both cases, restitution coefficient of colliding particles is $\varepsilon = 0.5$.
(b) Separation of the total viscosity in Fig. 1(a) into each component, translational (circle) collisional (triangle), and gravitational (square) viscosity for $\tau = 0.5$.

3 NUMERICAL RESULTS

In almost previous studies, self-gravity was ignored in calculation of the ring's viscosity. We first see the influence of self-gravity force between particles on the ring's viscosity. To do so, we performed simulations with various value of $r_h/2r_p$ for fixed τ and obtained the total viscosity. Our numerical results are shown in Fig. 1.

Figure 1(a) shows the total viscosity as a function of $r_h/2r_p$ for $\tau = 0.2$ (filled triangle) and $\tau = 0.5$ (filled circle). Simulations for $r_h/2r_p = 0$ correspond to the non self-gravitating particle cases and our results of the simulations are consistent with Araki and Tremaine (1986) and Wisdom and Tremaine (1988). This figure shows that for $r_h/2r_p < 0.5$, the values of the total viscosity in both optical depth cases are similar to these in non self-gravitating cases, whereas they are increasing with increase of $r_h/2r_p$ for the range of $r_h/2r_p > 0.5$. Such increase in the viscosity may be due to the effect of self-gravity of particles, since increase of $r_h/2r_p$ leads to the rather strong effect of self-gravity. This feature is independent on the optical depth, but the enhance rate of the viscosity would depend on optical depth. The Saturn's main ring satisfies the condition of $r_h/2r_p > 0.5$, so that our result indicates that the self-gravity play an important role on the transport mechanism of angular momentum in the ring. From Fig. 1(a), we can see that the viscosity for $\tau = 0.5$ is enhanced by factor 10 relative to non self-gravitating case with the same optical depth, and more than factor 2 even in relatively thin case of $\tau = 0.2$ at the typical B-ring's parameter of $r_h/2r_p$ ($r_h/2r_p = 0.82$). The observational value of the optical depth in the B-ring exceeds unity (e.g, Esposito 1993), so that our result indicates that the viscosity is at least 10 times larger than that considered before due to the effect of self-gravity.

As mentioned before, we separately calculated the translational, collisional, and gravitational viscosity. In order to examine what component of viscosity regulate the total viscosity which shows large increase for large $r_h/2r_p$ in Fig. 1(a), we next see the individual component of the viscosity. We divide the total viscosity shown in Fig. 1(a) into each component and plot them in Fig. 1(b). Note that Fig. 2 is a expanded view of Fig. 1(a) in the region from $r_h/2r_p = 0.5$ to $r_h/2r_p = 1.0$ and the case for $\tau = 0.5$ is only displayed. In this case, our simulations show the wake formation for $r_h/2r_p > 0.7$. The value of $r_h/2r_p$ for the wake formation would depend on the optical depth τ adopted in a simulation. For larger optical depth, we can see wake formation at rather small $r_h/2r_p$.

We can clearly see in Fig 1(b) that for large $r_h/2r_p$ where wake develops ($r_h/2r_p > 0.7$), translational and gravitational viscosity become the same order, but collisional viscosity is much smaller than these two. This means that the translational and gravitational viscosity is responsible for large increase in the total viscosity seen in Fig. 1(a). The same features can also be obtained by simulations with different optical depth in which wake formation occurs. The mechanism which dominates the viscosity in the ring where wake develops is quite different from that in the non self-gravitating particle case. According to Araki and Tremaine (1986) and Wisdom and Tremaine (1988), the viscosity in the non-gravitating particle case is determined by translational viscosity for low optical depth, whereas collisional viscosity is dominant for large optical depth where mean tree path is comparable with or less than particle radius. Our

result shows that when wakes develops due to self-gravity and collisional damping strongly, the viscosity is determined by translational and gravitational viscosity and collisional viscosity is less significance.

4 SUMMARY

In this study, we have investigated the ring's viscosity by local N-body simulations with self-gravitating and inelastic particles. Our simulations showed that the factor which determine the ring's viscosity is quite different from that obtained in pervious studies. The viscosity in ring where wake develops becomes more than 10 times larger than that obtained in previous studies without self-gravity force. Our simulations also shows that such increase in the total viscosity comes from translational and gravitational viscosity and increase in these components is related with the wake formation. By formation of non-axisymmetrical structure (wake), gravitational torque could be strengthened and it leads to rather larger momentum transport by self-gravity. As a result, gravitational viscosity increases. The reason of increase in translational viscosity is the coherent motion of particles in wakes induced by self-gravity force (Salo, 1995; Daisaka and Ida, 1999). Coherent motion could provide momentum transport rather larger than that due to real random motion of particles in wakes. Wake itself is induced by the effect of self-gravity and collisional damping of particles. So we can state that self-gravity regulates the ring's viscosity.

In this proceeding, we only introduce the results of simulations with various value of the ration $r_h/2r_p$ but fixed optical depth τ. As mentioned before, the system is characterized by these two parameters. We have also performed simulations with various value of τ. Together with simulations with such various parameters, we can obtain the description of the ring's viscosity where wake develops. We already find that the translational and gravitational viscosity is given by simple formula as

$$\nu_{\rm tot} \simeq \nu_{\rm trans} + \nu_{\rm grav} \simeq 10\frac{G^2\Sigma^2}{\Omega^3}, \tag{3}$$

where $\nu_{\rm tot}$, $\nu_{\rm trans}$, and $\nu_{\rm grav}$ represent the total, translational, and gravitational viscosity, and G, Ω, and Σ are the gravitational constant, the angular velocity, and surface mass density. This could be obtained from easy estimation of gravitational torque and momentum transport due to coherent motion and is the same formula with analytical expression proposed by Cameron and Ward (1978) and Lin and Pringle (1987).

More detail results would appear in the near future in Daisaka et al. (2000).

ACKNOWLEDGMENTS

The author thanks to H. Tanaka and S. Ida for useful discussions and comments. This manuscript is preparated with MN LaTeXstyle file v 1.4.

REFERENCES

ARAKI, S. AND S. TREMAINE, The Dynamics of Dense Particle Disks, *Icarus*, **65**, 83-109, 1986.

DAISAKA, H., AND S. IDA, Spatial Structure and coherent motion in dense planetary rings induced by self-gravitational instability, *Earth, Planet and Space*, **51**, 1195-1213, 1999.

DAISAKA, H., H. TANAKA, AND S. IDA, 2000, in preparation.

ESPOSITO, L. W., Understanding planetary rings, *Annu. Rev. Earth Planet. Sci*, **21**, 487-523, 1993.

GOLDREICH, P. AND S. TREMAINE, The Velocity Dispersion in Saturn's Rings, *Icarus*, **34**, 227-239, 1978.

JULIAN, W. H. AND A. TOOMRE, Non-axisymmetric responses of differentially rotating disks of starts, *Astrophys. J.*, **146**, 810-827, 1966.

LIN, D. N. C. AND P. BODENHEIMER, On the stability of Saturn's rings, *Astrophys. J. letter*, **248**, L83-L86, 1981.

LIN, D. N. C. AND J. E. PRINGLE, A viscosity prescription for a self-gravitating accretion disc, *Mon. Not. R. Astron. Soc.*, **225**, 607-613, 1987.

LUKKARI, J., Collisional amplification of density fluctuations in Saturn's rings, *Nature*, **292**, 433-435, 1981.

RICHARDSON, D. C., Tree code simulations of planetary rings, *Mon. Not. R. Astron. Soc.*, **269**, 493-511, 1994.

SALO, H., Numerical Simulations of Dense Collisional Systems, *Icarus*, **90**, 254-270, 1991.

SALO, H., Gravitational wakes in Saturn's rings, *Nature*, **395**, 619-621, 1992.

SALO, H., Simulations of Dense Planetary Rings. III. Self-Gravitating Identical Particles, *Icarus*, **117**, 287-312, 1995.

WARD, W. R., On the radial structure of Saturn's ring, *Geophys. Res. Let.*, **8**, 641-643, 1981.

WARD, W. R., AND A. G. W. CAMERON, Disc evolution within the Roche limit, *Proc. Lunar Planet Sci. conf. 9th*, 1205-1207, 1978.

WISDOM, J. AND S. TREMAINE, Local simulations of planetary rings, *Astron. J.*, **95**, 925-940, 1988.

The effects of a stellar encounter on a planetesimal disk

HIROSHI KOBAYASHI AND SHIGERU IDA

Department of Earth and Planetary Sciences, Faculty of Science
Tokyo Institute of Technology, Tokyo 152-8551, Japan
E-mail: hkobayas@geo.titech.ac.jp

We have investigated the effects of a passing stellar encounter on a planetesimal disk through orbital integrations and analytical calculations. When stars are born, they usually belong to a cluster, which would be dissolved on timescales of 10^8 years. Planetary systems around the stars in a cluster experience stellar encounters during their formation stage. Stellar encounters may have also affected the formation of the solar system.

We modeled a planetesimal disk as non-self-gravitating test particles rotating around a primary star and consider a single passing stellar encounter. We integrated orbits of 10000-body test particles in the disk encountering the star with various encounter parameters. The eccentricities e and inclinations i pumped-up by the stellar perturbations show similar functional form except for some scaling factors, irrespective of different encounter parameters. We found $e \propto (a/q)^{5/2}$ and $i \propto (a/q)^{3/2}$, for small a/q (in the case of parabolic encounter, $a/q \lesssim 0.25$), where a is semimajor axis of the particle and q is pericenter distance between the primary star and the passing star, We also derived approximate analytical formulae of the pumped-up e and i in this region, which completely agree with the results of orbital calculations. The formulae explicitly show how the pumped-up e and i depend on encounter parameters. For larger a/q, resonant interactions are important and e and i increase more rapidly with a. Using these results, we discuss the effects of stellar encounters on planetary formation and diversity planetary systems.

1 Introduction

In general, stars are born as members of an open cluster. Stellar clusters would be dissolved on timescales about 10^8 years (Kroupa 1995, 1998). This dissolution would be caused by gravitational interactions between stars, so that many stars experience gravitational perturbations of the other stars during the dissolution. More than half of T Tauri stars have protoplanetary disks (Beckwith and Sargent 1996), which would eventually form planetary systems. Planetary systems would also be affected by stellar encounters during their formation stage.

Laughlin & Adams (1998) suggested that a stellar encounter with pericenter distance $q \sim 200$ AU is likely before the dissolution of a dense cluster like Orion star forming region. Ida et. al (2000) have showed that high eccentricities e and inclinations i of outer Kuiper Belt objects may be explained by a stellar encounter with $q \sim$ 100-200 AU. Ida et. al (2000) and Kalas et al. (2000) suggested that commonly observed features of distortion in outer parts of dust-debris disks may be caused by stellar encounters.

Planets accrete from planetesimals that are formed in a protoplanetary disk. If stellar encounters pump up e and i highly enough that collision velocity between planetesimals exceeds their surface escape velocity, the collision would be disruptive (e.g., Safronov 1969, Ohtsuki 1993). Then, planetesimal accretion would be forestalled. As we will show below, e and i are pumped-up only in the outer disk and the radial gradient of e and i is rather steep. Planet formation is affected only in the outer region of the disk. Variety of stellar encounters may cause diversity of planetary systems, in particular, in outer region of the systems.

Thus stellar encounters may have significant effects on planet formation, however, no systematic study has been done about dynamics of stellar encounters with a planetesimal disk. Here we investigate the effects of stellar encounters on a planetesimal disk through orbital integrations and analytical calculations.

2 Model and Basic Equation

We model a planetesimal disk as non-self-gravitating, collisionless particles that initially have coplanar circular orbits around a primary star. This particle disk encounters a hypothetical passing star. The orbits of the test particles are determined by gravitational forces of the primary and the passing stars. Equation of motion of a planetesimal in inertial frame is

$$\frac{d^2\mathbf{R_0}}{dt^2} = -\frac{GM_1}{|\,\mathbf{R_0}-\mathbf{R_1}\,|^3}(\mathbf{R_0}-\mathbf{R_1}) - \frac{GM_2}{|\,\mathbf{R_0}-\mathbf{R_2}\,|^3}(\mathbf{R_0}-\mathbf{R_2}), \tag{1}$$

where M_1 and M_2 are masses of the primary and the passing stars, and $\mathbf{R_0}$, $\mathbf{R_1}$, and $\mathbf{R_2}$ are position vectors of the planetesimal, the primary star, and the passing star in the inertial frame, respectively. Since

$$\frac{d^2\mathbf{R_1}}{dt^2} = -\frac{GM_2}{|\,\mathbf{R_1}-\mathbf{R_2}\,|^3}(\mathbf{R_1}-\mathbf{R_2}), \tag{2}$$

the equation of motion of a planetesimal in the heliocentric frame (the frame with the primary star at rest) is

$$\frac{d^2\mathbf{r}}{dt^2} = -\frac{GM_1}{|\,\mathbf{r}\,|^3}\mathbf{r} + \frac{GM_2}{|\,\mathbf{R}-\mathbf{r}\,|^3}(\mathbf{R}-\mathbf{r}) - \frac{GM_2}{|\,\mathbf{R}\,|^3}\mathbf{R}, \tag{3}$$

where $\mathbf{r} = \mathbf{R_0} - \mathbf{R_1}$ and $\mathbf{R} = \mathbf{R_2} - \mathbf{R_1}$, which are position vectors of the planetsimal and the passing star relative to the position of the primary star. The first term in the r. h. s. corresponds to Kepler motion around the primary star, and the second and third terms are perturbing forces.

We scale length by pericenter distance q, mass by the primary star mass M_1, and time by $\Omega_{\rm Kep}^{-1}$ where $\Omega_{\rm Kep}$ is Keplerian frequency at $a = q$ given by $\sqrt{GM_1/q^3}$. Equation(3) is then transformed into

$$\frac{d^2\tilde{\mathbf{r}}}{d\tilde{t}^2} = -\frac{\tilde{\mathbf{r}}}{|\,\tilde{\mathbf{r}}\,|^3} - \frac{M_*(\tilde{\mathbf{r}} - \tilde{R})}{|\,\tilde{\mathbf{r}} - \tilde{R}\,|^3} + \frac{M_*\tilde{R}}{|\,\tilde{R}\,|^3}, \tag{4}$$

where $M_* = M_2/M_1$, $\tilde{\mathbf{r}} = \mathbf{r}/q$, $\tilde{\mathbf{R}} = \mathbf{R}/q$, and $\tilde{t} = \Omega_{\rm Kep}t$. We calculate changes in e and i of the planetesimal according to Eq.(3) or Eq.(4), through orbital integrations and analytical estimations.

3 Numerical Simulations

We integrated orbits of 10000 particles with surface number density $n_s \propto a^{-3/2}$. We integrate Eq.(4), using a fourth order predictor-corrector scheme. Many variations of encounter geometry, encounter velocity, and passing star mass were examined. Since the length is scaled by the pericenter distance of passing star q, parameters are the inclination of orbit of the passing star relative to the initial planetesimal disk (i_*), the orbital energy or orbital eccentricity of the passing star (e_*), the argument of perihelion(ω_*), and the scaled passing star mass (M_*). The encounter geometry is illustrated in Figure 1.

Figure 2 shows time evolution of e and i and corresponding face-on snapshots in the case with $e_* = 1$ (parabolic orbit), $i_* = 5$ degrees, $\omega_* = 90$ degrees, and $M_* = 1$. e and i of planetesimals are most excited when the passing star is near the perihelion. For $a/q \lesssim 0.25$, final pumped-up e and i (in radian) are $\lesssim$ 0.01-0.1. In this linear region, $e \propto (a/q)^{5/2}$ and $i \propto (a/q)^{3/2}$. Change in semimajor axis $\Delta a/a$ is much smaller than that in e and i. This is because angular velocity of the planetesimals, $\Omega_p = \sqrt{GM_1/a^3}$, in this regime is much larger than that of the passing star near perihelion, $\Omega_* \simeq \sqrt{G(M_1 + M_2)(1 + e_*)/q^3}$. The gravitational potential of the passing star is almost stationary for the planetesimals, which means their orbital energy and equivalently their a do not change.

For $a/q \gtrsim 0.25$, e and i increase more rapidly with a. Many particles are ejected for $a/q \gtrsim 0.3$. Some particles are captured by the passing star. In this region, Ω_p is of the same order of Ω_*, so that resonant interactions are important. Since locations of planetesimals at the pericenter passage of the star affect the resultant e and i in this region, e and i have some range for the same a.

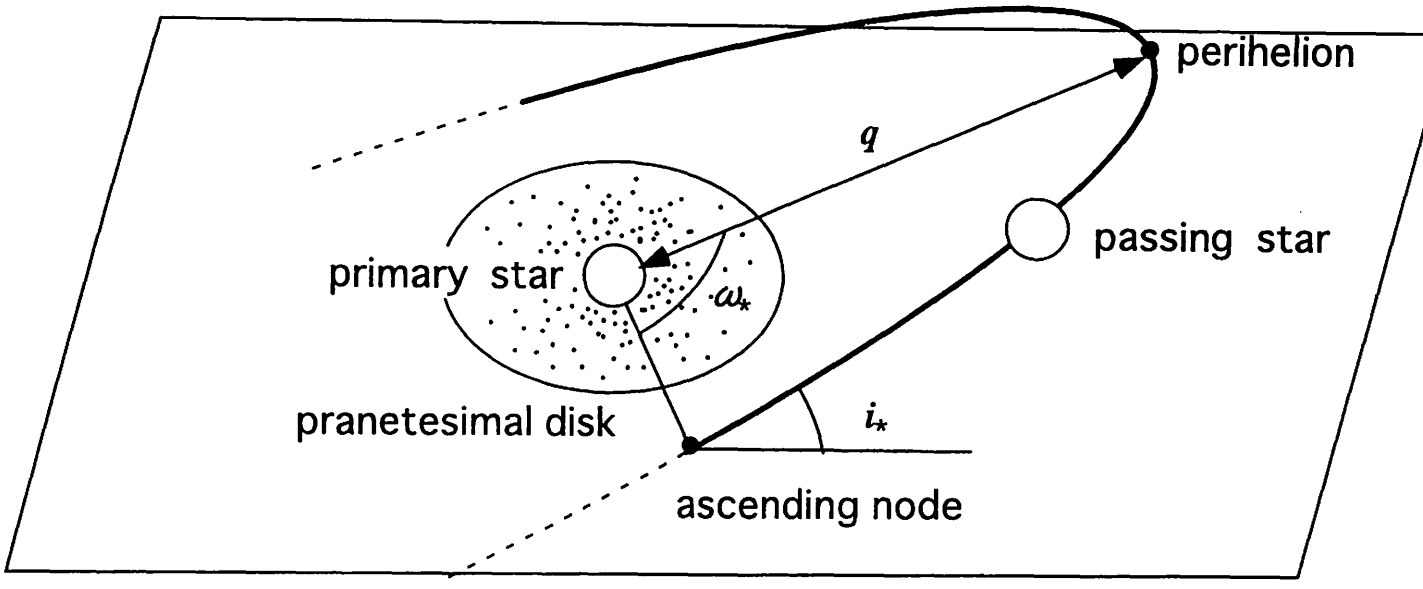

Figure 1: The encounter geometry

The condition of n : 1 commensurability is $\Omega_*/\Omega_p = (a/q)^{3/2}\sqrt{(1+M_*)(1+e_*)} = 1/n$. The n : 1 commensurability is located at $a/q = [(1+M_*)(1+e_*)n^2]^{-1/3}$. In the present case, the 4:1 and 3:1 are at $a/q \simeq 0.25$ and 0.30, respectively. The locations of 4:1 and 3:1 commensurabilities correspond to the abrupt increase in e and i and the ejection of many particles, respectively.

These features are almost independent of i_*, ω_*, and M_* except for the case with $i_* = 0$ where i is not pumped up at all. The graphs just shift upward or downward depending on these parameters. The dependence is analytically derived in section 4.

Figure 3 shows the dependence on e_* in the case with $i_* = 5$ degrees, $\omega_* = 90$ degrees, and $M_* = 1$. As e_* increases, the linear regime where $e \propto (a/q)^{5/2}$ and $i \propto (a/q)^{3/2}$ is restricted to smaller a/q, because the condition of the linear region is $\Omega_*/\Omega_p = (a/q)^{3/2}\sqrt{(1+M_*)(1+e_*)} \ll 1$. The 4 : 1 commensurability that may mark the boundary between the linear and resonant regions is at $a/q = 0.14$ and 0.07 for $e_* = 10$ and 100, respectively.

On the other hand, for large e_*, the region $\Omega_*/\Omega_p > 1$ is also important. $\Omega_*/\Omega_p > 1$ at $a/q > 0.17$ and 0.36 for $e_* = 100$ and 10, respectively (for $e_* = 1$, at $a/q > 0.63$). Figures 3 suggest some power-law dependence of e and i on a/q in this region, although

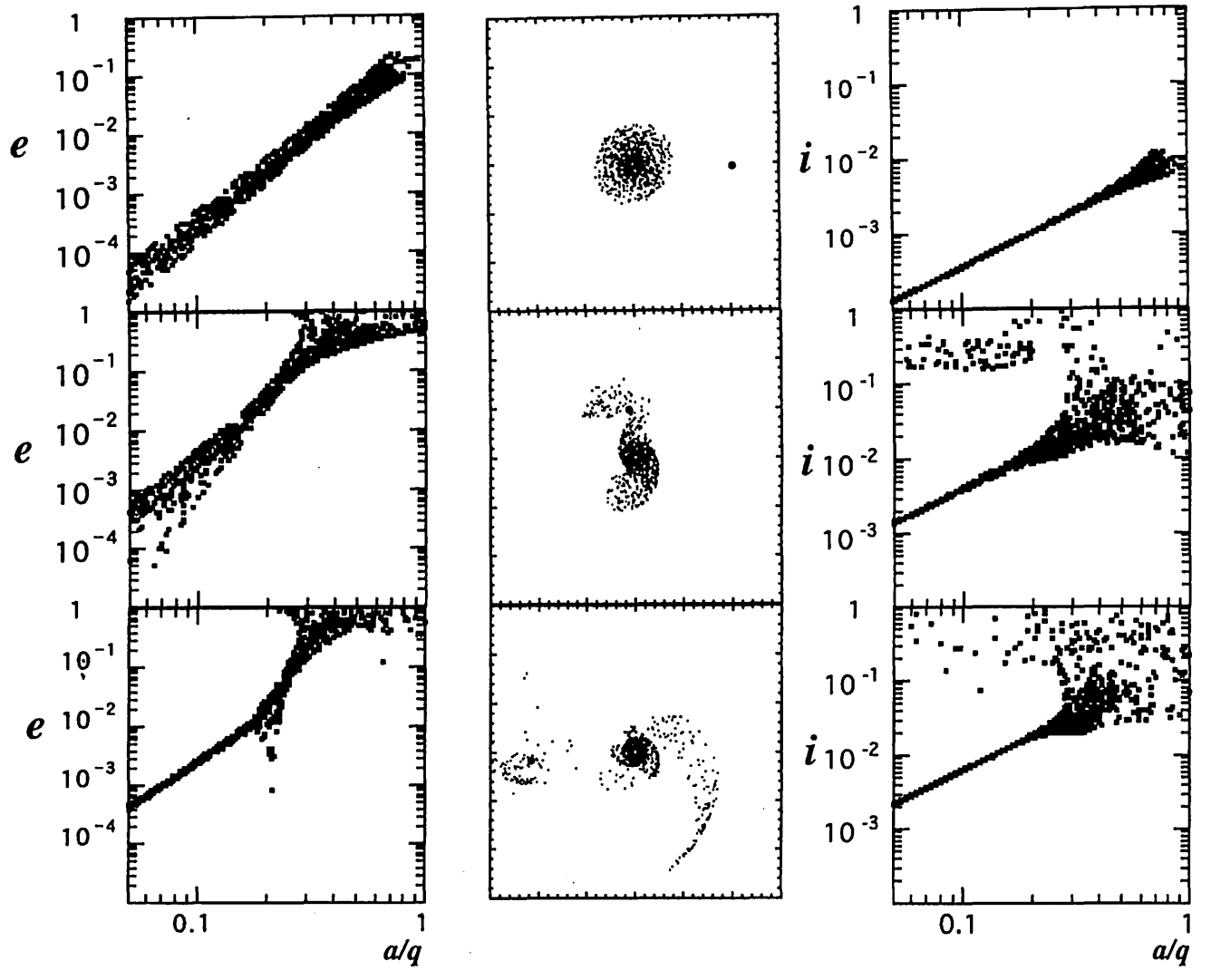

Figure 2: Right and left panels are evolution of orbital eccentricity e and inclination i of the particles pumped up by a passing star, as a function of semimajor axis a. Central panels are face-on snapshots of particles' disk and companion.

some divergence is caused by different locations of planetesimals at the pericenter passage of the star. The increase in e and i with a is less steep in this region than in the resonant region. Note that there is no commesurability of $\Omega_*/\Omega_p = n$ $(n > 1)$ while those of $\Omega_*/\Omega_p = 1/n$ $(n > 1)$ exist, because the passing star potential has Fourier components with $n\Omega_*$ but not $(1/n)\Omega_*$.

In summary, the features of the pumped-up e and i are divided into three regions : (1) The region with $\Omega_*/\Omega_p \ll 1$, where $e \propto (a/q)^{5/2}$ and $i \propto (a/q)^{3/2}$, (2) the region with $\Omega_*/\Omega_p \lesssim 1$, where resonant interactions are important and e and i rapidly increase with a, (3) the region with $\Omega_*/\Omega_p > 1$. In the next section, we derive analytical formula of e and i in the region (1).

4 Analytical Calculation

We derive analytical formula of pumped-up e and i in the linear region. Orbital integrations show that in that region, $e = e_0(a/q)^{5/2}$ and $i = i_0(a/q)^{3/2}$, where e_0 and i_0 are constant. The analytical formula explain these dependence on (a/q) as well as dependence of e_0 and i_0 on M_*, i_* and e_*.

4.1 Pumped-Up Inclination

We estimate change of perpendicular velocity, Δv_z, of the planetesimal. The change occurs mainly near the pericenter as the numerical simulations show. As seen in Eq.(3), near the pericenter where $\mid \mathbf{R} \mid \sim \mid \mathbf{R} - \mathbf{r} \mid \sim q$, the two perturbing forces in the r. h. d. of Eq.(3) almost cancel and the magnitude of net perturbing force in the z-direction (F_z) is

$$\mid F_z \mid \sim \frac{GM_2}{q^2}\frac{r}{q}\sin i_*. \tag{5}$$

In the linear region, the planetesimal orbit is primarily Keplerian orbit even during an encounter. v_z oscillates on Keplerian orbit. If dv_z/dt has different signs at the opposite points of the Keplerian orbit, the amplitude of v_z is secularly increased. F_z changes sign depending on whether $\mid \mathbf{r} - \mathbf{R_2} \mid > \mid \mathbf{R_1} - \mathbf{R_2} \mid$ or not, so that dv_z/dt has different signs at the opposite points. Thus, Δv_z secularly increases during the stellar encounter.

The effective time scale of the encounter is $\Delta t \sim 2q/v_*$ (e.g., Binney and Tremaine 1987) where v_* is passing speed near the pericenter. Since $v_* \sim \sqrt{G(M_1 + M_2)(1 + e_*)/q}$,$\Delta t \sim 2\left(\frac{q^3}{G(M_1+M_2)(1+e_*)}\right)^{1/2}$.(6)The total change of $\Delta\hat{v}_z$ is $\sim \mid F_z \mid \Delta t$. The change of inclination, Δi, is $\sim \Delta v_z/v_{\rm Kep}$ where $v_{\rm Kep}$ is Keplerian velocity of the planetesimal, which is given by

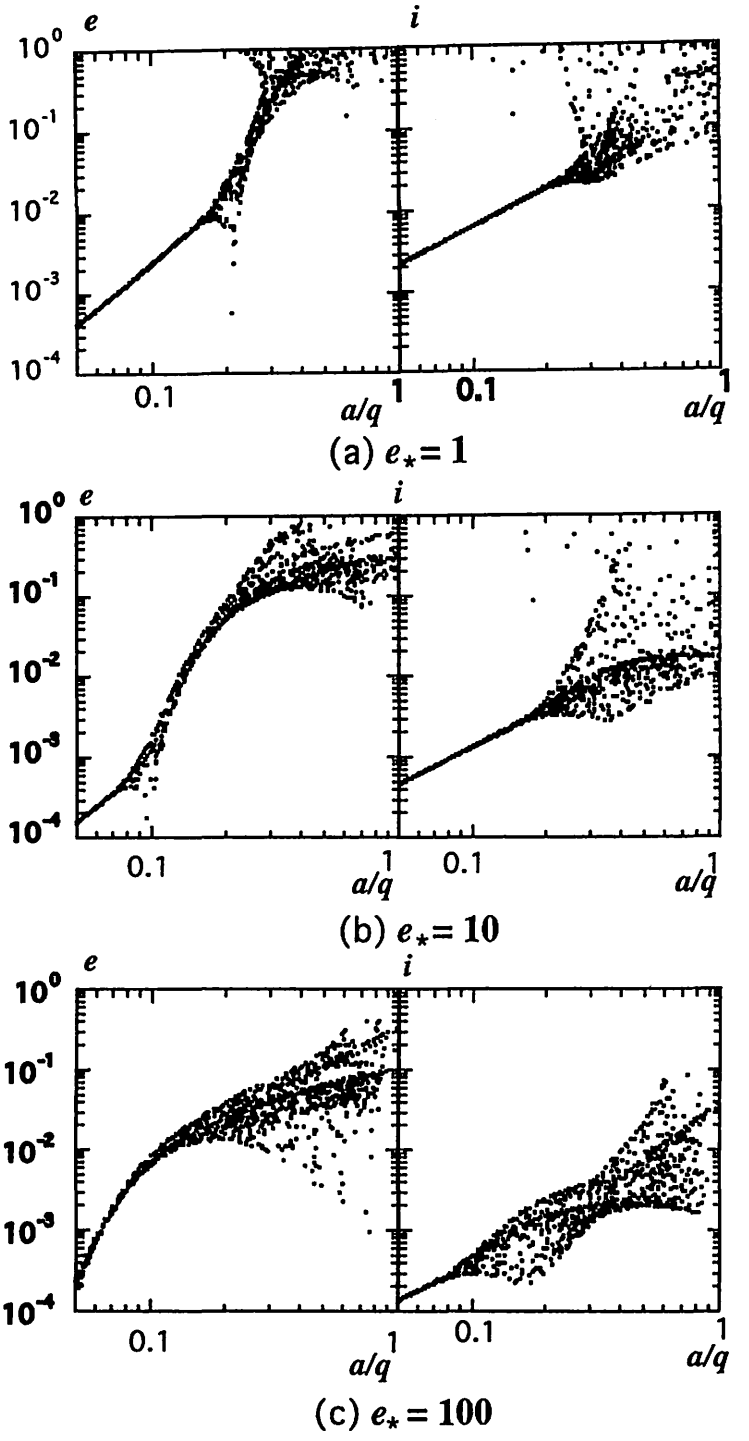

Figure 3: Orbital eccentricity e and inclination i of particles pumped-up by a passing star, as a function of semimajor axis a. $M_* = 1$, $i_* = 5$ degrees, $\omega = 90$ degrees are assumed for the passing star: (a) the case with $e_* = 1$, (b) the case with $e_* = 10$, (c) the case with $e_* = 100$.

$(GM_1/a)^{1/2}$. The total change of inclination is thus

$$\Delta i \sim \frac{M_*}{\sqrt{(1+M_*)(1+e_*)}} \left(\frac{a}{q}\right)^{3/2} \sin i_*. \tag{7}$$

4.2 Pumped-Up Eccentricity

We estimate change of velocity in the angular direction, Δv_θ, of the planetesimal. The magnitude of net perturbing force in the θ-direction is

$$\mid F_\theta \mid \sim \frac{GM_2}{q^2}\frac{a}{q}. \tag{8}$$

Also in this case, F_θ changes sign depending on whether $\mid \mathbf{r} - \mathbf{R_2} \mid > \mid \mathbf{R_1} - \mathbf{R_2} \mid$ or not. Furthermore, dv_θ/dt also has opposite signs between right and left hand sides from the line of sight between the primary and passing stars. Hence, Δv_θ almost cancels during Keplerian time ($t_{\rm Kep}$). Net change should be a/q times amplitude of Δv_θ during $t_{\rm Kep}$. The amplitude is $\sim F_\theta t_{\rm Kep}$. The rotation number during Δt is $\Delta t/t_{\rm Kep}$. Thereby, the total Δv_θ during the encounter is

$$\Delta v_{\theta,\rm tot} \sim \frac{a}{q} F_\theta \Delta t. \tag{9}$$

Since the change of eccentricity, Δe, is $\sim \Delta v_\theta / v_{\rm Kep}$, the total change of eccentricity is

$$\Delta e \sim \frac{M_*}{\sqrt{(1+M_*)(1+e_*)}} \left(\frac{a}{q}\right)^{5/2} \tag{10}$$

5 Conclusion & Discursion

We have studied the effect of a stellar encounter on a planetesimal disk through orbital integration and analytical calculations. Through our simulation, we found that the features of the pumped-up e and i are different in three cases. $\Omega_*/\Omega_p \ll 1$, $\Omega_*/\Omega_p \lesssim 1$ and $\Omega_*/\Omega_p > 1$, where Ω_* and Ω_p are the angular velocity of a passing star at perihelion and Keplerian angular velocity of particles. In the region with $\Omega_*/\Omega_p \ll 1$ (a/q is small), $e \propto (a/q)^{5/2}$ and $i \propto (a/q)^{3/2}$. In this region, we derided analytical formulas of e and i. They are consistent with the orbital calculations. This analytical calculation clearly shows the dependence of the pumped-up e and i on the parameters of the encounter.

In the outer disk with $\Omega_*/\Omega_p \lesssim 1$, resonant interactions are important and e and i rapidly increase with a. In the outermost region with $\Omega_*/\Omega_p > 1$. the increase in e and i with a becomes slow again, because there is no strong resonance there.

If e and i are pumped-up so highly that the collision velocity between planetesimals exceeds their surface escape velocity, the collisions would lead to disruption of the planetesimals. In this region, further planetesimal accretion would be inhibited. Since the radial gradient of pumped-up e and i is rather steep, the inhibition of planet formation would be shapely restricted to outer region of the disk. If probability of q is given, we can predict the diversity of planetary systems caused by stellar encounters, such as truncation size of a system and e and i of planets in outer region.

The disruptive collisions would produce a plenty of dusts that still have orbits of large e and i, which may account for observed distorted dust-debris disks.

In the case of slow velocity encounter, such as parabolic orbit encounter, the passing star capture the particles that originally rotate at the primary star. There may be planetesimals of extrasolar origin.

References

Beckwith, S. V. W. and Sargent, A. I. 1996, *Nature*, **383**, 139

Binney, J. and Tremaine, S. 1987, Galactic Dynamics, Princeton Univ. Press, Princeton, New Jersey

Ida, S., Larwood J. and Burkert A., 2000, *ApJ*, **528**, 351-356

Kalas, P., Larwood, J., Smith, B. A. and Schultz, A. 2000 *AJ*, **530**, L133-L137

Kroupa, P. 1995, *MNRAS*, **277**, 1507

Kroupa, P. 1998, *MNRAS*, **298**, 231

Laughlin G. and Adams F C., 1998, *ApJ*, **508**, 171-174

Ohtsuki, K. 1993, *Icarus*, **106**, 228

Safronov, V. S. 1969, Evolution of the Protoplanetary Cloud and Formation of the Earth and Planets. (Moscow: Nauka Press)

Long-term stability of our solar system

Takashi Ito and Kiyotaka Tanikawa
National Astronomical Observatory, Mitaka, Tokyo 181–8588, Japan
tito@cc.nao.ac.jp

This article is devoted to describe the strong stability of planetary motions in our solar system. In many kinds of long-term numerical integrations as well as in the results of secular perturbation theories, all the planets remain in the system stable near their own initial orbits in spite of their exhibition of chaotic dynamical characters. We present one of our trials of several long-term numerical integrations of planetary orbital motions over $O(10^9)$-year timespan. Time-series and time-frequency analyses of our numerical data show that the planetary motion, at least in our simple dynamical model, may be quite stable in this timespan. The innermost planet, Mercury, would show a symptom of some deficit in its angular momentum (i.e. eccentricity and inclination of the planet may be somewhat increased), the effect is not fatal on the global stability of whole planetary system due to the small mass of Mercury. The orbital motion of Earth which can have a potentially large effect on its surface climate system through solar insolation variations is also found to be stable.

1. Definition of the problem: what should we seek for?

The stability of our solar system has been argued over several hundred years, since the era of Newton. The problem has attracted many famous mathematicians over the period (Laplace, Lagrange, Poincaré, Arnold, etc.) and has played a central role in the development of nonlinear dynamics and chaos theory. However, we do not yet have any definite answer of the question: whether our solar system is stable or not. This is partly due because the definition of the term "stability" is quite vague when it is used on the problem of planetary motion in the solar system. Actually it is pretty difficult to give a clear, rigorous, and physically meaningful definition on the stability of our solar system. In other aspect, we can say that there are as many definitions of stability as the number of researchers for these hundreds of years.

Among many kinds of definition of stability, here we adopt the Hill stability criteria (Gladman, 1993); strictly speaking it is not a definition of stability, but of instability. We define that a system becomes unstable when a close encounter occurs somewhere, starting from certain initial configuration (Chambers *et al.*, 1996; Ito and Tanikawa, 1999). A system is defined to experience a close encounter when two bodies approach one another within the size of the larger Hill radius. Otherwise the system is considered to be stable. Definition of the instability here can be replaced by occurrence of any orbital crossing between either pair of planets, since we know by experiences that an orbital crossing soon leads to a close encounter in planetary and protoplanetary systems (Yoshinaga *et al.*, 1999).

Henceforward we state that our planetary system is dynamically stable if no close encounter happens in the age of our solar system, $T \sim \pm 5 \times 10^9$ years. Actually, our solar system seems to be far more stable than what is defined by the Hill stability criterion: not only no close encounter happens, but also orbital motions of planets remain quasiperiodic in that timespan, as shown in the following sections.

2. Equations of motion and initial conditions

To investigate the stability of our solar system, it is necessary to solve the equations of motion in the inertial space

$$\frac{d^2\boldsymbol{x}_i}{dt^2} = \sum_{\substack{j=0 \\ j\neq i}}^{N} \frac{Gm_j}{|\boldsymbol{x}_j - \boldsymbol{x}_i|^3} + \boldsymbol{a}_i, \tag{1}$$

where i denotes the index for each celestial body (Sun, Mercury, Venus, ..., Pluto), $\boldsymbol{x}_i$ and m_i is the position and mass of the i-th particle in the inertial space respectively, G is the gravitational constant, N is the number of particles, and $\boldsymbol{a}_i$ represents any small extra acceleration arising from sources other than Newtonian gravitational interactions between the planets and the Sun.

Equation (1) is rewritten in the relative coordinates to the Sun by using the relative position vector to the Sun $\boldsymbol{r}_i$ as

$$\frac{d^2\boldsymbol{r}_i}{dt^2} = -\frac{G(M_\odot + m_i)}{r_i^3}\boldsymbol{r}_i + \sum_{\substack{j=1 \\ j\neq i}}^{N} \frac{Gm_i}{|\boldsymbol{r}_i - \boldsymbol{r}_j|^3}(\boldsymbol{r}_i - \boldsymbol{r}_j) - \sum_{\substack{j=1 \\ j\neq i}}^{N} \frac{Gm_j}{|\boldsymbol{r}_j|^3}\boldsymbol{r}_j + \tilde{\boldsymbol{a}}_i, \tag{2}$$

where the first term in the right-hand side of equation (2) is the acceleration for Keplerian motion, and the second and third terms denote perturbation to the two-body orbital motion. $M_\odot$ denotes the solar mass.

The small acceleration $\boldsymbol{a}_i$ (or $\tilde{\boldsymbol{a}}_i$) includes for example (Tremaine, 1995): satellites, general relativity, asteroids, the galaxy, nearby stars, passing stars, and solar mass loss. In this chapter we neglect all the effect from $\boldsymbol{a}_i$ and other dissipative forces: we consider our planetary system as a nonlinear Hamiltonian system, dominated only by Newtonian gravitational force between the planets and the Sun.

At present, the longest numerical integrations published in a journal is Duncan and Lissauer (1998). Although their main target is the effect of post-main-sequence solar mass loss on the stability of our planetary system, they performed many integrations up to 10^{11} years of four jovian planets' orbital motion. The initial orbital elements of planets are the same as of our solar system, but the solar mass decreases relative to those of planets in their experiments. They found that orbit crossing times of planets, which can be a typical indicator of an instability timescale, are quite sensitive to the degree of the sun's mass decrease. The reduction of the sun's mass induces the reduction of the instability, probably increasing the mutual Hill radii among planets. However when the sun's mass is not so different from the present value, jovian planets remains stable over 10^{10} years, or perhaps more. They also performed four similar experiments on the orbital motion of seven planets (Venus to Neptune) which span $\sim 10^9$ years. Their experiments on the seven planets is not yet comprehensive, but it seems that terrestrial planets also remain stable during the period, keeping quasiperiodic oscillations similar to the present one.

Table 1 summarizes some historical investigations of the long-term evolution of our solar system. Many of them follow only the outer five planets (Jupiter to Pluto) since: (1) the masses of inner terrestrial planets are so small that the outer planets form an independent

dynamical system; (2) the orbital periods of the outer planets are longer so it is easier to follow the system for a given time.

A thorough understanding of the long-term evolution of planetary orbits would require integrating an ensemble of planetary systems for 5–10 Gyr. This task is still more than two or three orders of magnitude beyond our present capability for N-body integrations (Tremaine, 1995). Nevertheless, even by shorter integrations, we can understand several principal features of dynamical evolution of the planetary system over its lifetime as we show in the next section.

Table 1. Historical summary of major numerical integrations of solar system planetary orbital motion. Adapted and modified from Tremaine (1995). Δt is stepsize of the integration and T is the longest integration period.

Authors	Δt (d)	T (yr)	planets	used machine
Eckert *et al.* (1951)	40	3.5×10^2	outer 5	mainframe
Cohen & Hubbard (1965)	40	1.2×10^5	outer 5	mainframe
Cohen *et al.* (1973)	40	1.0×10^6	outer 5	mainframe
Newhall *et al.* (1983)	0.25	4.4×10^3	whole 9 +☾	mainframe
Kinoshita & Nakai (1984)	40	5.0×10^6	outer 5	mainframe
Applegate *et al.* (1986)	40	2.17×10^6	outer 5	special-purpose
Richardson & Walker (1989)	0.5	2.0×10^6	whole 9	mainframe
Sussman & Wisdom (1988)	32.7	8.45×10^8	outer 5	special-purpose
Nobili *et al.* (1989)	40	1.0×10^8	outer 5	vector super
Quinn *et al.* (1991)	0.75	$\pm 3.0 \times 10^6$	whole 9	workstation
Wisdom & Holman (1991)	1 (yr)	1.1×10^9	outer 5	workstation
Sussman & Wisdom (1992)	7.2	1.0×10^8	whole 9	special-purpose
Kinoshita & Nakai (1996)	40	$\pm 5.5 \times 10^9$	outer 5	PC (i386)
Ito *et al.* (1996)	400	4.3×10^{10}	outer 5	workstation
Duncan & Lissauer (1998)	—	$\sim 1 \times 10^{11}$	jovian 4	—
Duncan & Lissauer (1998)	—	$\sim 1 \times 10^9$	7 (♀ to ♆)	—

3. Longer-term integrations of planetary orbits

Laskar (1994, 1996) finds in his accurate perturbation theory that large and irregular variations appear in the eccentricities and inclinations of the terrestrial planets, especially Mercury and Mars in the timescale of several 10^9 years. Behavior of planetary orbits in such a long timespan has not been investigated by numerical integrations of equations of motion in detail so far. We performed seven long-term numerical integrations on whole nine planetary orbits which span several 10^9 years, and two integrations spanning $\pm 5 \times 10^{10}$ years (Table 2). Total elapsed time for whole integrations is more than five years using several dedicated PC compatibles, SPARC, DEC, and Hewlett-Packard workstations.

Table 2. Description of our 9 long-term numerical integrations. Top seven target whole 9 planets ($\Delta t = 8$d), and bottom two are for outer 5 planets ($\Delta t = 400$d). Initial orbital elements of the couples jan25 and emb-minus, and plus and plus_u03 are a little bit different. In addition, we slightly increase Sun's mass to make a different initial conditions in emb-plus-I integration. In 50G± integrations we incorporate the masses of inner four planets into Sun's mass.

ID	planets	direction	T (yr)	notes
minus	whole 9	past	4.1×10^9	Earth
emb-minus	whole 9	past	3.9×10^9	Earth–Moon baricenter
jan25	whole 9	past	4.1×10^9	Earth–Moon baricenter
plus	whole 9	future	1.7×10^9	Earth
plus_u03	whole 9	future	1.5×10^9	Earth
emb-plus	whole 9	future	5.0×10^9	Earth–Moon baricenter
emb-plus-I	whole 9	future	4.2×10^9	Earth–Moon baricenter, increased Sun's mass
50G−	outer 5	past	5.0×10^{10}	Sun incorporates inner planets' mass
50G+	outer 5	future	5.0×10^{10}	Sun incorporates inner planets' mass

3.1 Models and methods

We solved equations of motion (1) without any forces other than the mutual classical gravitation among planets, i.e. $\boldsymbol{a}_i = 0$ in (1). Effect of the Moon is bunched into the mass of Earth, or simply neglected in some experiments. Initial orbital elements are taken from the Development Ephemeris of JPL, DE245 (*cf.* Standish 1990).

We utilize the second-order Wisdom-Holman symplectic map as the main integration method (Wisdom and Holman 1991, Kinoshita *et al.* 1991) with a special start-up procedure to reduce the truncation error of angle variables, "warm start"(Saha and Tremaine 1992, 1994).

Stepsize for the numerical integrations is 8 days in the case of whole nine planets, which is about 1/11 of the shortest (Mercury's) orbital period. Wisdom and Holman (1991) performed numerical integration of jovian planets plus Pluto using the mapping method with the stepsize of 400 days, 1/10.83 of Jupiter's orbital period. Their result seems to be accurate enough, which partly justify our way of stepsize determination. We follow them in the case of outer five planets, choosing 400 days of stepsize.

We adopt Gauß's f- and g- functions in the mapping together with the third order Halley's method (Danby, 1992) as a solver of Kepler equations. Number of the maximum iteration in the Halley's method we set is 15, but it never reached the maximum in any of our integrations. As for the Kepler's equation solver, a series of recent work by Fukushima (福島, 1980; Fukushima, 1996; Fukushima, 1997e; Fukushima, 1997b; Fukushima, 1997d; Fukushima, 1997a; Fukushima, 1997c; Fukushima, 1998), which succeed to eliminate all transcendental functions in the solving algorithm of Kepler's equation, will be a powerful tool both in accuracy and computational speed. We have just begun to implement one of his methods in our simulation code.

Interval of data output is 200000 days ($\sim$ 547 years) for whole 9 planets calculation, and about 8000000 days ($\sim$ 21903 years) for outer 5 planets integration.

In some part of our integrations, mainly to check accuracy of main integrations, we also use

the Bulirsch-Stoer extrapolation method (Gragg, 1965; Bulirsch and Stoer, 1966; Hairer *et al.*, 1993) which can be well parallelized (福島, 1992; Ito and Fukushima, 1997).

The integration length of $\pm 5 \times 10^{10}$ years on the outer five planets seems to have no sense since the age of the solar system is thought to be 1×10^{10} years. Here our intention is to show the rigorous stability of outer solar system in this timespan using a simple numerical model, not to insist that the solar system really exists during that interval.

We are now planning to integrate more accurate equations of motion including the effect of Moon and general relativity (cf. Quinn *et al.* 1991), utilizing the Picard-Chebyshev numerical perturbation technique which can be quite suitable for vector integration (Fukushima, 1997d; Fukushima, 1997f).

3.1.1 Error estimation

The integration seems to be accurate enough: for example in the case of whole nine planets integration, the averaged relative errors of total energy ($\langle \delta E/E_0 \rangle \sim 10^{-9}$ where δE is the maximum change of the total energy and E_0 is its initial value) and of total angular momentum ($\langle \delta A/A_0 \rangle \sim 10^{-11}$ where δA is the maximum change of angular momentum and A_0 is its initial value) are kept nearly constant through the whole integration. Warm start reduces the averaged relative error of the total energy by one order of magnitude or more in this case compared with the symplectic map without it. In the case of outer five planets case, $\langle \delta E/E_0 \rangle \sim 10^{-6}$ and $\langle \delta A/A_0 \rangle \sim 10^{-10}$. These errors are plotted in Figure 1. Different operating systems (and math libraries) and hardwares produce different numerical errors through the way of round-off error handling and numerical algorithm.

Since symplectic integrators preserve total energy and total angular momentum of N-body systems inherently well, they may not be a good measure for accuracy of numerical integration. To estimate the numerical error in orbital integrations, we compare the result of main integration with some test integrations which is much more accurate than the main integrations. For this purpose, a very accurate integrations which span 3×10^5 years have been done by the parallelized Bulirsch-Stoer extrapolation method (Ito and Fukushima, 1997). Result of the time reversal test (starting from $t = 0$ to $t = 3 \times 10^5$ years, then going back to the starting point reversely, and measure the difference between the initial values) shows that the difference in Earth's mean anomaly is $\sim 0.0015°$ at $t = 0$ point. Since the error of longitudes increases linearly with time in the extrapolation method, we can extrapolate this value to the period of $\pm 5 \times 10^9$ years as $0.0015 \times (5 \times 10^9)/(3 \times 10^5) \sim 25°$. We should consider this quite small, so we adopt this integration by the extrapolation method as a measure of main integrations. Then we compare this accurate measure integration with main integrations. For the period of 3×10^5 years, a typical difference between these two integrations is $\Delta l_{earth} \sim 0.52°$, which can be extrapolated to the value $\sim 8700°$, about 25 rotations of Earth after 5 Gyr. Similarly, longitude error of Pluto can be estimated as $\Delta l_{pluto} \sim 12°$. This value for Pluto is much better than the result in Kinoshita and Nakai (1996) where $\Delta l_{pluto} \sim 60°$.

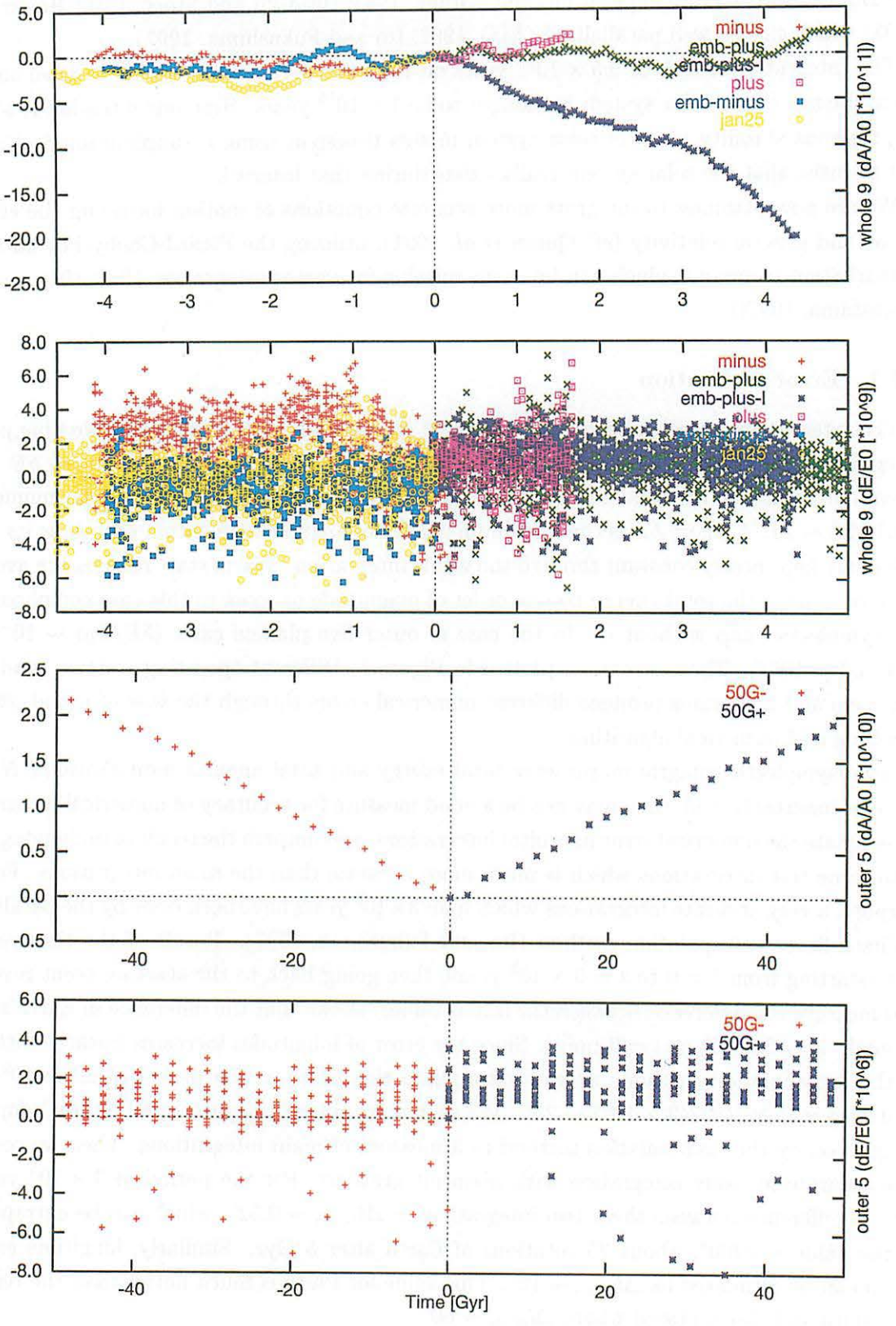

Figure 1. Relative numerical error of total angular momentum $\delta A/A_0$ and total energy $\delta E/E_0$ in the numerical integrations for whole nine planets (upper two panels, minus, plus, emb-plus-l, emb-minus, emb-plus, jan25) and for outer five planets (lower two panels, 50G+, 50G-).

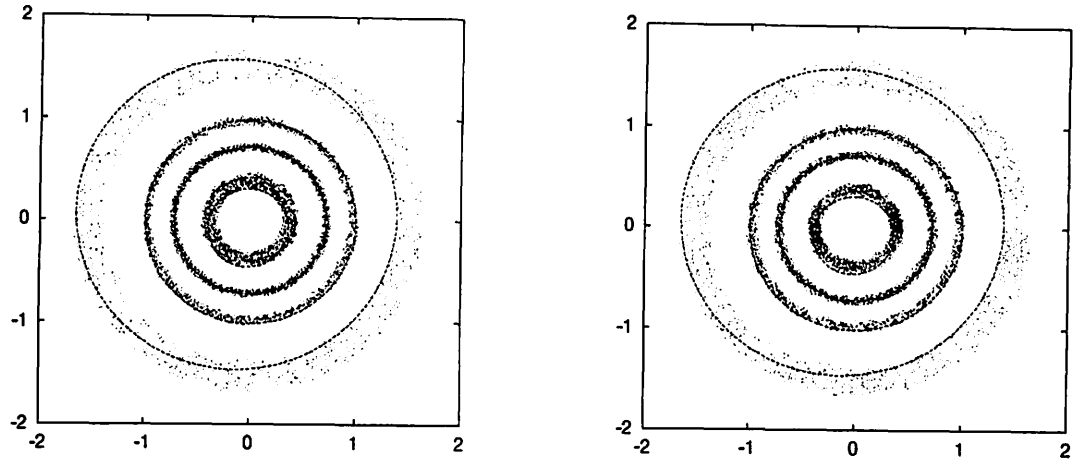

Figure 2. Vertical view of the four inner planetary orbits in leading (left, $t \sim 0$) and trailing (right, $t \sim +3 \times 10^8$ years) part of emb-plus-I series. Jacobi coordinates centered at the Sun is used. The unit of axes are AU. The xy-plane is set to the invariant plane of solar system angular momentum. Total 23684 points are plotted with an interval of about 2190 years during the total data-length of about 5.19×10^7 years.

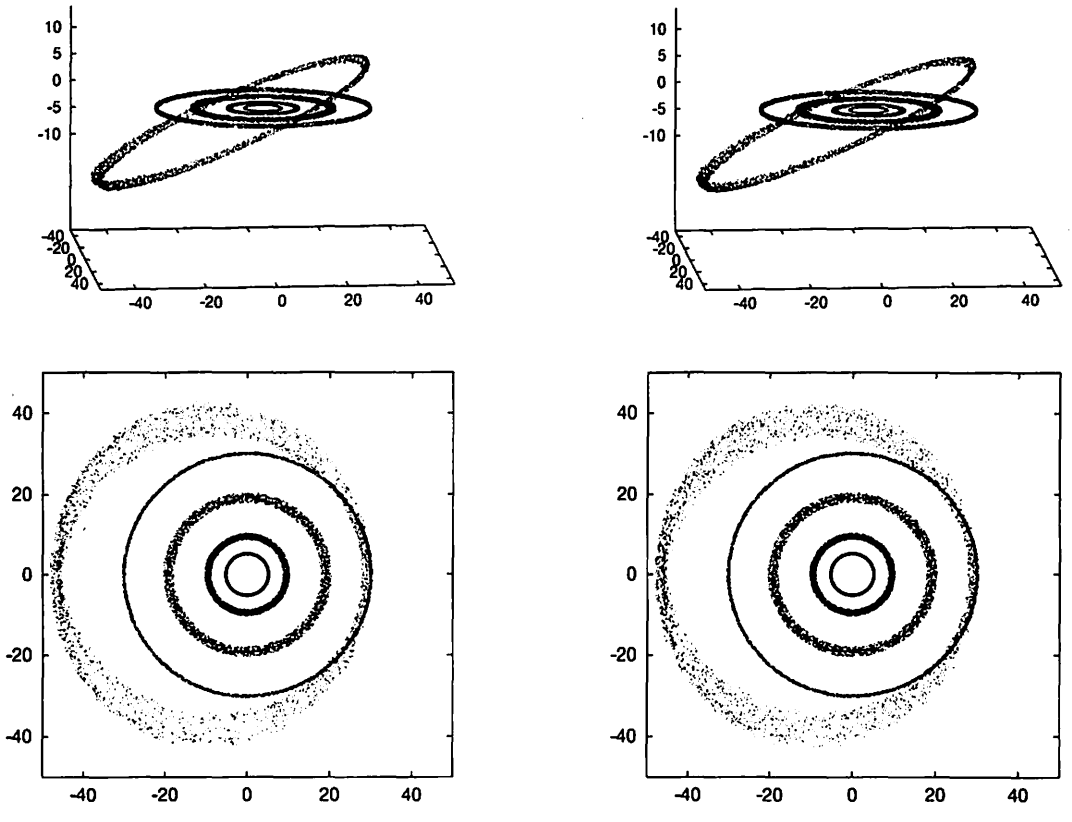

Figure 3. Orbital configuration of outer five planets in leading (left, $t \sim 0$) and trailing (right, $t \sim +5 \times 10^{10}$ years) part of 50G+ series. Total 23810 points are plotted with an interval of about 87611 years during the total data-length of about 2.09×10^8 years.

3.2 General description of the stability of planetary orbits

We briefly look at the general and specific characters of the stability of planetary orbits. In a word, orbital motion of our planetary system remains rigorously stable during the whole integration periods, which is partly shown in three-dimensional orbit configurations such as Figure 2.

Leading and trailing parts of eccentricities of four inner planets in minus and emb-plus-I datasets are shown in Figure 4 (panels in top and middle steps). Variation of Mercury's eccentricity seems to have changed a little bit between the leading and trailing parts in these integrations, especially in minus dataset. But the effect would not be fatal on the global stability of the whole planetary system due to the small mass of Mercury. Inclinations of the four planets also show similar stable behaviour. As for the extensive $\pm 5 \times 10^{10}$-year integrations on the outer five planets, they show much more rigorous stability than the inner four (Figure 3. Note that a rotation is applied to the coordinate system so that Pluto's ascending node always lies on x-axis. This transformation makes the figures easier to look at since inclination and eccentricity of Pluto is much larger than those of other planets). Leading and trailing parts of eccentricities of the $\pm 5 \times 10^{10}$-year integrations are shown in Figure 4 (panels in bottom step). Oscillations of eccentricity of all five planets indicate excellent quasi-periodicity.

These results support the fact that our planetary system remains stable during its whole age, though the motion of planets shows weak chaotic characters (cf. Milani and Nobili 1997, Pilat-Lohinger *et al.* 1999, Šidlichovský 1999).

3.2.1 Low-pass filtering and Delauney elements

Time variation of orbital elements is in a sense buried in short periodic oscillations as we can see in Figure 6. This means that the planetary orbital motion is nearly quasiperiodic and dominated by the harmonic oscillation of some canonical variables (h_i, k_i) and (p_i, q_i) where $h_i = e_i \sin \varpi_i$, $k_i = e_i \cos \varpi_i$, $p_i = \sin I/2 \sin \Omega_i$, $q_i = \sin I/2 \cos \Omega_i$, and $i = 1 \ldots 9$ (cf. Brouwer and van Woerkom 1950). However, what we want to know by the long-term numerical integrations is not the short periodic oscillation but longer-term evolution of the system. For this purpose we should remove the short periodic oscillation by some way and extract long-periodic, or if any, secular component buried in the raw data.

To extract the long-periodic or secular components, we applied low-pass filters on the raw orbital elements described in Figure 6. Specifications of the low-pass filters are listed in Table 3. When we denote filter coefficients as $h_j (j = 0, \ldots, \mathcal{M})$, input data x_i and output data y_i are related as (三上, 1998)

$$y_i = \sum_{j=0}^{\mathcal{M}} h_j x_{i-j} \tag{3}$$

where $\mathcal{M}$ is the degree of the filter. Filter coefficients in frequency and time domain are displayed in Figure 5 for whole nine planet case (cut-off period is 5×10^7 years). Characteristics of the filter in outer five planet case is the same except cut-off frequency.

An example of low-pass filtered orbital elements are depicted in Figure 7 whose raw orbital elements and their running averages are shown in Figure 6. Note that the absolute value of the

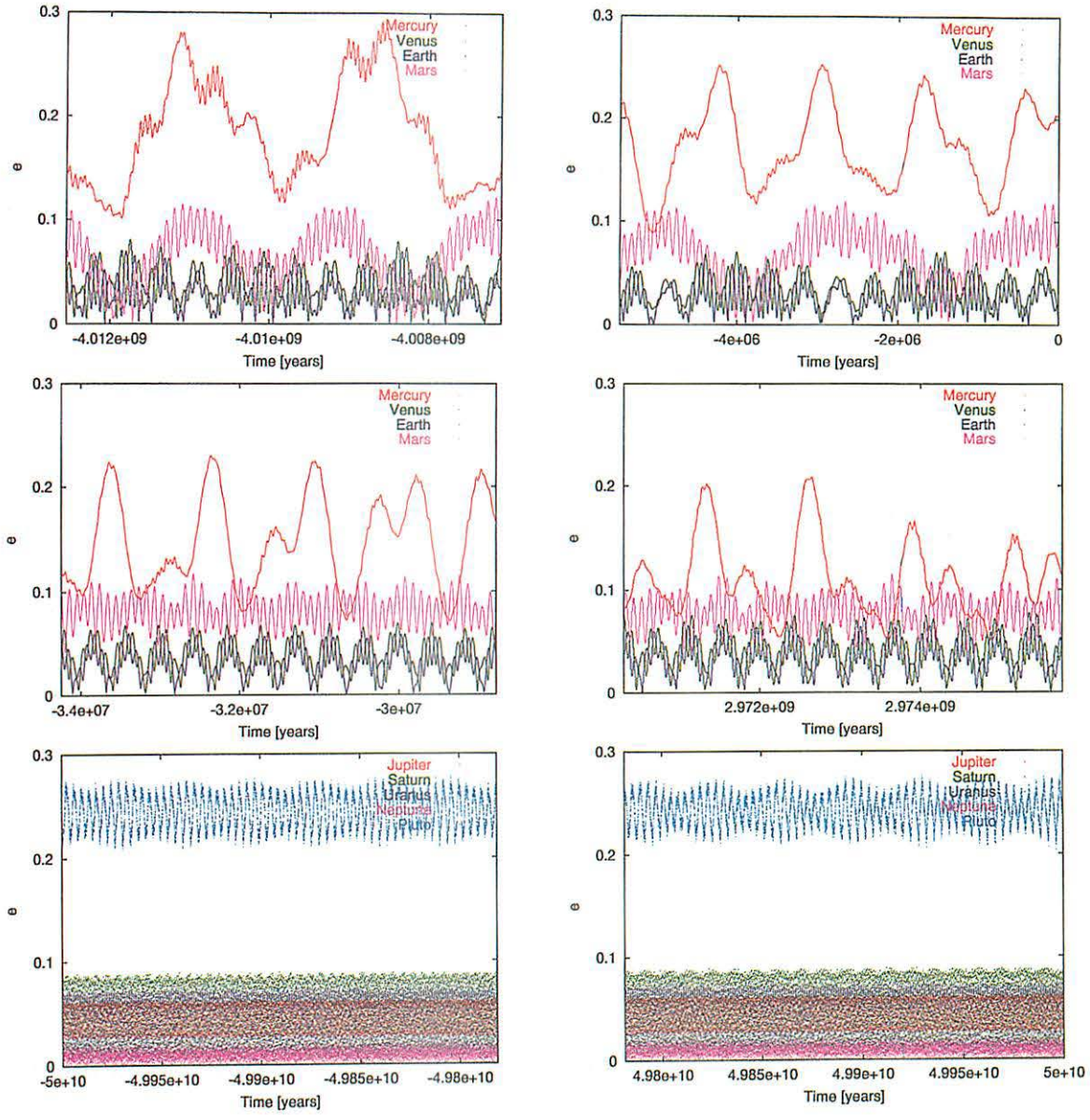

Figure 4. Top and middle: leading and trailing parts of eccentricities of four inner planets in minus dataset (top two. The leading part is right, and the trailing part is left) and emb-plus-l dataset (middle two. The leading part is left, and the trailing part is right). About 5×10^6-year data are plotted in each panel. Bottom: trailing parts of eccentricities of five outer planets in $\pm 5 \times 10^{10}$-year integrations in 50G- (left) and 50G+ (right) datasets. About 2.2×10^8-year data are plotted in each panel.

Table 3. Specification of low-pass filter used in this research.

	whole 9	outer 5
Cut-off period (year)	5×10^7	5×10^8
Degree of filter ($\mathcal{M}$)	5001	10001
Filter length (years)	$\sim 2.74 \times 10^8$	$\sim 2.19 \times 10^9$
Worst reduction ratio (dB)	100	

elements are somewhat reduced because of the nature of band-pass filters. However since the amplitude reduction is small (i.e. worst reduction ratio equals to 100 dB), we think the filtered elements are worthy of quantitative discussion.

To look at the exchange of physical quantity such as energy or angular momentum among planets, we calculate the Delauney elements from the low-pass filtered orbital elements. Delauney elements are a set of canonical variables which are defined by Kepler elements as follows:

$$\begin{aligned} L &= na^2 = \sqrt{\mu a}, & l &= l, \\ G &= L\sqrt{1-e^2} = \sqrt{\mu a\,(1-e^2)}, & g &= \omega, \\ H &= G\cos I = \sqrt{\mu a\,(1-e^2)}\cos I, & h &= \Omega. \end{aligned} \tag{4}$$

Angles l, g, h are just equivalent to mean anomaly, argument of perihelion, longitude of ascending node of Kepler orbital elements, respectively. Actions G and H are equivalent to angular momentum and its vertical component per unit mass of each planet. L is related to orbital energy E per unit mass as $E = -\mu^2/2L^2$.

An example of resulting Delauney action G based on the low-pass filtered orbital elements (Figure 7) is drawn in Figure 8. Note that all the variables are multiplied by mass of the planets.

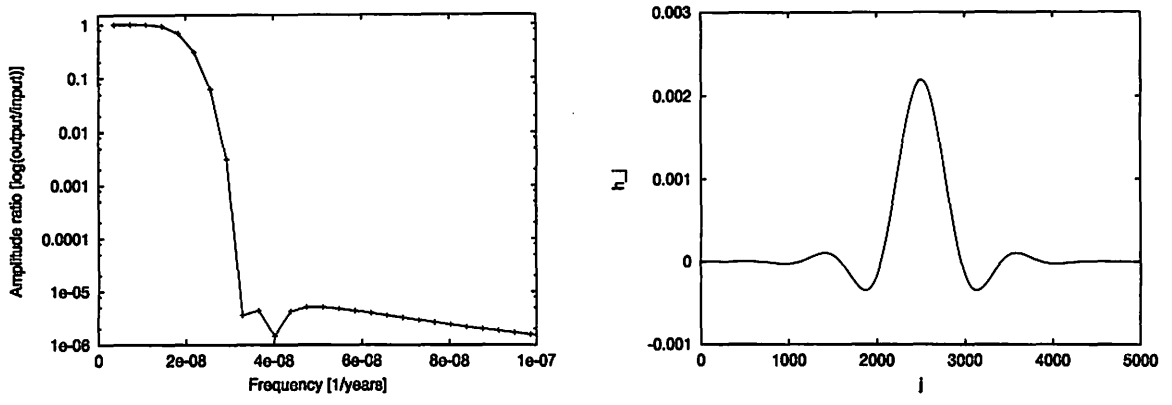

Figure 5. Frequency domain (left) and time domain (right) characteristics of low-pass filter adopted for whole 9 planets integrations (cut-off period $\sim 10^7$ years). Filter length is 5001 $\times$ dt where dt is the step-interval of original data ($dt = 2 \times 10^6$ days in these cases).

3.2.2 Long-term exchange of energy and angular momentum and stability

We obtain very low-frequency oscillation of planetary orbital motion by the low-pass filtering method. Using these filtered elements, we can calculate the variation of total energy and total angular momentum of the planetary system in very low-frequency domain.

If the system is completely linear, energy and angular momentum in each frequency-bin must be constant. Nonlinearity in the planetary system can cause the exchange of energy and angular momentum in frequency domain. In addition, amplitude of the lowest frequency oscillation should become larger if the system would be unstable and break down gradually. Such a symptom of instability was not found in our integrations, even in $\pm 5 \times 10^{10}$ timespan for outer five planets. It means that the present planetary system is rigorously stable, at least 10^9-year timescale.

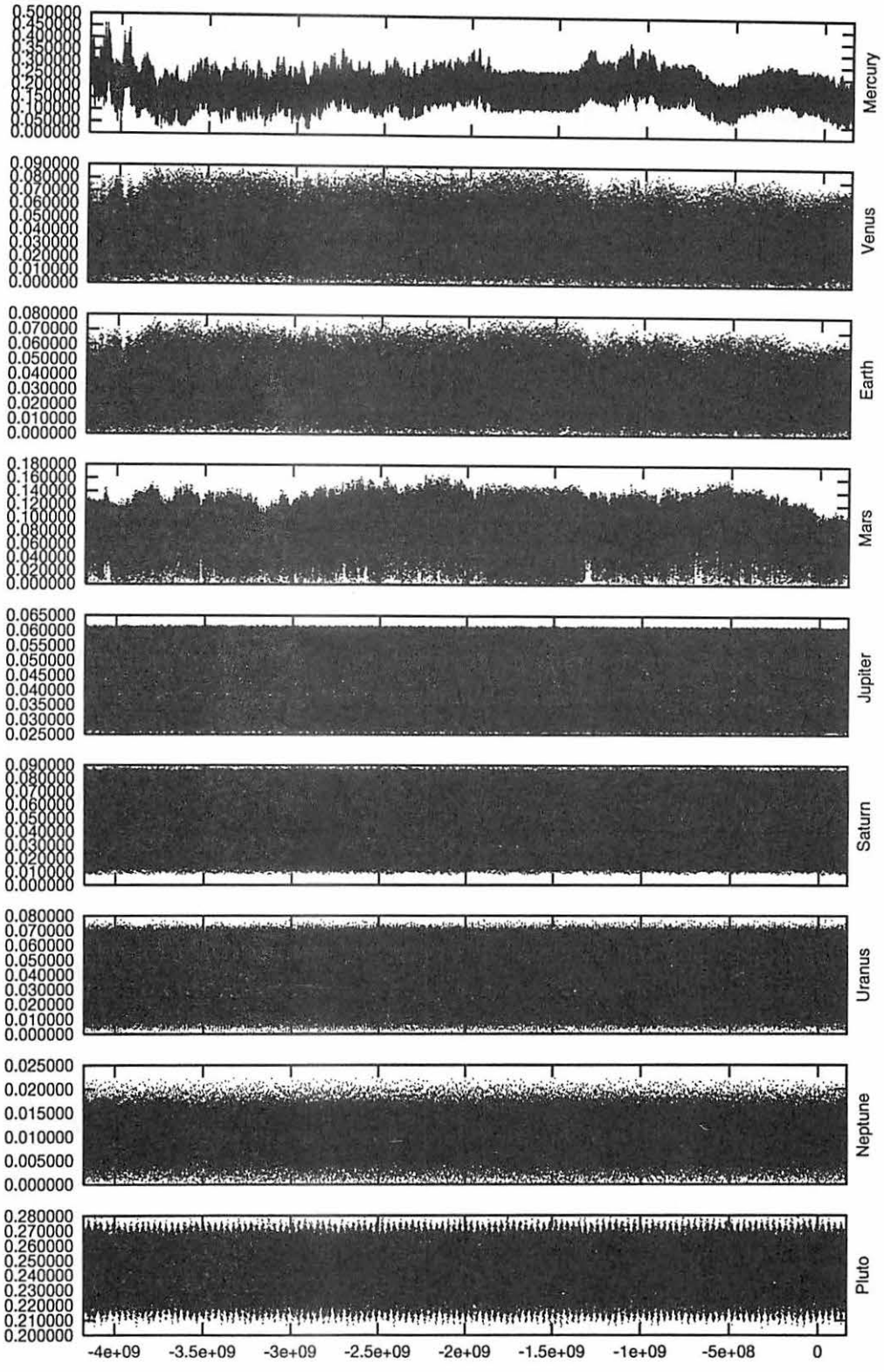

Figure 6. Time evolution of e in minus series. Raw orbital elements with its running averages are plotted.

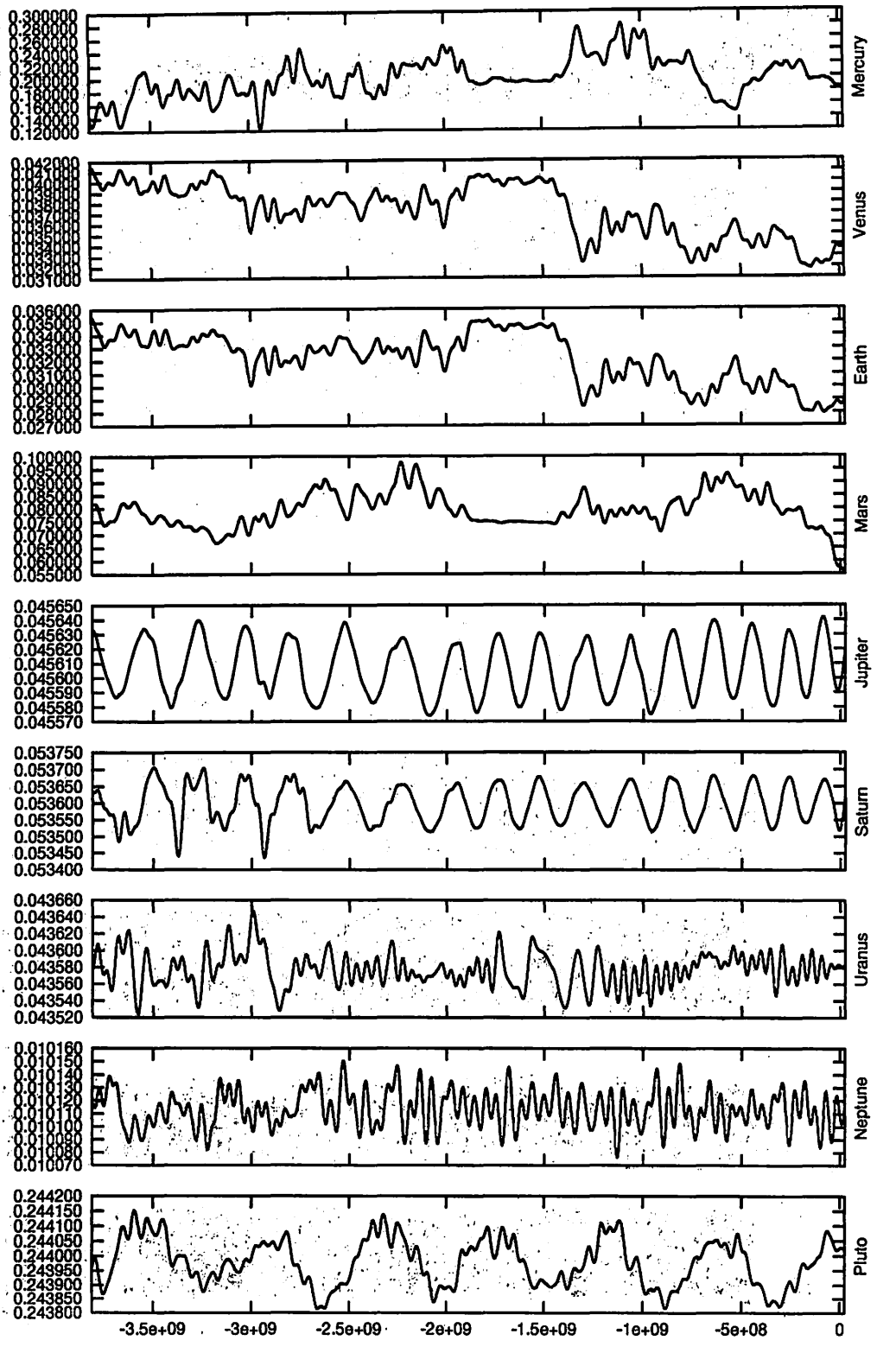

Figure 7. Time evolution of e in minus series. Short-periodic oscillations in the data plotted in Figure 6 are removed by a a low-pass filter whose cut-off period is about 5×10^7 years.

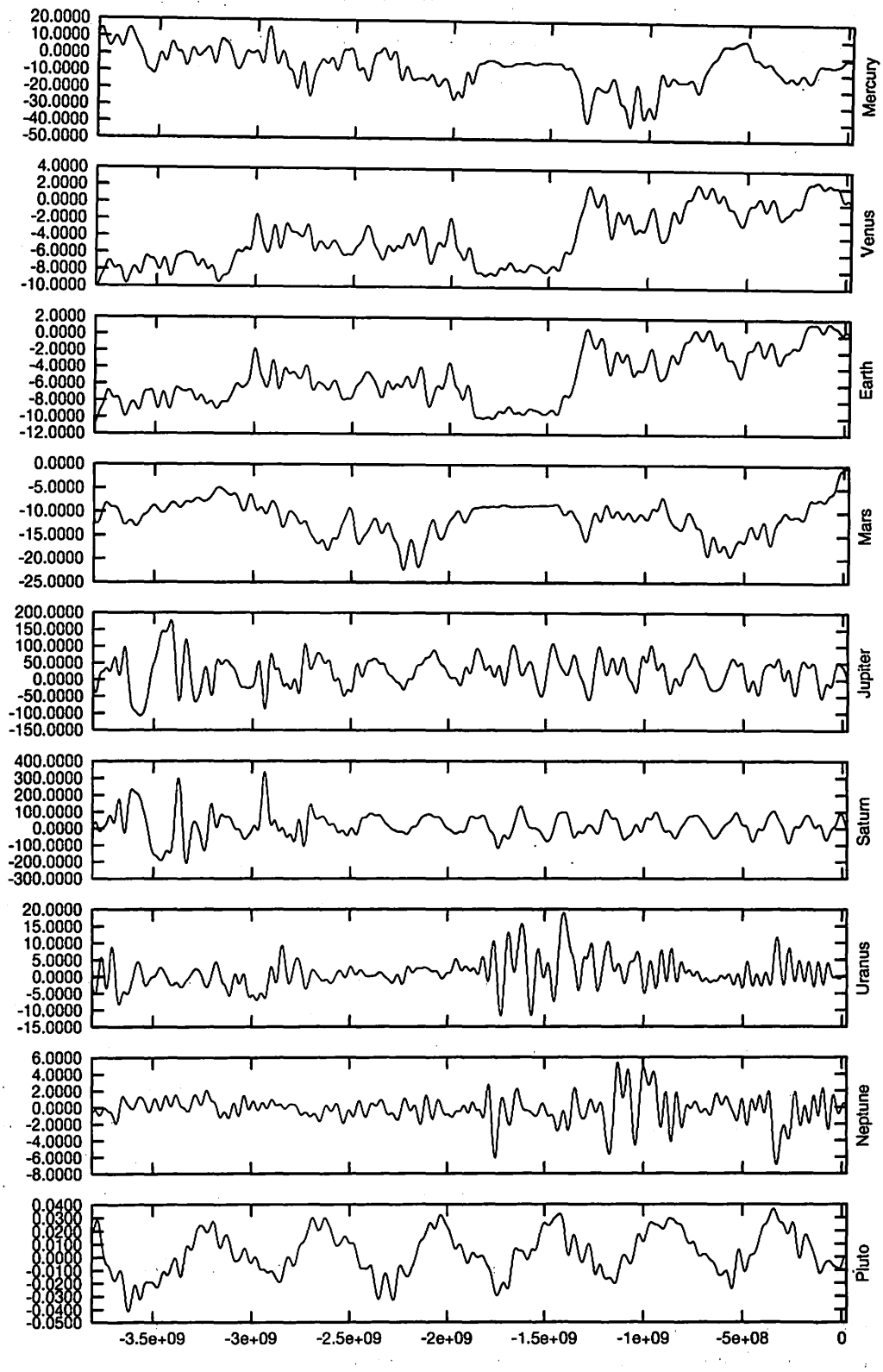

Figure 8. $m(G - G_0)$ in minus series using low-pass filtered Kepler orbital elements. The unit is $10^{-12} M_\odot \cdot \mathrm{AU}^2 \cdot \mathrm{day}^{-1}$.

In Figures 9 through 16 we show several panels for each time-series data which indicate the long-range variation of total energy and angular momentum. Upper three (or six) panels for each time-series show the long-periodic variation of total energy (noted as E-E0), total angular momentum (G-G0), and its vertical component (H-H0) calculated from the low-pass filtered orbital elements described in the previous section. E0, G0, H0 denotes the initial values of each quantity, and absolute difference from the initial values are plotted in the panels. For whole nine planets integrations (minus, plus, emb-minus, emb-plus, emb-plus-I, jan25), we add three more panels for each quantity (E-E0, G-G0, H-H0) of inner four terrestrial planets noted as inner 4. Unit of energy used here is $10^{-12} M_\odot \cdot \mathrm{AU}^2 \cdot \mathrm{day}^{-2}$, and that of angular momentum is $10^{-12} M_\odot \cdot \mathrm{AU}^2 \cdot \mathrm{day}^{-1}$.

As you can recognize from perturbation theories, the amplitude of long-periodic oscillation is much smaller than that of short-periodic one. So we have to be careful enough whether or not the apparent long-range variation of total energy and total angular momentum is a product of numerical error. To check it, we add two more panels (lower two ones) which indicate numerical errors of total energy En-En0 and total angular momentum An-An0, including all the frequency-bin. In the case of whole nine planets integration, amplitude of the long-range variation of total energy and angular momentum is significantly larger than that for the numerical error (e.g. Figure 9). In the case of outer five planet integration, amplitude of the angular momentum variation is large enough, but amplitude of the energy variation E-E0 seems to be somewhat smaller than the numerical error, En-En0 (*e.g.* Figure 16). The relatively large amplitude of numerical error perhaps results from the short-periodic terms of the error Hamiltonian of the symplectic map. Variation amplitude of time-averaged error Hamiltonian may be much smaller than what is shown as En-En0 in Figure 16, so the long-range energy variation shown in the figures is expected not to be unrealistic.

Comparing the variations of energy and angular momentum of inner 4 planets and total 9 planets, it is apparent that the amplitude of those of inner 4 planets are much smaller than those of total 9 planets; the amplitudes of outer 5 planets are much larger than those of inner 4 planets. This does not mean that the inner terrestrial planetary subsystem is more stable than the outer one: simply due to the smallness of four terrestrial planets' masses than masses of outer jovian planets, or to the negligibility of the gravitational effect of terrestrial planets on the stability of outer jovian planets. Rather, inner planetary subsystem can be unstable more rapidly than the outer one because of its shorter orbital timescales. This may be seen in the panels noted inner 4 in which the longer-periodic oscillations are more irregular than in the panels noted total 9, i.e. those of outer five planets. It may be a symptom that the inner terrestrial planetary subsystem is diffusing chaotically in the timespan of this 10^9 to 10^{10} years.

3.3 Specific description of the stability of planetary orbits

Besides the global stability of planetary motion described above, there are several specific points which we should notice in the integration results.

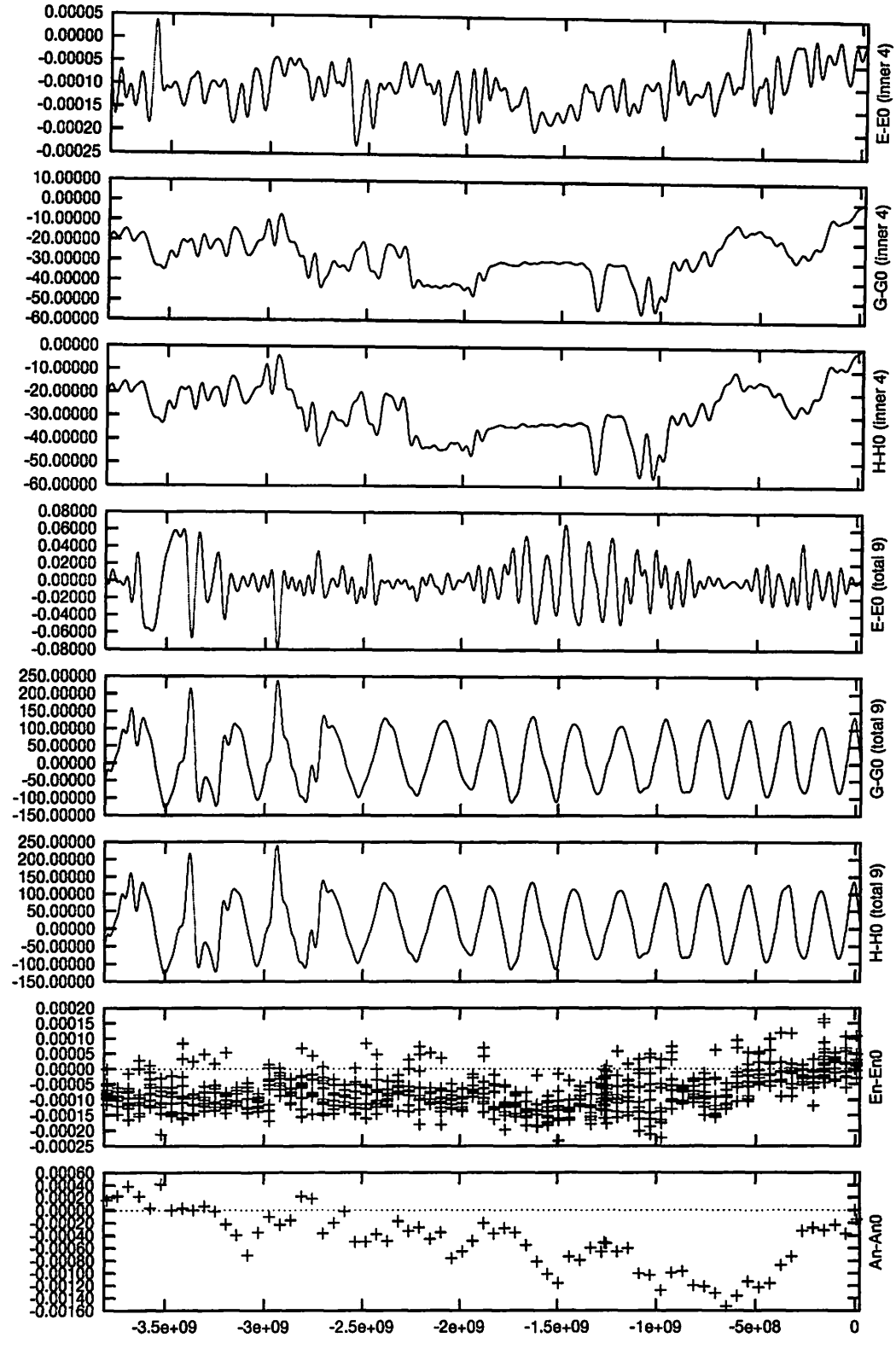

Figure 9. Upper six: total energy $(E - E_0)$, angular momentum $(G - G_0)$ and its vertical component $(H - H_0)$ calculated by the low-pass filtered orbital elements in **minus** series. E is calculated from one of the Delauney elements L as $E = -\mu^2/2L^2$. Lower two: numerical error for total energy $(E_n - E_{n0})$ and angular momentum $(A_n - A_{n0})$. The unit of energy is $10^{-12}M_\odot \cdot \mathrm{AU}^2 \cdot \mathrm{day}^{-2}$, and that of angular momentum is $10^{-12}M_\odot \cdot \mathrm{AU}^2 \cdot \mathrm{day}^{-1}$.

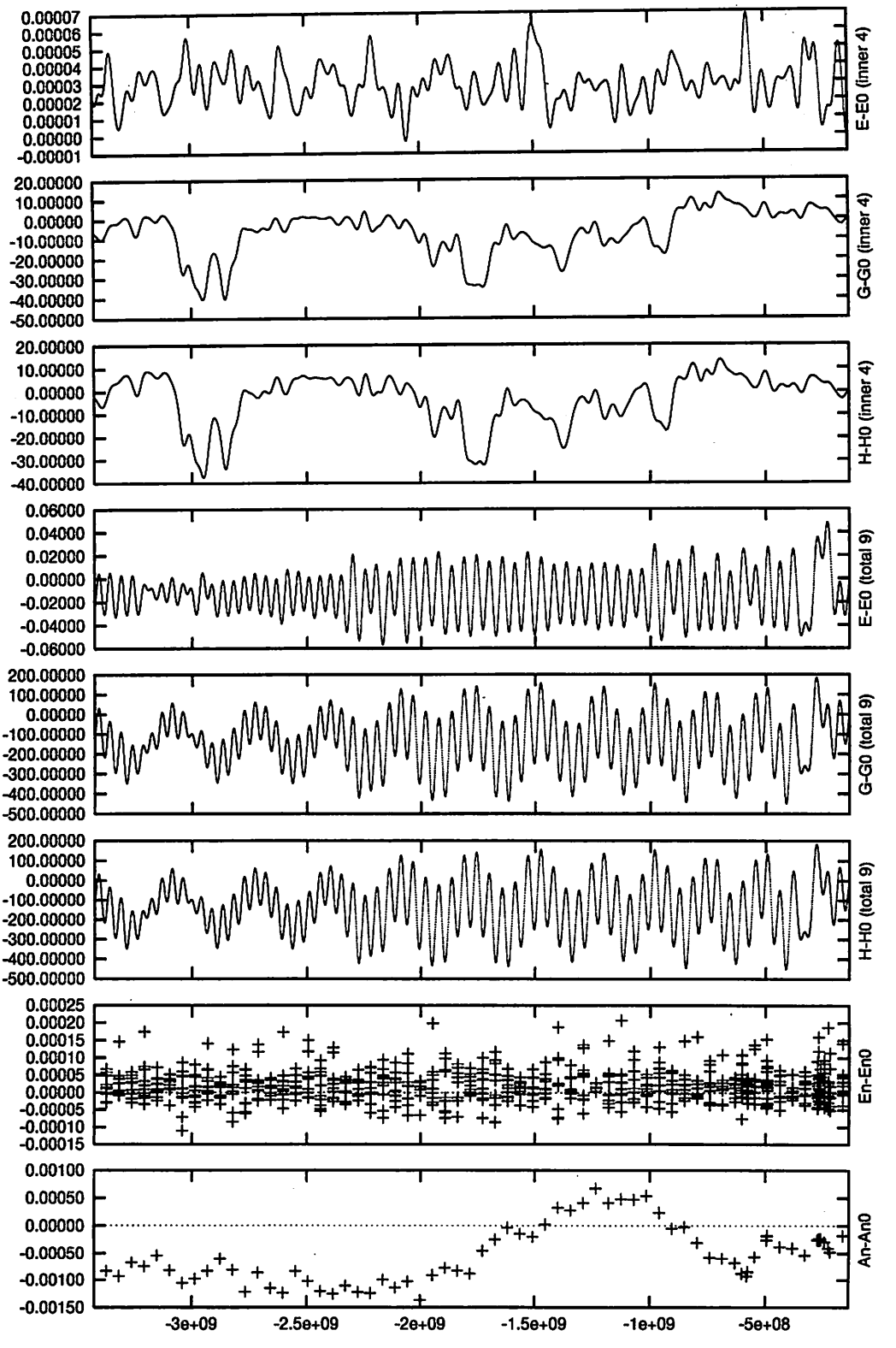

Figure 10. Same as Figure 9 for emb-minus series.

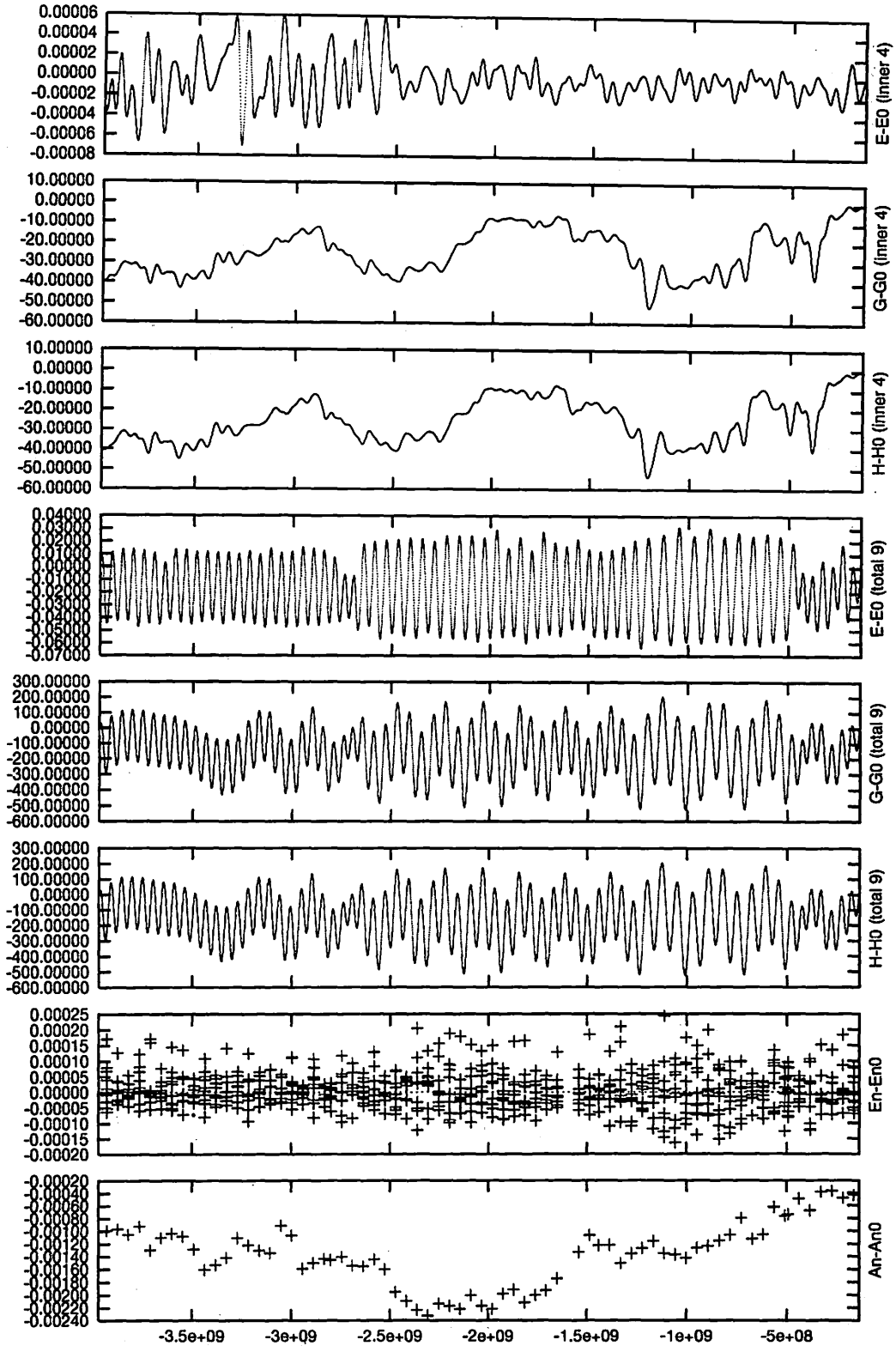

Figure 11. Same as Figure 9 for jan25 series.

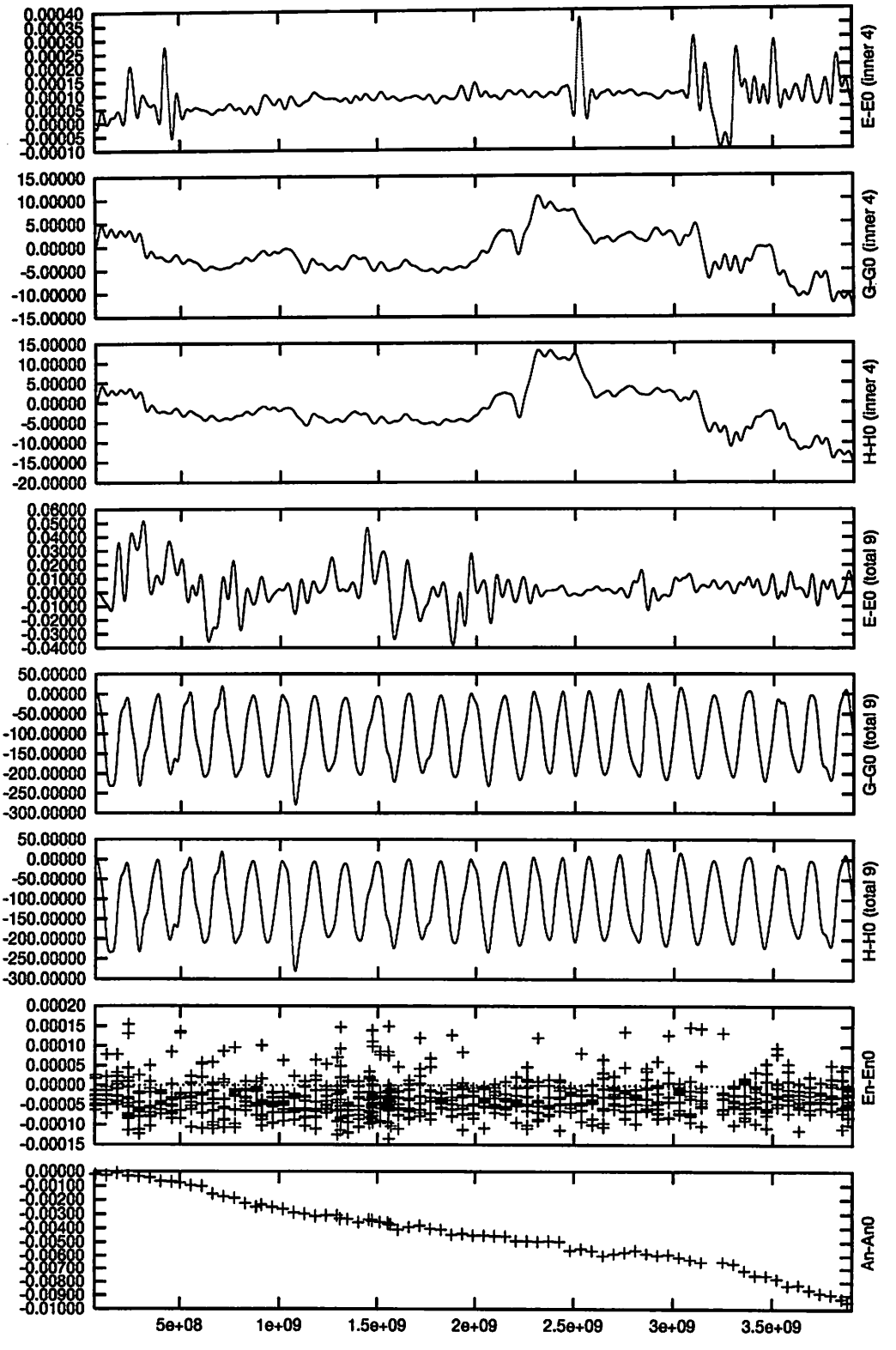

Figure 12. Same as Figure 9 for emb-plus-I series.

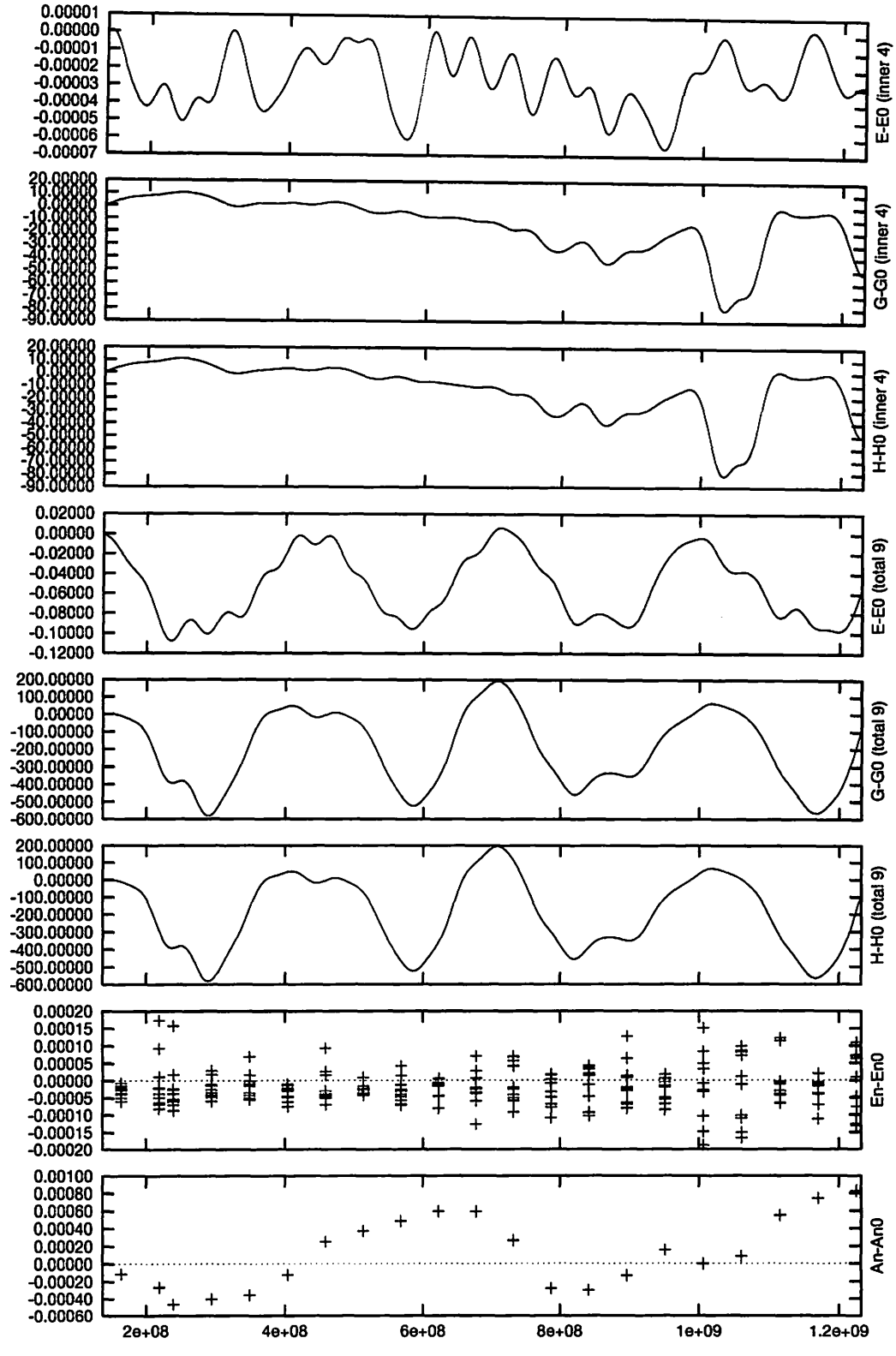

Figure 13. Same as Figure 9 for plus series.

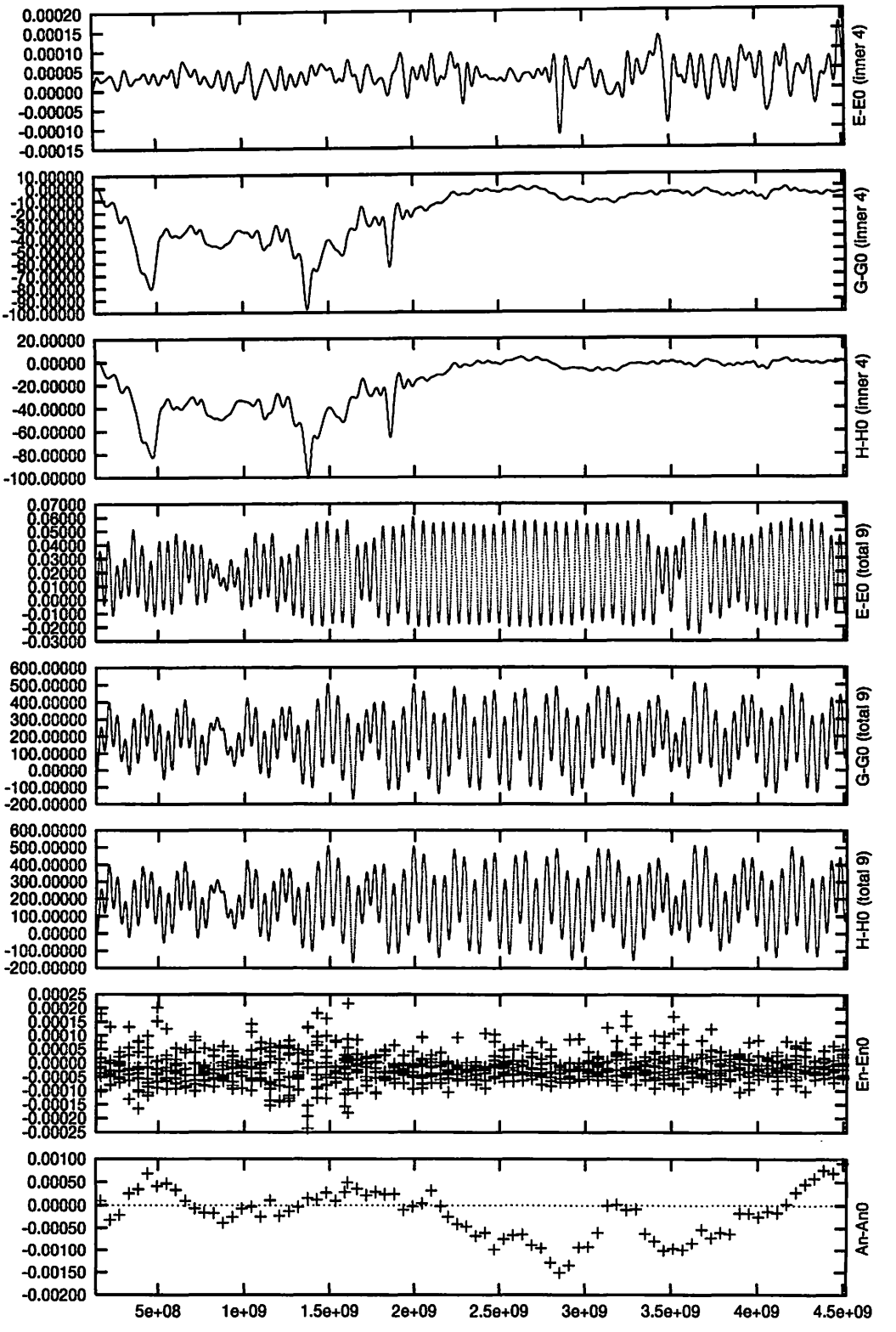

Figure 14. Same as Figure 9 for emb-plus series.

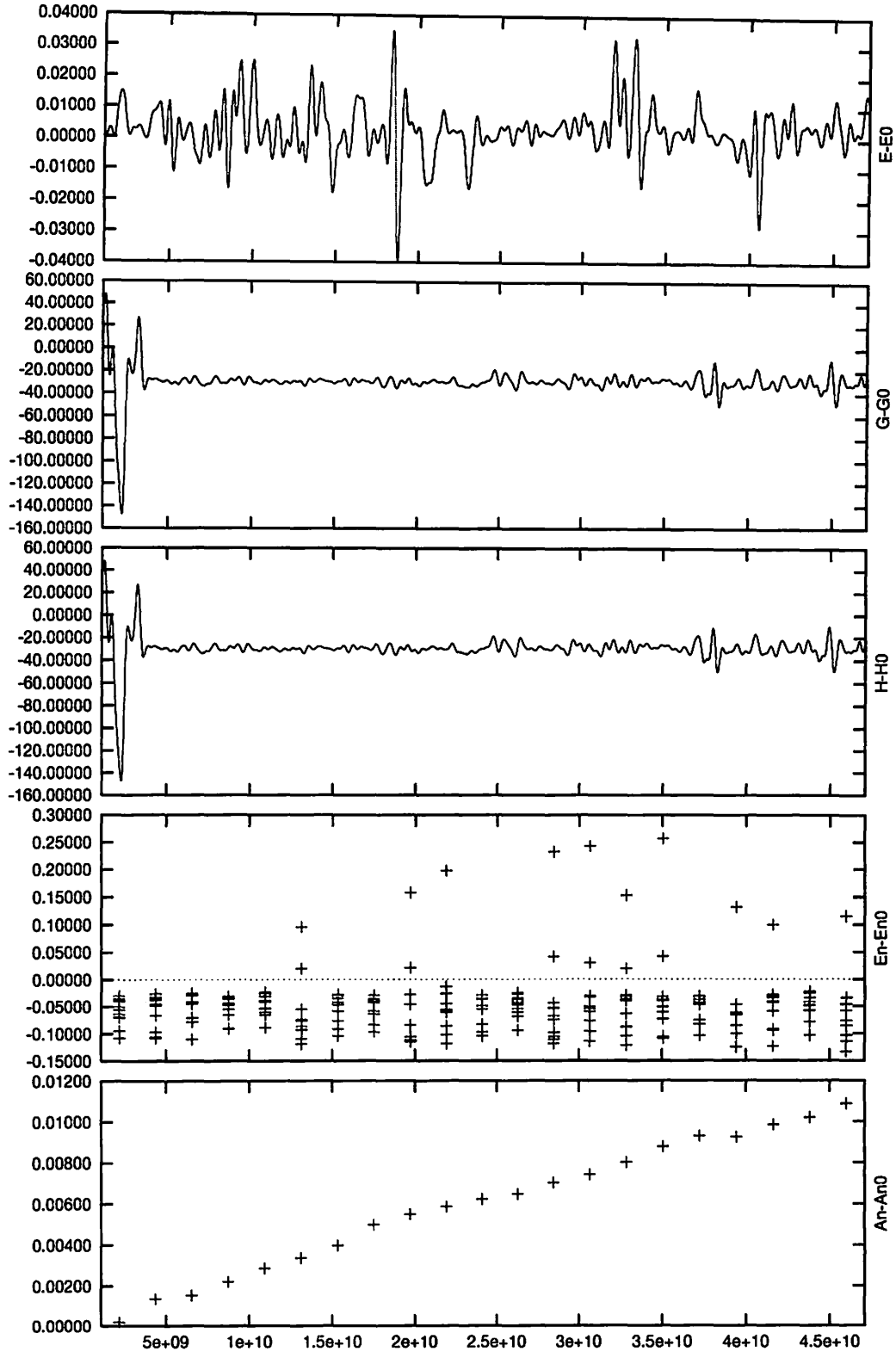

Figure 15. Same as Figure 9 for 50G+ series.

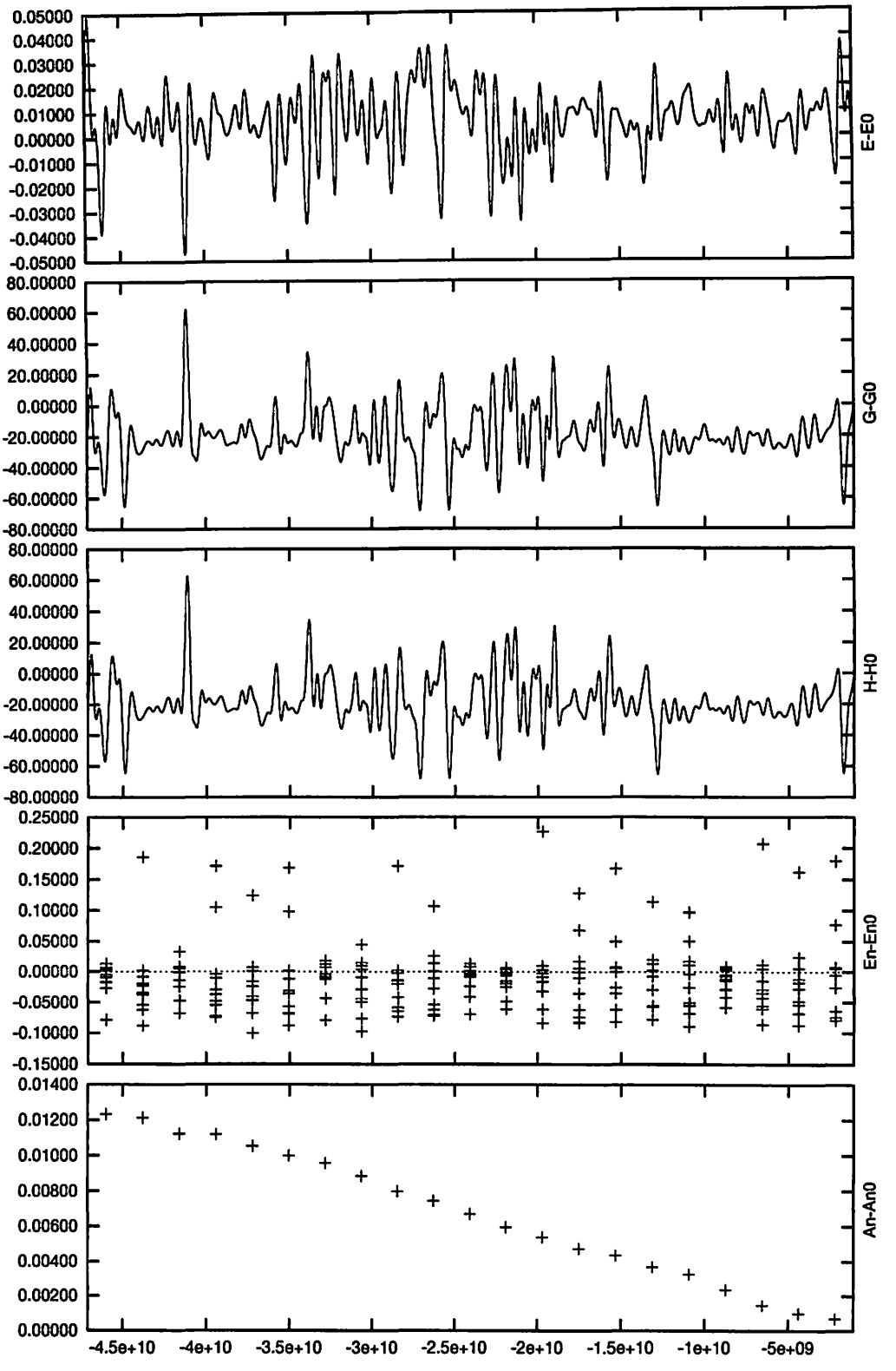

Figure 16. Same as Figure 9 for 50G- series.

3.3.1 Coupling of some neighboring planet pairs

We can see from the low-pass filtered orbital elements that some planets are coupled in terms of energy and angular momentum exchange. Venus and Earth make an apparent strong couple (Figures 17 to 20). They show negative correlation in exchange of energy and positive correlation in exchange of angular momentum. The negative correlation in exchange of energy means that the two planets compose a closed dynamical system in terms of orbital energy. Positive correlation in exchange of angular momentum (and also eccentricity) between any two planets means that orbits of the two planets are aligned, shepherded by outside disturber. A candidate of the perturber for the Venus–Earth system is Mercury and possibly Mars. Mercury and Mars show a weak negative correlation in exchange of angular momentum.

In the outer jovian planetary subsystem, Jupiter–Saturn and Uranus-Neptune can be considered to make couples with each other (Figures 21 and 22). They show negative correlation in exchange of both energy and angular momentum. But strength of the coupling is not so strong in this case, compared with Venus–Earth pair. This is partly because of the exchange of energy and momentum between low and high frequency domain is larger than the exchange in each planetary pair.

Absolute amplitudes of the orbital energy exchange are very small as perturbation theories expect, but it surely exists in our results. The sign of correlations in exchange of total energy is generally negative, which implies that the long-term energy exchange is limited only to neighboring pairs of planets, unlike the angular momentum exchange between the Venus–Earth system and other planet such as Mercury or Mars.

For comparison with the long-term exchange of such physical quantities, we consider shorter timescale cases. In shorter timescale, the Jupiter–Saturn and Venus–Earth pair show negative correlations in exchange of angular momentum. This is natural since these neighboring planets have masses of the same order, and must interact each other. This situation is seen in the result of a traditional secular perturbation theory as Figures 23 and 24.

In traditional secular perturbation theories, eccentricity, longitude of perihelion, orbital inclination, and longitude of ascending node of planetary orbits can be expressed by the following trigonometric series to the first order in masses and second order in eccentricity and inclination (Brouwer and van Woerkom, 1950; Brouwer and Clemence, 1961):

$$e_i \sin \varpi_i = \sum_{j=1}^{n} M_{i,j} \sin g_j t + \beta_j, \quad e_i \cos \varpi_i = \sum_{j=1}^{n} M_{i,j} \cos g_j t + \beta_j, \tag{5}$$

$$e_i \sin I_i \sin \Omega_i = \sum_{j=1}^{n} L_{i,j} \sin f_j t + \delta_j, \quad e_i \sin I_i \cos \Omega_i = \sum_{j=1}^{n} L_{i,j} \cos f_j t + \delta_j, \tag{6}$$

where we denote the number of planets by n. Characteristic frequencies (called "basic planetary frequencies") (g_i, f_i) are functions of masses and semimajor axes of planets, and are obtained by solving an eigenvalue problem of $n \times n$ matrix derived from the equations of motion. Corresponding eigenvectors $(M_{i,j}, L_{i,j})$ and initial phases (β_j, δ_j) are determined from the initial values of orbital elements. Values of $M_{i,j}$, $L_{i,j}$, g_j, f_j, β_j, and δ_j used in Brouwer and van Woerkom (1950)'s theory are listed in Tables 4 and 5.

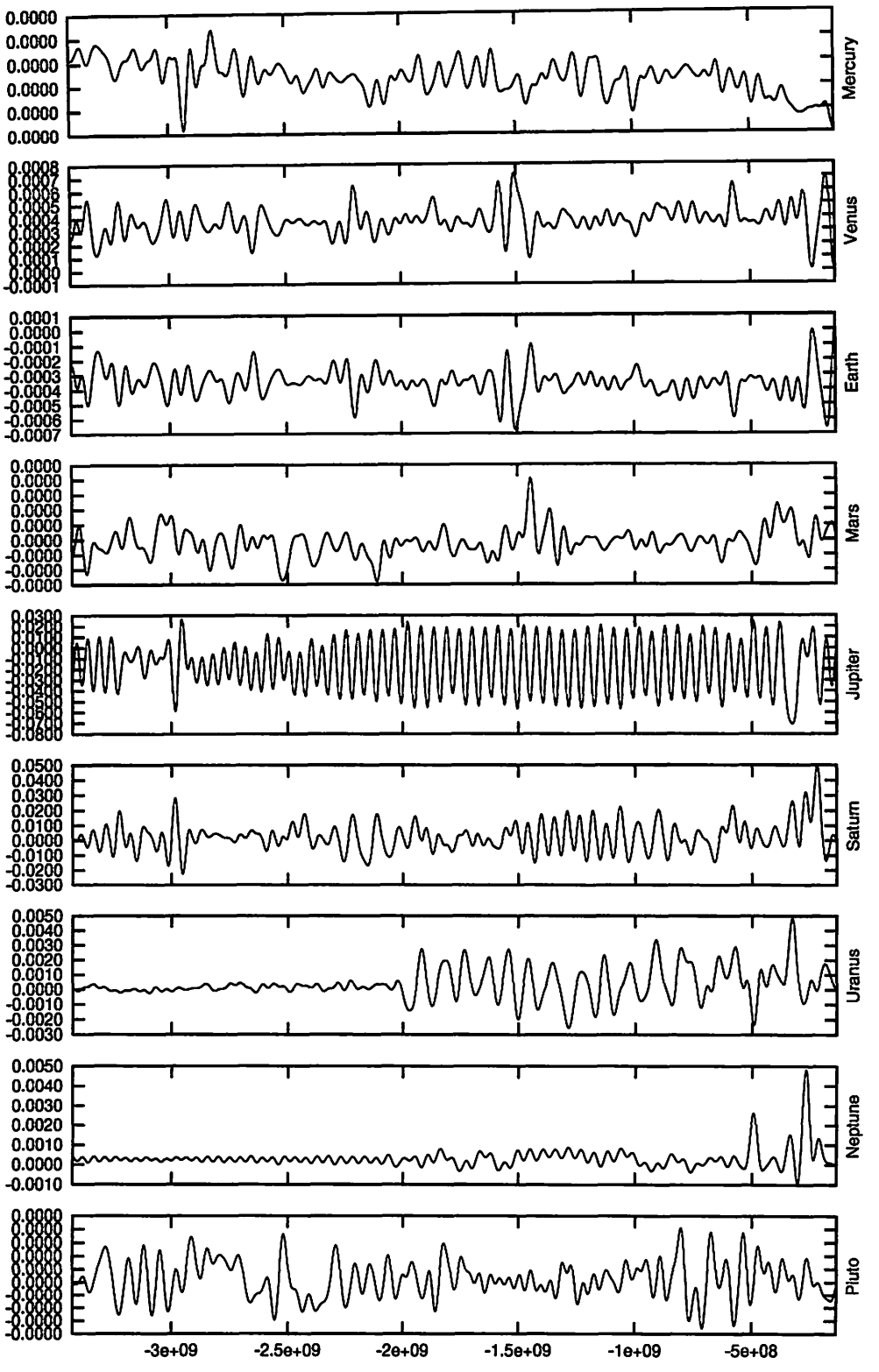

Figure 17. $m(E - E_0)$ in emb-minus series.

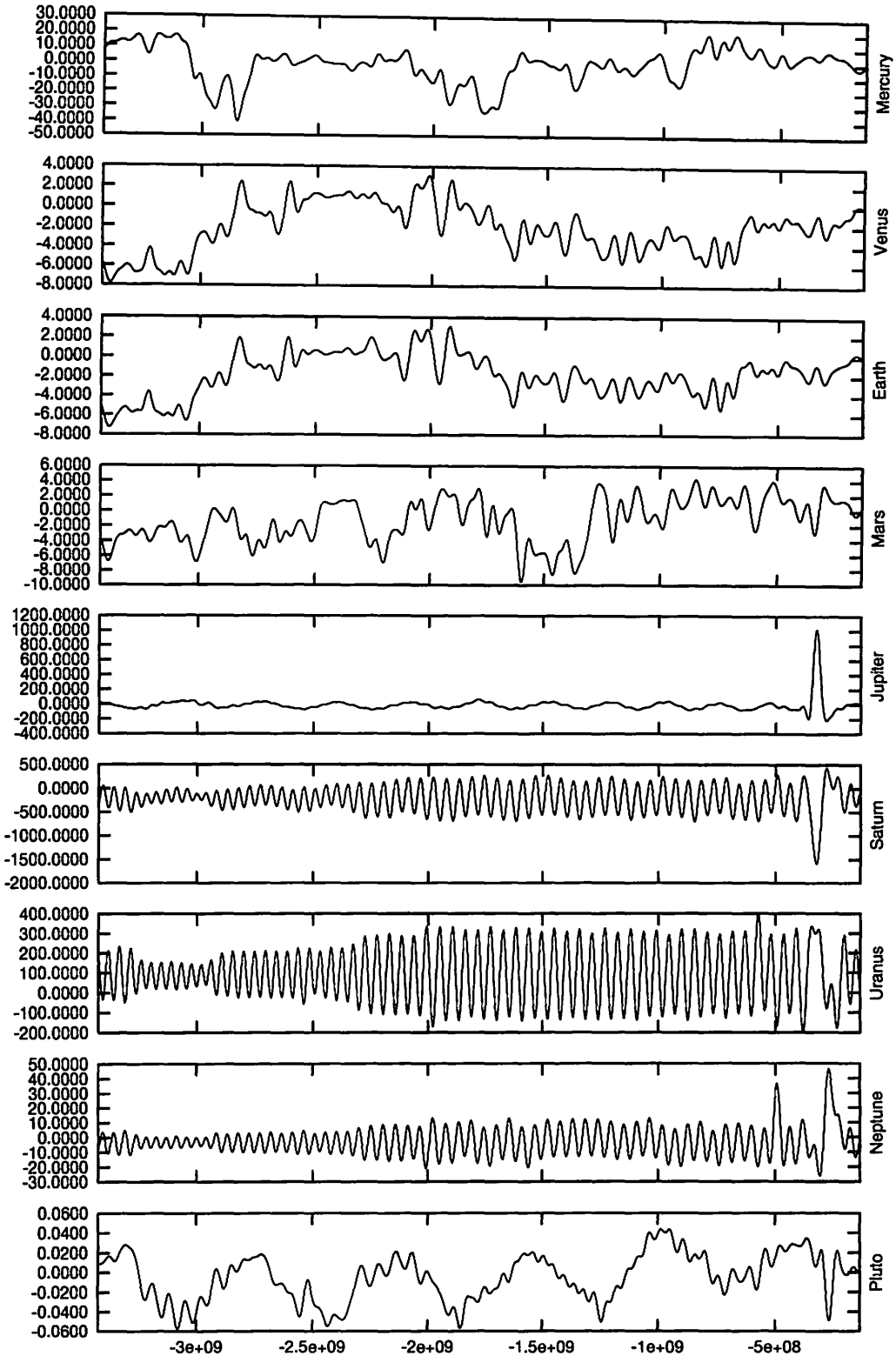

Figure 18. $m(G - G_0)$ in emb-minus series.

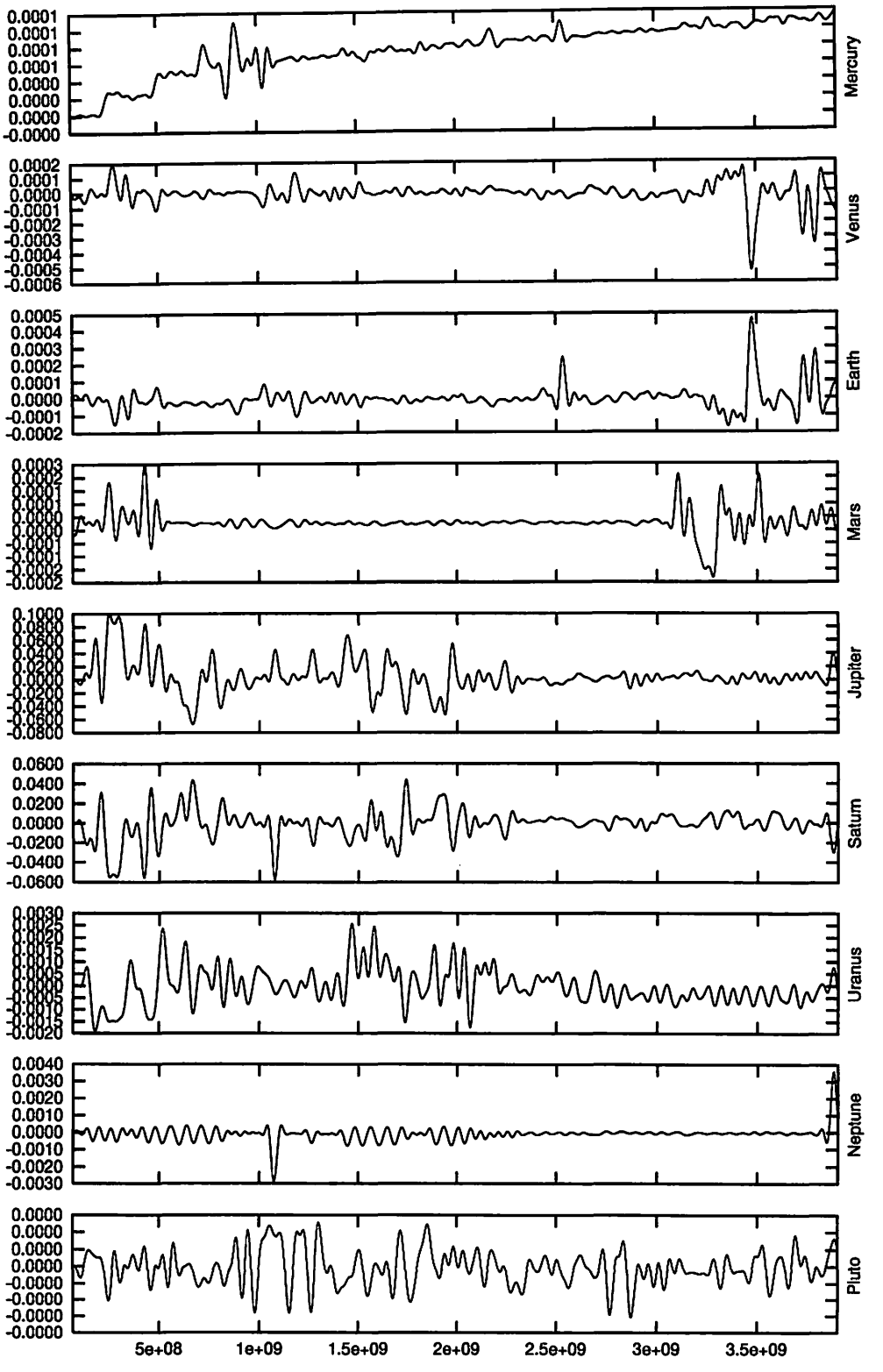

Figure 19. $m(E - E_0)$ in emb-plus-I series.

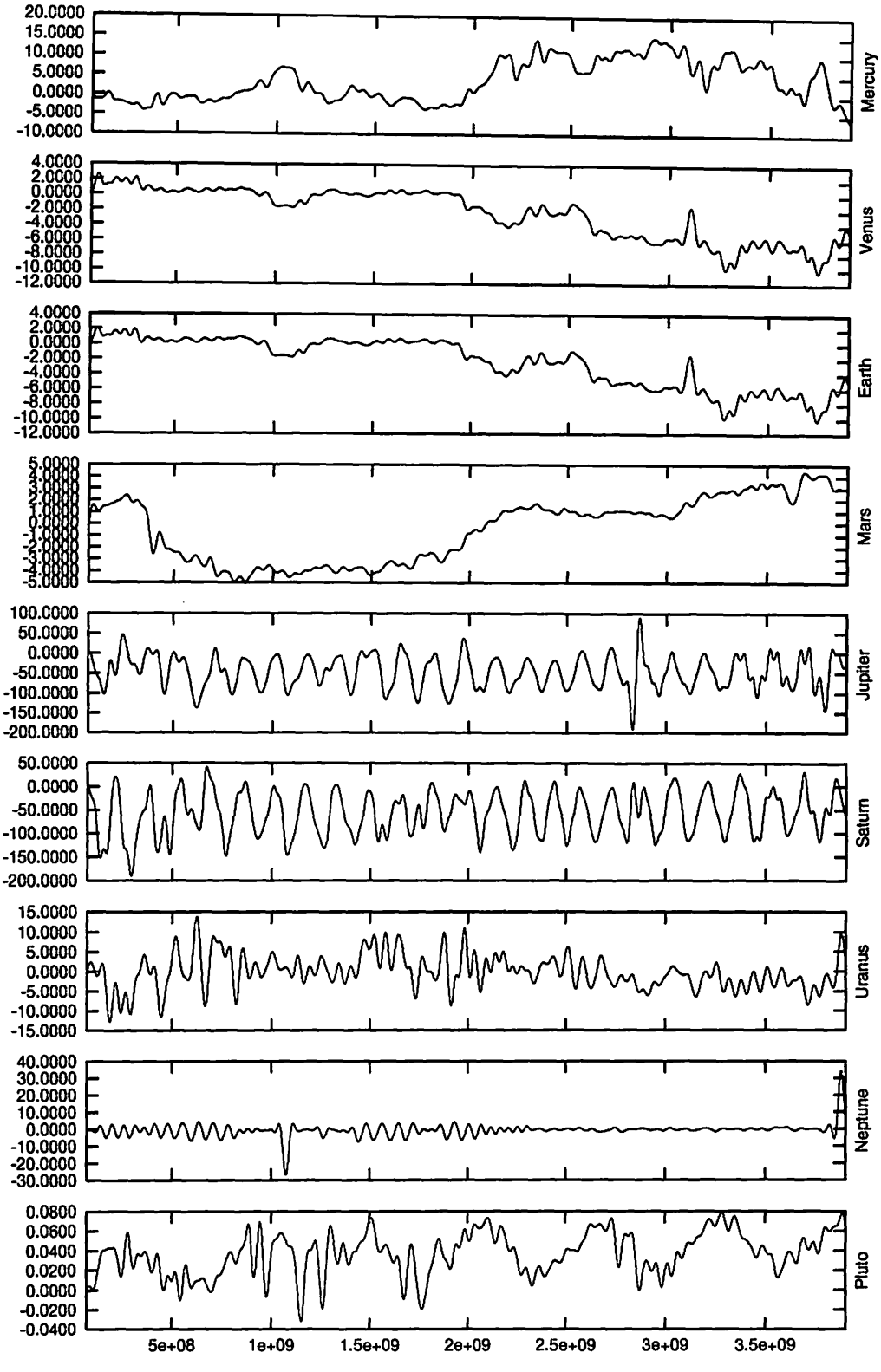

Figure 20. $m(G - G_0)$ in emb-plus-I series.

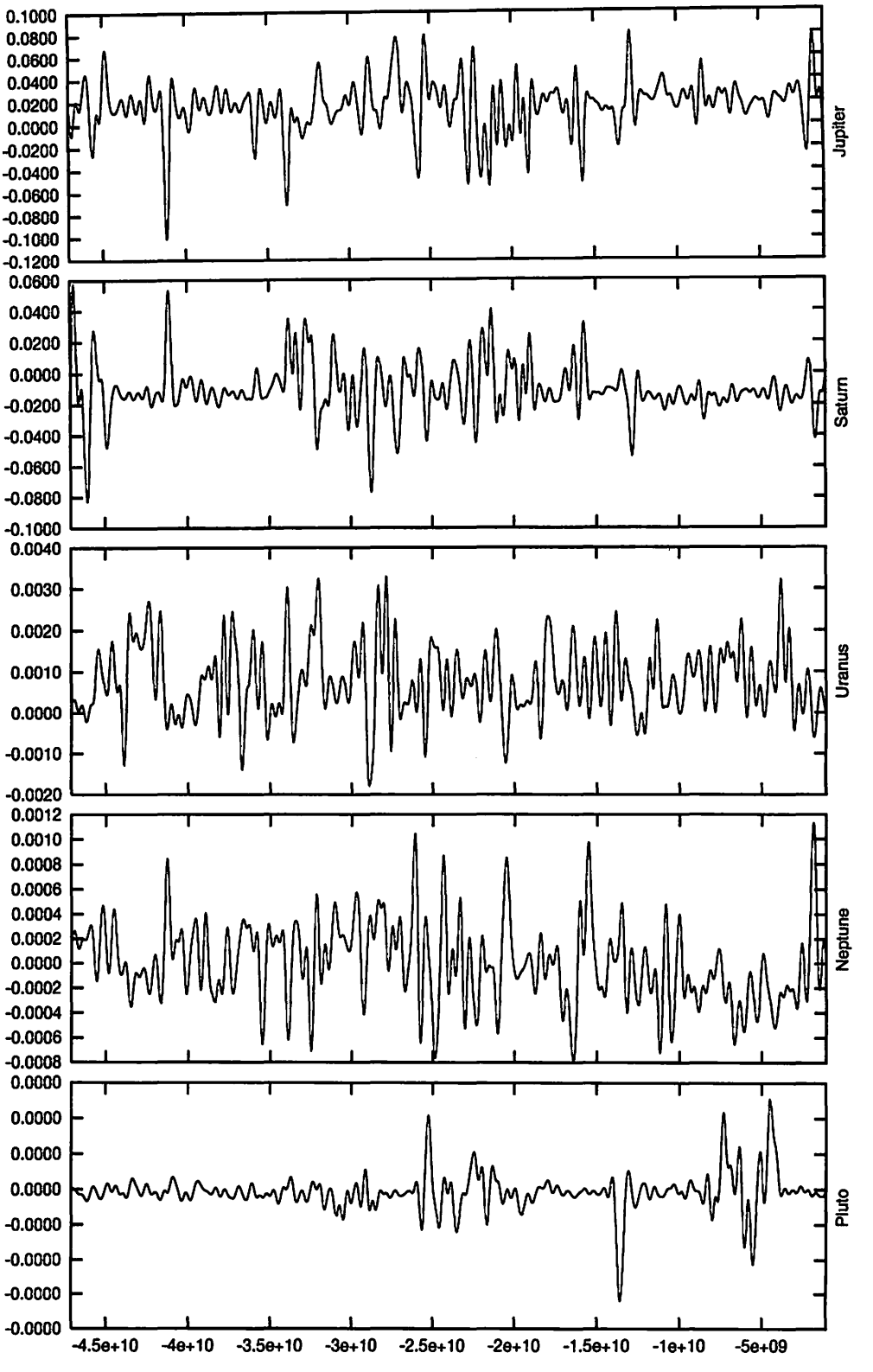

Figure 21. $m(E - E_0)$ in 50G- series.

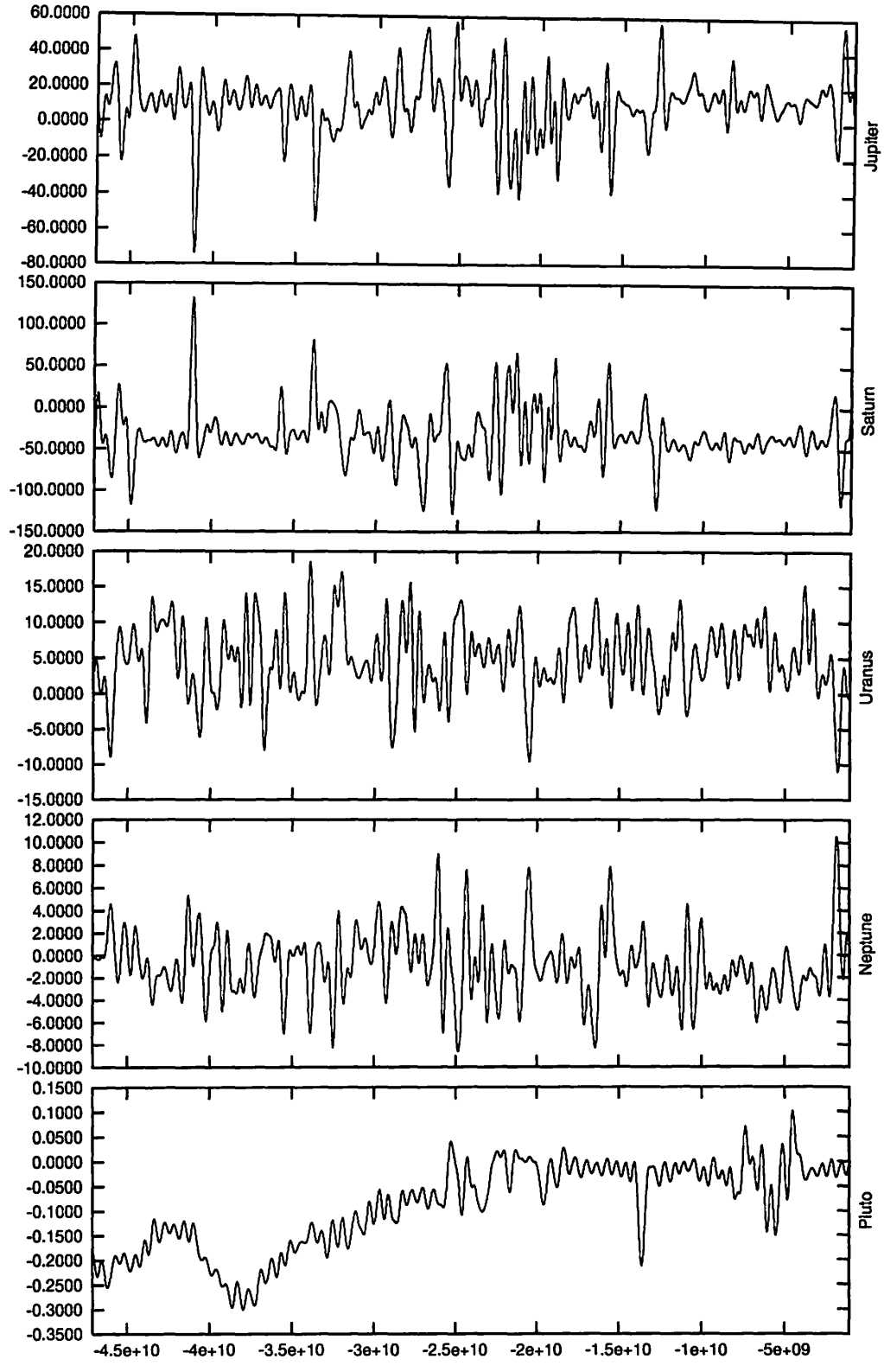

Figure 22. $m(G - G_0)$ in 50G- series.

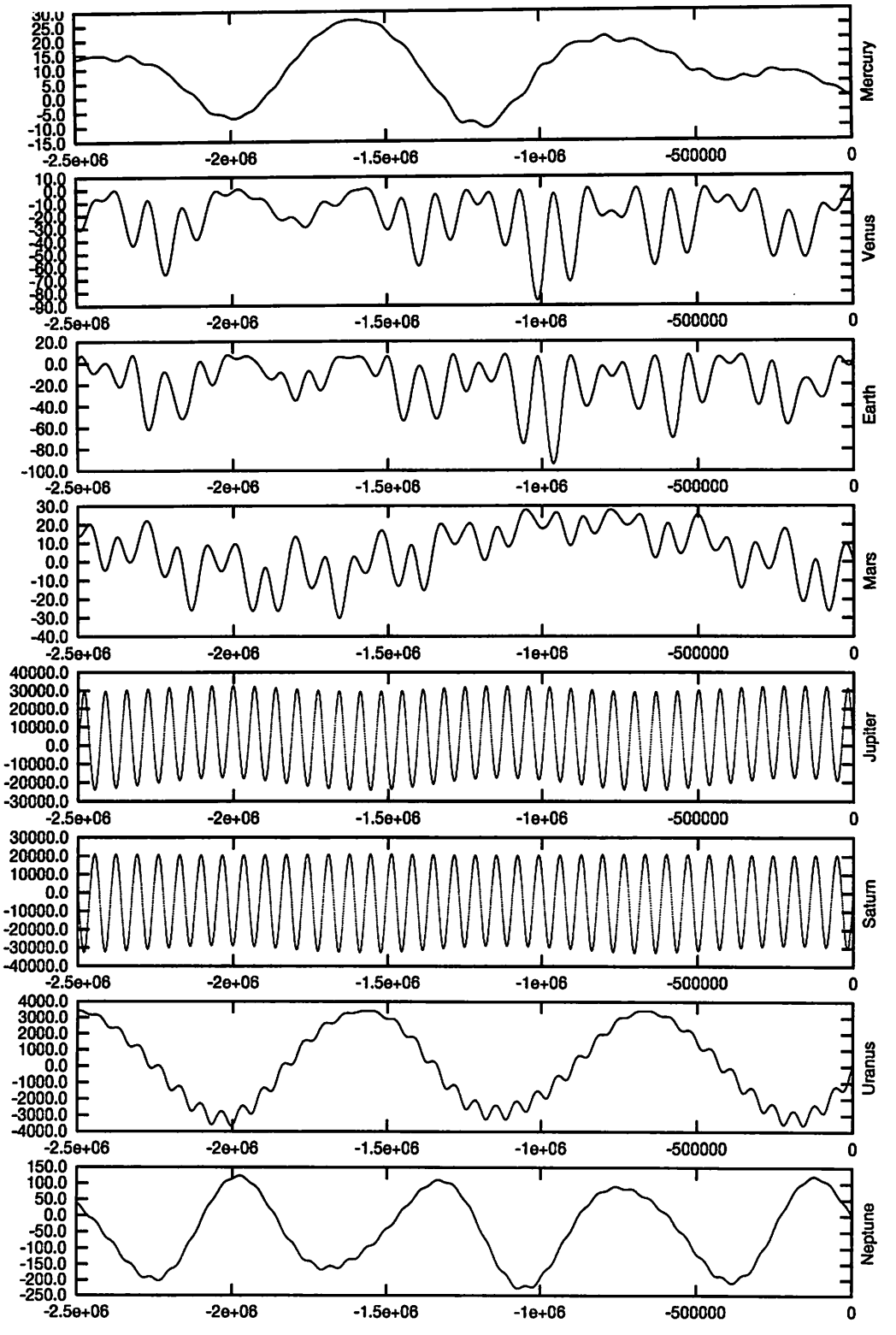

Figure 23. Short periodic variation of total angular momentum G calculated by the secular perturbation theory of Brouwer and van Woerkom (1950).

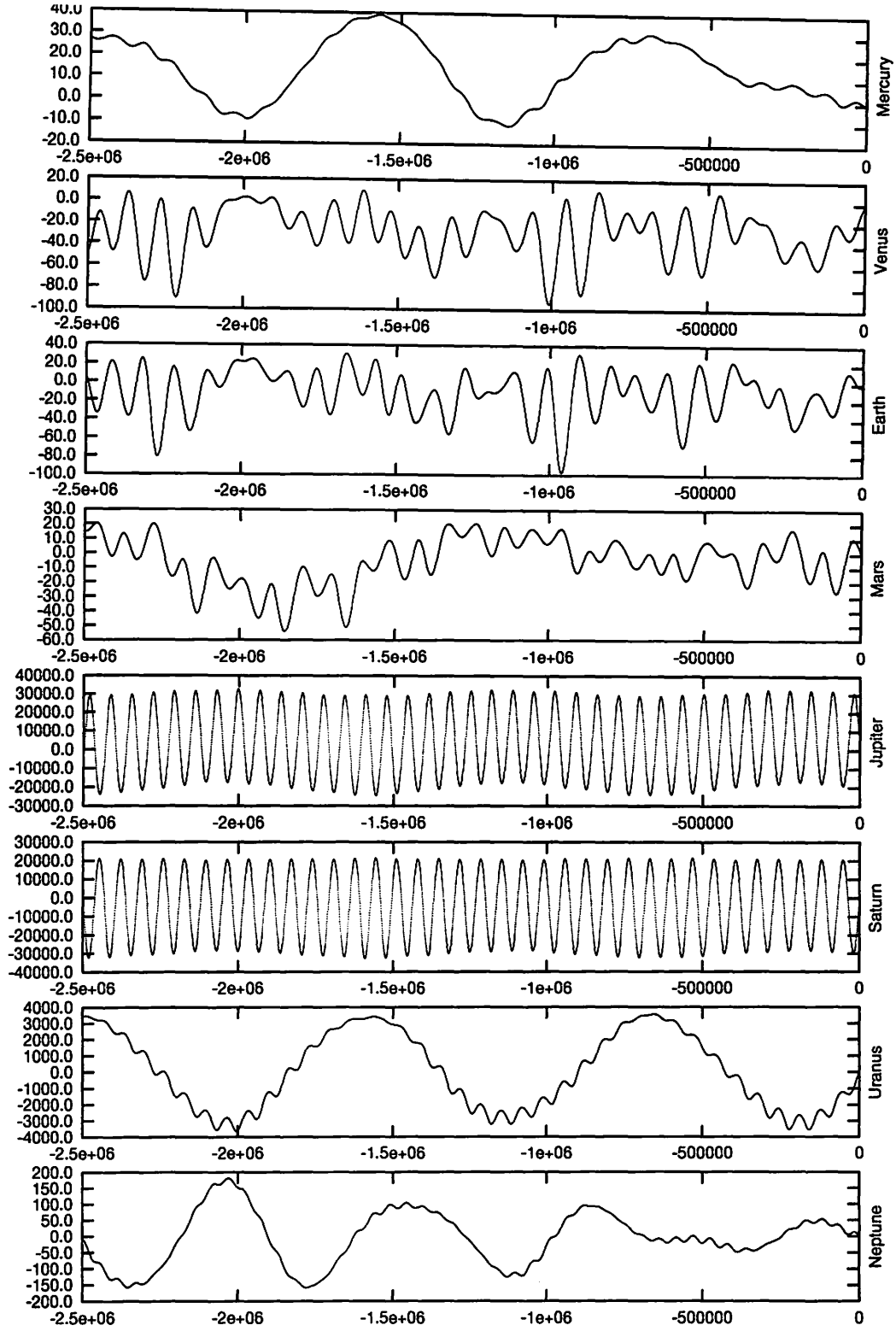

Figure 24. Short periodic variation of vertical component of total angular momentum H calculated by the secular perturbation theory of Brouwer and van Woerkom (1950).

Table 4. Planetary basic frequencies g_j, f_j, periods ($P_j^g = 2\pi/g_j$ and $P_j^f = 2\pi/f_j$), initial phases β_j and δ_j in (5) and (6) by Brouwer and van Woerkom (1950). Terms $j = 9$ and $j = 10$ are derived from the 5:2 mean motion commensurability between Jupiter and Saturn ("the great inequality"): $g_9 = 2g_5 - g_6$, $g_9 = 2g_6 - g_5$, $\beta_9 = 2\beta_5 - \beta_6$, $\beta_{10} = 2\beta_5 - \beta_6$. One of the f_j should be zero because of the preservation law of total angular momentum ($f_5 = 0$ here).

j	g_j (arcsec/y)	P_j^g (year)	β_j (degree)	f_j (arcsec/y)	P_j^f (year)	δ_j (degree)
1	5.463255	237221.22	92.18164	−5.201537	249157.12	190.43255
2	7.344791	176451.58	196.88119	−6.570802	197236.20	318.05685
3	17.328377	74790.62	335.22366	−18.743586	69143.65	255.03057
4	18.002327	71990.69	317.94813	−17.633305	73497.28	296.54103
5	4.128084	313947.10	31.17370	0	—	—
6	23.085793	56138.42	131.68619	−25.733549	50362.27	127.36669
7	2.718661	476705.26	131.94363	−2.902663	446486.55	315.06348
8	0.633254	2046572.15	69.43109	−0.677522	1912853.01	202.29272
9	−14.829625	87392.63	−69.33879	—	—	—
10	42.043502	30825.22	232.19868	—	—	—

Table 5. Amplitude M_{ij} and $L_{i,j}$ in integer format in (5) and (6) by Brouwer and van Woerkom (1950). Unit is 10^{-7}radian. Number of planets (i) are Mercury = ☿, Venus = ♀, Earth = ⊕, Mars = ♂, Jupiter = ♃, Saturn = ♄, Uranus = ♅, Neptune = ♆ from the left side.

	$M_{i,j}$							
j	☿	♀	⊕	♂	♃	♄	♅	♆
1	1745400	60961	39162	6382	−88	−81	35	1
2	−254981	209439	163395	28984	−128	−136	33	1
3	15369	−125529	104345	297221	−10	−70	4	0
4	−16918	148334	−148347	723712	−7	−77	4	0
5	357144	190892	183400	186080	448188	329124	−318825	6345
6	9596	582	28264	150176	−153546	486278	−24759	−1131
7	4270	4184	4427	5860	14701	14794	304341	−32297
8	65	99	115	183	531	642	14312	93764
9	−2089	−1088	−1218	−1992	−1591	−4896	1966	−29
10	1033	369	1471	6391	−5380	20200	−1575	−34
	$L_{i,j}$							
j	☿	♀	⊕	♂	♃	♄	♅	♆
1	1244934	117814	84889	18011	−207	−264	221	6
2	−354475	100420	80958	18012	−130	−184	−95	5
3	40948	−267985	244823	−358910	−2	−48	4	0
4	11625	−68514	45254	502516	−18	−183	17	2
6	2781	1212	28112	96481	−63064	157245	−6946	−771
7	−33230	−19160	−17308	−12561	−9571	−7803	175988	−20737
8	−14452	−13231	−12969	−12286	−11689	−11267	10958	117522

3.3.2 Resonances in Neptune-Pluto system

Kinoshita and Nakai (1995, 1996) integrated orbits of outer five planets over $\pm 5.5 \times 10^9$ years. They found that several resonances between Neptune and Pluto can be maintained during the whole integration period, and that the resonances may be one of the main causes of the stable existence of Pluto. Major four resonances found in previous researches are as follows:

1. Mean motion resonance between Neptune and Pluto (2:3). The critical argument $\theta_1 = 3\lambda_P - 2\lambda_N - \varpi_P$ librates around 180° with the amplitude about 80°, and the libration period is about 2×10^4 years.

2. Pluto's argument of perihelion $\omega_P = \theta_2 = \varpi_P - \Omega_P$ librates around 90° with the period of about 3.8×10^6 years. The dominant periodic variations of Pluto's eccentricity and inclination are synchronized with the libration of its argument of perihelion. The fact is expected from the secular perturbation theory constructed by Kozai (1962).

3. The longitude of Pluto's node referred to the longitude of Neptune's node, $\theta_3 = \Omega_P - \Omega_N$, circulates and the period of this circulation is equal to the period of θ_2 libration. When θ_3 becomes zero, i.e. longitudes of ascending nodes of Neptune and Pluto overlap, Pluto's inclination becomes maximum, eccentricity becomes minimum, and argument of perihelion becomes 90°. When θ_3 becomes 180°, Pluto's inclination becomes minimum, eccentricity becomes maximum, and argument of perihelion becomes 90° again. Williams and Benson (1971) expected the existence of this type of resonance, which was confirmed afterwards by Milani *et al.* (1989).

4. An argument $\theta_4 = \varpi_P - \varpi_N + 3(\Omega_P - \Omega_N)$ librates around 180° with very long period, about 5.7×10^8 years.

In our numerical integrations, the resonances 1, 2 and 3 are well maintained, and variation of the critical arguments $\theta_1, \theta_2, \theta_3$ remain similar during the whole integration period (Figures 25, 26, 27). However the fourth resonance shows an interesting behavior: the critical argument θ_4 alternates libration and circulation in $O(10^{10})$-year timescale (Figure 28). This is an interesting fact that Kinoshita and Nakai (1995, 1996)'s short integrations could not find.

In spite that the fourth resonance may not be maintained in this long timespan, Neptune–Pluto system remains completely stable. Thus it seems that the fourth resonance may have little effect on the stability of Neptune–Pluto system.

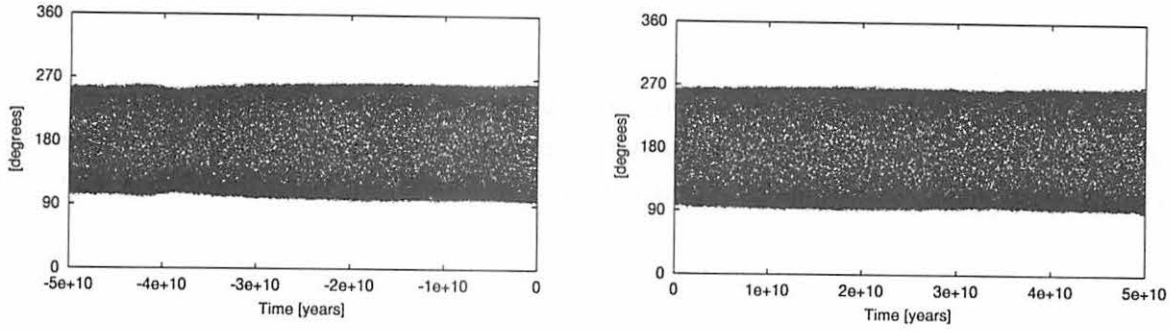

Figure 25. Critical argument θ_1 for 50G- (left) and 50G+ (right) series.

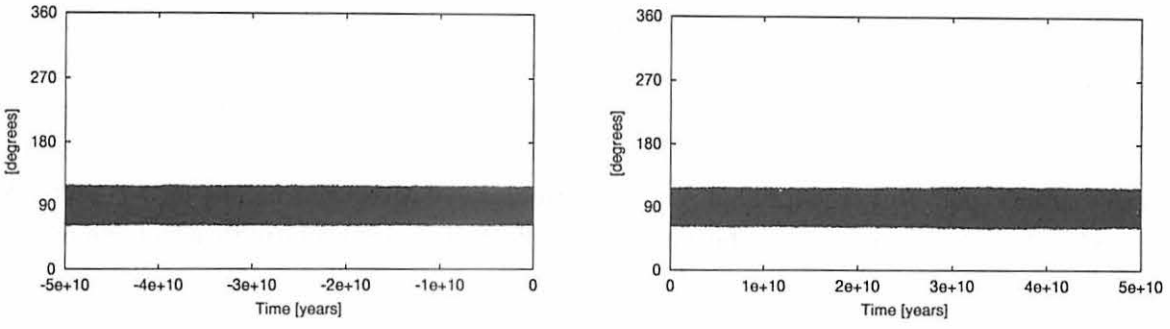

Figure 26. Critical argument θ_2 for 50G- (left) and 50G+ (right) series.

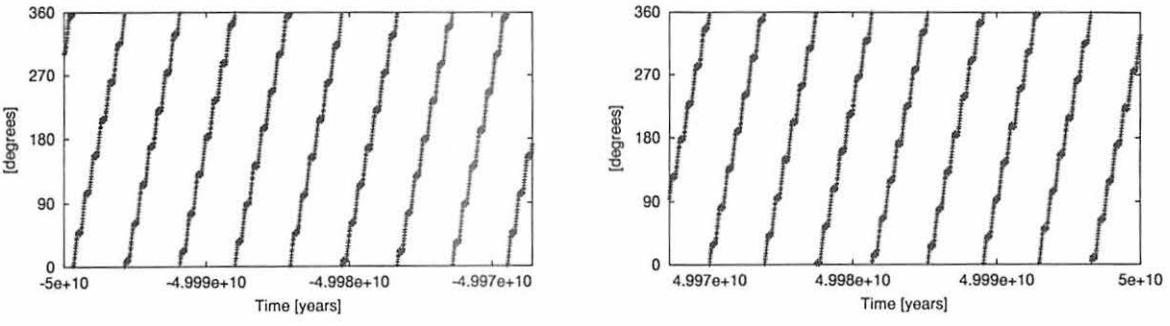

Figure 27. Critical argument θ_3 for trailing parts of 50G- (left) and 50G+ (right) series.

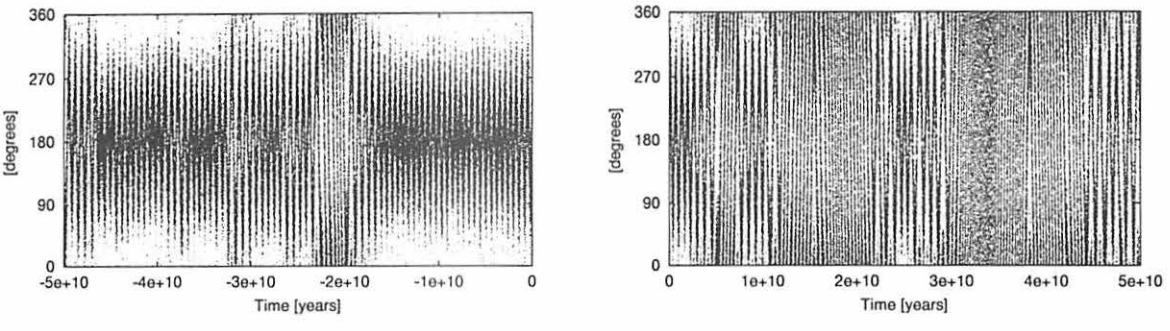

Figure 28. Critical argument θ_4 for 50G- (left) and 50G+ (right) series.

3.3.3 Time-frequency analysis

The orbital motion of planets shows global stability as we see in the previous sections: no orbital crossings nor close encounters between any pair of planet. However, chaotic nature of planetary dynamics can change the oscillatory period and amplitude slightly in such long timespans. Especially, variations of eccentricity and inclination of Earth have large effect on its surface climate system through solar insolation variation (Milankovitch, 1941; Berger, 1988; Шараф and Будникова, 1969a; Шараф and Будникова, 1969b).

We performed a simple time-frequency analysis using FFT (Fast Fourier Transformation). Some of the resulting periodgrams (such as Figure 29) indicate that the periodicity of eccentricity and inclination changes only slightly during the whole integration period. The rigorous stability of outer five planets is again prominently seen here (Figure 30).

For comparison, we show the FFT results by an accurate perturbation theory by Laskar (1988). Since the numerical models used here and there are different (Laskar's model is more accurate, including the effect of the general relativity), direct comparison of these two results has little meaning. However we can see that both results (Figure 29 and 31, or Figure 30 and 32) agree rather well. Only the difference in the periodicity of Mercury's eccentricity (Figure 29) is somewhat large. This is perhaps because of the effect of general relativity which we neglect in our calculation. The effect of general relativity acts most heavily on the nearest planet to Sun, i.e. Mercury.

Since the orbital elements calculated in Laskar (1988) uses the epoch of J2000.0 ecliptic, we recalculated orbital elements (e, I) on that epoch and draw FFT diagrams. Note that there is no result for Pluto in Figure 32 because Laskar's theory does not include the planet.

Moreover to see the change of periodicity in planetary orbital motion in more detail, we perform many FFTs along the time axis, and superpose the results to make two-dimensional time-frequency maps. Figures 33, 34, 35, 36, 37, and 38 are typical examples of such analyses which indicate time-frequency maps of each planet from Mercury to Neptune.

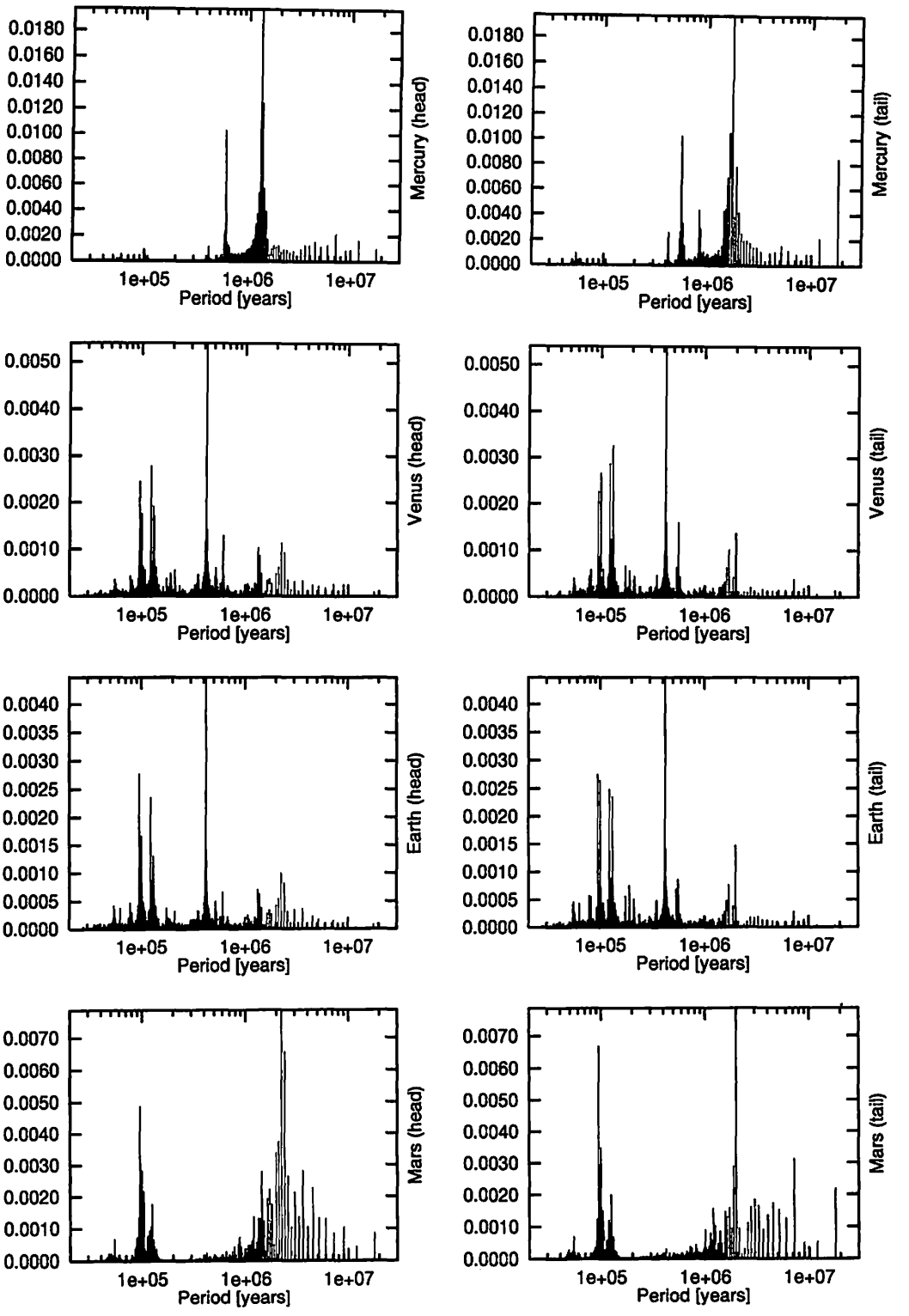

Figure 29. FFT periodgram of e in emb-minus series. (Left) leading 89713894.6 years. (Right) trailing 89713894.6 years.

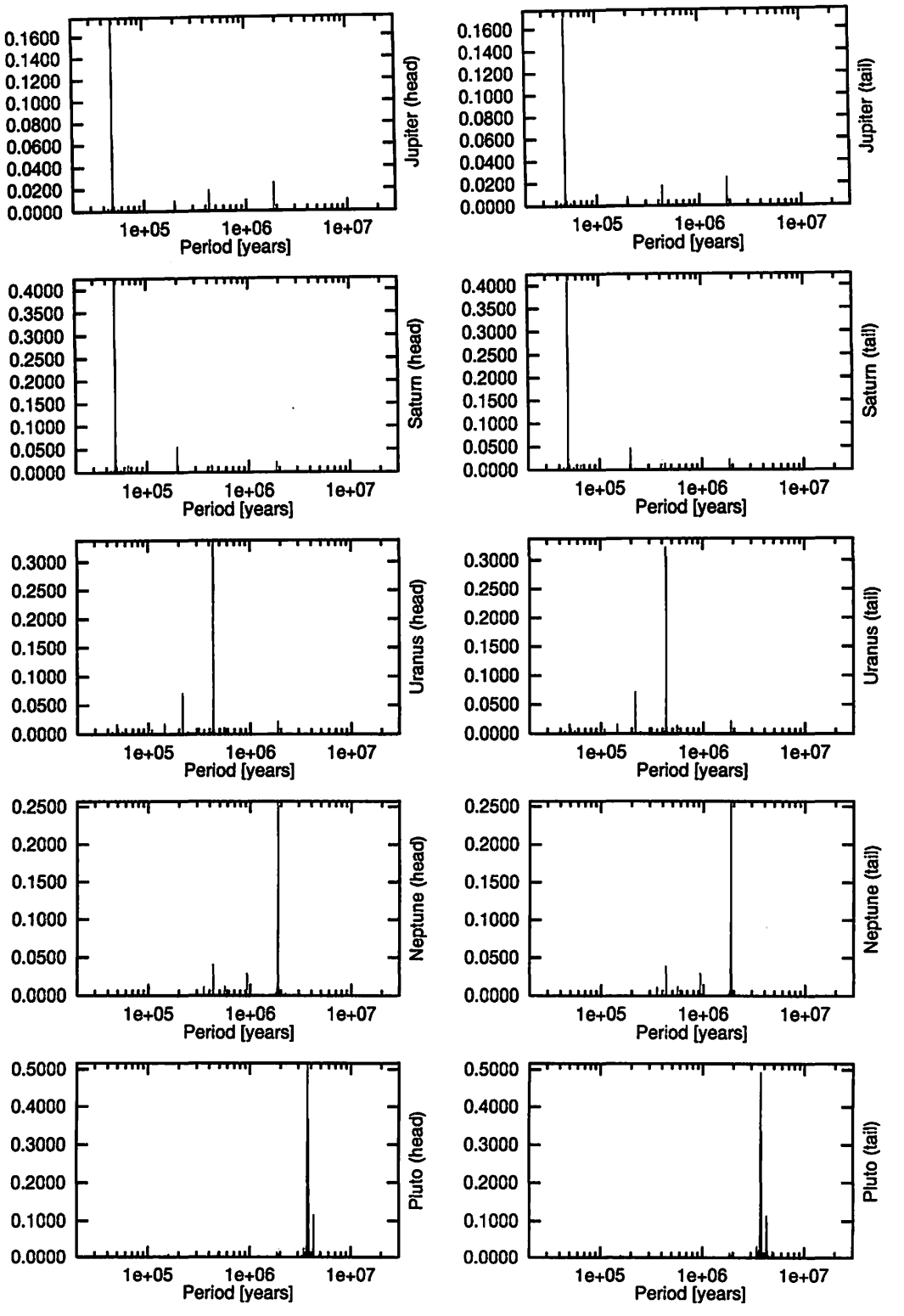

Figure 30. FFT periodgram of I in 50G+ series. (Left) leading 358855578.4 years. (Right) trailing 358855578.4 years.

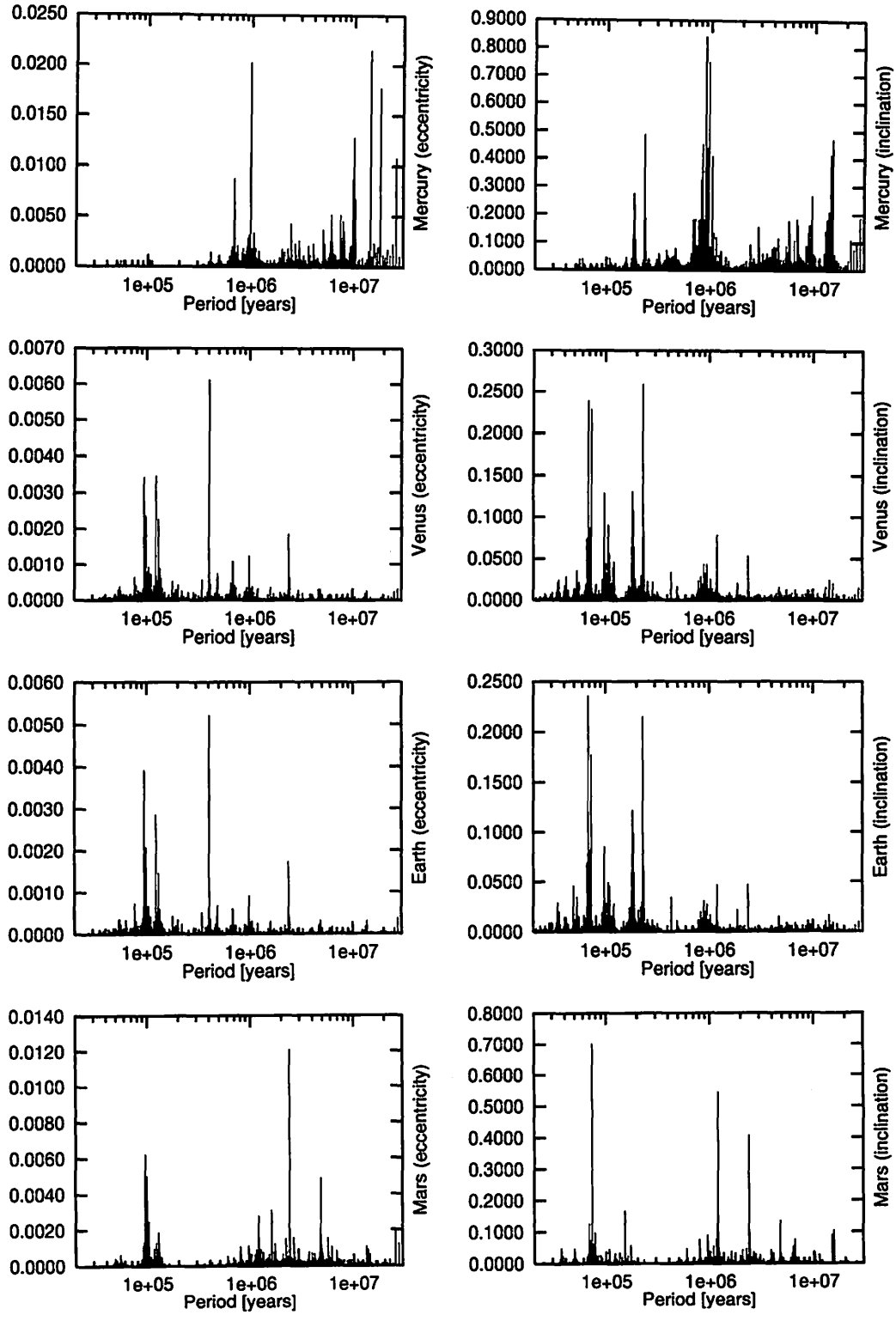

Figure 31. FFT periodgram of e (left) and I (right) from Laskar (1988) perturbation theory (inner four planets).

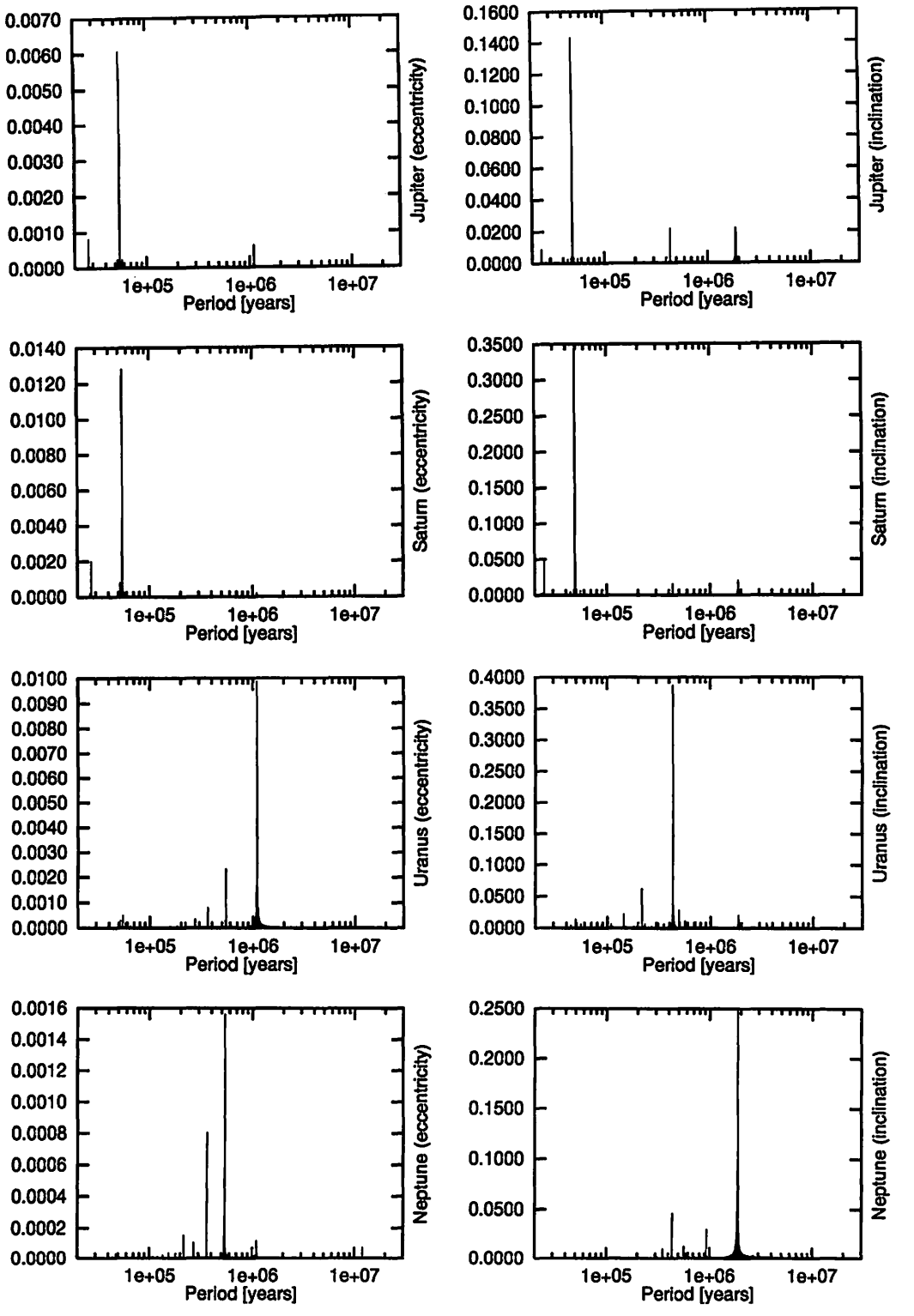

Figure 32. FFT periodgram of e (left) and I (right) from Laskar (1988) perturbation theory (outer four planets).

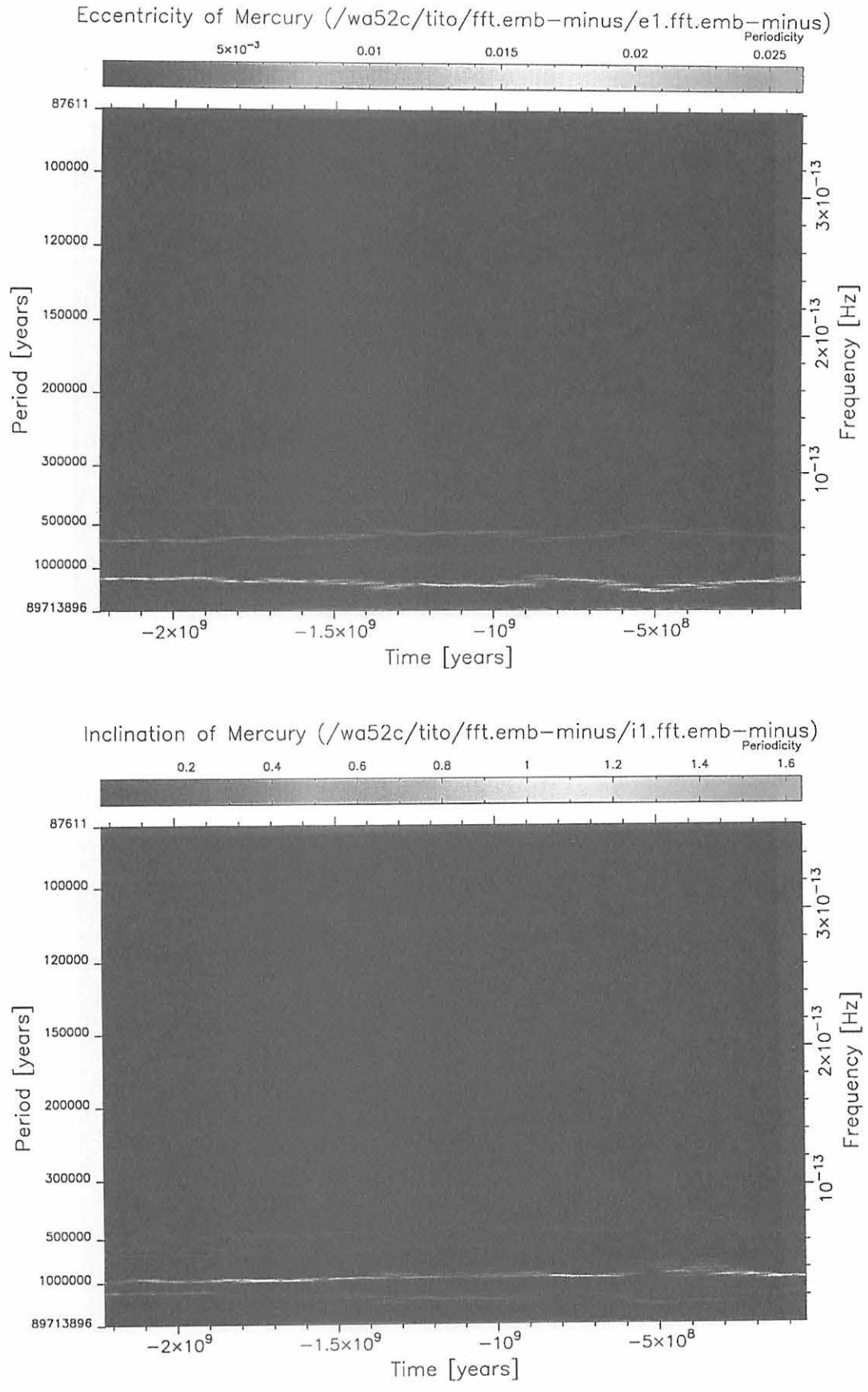

Figure 33. An example of time-frequency map for Mercury's e and I in emb-minus series.

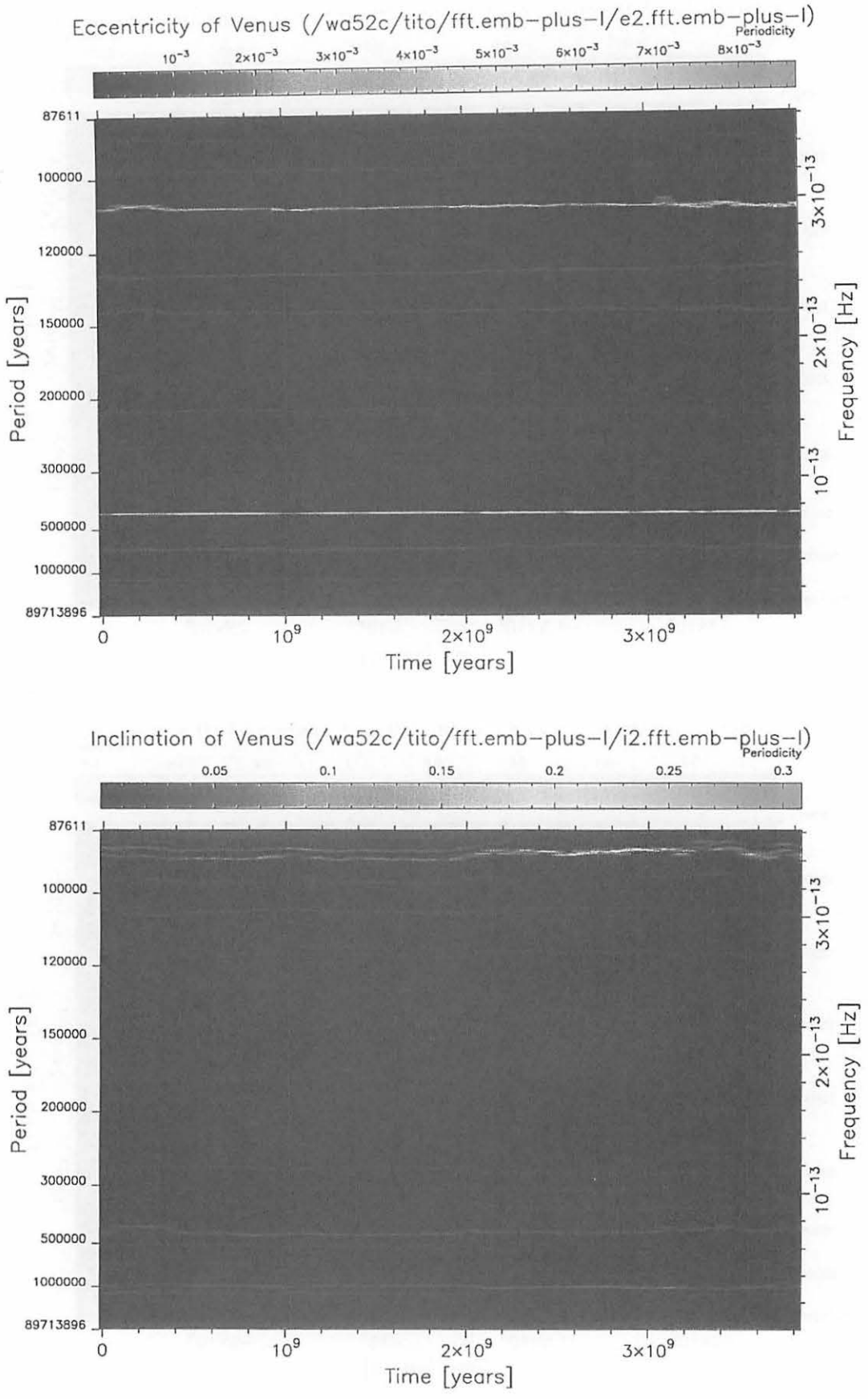

Figure 34. An example of time-frequency map for Venus's e and I in emb-plus-I series.

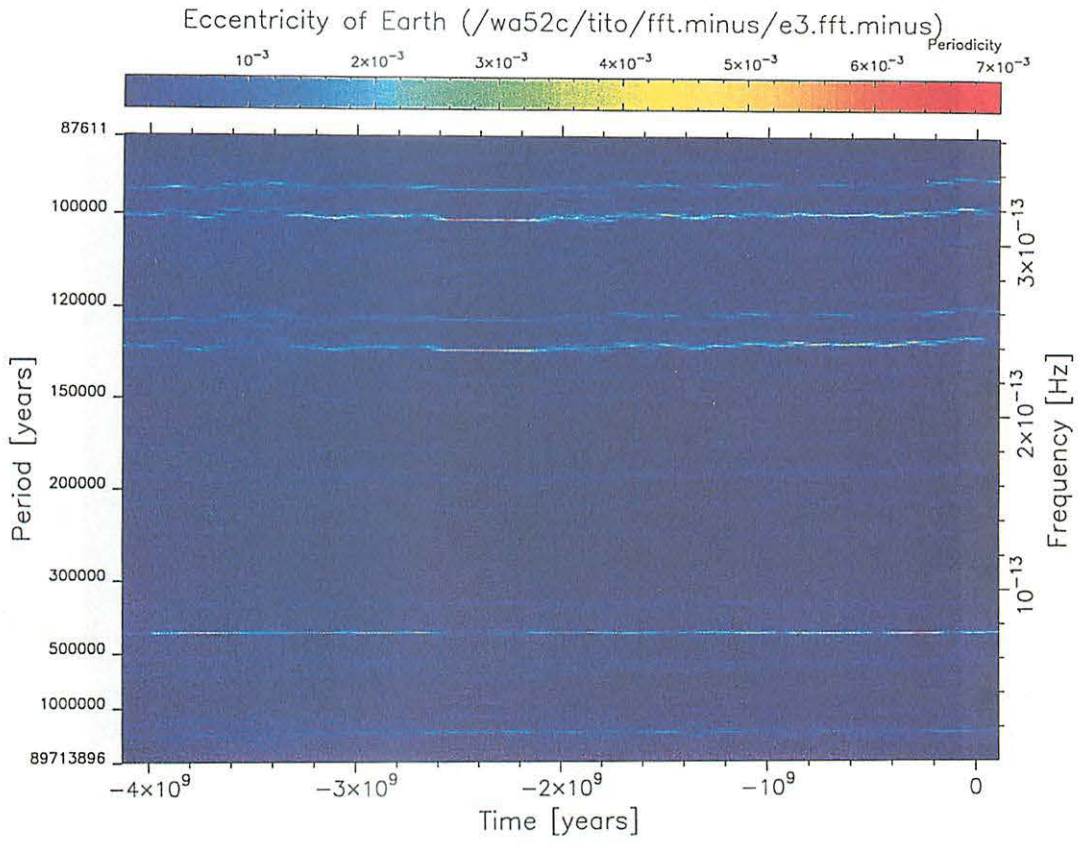

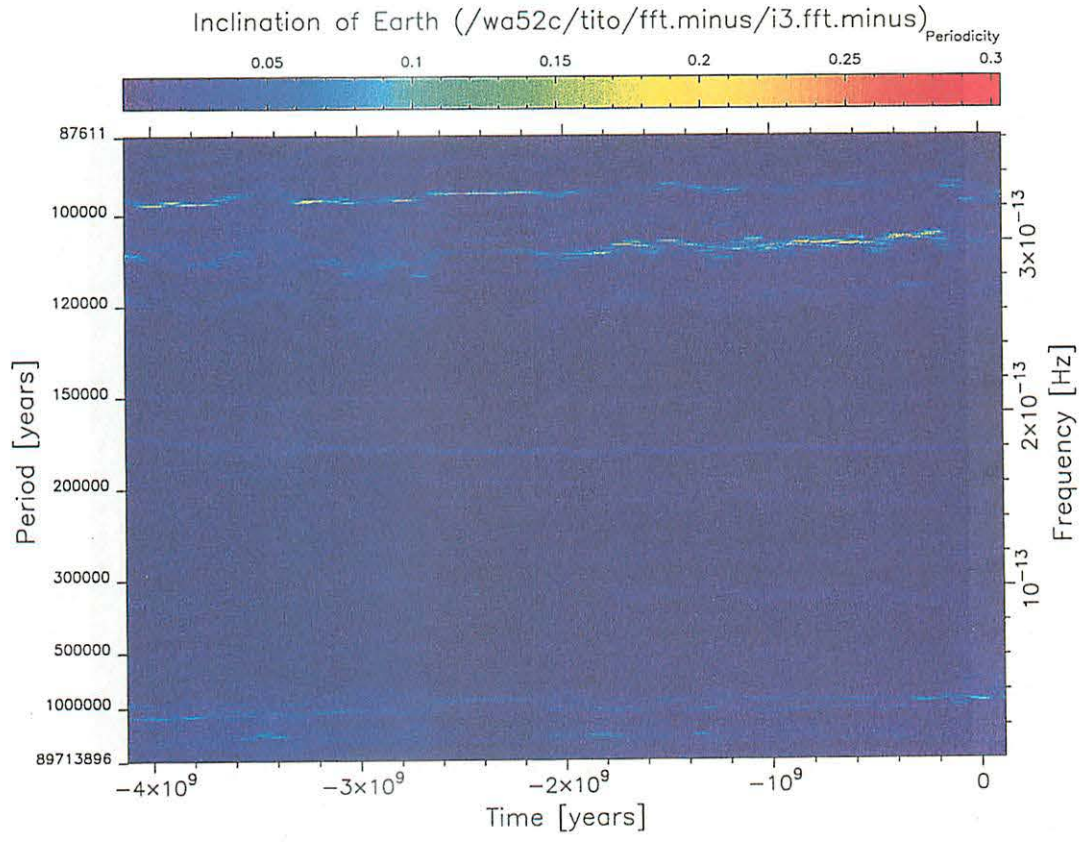

Figure 35. An example of time-frequency map for Earth's e and I in minus series.

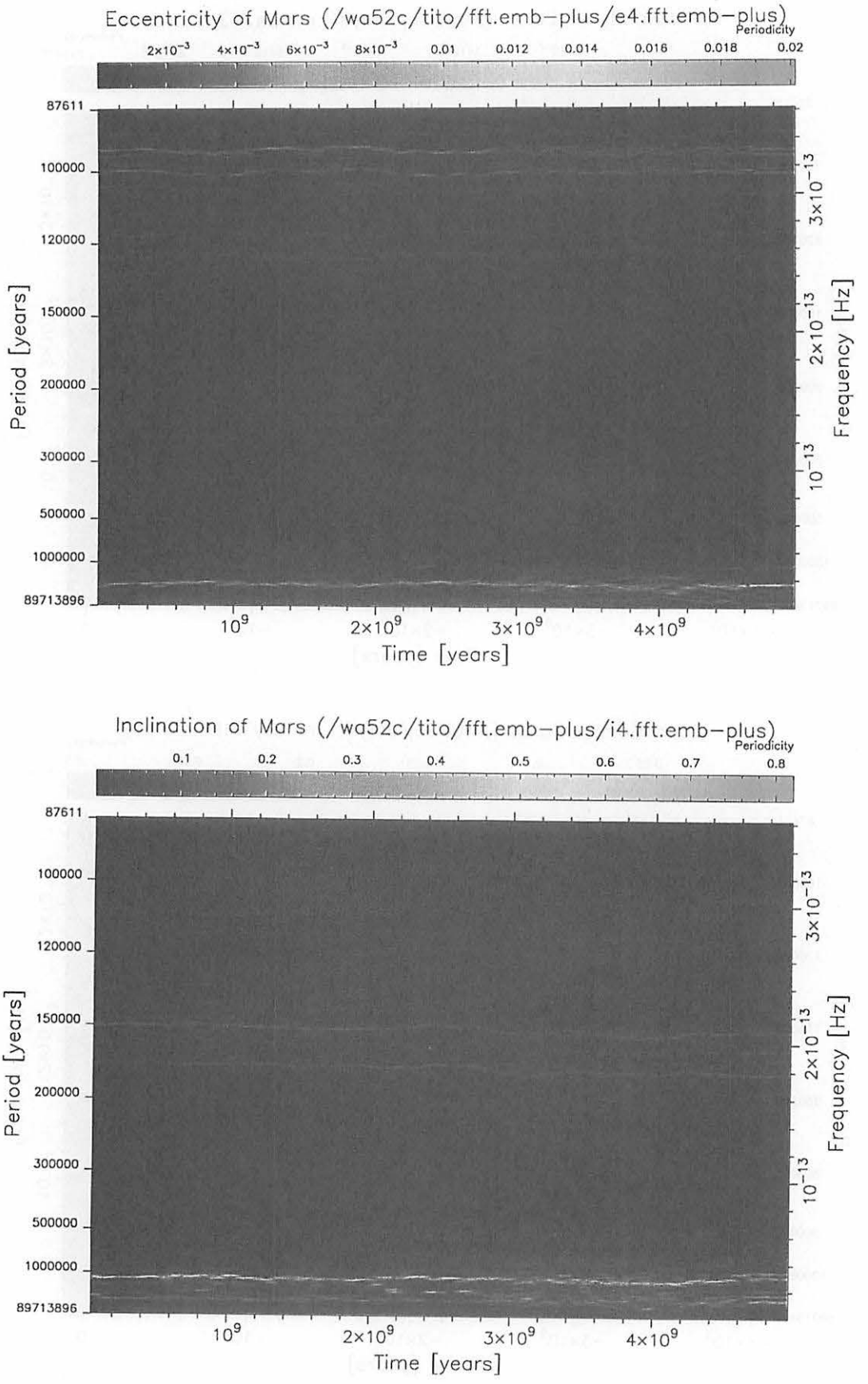

Figure 36. An example of time-frequency map for Mars's e and I in emb-plus series.

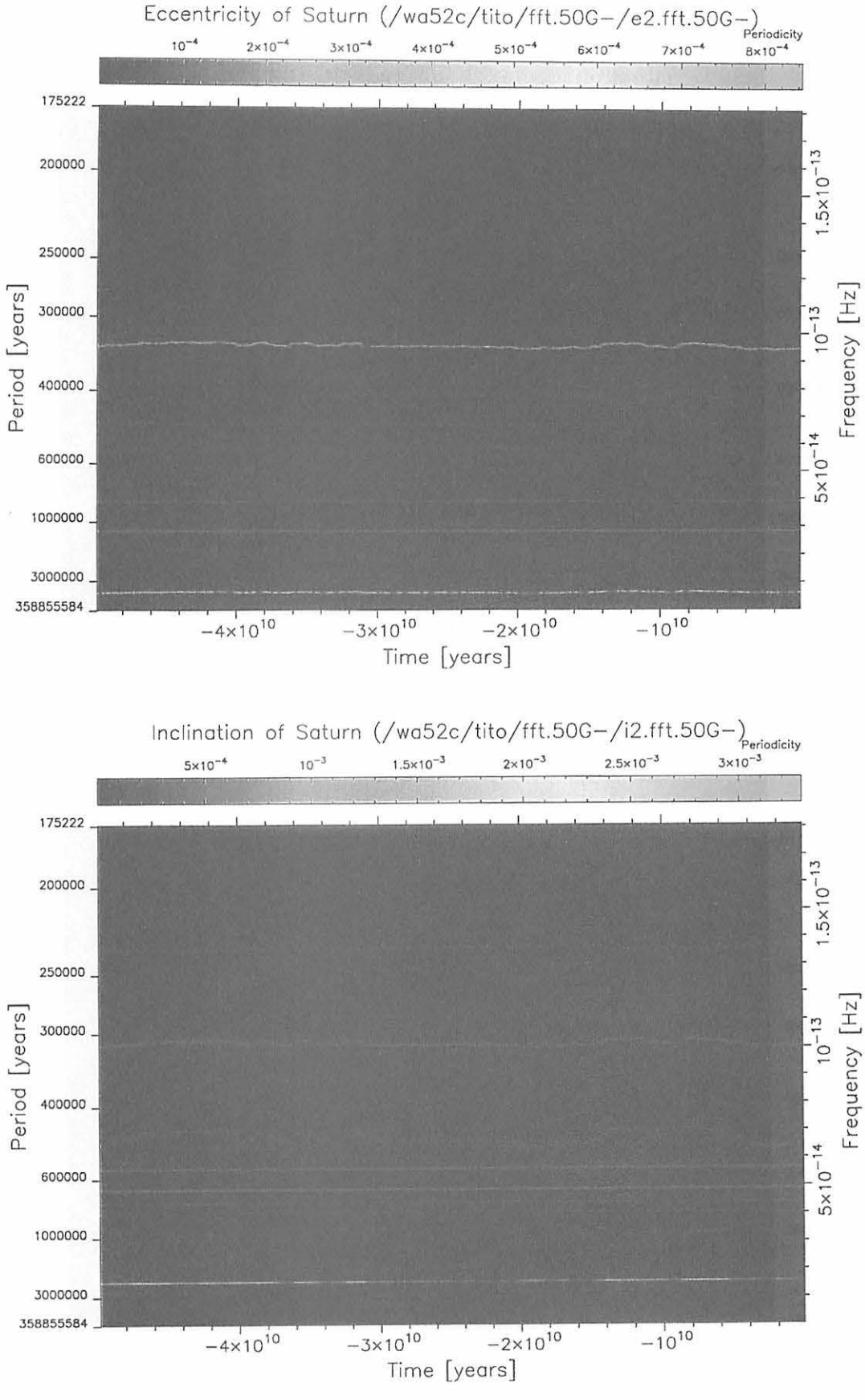

Figure 37. An example of time-frequency map for Saturn's e and I in 50G- series.

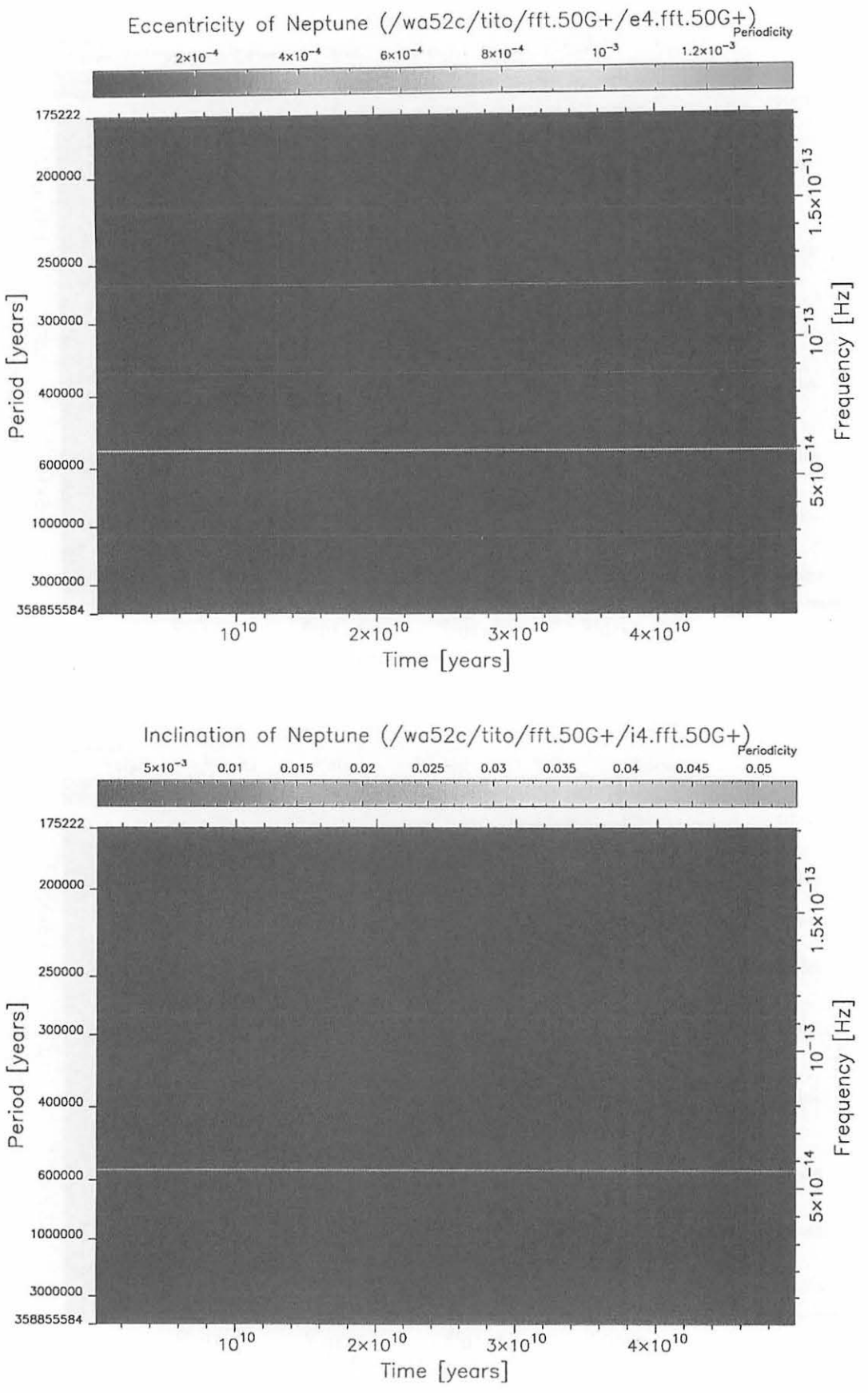

Figure 38. An example of time-frequency map for Neptune's e and I in 50G+ series.

References

Applegate, J.H., Douglas, M.R., Gürsel, Y., Sussman, G.J., and Wisdom, J. (1986) The outer solar system for 200 million years, *Astron. J.*, **92**, 176–94.

Berger, A.L. (1988) Milankovitch theory and climate, *Rev. Geophys.*, **26**, 624–657.

Brouwer, D. and Clemence, G.M. (1961) *Methods of Celestial Mechanics*, Academic Press, New York.

Brouwer, D. and van Woerkom, A.J.J. (1950) The secular variations of the orbital elements of the principal planets, *Astron. Pap. Amer. Ephemeris. Naut. Alm.*, **13**, 2, 81–107.

Bulirsch, R. and Stoer, J. (1966) Numerical treatment of ordinary differential equations by extrapolation methods, *Num. Math.*, **8**, 1–13.

Chambers, J.E., Wetherill, G.W., and Boss, A.P. (1996) The stability of multi-planet systems, *Icarus*, **119**, 261–268.

Cohen, C.J. and Hubbard, E.C. (1965) Libration of the close approaches of Pluto to Neptune, *Astron. J.*, **70**, 10–13.

Cohen, C.J., Hubbard, E.C., and Oesterwinter, C. (1973) Planetary elements for 10000000 years, *Celes. Mech.*, **7**, 438–448.

Danby, J.M.A. (1992) *Fundamentals of Celestial Mechanics (second edition, third printing)*, Willmann-Bell Inc., Richmond, Virginia.

Duncan, M.J. and Lissauer, J.J. (1998) The effects of post-main-sequence solar mass loss on the stability of our planetary system, *Icarus*, **134**, 303–310.

Eckert, W.J., Brouwer, D., and Clemence, G.M. (1951) Coordinates of the five outer planets, *Astron. Pap. Amer. Ephemeris. Naut. Alm.*, **12**.

Fukushima, T. (1996) A fast procedure solving Kepler's equation for elliptic case, *Astron. J.*, **112**, 2858–2861.

Fukushima, T. (1997a) A method solving Kepler's equation for hyperbolic case, *Celes. Mech. Dyn. Astron.*, **68**, 121–137.

Fukushima, T. (1997b) A method solving Kepler's equation without transcendental function evaluation, *Celes. Mech. Dyn. Astron.*, **66**, 309–319.

Fukushima, T. (1997c) A method solving Kepler's equation without transcendental function evaluations, *Celes. Mech. Dyn. Astron.*, **66**, 309–319.

Fukushima, T. (1997d) Picard iteration method, Chebychev polynomial approximation, and global numerical integration of dynamical motions, *Astron. J.*, **113**, 1909–1914.

Fukushima, T. (1997e) A procedure solving the extended Kepler's equation for the hyperbolic case, *Astron. J.*, **113**, 1920–1924.

Fukushima, T. (1997f) Vector integration of dynamical motions by the Picard-Chebychev method, *Astron. J.*, **113**, 2325–2328.

Fukushima, T. (1998) A fast procedure solving Gauss' form of Kepler's equation, *Celes. Mech. Dyn. Astron.*, **70**, 115–130.

Gladman, B. (1993) Dynamics of systems of two close planets, *Icarus*, **106**, 247–263.

Gragg, W.B. (1965) On extrapolation algorithms for ordinary initial value problems, *SIAM J. Numer. Anal.*, **2**, 384–403.

Hairer, E., Nørsett, S.P., and Wanner, G. (1993) *Solving Ordinary Differential Equation I – Nonstiff Problems* (second revised edition), Springer-Verlag, New York.

Ito, T. and Fukushima, T. (1997) Parallelized extrapolation method and its application to the orbital dynamics, *Astron. J.*, **114**, 1260–1267.

Ito, T. and Tanikawa, K. (1999) Stability and instability of the terrestrial protoplanet system and their possible roles in the final stage of planet formation, *Icarus*, **139**, 336–349.

Ito, T., Kinoshita, H., Nakai, H., and Fukushima, T. (1996) Numerical experiments to inspect the long-term stability of the planetary motion -1, in *Proc. 28th Symp. Celes. Mech.*, National Astronomical Observatory, Mitaka, Tokyo, 123–136.

Kinoshita, H. and Nakai, H. (1984) Motions of the perihelions of Neptune and Pluto, *Celes. Mech.*, **34**, 203–217.

Kinoshita, H. and Nakai, H. (1995) The motion of Pluto over the age of the solar system, in Ferraz-Mello, S. *et al.* ed., *Dynamics, ephemerides and astrometry in the solar system*, Kluwer Academic publishers, Dordrecht, 61–70.

Kinoshita, H. and Nakai, H. (1996) Long-term behavior of the motion of Pluto over 5.5 billion years, *Earth, Moon, and Planets*, **72**, 165–173.

Kinoshita, H., Yoshida, H., and Nakai, H. (1991) Symplectic integrators and their application to dynamical astronomy, *Celes. Mech. Dyn. Astron.*, **50**, 59–71.

Kozai, Y. (1962) Secular perturbations of asteroids with high inclination and eccentricity, *Astron. J.*, **67**, 591–598.

Laskar, J. (1985) Accurate methods in general planetary theory, *Astron. Astrophys.*, **144**, 133–146.

Laskar, J. (1986) Secular terms of classical planetary theories using the results of general theory, *Astron. Astrophys.*, **157**, 59–70.

Laskar, J. (1988) Secular evolution of the solar system over 10 million years, *Astron. Astrophys.*, **198**, 341–362.

Laskar, J. (1990) The chaotic motion of the solar system: A numerical estimate of the size of the chaotic zones, *Icarus*, **88**, 266–291.

Laskar, J. (1994) Large scale chaos in the solar system, *Astron. Astrophys.*, **287**, L9–L12.

Laskar, J. (1996) Large scale chaos and marginal stability in the solar system, *Celes. Mech. Dyn. Astron.*, **64**, 115–162.

Milani, A. and Nobili, A.M. (1997) Stable chaos in the asteroid belt, *Icarus*, **125**, 13–31.

Milani, A., Nobili, A.M., and Carpino, M. (1989) Dynamics of Pluto, *Icarus*, **82**, 200–217.

Milankovitch, M. (1941) *Kanon der Erdbestrahlung und seine Anwendung auf das Eiszeitproblem*, Vol. 133 of *Königlich Serbische Academie Publication*, Königlich Serbische Academie, 邦訳は『ミランコビッチ気候変動の天文学理論と氷河時代』, 柏谷健二・山本淳之・大村誠・福山薫・安成哲三 訳, 古今書院, 1992.

Newhall, X X., Standish, E.M., and Williams, J.G. (1983) DE102: a numerically integrated ephemeris of the Moon and planets spanning forty-four centuries, *Astron. Astrophys.*, **125**, 150–167.

Nobili, A.M., Milani, A., and Carpino, M. (1989) Fundamental frequencies and small divisors in the orbits of the outer planets, *Astron. Astrophys.*, **210**, 313–336.

Pilat-Lohinger, E., Dvorak, R., and Burger, Ch. (1999) Trojans in stable chaotic motion, *Celes. Mech. Dyn. Astron.*, **73**, 117–126.

Quinn, T.R., Tremaine, S., and Duncan, M. (1991) A three million year integration of the earth's orbit, *Astron. J.*, **101**, 2287–2305.

Richardson, D.L. and Walker, C.F. (1989) Numerical simulation of the nine-body planetary system spanning two million years, *J. Astronaut. Sci.*, **37**, 159–182.

Roy, A.E., Walker, I.W., Macdonald, A.J., Williams, K., I.P. Fox, Murray, C.D., Milani, A., Nobili, A.M., Message, P.J., Sinclair, A.T., and Carpino, M. (1988) Project LONGSTOP, *Vistas Astron.*, **32**, 95–116.

Saha, P. and Tremaine, S. (1992) Symplectic integrators for solar system dynamics, *Astron. J.*, **104**, 1633–1640.

Saha, P. and Tremaine, S. (1994) Long-term planetary integrations with individual time steps, *Astron. J.*, **108**, 1962 1969.

Шараф, Ш.Г. and Будникова, Н.А. (1969a) О вековых измененисых элементов орбиты Земли, влияющих на климаты геологического прощлого, БЮЛЛЕТЕНЬ ИНСТИТУТА ТЕОРЕТИЧЕСКОЙ АСТРОНОМИИ, **11**, 231–261, English translation is in NASA TT F–12, *467*, 1–37.

Шараф, Ш.Г. and Будникова, Н.А. (1969b) ВЕКОВЫЕ ИЗМЕНЕНИЯ ЭЛЕМЕНТОВ ОРБИТЫ ЗЕМЛИ И АСТРОНОМИЧЕСКАЯ ТЕОРИЯ КОЛЕБАНИЙ КЛИМАТА, ТРУДЫ ИНСТИТУТА ТЕОРЕТИЧЕСКОЙ АСТРОНОМИИ, **14**, 48–84, Japanese translation by K. Tanikawa is available from http://ataru.mtk.nao.ac.jp/list08/list08.html.

Šidlichovský, M. (1999) On stable chaos in the asteroid belt, *Celes. Mech. Dyn. Astron.*, **73**, 77–86.

Standish, E.M. (1990) The observational basis for JPL's DE200, the planetary ephemerides of the astronomical almanac, *Astron. Astrophys.*, **233**, 252–271.

Sussman, G.J. and Wisdom, J. (1988) Numerical evidence that the motion of Pluto is chaotic, *Science*, **241**, 433–437.

Sussman, G.J. and Wisdom, J. (1992) Chaotic evolution of the solar system, *Science*, **257**, 56–62.

Tremaine, S. (1995) Is the solar system stable?, CITA–95–3, in *Proceedings of Rosseland Centenary Symposium of Astrophysics*, Oslo, June 16–17, 1994.

Williams, J.G. and Benson, G.S. (1971) Resonances in the Neptune-Pluto system, *Astron. J.*, **76**, 167–177.

Wisdom, J. (1992) Long term evolution of the solar system, in *Chaos, resonance and collective dynamical phenomena in the solar system*, Kluwer Academic publishers, Dordrecht, 17–24.

Wisdom, J. and Holman, M. (1991) Symplectic maps for the N-body problem, *Astron. J.*, **102**, 1528–1538.

Wisdom, J. and Holman, M. (1992) Symplectic maps for the n-body problem: stability analysis, *Astron. J.*, **104**, 2022–2029.

Yoshinaga, K., Kokubo, E., and Makino, J. (1999) The stability of protoplanet systems, *Icarus*, **139**, 328–335.

中井宏, 木下宙 (1995) 外惑星系の数値シミュレーション, 第 27 回天体力学研究会集録, 国立天文台, 1–9.

福島登志夫 (1980) 補外法による多体問題の高精度数値積分, 昭和 55 年度水路観測所長会議, 海上保安庁水路部編暦課 編, 87–91.

福島登志夫 (1992) Extrapolation technique and multi-processor computers, 観山正見（編）, 超高速計算機による数値天文学の構築, 国立天文台, 73–75.

三上直樹 (1998) ディジタル信号処理の基礎, CQ 出版社.

IMPROVEMENT OF NON-RIGID EARTH NUTATION THEORY BY ADDING A MODEL FREE CORE NUTATION TERM

Toshimichi Shirai
University of Tokyo, Graduate School of Science, Department of Astronomy,
3-8-1, Hongoh, Bunkyo-ku, Tokyo 113-0033, Japan
t.shirai@nao.ac.jp

Toshio Fukushima
National Astronomical Observatory,
2-21-1, Ohsawa, Mitaka, Tokyo 181-8588, Japan

ABSTRACT

From the analysis of VLBI observational data compiled by USNO from 1979 to 1999, we showed that a strong peak around −400 sidereal days in the spectrum of their difference from the IERS96 nutation theory could be explained by adding a model Free Core Nutation (FCN) term of the form of a single damping oscillation. Then we developed a new analytical series of the non-rigid Earth nutation including thus chosen FCN model. We adopted RDAN98 (Roosbeek and Dehant 1998) as the rigid Earth nutation theory. Then it was convoluted with a transfer function by the numerical convolution in time domain (Shirai and Fukushima 2000). The form of the transfer function was the same as that of Herring (1995), however, its free parameters such as the complex amplitude and frequency of FCN were readjusted by fitting to the above VLBI data. Even after truncating the forced nutation series so as to contain only 180 terms, the weighted root mean square (WRMS) of the residuals in complex for the new nutation series is 0.312 mas, which is significantly smaller than 0.325 mas, that of the IERS96 nutation theory. As for the FCN term, we estimated its oscillatory period as -430.8 ± 0.6 sidereal days and Q-value as 16200 ± 1600. Also we estimated the correction to the precession constants as -0.042458 ± 0.000033 ″ in longitude and -0.005186 ± 0.000013 ″ in obliquity to offsets and -0.29297 ± 0.00047 ″/cy in longitude and -0.02430 ± 0.00019 ″/cy in obliquity to rates, respectively.

Subject headings: Astrometry and Celestial Mechanics — nutation, precession, free core nutation, reference system

1. Introduction

The nutation has two modes, the forced and the free modes. The forced nutation is due to the luni-solar and planetary tidal forces. The free mode appears because the Earth has a rotating and elliptical fluid core. Thus this mode was named as the free core nutation (FCN) by Toomre (1974). However the current IAU nutation theory, which is called as the IAU1980 nutation theory (Seidelmann 1982), does not include the FCN term. This is because, at the time of its creation, the FCN had not yet been observed directly and indisputably by the optical observation and the excitation mechanism was not clear (Sasao and Wahr 1981). The IERS96 nutation theory, which is in the best agreement with the VLBI observation, also does not contain the FCN term (McCarthy 1996). See Figure 1 for the difference between the VLBI data compiled by

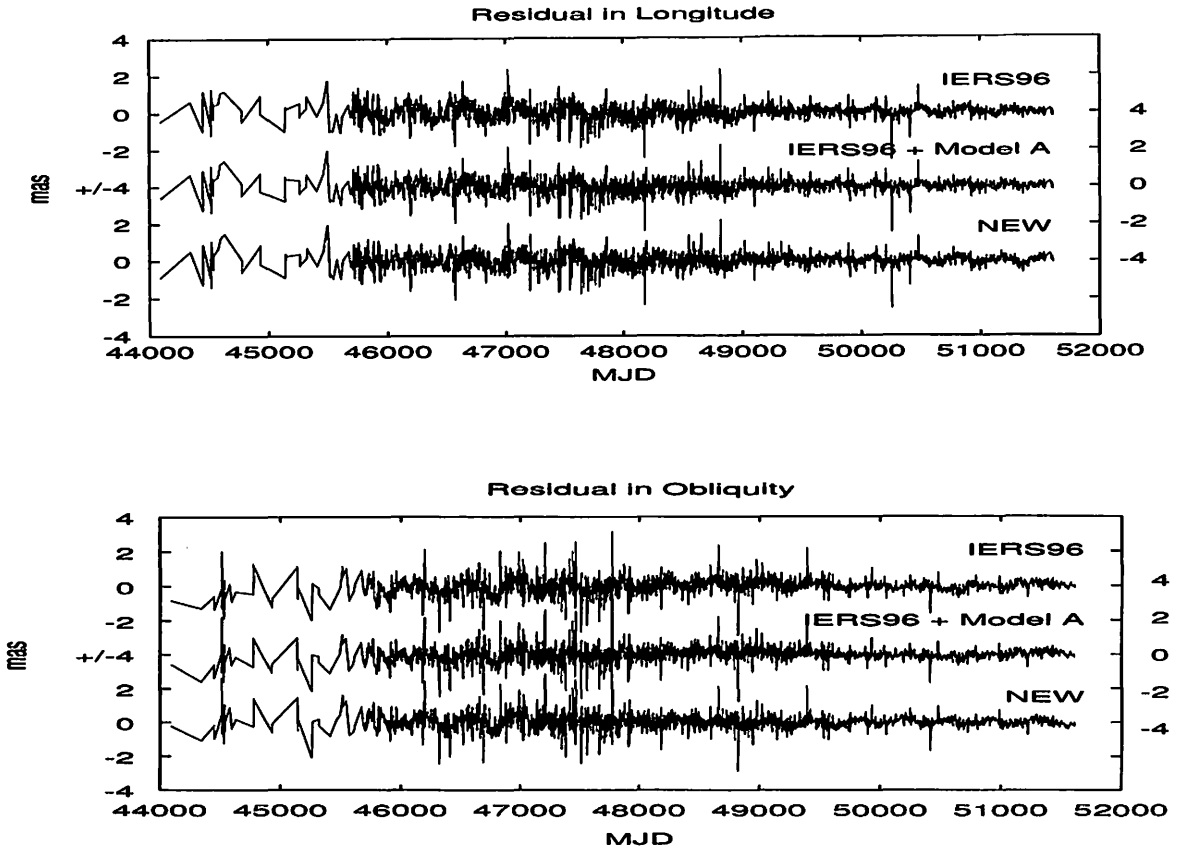

Fig. 1.— Residuals of IERS96 Nutation Theories with and without FCN Model and of New Series. Shown are differences from between the VLBI data compiled by USNO.

USNO (U.S. Naval Observatory) and IERS96 nutation theory for the period MJD 44089.994 to 51618.250. However, there remains a strong peak around −400 sidereal days period in its spectrum, Figure 2. Charlot et al. (1995) and Souchay et al. (1995) estimated the prograde and retrograde components with the given frequency of the FCN at some epochs. Charlot et al. adopted the FCN term as a sine wave with period −429.8 sidereal days. Then they estimated the amplitudes of prograde and retrograde components on 3 to 5 year intervals from the combined data of VLBI and LLR for the period 1978-1994. They suggested that the FCN has not varied significantly since 1988. Souchay et al. (1995) did in almost the same way but based on VLBI data only. They adopted the FCN term as a sine wave with period 433 sidereal days and estimated the amplitudes of prograde and retrograde components on two-year intervals for the period 1984-1993. They concluded that (1) the amplitudes are subject to significant changes, (2) but all of them correspond to a retrograde motion, as expected for the FCN, and (3) the retrograde component seems to be constant after 1988 at the value 0.16±0.03 mas. We remark that the FCN has the retrograde component only because the period of the FCN is not +431 sidereal days, but −431 sidereal days. Herring (1995) also estimated the amplitude and frequency of the FCN using the VLBI data for 1979 to 1994 when he developed the IERS96

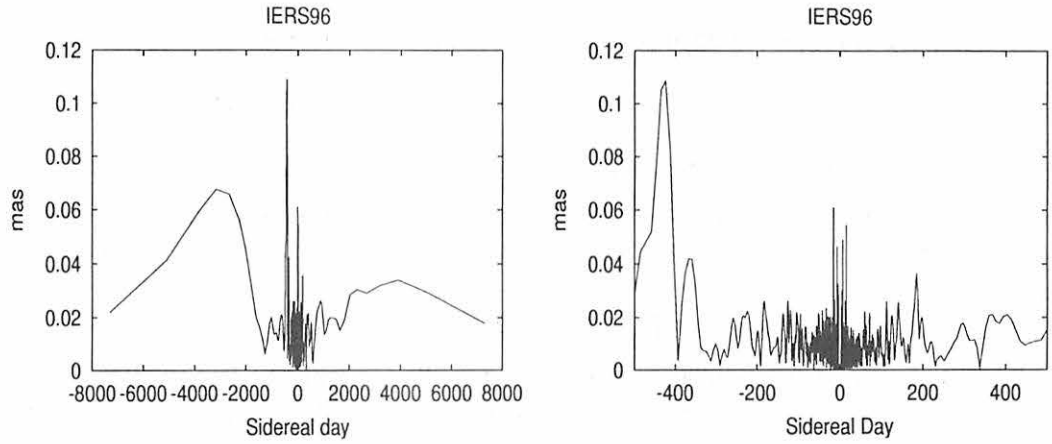

Fig. 2.— Frequency Spectra of Complex Residuals of IERS96 Nutation Theory with and without FCN Models. There is the strong peak around −400 sidereal days in the spectrum of the IERS96 nutation theory.

nutation theory. He first estimated the complex frequency of the FCN, next did its amplitude discretely, namely in every two years intervals. This method was the same with Souchay et al (1995). He concluded that the amplitude of the FCN showed a steady decrease during the period. Anyway he did not introduce any model of the FCN to the IERS96 nutation theory. This is probably because the strong peak in the spectrum of the residuals were believed to be explained by considering external excitations which vary with the periods close to that of the FCN. As shown by Gegout et al. (1998), the atmosphere is a good candidate for such exciting force, which means that the amplitude of such peaks cannot be predicted. Therefore the FCN has been considered not to be predicted but to be observed as the Chandler wobble is done. However, the strong peak may be explained appropriately by adding a model FCN term. In this paper, we will try to improve the analytical theory of the non-rigid Earth nutation by adding a simple model term of the FCN.

2. Models of FCN

Let us examine the existence of FCN by using the VLBI data. To do so, we first fixed the forced nutation theory as the IERS96 nutation theory. Next, we assumed that the period of FCN is constant (Roosbeek et al. 1999). Then we set the frequency of FCN as that of Herring (1995). As for the model of FCN, we considered the following two; (A) no excitation during the observation, and (B) frequent excitations during the observation. At first, we consider the model A. The energy of FCN is considered to dissipate due to the viscosity of the outer fluid core and the magnetic coupling of the mantle-core boundary. Then, it is reasonable that the FCN is of the form of a damping oscillation. If the FCN has no excitation during the observation, then it must be a single damping oscillation. In order to treat the energy dissipation of the FCN properly, we dealt the amplitude $C_{\rm FCN}$ and the frequency $\omega_{\rm FCN}$ of the FCN as complex values:

$$C_{\rm FCN} = C^r_{\rm FCN} + iC^i_{\rm FCN}, \quad \omega_{\rm FCN} = \omega^r_{\rm FCN} + i\omega^i_{\rm FCN} \tag{1}$$

In other words, the FCN in longitude $\Delta\psi_{\rm FCN}$ and in obliquity $\Delta\epsilon_{\rm FCN}$ in the model A are expressed compactly in a complex notation as

$$Z^A_{\rm FCN} \equiv \Delta\psi^A_{\rm FCN}\sin\epsilon_0 + i\Delta\epsilon^A_{\rm FCN} = C_{\rm FCN}e^{i\omega_{\rm FCN}t} \tag{2}$$

where ϵ_0 is the obliquity of ecliptic at J2000.0. The above expressions are rewritten in real forms as

$$\Delta\psi^A_{\rm FCN}\sin\epsilon_0 = e^{-\omega^i_{\rm FCN}t}(C^r_{\rm FCN}\cos\omega^r_{\rm FCN}t - C^i_{\rm FCN}\sin\omega^r_{\rm FCN}t), \tag{3}$$

$$\Delta\epsilon^A_{\rm FCN} = e^{-\omega^i_{\rm FCN}t}(C^i_{\rm FCN}\cos\omega^r_{\rm FCN}t + C^r_{\rm FCN}\sin\omega^r_{\rm FCN}t). \tag{4}$$

Next we consider the model B. If the FCN is excited frequently during the observation, it is regarded as a simple harmonic oscillation without damping whose (real) frequency ω is close to the real part of the FCN frequency as

$$Z^B_{\rm FCN} \equiv \Delta\psi^B_{\rm FCN}\sin\epsilon_0 + i\Delta\epsilon^B_{\rm FCN} = C_{\rm FCN}e^{i\omega t}. \tag{5}$$

Strictly speaking, this is not a free oscillation but a forced oscillation with the frequency which is so close to the resonant frequency that its amplitude is greatly magnified. The above expression is rewritten in real forms as

$$\Delta\psi^B_{\rm FCN}\sin\epsilon_0 = C^r_{\rm FCN}\cos\omega t - C^i_{\rm FCN}\sin\omega t, \tag{6}$$

$$\Delta\epsilon^B_{\rm FCN} = C^i_{\rm FCN}\cos\omega t + C^r_{\rm FCN}\sin\omega t. \tag{7}$$

Of course, there is a possibility that the excited oscillation contains multiple frequencies. However, as will be shown later, the analysis of residuals strongly suggests the singleness of excited frequency (if existing). Thus we will regard it as of a single frequency. This approach was different from those taken by Charlot et al. (1995) and Souchay et al. (1995). The main differences are (1) they estimated both the prograde and retrograde components while the model B estimated only the retrograde one, (2) they estimated the amplitudes at several epochs while the model B did only one, and (3) they fixed the frequency while model B searched the best frequency by fitting to VLBI data.

In both models, we estimated the complex amplitude $C_{\rm FCN}$ by the least square fitting to the residuals. In the model B, we did also the real frequency ω by fitting. So the number of parameters of the model B is greater by one than that of the model A. See Figure 3 for the frequency dependence of WRMS of the model B. These figures are regarded as an upside-down periodgram in the sense the smaller the WRMS is the larger the corresponding spectrum power is. In the left figure, we added the arrows indicating the FCN periods estimated by the IERS 96 nutation theory. As is shown clearly, the WRMS has 3 local minimum, -481.0 sidereal days, -428.0 sidereal days, and -363.5 sidereal days. However the variation of the WRMS is unimodal and very smooth around $-$ 431.2 sidereal days, the period of the FCN estimated by the IERS96 nutation theory. In the right figure, we added the arrows indicating the FCN periods estimated by the IERS96 nutation theory and by the new nutation theory, whose detail will be described in the next section. This indicates that, if the strong peak shown in the residual spectrum is caused by external excitations, the excitation frequency is single. We also calculated the magnification factor by the resonance. The value of the peak -431.2 sidereal days is about 40. That of -428.0 sidereal days which we adopted as the best excitation period is about 30. Also we estimated the absolute amplitude of FCN of the model B as 0.11 mas. Therefore the original of the external excitation, if this interpretation is correct, must be so small as of about 3.7 μas when the Earth is rigid. Now we compare these two models, A and B. Table 1 shows that the WRMS decreases significantly by adding a model FCN term anyway. Figure 4 has shown the spectra of the residuals for the IERS96 nutation theory itself and its combinations with two models. The strong peak in the spectrum around -400 sidereal days is clearly removed by adding a model FCN term. This is also

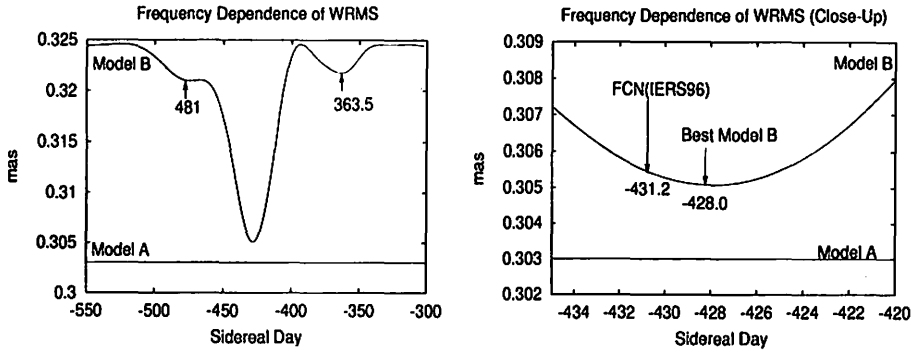

Fig. 3.— Frequency Dependence of WRMS of FCN Models. The left figure can be regarded as a periodgram in the sense the smaller the WRMS is the larger the corresponding spectrum power is. Arrows show the frequencies of possible local minima, −481 sidereal days and −363.5 sidereal days. The right figure is its close-up around −431.2 sidereal days estimated by IERS96 nutation theory.

Table 1: Comparison of Nutation Series in WRMS

	IERS96			NEW	
	w/o FCN	+ Model A	+ Model B	Full	Short
Complex	0.3250	0.3030	0.3051	0.3075	0.312
$\Delta\psi \sin\epsilon_0$	0.227	0.212	0.213	0.221	0.224
$\Delta\epsilon$	0.229	0.213	0.215	0.211	0.214

Note: The unit is mas. The column complex means WRMS of $\Delta\psi \sin\epsilon_0 + i\Delta\epsilon$. The model A adopted the FCN as a single damping oscillation and the model B did as a simple harmonic oscillation. WRMS of the model A is smaller than that of new series since the annual prograde nutation was adjusted.

seen from Figure 1 showing the post-fit residuals for the IERS96 nutation theory + model A. Apparently the model A is better than the model B in spite of the fact that its number of the adjusted parameters is less by one than that of the model B. Unfortunately the difference between these two models is of the order of the observational precision. Thus, if the period and/or precision of the observation will increase, it will be clear which model is really the better. Since the model A is of the form of a single damping oscillation, the past amplitude of FCN must have been much larger than the present one. However, the amplitude of FCN was at most about 0.1" a century ago. Until the rise of the VLBI technique, the precision of the optical observation had not been sufficiently accurate. Then it is no wonder that the FCN had not been noticed. Therefore the model A is consistent with the past observation. In conclusion, we adopt the model A to improve the nutation theory in this paper.

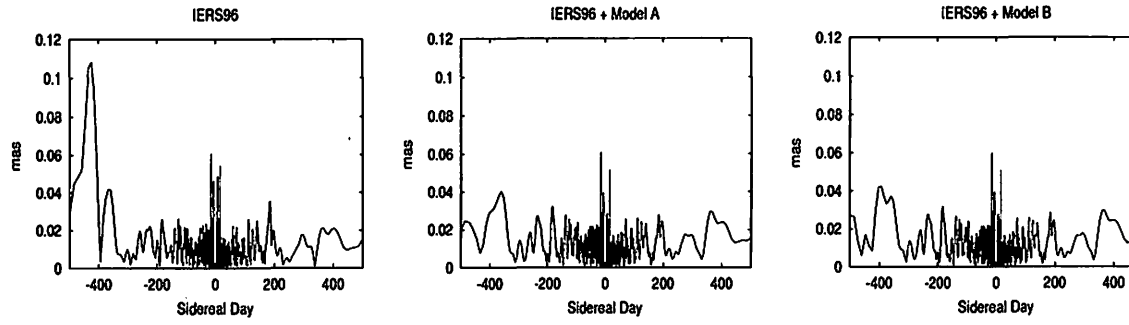

Fig. 4.— Frequency Spectra of Complex Residuals of IERS96 Nutation Theory with and without FCN Models. The strong peak in the spectrum of the IERS96 nutation theory around −400 sidereal days is clearly removed by adding a model FCN term.

3. Method

In order to explain the VLBI data better, we developed a new nutation series by incorporating a model FCN term discussed in the previous section. Usually the theory of the forced nutation is obtained as a combination of the rigid Earth nutation theory and the transfer function of the non-rigid Earth. As the former, we adopted the RDAN98 (Roosbeek and Dehant 1998) whose truncation level is 0.1 μas. The nutation series RDAN98 includes not only the luni-solar effects but the planetary effects. Next we removed very long periodic terms from RDAN98, namely the terms with the period longer than 150 years. As the transfer function, we selected the same functional form as that of Herring (1995);

$$g(\hat{\omega}) = R + R'\hat{\omega} + \frac{R_{\rm FCN}}{\hat{\omega} - \hat{\omega}_{\rm FCN}} + \frac{R_{\rm CW}}{\hat{\omega} - \hat{\omega}_{\rm CW}} \tag{8}$$

where $g(\hat{\omega})$ is the ratio of the nutation amplitude of the non-rigid Earth, $\hat{\omega}$ is the frequency normalized by the mean angular velocity of the Earth rotation Ω_0 as

$$\hat{\omega}_{\rm FCN} = \frac{\omega_{\rm FCN}}{\Omega_0} \tag{9}$$

where

$$\Omega_0 = 7.292115 \times 10^{-5} {\rm rads}^{-1} \tag{10}$$

and CW stands for the Chandler Wobble. Here we ignored the contribution of the inner solid core of the Earth whose effects to the nutation are very small. We convoluted the transfer function with the nutation theory of the rigid Earth by the numerical convolution in the time domain, which is much more precise than the current analytical method of convolution in the frequency domain (Shirai and Fukushima 2000). The convoluted values were stored at equal time intervals, namely every 1.5 hours. We used the VLBI data compiled by USNO for the period MJD 44089.994 to 51618.250. Since the VLBI data are scattered almost randomly. We interpolated the convoluted values by 4-points Lagrange's interpolation to obtain the values at data points. We confirmed that the interpolation errors are sufficiently small as of the order of 1 nano arcsecond. Next we removed the geodesic nutation discussed by Fukushima (1991) from the VLBI data because the geodesic nutation should not be influenced by the transfer function. The parameters

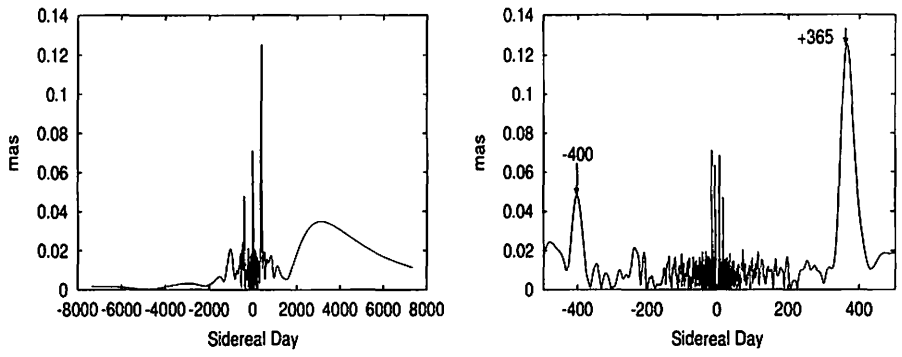

Fig. 5.— Frequency Spectrum of Complex Residuals of New Series. Same as Figure 2 but for the new nutation series. The period of the peak in the prograde band is that of the annual and that in the retrograde one is about −400 sidereal days.

$R, R', R_{\rm FCN}, R_{\rm CW}, \hat{\omega}_{\rm FCN}$, and $\hat{\omega}_{\rm CW}$ depend on the geophysical model. Following Herring, we first estimated the parameters $R, R', R_{\rm FCN}$, and $\hat{\omega}_{\rm FCN}$ from the VLBI data. When we additionally included $R_{\rm CW}$ and $\hat{\omega}_{\rm CW}$ to the parameters to be fitted, the resulting estimates became far from the geophysically predicted values. This is because the separation among the parameters was degraded due to strong correlations among them. Thus we fixed $R_{\rm CW}$ and $\hat{\omega}_{\rm CW}$ as their values geophysically estimated same with Herring (1995). On the other hand, we included to the parameters to be fitted the correction to the IAU1976 precession formula (Lieske et al. 1977), namely the offsets and rates of nutation. As we mentioned in the previous section, we adopted the model A to incorporate the FCN. Then we also included $C_{\rm FCN}$ to the parameters to be fitted. In summary, we simultaneously estimated 7 complex parameters comprised of (1) 4 complex parameters characterizing the transfer function, $R, R', R_{\rm FCN}$, and $\hat{\omega}_{\rm FCN}$, (2) 2 complex ones corresponding to the offsets and rates of nutations in longitude and in obliquity, and (3) the complex amplitude of the FCN, $C_{\rm FCN}$. The estimation was done by the weighted non-linear least square method. This approach is almost the same as that created the IERS96 nutation theory. The main differences are (1) the FCN term which we included while Herring did not, (2) the additional annual prograde term which Herring estimated while we did not, and (3) the period of VLBI data.

4. Result

4.1. Residual

See Table 1 again. The WRMS of the residuals for the new theory is 0.3075 mas, which is about 6% smaller than 0.312 mas that of the IERS96 nutation theory. Figure 1 has already shown the residuals for the new theory. Figure 5 does the periodgram of the new nutation theory for the prograde and the retrograde bands. There appears a strong peak in the prograde band which was not seen in the spectrum of the IERS96 nutation theory. The frequency of the peak is +365 sidereal days and therefore is quite close to the annual oscillation. Herring suggested that this eminent prograde nearly-annual nutation was influenced by the S_1

Table 2: Estimated Parameters of Nutation

	Unit	New	IERS96	Wahr	MBHS	DD
R^r		1.049018 ± 0.000011	1.04901828112	1.0496591879	1.05017	1.050419
R^i		0.00156 ± 0.000011	0.00150732471	...	...	...
R^{rr}		-0.2570 ± 0.0007	−0.25517427386	−0.282203701	−0.28510	−0.279056
R^{ri}		-0.0406 ± 0.0007	−0.03965769073	...	...	...
$R^r_{\rm FCN}$	10^{-4}	-1.1499 ± 0.0002	−1.1489752	−1.091387	−1.1021	−1.19
$R^i_{\rm FCN}$	10^{-6}	-2.17 ± 0.02	−2.1430	...	...	...
$\hat{\omega}^r_{\rm FCN}$	10^{-3}	-2.3206 ± 0.0025	−2.31888314	−2.1714	−2.1816	−2.3157
$\hat{\omega}^i_{\rm FCN}$	10^{-5}	3.06 ± 0.25	2.920327	...	...	...
$P_{\rm FCN}$	sidereal day	-430.8 ± 0.6	−431.2	−460.5	−457.1	−431.8
$C^r_{\rm FCN}$	μas	-78 ± 3	...	...	...	...
$C^i_{\rm FCN}$	μas	-0.6 ± 3	...	...	...	...

Note: MBHS and DD stand for Mathews et al. (1991) and Dehant & Defraigne (1997), respectively.

atmospheric tide. This is the reason why Herring estimated the amplitude of the annual prograde nutation together with other parameters. However, if the S_1 atmospheric tide influences the component the annual prograde nutation, it must also do the annual retrograde component. See the report of the IAU/IUGG Working Group on Nutation (Dehant et al. 1999). Unfortunately Figure 5 shows that there is no annual peak in the retrograde band. Thus the origin of the annual prograde oscillation seen in the residuals is unknown. Therefore we dare not to add this unknown term to the new theory in order only to decrease the post-fit WRMS. On the other hand there is a peak of the period of around −400 sidereal days in the retrograde band. This peak represents the remaining after our FCN term was removed. This means that the FCN could be a combination of the models A and B. We will reserve this issue for future researches.

4.2. Parameters of Nutation Theory

The best-fit parameters of the new theory were listed in Table 2 together with those of the other theories. As for the IERS96 nutation theory, we quoted only the values from the report of the IAU/IUGG Working Group on Nutation (Dehant et al. 1999). We estimated the parameters as if they are the complex values. The uncertainties we obtained indicate that all the imaginary parts are significant except $C^i_{\rm FCN}$. We estimated the oscillatory period of the FCN as -430.8 ± 0.6 sidereal days. This is about 6.5 % smaller than the geophysically estimated value −460.5 sidereal days by Wahr (1981), −457.1 sidereal days by Mathews et al. (1991), and in good agreement with that by Dehant and Defraigne (1997). The Q-value of the FCN was estimated as 16200 ± 1600.

4.3. Correction to Precession Formula

The best-fit corrections to the precession formula are estimated as

$$\begin{pmatrix} \Delta\psi_{\rm P} \\ \Delta\epsilon_{\rm P} \end{pmatrix} = \begin{pmatrix} \Delta\psi_0 \\ \Delta\epsilon_0 \end{pmatrix} + \begin{pmatrix} \Delta\psi_1 \\ \Delta\epsilon_1 \end{pmatrix} T \tag{11}$$

Table 3: Corrections to Precession Constants

Method & Reference		$\Delta\psi_1$ ("/cy)		$\Delta\epsilon_1$ ("/cy)	
		Value	σ	Value	σ
V	Fanselow *et al.* (1984)	−0.38	0.09		
V	Herring *et al.* (1986)	−0.239	0.013		
V	Sovers (1990)	−0.196	0.013		
V	Zhu *et al.* (1990)	−0.376	0.047	+0.017	0.017
S	Andrei & Elsmore (1991)	+0.01	0.15		
V	Herring *et al.* (1991)	−0.32	0.10	−0.040	0.050
L+V	Williams *et al.* (1991)	−0.27	0.04		
V	McCarthy & Luzum (1991)	−0.274	0.021	−0.005	0.007
P	Miyamoto & Soma (1993)	−0.27	0.03		
V	Walter & Ma (1994)	−0.359	0.114		
T	Williams (1994)	−0.2368		−0.0244	
L+V	Charlot *et al.* (1995)	−0.300	0.020	−0.020	0.008
V	Herring (1995)	−0.298	0.010	−0.024	0.005
V	Souchay *et al.* (1995)	−0.321	0.003	−0.026	0.001
V	Walter & Sovers (1996)	−0.31	0.01		
O	Vondrak (1999)	−0.1543	0.0043	−0.0131	0.0018
L	Chapront *et al.* (1999)	−0.3437	0.0040		
P	Vityazev (2000)	−0.28	0.08		
O	Vondrak and Ron (2000)	−0.216	0.005	−0.009 3	0.001 8
V	Petrov (2000)	−0.295	0.002	−0.027	0.009
V	Vondrak & Ron (2000)	−0.2990	0.0013	−0.02203	0.00067
V	Mathews *et al.* (2000)	−0.30010	0.00075	−0.02471	
V	Shirai & Fukushima (2000)	−0.29297	0.00047	−0.02430	0.00019

Note: Shown are the estimations of the corrections to be *added* to the precession constants, or the linear rates precisely speaking, given in the IAU 1976 precession formula (Lieske *et al.* 1977). The symbols of the methods are; V for the VLBI data, S for the short baseline radio interferometry, L for the LLR data, P for the proper motion data of M- and K-type giants, T for the theoretical consideration, O for the optical observation of latitude variations.

and

$$\Delta\psi_0 = -0".042458 \pm 0.000033, \quad \Delta\epsilon_0 = -0".005186 \pm 0.000013 \tag{12}$$

$$\Delta\psi_1 = -0".29297 \pm 0.00047, \quad \Delta\epsilon_1 = -0".02430 \pm 0.00019 \tag{13}$$

where T is the time measured in Julian centuries since J2000.0. We listed our estimated values to precession constants in Table 3 together with the other estimations. Figure 6 compares the values graphically. And we also listed our estimated values to offsets of celestial ephemeris pole in Table 4 together with the other estimations. The uncertainty of new estimates is the smallest of them. This is because separation of fitted parameters is good. All these values were estimated from the analysis of VLBI data except for (1) Andrei and Elsmore (1991) who obtained the corrections from the analysis of short baseline interferometry, (2) Williams et al. (1991) and Charlot et al. (1995) who based on the combined analysis of VLBI and LLR data, (3) Miyamoto & Soma (1993) and Vityazev (2000) who estimated from the analysis of proper motion of K-M giants , (4) Williams (1994) who predicted these values theoretically, (5) Chapront et al.(1999) who

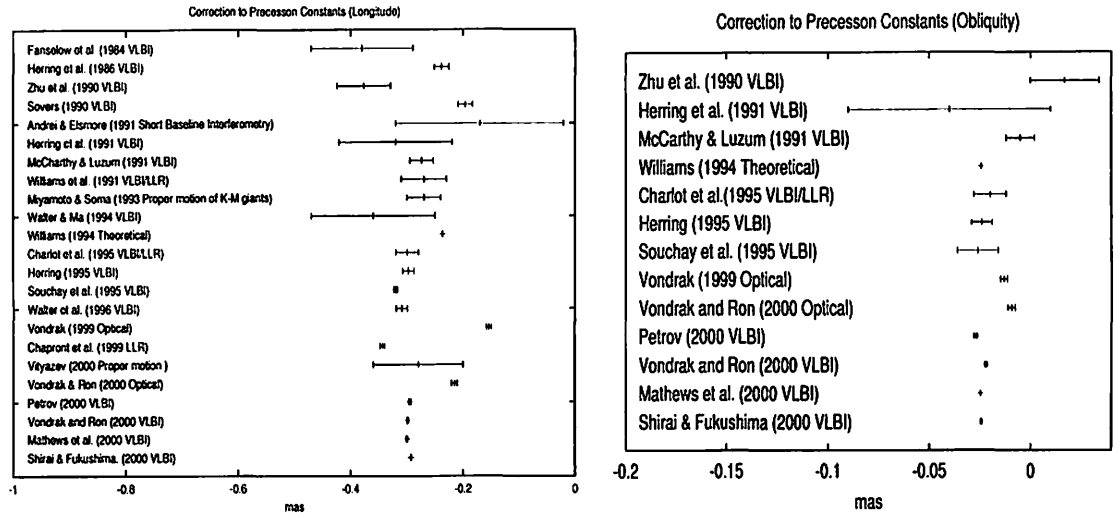

Fig. 6.— Estimated Corrections to Precession in Longitude and Obliquity. We listed the names of authors, the year of publishment, and the method based on. Numerical values are listed in Table 3.

estimated from analysis of LLR data, and (6) Vondrak (1999) and Vondrak & Ron (2000) who estimated by using the optical data for the period 1899.7-1992.0. The new estimated correction in obliquity is in good agreement with that of Williams. However this is not the case in longitude.

4.4. Expression of New theory

Finally we present the new theory explicitly. The theory consists of 4 parts:

$$\Delta\psi_{\rm NEW} = \Delta\psi_{\rm P} + \Delta\psi_{\rm F} + \Delta\psi_{\rm FCN} + \Delta\psi_{\rm G} \quad \Delta\epsilon_{\rm NEW} = \Delta\epsilon_{\rm P} + \Delta\epsilon_{\rm F} + \Delta\epsilon_{\rm FCN} \tag{14}$$

where the suffices P denotes the correction of the precession formula, F does the forced nutation series, FCN does the FCN term, and G does the geodesic nutation. The first part includes two terms, the offsets and the rates.

$$\begin{pmatrix} \Delta\psi_{\rm P} \\ \Delta\epsilon_{\rm P} \end{pmatrix} = \begin{pmatrix} \Delta\psi_0 \\ \Delta\epsilon_0 \end{pmatrix} + \begin{pmatrix} \Delta\psi_1 \\ \Delta\epsilon_1 \end{pmatrix} T \tag{15}$$

and

$$\Delta\psi_0 = -0".042458 \quad \Delta\epsilon_0 = -0".005186 \tag{16}$$

$$\Delta\psi_1 = -0".29297 \quad \Delta\epsilon_1 = -0".02430 \tag{17}$$

where T is the time measured in Julian centuries since J2000.0. Tables 5 and 6 show the main terms of luni-solar and planetary contributions of the second part, the forced nutation, respectively.

$$\Delta\psi_{\rm F} = \sum_{k=1}^{180} \left[(A_{c,k} + A'_{c,k} T) \cos\theta_k + (A_{s,k} + A'_{s,k} t) \sin\theta_k \right] \tag{18}$$

Table 4: Offsets of Celestial Ephemeris Pole at J2000.0

Method & Reference		$\Delta\psi_0 \sin\varepsilon_0$ (mas)		$\Delta\varepsilon_0$ (mas)	
		Value	σ	Value	σ
V	Herring (1995)	−17.3	0.2	−5.1	0.2
L	Chapront *et al.* (1999)	−18.3	0.4	−5.6	0.2
O	Vondrak & Ron (2000)	−12.3	0.7	−9.2	0.6
V	Vondrak & Ron (2000)	−17.10	0.05	−4.95	0.05
V	Mathews *et al.* (2000)	−16.18		−4.53	
V	Shirai & Fukushima (2000)	−16.889	0.013	−5.186	0.013

Table 7: Polynomial developments in T of argument (Simon el al.)

	Constant	T	T^2	T^3	T^4
ℓ	134°.96340251	1717915923".2178	31".8792	0".051635	−0".00024470
ℓ'	357°.52910918	129596581".0481	−0".5532	0".000136	−0".00001149
F	93°.27209062	1739527262".8478	−12".7512	−0".001037	0".00000417
D	297°.85019547	1602961601".2090	−6".3706	0".006539	−0".00003169
Ω	125°.04455501	−6962890".5431	7".4722	0".007702	−0".000059
V_e	181°.97980085	210664136".4335	...	...	...
M_a	355°.43299958	68905077".4940	...	...	...
J_u	34°.35151874	10925660".3780	...	...	...
S_a	50°.07744430	4399609".8557	...	...	...

$$\Delta\epsilon_{\rm F} = \sum_{k=1}^{180} \left[(B_{c,k} + B'_{c,k}T)\cos\theta_k + (B_{s,k} + B'_{s,k}t)\sin\theta_k \right] . \tag{19}$$

Here the argument θ is expressed as a linear form of basic angles as

$$\theta_k = \sum_j n_{j,k}\theta^{(j)} \tag{20}$$

where the basic angles are

$$\{\theta^{(j)}\} = \{\ell, \ell', F, D, \Omega, Ve, Ma, Ju, Sa, Me\}. \tag{21}$$

whose polynomial developments in T given by Simon el al. (1994) are quoted in Table 7. The third part, the FCN term, is expressed as

$$\Delta\psi_{\rm FCN} \sin\epsilon_0 = e^{-\omega^i_{\rm FCN}T}(-78\cos\omega^r_{\rm FCN}T + 0.6\sin\omega^r_{\rm FCN}T) \tag{22}$$

$$\Delta\epsilon_{\rm FCN} = e^{-\omega^i_{\rm FCN}T}(-0.6\cos\omega^r_{\rm FCN}T - 78\sin\omega^r_{\rm FCN}T) \tag{23}$$

where the unit is μas for the amplitude and

$$\omega^i_{\rm FCN} = 7.11 \quad \text{rad/cy} \quad \omega^r_{\rm FCN} = 1.10 \times 10^8 \quad \text{"/cy.} \tag{24}$$

The last part, the geodesic nutation, is expressed (Fukushima 1991) as

$$\Delta\psi_{\rm G} = -153.1\sin\ell' - 1.9\sin 2\ell' \tag{25}$$

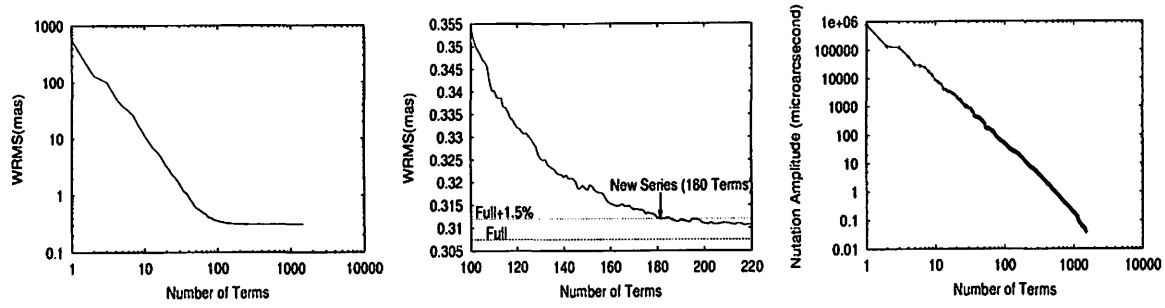

Fig. 7.— Number-of-Terms Dependence of WRMS and Nutation Amplitude. Clearly the WRMS does not decrease significantly after around 100 terms. On the other hand, the amplitude decrease linearly.

where the unit is μas for the amplitude.

The original RDAN98 contains 1501 terms. After the convolution by the transfer function, we sorted the series in the order of amplitude and kept only top 180 terms. This is because the WRMS for the abridged series, 0.3120 mas, was only 1.5 % lager than 0.3075 that of the full theory. See Figure 7 for the number-of-terms dependence of WRMS. The WRMS does not significantly decrease after the number of terms exceeds 180. On the other hand, Figure 7 shows the number-of-terms dependence of nutation amplitude of the new theory, which decreases linearly in the logscale. Thus, we conclude the truncated series shown in Tables 5 and 6 are precise enough for the practical purpose.

5. Conclusion

From the analysis of the VLBI data compiled by USNO for the period 1979 to 1999, we showed that a strong peak around -400 sidereal days in the spectrum of their residuals after the IERS96 nutation theory was subtracted could be explained by adding a predicted FCN term. We considered three models on the treatment of the FCN; (1) no FCN contribution, (2) the FCN with no excitation during the observation, and (3) the FCN excited frequently during the observation. The functional form of the FCN is a single damping oscillation in the second case and a simple harmonic oscillation in the last case. From the comparison of WRMS and spectra of the residuals obtained for these models, we adopted the second as the best model. Then we developed a new analytical theory of the non-rigid Earth nutation including thus determined FCN term. We adopted RDAN98 (Roosbeek and Dehant 1998) as the rigid Earth nutation theory. Then it was convoluted with a transfer function by the numerical convolution in the time domain (Shirai and Fukushima 2000). The form of the transfer function was the same as that of Herring (1995), however its free parameters were adjusted by fitting to the above VLBI data. Even after truncating the forced nutation series so short as to contain only 180 terms, the WRMS of the residuals for the new nutation series is sufficient small as 0.3120 mas. This significantly smaller than 0.3250 mas, that of the IERS96 nutation theory. As for the FCN term, we estimated its oscillatory period as -430.8 ± 0.6 sidereal days and Q-value as 16200 ± 1600. Also we estimated the correction to the precession constants as -0.042458 ± 0.000033 $''$ in longitude and -0.005186 ± 0.000013 $''$ in obliquity to offsets and -0.29297 ± 0.00047 $''$/cy in longitude and

-0.02430 ± 0.00019 "/cy in obliquity to rates, respectively. The f77 program to compute the new series is available from the author TS.

Acknowledgements. The authors wish to thank D.D. McCarthy for providing the VLBI observational data compiled by USNO.

REFERENCES

Andrei, A. H., and Elsmore, B., 1991, Proceedings of IAU Coll. No. 127, edited by J. A. Hughes, C. A. Smith, and G. H. Kaplan, 157

Chapront,J., Chapront-Touze, M., and Francou, G., 1999, A&A, 343, 624

Charlot, P., Sovers, O. J., Williams, J. G., and Newhall, X. X., 1995, AJ, 109, 418

Dehant, V., et al., 1999, Celest. Mech. Dyn. Astron., 72, 245

Dehant, V., and Defraigne, P., 1997, J. Geophys. Res., 102, 27659

Fanselow el al., 1984, AJ, 89, 987

Fukushima, T., 1991, A&A, 244, L11

Gegout, P., Hinerer, J., Legros, H., Greff, M., and Dehant, V., 1998, Phys. Earth. Planet. Inter., 106, 337

Herring, T. A., Gwinn, C. R., and Shapiro, I. I., 1986, J. Geophys. Res., 91, B5, 8259

Herring, T. A., Buffett, B. A., Mathews, P. M., and Shapiro, I. I., 1991, J. Geophys. Res., 96, 8259

Herring, T. A., 1995, Hightlights of Astronomy, 10, 222

Kinoshita, H., 1977, Celest. Mech., 15, 277

Kinoshita, H., Nakajima, J., Kubo, Y., Nakagawa, I., Sasao, T., and Yokoyama, K., 1979, Publs Int. Lat. Obs. Mizusawa, 12, 71

Lieske, J. H., Lederle, T., Fricke, W., and Morando, B., 1977, A&A, 58, 1

Mathews, P. M., Buffett, B. A., Herring, T. A., and Shaprio, I. I., 1991, J. Geophys. Res., 96, 8243

Mathews, P. M., Buffett, B. A., Herring, T. A., 2000, J. Geophys. Res., submitted

McCarthy, D. D., Luzum, B. J., 1991, AJ, 102, 1889

McCarthy, D. D., 1996, 'IERS Conventions', IERS Technical Note 21

Miyamoto, M., and Soma, M., 1993, AJ, 105, 691

Petrov, L., 2000, Proceedings IAU Coll. No. 180, in press

Roosbeek, F., and Dehant, V., 1998, Celest. Mech. Dyn. Astron., 70, 215

Roosbeek, F., Defraigne, P., Feissel, M., and Dehant, V., 1999, Geophys. Res. L., 26, 131

Sasao, T., and Wahr, J. M., 1981, Geophys. J. R. Astron. Soc., 64, 729

Seidelmann, P. K., 1982, Celest. Mech., 27, 79

Shirai, T., and Fukushima, T., 2000, AJ, 119, ?

Souchay, J., Feissel, M., Bizouard, C., Capitaine, N., and Bougeard, M., 1995, A&A, 299, 277

Sovers, O. J., Proceedings IAU Symp. No. 141, 261

Toomre, A., 1974, Geophys. J. R. Astron. Soc., 38, 335

Vityazev, V., 2000, Proceedings IAU Coll. No. 180, in press

Vondark, J., 1999, Celest. Mech. Dyn. Astron., 20, 169

Vondark, J., and Ron, C., 2000, Proceedings IAU Coll. No. 180, in press

Wahr, J. M., 1981, Geophys. J. R. Astron. Soc., 64, 705

Walter, H. G., and Ma C., 1994, A&A, 284, 1000

Walter, H. G., and Sovers O. J., 1996, A&A, 308, 1001

Williams,J. G., 1991, A&A, 241, L9

Williams, J. G., 1994, AJ, 108, 711

Zhu, S. Y., Groten, E., Reigber, Ch., 1990, AJ, 99, 1024

Table 5. Forced nutaion series for luni-solar part

	PERIOD	ARGUMENT					LONGITUDE				OBLIQUITY			
No	(days)	ℓ	ℓ'	F	D	Ω	A_c	A_s	A'_c	A'_s	B_c	B_s	B'_c	B'_s
1	6798.38	0	0	0	0	-1	3675.3	17206295.2	2.9	17409.5	9205361.1	-1534.8	885.7	-0.4
2	182.62	0	0	2	-2	2	-1457.3	-1317108.7	1.2	-156.8	573058.8	-483.9	-305.0	-0.2
3	13.66	0	0	2	0	2	288.6	-227664.1	0.2	-23.5	97843.2	145.4	-48.8	-0.1
4	3399.19	0	0	0	0	-2	-66.5	-207450.0	0.0	-21.4	-89754.2	26.8	46.9	0.0
5	365.26	0	1	0	0	0	923.5	147610.1	-2.2	-355.0	7410.2	-324.1	-18.2	0.8
6	121.75	0	1	2	-2	2	-56.3	-51685.8	0.2	122.6	22440.8	-18.7	-67.6	0.0
7	27.55	1	0	0	0	0	-99.9	71111.3	0.0	7.0	-684.6	40.1	0.0	0.0
8	13.63	0	0	2	0	1	38.1	-38740.3	0.1	-36.2	20070.0	34.8	1.6	0.0
9	9.13	1	0	2	0	2	82.1	-30128.3	0.0	-3.1	12893.9	37.7	-6.2	0.0
10	365.23	0	-1	2	-2	2	5.8	21581.8	0.1	-50.3	-9592.8	13.0	30.2	-0.1
11	177.84	0	0	2	-2	1	18.7	12822.1	0.0	13.3	-6899.0	4.1	-0.6	0.0
12	27.09	-1	0	2	0	2	1.8	12350.2	0.0	1.3	-5332.2	-0.6	2.7	0.0
13	31.81	-1	0	0	2	0	-19.4	15698.1	0.0	1.6	-125.4	9.0	0.0	0.0
14	27.67	1	0	0	0	1	3.0	6313.6	0.0	6.2	-3323.2	-1.1	-0.3	0.0
15	27.44	1	0	0	0	-1	-20.1	5796.1	0.0	6.1	3142.0	7.9	0.3	0.0
16	9.56	-1	0	2	2	2	15.1	-5961.2	0.0	-0.6	2552.6	7.0	-1.2	0.0
17	9.12	1	0	2	0	1	12.8	-5159.4	0.0	-4.6	2634.3	8.3	0.2	0.0
18	1305.48	-2	0	2	0	1	1.4	4592.5	0.0	4.5	-2424.4	1.3	-0.4	0.0
19	14.77	0	0	0	2	0	-16.1	6335.5	0.0	0.7	-123.5	3.3	0.0	0.0
20	7.10	0	0	2	2	2	15.5	-3851.3	0.0	-0.4	1642.5	6.9	-0.8	0.0
21	205.89	2	0	0	-2	0	-2.4	4771.2	0.0	0.5	47.9	2.7	0.0	0.0
22	6.86	2	0	2	0	2	13.1	-3099.5	0.0	-0.3	1321.3	5.8	-0.6	0.0
23	23.94	1	0	2	-2	2	-0.1	2860.2	0.0	0.3	-1234.1	-0.4	0.6	0.0
24	26.98	-1	0	2	0	1	1.0	2045.2	0.0	2.0	-1076.4	-0.4	0.0	0.0
25	13.78	2	0	0	0	0	-8.0	2922.4	0.0	0.3	-61.6	1.5	0.0	0.0
26	13.61	0	0	2	0	0	-7.2	2587.7	0.0	0.2	-55.4	1.3	0.0	0.0
27	386.00	0	1	0	0	1	8.7	-1407.8	0.0	3.7	856.9	-4.6	-2.1	0.0
28	31.96	-1	0	0	2	1	1.1	1517.4	0.0	1.5	-800.7	-0.1	0.0	0.0
29	91.31	0	2	2	-2	2	-1.6	-1579.6	0.0	7.7	685.1	-0.5	-3.8	0.0
30	173.31	0	0	2	-2	0	1.1	-2178.4	0.0	-0.2	-16.9	-1.3	0.0	0.0
31	31.66	-1	0	0	2	-1	-4.2	1286.7	0.0	1.3	695.6	1.6	0.0	0.0

Table 5 —Continued

	PERIOD	ARGUMENT					LONGITUDE			OBLIQUITY			
32	346.64	0	1	0	0	-1	6.5	1267.1	0.0	-4.0	642.2	-2.7	-1.6	0.0
33	182.63	0	2	0	0	0	-0.9	1669.2	0.0	-8.3	13.3	1.0	-0.1	0.0
34	9.54	-1	0	2	2	1	2.3	-1020.0	0.0	-0.9	521.9	1.5	0.0	0.0
35	5.64	1	0	2	2	2	4.2	-767.0	0.0	0.0	325.8	1.9	-0.1	0.0
36	13.17	0	1	2	0	2	-1.1	756.5	0.0	-1.7	-325.1	-0.5	0.9	0.0
37	1095.18	-2	0	2	0	0	-1.2	-1097.3	0.0	-0.5	10.1	0.3	0.0	0.0
38	7.09	0	0	2	2	1	2.5	-663.0	0.0	-0.6	334.5	1.5	0.0	0.0
39	14.19	0	-1	2	0	2	0.8	-714.1	0.0	1.6	307.1	0.4	-0.9	0.0
40	14.80	0	0	0	2	1	0.5	-629.9	0.0	-0.6	327.1	0.5	0.0	0.0
41	23.86	1	0	2	-2	1	0.2	580.4	0.0	0.6	-304.6	-0.2	0.0	0.0
42	199.84	2	0	0	-2	-1	-1.4	577.2	0.0	0.5	304.0	0.5	0.0	0.0
43	12.81	2	0	2	-2	2	-0.9	644.4	0.0	0.0	-276.8	-0.5	0.1	0.0
44	6.85	2	0	2	0	1	2.1	-534.0	0.0	-0.5	268.9	1.2	0.0	0.0
45	14.73	0	0	0	2	-1	-2.3	493.2	0.0	0.5	271.8	1.0	0.0	0.0
46	346.60	0	-1	2	-2	1	0.0	-477.3	0.0	-2.4	271.5	-0.4	-0.8	0.0
47	34.85	-1	-1	0	2	0	-0.8	735.0	0.0	-1.7	-5.2	0.4	0.0	0.0
48	212.32	2	0	0	-2	1	0.6	406.2	0.0	0.4	-220.5	0.1	0.0	0.0
49	9.61	1	0	0	2	0	-2.6	656.8	0.0	0.0	-20.2	0.3	0.0	0.0
50	119.61	0	1	2	-2	1	0.5	358.0	0.0	2.0	-191.0	0.1	0.5	0.0
51	29.80	1	-1	0	0	0	-0.6	472.5	0.0	-1.1	-4.1	0.3	0.0	0.0
52	1615.75	-2	0	2	0	2	-0.1	-300.5	0.0	0.0	130.6	-0.1	0.0	0.0
53	15.39	0	-1	0	2	0	-1.1	435.1	0.0	-1.0	3.0	0.3	0.0	0.0
54	5.49	3	0	2	0	2	1.7	-289.5	0.0	0.0	122.9	0.7	0.0	0.0
55	29.53	0	0	0	1	0	0.6	-422.6	0.0	0.0	3.7	-0.2	0.0	0.0
56	9.37	1	-1	2	0	2	0.8	-287.6	0.0	0.6	123.1	0.3	-0.3	0.0
57	411.78	1	0	0	-1	0	-37.1	-394.4	0.0	0.0	-53.5	14.7	0.0	0.0
58	9.81	-1	-1	2	2	2	0.7	-281.8	0.0	0.6	120.7	0.3	-0.3	0.0
59	26.88	-1	0	2	0	0	0.6	-405.6	0.0	0.0	4.0	-0.2	0.0	0.0
60	13.75	2	0	0	0	-1	-1.1	228.9	0.0	0.2	126.5	0.5	0.0	0.0
61	7.24	0	-1	2	2	2	1.0	-264.3	0.0	0.5	112.8	0.5	-0.3	0.0
62	8.91	1	1	2	0	2	-0.7	247.9	0.0	-0.5	-106.1	-0.3	0.3	0.0
63	13.81	2	0	0	0	1	-0.2	218.0	0.0	0.2	-112.9	-0.2	0.0	0.0

Table 5—Continued

	PERIOD	ARGUMENT					LONGITUDE			OBLIQUITY			
64	25.62	1	1	0	0	0	0.5	-339.0	0.0	0.8	3.6	-0.2	0.0	0.0
65	32.61	1	0	-2	2	-1	-0.6	198.7	0.0	0.2	107.3	0.2	0.0	0.0
66	9.11	1	0	2	0	0	-1.4	334.0	0.0	0.0	-11.0	0.1	0.0	0.0
67	3232.86	-1	1	0	1	0	0.1	334.0	0.0	0.0	-0.9	0.0	0.0	0.0
68	27.78	1	0	0	0	2	0.0	-198.1	0.0	0.0	85.4	0.0	0.0	0.0
69	3231.50	-1	0	1	0	1	-106.6	0.0	0.0	0.0	0.0	-88.8	0.0	0.0
70	9.34	0	0	2	1	2	-0.4	165.8	0.0	0.0	-71.0	-0.2	0.0	0.0
71	6164.10	-1	1	0	1	1	0.0	134.8	0.0	0.0	-70.3	0.0	0.0	0.0
72	5.80	-1	0	2	4	2	0.8	-151.6	0.0	0.0	64.5	0.3	0.0	0.0
73	6786.32	0	-2	2	-2	1	0.0	-129.7	0.0	0.0	69.8	0.0	0.0	0.0
74	5.64	1	0	2	2	1	0.7	-132.8	0.0	-0.1	66.1	0.4	0.0	0.0
75	27.33	1	0	0	0	-2	0.4	-140.6	0.0	0.0	-61.0	-0.2	0.0	0.0
76	14.63	-2	0	2	2	2	-0.1	138.4	0.0	0.0	-59.5	-0.1	0.0	0.0
77	22.47	1	1	2	-2	2	0.0	129.0	0.0	-0.3	-55.6	0.0	0.2	0.0
78	7.35	-2	0	2	4	2	0.5	-121.2	0.0	0.0	51.7	0.2	0.0	0.0
79	9.06	-1	0	4	0	2	-0.3	114.5	0.0	0.0	-49.0	-0.1	0.0	0.0
80	12.79	2	0	2	-2	1	-0.1	101.9	0.0	0.0	-52.7	-0.1	0.0	0.0
81	388.27	1	0	0	-1	-1	-3.5	-102.0	0.0	0.0	-49.6	1.4	0.0	0.0
82	4.68	2	0	2	2	2	0.8	-109.4	0.0	0.0	46.3	0.3	0.0	0.0
83	9.63	1	0	0	2	1	0.2	-97.0	0.0	0.0	49.6	0.1	0.0	0.0
84	9.18	3	0	0	0	0	-0.6	157.3	0.0	0.0	-5.1	0.1	0.0	0.0
85	169.00	0	0	2	-2	-1	0.2	-83.3	0.0	0.0	-44.0	-0.1	0.0	0.0
86	8.75	3	0	2	-2	2	-0.3	93.3	0.0	0.0	-39.9	-0.1	0.0	0.0
87	12.66	0	0	4	-2	2	-0.1	92.1	0.0	0.0	-39.5	-0.1	0.0	0.0
88	10.08	-1	0	0	4	0	-0.5	133.6	0.0	0.0	-3.9	0.1	0.0	0.0
89	13.14	0	1	2	0	1	-0.1	81.5	0.0	0.0	-42.1	-0.1	0.0	0.0
90	187.66	0	0	2	-2	3	0.0	123.9	0.0	0.0	-17.2	0.1	0.0	0.0
91	15.91	-2	0	0	4	0	-0.3	128.1	0.0	0.0	-2.3	0.1	0.0	0.0
92	35.03	-1	-1	0	2	1	0.1	74.1	0.0	-0.3	-39.2	0.0	0.0	0.0
93	943.23	-2	0	2	0	-1	-0.2	-70.3	0.0	0.0	-38.4	0.1	0.0	0.0
94	13.58	0	0	2	0	-1	-0.3	66.6	0.0	0.0	36.8	0.1	0.0	0.0
95	14.16	0	-1	2	0	1	0.1	-66.7	0.0	0.0	34.6	0.1	0.0	0.0

Table 5—Continued

	PERIOD	ARGUMENT					LONGITUDE			OBLIQUITY			
96	409.23	0	1	0	0	2	-0.7	69.3	0.0	-0.3	-32.7	0.3	0.0	0.0
97	25.42	0	0	2	-1	2	0.0	-70.4	0.0	0.0	30.4	0.0	0.0	0.0
98	131.67	2	1	0	-2	0	-0.1	101.5	0.0	0.0	0.4	0.1	0.0	0.0
99	4.79	0	0	2	4	2	0.5	-69.1	0.0	0.0	29.3	0.2	0.0	0.0
100	34.67	-1	-1	0	2	-1	-0.2	58.5	0.0	0.2	31.6	0.1	0.0	0.0
101	29.26	-1	1	0	2	0	0.1	-94.9	0.0	0.2	0.8	-0.1	0.0	0.0
102	29.93	1	-1	0	0	1	0.0	52.9	0.0	-0.2	-27.9	0.0	0.0	0.0
103	329.79	0	-1	2	-2	0	0.1	86.7	0.0	-0.2	2.9	0.0	0.0	0.0
104	329.82	0	1	0	0	-2	-0.1	-59.2	0.0	0.2	-25.3	0.1	0.0	0.0
105	5.73	1	-1	2	2	2	0.3	-58.8	0.0	0.1	25.0	0.1	0.0	0.0
106	9.60	1	0	0	2	-1	-0.3	49.0	0.0	0.0	27.5	0.1	0.0	0.0
107	9.31	-1	1	2	2	2	-0.1	56.9	0.0	-0.1	-24.4	-0.1	0.0	0.0
108	5.49	3	0	2	0	1	0.3	-50.2	0.0	0.0	24.9	0.1	0.0	0.0
109	6.96	0	1	2	2	2	-0.2	53.4	0.0	-0.1	-22.8	-0.1	0.0	0.0
110	23.77	1	0	2	-2	0	0.1	-76.5	0.0	0.0	0.9	0.0	0.0	0.0
111	38.74	-1	0	-2	4	-1	-0.1	45.3	0.0	0.0	24.4	0.1	0.0	0.0
112	9.80	-1	-1	2	2	1	0.1	-46.8	0.0	0.0	23.9	0.1	0.0	0.0
113	7.23	0	-1	2	2	1	0.2	-44.6	0.0	0.0	22.5	0.1	0.0	0.0
114	6.99	2	-1	2	0	2	0.2	-48.7	0.0	0.0	20.8	0.1	0.0	0.0
115	14.83	0	0	0	2	2	0.1	-46.8	0.0	0.0	20.1	0.0	0.0	0.0
116	25.22	-1	1	2	0	2	0.0	46.4	0.0	-0.1	-20.0	0.0	0.0	0.0
117	9.35	1	-1	2	0	1	0.1	-42.0	0.0	0.0	21.5	0.1	0.0	0.0
118	14.19	0	1	0	2	0	0.2	-67.3	0.0	0.1	1.4	0.0	0.0	0.0
119	117.54	0	1	2	-2	0	0.0	-65.8	0.0	0.2	-0.2	0.0	0.0	0.0
120	73.05	0	3	2	-2	2	0.0	-43.9	0.0	0.3	19.0	0.0	-0.1	0.0
121	29.66	0	0	0	1	1	0.0	-38.9	0.0	0.0	20.5	0.0	0.0	0.0
122	9.53	-1	0	2	2	0	-0.2	63.9	0.0	0.0	-2.0	0.0	0.0	0.0
123	6.73	2	1	2	0	2	-0.2	41.2	0.0	0.0	-17.6	-0.1	0.0	0.0
124	25.72	1	1	0	0	1	0.0	-36.1	0.0	0.2	19.0	0.0	0.0	0.0
125	7.13	2	0	0	2	0	-0.3	58.5	0.0	0.0	-2.5	0.0	0.0	0.0
126	8.90	1	1	2	0	1	-0.1	36.1	0.0	0.0	-18.4	-0.1	0.0	0.0
127	32.11	-1	0	0	2	2	0.0	-39.7	0.0	0.0	17.1	0.0	0.0	0.0

Table 5—Continued

	PERIOD	ARGUMENT					LONGITUDE				OBLIQUITY			
128	32.76	1	0	-2	2	0	0.1	-57.7	0.0	0.0	0.4	0.0	0.0	0.0
129	15.35	0	-1	0	2	-1	-0.1	33.4	0.0	0.0	18.4	0.1	0.0	0.0
130	6159.14	-1	0	1	0	2	36.4	0.0	0.0	0.0	0.0	17.4	0.0	0.0
131	27.32	0	1	0	1	0	-0.1	55.7	0.0	-0.1	-0.6	0.0	0.0	0.0
132	32.45	1	0	-2	2	-2	0.1	-35.4	0.0	0.0	-15.4	0.0	0.0	0.0
133	29.40	0	0	0	1	-1	0.1	-31.0	0.0	0.0	-16.8	0.0	0.0	0.0
134	29.67	1	-1	0	0	-1	-0.1	30.1	0.0	0.0	16.3	0.0	0.0	0.0
135	7.38	0	0	0	4	0	-0.2	49.2	0.0	0.0	-2.0	0.0	0.0	0.0
136	6.98	1	0	2	1	2	-0.1	33.6	0.0	0.0	-14.3	-0.1	0.0	0.0
137	9.87	1	-1	0	2	0	-0.2	49.1	0.0	0.0	-1.5	0.0	0.0	0.0
138	13.22	1	0	2	-1	2	0.1	-33.5	0.0	0.0	14.4	0.0	0.0	0.0
139	31.52	-1	0	0	2	-2	0.1	-31.0	0.0	0.0	-13.4	0.0	0.0	0.0
140	9.33	0	0	2	1	1	-0.1	28.0	0.0	0.0	-14.3	0.0	0.0	0.0
141	26.77	-1	0	2	0	-1	0.1	-25.2	0.0	0.0	-13.7	0.0	0.0	0.0
142	5.80	-1	0	2	4	1	0.1	-26.2	0.0	0.0	13.1	0.1	0.0	0.0
143	7.08	0	0	2	2	0	-0.2	41.5	0.0	0.0	-1.8	0.0	0.0	0.0
144	22.40	1	1	2	-2	1	0.0	24.5	0.0	0.1	-12.8	0.0	0.0	0.0
145	27.32	0	0	1	0	1	-16.2	0.0	0.0	0.0	0.0	-14.4	0.0	0.0
146	313.04	-1	0	2	-1	1	0.0	-22.3	0.0	0.0	12.4	0.0	0.0	0.0
147	14.60	-2	0	2	2	1	0.0	23.1	0.0	0.0	-12.0	0.0	0.0	0.0
148	14.32	2	-1	0	0	0	-0.1	37.5	0.0	0.0	-0.8	0.0	0.0	0.0
149	4.58	4	0	2	0	2	0.2	-25.7	0.0	0.0	10.9	0.1	0.0	0.0
150	12.38	2	1	2	-2	2	0.0	25.2	0.0	0.0	-10.8	0.0	0.0	0.0
151	9.11	0	1	2	1	2	0.1	-24.5	0.0	0.0	10.5	0.0	0.0	0.0

Note. — Unit is micro-arcsecond for amplitude

Table **6**. Foreced nutation series for planetary part

	PERIOD	ARGUMENT									LONGITUDE				OBLIQUITY			
No	(days)	ℓ	ℓ'	F	D	Ω	V_e	M_a	J_u	S_a	A_c	A_s	A'_c	A'_s	B_c	B_s	B'_c	B'_s
1	2954.56	0	0	5	-5	5	-3	0	0	0	4.0	178.8	-11.8	0.3	-87.7	4.4	-0.4	-6.3
2	2166.29	0	0	0	0	0	0	0	2	0	39.8	-107.3	-5.6	-1.0	46.3	22.4	0.5	-2.4
3	398.87	0	0	1	-1	1	0	0	-1	0	9.6	164.2	-4.1	0.1	15.7	-3.3	0.1	0.4
4	583.96	0	0	-1	1	-1	1	0	0	0	-4.7	-135.3	-3.4	-0.1	5.2	5.8	0.2	-0.1
5	38036.70	0	0	-1	1	0	0	2	0	0	50.5	75.0	1.4	-1.2	-30.1	26.9	0.7	0.0
6	125.27	0	0	3	-3	3	0	0	-1	0	-1.1	-53.5	1.3	0.0	23.2	-0.5	0.0	0.6
7	4964.16	0	0	-8	8	-7	5	0	0	0	-45.0	-2.4	-0.4	6.6	1.0	23.2	3.4	0.0
8	5767.54	0	0	-1	1	-1	0	2	0	0	-11.5	-61.0	-0.9	0.4	-12.2	-4.3	0.0	0.0
9	291.98	0	0	-2	2	-2	2	0	0	0	4.4	-68.4	-3.4	0.0	-2.1	-3.7	-0.2	0.1
10	727.80	0	0	-6	6	-6	4	0	0	0	7.7	-47.1	-4.7	-1.0	-18.6	-3.8	-0.4	1.8
11	182.58	0	0	-2	2	-2	0	8	-3	0	-42.9	-12.6	-1.2	4.2	5.5	-18.7	-1.8	-0.5
12	182.66	0	0	6	-6	6	0	-8	3	0	-42.8	12.7	-1.2	-4.2	-5.5	-18.7	1.8	-0.5
13	487.59	0	0	4	-4	4	-2	0	0	0	-7.6	-44.1	2.1	-0.5	18.4	-3.6	0.3	0.9
14	1455.61	0	0	-3	3	-3	2	0	0	0	-64.1	1.7	0.2	4.5	-0.6	1.3	0.0	0.0
15	6850.09	0	0	4	-4	3	0	-8	3	0	36.4	-10.4	1.0	3.5	-5.6	-19.5	1.9	0.0
16	6747.46	0	0	-4	4	-5	0	8	-3	0	35.6	10.2	1.0	-3.5	5.5	-19.1	-1.9	0.0
17	112.35	0	0	0	0	0	2	0	0	0	-1.7	39.5	2.0	0.0	-17.3	-0.8	0.0	0.9
18	416.76	0	0	-4	4	-4	3	0	0	0	51.4	-8.0	-0.8	-5.0	-3.1	-8.5	-0.8	0.3
19	4335.05	0	1	-1	1	-1	0	0	1	0	0.0	52.3	1.2	0.0	-0.1	0.0	0.0	0.0
20	4332.59	0	0	0	0	0	0	0	1	0	-42.9	-17.8	0.4	0.0	-5.4	7.8	-0.3	0.0
21	139.12	0	0	1	-1	1	1	0	0	0	2.6	34.3	0.8	0.0	-14.8	1.4	0.0	0.3
22	389.94	0	0	2	-2	2	0	-2	0	0	-0.7	-48.6	2.4	-0.1	-3.8	0.4	0.0	-0.2
23	2868.06	0	-1	-7	7	-7	5	0	0	0	-4.9	30.5	3.7	0.7	12.6	3.2	0.5	-1.5
24	6357.65	-2	0	2	0	2	0	0	-2	0	0.0	-43.6	2.1	0.0	0.1	0.0	0.0	0.0
25	13591.40	-2	0	2	0	1	0	0	-3	0	0.0	-25.4	1.2	0.0	-13.6	2.4	-0.1	0.0
26	199.43	0	0	2	-2	2	0	0	-2	0	2.0	40.9	-2.0	0.0	0.9	1.2	0.0	0.0
27	336.85	0	0	1	-1	1	0	0	1	0	-2.1	26.1	0.6	0.0	-11.9	-0.5	0.0	0.3
28	5379.61	0	0	0	0	0	0	0	0	2	22.6	-3.2	-0.5	-0.5	0.4	12.0	0.3	-0.2
29	10759.20	0	0	0	0	0	0	0	0	1	-7.6	24.9	-0.4	-0.2	8.3	6.1	-0.1	0.1

Note. — The unit for the period is day and amplitude is microarcsecond.

The Theory of Motion of Nereid II. Non-planar Case

Abdel-naby S. Saad[1] and **Hiroshi Kinoshita**[2]

[1] *Dept. of Astron. Sci., School of Mathematical and Physical Science, The Graduate Univ. For Advanced Studies, Mitaka, Tokyo 181-8588, Japan.*
E-mail : saad@pluto.mtk.nao.ac.jp

[2] *National Astronomical Observatory, Mitaka, Tokyo 181-8588, Japan.*
E-mail : Kinoshita@nao.ac.jp

Abstract

We have constructed an analytical model for the motion of the second Neptunian satellite Nereid in the frame work of the circular non-planar restricted three body problem using Lie transforms approach. The main perturbing forces due to the solar effects are only taken into account. The disturbing function is developed in powers of the ratio of the semimajor axes of the satellite and the Sun and put in a closed form with respect to the eccentricity. In a separate paper (Saad and Kinoshita 1999) we introduced the solution of the planar motion of Nereid. In this paper we present a complete theory which includes the short, intermediate and long periodic perturbations. The osculating orbital elements which describe the orbital motion of Nereid are evaluated analytically and got ephemerides of Nereid. The comparison with the numerical integration of the equations of motion gives an accuracy on the level of 0.3 km in the semi-major axis, 3×10^{-7} in the eccentricity and 10^{-5} degree in the angular variables over several hundred years. The results of the present theory satisfy the required accuracy for the observations.

Keywords: Celestial mechanics, satellite theory, osculating elements, ephemerides, Nereid

1 Introduction

By virtue of Voyager 2 encounter, Neptune's known satellite system consisted of one large retrograde highly inclined satellite, Triton, a smaller satellite, Nereid, in a prograde highly eccentric orbit, and six newly discovered satellites in the vicinity of their mother planet Neptune. Triton was discovered by Lassel in 1846, Nereid was discovered by Kuiper in 1949, while the other 6 satellites were discovered in 1989 during the Voyager 2 encounter with the Neptunian system (Stone and Miner 1989). Its highly elliptical orbit and faintness make the motion prediction of Nereid inaccurate by the usage of the classical models. Many authors have dealt with the orbital determinations of Nereid (Rose 1974; Mignard 1975, 1981; Veillet 1982, 1988; Oberti 1990; Jacobson 1990, 1991; Segerman and Richardson 1997). Rose fit van Biesbroeck's (1951, 1957) observations, while Veillet used the theory of Mignard (1975, 1981) which is based on Von Zeipel's method. Jacobson fit the numerically integrated Neptunian satellite orbits (Nereid and Triton) to Earth-based astrometric observations and Voyager spacecraft observations. The second order analytic theory by Oberti gives discripacies about a hundred of kilometers, while in the theory of Segerman and Richardson the disturbing function is expanded in eccentricity. However, most of the analytical theories which are expanded in eccentricity or/and inclination not very accurate for the case of highly eccentric orbits. That is because of the slow convergence of the power series of the disturbing function. In this paper we construct a third order analytical theory on the motion of Nereid which is chiefly perturbed by the Sun. The theory is based on Lie transforms approach advanced

by Hori(1966). The small parameter is the ratio of the mean motion of the Sun and Nereid $\sim 6 \times 10^{-3}$. The disturbing function is developed in this small parameter and put in a closed form with respect to eccentricity. The ephemerides evaluated by the analytic expressions of the present theory are compared with those computed by the numerical integrations of the equations of motion. The accuracy and the amplitudes of the osculating orbital elements of Nereid are shown by tables and figures in the last Section of this paper. In the following section we give the Hamiltonian equation of the nonplanar case. Sections 3 and 4 are devoted for the short-period, long-period and secular perturbations respectively. In Section 5 we give the osculating orbital elements. Then the discussion and conclusion.

2 Hamiltonian of the motion

The Hamiltonian equation of the nonplanar case is given by

$$F = \frac{\mu^2}{2L^2} + \nu G + F_2, \tag{1}$$

where

$$F_0 = \frac{\mu^2}{2L^2}, F_1 = \nu G, \tag{2}$$

$$F_2 = F_{21} + F_{22} + F_{23}, \tag{3}$$

$$\left.\begin{aligned} F_{21} &= \nu^2 a^2 \left(\frac{r}{a}\right)^2 \left\{(-\frac{1}{8} + \frac{3}{8}\theta^2) + \frac{3}{16}(1+\theta)^2 \cos(2f + 2y_2)\right\}, \\ F_{22} &= \nu^2 a^2 \left(\frac{r}{a}\right)^2 \left\{\frac{3}{8}(1-\theta^2)\left[\cos(2f+2g) + \cos(2g-2y_2)\right]\right\}, \\ F_{23} &= \nu^2 a^2 \left(\frac{r}{a}\right)^2 \left\{\frac{3}{16}(1-\theta)^2 \cos(2f + 4g - 2y_2)\right\}, \end{aligned}\right\} \tag{4}$$

ν is the mean motion of the Sun, $\theta = \cos i$, $y_2 = g + h - k$ and k defines the longitude of the Sun. The normalization of F_2 with respect to the mean anomaly of Nereid results in

$$F_{2s} = F_{21s} + F_{22s} + F_{23s}, \tag{5}$$

where

$$\left.\begin{aligned} F_{21s} &= \nu^2 a^2 \left\{(1 + \frac{3}{2}e^2)(-\frac{1}{8} + \frac{3}{8}\theta^2) + \frac{15}{32}e^2(1+\theta)^2 \cos(2y_2)\right\}, \\ F_{22s} &= \nu^2 a^2 \left\{\frac{15}{16}e^2(1-\theta^2)\cos(2g) + \frac{3}{8}(1 + \frac{3}{2}e^2)(1-\theta^2)\cos(2g - 2y_2)\right\}, \\ F_{23s} &= \nu^2 a^2 \left\{\frac{15}{32}e^2(1-\theta)^2 \cos(4g - 2y_2)\right\}. \end{aligned}\right\} \tag{6}$$

Then, the periodic part F_{2p} provides

$$F_{2p} = F_{21p} + F_{22p} + F_{23p}, \tag{7}$$

where

$$\left.\begin{aligned} F_{21p} &= \nu^2 a^2 \left\{A_{21} + B_{21}\cos(2y_2) + C_{21}\sin(2y_2)\right\}, \\ F_{22p} &= \nu^2 a^2 \left\{A_{22} + B_{22}\cos(2y_2) + C_{22}\sin(2y_2)\right\}, \\ F_{23p} &= \nu^2 a^2 \left\{B_{23}\cos(2y_2) + C_{23}\sin(2y_2)\right\}. \end{aligned}\right\} \tag{8}$$

The high eccentric orbit of Nereid precludes replacing functions of the true anomaly by expansions involving the mean anomaly. So, it is convenient to take the eccentric anomaly of

Nereid u as independent variable (Mignard 1975, Oberti 1990). In this regard, the expressions of A_{ij} and B_{ij} above yield

$$\left.\begin{aligned}
A_{21} &= \left(-\frac{1}{8}+\frac{3}{8}\theta^2\right)A,\\
B_{21} &= \frac{1}{16}(1+\theta)^2 B,\\
C_{21} &= \frac{1}{16}(1+\theta)^2 C,\\
A_{22} &= \frac{1}{8}(1-\theta^2)\{B\cos(2g)+C\sin(2g)\},\\
B_{22} &= \frac{3}{8}(1-\theta^2)A\cos(2g),\\
C_{22} &= \frac{3}{8}(1-\theta^2)A\sin(2g),\\
B_{23} &= \frac{1}{16}(1-\theta)^2\{B\cos(4g)+C\sin(4g)\},\\
C_{23} &= \frac{1}{16}(1-\theta)^2\{B\sin(4g)-C\cos(4g)\},
\end{aligned}\right\} \tag{9}$$

where A, B and C are given by

$$\left.\begin{aligned}
A &= -e^2-2e\cos u+\tfrac{1}{2}e^2\cos(2u),\\
B &= -3e^2-6e\cos u+(3-\tfrac{3}{2}e^2)\cos(2u),\\
C &= \eta(6e\sin u-3\sin(2u).
\end{aligned}\right\} \tag{10}$$

Notice that, all the analytical expressions in this case are put in a way such that anyone can easily get their correspondents in the planar case (Saad & Kinoshita 1999).

3 Short periodic perturbations

Elimination of the short periodic terms will be satisfied by finding a canonical transformation

$$(L,G,H;l,g,h,\lambda_\odot)\longrightarrow(L^*,G^*,H^*;l^*,g^*,h^*,\lambda_\odot), \tag{11}$$

where, $\lambda_\odot\equiv k$ defines the longitude of the Sun. In order that:

$$F(L,G,H;l,g,h,\lambda_\odot)\longrightarrow F^*(L^*,G^*,H^*;-,g^*,h^*,\lambda_\odot), \tag{12}$$

and the determining function S only includes the new variables $L^*,G^*,H^*;l^*,g^*,h^*,\lambda_\odot$. After eliminating the short-periodic terms, the orbital elements a^*, e^*, n^* and η^* are copmuted from

$$a^*=\frac{L^{*2}}{\mu},e^*=\sqrt{1-\left(\frac{G^*}{L^*}\right)^2},n^*=\frac{\mu^2}{L^{*3}},\eta^*=\frac{G^*}{L^*}. \tag{13}$$

In this Section for simplicity, the superscript * will be omitted from the orbital elements. Following the algorithm concerned the short-period terms, the new Hamiltonian and determining functions deliver

$$F_0^*=\frac{\mu^2}{2L^2},F_1^*=\nu G, \tag{14}$$

$$F_2^* = \nu^2a^2\left\{\left(1+\frac{3}{2}e^2\right)\left(-\frac{1}{8}+\frac{3}{8}\theta^2\right)+\frac{15}{16}e^2(1-\theta^2)\cos(2g)\right.$$

$$
\begin{aligned}
&+\frac{3}{8}\left(1+\frac{3}{2}e^2\right)(1-\theta^2)\cos(2k-2h)\\
&+\frac{15}{32}e^2(1+\theta)^2\cos(2k-2g-2h)\\
&+\frac{15}{32}e^2(1-\theta)^2\cos(2k+2g-2h)\Big\},
\end{aligned}
\tag{15}
$$

$S_1 = 0$ since the determining function has the identical transformation, consequently the Hamiltonian $F_3^* = 0$. The determining function S_2 is given by

$$
S_2 = S_{21} + S_{22} + S_{23}, \tag{16}
$$

where

$$
\left.
\begin{aligned}
S_{21} &= \frac{1}{4}\frac{\nu^2 a^2}{n}\left\{A_{21}^{(1)} + B_{21}^{(1)}\cos(2y_2) + C_{21}^{(1)}\sin(2y_2)\right\},\\
S_{22} &= \frac{1}{4}\frac{\nu^2 a^2}{n}\left\{A_{22}^{(1)} + B_{22}^{(1)}\cos(2y_2) + C_{22}^{(1)}\sin(2y_2)\right\},\\
S_{23} &= \frac{1}{4}\frac{\nu^2 a^2}{n}\left\{B_{23}^{(1)}\cos(2y_2) + C_{23}^{(1)}\sin(2y_2)\right\},
\end{aligned}
\right\} \tag{17}
$$

the symbols above $A_{2j}^{(1)}$, $B_{2j}^{(1)}$ and $C_{2j}^{(1)}$ have the expressions

$$
\left.
\begin{aligned}
A_{2j}^{(1)} &= \frac{1}{2\pi}\int_0^{2\pi} A_{2j}\,dl,\\
B_{2j}^{(1)} &= \frac{1}{2\pi}\int_0^{2\pi} B_{2j}\,dl,\\
C_{2j}^{(1)} &= \frac{1}{2\pi}\int_0^{2\pi} C_{2j}\,dl,
\end{aligned}
\right\} \tag{18}
$$

for $j = 1,2,3$, and $A_{23} = 0$. Here, we put $dl = (1 - e\cos u)du$ and consider the average relations

$$
\left.
\begin{aligned}
\langle\cos u\rangle &= -\frac{1}{2}e,\\
\langle\cos ju\rangle &= 0,\\
\langle\sin ju\rangle &= 0,
\end{aligned}
\right\} \tag{19}
$$

for $j \geq 2$. Thus, we obtain

$$
\begin{aligned}
S_{21} \;=\; &\frac{1}{4}\frac{\nu^2 a^2}{n}\left\{-\frac{1}{32}e(-2+e^2)(1+\theta)^2\sin(2k-2g-2h-3u)\right.\\
&-\frac{3}{32}(2+e^2)(1+\theta)^2\sin(2k-2g-2h-2u)\\
&-\frac{15}{32}e(-2+e^2)(1+\theta)^2\sin(2k-2g-2h-u)\\
&+\frac{1}{8}e(-8+3e^2)(-1+3\theta^2)\sin(u)\\
&+\frac{3}{8}e^2(-1+3\theta^2)\sin(2u)+\frac{1}{24}e^3(1-3\theta^2)\sin(3u)\\
&+\frac{15}{32}e(-2+e^2)(1+\theta)^2\sin(2k-2g-2h+u)\\
&+\frac{3}{32}(2+e^2)(1+\theta)^2\sin(2k-2g-2h+2u)\\
&+\frac{1}{32}e(-2+e^2)(1+\theta)^2\sin(2k-2g-2h+3u)
\end{aligned}
$$

$$
\begin{aligned}
&+ \eta \left(\frac{15}{16} e^2 (1+\theta)^2 \sin(2k - 2g - 2h) \right. \\
&+ \frac{1}{16} e (1+\theta)^2 \sin(2k - 2g - 2h - 3u) \\
&- \frac{3}{16} (1+e^2)(1+\theta)^2 \sin(2k - 2g - 2h - 2u) \\
&+ \frac{15}{16} e (1+\theta)^2 \sin(2k - 2g - 2h - u) \\
&+ \frac{15}{16} e (1+\theta)^2 \sin(2k - 2g - 2h + u) \\
&- \frac{3}{16} (1+e^2)(1+\theta)^2 \sin(2k - 2g - 2h + 2u) \\
&\left. + \frac{1}{16} e (1+\theta)^2 \sin(2k - 2g - 2h + 3u) \right) \Big\}, \qquad (20)
\end{aligned}
$$

$$
\begin{aligned}
S_{22} \;=\; & \frac{1}{4} \frac{\nu^2 a^2}{n} \left\{ \frac{1}{16} e (-2+e^2)(-1+\theta^2) \sin(2g - 3u) - \frac{1}{16} e^3 (-1+\theta^2) \right. \\
& * \sin(2k - 2h - 3u) + \frac{3}{16} (2+e^2)(-1+\theta^2) \sin(2g - 2u) \\
& + \frac{9}{16} e^2 (-1+\theta^2) \sin(2k - 2h - 2u) + \frac{15}{16} e (-2+e^2)(-1+\theta^2) \\
& * \sin(2g - u) + \frac{3}{16} e (-8+3e^2)(-1+\theta^2) \sin(2k - 2h - u) \\
& - \frac{15}{16} e (-2+e^2)(-1+\theta^2) \sin(2g + u) - \frac{3}{16} e (-8+3e^2)(-1+\theta^2) \\
& * \sin(2k - 2h + u) - \frac{3}{16} (2+e^2)(-1+\theta^2) \sin(2g + 2u) \\
& - \frac{9}{16} e^2 (-1+\theta^2) \sin(2k - 2h + 2u) - \frac{1}{16} e (-2+e^2)(-1+\theta^2) \\
& * \sin(2g + 3u) + \frac{1}{16} e^3 (-1+\theta^2) \sin(2k - 2h + 3u) \\
& + \eta \left(\frac{15}{8} e^2 (-2+e^2)(-1+\theta^2) \sin(2g) + \frac{1}{8} e (-1+\theta^2) \sin(2g - 3u) \right. \\
& - \frac{3}{8} (1+e^2)(-1+\theta^2) \sin(2g - 2u) + \frac{15}{8} e (-1+\theta^2) \sin(2g - u) \\
& + \frac{15}{8} e (-1+\theta^2) \sin(2g + u) - \frac{3}{8} (1+e^2)(-1+\theta^2) \sin(2g + 2u) \\
& \left. + \frac{1}{8} e (-1+\theta^2) \sin(2g + 3u) \right) \Big\}, \qquad (21)
\end{aligned}
$$

finally S_{23} is given by

$$
\begin{aligned}
S_{23} \;=\; & \frac{1}{4} \frac{\nu^2 a^2}{n} \left\{ -\frac{1}{32} e (-2+e^2)(-1+\theta)^2 \sin(2k + 2g - 2h - 3u) \right. \\
& - \frac{3}{32} (2+e^2)(-1+\theta)^2 \sin(2k + 2g - 2h - 2u) \\
& - \frac{15}{32} e (-2+e^2)(-1+\theta)^2 \sin(2k + 2g - 2h - u) \\
& + \frac{15}{32} e (-2+e^2)(-1+\theta)^2 \sin(2k + 2g - 2h + u) \\
& + \frac{3}{32} (2+e^2)(-1+\theta)^2 \sin(2k + 2g - 2h + 2u)
\end{aligned}
$$

$$
\begin{aligned}
&+\frac{1}{32}e(-2+e^2)(-1+\theta)^2\sin(2k+2g-2h+3u)\\
&+\eta\Big(-\frac{15}{16}e^2(-1+\theta)^2\sin(2k+2g-2h)\\
&-\frac{1}{16}e(-1+\theta)^2\sin(2k+2g-2h-3u)\\
&+\frac{3}{16}(1+e^2)(-1+\theta)^2\sin(2k+2g-2h-2u)\\
&-\frac{15}{16}e(-1+\theta)^2\sin(2k+2g-2h-u)\\
&-\frac{15}{16}e(-1+\theta)^2\sin(2k+2g-2h+u)\\
&+\frac{3}{16}(1+e^2)(-1+\theta)^2\sin(2k+2g-2h+2u)\\
&-\frac{1}{16}e(-1+\theta)^2\sin(2k+2g-2h+3u)\Big)\Big\}. \qquad (22)
\end{aligned}
$$

We intended removing any secular terms from the determining function by applying the mathematical operations

$$
\left.
\begin{aligned}
A_{2j}^{(1)} &= A_{2j}^{(1)} - \langle A_{2j}^{(1)}\rangle,\\
B_{2j}^{(1)} &= B_{2j}^{(1)} - \langle B_{2j}^{(1)}\rangle,\\
C_{2j}^{(1)} &= C_{2j}^{(1)} - \langle C_{2j}^{(1)}\rangle,
\end{aligned}
\right\} \qquad (23)
$$

for $j = 1, 2, 3$.

Substituting from equations (20), (21) and (22) in equation (16) we get the analytical expression of the determining function S_2. Here, $A_{2j}^{(1)}$, $B_{2j}^{(1)}$ and $C_{2j}^{(1)}$ are free from any angular variables, however they are factorized by $(1-\theta^2) \equiv \sin^2 i$. The small parameter in this theory is roughly of the order of 10^{-3}, this means that if the inclination of Nereid is $\sim 10^o$, then $\sin^2 i \sim \sqrt{\epsilon}$. Now we are going to the derivation of the fourth order Hamiltonian F_4^*. It can be given by the simple expression

$$
F_4^* = F_{41}^* + F_{42}^* + F_{43}^*, \qquad (24)
$$

where

$$
\left.
\begin{aligned}
F_{41}^* &= \frac{1}{2}\Big(\{F_{21p}, S_{21}\}_s + \{F_{21p}, S_{22}\}_s + \{F_{21p}, S_{23}\}_s\Big),\\
F_{42}^* &= \frac{1}{2}\Big(\{F_{22p}, S_{21}\}_s + \{F_{22p}, S_{22}\}_s + \{F_{22p}, S_{23}\}_s\Big),\\
F_{43}^* &= \frac{1}{2}\Big(\{F_{23p}, S_{21}\}_s + \{F_{23p}, S_{22}\}_s + \{F_{23p}, S_{23}\}_s\Big),
\end{aligned}
\right\} \qquad (25)
$$

the subscripts s and p define the secular and periodic parts respectively, F_{2jp} and S_{2j} for $j = 1, 2, 3$ are given by equations (8) and (17). Proceeding various mathematical derivations, the Poisson bracket $\{F_{2p}, S_2\}$ can be reduced to the form

$$
\begin{aligned}
\{F_{2p}, S_2\} \;=\; & \frac{\nu^4 a^2}{16n^2}\Big\{\Big(4\mathcal{D} + \frac{\eta^2}{e}\mathcal{D}_e\Big)\mathcal{D} - \frac{\eta}{e}\mathcal{D}_e(2\mathcal{E}) + \frac{\eta}{e}\mathcal{D}_g\mathcal{P}_c\\
&- \Big(7\mathcal{P} + \frac{\eta^2}{e}P_e\Big)\mathcal{D}_l + L\,(2\mathcal{E}\mathcal{D}_G - \mathcal{D}_g\mathcal{P}_G)\\
&- L\,(\mathcal{P}_H\mathcal{D}_h - \mathcal{P}_h\mathcal{D}_H)\Big\}, \qquad (26)
\end{aligned}
$$

where

$$
\mathcal{D} = \mathcal{D}_1 + \mathcal{D}_2 + \mathcal{D}_3, \qquad (27)
$$

$$\left.\begin{aligned}\mathcal{D}_1 &= A_{21} + B_{21}\cos(2y_2) + C_{21}\sin(2y_2),\\ \mathcal{D}_2 &= A_{22} + B_{22}\cos(2y_2) + C_{22}\sin(2y_2),\\ \mathcal{D}_3 &= B_{23}\cos(2y_2) + C_{23}\sin(2y_2),\end{aligned}\right\} \tag{28}$$

$$\mathcal{E} = \mathcal{E}_1 + \mathcal{E}_2 + \mathcal{E}_3, \tag{29}$$

$$\left.\begin{aligned}\mathcal{E}_1 &= -B_{21}^{(1)}\sin(2y_2) + C_{21}^{(1)}\cos(2y_2),\\ \mathcal{E}_2 &= -B_{22}^{(1)}\sin(2y_2) + C_{22}^{(1)}\cos(2y_2),\\ \mathcal{E}_3 &= -B_{23}^{(1)}\sin(2y_2) + C_{23}^{(1)}\cos(2y_2),\end{aligned}\right\} \tag{30}$$

similarly, $\mathcal{P}$ can be defined by the following form

$$\mathcal{P} = \mathcal{P}_1 + \mathcal{P}_2 + \mathcal{P}_3, \tag{31}$$

where

$$\left.\begin{aligned}\mathcal{P}_1 &= A_{21}^{(1)} + B_{21}^{(1)}\cos(2y_2) + C_{21}^{(1)}\sin(2y_2),\\ \mathcal{P}_2 &= A_{22}^{(1)} + B_{22}^{(1)}\cos(2y_2) + C_{22}^{(1)}\sin(2y_2),\\ \mathcal{P}_3 &= B_{23}^{(1)}\cos(2y_2) + C_{23}^{(1)}\sin(2y_2).\end{aligned}\right\} \tag{32}$$

Since $\mathcal{D}$ and $\mathcal{P}$ are functions of the eccentric anomaly u, then their partial derivatives $\mathcal{D}_e$ and $\mathcal{P}_e$ with respect to e deliver

$$\frac{\partial(\mathcal{D},\mathcal{P})}{\partial e} = \left(\frac{\partial(\mathcal{D},\mathcal{P})}{\partial e}\right) + \frac{\partial(\mathcal{D},\mathcal{P})}{\partial u}\frac{\partial u}{\partial e}, \tag{33}$$

Taking the secular part of the Poisson bracket $\{F_{2p}, S_2\}$, the analytical form of F_4^* arises

$$F_4^* = F_{4s}^* + F_{4p}^*, \tag{34}$$

where

$$\begin{aligned}F_{4s}^* = \frac{\nu^4 a^2}{n^2}\Big\{&\frac{1}{4096}\left(-8\left(47 + 282\theta^2 + 63\theta^4\right) - 63e^2\left(239 + 170\theta^2 + 143\theta^4\right)\right.\\ &\left. + 72e^2\left(377 + 190\theta^2 + 209\theta^4\right)\right) + \frac{1}{1024}\left(3e^2\left(-1+\theta^2\right)\left(-6\left(83 + 195\theta^2\right)\right.\right.\\ &\left.\left. + e^2\left(131 + 555\theta^2\right)\right)\right)\cos(2g) + \frac{1845}{4096}e^4\left(-1+\theta^2\right)^2\cos(4g)\Big\},\end{aligned} \tag{35}$$

and the periodic part has the form

$$\begin{aligned}F_{4p}^* = \frac{\nu^4 a^2}{n^2}\Big\{&-\frac{3}{4096}\left(56 - 1672e^2 + 1001e^4\right)\left(-1+\theta^2\right)^2\cos(4k-4h)\\ &+ \frac{615}{8192}e^4(1+\theta)^4\cos(4k-4g-4h) + \frac{15}{2048}e^2\left(-78+37e^2\right)(-1+\theta)\\ &* (1+\theta)^3\cos(4k-2g-4h) + \frac{15}{2048}e^2\left(-78+37e^2\right)(-1+\theta)^3(1+\theta)\\ &* \cos(4k+2g-4h) + \frac{615}{8192}e^4(-1+\theta)^4\cos(4k+4g-4h) + \frac{3}{1024}\left(-1+\theta^2\right)\\ &* \left(216 + 560^2 - 152e^2\left(13 + 110^2\right) + 7e^4\left(199 + 1430^2\right)\right)\cos(2k-2h)\\ &- \frac{615}{2048}e^4(-1+\theta)(1+\theta)^3\cos(2k-4g-2h) - \frac{3}{512}e^2(1+\theta)^2\\ &* \left(-222 + 3900 - 3900^2 + e^2\left(79 - 1850 + 1850^2\right)\right)\cos(2k-2g-2h)\\ &- \frac{3}{512}e^2(-1+\theta)^2\left(-6\left(37 + 650 + 650^2\right) + e^2\left(79 + 1850 + 1850^2\right)\right)\\ &* \cos(2k+2g-2h) - \frac{615}{2048}e^4(-1+\theta)^3\cos(2k+4g-2h)\Big\},\end{aligned} \tag{36}$$

where $g = \varpi - \Omega$. By the virtue of the powerful Mathematica software, we could evaluate and simplify the analytic formulae of both the Hamiltonian and the determining function of the present theory although their derivations were laborious. We give S_3 as follows

$$S_3 = S_{31} + S_{32} + S_{33}, \tag{37}$$

where

$$\left.\begin{aligned} S_{31} &= \frac{1}{4}\frac{\nu^3 a^2}{\eta^2}\mathcal{M}_1, \\ S_{32} &= \frac{1}{4}\frac{\nu^3 a^2}{\eta^2}\mathcal{M}_2, \\ S_{33} &= \frac{1}{4}\frac{\nu^3 a^2}{n^2}\mathcal{M}_3, \end{aligned}\right\} \tag{38}$$

$$\left.\begin{aligned} \mathcal{M}_1 &= -2B_{21}^{(2)}\sin(2y_2) + 2C_{21}^{(2)}\cos(2y_2), \\ \mathcal{M}_2 &= -2B_{22}^{(2)}\sin(2y_2) + 2C_{22}^{(2)}\cos(2y_2), \\ \mathcal{M}_3 &= -2B_{23}^{(2)}\sin(2y_2) + 2C_{23}^{(2)}\cos(2y_2), \end{aligned}\right\} \tag{39}$$

and

$$\left.\begin{aligned} B_{2j}^{(2)} &= \frac{1}{2\pi}\int_0^{2\pi} B_{2j}^{(1)} dl, \\ C_{2j}^{(2)} &= \frac{1}{2\pi}\int_0^{2\pi} C_{2j}^{(1)} dl, \end{aligned}\right\} \tag{40}$$

for $j = 1, 2, 3$. For the purpose of removing any secular term from the determining function, we subtracted the averages from the original expressions as follows

$$\left.\begin{aligned} B_{2j}^{(2)} &= B_{2j}^{(2)} - \langle B_{2j}^{(2)} \rangle, \\ C_{2j}^{(2)} &= C_{2j}^{(2)} - \langle C_{2j}^{(2)} \rangle. \end{aligned}\right\} \tag{41}$$

Then, the final form of S_3 is represented by its three parts S_{31}, S_{32} and S_{33}

$$\begin{aligned} S_{31} \;=\; & \frac{1}{4}\frac{\nu^3 a^2}{n^2}(1+\theta)^2 \left\{ -\frac{3}{32}e^2(-22+9e^2)\sin(2k-2g-2h) + \frac{1}{128}e^2(-2+e^2) \right. \\ & * \sin(2k-2g-2h-4u) + \frac{1}{96}e(10+e^2)\sin(2k-2g-2h-3u) \\ & + \frac{1}{32}(-6-19e^2+8e^4)\sin(2k-2g-2h-2u) - \frac{3}{32}e(-22+9e^2) \\ & \sin(2k-2g-2h-u) - \frac{3}{32}e(-22+9e^2)\sin(2k-2g-2h+u) \\ & + \frac{1}{32}(-6-19e^2+8e^4)\sin(2k-2g-2h+2u) \\ & + \frac{1}{96}e(10+e^2)\sin(2k-2g-2h+3u) + \frac{1}{128}e^2(-2+e^2) \\ & * \sin(2k-2g-2h+4u) + \eta\left(-\frac{1}{64}e^2\sin(2k-2g-2h-4u)\right. \\ & + \frac{1}{48}e(5+3e^2)\sin(2k-2g-2h-3u) - \frac{1}{16}(3+11e^2) \\ & * \sin(2k-2g-2h-2u) - \frac{3}{16}e(-11+4e^2)\sin(2k-2g-2h-u) \\ & + \frac{3}{16}e(-11+4e^2)\sin(2k-2g-2h+u) + \frac{1}{16}(3+11e^2) \\ & * \sin(2k-2g-2h+2u) - \frac{1}{48}e(5+3e^2)\sin(2k-2g-2h+3u) \\ & \left. \left. + \frac{1}{64}e^2\sin(2k-2g-2h+4u)\right)\right\}, \end{aligned} \tag{42}$$

$$
\begin{aligned}
S_{32} &= \frac{1}{4}\frac{\nu^3 a^2}{n^2}(-1+\theta^2)\left\{\frac{3}{16}e^2(-16+3e^2)\sin(2k-2h)+\frac{1}{64}e^4\sin(2k-2h-4u)\right.\\
&-\frac{11}{48}e^3\sin(2k-2h-3u)-\frac{1}{16}e^2(-21+4e^2)\sin(2k-2h-2u)\\
&+\frac{3}{16}e(-16+3e^2)\sin(2k-2h-u)+\frac{3}{16}e(-16+3e^2)\sin(2k-2h+u)\\
&-\frac{1}{16}e^2(-21+4e^2)\sin(2k-2h+2u)-\frac{11}{48}e^3\sin(2k-2h+3u)\\
&\left.+\frac{1}{64}e^4\sin(2k-2h+4u)\right\}, \qquad (43)
\end{aligned}
$$

and S_{33} is given by

$$
\begin{aligned}
S_{33} &= \frac{1}{4}\frac{\nu^3 a^2}{n^2}(-1+\theta)^2\left\{-\frac{3}{32}e^2(-22+9e^2)\sin(2k+2g-2h)+\frac{1}{128}e^2(-2+e^2)\right.\\
&*\sin(2k+2g-2h-4u)+\frac{1}{96}e(10+e^2)\sin(2k+2g-2h-3u)\\
&+\frac{1}{32}(-6-19e^2+8e^4)\sin(2k+2g-2h-2u)-\frac{3}{32}e(-22+9e^2)\\
&\sin(2k+2g-2h-u)-\frac{3}{32}e(-22+9e^2)\sin(2k+2g-2h+u)\\
&+\frac{1}{32}(-6-19e^2+8e^4)\sin(2k+2g-2h+2u)\\
&+\frac{1}{96}e(10+e^2)\sin(2k+2g-2h+3u)+\frac{1}{128}e^2(-2+e^2)\\
&*\sin(2k+2g-2h+4u)+\eta\left(-\frac{1}{64}e^2\sin(2k+2g-2h-4u)\right.\\
&+\frac{1}{48}e(5+3e^2)\sin(2k+2g-2h-3u)-\frac{1}{16}(3+11e^2)\\
&*\sin(2k+2g-2h-2u)+\frac{3}{16}e(-11+4e^2)\sin(2k-2g-2h-u)\\
&-\frac{3}{16}e(-11+4e^2)\sin(2k+2g-2h+u)-\frac{1}{16}(3+11e^2)\\
&*\sin(2k+2g-2h+2u)+\frac{1}{48}e(5+3e^2)\sin(2k+2g-2h+3u)\\
&\left.\left.-\frac{1}{64}e^2\sin(2k+2g-2h+4u)\right)\right\}, \qquad (44)
\end{aligned}
$$

where $u = k - \varpi$.

4 Long periodic perturbations

In this Section, we remove the long (intermediate) periodic terms which are related to the motion of the Sun. This will be achieved by building the canonical transformation

$$
(L^*, G^*, H^*; l^*, g^*, h^*, \lambda_\odot) \longrightarrow (L^{**}, G^{**}, H^{**}; l^{**}, g^{**}, h^{**}, \lambda_\odot), \qquad (45)
$$

In order that:

$$
F^*(L^*, G^*, H^*; l^*, g^*, h^*, \lambda_\odot) \longrightarrow F^{**}(L^{**}, G^{**}, H^{**}; -, g^{**}, -, -), \qquad (46)
$$

and the determining function S only includes the new variables $L^{**}, G^{**}, H^{**}; l^{**}, g^{**}, h^{**}, \lambda_\odot$. The new Hamiltonian F^{**} will be also free from h, since the disturbing potential becomes

axial symmetric. After eliminating the long (intermediate) terms, the orbital elements a^{**}, e^{**}, n^{**} and η^{**} are copmuted from

$$a^{**} = \frac{L^{**2}}{\mu}, e^{**} = \sqrt{1 - \left(\frac{G^{**}}{L^{**}}\right)^2}, n^{**} = \frac{\mu^2}{L^{**3}}, \eta^{**} = \frac{G^{**}}{L^{**}}. \tag{47}$$

In this section right now, the superscript ** will be omitted from the orbital elements. We follow the algorithm concerned the long-period terms to get the new Hamiltonian and determining functions as follows

$$F_0^{**} = \frac{\mu^2}{2L^2}, F_1^{**} = \nu G, \tag{48}$$

$$F_2^{**} = \nu^2 a^2 \left\{ \left(1 + \frac{3}{2}e^2\right) + \left(\frac{-1}{8} + \frac{3}{8}\theta^2\right) + \frac{15}{16}e^2(1-\theta^2)\cos(2g) \right\}, \tag{49}$$

$$\begin{aligned} S_1^* &= \nu a^2 \left\{ \frac{3}{16}\left(1 + \frac{3}{2}e^2\right)(1-\theta^2)\sin(2k-2h) + \frac{15}{64}e^2(1+\theta)^2 \right. \\ &\quad \left. * \sin(2k-2g-2h) + \frac{15}{64}e^2(1-\theta)^2\sin(2k+2g-2h) \right\}, \end{aligned} \tag{50}$$

$$F_3^{**} = \frac{\nu^3 a^2}{n}\eta \left\{ \frac{9}{128}\theta(2 - 2\theta^2 + e^2(33 + 17\theta^2)) + \frac{135}{128}e^2\theta(1-\theta^2)\cos(2g) \right\}, \tag{51}$$

$$\begin{aligned} S_2^* &= \frac{\nu^2 a^2}{n}\eta \left\{ \frac{9}{128}(-2 + 17e^2)\theta(1-\theta^2)\sin(2k-2h) \right. \\ &\quad + \frac{45}{256}e^2(1+\theta)^2(-2+3\theta)\sin(2k-2g-2h) \\ &\quad \left. + \frac{45}{256}e^2(1-\theta)^2(2+3\theta)\sin(2k+2g-2h) \right\}, \end{aligned} \tag{52}$$

$$\begin{aligned} F_4^{**} &= \frac{\nu^4 a^2}{n^2}\left\{ \frac{1}{8192}(8(-67 - 726\theta^2 + 9\theta^4) + 144e^2(329 + 253\theta^2 + 344\theta^4) \right. \\ &\quad - 9e^4(2527 + 2794\theta^2 + 5407\theta^4)) + \frac{3}{2048}e^2(-1+\theta^2)(-12(68 + 345\theta^2) \\ &\quad \left. + e^2(307 + 4035\theta^2))\cos(2g) + \frac{315}{8192}e^4(-1+\theta^2)^2\cos(4g) \right\}, \end{aligned} \tag{53}$$

while S_3^* has the analytical expression

$$\begin{aligned} S_3^* &= \frac{\nu^3 a^2}{n^2}\left\{ (-1+\theta^2)^2\left(-\frac{69}{1024} + \frac{3}{4}e^2 + \frac{123}{8192}e^4\right)\sin(4k-4h) \right. \\ &\quad + \frac{1905}{16384}e^4(1+\theta)^4\sin(4k-4g-4h) \\ &\quad + (-1+\theta)(1+\theta)^3\left(-\frac{315}{1024}e^2 - \frac{645}{4096}e^4\right)\sin(4k-2g-4h) \\ &\quad + (-1+\theta)(1+\theta)^3\left(-\frac{315}{1024}e^2 - \frac{645}{4096}e^4\right)\sin(4k+2g-4h) \\ &\quad + \frac{1905}{16384}e^4(1+\theta)^4\sin(4k+4g-4h) + (-1+\theta^2) \\ &\quad \left. * \left(\frac{171}{256} - \frac{39}{256}\theta^2 - \frac{3}{256}e^2(215 + 904\theta^2) + \frac{3}{2048}e^4(1355 + 8131\theta^2)\right) \right. \end{aligned}$$

$$
\begin{aligned}
&* \sin(2k-2h) + \frac{795}{4096}e^4(-1+\theta)(1+\theta)^3\sin(2k-4g-2h) + (1+\theta)^2 \\
&* \left(\frac{9}{512}e^2(79-175\theta+310\theta^2) - \frac{3}{1024}e^4(563-1315\theta+2125\theta^2)\right) \\
&* \sin(2k-2g-2h) + (-1+\theta)^2\left(\frac{9}{512}e^2(79+175\theta+310\theta^2)\right. \\
&\left. - \frac{3}{1024}e^4(563+1315\theta+2125\theta^2)\right)\sin(2k+2g-2h) \\
&\left. + \frac{795}{4096}e^4(-1+\theta)^3(1+\theta)\sin(2k+4g-2h)\right\}. \qquad (54)
\end{aligned}
$$

Notice that all the above analytical expressions satisfy d'Alembert characteristics. This may prove the validity of these expressions from the analytical point of view. Up to this stage, the Hamiltonian system is still include the long terms g. Omitting these terms can be done by two ways, the first one (which is analogue to the previous procedures) is to build a new canonical transformation

$$
(L^{**}, G^{**}, H^{**}; l^{**}, g^{**}, h^{**}, \lambda_{\odot}) \longrightarrow (L^{***}, G^{***}, H^{***}; l^{***}, g^{***}, h^{***}, \lambda_{\odot}) \qquad (55)
$$

in order that:

$$
F^{**}(L^{**}, G^{*}, H^{**}; -, g^{**}, -, -) \longrightarrow F^{***}(L^{***}, G^{***}, H^{***}; -, -, -, -) \qquad (56)
$$

and the final results give the mean elements. The second way is to use the Jacobian elliptic functions (Kinoshita and Nakai 1991, 1999) in solving the Hamiltonian equations system

$$
\left.
\begin{aligned}
&L^{**} = \text{const.}, \frac{dl^{**}}{dt} = -\frac{\partial F^{**}}{\partial L^{**}}, \\
&\frac{dG^{**}}{dt} = \frac{\partial F^{**}}{\partial g^{**}}, \frac{dg^{**}}{dt} = -\frac{\partial F^{**}}{\partial G^{**}}, \\
&H^{**} = \text{const.}, \frac{dh^{**}}{dt} = -\frac{\partial F^{**}}{\partial H^{**}},
\end{aligned}
\right\} \qquad (57)
$$

and the final results are also mean elements. In this theory we adopt the latter's method to remove g from the new Hamiltonian system.

5 The osculating orbital elements

In the previous sections we discussed the analytical expressions of the short-period, long-period and the secular perturbations. This Section is devoted for evaluating the osculating orbital elements of the nonplanar problem. In order that we consider for simplicity (and saving the area of this paper), the partial derivatives of S_j $(j = 2, 3)$ with respect to L', G', H', l', g', h' are given by $\mathcal{P}_i$ $(i = 1, 2, ..., 12)$ and the derivatives of S_ℓ^* $(\ell = 1, 2, 3)$ with respect to L'', G'', H'', g'', h'' stand for $\mathcal{K}_s$ $(s = 1, 2, ..., 15)$. In what follows, we implement the above analytical expressions for digital computations by constructing the following algorithm described by its purpose, input and its computational sequence:

5.1 Computational algorithm

- *Purpose*: To compute the osculating orbital elements a, e, I, ω, Ω, l of Nereid for the nonplanar case. Nereid is inclined to the orbital plane of Neptune and perturbed by the solar effects.

- *Input*: the initial values a_0'', e_0'', I_0'', Ω_0'', l_0'', t_0, t_{end}, and tol (specified tolerance).
- Units measurement: Masses are given in solar unit, distances are in AU, time in days while the angles are given in radians.
- *Computational Sequence*:

(1) Compute the mean elements e'', I'', ω'', Ω'', l'', by solving the equations system (57).
(2) Compute the long (intermediate)-periodic variations from the following sequence
(a) As for the eccentricity:

$$\left.\begin{aligned}
\Phi_1 &= -\frac{\eta}{ena^2}\mathcal{K}_4 \equiv \delta_1 e,\\
\Phi_2 &= -\frac{\eta}{ena^2}\mathcal{K}_9,\\
\Phi_3 &= \left(\left(\frac{\partial\Phi_1}{\partial G} - \frac{\eta}{ena^2}\frac{\partial\Phi_1}{\partial e}\right)\mathcal{K}_4 - \frac{\partial\Phi_1}{\partial g}\mathcal{K}_2\right) + \left(\frac{\partial\Phi_1}{\partial H}\mathcal{K}_5 - \frac{\partial\Phi_1}{\partial h}\mathcal{K}_3\right),\\
\Phi_4 &= \Phi_2 + \frac{\Phi_3}{2} \equiv \delta_2 e,\\
\Phi_5 &= -\frac{\eta}{ena^2}k_{14},\\
\Phi_6 &= \left(\left(\frac{\partial\Phi_1}{\partial G} - \frac{\eta}{ena^2}\frac{\partial\Phi_1}{\partial e}\right)k_9 - \frac{\partial\Phi_1}{\partial g}k_7\right) + \left(\frac{\partial\Phi_1}{\partial H}k_{10} - \frac{\partial\Phi_1}{\partial h}k_8\right),\\
\Phi_7 &= \left(\left(\frac{\partial\Phi_2}{\partial G} - \frac{\eta}{ena^2}\frac{\partial\Phi_2}{\partial e}\right)k_4 - \frac{\partial\Phi_2}{\partial g}k_2\right) + \left(\frac{\partial\Phi_2}{\partial H}k_5 - \frac{\partial\Phi_2}{\partial h}k_3\right),\\
\Phi_8 &= \left(\left(\frac{\partial\Phi_3}{\partial G} - \frac{\eta}{ena^2}\frac{\partial\Phi_3}{\partial e}\right)k_4 - \frac{\partial\Phi_3}{\partial g}k_2\right) + \left(\frac{\partial\Phi_3}{\partial H}k_5 - \frac{\partial\Phi_3}{\partial h}k_3\right),\\
\Phi_9 &= \Phi_5 + \frac{(\Phi_6+\Phi_7)}{2} + \frac{\Phi_8}{6} \equiv \delta_3 e,\\
e'_{long} &= e'' + \delta_1 e' + \delta_2 e' + \delta_3 e',
\end{aligned}\right\} \tag{58}$$

(b) Inclination: in this case we use the notation $I = \arccos(H/G)$ as follows
(b1) to get the angular momentum G' make the following changes in item (a)

$$\left.\begin{aligned}
\Phi_1 &= \mathcal{K}_4,\\
\Phi_2 &= \mathcal{K}_9,\\
\Phi_5 &= \mathcal{K}_{14},
\end{aligned}\right\} \tag{59}$$

then apply all the steps in (a) to get

$$G'_{long} = G'' + \delta_1 G' + \delta_2 G' + \delta_3 G'. \tag{60}$$

(b2) to get the angular momentum H' make the following changes in item (a)

$$\left.\begin{aligned}
\Phi_1 &= \mathcal{K}_5,\\
\Phi_2 &= \mathcal{K}_{10},\\
\Phi_5 &= \mathcal{K}_{15},
\end{aligned}\right\} \tag{61}$$

then apply all the steps in (a) to get

$$H'_{long} = H'' + \delta_1 H' + \delta_2 H' + \delta_3 H'. \tag{62}$$

(b3) then we can get I'_{long} using the definition

$$I'_{long} = \arccos\left(H'_{long}/G'_{long}\right). \tag{63}$$

(c) for the argument of pericenter ω', in the above equations put

$$\left.\begin{aligned}\Phi_1 &= -\mathcal{K}_2,\\ \Phi_2 &= -\mathcal{K}_7,\\ \Phi_5 &= -\mathcal{K}_{12},\end{aligned}\right\} \tag{64}$$

then apply all the steps mentioned in eccentricity case to get

$$\omega'_{long} = \omega'' + \delta_1\omega' + \delta_2\omega' + \delta_3\omega'. \tag{65}$$

(d) for the longitude of ascending node Ω', change

$$\left.\begin{aligned}\Phi_1 &= -\mathcal{K}_3,\\ \Phi_2 &= -\mathcal{K}_8,\\ \Phi_5 &= -\mathcal{K}_{13},\end{aligned}\right\} \tag{66}$$

then apply all the steps mentioned in item (a) to get

$$\Omega'_{long} = \Omega'' + \delta_1\Omega' + \delta_2\Omega' + \delta_3\Omega'. \tag{67}$$

(e) in case of the mean anomaly l' put

$$\left.\begin{aligned}\Phi_1 &= -\mathcal{K}_1,\\ \Phi_2 &= -\mathcal{K}_6,\\ \Phi_5 &= -\mathcal{K}_{11},\end{aligned}\right\} \tag{68}$$

then apply all the steps mentioned in the case (a) to get:

$$l'_{long} = l'' + \delta_1 l' + \delta_2 l' + \delta_3 l'. \tag{69}$$

(3) Compute the short-periodic variations as follows
Call Kepler
(a) semi-major axis:

$$\left.\begin{aligned}\delta_2 a &= \frac{2}{na}\mathcal{P}_4,\\ \delta_3 a &= \frac{2}{na}\mathcal{P}_{10},\\ \delta a_{sho} &= \delta_2 a + \delta_3 a,\end{aligned}\right\} \tag{70}$$

(b) eccentricity:

$$\left.\begin{aligned}\delta_2 e &= \frac{\eta^2}{ena^2}\mathcal{P}_4 - \frac{\eta}{ena^2}\mathcal{P}_5,\\ \delta_3 e &= \frac{\eta^2}{ena^2}\mathcal{P}_{10} - \frac{\eta}{ena^2}\mathcal{P}_{11},\\ \delta e_{sho} &= \delta_2 e + \delta_3 e,\end{aligned}\right\} \tag{71}$$

(c) Inclination: in this case we use also the notation $I = \arccos(H/G)$
(c1) to get the angular momentum G

$$\left.\begin{aligned}\delta_2 G &= \mathcal{P}_5,\\ \delta_3 G &= \mathcal{P}_{11},\\ \delta G_{sho} &= \delta_2 G + \delta_3 G\end{aligned}\right\} \tag{72}$$

(c2) to get the angular momentum H

$$\left.\begin{aligned} \delta_2 H &= \mathcal{P}_6, \\ \delta_3 H &= \mathcal{P}_{12}, \\ \delta H_{sho} &= \delta_2 H + \delta_3 H \end{aligned}\right\} \tag{73}$$

(d) Argument of pericenter:

$$\left.\begin{aligned} \delta_2 \omega &= -\mathcal{P}_2, \\ \delta_3 \omega &= -\mathcal{P}_8, \\ \delta \omega_{sho} &= \delta_2 \omega + \delta_3 \omega \end{aligned}\right\} \tag{74}$$

(e) Longitude of ascending node:

$$\left.\begin{aligned} \delta_2 \Omega &= -\mathcal{P}_3, \\ \delta_3 \Omega &= -\mathcal{P}_9, \\ \delta \Omega_{sho} &= \delta_2 \Omega + \delta_3 \Omega \end{aligned}\right\} \tag{75}$$

(f) in case of the mean anomaly

$$\left.\begin{aligned} \delta_2 l &= -\mathcal{P}_1, \\ \delta_3 l &= -\mathcal{P}_7, \\ \delta l_{sho} &= \delta_2 l + \delta_3 l. \end{aligned}\right\} \tag{76}$$

(4) Compute the osculating orbital elements from the equations

$$\left.\begin{aligned} a_{osc} &= a_0'' + \delta a_{sho}, \\ e_{osc} &= e'_{long} + \delta e_{sho}, \\ G_{osc} &= G'_{long} + \delta G_{sho}, \\ H_{osc} &= H'_{long} + \delta H_{sho}, \\ I_{osc} &= \arccos\left(H_{osc}/G_{osc}\right), \\ \omega_{osc} &= \omega'_{long} + \delta \omega_{sho}, \\ \Omega_{osc} &= \Omega'_{long} + \delta \Omega_{sho}, \\ l_{osc} &= l'_{long} + \delta l_{sho}. \end{aligned}\right\} \tag{77}$$

(5) The algorithm is completed up to the third order.

6 Discussion and conclusion

We have offered a complete theory on the motion of Nereid which includes the short, intermediate and long periodic perturbations. The osculating orbital elements which describe the orbital motion of Nereid are evaluated analytically and got ephemerides of Nereid. The comparison with the numerical integration of the equations of motion gives an accuracy on the level of 0.3 km in the semi-major axis, 3×10^{-7} in the eccentricity and 10^{-5} degree in the angular variables over several hundred years. Figures 1 and 2 show the behaviour of the osculating elements of Nereid over 5 and 300 years respectively. The direct difference between the analytical and numerical results for short period interval is given by figure 3, while figure 4 exhibits the residuals in the elements using least square fitting. The check of the reliability and accuracy of the theory for a relatively long interval is given in figures 5 and 6. Figure 7 represents the accuracy in the elements after making corrections in the mean motions of ℓ, g and h. These corrections are coming from the linear part of figure 5. Finally, the residuals in the osculating elements are adjusted and exhibited in figure 8.
Tables I and II show the amplitudes and the accuracy in the osculating orbital elements for both short and long periodic perturbations respectively. The results of the present theory satisfy the required accuracy for the observations.

References

Hori, G. 1966. Theory of general perturbations with unspecified canonical variables. *Publ. Astron. Soc. Japan* **18**, 287-296.

Jacobson, R. A. 1990. The orbits of the satellites of Neptune. *Astron. Astrophys.* **231**, 241-250.

Jacobson, R. A., Riedel, J. E. and Taylor, A. H. 1991. The orbits of triton and Nereid from spacecraft and Earthbased observations. *Astron. Astrophys.* **247**, 565-575.

Kinoshita, H. and Nakai, H. 1991. Secular perturbations of fictitious satellites of Uranus. *Celestial Mechanics and Dynamical Astronomy* **52**, 293-303.

Kinoshita, H. and Nakai, H. 1999. Analytical solution of the Kozai resonance and its application. *Celestial Mechanics and Dynamical Astronomy* **75**, 125-147.

Mignard, F. 1975. Satellite with high eccentricity. Application to Nereid', *Astron. Astrophys.* **43**, 359-379.

Mignard, F. 1981. The mean elements of Nereid. *Astron. J.* **86**, 1728-1729.

Oberti, P. 1990. An accurate solution for Nereid's motion. I. Analytic modeling. *Astron. Astrophys.* **239**, 381-386.

Rose, L. E. 1974. Orbit of Nereid and the mass of Neptune. *Astron. J.* **79**, 489-490.

Saad, A. S. and H. Kinoshita 1999. An anayltical theory on a satellite motion with highly eccentric orbit. *Proceedings of the 31st Symposium on Celestial Mechanics*, Kashima, Ibaraki, Japan, March 3-5,(H. Umehara, ed.), pp. 249-268.

Segerman, A. M. and Richardson, D. L. 1997. An analytical theory for the orbit of Nereid. *Celestial Mechanics* **66**, 321-344.

Veillet, C. 1982. Orbital elements of Nereid from new observations. *Astron. Astrophys.* **112**, 277-280.

Van Biesbroeck, G. 1951. The orbit of Nereid, Neptune's second satellite. *Astron. J.* **56**, 110-111.

Figure Captions

Fig. 1. The osculating orbital elements of Nereid for the nonplanar case over 5 years:
(1) semi-major axis,
(2) eccentricity,
(3) argument of pericenter,
(4) inclination,
(5) longitude of ascending node,
(6) periodic part of the mean anomaly.

Fig. 2. The osculating orbital elements of Nereid for the nonplanar case over 300 years:
(1) semi-major axis,
(2) eccentricity,
(3) periodic part of the argument of pericenter,
(4) inclination,
(5) periodic part of the longitude of ascending node,
(6) periodic part of the mean anomaly.

Fig. 3. Difference between analytical and numerical results of the orbital elements of Nereid during 5 years:
(1) semi-major axis (in km),

(2) eccentricity (in radians),
(3) argument of pericenter (in degree),
(4) inclination (in degree),
(5) longitude of ascending node (in degree),
(6) the mean anomaly (in degree).

Fig. 4. Residuals in the orbital elements of Nereid during 5 years by using least-square fitting :
(1) semi-major axis (in km),
(2) eccentricity (in radians),
(3) argument of pericenter (in degree),
(4) inclination (in degree),
(5) longitude of ascending node (in degree),
(6) the mean anomaly (in degree).

Fig. 5. Difference between analytical and numerical results of the orbital elements of Nereid over 300 years:
(1) semi-major axis (in km),
(2) eccentricity (in radians),
(3) argument of pericenter (in degree),
(4) inclination (in degree),
(5) longitude of ascending node (in degree),
(6) the mean anomaly (in degree).

Fig. 6. Residuals in the orbital elements of Nereid over 300 years by using least-square fitting :
(1) semi-major axis (in km),
(2) eccentricity (in radians),
(3) argument of pericenter (in degree),
(4) inclination (in degree),
(5) longitude of ascending node (in degree),
(6) the mean anomaly (in degree).

Fig. 7. Difference between analytical and numerical results of the orbital elements of Nereid over 300 years after making corrections in the mean motions of ℓ, g and h:
(1) semi-major axis (in km),
(2) eccentricity (in radians),
(3) argument of pericenter (in degree),
(4) inclination (in degree),
(5) longitude of ascending node (in degree),
(6) the mean anomaly (in degree).

Fig. 8. Residuals in the osculating orbital elements of Nereid over 300 years by using least-square fitting, and after making corrections in the mean motions of ℓ, g and h:
(1) semi-major axis (in km),
(2) eccentricity (in radians),
(3) argument of pericenter (in degree),
(4) inclination (in degree),
(5) longitude of ascending node (in degree),
(6) the mean anomaly (in degree).

Tables and Figures

TABLE I

Amplitudes of the osculating elements

Elements	Short-period	Long-period
semi-major axis	747.989	1196.78
eccentricity	0.0004	0.0115
arg. of pericenter	0.006	0.7
inclination	0.0025	0.16
long. of asc. node	0.01	0.17
mean anomaly	0.0325	2.0

TABLE II

Accuracy of the osculating elements

Elements	Short-period	Long-period
semi-major axis	0.3	0.3
eccentricity	3×10^{-8}	1×10^{-7}
arg. of pericenter	3×10^{-6}	7×10^{-4}
inclination	1.5×10^{-6}	1×10^{-4}
long. of asc. node	3×10^{-6}	7×10^{-4}
mean anomaly	2.5×10^{-5}	6×10^{-5}

where the semi-major axis is given in km, eccentricity in radian, and the argument of pericenter, longitude of ascending node and the mean anomaly are given in degree.

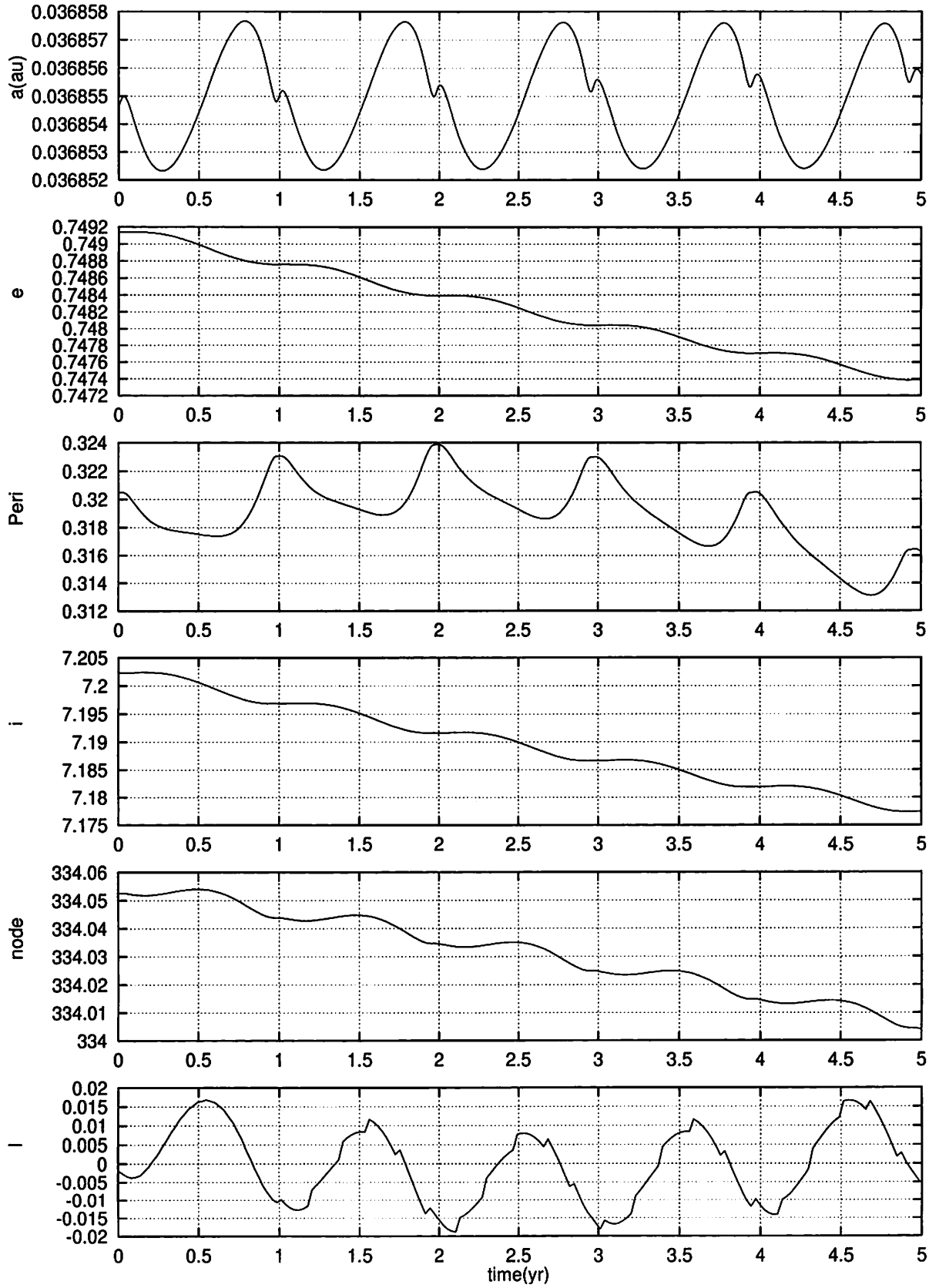
a(au)
0.036858
0.036857
0.036856
0.036855
0.036854
0.036853
0.036852
0 0.5 1 1.5 2 2.5 3 3.5 4 4.5 5
(1)
e
0.7492
0.749
0.7488
0.7486
0.7484
0.7482
0.748
0.7478
0.7476
0.7474
0.7472
0 0.5 1 1.5 2 2.5 3 3.5 4 4.5 5
(2)
Peri
0.324
0.322
0.32
0.318
0.316
0.314
0.312
0 0.5 1 1.5 2 2.5 3 3.5 4 4.5 5
(3)
i
7.205
7.2
7.195
7.19
7.185
7.18
7.175
0 0.5 1 1.5 2 2.5 3 3.5 4 4.5 5
(4)
node
334.06
334.05
334.04
334.03
334.02
334.01
334
0 0.5 1 1.5 2 2.5 3 3.5 4 4.5 5
(5)
l
0.02
0.015
0.01
0.005
0
-0.005
-0.01
-0.015
-0.02
0 0.5 1 1.5 2 2.5 3 3.5 4 4.5 5
time(yr)
(6)

Fig. 1

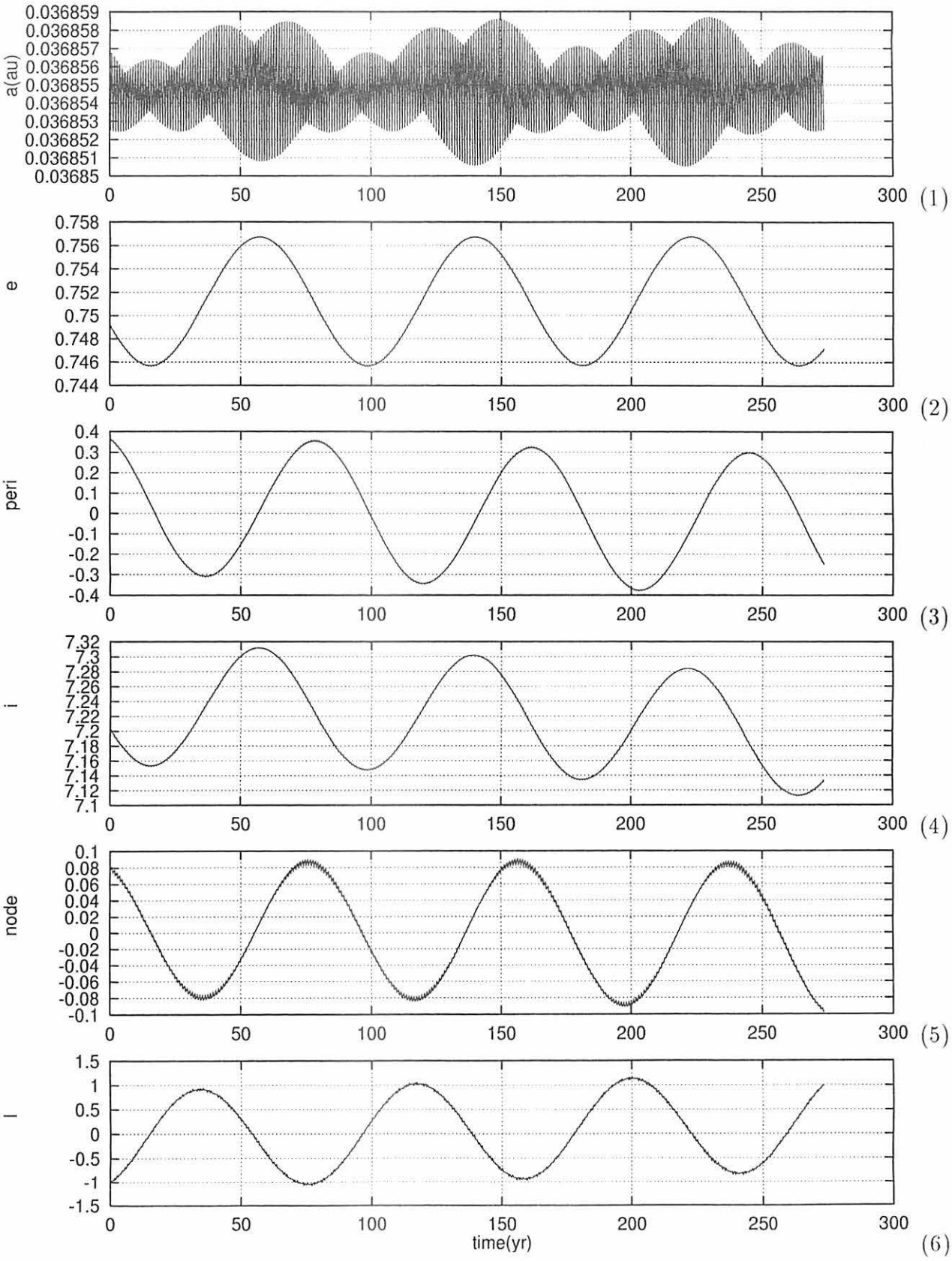
a(au)
0.036859
0.036858
0.036857
0.036856
0.036855
0.036854
0.036853
0.036852
0.036851
0.03685
0 50 100 150 200 250 300
(1)
e
0.758
0.756
0.754
0.752
0.75
0.748
0.746
0.744
0 50 100 150 200 250 300
(2)
peri
0.4
0.3
0.2
0.1
0
-0.1
-0.2
-0.3
-0.4
0 50 100 150 200 250 300
(3)
i
7.32
7.3
7.28
7.26
7.24
7.22
7.2
7.18
7.16
7.14
7.12
7.1
0 50 100 150 200 250 300
(4)
node
0.1
0.08
0.06
0.04
0.02
0
-0.02
-0.04
-0.06
-0.08
-0.1
0 50 100 150 200 250 300
(5)
l
1.5
1
0.5
0
-0.5
-1
-1.5
0 50 100 150 200 250 300
time(yr)
(6)

Fig. 2

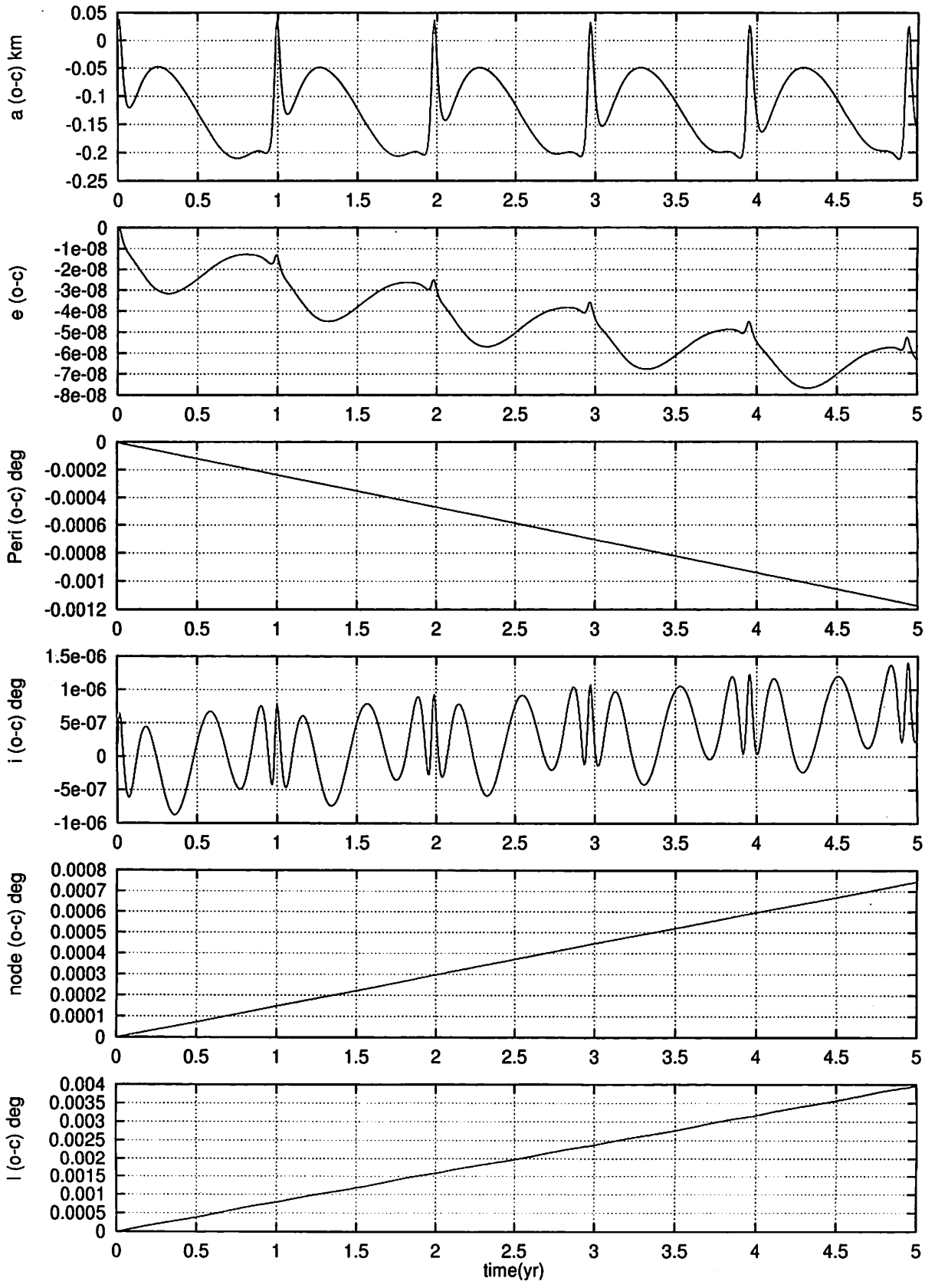
a (o-c) km
0.05
0
-0.05
-0.1
-0.15
-0.2
-0.25
(1)
e (o-c)
0
-1e-08
-2e-08
-3e-08
-4e-08
-5e-08
-6e-08
-7e-08
-8e-08
(2)
Peri (o-c) deg
0
-0.0002
-0.0004
-0.0006
-0.0008
-0.001
-0.0012
(3)
i (o-c) deg
1.5e-06
1e-06
5e-07
0
-5e-07
-1e-06
(4)
node (o-c) deg
0.0008
0.0007
0.0006
0.0005
0.0004
0.0003
0.0002
0.0001
0
(5)
l (o-c) deg
0.004
0.0035
0.003
0.0025
0.002
0.0015
0.001
0.0005
0
0 0.5 1 1.5 2 2.5 3 3.5 4 4.5 5
time(yr)
(6)

Fig. 3

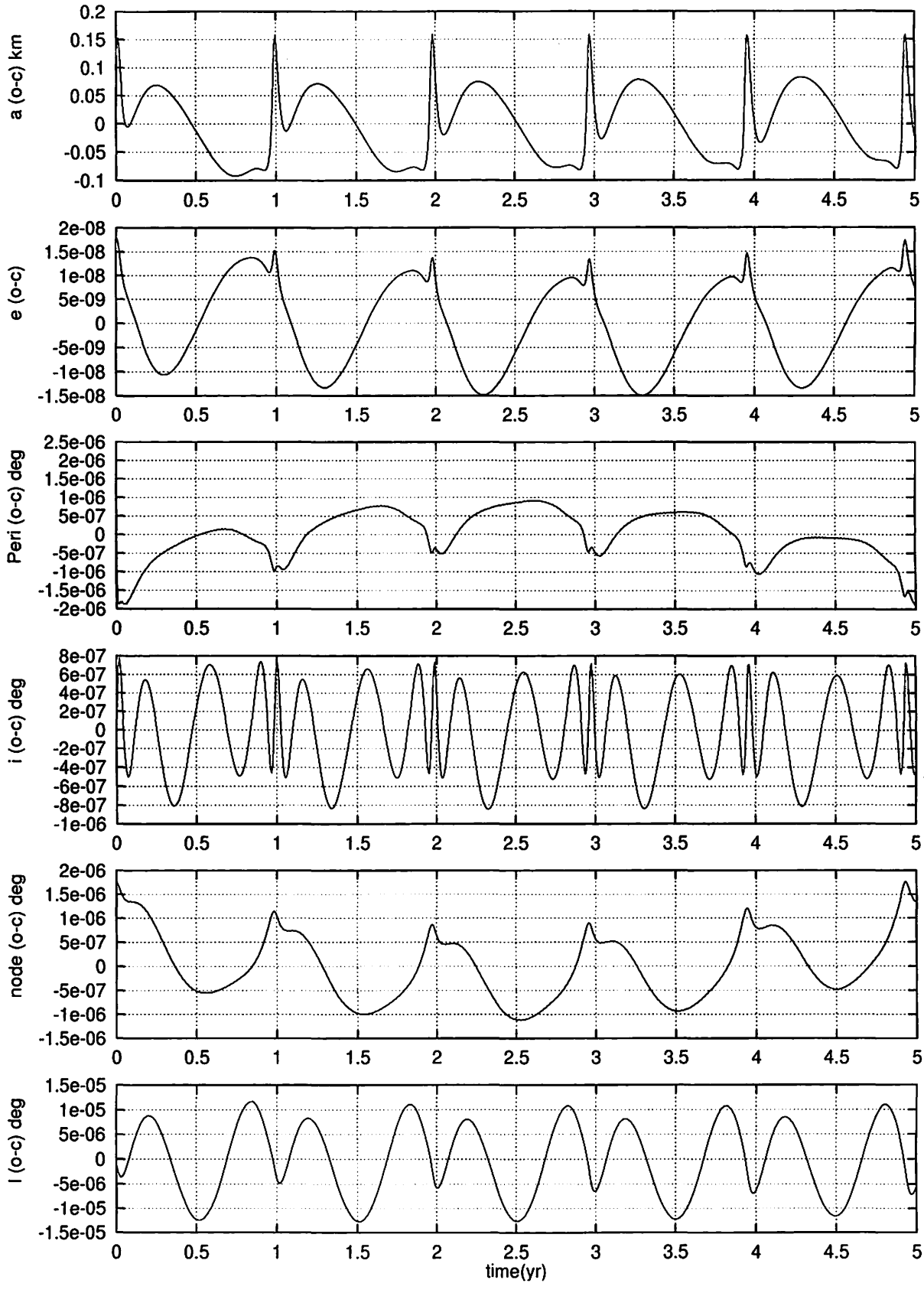
a (o-c) km
0.2
0.15
0.1
0.05
0
-0.05
-0.1
0 0.5 1 1.5 2 2.5 3 3.5 4 4.5 5
(1)
e (o-c)
2e-08
1.5e-08
1e-08
5e-09
0
-5e-09
-1e-08
-1.5e-08
0 0.5 1 1.5 2 2.5 3 3.5 4 4.5 5
(2)
Peri (o-c) deg
2.5e-06
2e-06
1.5e-06
1e-06
5e-07
0
-5e-07
-1e-06
-1.5e-06
-2e-06
0 0.5 1 1.5 2 2.5 3 3.5 4 4.5 5
(3)
i (o-c) deg
8e-07
6e-07
4e-07
2e-07
0
-2e-07
-4e-07
-6e-07
-8e-07
-1e-06
0 0.5 1 1.5 2 2.5 3 3.5 4 4.5 5
(4)
node (o-c) deg
2e-06
1.5e-06
1e-06
5e-07
0
-5e-07
-1e-06
-1.5e-06
0 0.5 1 1.5 2 2.5 3 3.5 4 4.5 5
(5)
l (o-c) deg
1.5e-05
1e-05
5e-06
0
-5e-06
-1e-05
-1.5e-05
0 0.5 1 1.5 2 2.5 3 3.5 4 4.5 5
time(yr)
(6)

Fig. 4

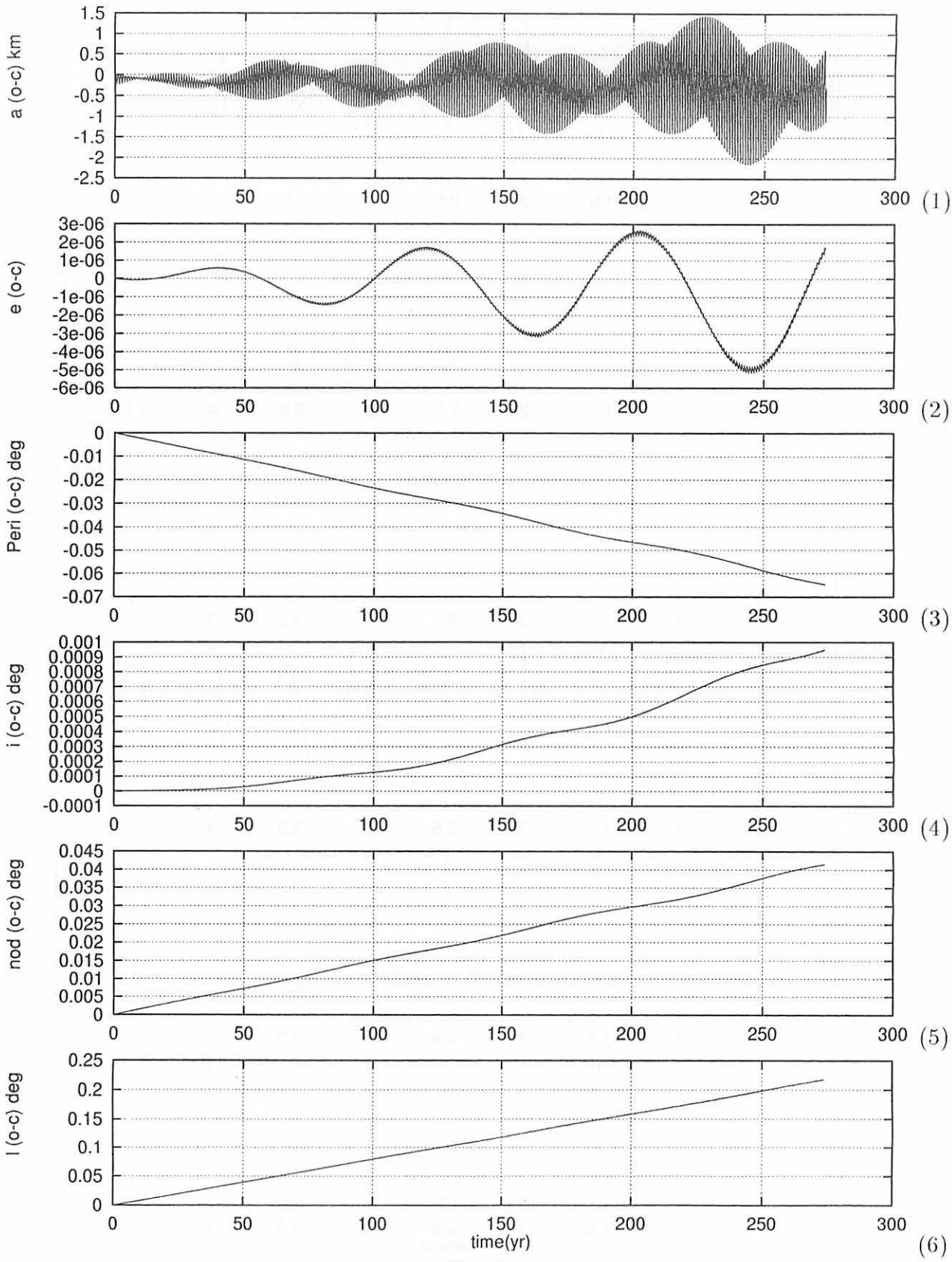
a (o-c) km
1.5
1
0.5
0
-0.5
-1
-1.5
-2
-2.5
0
50
100
150
200
250
300
(1)
e (o-c)
3e-06
2e-06
1e-06
0
-1e-06
-2e-06
-3e-06
-4e-06
-5e-06
-6e-06
(2)
Peri (o-c) deg
0
-0.01
-0.02
-0.03
-0.04
-0.05
-0.06
-0.07
(3)
i (o-c) deg
0.001
0.0009
0.0008
0.0007
0.0006
0.0005
0.0004
0.0003
0.0002
0.0001
0
-0.0001
(4)
nod (o-c) deg
0.045
0.04
0.035
0.03
0.025
0.02
0.015
0.01
0.005
0
(5)
l (o-c) deg
0.25
0.2
0.15
0.1
0.05
0
time(yr)
(6)

Fig. 5

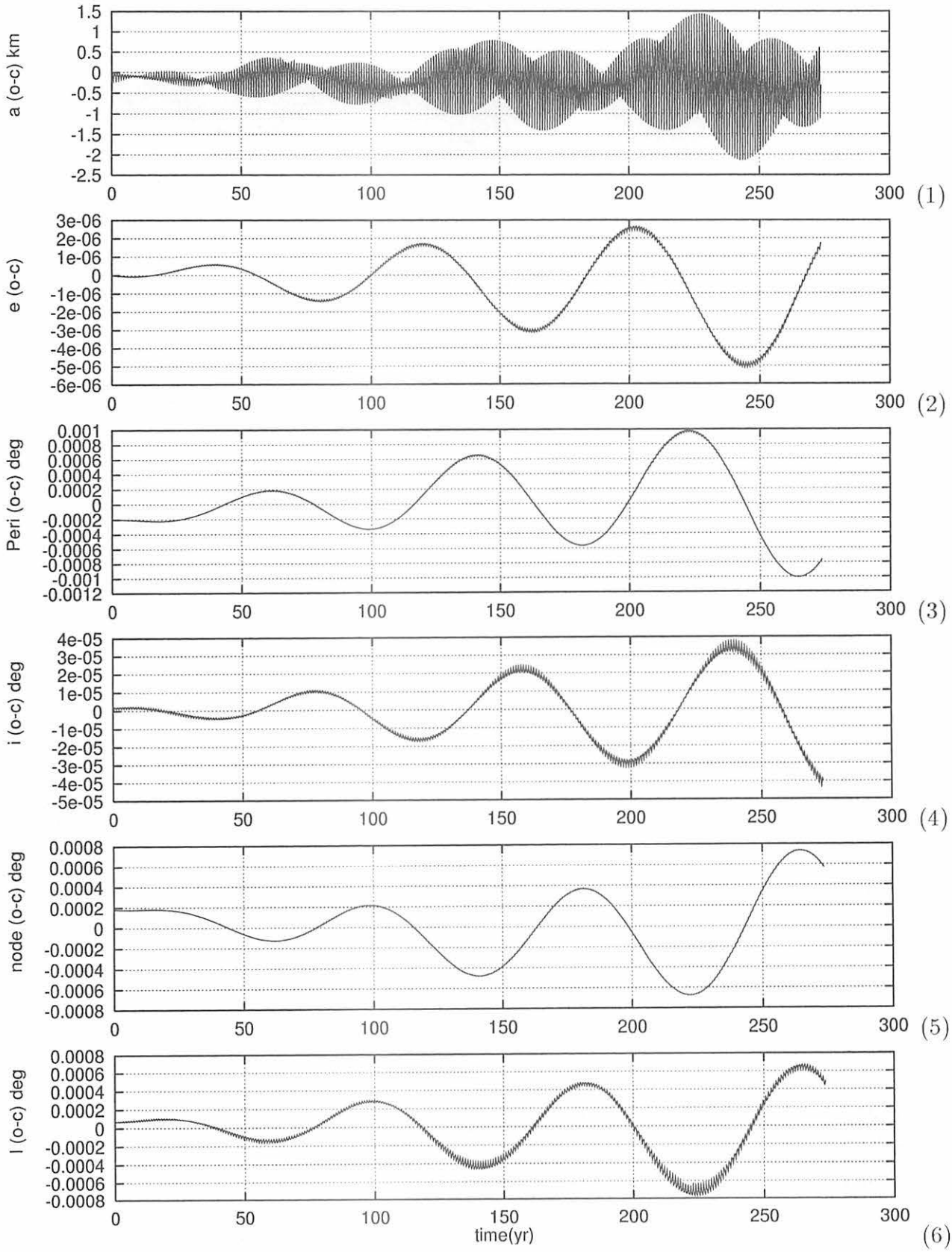
a (o-c) km
1.5
1
0.5
0
-0.5
-1
-1.5
-2
-2.5
0
50
100
150
200
250
300
(1)
e (o-c)
3e-06
2e-06
1e-06
0
-1e-06
-2e-06
-3e-06
-4e-06
-5e-06
-6e-06
(2)
Peri (o-c) deg
0.001
0.0008
0.0006
0.0004
0.0002
0
-0.0002
-0.0004
-0.0006
-0.0008
-0.001
-0.0012
(3)
i (o-c) deg
4e-05
3e-05
2e-05
1e-05
0
-1e-05
-2e-05
-3e-05
-4e-05
-5e-05
(4)
node (o-c) deg
0.0008
0.0006
0.0004
0.0002
0
-0.0002
-0.0004
-0.0006
-0.0008
(5)
l (o-c) deg
time(yr)
(6)

Fig. 6

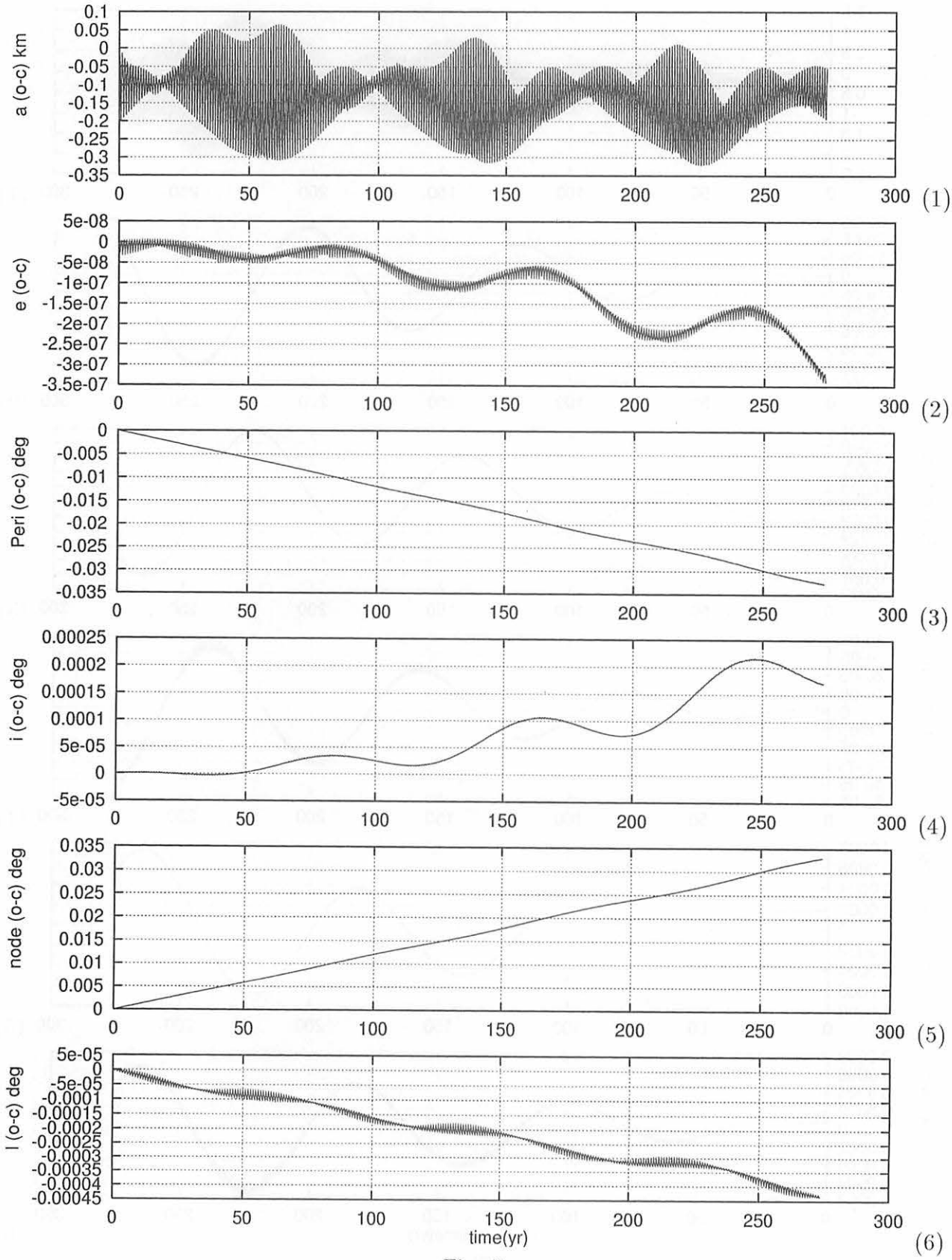
a (o-c) km
0.1
0.05
0
-0.05
-0.1
-0.15
-0.2
-0.25
-0.3
-0.35
0
50
100
150
200
250
300
(1)
e (o-c)
5e-08
0
-5e-08
-1e-07
-1.5e-07
-2e-07
-2.5e-07
-3e-07
-3.5e-07
(2)
Peri (o-c) deg
0
-0.005
-0.01
-0.015
-0.02
-0.025
-0.03
-0.035
(3)
i (o-c) deg
0.00025
0.0002
0.00015
0.0001
5e-05
0
-5e-05
(4)
node (o-c) deg
0.035
0.03
0.025
0.02
0.015
0.01
0.005
0
(5)
l (o-c) deg
5e-05
0
-5e-05
-0.0001
-0.00015
-0.0002
-0.00025
-0.0003
-0.00035
-0.0004
-0.00045
time(yr)
(6)

Fig. 7

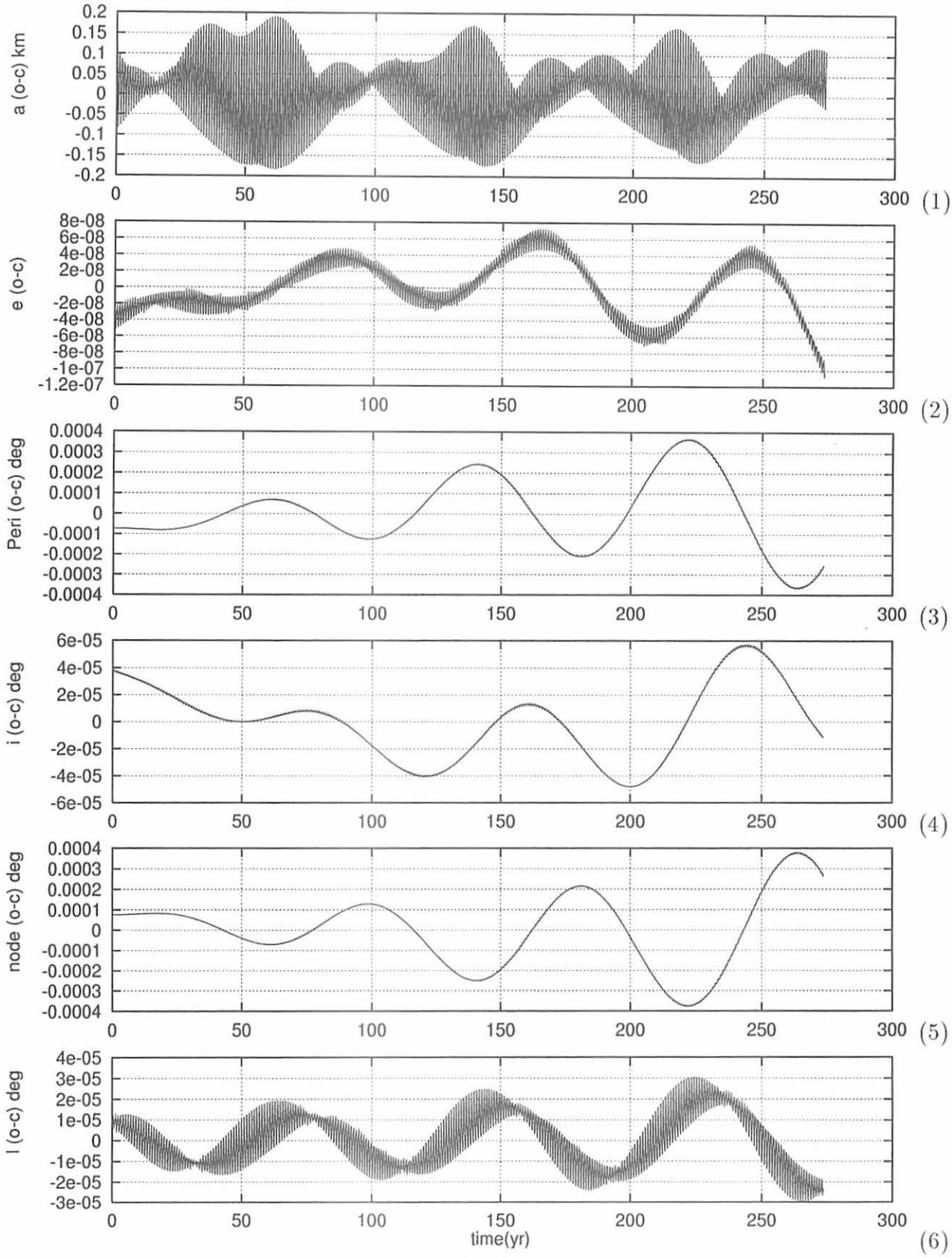
a (o-c) km
0.2
0.15
0.1
0.05
0
-0.05
-0.1
-0.15
-0.2
0
50
100
150
200
250
300
(1)
e (o-c)
8e-08
6e-08
4e-08
2e-08
0
-2e-08
-4e-08
-6e-08
-8e-08
-1e-07
-1.2e-07
(2)
Peri (o-c) deg
0.0004
0.0003
0.0002
0.0001
-0.0001
-0.0002
-0.0003
-0.0004
(3)
i (o-c) deg
6e-05
4e-05
2e-05
-2e-05
-4e-05
-6e-05
(4)
node (o-c) deg
(5)
l (o-c) deg
4e-05
3e-05
2e-05
1e-05
-1e-05
-2e-05
-3e-05
time(yr)
(6)

Fig. 8

Orbital Evolution of Kuiper Belt Objects Caused by the Sweeping Resonances

Makiko NAGASAWA°, Shigeru IDA
Department of Earth and Planetary Sciences,
Tokyo Institute of Technology, Meguro-ku, Tokyo 152-8851
E-mail: nagasawa@geo.titech.ac.jp

Sweeping secular resonances due to a depletion of a solar nebula in the outer Kuiper belt was studied. We analytically estimated the regions where the secular resonances sweep, and the increments of eccentricities and inclinations of Kuiper belt objects (KBOs). We found that the inclinations of the KBOs are largely excited by the sweeping secular resonances, if the residual nebula is uniformly depleted in a timescale of the order of 10^7 years with present planetary system. We also studied the effects of planets on the secular resonances changing planetary semi-major axis. In the case that Neptune had smaller semi-major axis (~-7AU), the required time scale of nebula depletion to obtain e~0.1 is 10^8 years. Since the required nebula depletion timescale of 10^8 years seems longer than that inferred from observations of T Tauri stars (10^6~10^7 years), it is favorable that the present planetary system is completed before the starting of the nebula depletion.

1. Introduction

As observational instruments develop, a lot of small bodies have been recently detected one after another in the Kuiper Belt region. At present, more than 150 objects were identified in this region. The distribution of KBOs is roughly separated into two regions (Fig.1). They are inner belt region and outer (classical) belt region. In the inner belt, both the eccentricities and the inclinations are largely excited (Fig.1 & Fig.2). Figure 1 and Fig. 2 show the distributions of eccentricities and inclination s of KBOs, respectively [1]. Root mean squares of the eccentricities and inclinations are about 0.2 and 0.23, respectively. Almost all bodies in this region are in mean motion resonances with Neptune. On the other hand, the eccentricities of the KBOs in the outer belt are substantially smaller than 0.2, and the root mean squares is only about 0.1. The inclinations of the KBOs in the outer belt are nearly equal to those of the inner belt. These large values are not explained by present planetary perturbations alone. As for the inner belt, the mechanism of sweeping 3:2 mean-motion resonance caused by Neptunian migration Malhotra [2] nicely explained the observed eccentricity. Although many studies were done to explain the origin of these large values of outer belt (e.g., sweeping of the 2:1 mean motion resonance [3], hypothetical stellar encounters [4], and Earth-sized hypothetical planetesimals, which scattered by Neptune [5]), the origin of the large inclination is not well known yet.

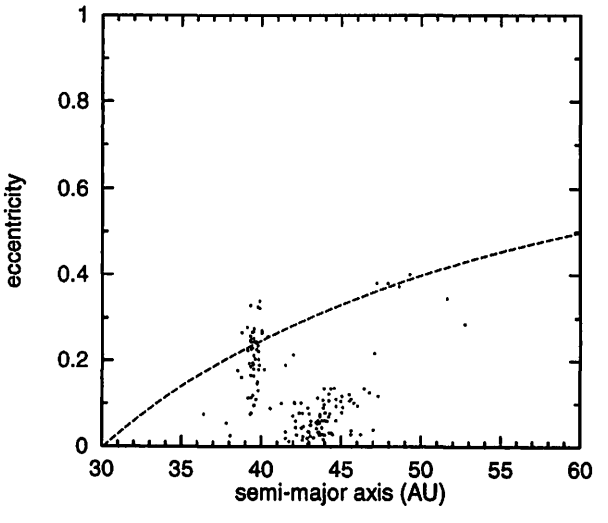

Fig.1. The distribution of eccentricities versus semi-major axes of the present Kuiper belt objects [1]. Above the dotted line, the KBOs orbits cross Neptunian orbit. The eccentricities in the outer belt are about 0.2, and the root mean squares is only about 0.1.

In this paper we investigate the effects of the sweeping secular resonances caused by the depletion of the primitive solar nebula. The importance of the sweeping secular resonances for the terrestrial planets and asteroids is shown by [6], [7], [8], [9] and [10]. With this excitation

mechanism, we will show that the eccentricities and inclinations of KBOs are excited to the observational level during the solar nebula depletion.

2. The sweeping secular resonances

Secular resonances occur when the rotation speed of the longitude of the perihelion or that of the ascending node of an object coincides with one of the eigenfrequencies of the planetary precessions. Coincidence of the longitude of the perihelion causes the excitation of the eccentricity, and that of ascending node causes the excitation of the inclination. With Sun and four Jovian planets in the present solar system configuration, seven secular resonances exist beyond the location of Neptune. Four resonances, which excite the eccentricity, take place at 31.7, 34.3, 35.0, and 41.0AU from the Sun. The resonances, which excite the inclination, exist at 31.6, 34.8 and 40.6AU. However, the nebula potential would significantly alter these locations of the secular resonances. As the nebula is depleted, the secular resonances move from the initial locations to the present locations. When the secular resonance passes through, the eccentricities and inclinations of the field bodies are excited.

3. Models and calculation methods

The region where the secular resonance sweeps depends strongly on the mass distribution of the proto-planetary system. The considering system consists of the Sun, four Jovian planets, a massless particle, and the nebula. The first model assumes present-day masses and orbits of Jupiter, Saturn, Uranus, and Neptune. The semi-major axes are 5.20, 9.55, 19.2, and 30.1AU, respectively. The eccentricities are 0.0482, 0.0539, 0.0513, and 0.00496. The inclinations are 0.0228, 0.0434, 0.0135, and 0.0309 in radian.

According to Malhotra [2], we consider the effects of gradual expansion of separations between the planetary orbits. In this case, the semi-major axes of four Jovian planets are 5.4, 8.7, 16.3, and 23.2 AU. For planetary masses, the present

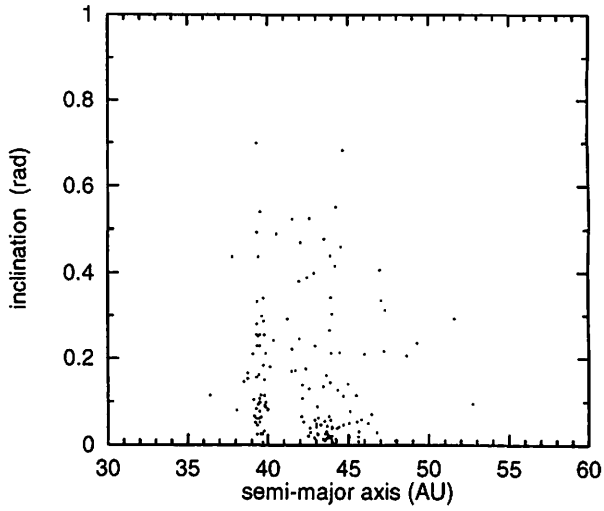

Fig.2. The distribution of inclinations versus semi-major axes of the KBOs. The inclinations of the KBOs are about 0.2. Inclinations are given in radian.

values are taken. After the nebula depletion, we calculated orbital evolution of KBOs by changing the semi-major axis of Neptune to see how the orbits of KBOs change by the sweeping of the mean-motion resonances.

The structure of the primitive solar nebula and the mechanisms of its depletion are not obvious in the outer region of the solar system. For the 'starting' nebula model, the minimum mass solar nebula [11] extending to 150AU was basically employed. We assume the nebula orbits cylindrical symmetrically around the Sun and is also symmetrical with respect to the ecliptic plane. We also assume the nebula is depleted exponentially with time and uniformly as follows:

$$\rho(r, z, t) = \rho(r, z, 0) \exp(-t / \tau), \quad (1)$$

where τ is a nebula depletion timescale (a constant parameter) and ρ is the nebula density.

We used secular perturbation theory to determine the location of the secular resonances. The disturbing functions are obtained using the expanding three-dimensional nebula potential. We calculated the rotation speed of the longitude of the perihelion or that of the ascending node of KBOs and eigenfrequencies of the planetary precessions at every stage of the nebula depletion. We

determined the location of the secular resonances and estimated their strength.

4. Results

4.1 Location of secular resonances and excitation magnitudes of eccentricities and inclinations

We found that the inclination of KBOs is excited to the observational level by the sweeping secular resonances.

Figure 3 shows the locations of the eccentricity's secular resonances as a function of the degree of nebula depletion u= ρ (t)/ ρ (0). The υ_5, υ_6, υ_7 and υ_8 secular resonances sweep the Kuiper Belt region. The eccentricity's resonances sweep the Kuiper Belt from outside to inside and nearly settled to the present locations when the nebula density decreases to 1/100 of the initial value. Figure 4 shows the location of the inclination's secular resonances as a function of the degree of nebula depletion. The υ_{15}, υ_{16}, υ_{17} and υ_{18} secular resonances sweep the Kuiper Belt from inside to outside. The υ_{15} starts to pass the KBOs region when the nebula density decreases to 1/200 of the initial density and reaches at infinity across the KBOs region when the nebula density becomes 1/2000 of the initial density. The υ_{18} resonance is the most important for the inclination excitation near the 3:2 resonance (~39.5AU), while the υ_{15} resonance is the most important in the classical belt (>42AU). The υ_{15} resonance is closely related Jovian motion. Jupiter is essentially responsible for excitation of inclination in the classical belt.

In Fig.5 and Fig. 6, the excited magnitude of eccentricity and inclination are plotted. The solid, dotted and dashed lines show the case of $\tau = 10^7$, 10^6, and 10^5 years, respectively. The excitation in eccentricity and inclination are obtained as a summation of excitations caused by sweeping of individual resonances. Circles show observed values. These lines correspond to the maximum excitation and KBOs distribute under these lines.

For the excitation of the eccentricity and the inclination to the observed level, the required timescales of the nebula depletion become approximately the same. These timescales are about 10^7 years.

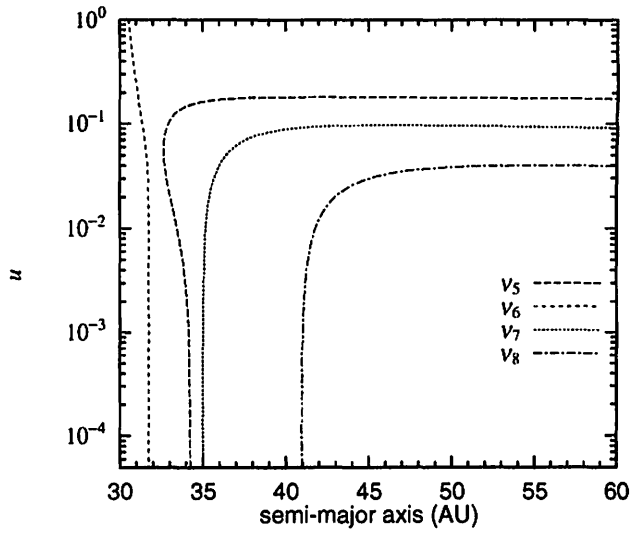

Fig.3. The location of the υ_5, υ_6, υ_7 and υ_8 secular resonances, which pump up eccentricities. They pass through the Kuiper Belt.

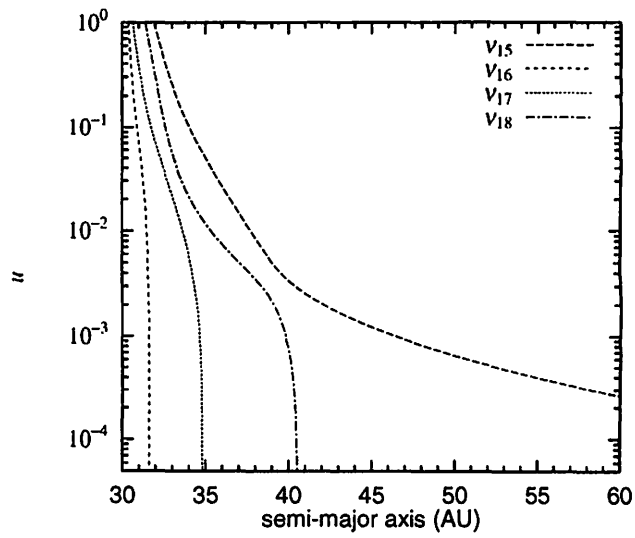

Fig.4. The location of the υ_{15}, υ_{16}, υ_{17} and υ_{18} secular resonances, which pump up inclinations. They pass through the Kuiper Belt region after the major fraction of the nebula had been depleted.

4.2 The nebula depletion followed by Neptunian migration

Although the observed KBOs are concentrated in the location of the 3:2 mean motion resonance, our mechanism of the sweeping secular resonance can not explain this feature. If the location of the

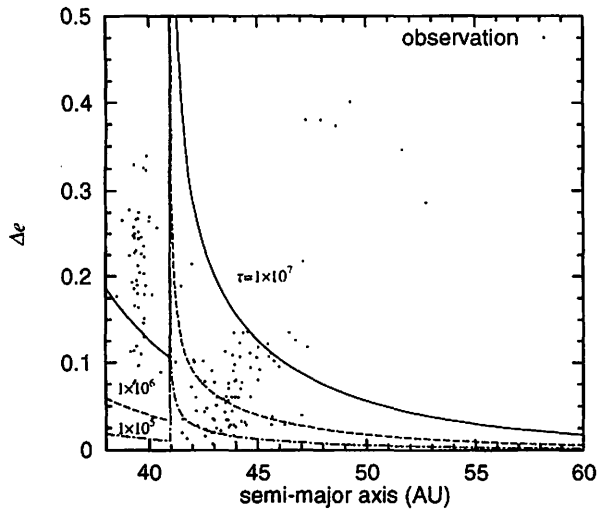

Fig.5. The estimated excitations in eccentricity in the present-day model. Solid, dotted and dashed lines show the cases that depletion time scale is 10^7 10^6 and 10^5 years, respectively.

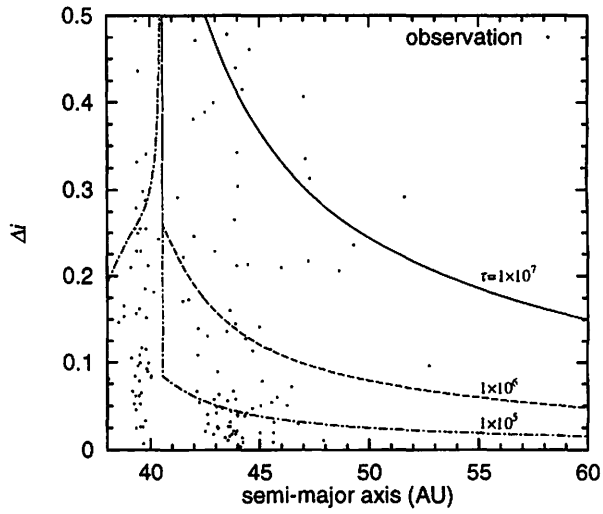

Fig.6. The estimated excitations in inclination in the present-day model. Solid, dotted and dashed lines show the cases that depletion time scale is 10^7 10^6 and 10^5 years, respectively.

3:2 resonance migrates by planetary migration (Malhotra [3]) after the nebula depletion, the KBOs in inner belt are captured into the 3:2 resonance. Figure 7 and Fig.8 shows the results of orbital integration. We estimated the excitation of eccentricities and inclinations after the nebula depletion by putting the semi-major axes of four Jovian planets to be 5.4, 8.7, 16.3, and 23.2 AU. We take $\tau = 10^8$ years, here. Using these excitation magnitudes, we calculate orbits of massless particles by changing the semi-major axis of Neptune. We integrate orbits for 10^7 years after the nebula depletion. In Fig.7 and Fig. 8, the particles in stable orbits are shown open symbols and particles in unstable orbits are shown cross symbols. We can see that the trapping mechanism is effective even if the inclinations of particles are high. However, if the secular resonance sweeping precedes the mean motion resonance sweeping, the long depletion timescale (~10^8 years) are required to explain present e and i. We also find that many particles are trapped into the 2:1 mean motion resonance. The long depletion timescale and concentration of particles in the 2:1 resonance are not favorable. Hence, the planetary migration would precede the secular resonance sweeping.

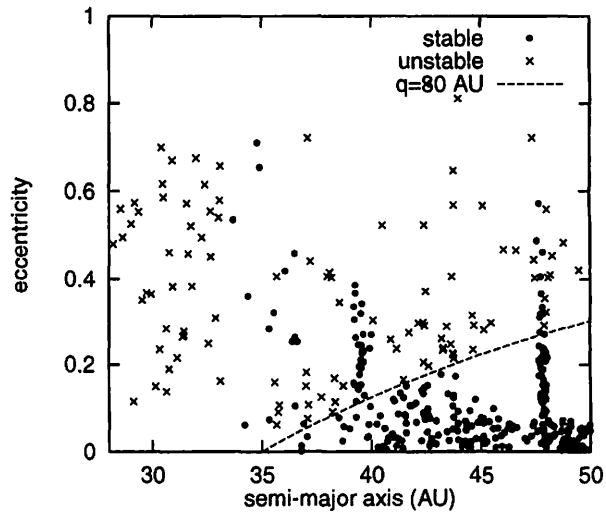

Fig.7. The eccentricity's distribution of massless particles after the nebula depletion followed by the planetary migration. Filled circles show the particles in stable orbit (around mean-motion resonances or ones pericentric distances q is smaller than 35AU). Crosses show the particles in unstable orbits. Dashed line show the q=30AU. Over this line, the orbits of particles cross Neptunian orbit.

5. Summaries and Discussions

We have investigated orbital excitations of KBOs caused by the sweeping secular resonances during the primitive solar nebula depletion.

We found that the sweeping of secular resonances well explain the trend of the large inclinations correspond with the eccentricities in the outer belt (Fig. 5 and Fig. 6). The inclination of the bodies in the outer belt is excited to the observational level if the nebula density uniformly decreases from 1/200 to 1/2000 of the initial nebula in a timescale of 10^7 years. For the excitation of inclinations, Jovian perturbations and nebula potential are the most important. On the other hand, the excitation of eccentricity depends on Neptune. This means that, even if Uranus and Neptune has not been completed before the starting of the nebula depletion, the inclination of KBOs are easily excited by the Jovian sweeping secular resonance. Previous mechanisms, which have been proposed to explain eccentricities and inclinations of the KBOs in the outer belt (the sweeping of 2:1 mean-motion resonance [4], hypothetical stellar encounter [5], Neptune-scattered planetesimals [6]), are not easy to explain the high inclinations. Our sweeping secular resonances in the present paper may be responsible for high inclination of KBOs.

We note that predicted eccentricities and inclinations beyond 50AU are quite different among proposed models. In the case of sweeping of 2:1 mean-motion resonance, eccentricities and inclinations are hardly excited beyond 50AU since there is not strong mean-motion resonance between the 2:1 resonance and the 3:1 resonance. The model of hypothetical stellar encounter predicts that e and i rapidly increase beyond 50AU since the effect of a passing star sensitively depends on distance from the star. Neptune-scattered planetesimal model would not show systematic trend of eccentricities and inclinations. If future observation finds so many objects beyond 50AU to allow statistical discussion, it would judge the above models and consequently give important clues on what happened in the outer solar system in the formation stage.

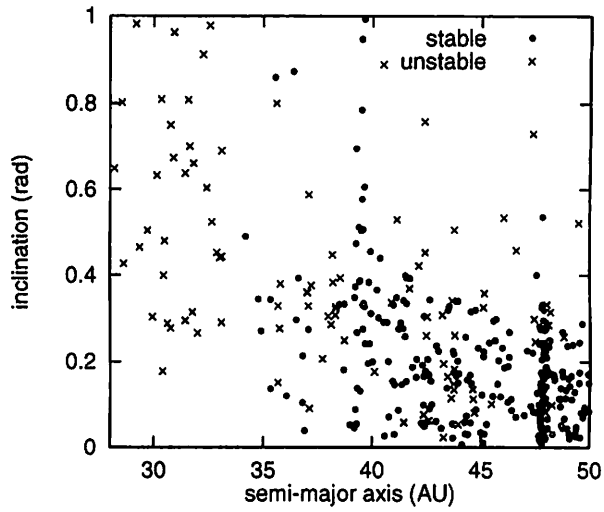

Fig.8. The inclination's distribution of mass less particles after the nebula depletion followed by the planetary migration. Filled circles show the particles in the stable orbits and crosses show the particles in the unstable orbits.

References

[1]http://cfa-www.harvard.edu/~graff/lists/TNOs.html

[2]Malhotra, R. 1993, *Nature*, 365, 819

[3]Hahn, J. M. & Malhotra, R. 1999, *AJ*, 3041

[4]Ida, S., Larwood, J., & Burkert, A. 2000, *AJ*, Preprint

[5]Morbidelli, A., & Valsecchi, G.B. 1997, *Icarus*, 128, 464

[6]Ward, W. R., Colombo, G., & Franklin, F. A. 1976, *Icarus*, 28, 441

[7]Heppenheimer, T. A. 1980, *Icarus*, 41, 76

[8]Ward, W. R. 1981, Icarus, 47, 234

[9]Lecar, M., & Franklin, F. 1997, *Icarus*, 129, 134

[10]Nagasawa, M., Tanaka, H., & Ida, S. 2000, *AJ*, 119, 1480

[11]Hayashi, C. 1981, *Prog. Theor. Phys. Suppl.*, 70, 35

水星近日点前進の問題 Newcombの場合
Newcomb's case for the appearance of the excess advance in the longitude of the perihelion of Mercury

井上　猛　（京都産業大学）
T. Inoue
Kyoto Sangyo University

Abstract. It is Le Verrier who pointed out the first the existence of the excess advance in the longitude of the perihelion of Mercury (Le Verrier, 1859). This is understood that the excess amount corresponds to a disrepancy between his theory of the motion of Mercury and the observations of Mercury's transits on the disk of the Sun. After him, it is Newcomb who verified the phenomenon (Newcomb, 1895).
We now know that this quantity is of the order of 43 arcseconds per century and that it is the Einstein's general theory of relativity which solved totally this problem in forcing to change our comprehension about the space and the time.
On the contrary, we insisted to reexamine the Le Verrier's theory of the motion of Mercury (Inoue, 1992). The Newcomb's theory is also the case and we found here the very reason why such a discrepancy appears in the motion of Mercury.
Our result shows that the Newtonian Mechanics is perfect to describe the motion of whole celestial bodies.

1．『水星近日点黄経に於ける余剰永年変化の問題は、“余剰前進”の存在を最初に指摘した Le Verrier (1859)の研究、更にはそれが確かであるとした Newcomb(1895)の研究にまで遡って調べられなければならない事柄である。Einstein (1915) の一般相対論に依る議論は、斯かる調査が済んでからである。』と、**“一貫して”**主張して来て居る処である(Inoue, 1992)。

此の中の Le Verrier の場合は、曲折を経ながらも我々の立場での解決を見る事が出来た(井上、1998)。 これに対して、Newcomb の場合は、扱いが Le Verrier の夫とは**“微妙に異なって居る”**のである。それにも拘らず、余剰前進は同様に生ずると云うのであるから仲々に解決する事が出来ないで居た。此の度、解決する事が出来て結果を見てみるならば両者が相互に強く関連し合って居るのに気付かされる。従って、Newcomb の場合を論ずるのに、 Le Verrier の場合の議論が有効となって来る事になる。

そこで、改めて Le Verrier の場合が如何様であったかを一通り整理して置く事にする。

①水星の運動を記述する為に、中心差および動径を、平均近点離角 M の Fourier級数に展開する。此の表式中の sin M および cos M に比例する項の中に、金星に依る影響を水星軌道の離心率を**“二様に”**改変する形で取り込んだ。
②二様に為された改変量は、夫々に微小であり、改変量同士の“差”に至っては更に微小である。しかし、 Le Verrier 理論の精度からすれば、此の“差”の存在を無視する事は許されない。斯くして得られた表式群は、二体問題の解が表わすもの（楕円軌道のそれ）とは明らかに異なるものとなって居る。
③上記表式群が表わす軌道が如何なるものであるか、中でも、楕円軌道と如何なる関係にあるかは明らかにされるべき事柄である。これは可能なのであって、結果は、一世紀当り43秒角、近日点黄経 ϖ に永年後退が存在して居る楕円軌道であると云う事になった。
④ Le Verrier 採用の摂動処理法では、初発の水星軌道が斯かる後退軌道となって仕舞うのである。然るに、彼は斯かる事態の発生に気付かず、従って、補正も修正も加える事はしなかった。これが、後に、“一世紀当り43秒角 (Le Verrierの結果は 38.″3/100年)合わない”と言われる問題を惹起する事になる。

⑤ Le Verrier が採用した“手法”が齎らす処のものを、端的に示す目的で、以下の様な式群で表わされる、二個の‘離心率’を有する『中間軌道』を提示した (Inoue, 1992)。

$$(1)\qquad u - e_M \sin u = M \ , \quad M = \int_{t0}^{t} n\,dt + \chi \ ;$$

$$(2)\qquad n \equiv \sqrt{\{\mu / a^3\}} \ , \quad \mu = G(m_{太陽} + m_{水星}) \ ;$$

$$(3)\qquad \tan(f/2) = \sqrt{\{(1+e_M)/(1-e_M)\}} \cdot \tan(u/2) \ ;$$

$$(4)\qquad r = a(1 - e_r \cos u) \ , \quad \phi = \varpi + f \ ;$$

$$(5)\qquad e_r - e_M \equiv +1.53\ 8156 \times 10^{-8} \ .$$

ここで、a、e_M 及び ϖは、長半径、離心率及び近日点黄経に類似の定数を、M、u 及び f は平均近点離角、離心近点離角及び真近点離角に類似の変数を表わすものとする。変量 r 及びϕは、動径及び真黄経を表わす事になって居る。

2. 我々が、何の故に上記の如き表式群を提示したかと言えば、Paris 天文台報・第二巻に所載の Le Verrier の扱いが以下の様であったからである (Le Verrier, 1856)。

軌道の離心率 e 及び近日点黄経 ϖ に微小な変化量 Δe 及び$\Delta\varpi$ が存在して居たとすると、真黄経ϕ及び動径 r に、次式で与えられる変化量 $\Delta\phi$ 及びΔr が生ずる事になる。

$$(6)\qquad \Delta\phi = 2\Delta e \sin M - 2e\Delta\varpi \cos M \ ;$$

$$(7)\qquad \Delta r = -ae\Delta\varpi \sin M - a\Delta e \cos M \ .$$

金星に依る真黄経ϕ及び動径 r に於ける摂動 $\delta\phi$ 及び δr は、次の形に与えられて居る。真黄経の方には、金星に依る摂動 $S_♀$、$C_♀$の他に、地球および木星に依る摂動 $S_{地球}$、$C_{地球}$ および$S_{水星}$、$C_{水星}$ も存在して居るのであるが、必要無いので此処では考えない事にする。

$$(8)\qquad \delta\phi = S_♀ \sin M + C_♀ \cos M \ ;$$

$$(9)\qquad \delta r = S^*_♀ \sin M + C^*_♀ \cos M \ .$$

両者を合成して次を得る。

$$(10)\qquad d\phi \equiv \Delta\phi + \delta\phi = (2\Delta e + S_♀) \sin M - (2e\Delta\varpi - C_♀) \cos M \ ;$$

$$(11)\qquad dr \equiv \Delta r + \delta r = -(ae\Delta\varpi - S^*_♀) \sin M - (a\Delta e - C^*_♀) \cos M \ .$$

そうして、(10)式に於ける Δe 及び $\Delta\varpi$に、次の等式の成立を要求するのである。

$$(12)\qquad 2\Delta e + S_♀ = 0 \ , \quad 2e\Delta\varpi - C_♀ = 0 \ .$$

これに依って、次の表式が得られる事になる。

$$(13)\qquad d\phi = 0 \ ;$$

$$(14)\qquad dr = -(aC/2 - S^*_♀) \sin M + (aS/2 + C^*_♀) \cos M \ .$$

金星に依る真黄経ϕに於ける摂動$\delta\phi$を、上記の形で取り込むと、その皺寄せが動径 r に(14)式の様に及ぶ事になる訳である。これはこれで良い。問題は無い。

３．　ところが“実際の水星の運動理論は、此の様には構築されては居ない”と見る事が出来るのである。事は仲々に微妙であって、我々の“読み取り”が的を射たものであるか否かは、改めて問われなければならないのかも知れない。問題は、Paris 天文台報・第五巻に所載の Le Verrier の主張の中に在る (Le Verrier, 1859)。

*Il entre, dans l'expression des perturbations de la longitude, des termes dépendant uniquement de la longitude de Mercure même. On sait qu'on peut les négliger, pourvu qu'on ajoute au rayon certains termes dépendant du même argument (Chapitre VI, Tome II). **Mais ces derniers termes sont insensibles, si ce n'est dans l'action de Vénus sur Mercure ; et, dans cette dernière théorie, ils se trouvent égaux et de signes contraires aux termes** $-0.''011 \sin \ell$ **et** $-0.''003 \cos \ell$ **provenant d'une autre source. Il résulte de ces considérations que les termes des perturbations qui dépendent uniquement de la longitude de Mercure peuvent être négligés soit dans la longitude, soit dans le rayon de Mercure(*).***

(*) C'est ce qui a été fait en réduisant en Tables les inégalités produites dans le mouvement de Mercure par l'action de Vénus. En calculant relatives aux inégalités produites dans la longitude par les actions de la Terre et de Jupiter, on a, par mégarde, conservé les termes en sin ℓ *et cos* ℓ *. Peu importe, puisque l'une et l'autre voie sont également légitimes.*

上の四行は、我々が既に前頁で扱った処を述べて居るに過ぎないのであるが、続く太字で示した部分は甚だ意味深長である。水星の動径ｒに於ける金星の影響：$-0.''011 \sin \ell$ 及び $-0.''003 \cos \ell$ を相殺するが如き“外からの作用”が在るとすれば、これ等の項は無視可能になると云うのである。此処に、量 ℓ は $\ell = \varpi + M$ で与えられる平均黄経を表わす。

此処の処を、我々は“彼は以下の様に扱った”と捉えたのであった (Inoue, 1992)： 即ち先に、(12)式の成立を要求する事に依って、(13)式で $d\phi = 0$ を得た様に、(11)式での dr にも、(12)式に類似の等式の成立を要求して、 $dr = 0$ が実現する様に図ったのであると。詰り、(11)式に於ける Δe 及び $\Delta\varpi$ に、(10)式に於けるのとは独立に次の等式の成立を課すのである。

(15)　　$a\, e\, \Delta\varpi_r - S^*_\varphi = 0$,　　$a\, \Delta e_r - C^*_\varphi = 0$.

これに合わせるべく、改めて(12)式を次の形に書いて置く事にする。

(16)　　$2\, \Delta e_M + S_\varphi = 0$,　　$2 e\, \Delta\varpi_M - C_\varphi = 0$.

此の様な事は一般には許されない。しかし“Le Verrier は斯く扱った”と考えられる。只今の流れで捉えた結果を、端的に表わしたのが、表式群：(1)、(2)、(3)、(4)、(5)と云う訳である。これらを‘離心率’ｅの一次の精度で展開すれば、先に①で示したものが得られる事になって居る。先に用いた e_M 及び e_r は次の様に与えられるとする。

(17)　　$e_M \equiv e + \Delta e_M = e - S_\varphi/2$,　　$e_r \equiv e + \Delta e_r = e + C^*_\varphi/a$.

これらを考慮しつつ、件の表式群を展開してみるならば、“妙な形で”金星の影響を取り込んだ関係式が得られる事になる。楕円軌道が表わすものでは無い事は一目瞭然。

(18)　　$\phi = \varpi + f = \varpi + M + (f - M) = \ell + 2 e_M \sin M + \cdots$,

(19)　　$r = a(1 - e_r \cos M) = a(1 + e^2/2) - a\, e_r \cos M + \cdots$.

4．　Le Verrier の場合にも Newcombの場合にも真黄経に於ける周期摂動および動径に於ける周期摂動の取り扱いが、水星の運動理論の構築に際して重要な鍵を握る事になって居る。そこで、Paris 天文台報・第五巻所載の諸量を抜き出して、以下に記して置く事にする (Le Verrier, 1859)。此の中の真黄経の部分は、そっくりその儘を Clemence が引用する処となるものである (Clemence, 1943)。

惑　星	真黄経に於ける摂動　$\delta\phi$ sin ℓ の係数	cos ℓ の係数	動径に於ける摂動　δr sin ℓ の係数	cos ℓ の係数
金　星	＋0．″017	－0．″063	－0．″011	－0．″003
地　球	＋0．″005	－0．″017	＊　＊　＊	＊　＊　＊
木　星	＋0．″008	－0．″031	＊　＊　＊	＊　＊　＊

先に述べた議論では、平均近点離角 M が登場して来て居るので、関係 : $\ell = \varpi + M$ を用いて、上記の表を次の形に書き換えて置く。 Le Verrier が採用した近日点黄経ϖの値 $\varpi = 75°\ 7'\ 1.''03$ を考慮する事、勿論である。

惑　星	真黄経に於ける摂動　$\delta\phi$ sin M の係数	cos M の係数	動径に於ける摂動　δr sin M の係数	cos M の係数
金　星	+0.″065 2528	+0.″000 2483	+0.″000 0740	-0.″011 4015
地　球	+0.″017 7139	+0.″000 4658	＊　＊　＊	＊　＊　＊
木　星	+0.″032 0147	-0.″000 2306	＊　＊　＊	＊　＊　＊
総　和	+0.″114 9815	+0.″000 4835	+0.″000 0740	-0.″011 4015

これに依れば、(16)式で定められるΔe_M、及び(15)式で定められるΔe_rの値が、夫々計算出来る事になる。

(20)　$+ 2\Delta e_M + 0.''065\ 2528 = 0$　（$d\phi$に於ける sin M の係数から），

(21)　$-a\Delta e_r - 0.''011\ 4015 = 0$　（drに於ける cos M の係数から）；

(22)　$\Delta e_M = -0.''032\ 6264$　，

(23)　$\Delta e_r = -0.''029\ 4537$　．

‘長半径’ a には、 Le Verrier の値 $a = 0.387\ 0987$ を代入した。‘離心率’に於ける二様の改変値間の“差” 0.″003 は、 Le Verrier の理論構築の精度からすれば無視する事は許されない。これは、 Le Verrier 流の“金星の影響の取り込みを行なったもの”は“単一の離心率を有する楕円軌道で把捉する”のが困難であると云う事を表わして居る。

既に(5)式で与えた微少量は、上記の“差”に外ならないものである。

(24)　$\Delta e \equiv e_r - e_M = \Delta e_r - \Delta e_M = 3.''17\ 2675\times10^{-3} = 1.53\ 8156\times10^{-8}$　．

これが、一世紀当り43秒角“後退する楕円”を与える“源”であった (Inoue, 1992)。

5． 水星の運動理論樹立に際して、Newcomb は Le Verrier とは少しく異なる取り扱いをする。しかし、 Le Verrier の結果を追認する形で、近日点黄経に於ける余剰前進量を同じ様に見い出して居るのである (Chebotarev, 1967)。その理由を以下で見て行く。

先ずは、Newcomb が如何様に扱ったかを見る目的で、 Clemence 所論の水星運動理論から次の記述を引用して置く (Clemence, 1943)。

> We now consider the eccentricities and longitudes of the perihelia. Here the situation is complicated by the existence of perturbations of the longitudes having the same periods as the mean anomalies, which therefore are easily confounded with the elliptic elements.
> .....
> In Leverrier's theory of Mercury (*Annales de l'Observatoire de Paris*, Vol. V), there are three perturbations of the class mentioned. These are :
>
> Action of Venus, $+0.''017 \sin \ell - 0.''063 \cos \ell$,
> Action of the Earth, $+0.''005 \sin \ell - 0.''017 \cos \ell$,
> Action of Jupiter, $+0.''008 \sin \ell - 0.''031 \cos \ell$,
>
> where ℓ is the mean ecliptic longitude of Mercury.
> **Newcomb, supposing that these terms had been included in the Tables as perturbations of the longitude, and wishing to include them in the elliptic elements, took their sum (*A. C.* p. 180) and converted it into corrections to the eccentricities and perihelion, obtaining $\delta e = +0.''058$, $\delta \pi = 0.''0$.** In fact, however, Leverrier included only the last two of the terms mentioned in his tables of the perturbations. He says (*op. cit.*, p. 16), "En calculant les Tables relatives aux inégalités produites dans la longitude par les actions de la Terre et de Jupiter, on a, par mégarde, conservé les termes en sin ℓ et cos ℓ".
>
> Changing the argument of the perturbation due to the action of Venus to g, the mean anomaly, we have
> $+0.''066 \sin g + 0.''000 \cos g$,
> which gives $\delta e = +0.''033$, $\delta \pi = 0.''0$.
> .....

ここで、 Clemence が $\delta\pi$ 及び g と表記したものは、近日点黄経に対する改変量 $\Delta\varpi$ 及び平均近点離角 M を表わす。これで明らかなる如く、 Le Verrier が水星の真黄経 ϕ 及び動径 r に於ける金星に依る摂動 : S_{φ} 、C_{φ} 及び S^{*}_{φ} 、C^{*}_{φ} を考慮して“離心率の値を変えた”のに対して、Newcomb は、動径に於ける摂動は一切考えずして、真黄経に於ける金星 ・地球 ・木星に依る摂動 : S_{φ} 、$S_{地球}$、$S_{木星}$ を、“水星の離心率に加え合わせる”と云う方法を採って居る。詰り、Newcomb は、離心率の値が少しだけ異なる楕円軌道で以て当該摂動を内包した運動理論が構築出来ると考えた訳である。 Clemence が、金星のみの影響を考慮して、離心率に於ける改変量を $\delta e = +0.''033$ としたのに対して、Newcomb はこれを $\delta e = +0.''058$ として居るのである。

当然ながら、Newcomb は、 Le Verrier が用いた軌道が有するものとは、数量的に異なる値を有する軌道を採用した事になる。これに依る影響が、どの様な形で現われ、どの様に処理され得るかを見て行く事にしよう。両者を区別する目的で、脚符「$_L$」及び「$_N$」を夫々「Le Verrier」及び「Newcomb」の意味で用いる事にする。 Le Verrier が用いた楕円軌道の離心率を e_L と表記する時、Newcomb のそれ e_N は次の様であると考えられる。

(25) $\quad e_N = e_L + S/2$, $\quad (S \equiv S_{\varphi} + S_{地球} + S_{木星})$.

この事に付いては、Newcomb が採用した水星の質量に関連させて議論する必要がある。

彼は、 Le Verrier が水星の質量 $m_{水星}$ を太陽質量 $m_{太陽}$ の三百万分の一としたのに対し六百万分の一として居るのである (Chebotarev, 1967)。質量が変ると平均運動が変る事になる。それでは、Newcomb の運動把捉は、 Le Verrier のそれと大きく異なって居るのであろうか？

平均運動　n　：

(26)　$n_N = \sqrt{\{\mu_N / a_N^3\}}$　,　$\mu_N \equiv G(m_{太陽} + m_{水星N})$　;

(27)　$n_L = \sqrt{\{\mu_L / a_L^3\}}$　,　$\mu_L \equiv G(m_{太陽} + m_{水星L})$　.

質量比　$m_{水星} / m_{太陽}$　：

(28)　$m_{水星N} / m_{太陽} = (1/6) \times 10^{-6}$　,

(29)　$m_{水星L} / m_{太陽} = (1/3) \times 10^{-6}$　.

ここで、平均黄経 ℓ に、$\ell_N \neq \ell_L$ の如き不一致が生じたのでは、水星の運動把捉上に大きな支障を来たすこと必定なので、これは回避する事にする。従って、次を要求する。

(30)　$n_N \equiv n_L$　.

これは、長半径 a に、次の関係を要求する事になる。

(31)　$a_N / a_L = (\mu_N / \mu_L)^{1/3} \fallingdotseq \{1 - m_{水星L} / (2m_{太陽})\}^{1/3} \fallingdotseq 1 - 5.55 \times 10^{-8}$　.

我々は、此処の処を以下の様に捉える事で“納得”する事にした。

平均近点離角に依る、動径の平均値 $a(1 + e^2/2)$ に着目する。先の(25)式に於ける量 : $S/2 = 0.''058$ は約 2.81×10^{-7} に相当するので、次の様な計算が出来る事になる。

(32)　$a_N(1 + e_N^2/2) = \{(1 - 5.55 \times 10^{-8}) a_L\} \times \{1 + (e_L + 2.81 \times 10^{-7})^2/2\} =$
$\fallingdotseq (1 - 5.55 \times 10^{-8}) \times (1 + 5.66 \times 10^{-8}) a_L(1 + e_L^2/2) =$
$\fallingdotseq (1 + 0.11 \times 10^{-8}) \times a_L(1 + e_L^2/2) =$
$\fallingdotseq a_L(1 + e_L^2/2)$　.

これは、水星軌道の離心率の改変、及び水星質量の改変に依っても、平均運動にも動径の平均値にも何らの変化も生じさせない事を表わすものである。我々が、“納得”する事にした所以のものが此処に存する。但し、水星の離心率として $e_L = 0.2056105$ を用いた。

6．　Newcomb の楕円軌道を、 Le Verrier のそれと比較してみるならば、離心率 e_L を e_N に変えたのに対応させて、質量 $m_{水星L}$ を $m_{水星N}$ に変え、長半径 a_L も a_N に変えたと見る事が出来る。量 : a_L、e_L ; $m_{水星L}$ は、 Le Verrier の、摂動を考えに入れる前の軌道、楕円軌道を記述するものである。従って、量 : a_N、e_N ; $m_{水星N}$ は、摂動を考えに入れる前の、Newcomb の楕円軌道を記述するものである、と見做す事が出来る。

此の段階での「Newcomb 軌道」には、未だ、$S_{♀}$ 、$S_{地球}$、$S_{木星}$ および $C^*_{♀}$ に関連した摂動が“真黄経および動径に考慮されなければならないものとして残って居る”のである。先で Newcomb は、$S_{♀}$ 、$S_{地球}$、$S_{木星}$ に依る摂動の、総てを取り込んだ事になって居るが、我々は中心差の方に取り込まれて居るのは、此の中の $S_{♀}$ のみであると捉える。そうして、残る $S_{地球}$ 、$S_{木星}$ に依る摂動は、正しく摂動計算の手法に従って計算されるべきであると考えて居る。量 S を取り込んだ事で、“Newcomb の運動理論は、これらに依る摂動計算は総てした事になって居るとする捉え方はしない”とは上で述べた処である。Newcomb は、此の $S_{地球}$、$S_{木星}$ に依る摂動は、計算しては居ないのである。

上の離心率 e_Nに、量 $S_♀/2$を加える形で、真黄経ϕに於ける金星に依る摂動を取り込む事を考える。従って、中心差 : f－M の計算に、此の e を用いる事になる。

(33)　$e \equiv e_N + S_♀/2$　.

只今の扱いに依って、当然の事ながら、動径 : $r = a(1 - e_N \cos u)$ に影響が及ぶ。動径 r に於ける金星に依る摂動 $C^*_♀$ の取り込みも同時に考える事にすれば、以下の様になるであろう。

(34)　$r + \delta r = a\{1 - (e - S_♀/2) \cos u\} + C^*_♀ \cos M =$
$\fallingdotseq a(1 - e \cos u) + (a S_♀/2 + C^*_♀) \cos M$　.

ここで、(17)式および(24)式から、次の表記の可能なる事を知る。

(35)　$\Delta e = S_♀/2 + C^*_♀/a$

従って、動径 r が、次の形に表わされ得るのが知れる。

(36)　$r + \delta r \fallingdotseq a\{1 - (e - \Delta e) \cos u\}$　.

此の量 $a\Delta e \cos u$ を、Newcomb は計算しては居ないのである。上記の量 $e - \Delta e$ の処が、Le Verrier の場合は $e + \Delta e$ となって居た。その場合は、一世紀当り43秒角の“後退”が、近日点黄経ϖに現われるのであった。従って、Δe の存在を考慮しなかった Newcomb の場合には、一世紀当り43秒角の“前進”が欠如する事になる訳である。これが「観測」と「理論」との間に、Newcomb の場合に、“43秒角 /世紀”の食い違いを生ずる事になった原因なのである。

ところで、地球および木星に依る摂動 $S_{地球}$、$S_{木星}$ はどうなるのであろう？　此処の処を彼の Le Verrier は、正しく計算して居るので、彼の場合には問題は無い。Newcomb はと言えば、計算しては居ないのである。これらの量の存否は、近日点黄経ϖの永年変化には無関係なのである。更に、本節の此処までの議論では、摂動 $C_♀$、$S^*_♀$; $C_{地球}$、$C_{木星}$ に関して、一切触れないで来た。それは、第４節の表で明らかな様に、何れもが無視可能な微小量である為に、取り上げる必要が無かったからである。

「Newcomb の運動理論」を理解する目的で、次の『中間軌道』の導入を図る事にする。

(37)　$u - e \sin u = M$,　$M = \int_{t0}^{t} n\,dt + \chi$　;

(38)　$n \equiv \sqrt{\{\mu_N / a_N^3\}}$,　$\mu_N = G(m_{太陽} + m_{木星N})$　;

(39)　$\tan(f/2) = \sqrt{\{(1+e^*)/(1-e^*)\}} \cdot \tan(u/2)$;

(40)　$e^* \equiv e + \Delta E$　,　$\Delta E \equiv S_{地球} + S_{木星}$　.

(41)　$r = a_N\{1 - (e - \Delta e) \cos u\}$　,

(42)　$\phi = \varpi + f$　;

(43)　$p_r = n a_N (e - \Delta e) \sin u / (1 - e \cos u)$　,

(44)　$p_\phi = r^2 n \sin f / \{\sin u (1 - e \cos u)\}$　.

先に Le Verrier の場合に見た（井上、1998)のと同様にして、以下、此の『中間軌道』に着目して、我々の見方を開陳して行く事にする。

7．　只今の『中間軌道』の系は、次の形の「エネルギー積分」を有する。

(45)　　$H \equiv -\mu_N/(2a_N) = (p_r^2 + p_\phi^2/r^2) - \{\mu_N/r + \varepsilon R_N\}$　，

(46)　　$\varepsilon R_N \equiv \mu_N(\Delta e/e)\{1/a - 3/r + a/r^2 + a^2(1-e^2)/r^3\} +$

$$+\mu_N(\Delta E/e)\{-a/r^2 + a^2(1-e^2)/r^3\} \quad .$$

量 H を Hamilton 函数であるとして、以下の形の運動方程式を書き出して置く。

(47)　　$dr/dt = \partial H/\partial p_r = p_r - \partial \varepsilon R_N/\partial p_r$　，

(48)　　$d\phi/dt = \partial H/\partial p_\phi = p_\phi/r^2 - \partial \varepsilon R_N/\partial p_\phi$　；

(49)　　$dp_r/dt = -\partial H/\partial r = p_\phi^2/r^3 - \mu_N/r^2 + \partial \varepsilon R_N/\partial r$　，

(50)　　$dp_\phi/dt = -\partial H/\partial \phi = 0 + \partial \varepsilon R_N/\partial \phi$　.

此の系を、要素変化の方法で近似的に解く事を考える。そこで、我々の言う『人工系』の導入を図る（井上,1995)。次の「二体問題の系」を、これに充てる事にする。外でもない Le Verrierや Newcombと同じ土俵で論じたいが為である。彼らは、水星の太陽面通過観測の整約を楕円要素で以て為し、件の余剰の永年変化を見い出したのであったからである。

(51)　　$dr^*/dt = p_r^*$　，

(52)　　$d\phi^*/dt = p_\phi^*/r^{*2}$　；

(53)　　$dp_r^*/dt = p_\phi^{*2}/r^{*3} - \mu_N/r^{*2}$　，

(54)　　$dp_\phi^*/dt = 0$　.

一見、煩瑣ではあるが、飽く迄も『人工系』である事を強調する目的で、「* 印」を付す事にした。此の系を満たす積分定数である楕円要素を、c_1、c_2 ; c_3、c_4 と表記する事にして、「二体問題の系の解表式」を以下の表記で表わすものとする。『中間軌道』を記述する為に導入された定数 ：a、e ; ϖ、χ は、断じて、只今の楕円要素と混同する様な事はあってはならない。要注意事項である。

(55)　　$r^* = \Phi_r(c_1, c_2 ; c_3, c_4 ; t)$　，

(56)　　$\phi^* = \Phi_\phi(c_1, c_2 ; c_3, c_4 ; t)$　；

(57)　　$p_r^* = \Psi_r(c_1, c_2 ; c_3, c_4 ; t)$　，

(58)　　$p_\phi^* = \Psi_\phi(c_1, c_2 ; c_3, c_4 ; t)$　.

斯くして、「変数変換の式」及び「新変数」を、次の「対応関係」で設定すれば、我々の言う『人工系の方法』の適用は完成する。

(59)　　$(r^*, \phi^* ; p_r^*, p_\phi^*) \longrightarrow (r, \phi ; p_r, p_\phi)$　，

(60)　　$(c_1, c_2 ; c_3, c_4) \longrightarrow (\zeta_1, \zeta_2 ; \zeta_3, \zeta_4)$　.

ここで、量 $(\zeta_1, \zeta_2 ; \zeta_3, \zeta_4)$ が、初発の系の変数 $(r, \phi ; p_r, p_\phi)$ に取って代るべき「新変数」に外ならないものである。従って、新旧の両変数を結び付けるものとして次の関係式が登場して来る事になる。

(61) $$r = \Phi_r(\zeta_1, \zeta_2 ; \zeta_3, \zeta_4 ; t) ,$$

(62) $$\phi = \Phi_\phi(\zeta_1, \zeta_2 ; \zeta_3, \zeta_4 ; t) ;$$

(63) $$p_r = \Psi_r(\zeta_1, \zeta_2 ; \zeta_3, \zeta_4 ; t) ,$$

(64) $$p_\phi = \Psi_\phi(\zeta_1, \zeta_2 ; \zeta_3, \zeta_4 ; t) .$$

新しい変数、楕円要素 $(\zeta_1, \zeta_2 ; \zeta_3, \zeta_4)$ に対する微分方程式系は、次で与えられる。

(65) $$d\zeta_k/dt = \sum_{j=1}^{4} \{\zeta_j, \zeta_k\} \partial\, \varepsilon R_N^\spadesuit / \partial \zeta_j \quad , \quad (k=1,2,3,4) \quad ;$$

(66) $$\varepsilon R_N^\spadesuit = \varepsilon R_N^\spadesuit(\zeta_1, \zeta_2 ; \zeta_3, \zeta_4 ; t) =$$

$$= \varepsilon R_N (r, \phi ; p_r, p_\phi) =$$

$$= \mu_N(\Delta e/e)\{1/a - 3/r + a/r^2 + a^2(1-e^2)/r^3\} +$$

$$+ \mu_N(\Delta E/e)\{-a/r^2 + a^2(1-e^2)/r^3\} \quad .$$

表記 $\{\zeta_j, \zeta_k\}$, $(j,k=1,2,3,4)$ は、Poisson 括弧を表わす。

8. 楕円要素 $(\zeta_1, \zeta_2 ; \zeta_3, \zeta_4)$ と言っても、これでは判り難いので、通常の表記を用いたい処であるが、混同は避けなければならないので、表記 : $a^\spadesuit, e^\spadesuit ; \varpi^\spadesuit, \chi^\spadesuit$ で以て書き分ける事にする。特別の関心があるのは、近日点黄経 $\varpi^\spadesuit$ に於ける永年変化である。そこで、上の摂動函数 $\varepsilon R_N^\spadesuit$ の永年部 $\varepsilon R_{N(s)}^\spadesuit$ を抽出して、その変化を見てみる事にする。

(67) $$\varepsilon R_{N(s)}^\spadesuit = \mu_N(\Delta e/e^\spadesuit)\{-2/a^\spadesuit + 2/(a^\spadesuit \eta^\spadesuit)\} +$$

$$+ \mu_N(\Delta E/e^\spadesuit) \times 0 \quad ;$$

(68) $$\eta^\spadesuit \equiv \sqrt{\{1-e^{\spadesuit 2}\}} \quad , \quad n^\spadesuit \equiv \sqrt{\{\mu_N/a^{\spadesuit 3}\}} \quad .$$

(69) $$d\varpi_{(s)}^\spadesuit/dt = \{\eta^\spadesuit/(n^\spadesuit a^{\spadesuit 2} e^\spadesuit)\} \partial\, \varepsilon R_{N(s)}^\spadesuit / \partial e^\spadesuit =$$

$$= +(\Delta e/e^\spadesuit)\{2/(1+\eta^\spadesuit)\}\{1/\eta^\spadesuit + (e^\spadesuit/\eta^\spadesuit)^2\} n^\spadesuit .$$

(70) $$\delta \varpi_{(s)}^\spadesuit \equiv \int_{t0}^{t} \{d\varpi_{(s)}^\spadesuit/dt\} \times dt =$$

$$= (\Delta e/e^\spadesuit)\{2/(1+\eta^\spadesuit)\}\{1/\eta^\spadesuit + (e^\spadesuit/\eta^\spadesuit)^2\} \times (M^\spadesuit - \chi^\spadesuit) .$$

これに、Newcomb の場合の数値として : $e^\spadesuit = e_L + S/2 = 0.205\ 6105 + 0.000\ 0002\ 8$ を用いる事にすれば、次の大きさの近日点黄経の永年変化 $\delta \varpi_{(s)}^\spadesuit$ が求められる。

(71) $$\delta \varpi_{(s)}^\spadesuit = +8.060\ 5728 \times 10^{-8} \times (M^\spadesuit - \chi^\spadesuit) \quad ,$$

(72) $$\delta \dot{\varpi}_{(s)}^\spadesuit : +43.374\ 8296 \text{秒角/世紀} \quad .$$

ここで、地球および水星の公転周期として、 Le Verrier の数値 : 365.25 63744 および 87.96 92580 を用いた (Le Verrier, 1856)。

先に Le Verrier の取り扱いを、『中間軌道』把捉で以て論じ、余剰前進の問題に決着を付ける事を試みた（井上、1998)。本小論の表式群（1)、(2)、(3)、(4)、(5) が、それであるが、Newcomb の場合の『中間軌道』：(37)、(38)、(39)、(40)、(41)、(42)、(43)、(44)の表式群に呼応させた形に、Le Verrier の場合のも書いて置く事にしよう。

(73) $$u - e_L \sin u = M \ , \quad M = \int_{t0}^{t} n\,dt + \chi \ ;$$

(74) $$n \equiv \sqrt{\{\mu_L / a_L{}^3\}} \ , \quad \mu_L = G(m_{太陽} + m_{水星\ L}) \ ;$$

(75) $$\tan(f/2) = \sqrt{\{(1+e_L)/(1-e_L)\}} \cdot \tan(u/2) \ ;$$

(76) $$r = a_L\{1 - (e_L + \Delta e)\cos u\} \ ,$$

(77) $$\phi = \varpi + f \ ;$$

(78) $$p_r = n a_L (e_L + \Delta e) \sin u / (1 - e_L \cos u) \ ,$$

(79) $$p_\phi = r^2 n \sin f / \{\sin u (1 - e_L \cos u)\} \ .$$

此の系に対する「エネルギー積分」は、次の形を取る。

(80) $$H \equiv -\mu_L/(2a_L) = (p_r{}^2 + p_\phi{}^2/r^2) - \{\mu_L/r + \varepsilon R_L\} \ ,$$

(81) $$\varepsilon R_L \equiv \mu_L(\Delta e/e_L)\{-1/a_L + 3/r - a_L/r^2 - a_L p_L/r^3\} \ ;$$

(82) $$p_L \equiv a_L \eta_L{}^2 \ , \quad \eta_L \equiv \sqrt{\{1 - e_L{}^2\}} \ .$$

此の場合にも、「二体問題の系」を『人工系』に選び、摂動函数 $\varepsilon R_L{}^\bullet$ の永年部を抽出し近日点黄経 $\varpi^\bullet$ の永年的な振舞いに付いて調べる事が出来るのであった（井上、1998)。

(83) $$\varepsilon R_{L(s)}{}^\bullet \equiv \mu_L(\Delta e/e^\bullet)\{2/a^\bullet - 2/(a^\bullet \eta^\bullet)\} \ ;$$

(84) $$\delta \varpi^\bullet{}_{(s)} = -(\Delta e/e^\bullet)\{2/(1+\eta^\bullet)\}\{1/\eta^\bullet + (e^\bullet/\eta^\bullet)^2\} \times (M^\bullet - \chi^\bullet) \ .$$

只今の Le Verrier の場合には、その大きさは、Newcomb の場合のに一致するのであるが符号が逆になって“後退”する事になって居るのであった（Inoue, 1992)。

(85) $$\delta \varpi^\bullet{}_{(s)} : -43.374\ 896 \text{ 秒角/世紀} \ .$$

そこで、我々の理解する処を、以下の様に整理して置く。

☆ Le Verrier は、“金星の摂動”を、中心差用の離心率 e_M と動径用の離心率 e_r の二個を、別々に用いた。此の様な扱いをすると、43秒角だけ、後退する軌道となって来て仕舞うのである。然るに、彼はその事に思い至らず「楕円軌道で計算して居る」と思い込んで居たのである。
これでは、如何に精緻な彼の理論で予報したとしても、観測を説明する事は不可能であったと言う訳である。

☆ Newcomb は、“金星・地球・木星に依る摂動”を、水星の離心率を改変した単一の楕円軌道で以て把捉可能であると考えた。しかし、これだけでは不充分なのである。金星に依る、動径に於ける摂動量を計算しなければ、水星の運動を正しく捉える事は出来ないのである。真黄経および動径への摂動が両者相俟って、43秒角だけ前進する軌道を与えるのである。これが正しい運動の姿であるのに、Newcomb は、これを計算しては居ないのである。それ故に、43秒角不足すると云う事態が発生したのである。

９．　我々は、Newcomb の扱いが齎らす処のものを、一つの『中間軌道』で以て把捉する事を試みた。果たして、我々の期待通りのものが、此の『中間軌道』に盛られて居るのであろうか？　先の (37)、(38)、(39)、(40)、(41)、(42)、(43)、(44)式を展開して、近似表式を導き、これを見て置く事にしよう。以下、計算をして行く。

◎　$u = M + e \sin u \fallingdotseq M + e \sin M + (e^2/2) \sin 2M$　,

◎　$\cos u \fallingdotseq \cos (M + e \sin M) \fallingdotseq -e/2 + \cos M + (e/2) \cos 2M$　,

◎　$r = a_N\{1 - (e - \Delta e) \cos u\} = a_N(1 - e \cos u) +$

$+ a_N \Delta e \cos u \fallingdotseq a_N(1 - e \cos u) + a_N \Delta e \cos M$　;

此処で　$\Delta e = S_♀/2 + C^*_♀/a$　であった。

◉動径　$r \fallingdotseq a_N(1 - e \cos u) + a_N(S_♀/2 + C^*_♀/a) \cos M$　.

◎　$f \fallingdotseq u + e^* \sin u + (e^{*2}/4) \sin 2u =$

$\fallingdotseq \{M + e \sin M + (e^2/2) \sin 2M\} +$

$+ e^*\{\sin M + (e/2) \sin 2M\} + (e^{*2}/4) \sin 2M =$

$= M + (e + e^*) \sin M + \{(e^2/2) + (e^* e/2) + (e^{*2}/4)\} \sin 2M$　;

此処で　$e^* = e + (S_{地球} + S_{木星})$　であった。

◉中心差　$f - M \fallingdotseq \{2e + (S_{地球} + S_{木星})\} \sin M + \{(5e^2/4) + e\Delta E\} \sin 2M$　.

これは、 sin M の係数を $2\times\{e + (S_{地球} + S_{木星})/2\}$ と書いてみれば明らかな様に、地球及び木星の影響を離心率 e に取り込んだ事を表わして居る。それ故に、Newcomb の取り扱いが齎らす処のものを余す処無く表現し得うる事を、我々の『中間軌道』把捉は教えて呉れて居る。

断って置くが、上記の動径 r に対する表式中、$a_N(S_♀/2 + C^*_♀/a) \cos M$ なる項を Newcomb は、計算しては居ないのである。我々の『中間軌道』は、計算すべき処の式群を手際良く、表現して居るのである。

１０．斯くして、次の事が明らかとなった。

（甲）金星に依る影響を正しく計算して、水星の位置予報を行なえば
理論と観測との間には、如何なる食い違いも生ずる事は無い。

（乙）未知惑星存在の仮定も不要なら、引力法則の改変も不要である。

(00506S)

参考文献

1. Chebotarev, G. A. : 1967, *Analytical and Numerical Methods of Celestial Mechanics*, Elsevier Publishing Company, INC.

2. Clemence, G. M. : 1943, *Astronomical Papers of the American Ephemeris*, XI.

3. Einstein, A. : 1915, *Preuss. Akad. Wiss. Berlin*, 47.

4. Inoue, T. : 1992, *Proceedings of the Twenty-Fifth Symposium on Celestial Mechanics.*

5. 井上　猛 : 1995, 第２７回天体力学研究会集録.

6. 井上　猛 : 1998, 第３０回天体力学研究会集録.

7. Le Verrier, U. J. : 1856, *Annales de l'Observatoire Impérial de Paris*, II.

8. Le Verrier, U. J. : 1859, *Annales de l'Observatoire Impérial de Paris*, V.

9. Newcomb, S. : 1895, *Astronomical Papers of the American Ephemeris*, VI.

Schwarzschild 問題の中間軌道による解

A Solution of the Schwarzschild Problem by Intermediary Orbit

山本　一登

Tadato YAMAMOTO

Department of Physics, Kyoto Sangyo University,
Motoyama, Kamigamo, Kita-ku, Kyoto, 603-8555, Japan

e-mail : tadato@cc.kyoto-su.ac.jp

ABSTRACT

The Schwarzschild problem is solved by means of the intermediary orbit method up to the first order of the small quantity, namely the solar gravitational radius m.

The present intermediary orbit is slightly different from the ordinary elliptic orbit but it incorporates all the first-order secular perturbations. That is to say that this orbit represents a main part of the real motion under the conditons that the second-order variations are negligible. The remaining perturbations are only periodic ones.

The first-order periodic perturbations are calculated for the parameters which describe the intermediary orbit.

1　はじめに

Le Verrier は、17 世紀の終りから彼の時代に亘る 150 年間に為された水星の太陽面通過の観測時刻を、彼が確立した水星の運動理論で予報することを試みた [1]。その結果、彼が用いた軌道要素には、いずれも要素改良の必要があった。中でも近日点黄経 ϖ には、誤差の範囲を超える量、1 世紀当り角度で 38.3 秒の補正が必要であった。これが有名な「水星の近日点前進問題」の発端である。現在では Einstein の一般相対論が、この問題を完全に解いたことになっている。ただ、この問題に対する de Sitter や Eddington の扱いは、天体力学における基本的、かつ伝統的な要素変化の式を通じてのものではない [2][3]。

両者を比較するためには、先ず、一般相対論で用いられている四次元時空変数 (r , ϕ , θ ; ct) の中の (r , ϕ , θ) が Newton 力学での相対極座標を、t が絶対時間を表すとし、要素変化の式を通じて、Schwarzschild 問題を論ずるのが適切な方法である。このような立場で、Schwarzschild 問題を部分的に扱ったものは既に幾つか存在している [4][5]。この立場で詳細に論じたものに Brumberg [6] がある。彼は Kepler 運動の Osculating Elements に、定数変化法を適用して、微小正数 m の一次の精度でこの問題を解いている。我々も、Brumberg と同じ立場であるが、彼とは異なる方法でこの Schwarzschild 問題を扱う。

ここで、改めて「定数変化の方法」を次のように整理しておく。

(1) 与えられた微分方程式系に“近い”もので積分可能な系を創る。
ここでは、これを「人工系」と呼ぶ[7]。

(2) (1)「で得られた「積分定数」を「新変数」とし、
得られた「解表式」を「変数変換の式」とする。

(3) 与えられた微分方程式を(2)で定義した新変数で書き換える。
このようにして得られる微分方程式を「要素変化の式」と言う。

以上の流れに沿って議論してゆくとき、「人工系」として Kepler 運動を与える二体問題の系を選ばなければならないと云う必然性はない。事実、Sterne や Garfinkel は、人工衛星の運動理論構築に際して、楕円軌道とは異なる軌道、「中間軌道」を導入した。中間軌道とは月や人工衛星などの複雑な運動を表現する足場として使われる軌道で、Kepler 軌道よりも真の軌道に近い軌道のことを言う。人工衛星の場合に Sterne が初めて摂動に永年変化が現れない中間軌道を発表した。その後 Sterne の理論を含み摂動に永年変化が現れない人工系捜しを、「未定定数」の導入に依って達成したのが Garfinkel [8] である。

我々は、この Garfinkel の方法を Schwarzschild 問題に適用して、微小正数 m の一次の精度でこれを解くことを試みた。その結果、要素変化の式に一次の永年変化を一切含ませることなく、周期変化のみでこれを表現することができた。このことは、我々の中間軌道が与えられた方程式の解の主要部分を含んでいることを意味している。さらに、我々の中間軌道を与えるポテンシャルが距離の逆数および逆自乗に比例する項のみから成立していることにも注目すべきである。それは、Schwarzschild 問題の場合、そのポテンシャルは距離の逆三乗に比例する項を含んでいて、これを解く際には楕円積分が必要となるが、我々の解は、三角関数のみで、高精度の近似解を与えているからである。我々が求めた「中間軌道」のこのような性質を通して、改めて Schwarzschild 問題が内包しているものを問い直すのは意味のあることであろう。

2 人工系の構築

2.1 Schwarzschild 問題の Lagrangian および Hamiltonian

Parameterized Post Newtonian (PPN) の立場での Schwarzschild 問題の Lagrangian は

$$L=\frac{1}{2}(\dot{\boldsymbol{r}}\cdot\dot{\boldsymbol{r}})+\frac{\mu}{r}+\frac{1}{8}c^{-2}(\dot{\boldsymbol{r}}\cdot\dot{\boldsymbol{r}})^2+ \\ +\frac{m}{r}\left\{\left(\gamma+\frac{1}{2}-\alpha\right)(\dot{\boldsymbol{r}}\cdot\dot{\boldsymbol{r}})+\left(-\beta+\frac{1}{2}+\alpha\right)\frac{\mu}{r}+\alpha\frac{(\boldsymbol{r}\cdot\dot{\boldsymbol{r}})^2}{r^2}\right\} \qquad (1)$$

(α, β, γ : PPN Parameter)

である[9]。ここで m は後述するように、微小な正の定数を表す。また c および μ も定数である。我々は、m の二次以上の項は微小であるとし、全体を通して無視することにする。

この Lagrangian で $\alpha=\beta=\gamma=1$ とすれば、Einstein の一般相対論における Schwarzschild 問題になる。我々は Einstein の立場で、Schwarzschild 問題を扱うことにして、Lagrangian を書き直す。その際にベクトル表示も極座標表示に直すと

$$L=\frac{1}{2}\left(\dot{r}^2+r^2\dot{\phi}^2\right)+\frac{\mu}{r}+m\left\{\frac{1}{8\mu}\left(\dot{r}^2+r^2\dot{\phi}^2\right)^2+\frac{1}{2r}\left(\dot{r}^2+r^2\dot{\phi}^2\right)+\frac{\mu}{2r^2}+\frac{\dot{r}^2}{r}\right\} \qquad (2)$$

となる。この Lagrangian を Hamiltonian へ変換すると

$$H=\frac{1}{2}\left({p_r}^2+\frac{{p_\phi}^2}{r^2}\right)-\frac{\mu}{r}-m\left\{\frac{1}{8\mu}\left({p_r}^2+\frac{{p_\phi}^2}{r^2}\right)^2+\frac{1}{2r}\left({p_r}^2+\frac{{p_\phi}^2}{r^2}\right)+\frac{\mu}{2r^2}+\frac{{p_r}^2}{r}\right\} \qquad (3)$$

となる。この Hamiltonian の下での正準運動方程式は、次のようになる。

$$\begin{cases} \dfrac{dr}{dt} = \dfrac{\partial H}{\partial p_r} = p_r - m\left\{ \dfrac{1}{2\mu}\left({p_r}^2 + \dfrac{{p_\phi}^2}{r^2} \right) p_r + 3\dfrac{p_r}{r} \right\} & (4) \\ \dfrac{d\phi}{dt} = \dfrac{\partial H}{\partial p_\phi} = \dfrac{p_\phi}{r^2} - m\left\{ \dfrac{1}{2\mu}\left({p_r}^2 + \dfrac{{p_\phi}^2}{r^2} \right) \dfrac{p_\phi}{r^2} + \dfrac{p_\phi}{r^3} \right\} & (5) \end{cases}$$

$$\begin{cases} \dfrac{dp_r}{dt} = -\dfrac{\partial H}{\partial r} = \dfrac{p_\phi^2}{r^3} - \dfrac{\mu}{r^2} - m\left\{ \dfrac{1}{2\mu}\left({p_r}^2 + \dfrac{{p_\phi}^2}{r^2} \right) \dfrac{p_\phi^2}{r^3} + \dfrac{3}{2}\left({p_r}^2 + \dfrac{{p_\phi}^2}{r^2} \right) \dfrac{1}{r^2} + \dfrac{\mu}{r^3} \right\} & (6) \\ \dfrac{dp_\phi}{dt} = -\dfrac{\partial H}{\partial \phi} = 0 & (7) \end{cases}$$

この微分方程式系は、平易には解けない。そこで、我々は定数変化法を適用し、m の一次の精度で解くことを考える。

2.2 平面 Kepler 運動

Schwarzschild 問題が平面運動を与えるものであり、Newton 力学での二体問題と深い関連を持っているので、まず、Kepler 運動について述べておく。この Kepler 運動が描く軌道は楕円軌道である。以後、Kepler 運動が描く軌道のことを単に、楕円軌道と呼ぶことにする。ここでは太陽に対する相対運動および運動平面を基準面に選んだ場合の解表式を示しておく。

楕円軌道の解表式

$$H = \frac{1}{2}\left({p_r}^2 + \frac{{p_\phi}^2}{r^2} \right) - \frac{\mu}{r} = -\frac{\mu}{2a} \tag{8}$$

$$u - e\sin u = M \tag{9}$$

$$M \equiv n(t - t_0) + \sigma \tag{10}$$

$$\tan\frac{f}{2} = \sqrt{\frac{1+e}{1-e}}\tan\frac{u}{2} \tag{11}$$

$$\begin{cases} r = \dfrac{a(1-e^2)}{1 + e\cos f} & (12) \\ \phi = f + \varpi & (13) \end{cases}$$

$$\begin{cases} p_r = \dfrac{na}{\eta} e\sin f & (14) \\ p_\phi = na^2\eta & (15) \end{cases}$$

$$\mu \equiv G(m_\odot + m_p) \tag{16}$$

$$n \equiv \sqrt{\frac{\mu}{a^3}} \tag{17}$$

$$\eta \equiv \sqrt{1 - e^2} \tag{18}$$

文字記号の約束は次のようである。

$$\left[\begin{array}{ll} G & : \text{重力定数} \\ m_\odot & : \text{太陽の質量} \\ m_p & : \text{惑星の質量} \\ r & : \text{動径} \\ \phi & : \text{経度} \end{array}\right] \quad \left[\begin{array}{ll} a & : \text{軌道長半径} \\ e & : \text{離心率} \\ \varpi & : \text{近日点経度} \\ \sigma & : \text{元期における平均近点離角} \\ t_0 & : \text{元期} \end{array}\right] \quad \left[\begin{array}{ll} n & : \text{平均運動} \\ M & : \text{平均近点離角} \\ u & : \text{離心近点離角} \\ f & : \text{真近点離角} \end{array}\right]$$

先程の (1) 式で用いた m は次式で定義される。

$$m \equiv \frac{\mu}{c^2} \quad , \quad (c : \text{光速}) \tag{19}$$

2.3 人工系の Hamiltonian および積分

定数変化法を適用するために先ず、積分可能な系として、未定定数を含む人工系を設定する。我々は、これが次のような Hamiltonian で記述されるものとした。人工系であることを強調するために r , ϕ ; p_r , p_ϕ の右肩に☆印を付ける。

$$H_0 = \frac{1}{2}\left(p_r^{\star 2} + \frac{p_\phi^{\star 2}}{r^{\star 2}}\right) - (1+mA)\frac{\mu}{r^\star} - mB\frac{\mu}{r^{\star 2}} \quad , \quad (A, B : \text{未定定数}) \tag{20}$$

$A = 0$, $B = 0$ とすれば、楕円軌道を表す Hamiltonian に帰着する。
この系の運動方程式は次のようになる。

$$\left\{\begin{array}{l} \dfrac{dr^\star}{dt} = \dfrac{\partial H_0}{\partial p_r^\star} = p_r^\star \qquad (21) \\ \dfrac{d\phi^\star}{dt} = \dfrac{\partial H_0}{\partial p_\phi^\star} = \dfrac{p_\phi^\star}{r^{\star 2}} \qquad (22) \end{array}\right.$$

$$\left\{\begin{array}{l} \dfrac{dp_r^\star}{dt} = -\dfrac{\partial H_0}{\partial r^\star} = \dfrac{p_\phi^{\star 2}}{r^{\star 3}} - (1+mA)\dfrac{\mu}{r^{\star 2}} - 2mB\dfrac{\mu}{r^{\star 3}} \qquad (23) \\ \dfrac{dp_\phi^\star}{dt} = -\dfrac{\partial H_0}{\partial \phi^\star} = 0 \qquad (24) \end{array}\right.$$

この系の解を楕円軌道の場合と区別すること、および人工系であることを強調するために積分定数の右肩に $*$ 印を付ける。

まず H_0 は時間 t を含んでいないので

$$\frac{dH_0}{dt} = 0 \tag{25}$$

これは直ちに積分できて

$$H_0 = -\frac{\mu}{2a^*} \quad , \quad (a^* : \text{積分定数「第一要素」}) \tag{26}$$

同じく $p_\phi^\star$ も

$$\frac{dp_\phi^\star}{dt} = 0 \tag{27}$$

より、

$$p_\phi^\star = \sqrt{\mu p^*} \quad , \quad (p^* : \text{積分定数}) \tag{28}$$

ここで積分定数 p^* を次のように定義する。

$$p^* \equiv a^*(1-e^{*2}) \quad , \quad (e^* : \text{積分定数「第二要素」}) \tag{29}$$

ただし、e^* は正の量に選ぶ。

これらの量によってエネルギー積分は次の形になる。

$$\frac{1}{2}\left(p_r^{\star 2}+\frac{p_\phi^{\star 2}}{r^{\star 2}}\right)-(1+mA)\frac{\mu}{r^\star}-mB\frac{\mu}{r^{\star 2}}=-\frac{\mu}{2a^*} \tag{30}$$

これを $r^\star$ に関する方程式に書き換えると

$$\left(\frac{dr^\star}{dt}\right)^2=-\left(1-\frac{2m}{p^*}B\right)\frac{\mu p^*}{r^{\star 2}}+2(1+mA)\frac{\mu}{r^\star}-\frac{\mu}{a^*} \tag{31}$$

となる。

これは楕円軌道の場合の方程式の形に酷似しているので、次のように置き換える。

$$\left(1-\frac{2m}{p^*}B\right)\mu p^* \equiv \mu^\star p^\star \quad , \quad (1+mA)\mu \equiv \mu^\star \tag{32}$$

$$\frac{\mu}{a^*} \equiv \frac{\mu^\star}{a^\star} \quad , \quad p^\star \equiv a^\star(1-e^{*2}) \tag{33}$$

このように置けば、まさに楕円軌道の場合に類似の形式になり積分可能なことが分かる。
よって

$$a^\star=(1+mA)a^* \quad , \quad p^\star=(1+mA)p^* \tag{34}$$

となる。これらを (32) 式に代入すると、未定定数 A , B の間に一つの従属関係が存在することがわかる。

$$\left(1-\frac{2m}{p^*}B\right)\mu p^*=(1+mA)^2\mu p^* \tag{35}$$

m の二次以上は無視するので次のようになる。

$$mA=-\frac{m}{p^*}B \tag{36}$$

しかし、この関係は A , B が純粋定数に対し、p^* は力学変数であるのでこの従属関係は許されないものである。今回の場合は (28) 式より p^* が積分定数であるのでこの p^* を数値としての p^* と考えればこの従属関係は成立する。

先程の関係式を使えば (31) 式は

$$\left(\frac{dr^\star}{dt}\right)^2=-\frac{\mu^\star p^\star}{r^{\star 2}}+2\frac{\mu^\star}{r^\star}-\frac{\mu^\star}{a^\star} \tag{37}$$

となる。ここで、動径 $r^\star$ を補助変数 f^* に変換する。ここでも人工系であることを強調するために補助変数の右肩に※印を付ける。

$$r^\star \equiv \frac{p^\star}{1+e^*\cos f^*} \tag{38}$$

(38) 式より

$$\frac{dr^\star}{dt}=\frac{r^{\star 2}}{p^\star}e^*\sin f^*\cdot\frac{df^*}{dt} \tag{39}$$

(38) 式、(39) 式を (37) 式に代入し、$\sin 0$ および $\sin \pi$ 以外では $\sin f^* \neq 0$ であるから開平して正の符号をとれば次のようになる。

$$r^{\star 2}\frac{df^*}{dt} = (1+mA)\sqrt{\mu p^*} \tag{40}$$

また (22) 式、(28) 式より

$$r^{\star 2}\frac{d\phi^\star}{dt} = \sqrt{\mu p^*} \tag{41}$$

である。故に、(40) 式と (41) 式から次の積分が得られる。

$$\phi^\star = (1-mA)(f^* + \varpi^*) \quad , \quad (\varpi^* : \text{積分定数「第三要素」}) \tag{42}$$

最後に、軌道上の位置と時間 t との関係を導くために、(37) 式の動径 $r^\star$ を新たな補助変数 u^* に置き換える。

$$r^\star \equiv a^\star(1 - e^* \cos u^*) \tag{43}$$

(43) 式より

$$\frac{dr^\star}{dt} = a^\star e^* \sin u^* \cdot \frac{du^*}{dt} \tag{44}$$

を経て、先程と同様に (43) 式、(44) 式を (37) 式に代入し、$\sin 0$ および $\sin \pi$ 以外では $\sin u^* \neq 0$ であるから開平して正の符号をとれば次のようになる。

$$r^\star \frac{du^*}{dt} = \sqrt{\frac{\mu^\star}{a^\star}} \tag{45}$$

補助量 n^* を

$$n^* \equiv \sqrt{\frac{\mu}{a^{*3}}} \tag{46}$$

と導入すれば

$$(1 - e^* \cos u^*)\frac{du^*}{dt} = \sqrt{\frac{\mu^\star}{a^{\star 3}}} = (1-mA)\sqrt{\frac{\mu}{a^{*3}}} = (1-mA)n^* \tag{47}$$

となる。積分すると

$$u^* - e^* \sin u^* = (1-mA)n^*(t-t_0) + \sigma^* \quad , \quad (\sigma^* : \text{積分定数「第四要素」}) \tag{48}$$

となり、これは Kepler 方程式に類似のものである。

2.4 解表式

以上で我々の必要とする 4 個の積分定数が滞りなく求まった。これらを整理してまとめる。

人工系の解表式

$$H_0 = \frac{1}{2}\left(p_r^{\star 2} + \frac{p_\phi^{\star 2}}{r^{\star 2}}\right) - (1+mA)\frac{\mu}{r^\star} - mB\frac{\mu}{r^{\star 2}} = -\frac{\mu}{2a^*} \tag{49}$$

$$u^* - e^* \sin u^* = M^* \tag{50}$$

$$M^* \equiv (1-mA)n^*(t-t_0) + \sigma^* \tag{51}$$

$$\tan\frac{f^*}{2} = \sqrt{\frac{1+e^*}{1-e^*}}\tan\frac{u^*}{2} \tag{52}$$

$$\begin{cases} r^{\star} = \varphi_r(a^{*}, e^{*}; f^{*}) = (1+mA)\dfrac{a^{*}(1-e^{*2})}{1+e^{*}\cos f^{*}} & (53) \\ \phi^{\star} = \varphi_\phi(\varpi^{*}; f^{*}) = (1-mA)(f^{*}+\varpi^{*}) & (54) \end{cases}$$

$$\begin{cases} p_r^{\star} = \psi_r(a^{*}, e^{*}; f^{*}) = \dfrac{n^{*}a^{*}}{\eta^{*}} e^{*}\sin f^{*} & (55) \\ p_\phi^{\star} = \psi_\phi(a^{*}, e^{*}) = n^{*}a^{*2}\eta^{*} & (56) \end{cases}$$

$$n^{*} = \sqrt{\frac{\mu}{a^{*3}}} \quad , \quad p^{*} = a^{*}(1-e^{*2}) \tag{57}$$

$$\eta^{*} \equiv \sqrt{1-e^{*2}} \tag{58}$$

$(a^{*}, e^{*}; \varpi^{*}, \sigma^{*})$: 積分定数

A, B : 未定定数

この解表式は楕円軌道の場合に酷似している。しかし、両者の間に存在している相違には注意が必要である。

また、この人工系の解表式のもとで成立する関係式を以下に列挙しておく。

(52) 式と

$$r^{\star} = (1+mA)a^{*}(1-e^{*}\cos u^{*}) \tag{59}$$

の関係を使うことで

$$\sin f^{*} = \frac{2\tan\dfrac{f^{*}}{2}}{1+\tan^2\dfrac{f^{*}}{2}} = \frac{\sqrt{1-e^{*2}}\sin u^{*}}{1-e^{*}\cos u^{*}} = (1+mA)\frac{a^{*}\eta^{*}}{r^{\star}}\sin u^{*} \tag{60}$$

(40) 式から

$$r^{\star 2}\frac{df^{*}}{dt} = (1+mA)\sqrt{\mu p^{*}} = (1+mA)n^{*}a^{*2}\eta^{*} \tag{61}$$

である。故に

$$n^{*}dt = (1-mA)\frac{r^{\star 2}}{a^{*2}\eta^{*}}df^{*} \tag{62}$$

また、(59) 式と (47) 式より

$$n^{*}dt = \frac{r^{\star}}{a^{*}}du^{*} \tag{63}$$

さらに、(51) 式から

$$dM^{*} = (1-mA)n^{*}dt \tag{64}$$

となる。まとめると以下のようになる。

$$n^{*}dt = (1+mA)dM^{*} = \frac{r^{\star}}{a^{*}}du^{*} = (1-mA)\frac{r^{\star 2}}{a^{*2}\eta^{*}}df^{*} \tag{65}$$

3 要素変化の式

3.1 新変数および変数変換

要素変化の式を導出するために変数変換の式としての解表式、および新変数としての積分定数 (a^* , e^* ; ϖ^* , σ^*) を求めることができたので、次の文字記号の置き換えを行う。

$$r^\star\,,\,\phi^\star\,;\,p_r^\star\,,\,p_\phi^\star \quad\Longrightarrow\quad r\,,\,\phi\,;\,p_r\,,\,p_\phi$$

$$a^*\,,\,e^*\,;\,\varpi^*\,,\,\sigma^* \quad\Longrightarrow\quad a^\triangle\,,\,e^\triangle\,;\,\varpi^\triangle\,,\,\sigma^\triangle$$

補助変数についても

$$M^*\,;\,u^*\,,\,f^* \quad\Longrightarrow\quad M^\triangle\,;\,u^\triangle\,,\,f^\triangle$$

とする。以後、新変数および新補助変数は ($a^\triangle$, $e^\triangle$; $\varpi^\triangle$, $\sigma^\triangle$; $M^\triangle$; $u^\triangle$, $f^\triangle$) と書くべきであるが、煩瑣を避けるために単に (a , e ; ϖ , σ ; M ; u , f) と書くことにする。ただし、これらを楕円軌道の要素および補助変数と混同してはならない。

従って次が変換式になる。

$$\begin{cases} r = \varphi_r(\,a\,,\,e\,;\,f\,) = (1+mA)\dfrac{a(1-e^2)}{1+e\cos f} & (66) \\ \phi = \varphi_\phi(\,\varpi\,;\,f\,) = (1-mA)(f+\varpi) & (67) \end{cases}$$

$$\begin{cases} p_r = \psi_r(\,a\,,\,e\,;\,f\,) = \dfrac{na}{\eta}e\sin f & (68) \\ p_\phi = \psi_\phi(\,a\,,\,e\,) = na^2\eta & (69) \end{cases}$$

$$u - e\sin u = M \tag{70}$$

$$M = (1-mA)n(t-t_0)+\sigma \tag{71}$$

$$\tan\frac{f}{2} = \sqrt{\frac{1+e}{1-e}}\tan\frac{u}{2} \tag{72}$$

$$n = \sqrt{\frac{\mu}{a^3}} \quad , \quad p = a(1-e^2) \tag{73}$$

$$\eta = \sqrt{1-e^2} \tag{74}$$

ここで要素 σ を新たな要素 χ で置き換える。この関係を次のように定義する [10]。

$$(1-mA)n(t-t_0)+\sigma \equiv \int_{t_0}^{t}(1-mA)n\,dt + \chi \tag{75}$$

ここでも未定定数 A , B については定数扱いすることに注意する。

(66) 式～(75) 式における新変数 (a , e ; ϖ , χ) をすべて定数であると見做して定められる解表式が「中間軌道」である。この中間軌道と真の解が記述する軌道との間には食い違いが存在している。この食い違いを正しく算出するのに供されるのが要素変化の式である。

与えられた Hamiltonian H と中間軌道の Hamiltonian H_0 の関係は

$$H = H_0 + (H - H_0) \equiv H_0 + \varepsilon H_1 \tag{76}$$

である。また Hamiltonian H には ϕ は含まれていないので、ϕ がないという意味で「-」で書くと、次のようになる。

$$\varepsilon H_1 = \varepsilon H_1(r\ ,\ -\ ;\ p_r\ ,\ p_\phi\ ) =$$

$$= -m\left\{ \frac{1}{8\mu}\left({p_r}^2 + \frac{{p_\phi}^2}{r^2}\right)^2 + \frac{1}{2r}\left({p_r}^2 + \frac{{p_\phi}^2}{r^2}\right) + \frac{\mu}{2r^2} + \frac{{p_r}^2}{r} - A\frac{\mu}{r} - B\frac{\mu}{r^2} \right\} \tag{77}$$

3.2 補助変数 u , f の微分

補助変数 u , f の微分関係は、何れの場合も楕円軌道の時とは異なった形になるので注意を要する。
(70) 式を (71) 式、(75) 式を用いて書き換えると、以下のようになる。

$$u - e\sin u = \int_{t_0}^{t} (1 - mA)n dt + \chi \tag{78}$$

この関係式を微分すると

$$(1 - e\cos u)\frac{du}{dt} - \frac{de}{dt}\sin u = (1 - mA)n + \frac{d\chi}{dt} \tag{79}$$

となる。ここで (59) 式と (60) 式の関係を使えば、u の微分は次のようになる。

$$\frac{du}{dt} = \frac{na}{r} + \frac{1}{\eta}\sin f\frac{de}{dt} + (1 + mA)\frac{a}{r}\frac{d\chi}{dt} \tag{80}$$

次に (72) 式を微分すると以下の関係が得られる。

$$\frac{1}{\sin f}\frac{df}{dt} = \frac{1}{\sin u}\frac{du}{dt} + \frac{1}{\eta^2}\frac{de}{dt} \tag{81}$$

よって、(80) 式と (60) 式より

$$\frac{df}{dt} = \frac{\sin f}{\sin u}\frac{du}{dt} + \frac{\sin f}{\eta^2}\frac{de}{dt} =$$

$$= (1 + mA)\frac{na^2\eta}{r^2} + \left\{(1 + mA)\frac{a}{r} + \frac{1}{\eta^2}\right\}\sin f\frac{de}{dt} + (1 + 2mA)\frac{a^2\eta}{r^2}\frac{d\chi}{dt} \tag{82}$$

となる。ここで

$$\xi \equiv 1 + e\cos f = (1 + mA)\frac{a\eta^2}{r} \tag{83}$$

と定義すれば、f の微分は次のようになる。

$$\frac{df}{dt} = (1 - mA)\frac{n\xi^2}{\eta^3} + \frac{\xi + 1}{\eta^2}\sin f\frac{de}{dt} + \frac{\xi^2}{\eta^3}\frac{d\chi}{dt} \tag{84}$$

3.3 偏微分係数

旧変数 (r , ϕ ; p_r , p_ϕ) で書かれた微分方程式系 (21) 式～(24) 式を、新変数 (a , e ; ϖ , χ) で書き表すために必要となる関係式を、一覧表の形でまとめておく。

$$\left\{\begin{array}{l} \dfrac{\partial r}{\partial a} = (1+mA)\dfrac{\eta^2}{\xi} \\ \dfrac{\partial r}{\partial e} = -(1+mA)\dfrac{a}{e}(\xi-1) \\ \dfrac{\partial r}{\partial \varpi} = 0 \\ \dfrac{\partial r}{\partial \chi} = (1+mA)\dfrac{a}{\eta}e\sin f \end{array}\right. \qquad \left\{\begin{array}{l} \dfrac{\partial \phi}{\partial a} = 0 \\ \dfrac{\partial \phi}{\partial e} = (1-mA)\dfrac{\xi+1}{\eta^2}\sin f \\ \dfrac{\partial \phi}{\partial \varpi} = (1-mA) \\ \dfrac{\partial \phi}{\partial \chi} = (1-mA)\dfrac{\xi^2}{\eta^3} \end{array}\right. \tag{85}$$

$$\left\{\begin{array}{l} \dfrac{\partial p_r}{\partial a} = -\dfrac{n}{2\eta}e\sin f \\ \dfrac{\partial p_r}{\partial e} = \dfrac{na\xi^2}{\eta^3}\sin f \\ \dfrac{\partial p_r}{\partial \varpi} = 0 \\ \dfrac{\partial p_r}{\partial \chi} = \dfrac{na\xi^2(\xi-1)}{\eta^4} \end{array}\right. \qquad \left\{\begin{array}{l} \dfrac{\partial p_\phi}{\partial a} = \dfrac{na\eta}{2} \\ \dfrac{\partial p_\phi}{\partial e} = -\dfrac{na^2e}{\eta} \\ \dfrac{\partial p_\phi}{\partial \varpi} = 0 \\ \dfrac{\partial p_\phi}{\partial \chi} = 0 \end{array}\right.$$

ここで、 χ での偏微分は以下の微分関係を用いた。

$$\frac{\partial r}{\partial \chi} = \frac{\partial r}{\partial f}\frac{\partial f}{\partial \chi} \quad , \quad \frac{\partial \phi}{\partial \chi} = \frac{\partial \phi}{\partial f}\frac{\partial f}{\partial \chi} \quad , \quad \frac{\partial p_r}{\partial \chi} = \frac{\partial p_r}{\partial f}\frac{\partial f}{\partial \chi} \tag{86}$$

f での偏微分は (66) 式～(68) 式より

$$\frac{\partial r}{\partial f} = (1+mA)\frac{a\eta^2}{\xi^2}e\sin f \tag{87}$$

$$\frac{\partial \phi}{\partial f} = (1-mA) \tag{88}$$

$$\frac{\partial p_r}{\partial f} = \frac{na}{\eta}(\xi-1) \tag{89}$$

であり、(84) 式より

$$\frac{\partial f}{\partial \chi} = \frac{\xi^2}{\eta^3} \tag{90}$$

である。

3.4 要素（新変数）による運動方程式

Hamiltonian $H = H_0 + \varepsilon H_1$ の下での運動方程式は次のようになる。

$$\begin{cases} \dfrac{dr}{dt} = \dfrac{\partial H}{\partial p_r} = \dfrac{\partial H_0}{\partial p_r} + \dfrac{\partial \varepsilon H_1}{\partial p_r} = p_r + \dfrac{\partial \varepsilon H_1}{\partial p_r} & (91) \\ \dfrac{d\phi}{dt} = \dfrac{\partial H}{\partial p_\phi} = \dfrac{\partial H_0}{\partial p_\phi} + \dfrac{\partial \varepsilon H_1}{\partial p_\phi} = \dfrac{p_\phi}{r^2} + \dfrac{\partial \varepsilon H_1}{\partial p_\phi} & (92) \end{cases}$$

$$\begin{cases} \dfrac{dp_r}{dt} = -\dfrac{\partial H}{\partial r} = -\dfrac{\partial H_0}{\partial r} - \dfrac{\partial \varepsilon H_1}{\partial r} = \dfrac{{p_\phi}^2}{r^3} - (1+mA)\dfrac{\mu}{r^2} - 2mB\dfrac{\mu}{r^3} - \dfrac{\partial \varepsilon H_1}{\partial r} & (93) \\ \dfrac{dp_\phi}{dt} = -\dfrac{\partial H}{\partial \phi} = -\dfrac{\partial H_0}{\partial \phi} - \dfrac{\partial \varepsilon H_1}{\partial \phi} = 0 - \dfrac{\partial \varepsilon H_1}{\partial \phi} & (94) \end{cases}$$

r については (91) 式と (66) 式を微分したものより、以下の関係式が得られる。

$$\frac{dr}{dt} = p_r + \frac{\partial \varepsilon H_1}{\partial p_r} =$$

$$= \frac{nae}{\eta}\sin f + \frac{r}{a}\frac{da}{dt} - (1+mA)a\cos f\frac{de}{dt} + (1+mA)\frac{ae}{\eta}\sin f\frac{d\chi}{dt} \qquad (95)$$

故に、次のようになる。

$$\frac{r}{a}\frac{da}{dt} - (1+mA)a\cos f\frac{de}{dt} + (1+mA)\frac{ae}{\eta}\sin f\frac{d\chi}{dt} = \frac{\partial \varepsilon H_1}{\partial p_r} \qquad (96)$$

同様に ϕ については、次のようになる。

$$\frac{d\phi}{dt} = \frac{p_\phi}{r^2} + \frac{\partial \varepsilon H_1}{\partial p_\phi} =$$

$$= \frac{na^2\eta}{r^2} + \left\{\frac{a}{r} + (1-mA)\frac{1}{\eta^2}\right\}\sin f\frac{de}{dt} + (1-mA)\frac{d\varpi}{dt} + (1+mA)\frac{a^2\eta}{r^2}\frac{d\chi}{dt} \qquad (97)$$

故に、

$$\left\{\frac{a}{r} + (1-mA)\frac{1}{\eta^2}\right\}\sin f\frac{de}{dt} + (1-mA)\frac{d\varpi}{dt} + (1+mA)\frac{a^2\eta}{r^2}\frac{d\chi}{dt} = \frac{\partial \varepsilon H_1}{\partial p_\phi} \qquad (98)$$

p_r , p_ϕ についても同様で

$$\frac{dp_r}{dt} = \frac{{p_\phi}^2}{r^3} - (1+mA)\frac{\mu}{r^2} - 2mB\frac{\mu}{r^3} - \frac{\partial \varepsilon H_1}{\partial r} =$$

$$= (1+mA)\frac{n^2a^3}{r^2}\left\{(1+mA)\frac{a\eta^2}{r} - 1\right\} - \frac{n}{2\eta}e\sin f\frac{da}{dt} +$$

$$+ (1+2mA)\frac{na^3\eta}{r^2}\sin f\frac{de}{dt} + (1+2mA)\frac{na^3}{r^2}e\cos f\frac{d\chi}{dt} \qquad (99)$$

故に、

$$-\frac{n}{2\eta}e\sin f\frac{da}{dt} + (1+2mA)\frac{na^3\eta}{r^2}\sin f\frac{de}{dt} + (1+2mA)\frac{na^3}{r^2}e\cos f\frac{d\chi}{dt} = -\frac{\partial \varepsilon H_1}{\partial r} \qquad (100)$$

$$\frac{dp_\phi}{dt} = 0 - \frac{\partial \varepsilon H_1}{\partial \phi} =$$

$$= \frac{1}{2} na\eta \frac{da}{dt} - \frac{na^2 e}{\eta}\frac{de}{dt} \tag{101}$$

故に、

$$\frac{1}{2} na\eta \frac{da}{dt} - \frac{na^2 e}{\eta}\frac{de}{dt} = -\frac{\partial \varepsilon H_1}{\partial \phi} \tag{102}$$

εH_1 に ϕ は含まれていないので

$$\frac{\partial \varepsilon H_1}{\partial \phi} = 0 \tag{103}$$

であるが、一般性を考慮して (102) 式の右辺では残しておいた。

以上で新変数 (a , e ; ϖ , χ) に対する微分方程式系が得られたので、これらを正規型に書き換えると次のようになる。

$$\frac{da}{dt} = -\frac{2}{n\eta} e \sin f \frac{\partial \varepsilon H_1}{\partial r} - \frac{2\xi^2}{na\eta^3}\frac{\partial \varepsilon H_1}{\partial \phi} - (1 - mA)\frac{2\xi^2(\xi - 1)}{\eta^4}\frac{\partial \varepsilon H_1}{\partial p_r} \tag{104}$$

$$\frac{de}{dt} = -\frac{\eta}{na} \sin f \frac{\partial \varepsilon H_1}{\partial r} - \frac{\xi^2 - \eta^2}{na^2 e\eta}\frac{\partial \varepsilon H_1}{\partial \phi} - (1 - mA)\frac{\xi^2(\xi - 1)}{a\eta^2 e}\frac{\partial \varepsilon H_1}{\partial p_r} \tag{105}$$

$$\frac{d\varpi}{dt} = \frac{\eta(\xi - 1)}{nae^2}\frac{\partial \varepsilon H_1}{\partial r} - \frac{\xi + 1}{na^2\eta e} \sin f \frac{\partial \varepsilon H_1}{\partial \phi} +$$

$$- (1 - mA)\frac{\xi^2}{a\eta^2 e} \sin f \frac{\partial \varepsilon H_1}{\partial p_r} + (1 + mA)\frac{\partial \varepsilon H_1}{\partial p_\phi} \tag{106}$$

$$\frac{d\chi}{dt} = -\frac{\eta^2(\xi^2 - \xi - 2e^2)}{nae^2\xi}\frac{\partial \varepsilon H_1}{\partial r} + \frac{\xi + 1}{na^2 e} \sin f \frac{\partial \varepsilon H_1}{\partial \phi} +$$

$$+ (1 - mA)\frac{\xi^2 - e^2}{a\eta e} \sin f \frac{\partial \varepsilon H_1}{\partial p_r} \tag{107}$$

Hamiltonian εH_1 の引数 (r , ϕ ; p_r , p_ϕ) に変換式 (66) 式～(69) 式を代入する。その際に天体力学での慣習に合わせるために符号を変えて εV を摂動関数とする。

$$\varepsilon V(a, e; \varpi, \chi; t) = -\varepsilon H_1(r, -; p_r, p_\phi) =$$

$$= m\mu\left\{ \frac{1}{8a^2} - \frac{2}{ar} + \frac{4}{r^2} - \frac{p}{r^3} - A\frac{1}{r} - B\frac{1}{r^2} \right\} \tag{108}$$

これによって (104) 式～(107) 式は以下のように書ける。このとき εH_1 すなわち εV が m を含んでいることを考慮する。

$$\frac{da}{dt} = -\frac{2}{na}\left(\frac{\partial r}{\partial \chi}\frac{\partial \varepsilon H_1}{\partial r} + \frac{\partial \phi}{\partial \chi}\frac{\partial \varepsilon H_1}{\partial \phi} + \frac{\partial p_r}{\partial \chi}\frac{\partial \varepsilon H_1}{\partial p_r}\right) = \frac{2}{na}\frac{\partial \varepsilon V}{\partial \chi} \tag{109}$$

$$\frac{de}{dt} = -\frac{\eta^2}{na^2 e}\left(\frac{\partial r}{\partial \chi}\frac{\partial \varepsilon H_1}{\partial r} + \frac{\partial \phi}{\partial \chi}\frac{\partial \varepsilon H_1}{\partial \phi} + \frac{\partial p_r}{\partial \chi}\frac{\partial \varepsilon H_1}{\partial p_r}\right) + \frac{\eta}{na^2 e}\frac{\partial \phi}{\partial \varpi}\frac{\partial \varepsilon H_1}{\partial \phi} =$$

$$= \frac{\eta^2}{na^2 e}\frac{\partial \varepsilon V}{\partial \chi} - \frac{\eta}{na^2 e}\frac{\partial \varepsilon V}{\partial \varpi} \tag{110}$$

$$\frac{d\varpi}{dt} = -\frac{\eta}{na^2e}\left(\frac{\partial r}{\partial e}\frac{\partial \varepsilon H_1}{\partial r} + \frac{\partial \phi}{\partial e}\frac{\partial \varepsilon H_1}{\partial \phi} + \frac{\partial p_r}{\partial e}\frac{\partial \varepsilon H_1}{\partial p_r} + \frac{\partial p_\phi}{\partial e}\frac{\partial \varepsilon H_1}{\partial p_\phi}\right) = \frac{\eta}{na^2e}\frac{\partial \varepsilon V}{\partial e} \tag{111}$$

$$\frac{d\chi}{dt} = \frac{\eta^2}{na^2e}\left(\frac{\partial r}{\partial e}\frac{\partial \varepsilon H_1}{\partial r} + \frac{\partial \phi}{\partial e}\frac{\partial \varepsilon H_1}{\partial \phi} + \frac{\partial p_r}{\partial e}\frac{\partial \varepsilon H_1}{\partial p_r}\right) + \frac{2}{na}\left(\frac{\partial r}{\partial a}\frac{\partial \varepsilon H_1}{\partial r} + \frac{\partial p_r}{\partial a}\frac{\partial \varepsilon H_1}{\partial p_r}\right) =$$

$$= -\frac{\eta^2}{na^2e}\frac{\partial \varepsilon V}{\partial e} - \frac{2}{na}\left(\frac{\partial \varepsilon V}{\partial a}\right) \tag{112}$$

これは天体力学で馴染みのある、εV を摂動関数とする楕円要素に対する要素変化の式に、結果として、同型のものとなった。

ここで、表記

$$\left(\frac{\partial \varepsilon V}{\partial a}\right)$$

は、εV を r 経由の a で偏微分したことを意味するものとする [10]。

以上を整理してまとめて書くと次のようになる。

$$\frac{da}{dt} = \frac{2}{na}\frac{\partial \varepsilon V}{\partial \chi} \tag{113}$$

$$\frac{de}{dt} = \frac{\eta^2}{na^2e}\frac{\partial \varepsilon V}{\partial \chi} - \frac{\eta}{na^2e}\frac{\partial \varepsilon V}{\partial \varpi} \tag{114}$$

$$\frac{d\varpi}{dt} = \frac{\eta}{na^2e}\frac{\partial \varepsilon V}{\partial e} \tag{115}$$

$$\frac{d\chi}{dt} = -\frac{\eta^2}{na^2e}\frac{\partial \varepsilon V}{\partial e} - \frac{2}{na}\left(\frac{\partial \varepsilon V}{\partial a}\right) \tag{116}$$

$$\varepsilon V = m\mu\left\{\frac{1}{8a^2} - \frac{2}{ar} + \frac{4}{r^2} - \frac{p}{r^3} - A\frac{1}{r} - B\frac{1}{r^2}\right\} \tag{117}$$

4 永年摂動の消去

4.1 摂動の永年変化部分

我々が人工系に未定定数を導入した目的は、真の軌道と中間軌道との間に永年的な変化を生じさせないためである。この目的のためには、摂動の永年部分のみを抽出し要素変化の式を計算すれば充分なので、必要としない周期変化部分を消去するために力学的量 εV の時間平均値を求める。

εV の永年部分を secular の s を採って $\varepsilon V_{(s)}$ と表現し、周期を T とする。ここでも、m の二次以上の項は微小であるため無視する。

$$\varepsilon V_{(s)} = \frac{1}{T}\int_0^T \varepsilon V dt \quad , \quad T = \frac{2\pi}{n} \tag{118}$$

積分変数の変換には関係式

$$ndt = (1+mA)dM = \frac{r}{a}du = (1-mA)\frac{r^2}{a^2\eta}df \tag{119}$$

を用いると $\varepsilon V_{(s)}$ は

$$\varepsilon V_{(s)} = \frac{n}{2\pi}\int_0^T \varepsilon V dt = \frac{1}{2\pi}\int_0^{2\pi} \varepsilon V dM =$$

$$= \frac{1}{2\pi}\int_0^{2\pi} m\mu\left\{ \frac{1}{8a^2} - \left(\frac{2}{a}+A\right)\frac{1}{r} + (4-B)\frac{1}{r^2} - \frac{p}{r^3} \right\} dM =$$

$$= \frac{1}{2\pi}\int_0^{2\pi} m\mu\left\{ \frac{1}{8a^2}dM - \left(\frac{2}{a}+A\right)\frac{1}{a}du + (4-B)\frac{\eta^3}{p^2}df - \frac{\eta^3}{p^2}d(f+e\sin f) \right\} =$$

$$= m\mu\left\{ -\frac{15}{8a^2} + \frac{3}{a^2\eta} - \frac{1}{a}A - \frac{1}{a^2\eta}B \right\} \tag{120}$$

となるので、

$$\varepsilon V_{(s)} = \varepsilon V_{(s)}(a, e; \ , \ ) =$$

$$= m\mu\left\{ -\frac{15}{8a^2} + \frac{3}{a^2\eta} - \frac{1}{a}A - \frac{1}{a^2\eta}B \right\} \tag{121}$$

これで永年変化部分が取り出せた。このことから

$$\frac{da_{(s)}}{dt} = \frac{2}{na}\frac{\partial \varepsilon V_{(s)}}{\partial \chi} = 0 \tag{122}$$

$$\frac{de_{(s)}}{dt} = \frac{\eta^2}{na^2 e}\frac{\partial \varepsilon V_{(s)}}{\partial \chi} = 0 \tag{123}$$

$$\frac{d\varpi_{(s)}}{dt} = \frac{\eta}{na^2 e}\frac{\partial \varepsilon V_{(s)}}{\partial e} = m\mu\frac{\eta}{na^2 e}\left(-\frac{3}{a^2\eta^2} + \frac{B}{a^2\eta^2}\right)\left(-\frac{e}{\eta}\right) \tag{124}$$

$$\frac{d\chi_{(s)}}{dt} = -\frac{\eta^2}{na^2 e}\frac{\partial \varepsilon V_{(s)}}{\partial e} - \frac{2}{na}\left(\frac{\partial \varepsilon V_{(s)}}{\partial a}\right) =$$

$$= -m\mu\frac{\eta^2}{na^2 e}\left(-\frac{3}{a^2\eta^2} + \frac{B}{a^2\eta^2}\right)\left(-\frac{e}{\eta}\right) - m\mu\frac{2}{na}\left(\frac{15}{4a^3} - \frac{6}{a^3\eta} + \frac{1}{a^2}A + \frac{2}{a^3\eta}B\right) \tag{125}$$

となり、ϖ と χ が永年変化に関係することがわかる。

4.2 未定定数の決定

前節で、永年変化に関係するのは ϖ と χ のみであったので、これらの永年項を消去するような未定定数 A, B を見つければ、我々の目的は達成される。しかし、従属関係 (36) 式

$$mA = -\frac{m}{p}B \tag{126}$$

があるので

$$\frac{d\varpi_{(s)}}{dt} = 0 \tag{127}$$

$$\frac{d\chi_{(s)}}{dt} = 0 \tag{128}$$

を同時に満すことはできない。そこで、χ については後に議論するとして、ϖ について (127) 式を実現する方を選ぶと、(124) 式から未定定数の値が

$$B = 3 \tag{129}$$

となり、同時に

$$A = -\frac{3}{p} \tag{130}$$

となる。この未定定数が ϖ の永年項を消去するものである。

未定定数

$$\boxed{A = -\frac{3}{p}} \tag{131}$$

$$\boxed{B = 3} \tag{132}$$

また (124) 式、(125) 式を積分した形として以下のような表現を定義する。

$$\delta\varpi_{(s)} \equiv \int \frac{d\varpi_{(s)}}{dt} dt \tag{133}$$

$$\delta\chi_{(s)} \equiv \int \frac{d\chi_{(s)}}{dt} dt \tag{134}$$

上の結果から要素 χ は次のようになる。

$$\frac{d\chi_{(s)}}{dt} = -\eta \frac{d\varpi_{(s)}}{dt} - m\mu \frac{2}{na}\left(\frac{15}{4a^3} - \frac{6}{a^3\eta} + \frac{1}{a^2}A + \frac{2}{a^3\eta}B\right) \tag{135}$$

よって

$$\delta\chi_{(s)} = -\eta\delta\varpi_{(s)} - \frac{m}{p}\left\{\frac{15}{2}\eta^2 - 12\eta + 2a\eta^2 A + 4\eta B\right\}M \tag{136}$$

ここで A , B の値を代入すると

$$\delta\chi_{(s)} = -\frac{3}{2}\frac{m}{p}(5\eta^2 - 4)M \tag{137}$$

となり、χ には永年項が残る。しかし χ は常に

$$M = \int_{t_0}^{t} (1 - mA)n dt + \chi \tag{138}$$

の形でしか入ってこない。つまり M に永年項が残らないようにすれば、永年項を含まない中間軌道樹立の目的は達成されることになる。

そこで、平均近点離角に類似の M は、長半径に類似の a の変化を通じて変化しているので、a の変化 δa を

$$\delta a \equiv \int \frac{da}{dt} dt \tag{139}$$

と表すことにすれば、関係

$$\mu = n^2 a^3 \tag{140}$$

を通じて量 n が

$$\delta n = -\frac{3}{2}\frac{n}{a}\delta a =$$

$$= -m\frac{3n}{a\eta^4}\left\{-(2 + aA)\frac{a\eta^4}{r} + (4 - B)\frac{a^2\eta^4}{r^2} - \frac{a^3\eta^6}{r^3} + \frac{1}{2}C_a^*\right\} \tag{141}$$

(C_a^* ： 積分定数)

のように変化する。これを (138) 式の右辺第一項に考慮すれば次のようになる。

$$\int (1 - mA)\delta n dt = -m\frac{3n}{a\eta^4}\int\left\{-(2 + aA)\frac{a\eta^4}{r} + (4 - B)\frac{a^2\eta^4}{r^2} - \frac{a^3\eta^6}{r^3} + \frac{1}{2}C_a^*\right\}dt =$$

$$= m\frac{3}{a\eta^4}\int\left\{(2 + aA)\eta^4 du - (4 - B)\eta^3 df + \eta^3(1 + e\cos f)df - \frac{1}{2}C_a^* dM\right\} \tag{142}$$

$\int(1-mA)\delta ndt$ の永年部分 $\int(1-mA)\delta ndt_{(s)}$ は

$$\int(1-mA)\delta ndt_{(s)} = m\frac{3}{p}\left\{(2+aA)\eta^2 u-(3-B)\eta f-\frac{1}{2\eta^2}C_a^* M\right\} \tag{143}$$

A , B の値を代入すると

$$\int(1-mA)\delta ndt_{(s)} = m\frac{3}{p}\left\{\left(2-\frac{3}{\eta^2}\right)\eta^2 u-\frac{1}{2\eta^2}C_a^* M\right\} \tag{144}$$

となる。故に M の永年変化部分を $\delta M_{(s)}$ と表記すれば

$$\begin{aligned}\delta M_{(s)} &= \int(1-mA)\delta ndt_{(s)}+\delta\chi_{(s)} = \\ &= m\frac{3}{p}\left\{\left(2-\frac{3}{\eta^2}\right)\eta^2 u-\frac{1}{2\eta^2}C_a^* M\right\}+m\frac{1}{p}\left(-\frac{15}{2}\eta^2+6\right)M\end{aligned} \tag{145}$$

となる。$u\approx M\approx f$ であるとすれば

$$\delta M_{(s)} = m\frac{3}{p}\left(-\frac{1}{2}\eta^2-1-\frac{1}{2\eta^2}C_a^*\right)M \tag{146}$$

となる。これより M に永年項が残らないようにするには

$$C_a^* = -\eta^2(\eta^2+2) \tag{147}$$

であればよいことになる。

5 Schwarzschild 問題の一次の精度での解

5.1 中間軌道

要素 (a , e ; ϖ , χ) を定数とし、未定定数の値を代入したとき、次の式が表すものが中間軌道である。

$$\begin{cases} r=\varphi_r(a\,,\,e\,;\,f\,)=\left(1-\dfrac{3m}{p}\right)\dfrac{a(1-e^2)}{1+e\cos f} & (148)\\ \phi=\varphi_\phi(\varpi\,;\,f\,)=\left(1+\dfrac{3m}{p}\right)(f+\varpi) & (149)\end{cases}$$

$$\begin{cases} p_r=\psi_r(a\,,\,e\,;\,f\,)=\dfrac{na}{\eta}e\sin f & (150)\\ p_\phi=\psi_\phi(a\,,\,e\,)=na^2\eta & (151)\end{cases}$$

$$u-e\sin u=M \tag{152}$$

$$M=\int_{t_0}^{t}\left(1+\frac{3m}{p}\right)ndt+\chi \tag{153}$$

$$\tan\frac{f}{2}=\sqrt{\frac{1+e}{1-e}}\tan\frac{u}{2} \tag{154}$$

$$n=\sqrt{\frac{\mu}{a^3}}\quad,\quad p=a(1-e^2) \tag{155}$$

$$\eta=\sqrt{1-e^2} \tag{156}$$

ここでは n は定数なので M を積分の形で書く必要はないが、次の段階、要素変化の式を解く際には必要な表式になるので (153) 式の形のまま書いておく。

この我々の中間軌道が Schwarzschild 問題の高い精度での近似解になっていることは次節で明らかになる。

5.2 近似解

上記、中間軌道を与えた要素 (a , e ; ϖ , χ) を変数とし、要素変化の式を適用すれば m の一次の精度での解が得られる。結果は以下の通りである。

$$a = a_0 + \delta a - \delta a_0 \tag{157}$$

$$e = e_0 + \delta e - \delta e_0 \tag{158}$$

$$\varpi = \varpi_0 + \delta\varpi - \delta\varpi_0 \tag{159}$$

$$\chi = \chi_0 + \delta\chi - \delta\chi_0 \tag{160}$$

ここで、

$$\begin{aligned} \delta a &\equiv \int \frac{da}{dt}dt \quad , \quad \delta e \equiv \int \frac{de}{dt}dt \\ \delta\varpi &\equiv \int \frac{d\varpi}{dt}dt \quad , \quad \delta\chi \equiv \int \frac{d\chi}{dt}dt \end{aligned} \tag{161}$$

である。なお、 a_0 , e_0 ; ϖ_0 , χ_0 および δa_0 , δe_0 ; $\delta\varpi_0$, $\delta\chi_0$ は元期 t_0 における、変数 a , e ; ϖ , χ および周期摂動 δa , δe ; $\delta\varpi$, $\delta\chi$ の値を表すものとする。

$$\delta a = m\frac{1}{\eta^4}\left\{\left(6+\frac{5}{2}e^2-2Ap-4B\right)e\cos f+(1-B)e^2\cos 2f-\frac{1}{2}e^3\cos 3f+C_a\right\} \tag{162}$$

$$\delta e = m\frac{1}{p}\left\{\left(3+\frac{5}{4}e^2-Ap-2B\right)\cos f+\frac{1}{2}(1-B)e\cos 2f-\frac{1}{4}e^2\cos 3f+C_e\right\} \tag{163}$$

$$\delta\varpi = m\frac{1}{p}\left\{(3-B)f+\left(3+\frac{7}{4}e^2-Ap-2B\right)\frac{1}{e}\sin f+ \right. \\ \left. +\frac{1}{2}(1-B)\sin 2f-\frac{1}{4}e\sin 3f+C_\varpi\right\} \tag{164}$$

$$\delta\chi = -m\frac{\eta}{p}\left\{-\frac{1}{2}\eta M+\left(8\eta+2A\frac{p}{\eta}\right)u+(-9+3B)f+ \right. \\ \left. +\left(3+\frac{23}{4}e^2-Ap-2B\right)\frac{1}{e}\sin f+\frac{1}{2}(1-B)\sin 2f-\frac{1}{4}e\sin 3f+C_\chi\right\} \tag{165}$$

$$\delta M = m\frac{\eta}{p}\left\{-\frac{3}{2\eta^3}C_a^{''}M+\frac{1}{2}\eta M+\left(-2\eta+A\frac{p}{\eta}\right)u+ \right. \\ \left. +\left(-3-\frac{11}{4}e^2+Ap+2B\right)\frac{1}{e}\sin f+\frac{1}{2}(B-1)\sin 2f+\frac{1}{4}e\sin 3f+C_M\right\} \tag{166}$$

(C_a , C_e , C_ϖ , C_χ , C_M ： 積分定数)

$$\boxed{A = -\frac{3}{p} \quad , \quad B = 3} \tag{167}$$

$$\boxed{\begin{aligned} C_a &= C_a^* + 2(1 - B - Ap) + (5 - B)e^2 \qquad (168) \\ C_a^* &= -\eta^2(\eta^2 + 2) \qquad (169) \end{aligned}}$$

未定定数 A , B および定数 C_a^* によって、ϖ と M に永年項が残らないようにすることが実現でき、このことによって、我々の中間軌道がSchwarzschild 問題の精度の高い近似解であることがわかる。

最後に未定定数および積分定数を代入すれば次のようになる。

$$\begin{cases} \delta a = m\dfrac{1}{\eta^4}\left\{\dfrac{5}{2}e^3\cos f - 2e^2\cos 2f - \dfrac{1}{2}e^3\cos 3f + C_a\right\} & (170) \\ \delta e = m\dfrac{1}{p}\left\{\dfrac{5}{4}e^2\cos f - e\cos 2f - \dfrac{1}{4}e^2\cos 3f + C_e\right\} & (171) \\ \delta\varpi = m\dfrac{1}{p}\left\{\dfrac{7}{4}e\sin f - \sin 2f - \dfrac{1}{4}e\sin 3f + C_\varpi\right\} & (172) \\ \delta\chi = -m\dfrac{\eta}{p}\left\{-\dfrac{1}{2}\eta M + \left(8\eta - \dfrac{6}{\eta}\right)u + \dfrac{23}{4}e\sin f - \sin 2f - \dfrac{1}{4}e\sin 3f + C_\chi\right\} & (173) \end{cases}$$

$$\delta M = m\frac{\eta}{p}\left\{-\frac{11}{4}e\sin f + \sin 2f + \frac{1}{4}e\sin 3f + C_M\right\} \tag{174}$$

我々が得た、$\frac{1}{r}$ および $\frac{1}{r^2}$ に比例する項からなる中間軌道の Hamiltonian は次式で与えられる。

$$\begin{aligned} H_0 &= \frac{1}{2}\left({p_r}^2 + \frac{{p_\phi}^2}{r^2}\right) - (1 + mA)\frac{\mu}{r} - mB\frac{\mu}{r^2} \\ A &= -\frac{3}{p} \quad , \quad B = 3 \end{aligned} \tag{175}$$

5.3 中間軌道が描く軌跡

我々の中間軌道がどのような軌跡を描くかを原点を太陽にしたときの水星の場合を例にまず見てみる。

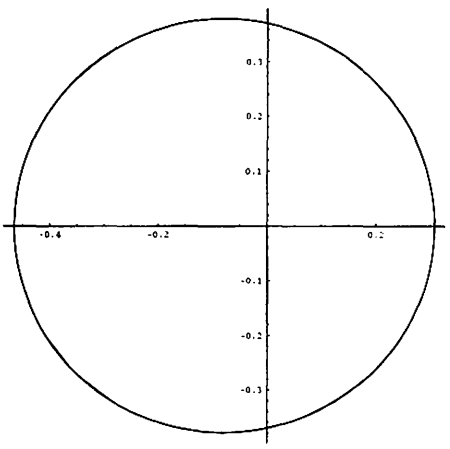

このとき用いた軌道要素および物理定数を以下に示す。

$$a = 0.38710\,a.u. \quad , \quad e = 0.20563$$

$$c = 299792458\,m/s \quad , \quad G = 6.672 \times 10^{-11}\,m/kg{\cdot}s^2$$

$$m_\odot = 1.9891 \times 10^{30}\,kg$$

図1：水星の軌道 ($f = 0 \rightarrow 5\pi$)

この図を見る限りでは軌道が動いている様子がわかりにくいので次に離心率と太陽質量の値を変えて描かせた図を示す。

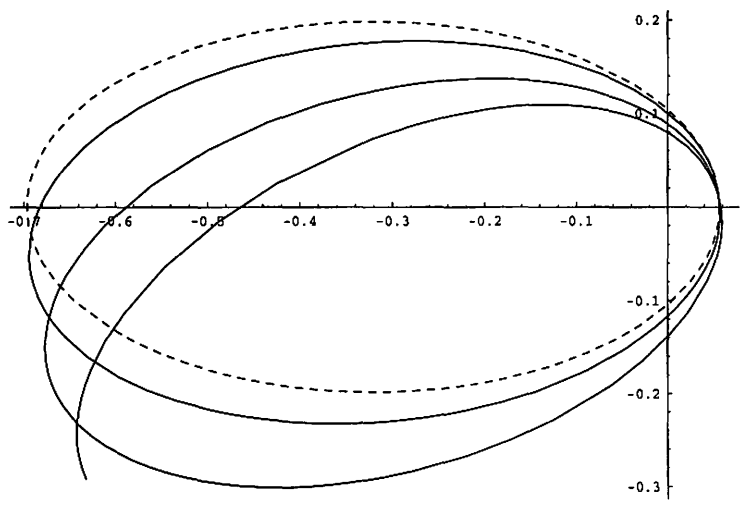

以下にこのとき用いた数値を示す。

$$e = 0.85$$

$$m_\odot = 1.9891 \times 10^{30} \times 10^5\,kg$$

図2：離心率と太陽質量を変えた場合の軌道 ($f = 0 \rightarrow 5\pi$)

実線：中間軌道、点線：楕円軌道

実線が中間軌道が描く軌跡を表し、点線が出発点を中間軌道のそれと同じにした場合の楕円軌道が描く軌跡を表している。

6 まとめ

Schwarzschild 問題を、(r , ϕ , θ) を絶対空間の相対極座標、t を絶対時間とする立場で、未定定数を含む中間軌道の方法で解いた。

未定定数に適切な値を与えることによって、摂動に微小正数 m の一次の大きさの永年変化が一切現れないようにすることができた。これによって、我々の中間軌道は、摂動補正 δa , δe ; $\delta\varpi$, $\delta\chi$ を考慮せずとも充分に精度の高い Schwarzschild 問題の近似解となっているのがわかる。

本小論では、楕円積分を必要とせずに、三角関数のみで、精度の高い Schwarzschild 問題の近似解が得られることを示した。

参考文献

[1] Le Verrier, U.J. : 1859, Théorie du mouvement de Mercure, *Annales de l' Observatoire Impérial de Paris*

[2] de Sitter, W. : 1916, On Einstein's Theory of Gravitation, and its Astronomical Consequences, *Monthly Notices of the Royal Astronomical Society*, **76**, 724

[3] Eddington, A.S. : 1975, *The mathematical theory of relativity*, Chelsea, 88

[4] 萩原　雄祐 : 1930, 萬有引力法則の吟味, 日本天文學會要報, 18

[5] 平山　清次 : 1930, 天體力學, 岩波講座, 69

[6] Brumberg, V.A. : 1991, *Essential Relativistic Celestial Mechanics*, Adam Hilger, 93

[7] 井上　猛 : 1995, 定数変化法と云うもの, 第２７回天体力学研究会集録, 155-161

[8] Garfinkel, B. : 1958, On the motion of a satellite of an oblate planet, *The Astronomical Journal*, **63**, 88-96

[9] Brumberg, V.A. : loc.cit., 82

[10] Brouwer, D. and Clemence G. M. : 1961, *Methods of Celestial Mechanics*, Academic Press, 285

Lifespan of Organisms and the Secular Change of the Environment

Kiyotaka Tanikawa[1], Toshihiro Handa[2], and Takashi Ito[1]
[1]National Astronomical Observatory
Mitaka, Tokyo, 181-8588 Japan
[2]Institute of Astronomy
University of Tokyo
Mitaka, Tokyo, 181-0015 Japan

Abstract

Effects of the secular change of the environment on the lifespan of organisms are studied. Simple one-dimensional models, i.e., one-dimensional discrete dynamical systems, are devised. These models have several parameters: the dispersion of character of successive generations, the dispersion of admissibility of the environment, the rate of the secular change, the reproduction rate, and the change of reproduction rate. The change of population over generations is numerically pursued. It is found, as expected, that small dispersions of characters and long lifespans are disadvantageous for survival.

1 Introduction

It is well known that a rapid change of the environment has taken place in the early Earth. There have been secular changes in various physical and chemical quantities: the amount of dangerous radiation(Boothroyd et al., 1990), the total area of continents(Condie, 1989), the total amount of carbon dioxide in the atmosphere and in the sea(Tajika, 1992), the average temperature of the atmosphere and in the interior of the Earth, the amount of O_3, the spin rate of the Earth(Tajika, 1992), the distance to the moon, the gravitational flattening of the Earth, Solar insolation(Ito et al., 1993), the strength of geomagnetism, the frequency of magnetic reversal, and so on.

These changes must have given a strong restriction to all living things. Organisms must have adapted to a new environment(Losos et al., 1997). In order to do that, the only way is to produce the next generation which has characters far from the parents. We naturally expect that long lifespan is inhibited by the rapid change. Our basic question is: what kind of effects the secular change of environments had on the evolution of organisms, in particular on their lifespan.

In this report, we construct a one-dimensional discrete dynamical system which simulates the population (density) change of a species in the environment changing secularly. We take into account the adjustment of reproduction rate by the species itself.

We summarize our motivation as a form of questions:

1) Why organic beings have programmed lifespans?

2) Is lifespan a product of evolution?

3) What is the role of the supposed secular change of environment in the past?

4) Is the dispersion of characters particularly important when the environment changes secularly?

5) Is the birth of multicellular organisms a result of the slowdown of the secular change?

2 Formulation

In order to formulate the problem, we first present basic assumptions.

Basic Assumption 1. The problem is one-dimensional, i.e., the variable x expresses the characteristics of the environment. Genetic characters are also expressed by x.

Basic Assumption 2. Evolution is neutral(Kimura, 1983), i.e., the distribution of characters of offspring is probabilistic as a function of $x' - x$, where x' and x are the values of characters for the parent and offspring, respectively.

Basic Assumption 3. Survivability is determined by the difference $x - x_E$, where x_E is the central character of the environment.

We postulate additional assumptions in order to concretely construct a model.

Additional Assumption 1. Parents die as soon as they create the next generation, i.e., there is no overlapping between different generations.

Additional Assumption 2. The number of offspring from one parent is constant in the stationary environment.

Additional Assumption 3. Probability distributions given in Basic Assumptions 2 and 3 are Gaussian.

Additional Assumption 4. The dispersion of the probability distribution for a species is constant for different generations.

We search for equations describing the population evolution for generations of a species based on the above Assumptions. For this purpose, let us introduce notations. Let N be the population of the n-th generation. Let $x_E(t)$ be the the center of environmental characteristics at time t. $f(n, x)$ is the probability distribution of characters of the species at the n-th generation. We take $t = 0$ as the starting time. Without loss of generality, we take $x_E(t = 0) = 0$. The lifespan of one generation is Δt. We have $t = n\Delta t$.

The probability distribution of characters is given by $g(x-x')$ where x' is the character of parents. By Additional Assumption 2, the number distribution of the character of offspring from parents x' is $cg(x-x')$, where c is the reproduction rate. The number distribution of offspring for the succeeding generation is given by $\int f(n,x')cg(x-x')dx'$. The survival probability of offspring with character x is $s(x-x_E(t))$.

Then the probability distribution with respect to x of $(n+1)$-st generation is

$$f(n+1,x) = s(x-x_E)\int f(n,x')cg(x-x')dx'. \tag{1}$$

The population is given by

$$N(n) = \int f(n,x)dx. \tag{2}$$

3 Stationary Solution

Assuming the invariant environment, let us obtain the stationary population distribution. We have $x_E(t) = 0$ by assumption. For simplicity, the initial population distribution is taken to be Gaussian with center at $x = x_E(0)$.

$$f(n,x-x_E) = N(n)\mathrm{Gauss}(x-x_E,\sigma_n) \tag{3}$$

where we use the notation

$$\mathrm{Gauss}(x,\sigma) = \frac{1}{\sqrt{\pi}\sigma}\exp\left(-\frac{x^2}{\sigma^2}\right). \tag{4}$$

The character distribution function $g(x-x')$ and survivability distribution function $s(x-x_E)$ are both Gaussian by Additional Assumption 3. We have

$$\begin{array}{rl} g(x-x') = & \mathrm{Gauss}(x-x',\sigma_g), \\ s(x-x_E) = & \sqrt{\pi}\sigma_E\mathrm{Gauss}(x-x_E,\sigma_E) \end{array} \tag{5}$$

where $x_E = 0$. σ_E, σ_g, and c are constant since the environment is invariant and by Additional Assumptions 4 and 2.

Substituting (5) into (1), we obtain the equation describing the evolution as

$$\begin{aligned} f(n+1,x) &= s(x-x_E)\int f(n,x')cg(x-x')dx' \\ &= N(n)\sqrt{\pi}\sigma_E\mathrm{Gauss}(x,\sigma_E)\int \mathrm{Gauss}(x',\sigma_n)c\mathrm{Gauss}(x-x',\sigma_g)dx' \\ &= N(n)c\sqrt{\pi}\sigma_E\mathrm{Gauss}(x,\sigma_E)\mathrm{Gauss}\left(x,\sqrt{\sigma_n^2+\sigma_g^2}\right) \\ &= cN(n)\sigma_E/\sqrt{\sigma_n^2+\sigma_g^2+\sigma_E^2}\mathrm{Gauss}\left(x,\sigma_E\sqrt{\sigma_n^2+\sigma_g^2}/\sqrt{\sigma_n^2+\sigma_g^2+\sigma_E^2}\right) \end{aligned} \tag{6}$$

We see that if the n-th generation has a Gaussian distribution, then the $(n+1)$-st generation does so.

The necessary condition for stationarity is that the form of the distribution is invariant in time. The condition reads

$$\sigma_{n+1} = \sigma_E \frac{\sqrt{\sigma_n^2 + \sigma_g^2}}{\sqrt{\sigma_n^2 + \sigma_g^2 + \sigma_E^2}} \tag{7}$$

from which we obtain the stationary dispersion as

$$\sigma_\infty^2 = \frac{\sigma_g}{2}(-\sigma_g + \sqrt{\sigma_g^2 + 4\sigma_E^2}) \tag{8}$$

For convenience, let us normalize dispersions by σ_g.

$$\begin{aligned} s_n &= (\sigma_n/\sigma_g)^2, \\ s_E &= (\sigma_E/\sigma_g)^2 \end{aligned} \tag{9}$$

Then Equation (7) becomes

$$s_{n+1}(s_n + s_E + 1) = s_E(s_n + 1) \tag{10}$$

We also get the following relation from (8).

$$s_\infty = (\sigma_\infty/\sigma_g)^2 = \frac{1}{2}(\sqrt{1 + 4s_E} - 1) = \frac{1}{2}(a_E - 1), \tag{11}$$

where

$$a_E = \sqrt{1 + 4s_E}. \tag{12}$$

Let us obtain the general solution for the n-th generation assuming the Gaussian distribution Gauss(x, σ_0) for the 0-th generation. The distribution is Gaussian and its dispersion is given(see Appendix A for derivation) by

$$\begin{aligned} s_n &= s_\infty + a_E \left[\left(\frac{a_E + 1}{a_E - 1} \right)^{2n} \left(\frac{2s_0 + a_E + 1}{2s_0 - a_E + 1} \right) - 1 \right]^{-1} \\ &= s_\infty + \frac{a_E(a_E - 1)^{2n}(2s_0 - a_E + 1)}{(a_E + 1)^{2n}(2s_0 + a_E + 1) - (a_E - 1)^{2n}(2s_0 - a_E + 1)} \end{aligned} \tag{13}$$

Since $a_E > 1, s_0 > 0$, the quantity of the right hand side in Eq.(13) becomes large indefinitely with n. So, s_n always converges for $n \to \infty$ giving $s_n \to s_\infty$. The rate of convergence is larger for a_E closer to 1 or equivalently for smaller s_E. This implies that the stronger the selection, the faster the convergence.

In order that the population is stationary, c satisfies

$$c^2 = \frac{s_\infty + s_E + 1}{s_E}. \tag{14}$$

Unless $s_n = s_\infty$, s_n is not constant, implying the non-stationarity.

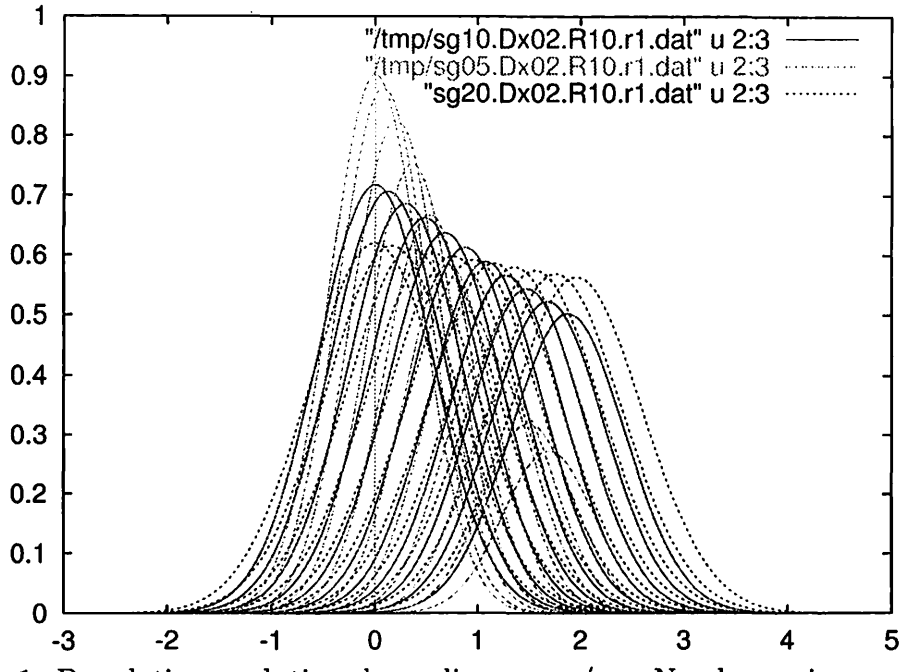

Figure 1: Population evolution depending on σ_g/σ_E. No change in reproduction rate.

The general solution for the population(see Appendix B for derivation) is

$$\log\left(\frac{N(n)}{N(0)}\right) = \frac{n}{2}\log\left(c^2 \cdot s_E\right) \\ -\frac{1}{2}\sum_{i=0}^{n-1}\left\{\log\left(\frac{1}{4}(a_E+1)^2 + a_E\left[\left(\frac{a_E+1}{a_E-1}\right)^{2i}\left(\frac{2s_0+a_E+1}{2s_0-a_E+1}\right)-1\right]^{-1}\right)\right\}, \tag{15}$$

or if we write

$$\varepsilon_i = \frac{4a_E}{(a_E+1)^2}\left[\left(\frac{a_E+1}{a_E-1}\right)^{2i}\left(\frac{2s_0+a_E+1}{2s_0-a_E+1}\right)-1\right]^{-1} \tag{16}$$

then, Eq.(15) assumes a simple form:

$$N(n) = N(0)\exp\left(-\frac{1}{2}\sum_{i=0}^{n-1}\log(1+\varepsilon_i)\right). \tag{17}$$

Let us summarize the results.

1. When the environment does not vary, and when the initial distribution is given by $f(0,x) = N(0)\mathrm{Gauss}(x,\sigma_0)$, then the distribution tends to the same Gaussian distribution $N(\infty)\mathrm{Gauss}(x,\sigma_\infty)$ irrespective neither of σ_0 nor $N(0)$.
2. The rate of convergence is smaller for a smaller σ_E/σ_g.
3. The reproduction rate c has a fixed value for the stationary distribution. However, in the transient phase, the total population is not constant for any c.

4 Initial parameters, initial conditions, and method of numerical integration

In this section, we fix our model. We assume that the starting distribution is the stationary one for $x_E = 0$ and that the rate of the environmental change is measured in the unit of generation. The rate of the environmental change per generation is Δx_E. When we want to compare the population evolution of species with different lifespans, we simply change Δx_E.

4.1 Parameters and initial conditions

Parameters to be given at the start are σ_g and σ_E. All the parameters can be normalized by σ_E. So we put $\sigma_E = 1$. Then, σ_g in the only changeable parameter from model to model. The remaining parameters are given by σ_g and σ_E as

$$\sigma_\infty^2 = \frac{\sigma_g}{2}(-\sigma_g + \sqrt{\sigma_g^2 + 4\sigma_E^2}) \tag{18}$$

$$s_E = (\sigma_E/\sigma_g)^2 \tag{19}$$

$$a_E = \sqrt{1 + 4s_E} \tag{20}$$

$$s_\infty = \frac{1}{2}(a_E - 1) \tag{21}$$

$$c^2 = \frac{s_\infty + s_E + 1}{s_E} \tag{22}$$

We take the position of environment $x_E = 0$ and the initial coefficient of population distribution $N(0) = 1$. We fix the rate of environmental change Δx_E. The initial dispersion of the distribution is of stationary value σ_∞.

4.2 Numerical quadrature

We numerically carry out the convolution of the form

$$f(n, x) = s(x - n\Delta x_E) \int_{-\infty}^{+\infty} f(n-1, x') c\mathrm{Gauss}(x - x', \sigma_g) dx'. \tag{27}$$

The integrand can be any function. The value of Gaussian distribution decreases very quickly off the center. The environmental change is directed to the positive x-axis. So, we restrict the integration range to $-10 \leq x \leq 30$. This length depends on how long we follow the evolution.

We use trapezoidal or Simpson formula with fixed divisions. We divide $X_{min} \leq x \leq X_{max}$ into m subintervals. For example, $X_{min} = -10$, $X_{max} = 30$, $m = 2000$.

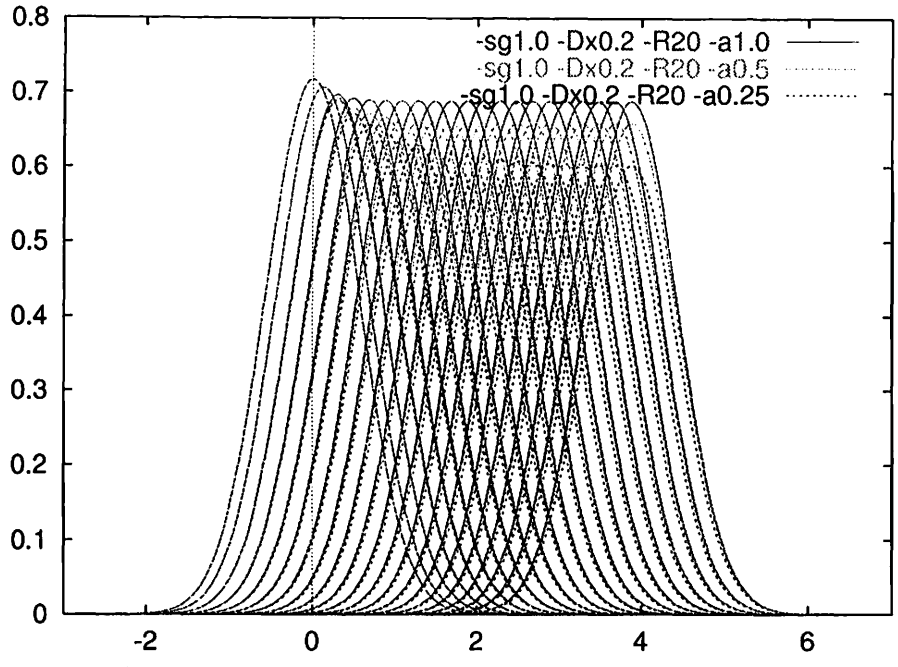

Figure 2: Population evolution depending on the change of reproduction rate. $\Delta x_E = 0.2, \sigma_g = 1.0$, $\alpha = 1.0, 0.5, 0.25$.

4.3 Transition to the stationary state

For the numerical check of the procedure, we fix the environment and follow the evolution of the form of the population distribution. We consider two cases for the position of the initial distribution: the case where the center of the initial distribution coincides with the center of environment; the case where the center of the initial distribution does not coincide with the center of environment. We consider three cases for the form of the distribution: Gaussian, Gaussian $\times \cos x$, and double peak distributions.

In all the cases, the distribution seems tend toward a Gaussian form. From this we judge that our procedure works.

5 Secular change of the environment and evolution of population

5.1 Adjustment of the reproduction rate

All species may extinguish under secular change of the environment if their reproduction rates are fixed. This is not realistic. To avoid extinction, species might have adjusted their reproduction rate. In this section, we introduce the change of reproduction rate and follow the evolution of population.

Our idea is as follows. A given species knows that the stationary state is the best. If the population becomes larger than that for stationary state, the species

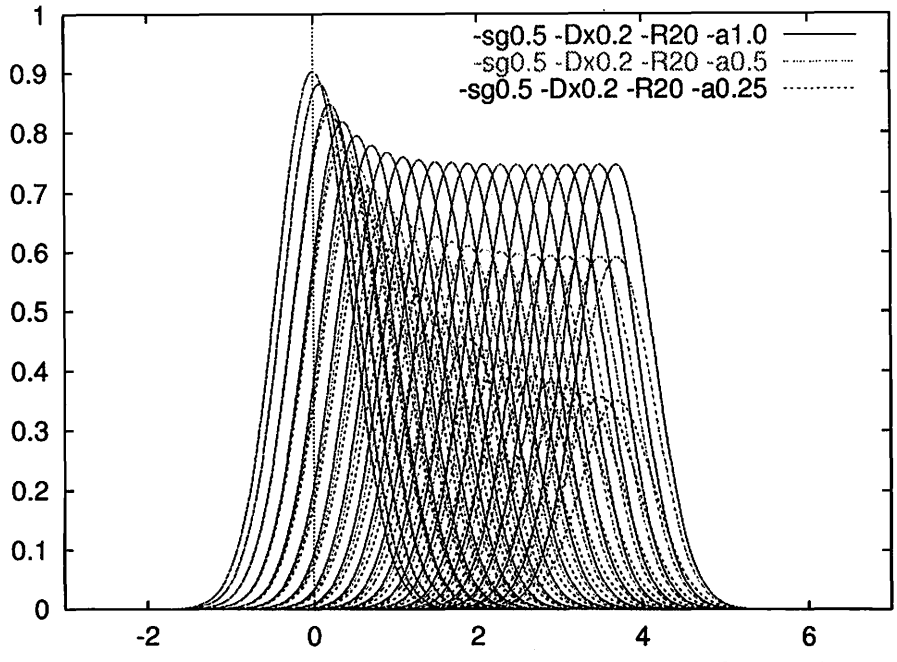

Figure 3: Population evolution depending on the change of reproduction rate. $\Delta x_E = 0.2, \sigma_g = 0.5$, $\alpha = 1.0, 0.5, 0.25$.

decreases the reproduction rate. In the reverse case, the reproduction rate increases. The reproduction rate changes as a function of the difference between the present population and the stationary population.

The simplest form may be

$$c = c_{\text{stat}} f(N_n) \tag{28}$$

Here, we consider the following three cases:

$$f_0(x) = 1 \tag{29}$$

$$f_1(x) = 1 + \alpha \frac{N_0 - x}{N_0}, \tag{30}$$

$$f_2(x) = 1 + \frac{2}{\pi} \arctan\left(\alpha \frac{N_0 - x}{N_0}\right), \tag{31}$$

where α is a parameter expressing the strength of the negative feedback. The larger α implies the stronger response to the change of population.

5.2 $f(x) = f_0(x)$

We follow the evolution of the population of organisms under the linear change in time of the environment. We want to know the dependence of the result on σ_g/σ_E. Numerical results are shown in Fig.1. The figure shows the results for $\sigma_g/\sigma_E = 0.5, 1.0, 2.0$. The interpretation is almost trivial.

1. Any species extinguish as long as the reproduction rate is of stationary value. The difference is the time until extinction.

2. The larger the dispersion of characters of offspring, the slower the extinction. The large σ_g is disadvantageous when the environment is fixed, whereas it is advantageous when the environment changes secularly.

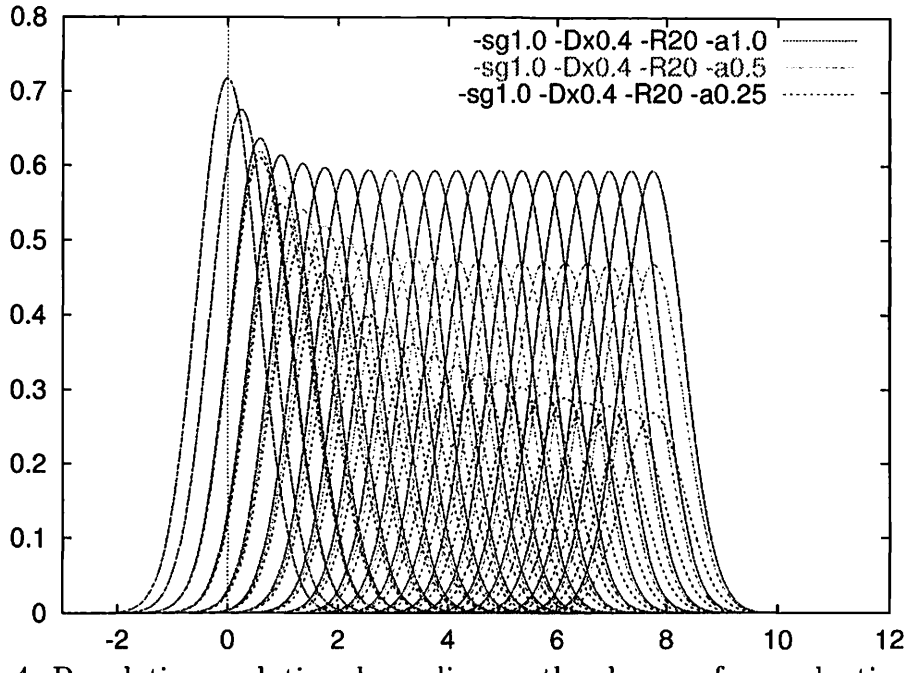

Figure 4: Population evolution depending on the change of reproduction rate. $\Delta x_E = 0.4, \sigma_g = 0.5$, $\alpha = 1.0, 0.5, 0.25$.

5.3 $f(x) = f_1(x)$

Let us next examine the population change under the linear response rule (30). We carry out four kinds of simulation to see the dependence of the result on σ_g, α, and lifespan. The results for $\Delta E = 0.2$, $\sigma_g = 1$ and $\alpha = 1.0, 0.5, 0.25$ are depicted in Fig.2. The species does not extinguish. In particular for $\alpha = 1$, the population goes back to its stationary value. This means that slow environmental change does not affect the population of species.

If we change σ_g to $\sigma_g = 0.5$ keeping other parameters fixed, then the population decreases rather rapidly. The result is exhibited in Fig.3. For the case $\alpha = 0.25$, the species may become extinct.

The rate of change of environment becomes double when $\Delta E = 0.4$. From a different view point, this is equivalent to look at the population change of a species with doubled lifespan. The results are shown in Figs.4 and 5. We should compare Figs.2 and 4 to see the effect of the difference of lifespans. Also Figures 3 and 5 should be compared. We observe two extinction in Fig.5.

5.4 $f(x) = f_2(x)$

In order to see the effect of the dispersion σ_g of the characters of species, the change of reproduction rate, and the life span, we carry out a two-dimensional survey of the stability of the population.

The results are shown in Figs.6 and 7. We fix the rule of the adjustment of the reproduction rate to $f_2(x)$. We change parameters α and σ_g. To see the effect on the lifespan, we carry out simulations for $\Delta E = 0.2$ and 0.4. In the figures, square and $+$ show the extinction and unstable oscillation of population, respectively. Symbol $\times$ shows a damped oscillation and $*$ shows a simple damping to a finite non-zero value. We interpret that regions with $\times$ and $*$ represent stable parameters.

It is apparent from the figures that extinction occurs when the dispersion of characters is small. That is, if the parents produce offspring whose characters are not so different from their own, then the species becomes easily extinct when the environment changes quickly. In addition, if the feedback coefficient α is smaller, the extinction occurs easier.

The largest difference of the structure of Figs.6 and 7 is that the area for extinction is very large in Fig.7. If the lifespan is twice, the extinction occurs very easily for small σ_g. This clearly shows that a long lifespan is disadvantageous.

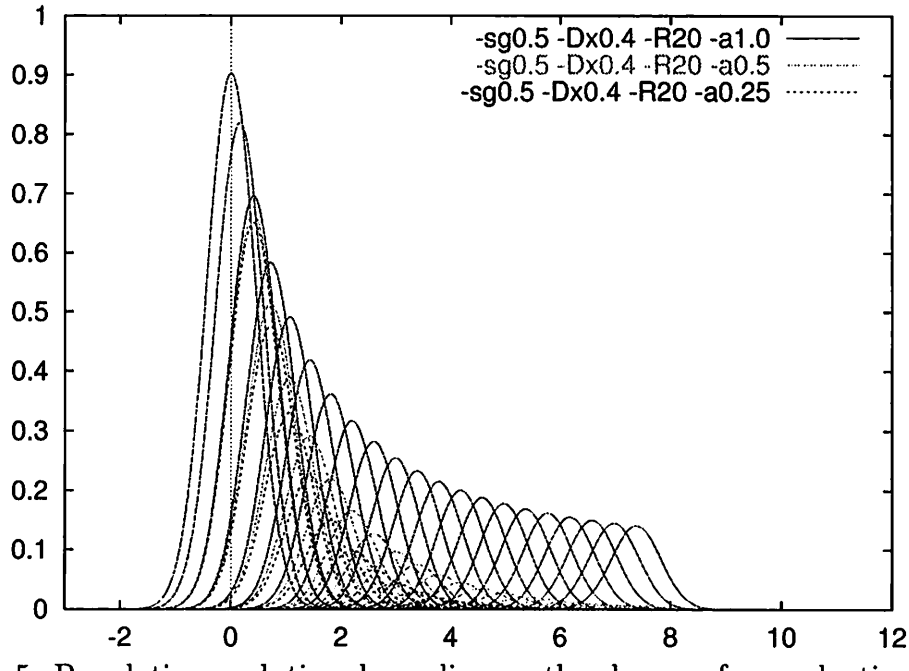

Figure 5: Population evolution depending on the change of reproduction rate. $\Delta x_E = 0.4, \sigma_g = 0.5$, $\alpha = 1.0, 0.5, 0.25$.

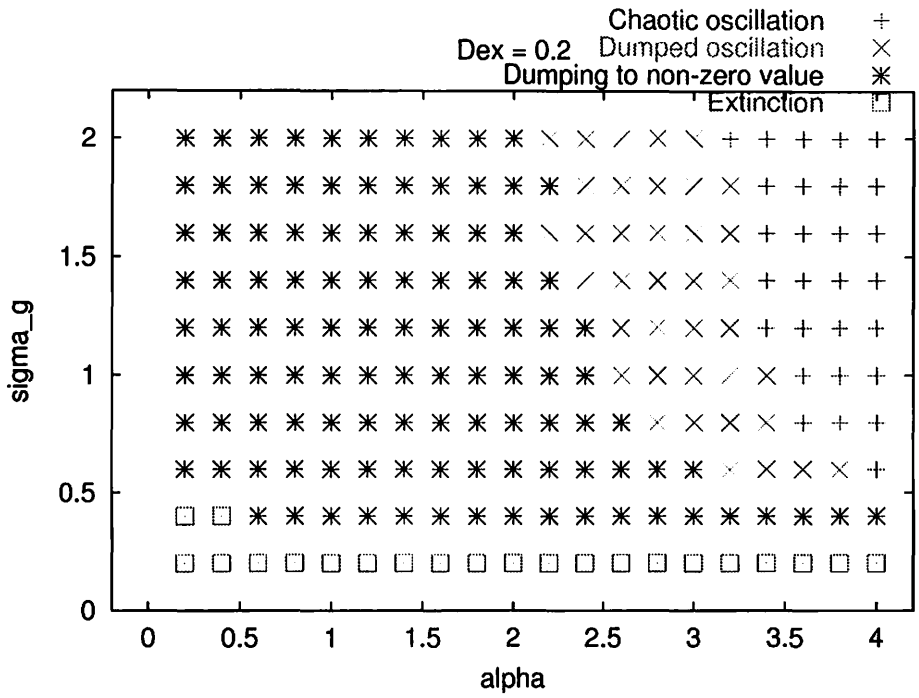

Figure 6: Parameter Dependence of the Fate of Species. The reproduction rate changes according to Eq.(31). $\Delta x_E = 0.2, \sigma_g = 0 - 2.0$, $\alpha = 0 - 4.0$. $+$, chaotic oscillation; $\times$, a damped oscillation to a non-zero value; $*$, a damping to a nonzero value; and $\square$, extinction.

6 Summary

1. As long as the reproduction rate does not change, every species becomes extinct under the secular environmental change. In this case, the large dispersion of characters slow down the extinction.

2. When the reproduction rate depends on the population according to the rule (30) or (31), 1) There are species which survive; 2) There are species which becomes extinct sensitively responding to the environmental change; 3) Species with smaller dispersion is likely to become extinct; 4) Species with longer lifetime is likely to become extinct.

Our results are very simple. However, their implications may be important.

(1) The above results explain why there were only organic beings of short life on the early Earth where the environment changed very rapidly.

(2) Diversity of life can be interpreted to be created after the cease of large scale secular change.

(3) Having diverse characters is a disadvantageous strategy in a quiet environment. But it is an advantageous strategy in a rapidly changing environment.

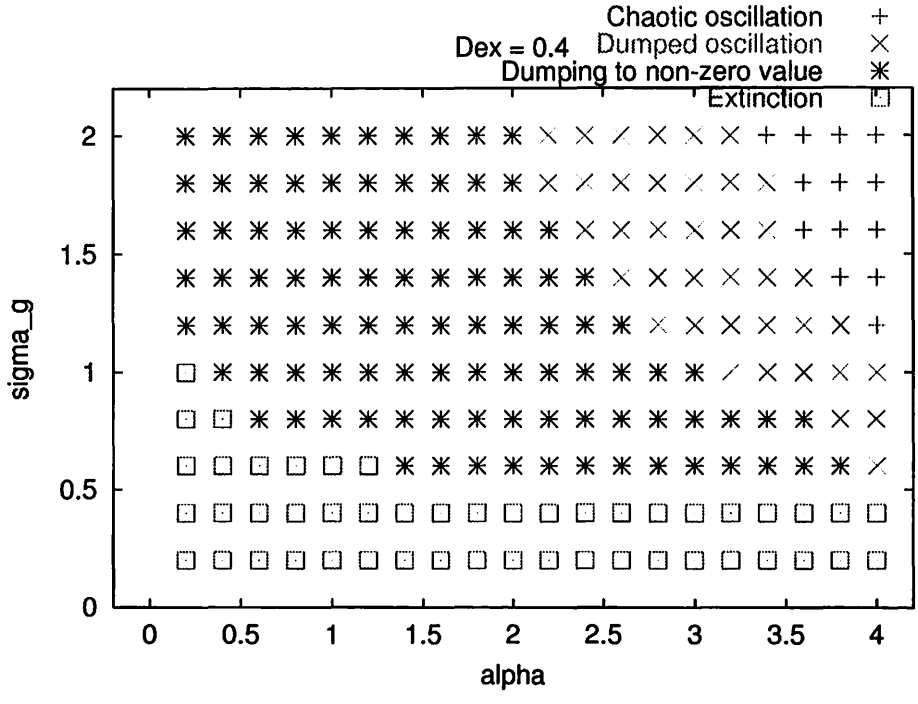

Figure 7: Parameter Dependence of the Fate of Species. The reproduction rate changes according to Eq.(31). $\Delta x_E = 0.4, \sigma_g = 0 - 2.0$, $\alpha = 0 - 4.0$.

Acknowledgment

The authors express thanks to Drs. M. Shimada and I. Isozaki(University of Tokyo) for suggestions.

References

1. Boothroyd, A.I., Sackmann, I.-J., and Fowler, W.A.: 1990, Our Sun. I. The standard model: successes and failures, Astrophys. J., vol.360, 727-736.
2. Condie, K.C.: 1989, Plate tectonics & crustal evolution, 3rd ed. Pergamon Press, Oxford.
3. Ito, T., Kumazawa, M., Hamano, Y., Matsui, T., and Masuda ,K.: 1993, Long term evolution of the solar insolation variation over 4Ga, Proc. Jpn. Acad., Ser. B **69**, 233-237(1993).
4. Kimura, M.: 1983, *The neutral theory of molecular evolution*, Cambridge University Press, Cambridge.
5. Losos, J.B., Warheit, K.I., and Schoener, T.W.: 1997, Adaptive differentiation following experimental island colonization in Anolis lizards, *Nature* **387**, 70-73.

6. Tajika, E.: 1992, *Evolution of the atmosphere and ocean of the Earth: global geochemical cycles of C, H, O, N, and S, and degassing history coupled with thermal history*, PhD Dissertation(University of Tokyo).

Appendix A.

We derive Eq.(13)

$$s_n = s_\infty + a_E \left[\left(\frac{a_E + 1}{a_E - 1} \right)^{2n} \left(\frac{2s_0 + a_E + 1}{2s_0 - a_E + 1} \right) - 1 \right]^{-1} \tag{13}$$

We start from the recursion formula

$$s_{n+1}(s_n + s_E + 1) = s_E(s_n + 1). \tag{10}$$

Let us introduce $t_n = s_n - s_\infty$ and change Eq.(10) into a recursion formula for t_n. Then

$$(t_{n+1} + s_\infty)(t_n + s_\infty + s_E + 1) = s_E(t_n + s_\infty + 1) \tag{A.1}$$

After a straight forward calculation, we obtain the following expression using $s_\infty^2 + s_\infty = s_E$(Eq.(11)).

$$t_{n+1} = t_n \frac{s_E - s_\infty}{t_n + s_\infty + s_E + 1}. \tag{A.2}$$

We further introduce

$$x_n = \frac{1}{t_n}. \tag{A.3}$$

Then

$$x_{n+1} = x_n \frac{s_E + s_\infty + 1}{s_E - s_\infty} + \frac{1}{s_E - s_\infty}. \tag{A.4}$$

This is of the form

$$x_{n+1} - \alpha = \beta(x_n - \alpha) \tag{A.5}$$

where

$$\begin{aligned} \alpha &= -\frac{1}{1 + 2s_\infty} = -\frac{1}{\sqrt{1 + 4s_E}} = -\frac{1}{a_E} \\ \beta &= \frac{s_E + s_\infty + 1}{s_E - s_\infty} \end{aligned} \tag{A.6}$$

Solving (A.6), we obtain

$$\begin{aligned} x_n &= \beta^n (x_0 - \alpha) + \alpha \\ &= \left(\frac{a_E + 1}{a_E - 1} \right)^{2n} \left(x_0 + \frac{1}{a_E} \right) - \frac{1}{a_E}. \end{aligned} \tag{A.7}$$

Going back to t_n, we have

$$t_n = \frac{1}{\left(\frac{a_E + 1}{a_E - 1} \right)^{2n} \left(\frac{1}{t_0} + \frac{1}{a_E} \right) - \frac{1}{a_E}}. \tag{A.8}$$

From this we finally get

$$s_n = s_\infty + \frac{a_E}{\left(\frac{a_E+1}{a_E-1}\right)^{2n}\left(\frac{a_E}{s_0-s_\infty}+1\right)-1}. \tag{A.9}$$

Noting the equality

$$\frac{a_E}{s_0-s_\infty}+1 = \frac{2a_E}{2s_0-a_E+1}+1 = \frac{2s_0+a_E+1}{2s_0-a_E+1} \tag{A.10}$$

we rewrite (A.9) as

$$\begin{aligned} s_n &= s_\infty + a_E\left[\left(\frac{a_E+1}{a_E-1}\right)^{2n}\left(\frac{2s_0+a_E+1}{2s_0-a_E+1}\right)-1\right]^{-1} \\ &= s_\infty + \frac{a_E(a_E-1)^{2n}(2s_0-a_E+1)}{(a_E+1)^{2n}(2s_0+a_E+1)-(a_E-1)^{2n}(2s_0-a_E+1)} \end{aligned} \tag{A.11}$$

Appendix B

We derive

$$\begin{aligned} &\log\left(\frac{N(n)}{N(0)}\right) = \frac{n}{2}\log\left(c^2\cdot s_E\right) \\ &-\frac{1}{2}\sum_{i=0}^{n-1}\left\{\log\left(\frac{1}{4}(a_E+1)^2 + a_E\left[\left(\frac{a_E+1}{a_E-1}\right)^{2n}\left(\frac{2s_0+a_E+1}{2s_0-a_E+1}\right)-1\right]^{-1}\right)\right\}. \end{aligned} \tag{15}$$

and

$$\log\left(\frac{N(n)}{N(0)}\right) = -\frac{1}{2}\sum_{i=0}^{n-1}\log(1+\varepsilon_i).$$

where

$$\varepsilon_i = \frac{4a_E}{(a_E+1)^2}\left[\left(\frac{a_E+1}{a_E-1}\right)^{2i}\left(\frac{2s_0+a_E+1}{2s_0-a_E+1}\right)-1\right]^{-1}$$

The condition that the population is stationary is

$$c^2 = \frac{\sigma_\infty^2+\sigma_g^2+\sigma_E^2}{\sigma_E^2}. \tag{B.1}$$

From Eq.(6), the population change from generation to generation is given by

$$\frac{N(n+1)}{N(n)} = c\left(\frac{\sigma_E^2}{\sigma_n^2+\sigma_E^2+\sigma_g^2}\right)^{1/2} = c\left(\frac{s_E}{s_n+s_E+1}\right)^{1/2} \tag{B.2}$$

If we introduce $\tilde{N}_n = \log N(n)$, then (B.2) becomes

$$\tilde{N}_{n+1}-\tilde{N}_n = \log c + \frac{1}{2}\log s_E - \frac{1}{2}\log(s_n+s_E+1). \tag{B.3}$$

from which we obtain

$$\begin{aligned}\tilde{N}_n &= \tilde{N}_0 + \sum_{i=0}^{n-1}\left(\log c + \frac{1}{2}\log s_E - \frac{1}{2}\log(s_i + s_E + 1)\right) \\ &= \tilde{N}_0 + n\left(\log c + \frac{1}{2}\log s_E\right) - \frac{1}{2}\sum_{i=0}^{n-1}\log(s_i + s_E + 1)\end{aligned} \tag{B.4}$$

Let us evaluate the third term in the right hand side of the above equation.

$$s_i + s_E + 1 = s_\infty + s_E + 1 + a_E\left[\left(\frac{a_E+1}{a_E-1}\right)^{2n}\left(\frac{2s_0 + a_E + 1}{2s_0 - a_E + 1}\right) - 1\right]^{-1} \tag{B.7}$$

or

$$s_i + s_E + 1 = \frac{1}{4}(a_E+1)^2 + a_E\left[\left(\frac{a_E+1}{a_E-1}\right)^{2n}\left(\frac{2s_0 + a_E + 1}{2s_0 - a_E + 1}\right) - 1\right]^{-1} \tag{B.8}$$

the required equation directly from this.

$$\begin{aligned}&\log\left(\frac{N(n)}{N(0)}\right) = \frac{n}{2}\log\left(c^2 \cdot s_E\right) \\ &-\frac{1}{2}\sum_{i=0}^{n-1}\left\{\log\left(\frac{1}{4}(a_E+1)^2 + a_E\left[\left(\frac{a_E+1}{a_E-1}\right)^{2i}\left(\frac{2s_0 + a_E + 1}{2s_0 - a_E + 1}\right) - 1\right]^{-1}\right)\right\}.\end{aligned} \tag{B.9}$$

Since $c^2 \cdot s_E = \frac{1}{4}(a_E+1)^2$, we have

$$\begin{aligned}&\log\left(\frac{N(n)}{N(0)}\right) = n\log\left(\frac{1}{2}(a_E+1)\right) \\ &-\frac{1}{2}\sum_{i=0}^{n-1}\left\{\log\left(\frac{1}{4}(a_E+1)^2 + a_E\left[\left(\frac{a_E+1}{a_E-1}\right)^{2i}\left(\frac{2s_0 + a_E + 1}{2s_0 - a_E + 1}\right) - 1\right]^{-1}\right)\right\}.\end{aligned} \tag{B.10}$$

If we define

$$\varepsilon_i = \frac{4a_E}{(a_E+1)^2}\left[\left(\frac{a_E+1}{a_E-1}\right)^{2i}\left(\frac{2s_0 + a_E + 1}{2s_0 - a_E + 1}\right) - 1\right]^{-1} \tag{B.11}$$

Then (B.10) becomes of a simpler form as

$$\log\left(\frac{N(n)}{N(0)}\right) = -\frac{1}{2}\sum_{i=0}^{n-1}\log(1+\varepsilon_i). \tag{B.12}$$

An estimation of upper limit masses of υ Andromedae planets

Takashi Ito and Shoken M. Miyama

National Astronomical Observatory, Mitaka, Tokyo 181-8588, Japan

tito@cc.nao.ac.jp

ABSTRACT

An estimation of upper limit masses of an extrasolar planetary system, υ Andromedae, is described. Doppler observation of extrasolar planets through the radial velocity displacement of their host stars can only determine lower limits of planetary masses, and inevitably includes uncertainties due to the unknown line-of-sight inclination of planetary orbits, $1/\sin i$. However, this inherent uncertainty about mass determination included in the Doppler measurement may be supplemented by long-term numerical integrations of planetary orbital motions. Our numerical integrations described in this letter, though only two outer companions around υ Andromedae are included, intend to find any relation between the planetary masses and their dynamical timescales of instability. We integrate the planetary orbits with various initial conditions of masses and angle variables to investigate which kind of initial configuration produces the stable orbits during the timescale of υ Andromedae host star's age. According to the numerical results starting from Lick observatory dataset, υ Andromedae planetary system is likely to remain stable over the timescale of its host star's age if $\sin i \geq 0.8$. In this case we may estimate that the upper limit masses of υ Andromedae planets in our model is about $1/0.8 \sim 1.25$ times larger than its minimum (i.e. when $\sin i = 1$). Another interesting feature in the orbital motion of υ Andromedae planets is that the longitudes of pericenter of outer two companions are likely to align, which leads to stabilize the system. Systems where this orbital alignment is not well achieved are easy to become unstable.

Subject headings: planets and satellites: general — celestial mechanics — stars: individual (υ Andromedae)

1. Introduction

Researches of dynamical evolution of extrasolar planetary systems are important when we consider the origin of the systems. Among such researches, the investigation of long-term stability of planetary orbits, is in some degree related to uncertainties in observational data of orbital elements. Determined orbital elements of extrasolar planets must contain some uncertainties by

observational errors, which can lead to a large diversity in orbital evolutions afterwards due to chaotic characters in planetary motion. But since most of the extrasolar planetary systems so far discovered had only one planet around their host stars, they could not have been served as dynamical tests of stability.

Recently, a quite suitable example for the dynamical test of stability has been found — three planets around υ Andromeda (Butler et al. 1999; Lissauer 1999). This planetary system is known by its highly chaotic dynamical character. Since the maximum Lyapunov exponent is estimated as $\sim 1/5000$ years^{-1} (Laughlin & Adams 1999), the planets' future behavior is quite sensitive to starting initial conditions. An ensemble of numerical integrations are necessary to grasp the dynamical stability of υ Andromedae planetary system beginning from different initial conditions.

There are mainly two purposes in our numerical integrations on υ Andromedae planets. One is to check the degree of divergence in their orbital evolutions, especially the diversity of instability timescales. We want to know the possible variation range of instability timescales of the planets due to the observational uncertainties in initial orbital elements and masses. The other, which we think is more meaningful for astronomy, is to estimate the upper limit of υ Andromedae planetary masses by numerical integrations. Among the several methods to detect extrasolar planets, Doppler observation of the radial velocity displacement of central stars is currently most powerful and popular technique. Most of extrasolar planets including υ Andromedae have been detected by the Doppler observation (Marcy et al. 2000). However, there is an inevitably weak character in the Doppler measurement. Since the Doppler measurement can only determine a product $m \sin i$ (where m is the planetary mass and i is the inclination angle between the line-of-sight of observers and a normal to the orbital plane of planets), planetary mass m itself cannot be determined uniquely except for its lower limit. When $\sin i = 1$ (i.e. viewing the planetary orbits "edge-on"), actual planetary masses should be smallest. In contrast when $\sin i \to 0$ (i.e. "face-on" view of the planetary orbits), actual masses should be very large, and they are quite difficult to be accurately determined. Although an analysis of Hipparcos astrometric measurements gives the mass of the outermost companion (d), it contains a large uncertainty such as $m_d = 10.1^{+4.7}_{-4.6}$ Jupiter mass (Mazeh et al. 1999). No sign of the innermost planet (b)'s transit in front of the υ Andromedae host star implies that $i < 83°$, which means $\sin i < 0.993$ (Lissauer 1999). This, however, also serves only as a weak constraint for planetary masses.

Nevertheless, this inherent uncertainty about mass determination included in the Doppler observation may be somewhat supplemented by numerical integrations of planetary orbital motions due to following facts: (1) Planetary systems which contain more than one planet generally becomes unstable within finite timespans, (2) this instability timescale becomes shorter when gravitational interaction among planets is stronger, and (3) it is natural to consider that existing planetary systems have been kept dynamically stable at least during the timescale of its host star's age.

As for this topic we can consult an intensive numerical study by Chambers, Wetherill and Boss (1996, hereafter called CWB) which provides a detail on the dynamical stability of protoplanetary

systems. CWB defined and measured the instability timescale T_I as being the time elapsing between the initial stable configuration and the first close encounter, varying the strength of interaction among particles. Then, the resulting relationship between the logarithm of T_I and initial separation normalized by the mutual Hill radius (proportional to $m^{1/3}$ and distance from its central mass) is well approximated by a linear function, which was confirmed by Yoshinaga et al. (1999) and Ito & Tanikawa (1999) afterwards. The methods and results by CWB are applicable to υ Andromedae planetary system. Instability timescale T_I of υ Andromedae planetary orbits will be very long if we adopt small planetary masses. But if we adopt large planetary masses, the instability timescale will become shorter; we may find a certain upper limit of planetary masses where the instability timescale of the system is shorter than the timescale of the host star's age, $\sim 2.6 \times 10^9$ years. Thus we can possibly estimate the upper limit of planetary masses m, and at the same time, the line-of-sight inclination of planetary orbits i.

In this letter we describe our first step to estimate the upper limit masses of υ Andromedae planets using a two-dimensional and two-companion dynamical model. The orbital motions of υ Andromedae planets themselves are interesting in terms of celestial mechanics, which can be understood as a kind of secular resonance between two planetary orbits and be partly explained by averaged-Hamiltonian map.

2. Dynamical model and numerical method

Although υ Andromedae planetary system compose a typical few-body point mass system, total degrees of freedom end up with 18 when we consider whole three planets in three dimensional space. Hence we only take outer two companions (c and d) in coplanar orbits into account to save the amounts of numerical computation here. The neglect of the innermost companion (b) can be somewhat justified because the dynamical coupling between the middle (c) and outermost (d) planet is much stronger than that between innermost (b) and middle (c) ones: normalized distance by the mutual Hill radii between the companion b and c is 19.6, whereas that between c and d is 8.5 when $\sin i = 1$. In addition, we supplement our omission of the companion b by incorporation of a circular ring potential which represents the time-averaged effect of the innermost planet (Nacozy & Diehl 1978). All the orbital elements and masses used in our numerical integrations are adopted from Butler et al. (1999), and are listed in Table 1. No consideration is given to relativity, gas drag, and other non-gravitational or dissipative effects.

Reduced degrees of freedom by adopting coplanar orbits apparently seem to shorten the timescale of instability compared with three dimensional orbits. However, three-dimensional orbits may not significantly increase the time required for becoming unstable, since the angular momentum deficit can be exchanged between eccentricities and inclinations and may helps the planets to avoid interact so strongly.

As for the mass of υ Andromedae host star we take $M = 1.3 M_\odot$ where $M_\odot$ is the solar mass.

Semimajor axes a of planets are determined by the Kepler's third law, $G(M+m) = (2\pi/P)^2 a^3$ where G is the gravitational constant and P is the orbital period. Fixing initial eccentricities e and orbital periods P (and hence initial semimajor axes a) as their nominal values, we vary longitudes of pericenter ϖ and mean anomalies l randomly within their observational uncertainties in Table 1. Mean anomalies l are converted from the pericenter passage time T_p using the time epoch of J2000.0.

We have defined the instability timescale T_I as being the time elapsing between the initial stable configuration and the final unstable configuration. A system is defined unstable when either planet's eccentricity becomes unity: then the particle is ejected out of the system, or falls into the central star. When a system does not experience any close encounter, integration is terminated after 3×10^9 years at most. Final results are gathered and plotted on $(\sin i, T_I)$ diagrams. Eight to twenty integrations per one $\sin i$ bin are performed using different initial orbital elements from $\sin i = 0.4$ to $\sin i = 1.0$ stepping 0.1.

As a numerical integration scheme, we mainly utilize the second-order symplectic map (Wisdom & Holman 1991; Kinoshita et al. 1991) with a special "warm start" procedure (Saha & Tremaine 1992, 1994). We take small stepsizes (2 or 4 days) for the integrations.

All of our integrations are forward; progressing to future direction in time axis. But we do not intend to inspect the actual fate of the planetary system in the real future. Our intention is simply to give any constraints on the long-term stability and planetary masses of the system. For this purpose, we adopt the timescale of the host star's age as our longest integration period; we consider the timescale as a minimum measure of "long-term" here.

3. $(\sin i, T_I)$ diagrams of υ Andromedae planets

Results of our numerical integrations for two kinds of dataset (Lick and AFOE. See Butler et al. (1999) for detail) are shown in Figures 1 (Lick) and 2 (AFOE) as filled and open circles. Note that all the open symbols indicate that although the numerical integrations have been stopped there for certain reasons, the systems were still stable; instability timescales should be much longer than actually shown by the open symbols there. Numbers located rightside at the open circles denote that the results of several integrations are overlapped at the open circles: for example, "$\bigcirc^5$" near at $(\sin i, T_i) = (0.9, 3 \times 10^9)$ means that the open circle represents the results from five numerical integrations altogether. We also plot the results in other papers in the figures: Rivera and Lissauer (2000, filled and open triangles) and two other results based on Lick/AFOE combined dataset, Laughlin and Adams (1999, upside-down filled triangles), and Nakai and Kinoshita (2000, in preparation; filled and open squares). Rivera and Lissauer (2000)'s results based on the combined dataset are not plotted.

We can find major four viewpoints in Figures 1 and 2. (i) Instability timescales are lengthen exponentially as $\sin i$ increases in both figures. This trend is essentially the same which was pointed

Table 1: Initial orbital elements and masses used in the integrations.

	Companion c		Companion d	
	Lick	AFOE	Lick	AFOE
$m \sin i$ (M_J)	1.98	1.96	4.11	5.70
e	0.23	0.22	0.36	0.44
P (days)	242.0	234.5	1269.0	1481.2
ϖ (deg)	261.0 ± 47	219.2 ± 14	236.0 ± 14.6	245.9 ± 5.9
T_p (JD)	2451131.24 ± 23.4	2450140.4 ± 8.3	2453813.46 ± 32.0	2450046.8 ± 16.1

P is orbital period, T_p is pericenter passage time whose epoch is J2000.0, e is eccentricity, ϖ is longitude of pericenter, $m \sin i$ is the product of planetary mass and the inclination between the line-of-sight of observers and a normal to the orbital plane. The unit of mass is Jupiter's mass, M_J. As for e and P, only their nominal values are adopted.

Fig. 1.— $(\sin i, T_l)$ diagram for numerical integrations using Lick orbital elements. Our results are represented by filled and open circles. All the open symbols indicate that although the numerical integrations have been stopped there for certain reasons, the systems were still stable; instability timescales should be much longer than actually shown by the open symbols there. Numbers located rightside at the open circles denote that the results of several integrations are overlapped at the open circles. Results in other papers are also plotted: Rivera and Lissauer (2000, filled and open triangles), Laughlin and Adams (1999, upside-down filled triangles; based on Lick/AFOE combined dataset), and Nakai and Kinoshita (2000, in preparation, filled and open squares; based on Lick/AFOE combined dataset). Note that horizontal positions of our open circles are slightly shifted toward the rightward direction (larger $\sin i$) to avoid overlapping with other filled symbols. They originally locate just on the same x-position as filled circles. The open triangle and open square around $(1.0, 1 \times 10^9)$ points are also shifted slightly leftward and rightward for the same reason.

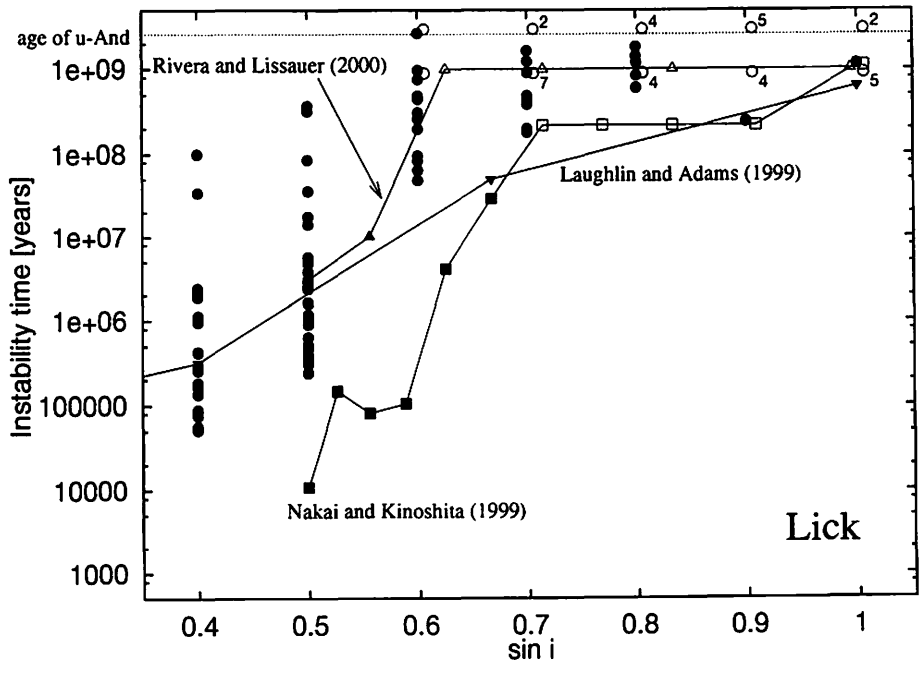

Fig. 2. Same as Figure 1, but for AFOE dataset.

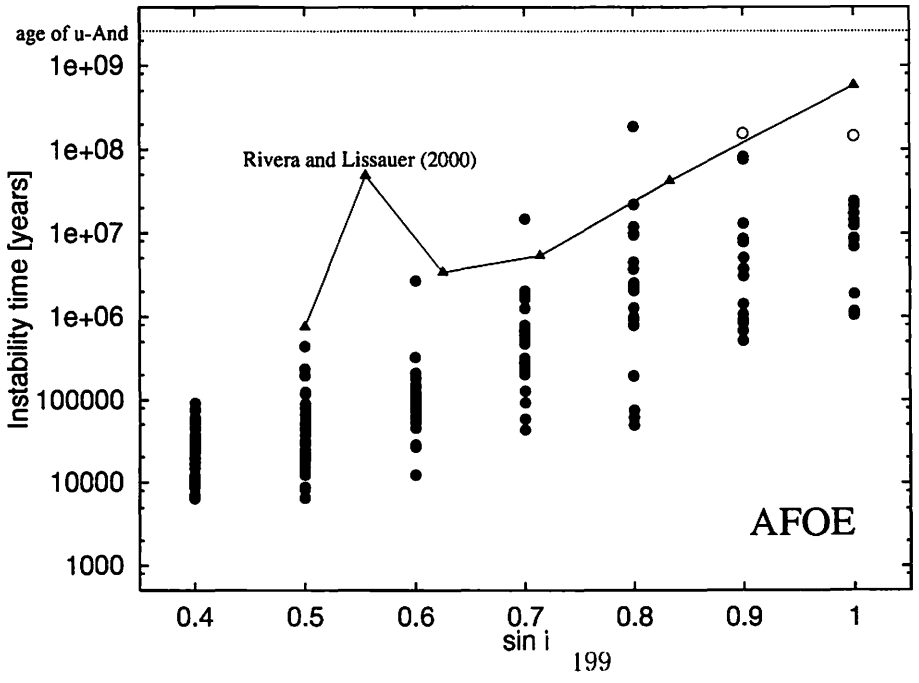

out by CWB for the terrestrial protoplanet system. (ii) There is a wide variety in instability timescales of υ Andromedae planets, two or three, even four orders of magnitude especially in small $\sin i$ (= large mass) area. It reflects the chaotic character of this planetary system as pointed out by Laughlin and Adams (1999). (iii) When using Lick dataset (Figure 1), most integrations (80 out of 82) in $\sin i \leq 0.6$ are likely to become unstable before they reach the timescale of the host star's age. When $\sin i = 0.7$, 8 integrations became unstable and 9 integrations survived, though 7 of 9 stable integrations were truncated after 1×10^9 years. When $\sin i \geq 0.8$, there are much more open circles (24) than filled circles (9) which indicate that the system are likely to remain stable over the host star's age in many orbits. Although the number of integration is still not enough to derive some definite statistical conclusions, the upper limit of υ Andromedae planetary masses may be set as $1/0.8 = 1.25$ times larger than their minimum (i.e. $\sin i = 1$) since the system's probability of being kept stable during the host star's age largely exceeds the probability of becoming unstable when $\sin i \geq 0.8$. (iv) When using AFOE dataset (Figure 2), almost all integrations (176 out of 178) became unstable before they reached the host star's age. It is probably due to the relatively large nominal eccentricity and mass of the outermost planet (companion d) in AFOE dataset ($e_d = 0.44$ and $m_d \sin i = 5.70 M_J$) compared with Lick dataset ($e_d = 0.36$ and $m_d \sin i = 4.11 M_J$). Inclusion of the AFOE initial orbital elements in the combined dataset may be one of the causes of rather shorter instability timescales in Laughlin and Adams (1999) and Nakai and Kinoshita (2000) indicated in Figure 1. Some of our preliminary calculations using minimum planetary eccentricities and masses of AFOE dataset show much more stable orbital evolution.

In some integrations using AFOE dataset, 1:6 mean motion resonance is recognized for some time interval. But the resonance is not so strong, and is likely to break up into instability in rather short timescale, $\sim 10^5$ to $\sim 10^6$ years.

4. Orbital alignment and stability

Large diversity of instability timescales in υ Andromedae planetary systems as in Figures 1 and 2 can be better understood by viewing the evolution of planetary orbital elements. Examples of the orbital evolution in two numerical integrations for Figure 1 are shown as Figures 3 and 4. Both of the two integrations start from the nominal eccentricities ($e_c = 0.23, e_d = 0.36$). Initial longitudes of pericenter are ($\varpi_c = 222.7°, \varpi_d = 234.7°$) in Figure 3, and ($\varpi_c = 275.2°, \varpi_d = 232.3°$) in Figure 4, respectively. Planetary masses are the largest, i.e. $\sin i = 0.4$ in both cases. One integration (shown in Figure 4) was terminated after about 2.7×10^5 years because the eccentricity of the inner planet (c) has reached unity, while the other (Figure 4) remained stable for several 10^7 years.

One of the major reasons which produces such large difference in orbital evolutions of above two cases is the alignment of longitudes of pericenter. In many of stable orbits in Figure 1 using Lick dataset, pericenters of the two companions align: $\delta\varpi = \varpi_c - \varpi_d$ is kept small, which can help the planets to avoid close encounters and keep the system stable for long timespan. This orbital

Fig. 3.— Eccentricities (e_c, e_d) and difference in longitudes of pericenter $(\delta\varpi = \varpi_c - \varpi_d)$ of the two planets in a numerical integration starting from Lick dataset, $\sin i = 0.4$. Initial elements are $e_c = 0.23$, $\varpi_c = 222.7°$, $e_d = 0.36$, $\varpi_d = 234.7°$.

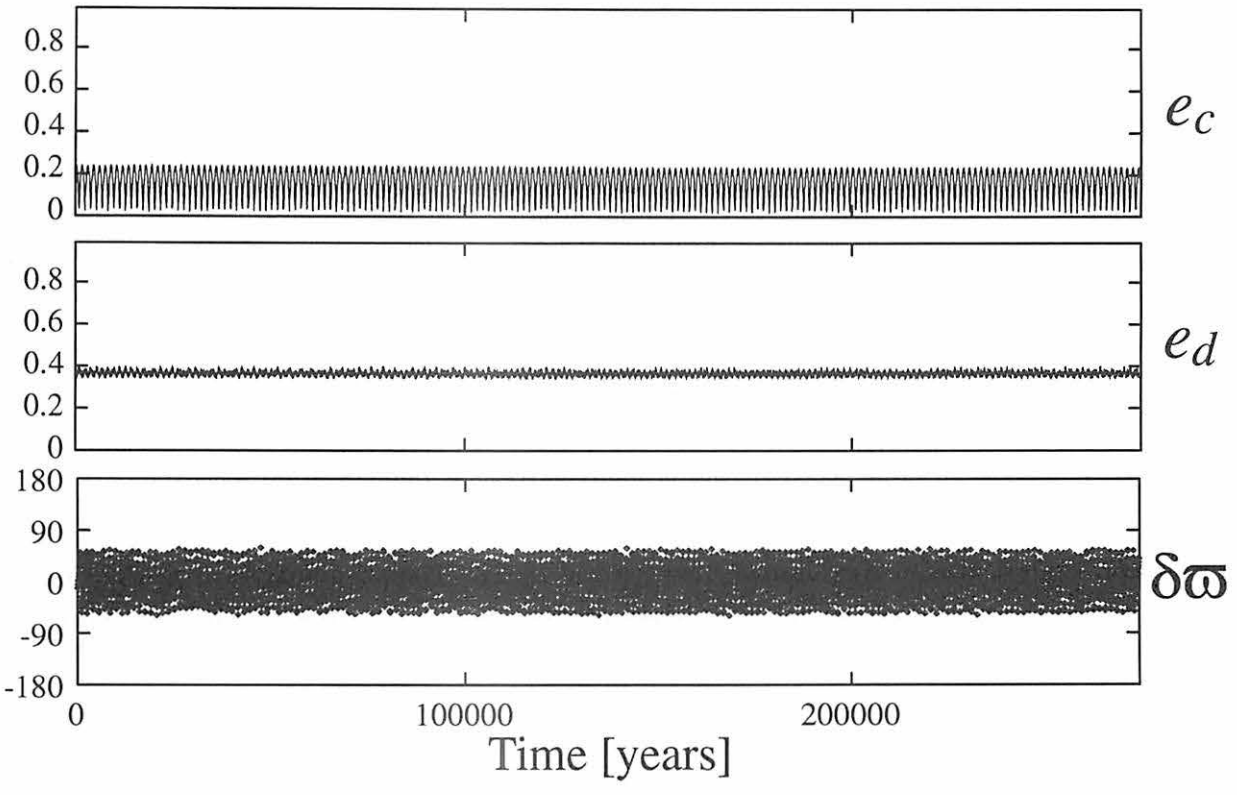

Fig. 4.— Same as Figure 3, but with different initial orbital elements. Initial eccentricities and longitudes of pericenter are $e_c = 0.23$, $\varpi_c = 275.2°$, $e_d = 0.36$, $\varpi_d = 232.3°$.

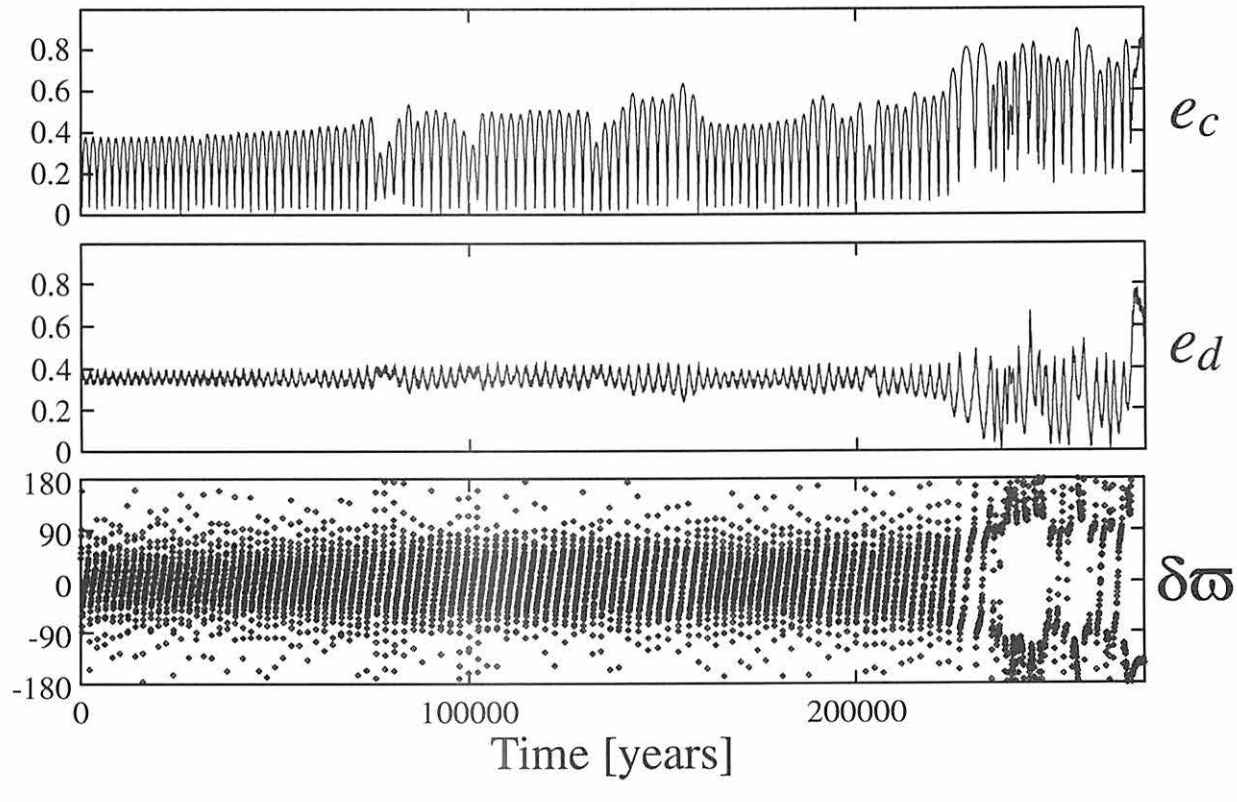

alignment is a typical example of so-called secular orbit-orbit resonances frequently found in planet–satellite systems in our solar system, such as Saturn's satellites Titan and Rhea (Greenberg 1977; Pauwels 1983).

Variation of eccentricity is regular and stable in the aligned system (Figure 3), while it is somewhat irregular and invokes instability in the non-aligned system (Figure 4). Libration of $\delta\varpi$ is not so rigid in Figure 4, altering to circulation after several 10^5 years. Due to this destruction of the orbital alignment, eccentricities of planetary orbits are pumped up, and the companion c is finally ejected out of the system.

Such ejection of middle planet is the most typical feature of the final state of υ Andromedae planetary system in our integrations. Though our integrations are terminated when the ejection occurs, another planet will remain in highly eccentric orbit afterwards due to the close encounter. This may be a cause of large eccentricities of many extrasolar planets so far discovered.

The difference between the aligned and non-aligned systems is qualitatively explained by drawing a semi-analytical equi-Hamiltonian map (Kozai 1962). The semi-analytical method is often used when analyzing global behaviour of small particles such as asteroids or Kuiper-belt objects (Nakai & Kinoshita 1985; Yoshikawa 1989). Here we consider the companion c as a massless particle which moves along the equi-potential field dominated by the host star and more massive companion, d. When the Hamiltonian of υ Andromedae planets $H(a_c, e_c, \varpi_c, l_c; a_d, e_d, \varpi_d, l_d)$ is averaged in terms of short periodic variables l_c and l_d, conjugate semimajor axes a_c and a_d become constant. Then, final form of the averaged Hamiltonian $\overline{H}$ whose degree of freedom is reduced to unity is expressed as $\overline{H}(e_c, \varpi_c - \varpi_d)$ when we fix the eccentricity of the perturber, e_d. Thus the companion c's eccentricity is represented as a function of only $\varpi_c - \varpi_d (= \delta\varpi)$. An example of such equi-Hamiltonian map is drawn as Figure 5 for $\sin i = 0.4$ in Lick dataset. Results of the two numerical integrations are plotted together on Figure 5 as crosses (for the aligned system in Figure 3) and open circles (for the non-aligned system in Figure 4). Though the libration area indicated by the numerical results for the aligned system (crosses) lies in somewhat lower eccentricity region than that of the semi-analytical curves, we can see that such a crude approximation of companion c's dynamical behaviour as a massless particle fairly well reflects the actual motion obtained from numerical integrations. Initial starting points of the aligned and non-aligned systems locate not so far: $(e_c, \delta\varpi) = (0.23, -12.0)$ for the aligned system, and $(e_c, \delta\varpi) = (0.23, 42.9)$ for the non-aligned system. However, the two starting points seem to be decoupled in and out of the libration area beyond a separatrix.

In Figure 5, strong mutual perturbation among the planets makes a difference between the semi-analytical and numerical results. Short periodic oscillations in numerical results become more remarkable when the the mutual interaction is strong, which makes the particle easy to move around among several energy contours. Thus in a large mass (i.e. small $\sin i$) system as shown in Figure 5, the companion c is likely to leave its initially given track. This pumps up the planet's eccentricity, leading to instability of the system. When the planetary masses are small (i.e. large $\sin i$), mutual

Fig. 5.— Background continuous curves represent the semi-analytical equi-Hamiltonian contours in $(e_c, \delta\varpi = \varpi_c - \varpi_d)$ phase space when $e_d = 0.36$ and $\sin i = 0.4$. Crosses ($\times$) and open circles ($\bigcirc$) represent the results of the two numerical integrations described in Figures 3 and 4, respectively. Initial positions are $(e_c, \delta\varpi) = (0.23, -12.0)$ for the crosses and $(e_c, \delta\varpi) = (0.23, 42.9)$ for the open circles.

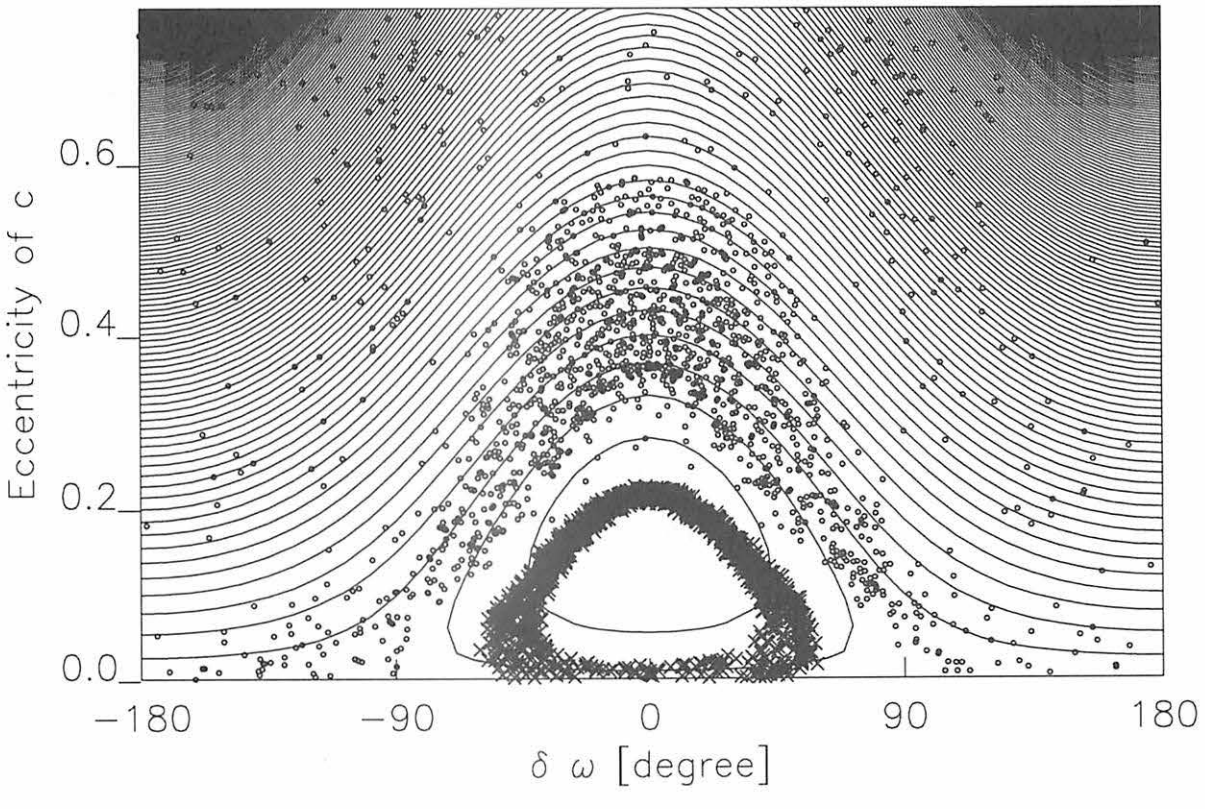

interaction is weak. In this case, the planet is well trapped on its initial track, not moving around among neighboring contours so freely.

5. Discussion

Our numerical integrations partly indicate that υ Andromedae planetary system can survive stably during the timescale of the host star's age if $\sin i \geq 0.8$. Of course, the chaotic nature of the system needs more and more numerical integrations. Future inclusion of mutual planetary orbital inclination in our dynamical model will require further increase in the number of numerical integrations.

On the other hand, longer-term observations of υ Andromedae planets, especially that of the outermost and most massive companion (d) whose orbital period is much longer than others, should give us their revised orbital elements such as described in Laughlin and Adams (1999, for Lick dataset). Eccentricity of the companion d is reduced much in the revised Lick dataset in Laughlin and Adams (2000, $e_d = 0.30 \pm 0.05$), and also according to our private communication to Geoffrey Marcy (2000; $e_d = 0.31$) who is one of the discoverers of υ Andromedae planets. This fact will lead to more stable feature of the planetary system.

The authors have greatly benefited from stimulating discussions with and encouragement from Hiroshi Nakai and Kiyotaka Tanikawa. This study was supported by the ADAC scientific simulation project, National Astronomical Observatory of Japan (dti02-1999).

REFERENCES

Butler, R.P., Marcy, G.W., Fischer, D.A., Brown, T.W., Contos, A.R., Korzennik, S.G., Nisenson, P., & Noyes, R.W. 1999, ApJ, 526, 916.

Chambers, J.E., Wetherill, G.W., & Boss, A.P. 1996, Icarus, 119, 261.

Greenberg, R. 1977, Vistas Astron., 41, 209.

Ito, T. & Tanikawa, K. 1999, Icarus, 139, 336.

Kinoshita, H., Yoshida, H., & Nakai, H. 1991, Celes. Mech. Dyn. Astron., 50, 59.

Kozai, Y. 1962, AJ, 67, 591.

Laughlin, G. & Adams, F.C. 1999, ApJ, 526, 881.

Lissauer, J.J. 1999, nature, 398, 659.

Marcy, G.W., Cochran, W.D., & Mayor, M. 2000, in Protostars and Planets IV, ed. Mannings, V., Boss, A.P., & Russell, S.S. (Tucson: University of Arizona Press), in press.

Mazeh, T., Zucker, S., Torre, A.D., & van Leeuwen, F. 1999, ApJ, 522, L149.

Nacozy, P.E. & Diehl, R.E. 1978, AJ, 83, 522.

Nakai, H. & Kinoshita, H. 1985, Celes. Mech., 36, 391.

Pauwels, T. 1983, Celes. Mech., 30, 229.

Rivera, E.J. & Lissauer, J.J. 2000, ApJ, submitted.

Saha, P. & Tremaine, S. 1992. AJ, 104, 1633.

Saha, P. & Tremaine, S. 1994. AJ, 108, 1962.

Wisdom, J. & Holman, M. 1991. AJ, 102, 1528.

Yoshikawa, M. 1989, A&A, 213, 436.

Yoshinaga, K., Kokubo, E., & Makino, J. 1999, Icarus, 139, 328.

υ Andromedae 惑星系の安定性
Stability of the υ Andromedae planetary system

中井宏、木下宙（国立天文台）
H. Nakai and H. Kinoshita
National Astronomical Observatory

Abstract

We investigate the stability of the υ Andromedae planetary system based on the various values of the masses of planets and the mean longitudes of planets. Using the semi-analytical theory, the differences in the londitudes of periastron between outer two planets librate around 0° with about 70° amplitudes. This results of the theory agree qualitatively with the results obtained by the numerical integrations. As its amplitude of libration increases, the stability of the system decreases in general. The planetary system is stable when the difference in the longitudes of periastron between outer two planets librates less than about 60° regularly, but the system is unstable when the difference in the longitudes of periastron circulates. There are chaotic regions between stable and unstable regions. It is necessary that the difference in the longitudes of periasron between outer planets librates for the stability of the υ Andromedae planetary system.

1 はじめに

LickグループやAFOEグループによるドップラー観測からバトラー達はυ Andromedae の３惑星の軌道を決定した。しかし、決定された軌道要素には不確定な部分があり、特に、平均近点離角、軌道傾斜角、惑星の質量等は正確に決定されていない。不確定な軌道要素が惑星系の安定性にどう影響するかを調べた。質量、平均経度等を強制的に変化させた種々の初期値で数値積分を行い、長期間惑星系が安定であるための条件について検討した。

2 数値積分

2.1 初期値

表１にバトラー達(1999)によって決定されたLickグループ、AFOEグループ、Lick/AFOE混合データから求まった３惑星の軌道要素を示す。AFOEグループとLick/AFOEの軌道要素を数値積分の初期値とし両者の差を検討した。軌道傾斜角、昇交点経度は不確定なため３惑星(b,c,d) の軌道傾斜角をそれぞれ１度、３度、１度とし、各惑星の昇交点経度は全て０度と仮定した。

ドップラー観測から推定される惑星質量(M^*)は軌道面の法線と視線方向のなす角をiとすると、$M^* = M \cdot \sin i$ でしか決定することができない。ただし、Mは惑星の質量である。そのため、i の値によって実際の惑星質量は M^* より大きくなる可能性がある。質量に対する軌道の安定性を検討するために、今回の数値積分では$1/\sin i$ を1.0から2.0 まで変化させた。

計算元期の選び方により惑星の軌道上の配置が異なり、惑星系の安定性に影響する。惑星配置による惑星系の安定性を検討するため、最外惑星の初期の平均経度（λ_{d0}）と中間の惑星の初期の平均経度（λ_{c0}）が$\lambda_{c0} = \lambda_{d0} + 30n, (n = 0, 1, 2, \cdots, 11)$ になるように惑星の配置を強制的に決めた仮想惑星系について数値シミュレーションを行った。同様に惑星ｃｄの初期の近星点経度の差($\Delta\varpi_{cd} = \varpi_{c0} - \varpi_{d0}$) が惑星系の安定性にどう影響するかを調べるために$\varpi_{c0} = \varpi_{d0} + 30n, (n = -6, -5, \cdots, 0, \cdots, 6)$ と変化させ数値シミュレーションを行った。

2.2 積分法

線形対称係数多段法 (Symmetric method)、外挿法(Extrapolation method) を用いて数値積分を行った。外挿法は可変キザミ幅で計算し、線形対称係数多段法のキザミ幅は固定で、3惑星系(b,c,d) の数値積分では0.04 日、外側2惑星系(c,d) では2 日で計算した。長期間軌道が安定である系 (初期値) のシミュレーションの結果では、線形対称係数多段法と外挿法との差は殆どなかった。しかし、初期値依存性の大きな系の結果は積分法によって差が生じた。ここでは主に線形対称係数多段法を使用し、期間が短く高精度を必要とする場合は外挿法を使用した。

3 永年共鳴による近星点経度差と離心率

2惑星が同一平面内を運動している場合を考え、υ Andromedae 惑星系の外側2惑星の近星点経度の運動を半解析的手法を用いて検討した。短周期成分である平均経度を平均操作により消去すると摂動関数 Rは $e_c, e_d, \varpi_c - \varpi_d$ だけの関数となり角運動量を一定とすると $\varpi_c - \varpi_d$: e_c または $\varpi_c - \varpi_d$: e_d の関係が分かる。惑星cdだけの2惑星系でAFOEデータの場合の等エネルギーカーブを図1の実線で示している。2惑星の近星点が連動する最大の振幅は約80度でそれ以上になると近星点の連動は崩れる。実際の数値積分 (AFOEデータ, 計算元期JD=2450001.99) の結果を点で示している。理論と数値積分の結果では、近星点が秤動する離心率の値は少し異なるがそれ以外は良く一致している。

4 軌道の安定性

4.1 惑星質量(M) と軌道の安定性

ドップラー観測から決定される惑星質量M^*は$M^* = M \cdot \sin i$でしか決められない。ただし、Mは実際の惑星質量である。そのため、iの値によってMは変わる可能性がある。Lick/AFOEデータで、$1/\sin i$を1.0から2.0まで変化させ2.2億年間の数値積分を行った。図2a,2bは最内惑星(b)を無視し、外側2個の惑星(c,d)を考慮した2惑星系についての結果である。図中○印は積分期間(2.2億年,$1/\sin i = 1.0$は11億年)軌道が安定であったことを示し、矢付き○印は惑星系の安定な期間が積分期間より永いことを示している。●印は2.2億年より短い期間で軌道が不安定 (惑星の離心率が1を超える) になったことを示す。$1/\sin i$が1.0から1.4までは積分期間2.2億年($1/\sin i = 1.0$は11億年)の間軌道は安定で、惑星cdの近星点経度の差($\delta\varpi_{cd} = |\varpi_c - \varpi_d|$) の振幅の最大値は約60度以下である。$1/\sin i$ が1.7以上になると$\delta\varpi_{cd}$の振幅は大きくなり70度を超えると惑星cdの近星点の連動が崩れ、惑星系の寿命 (惑星の離心率が1以下の期間) は短くなり軌道は不安定になっている。惑星cdの初期値の近星点経度差($\Delta\varpi_{cd} = \varpi_{c0} - \varpi_{d0}$) の振幅が0度になるように、惑星cdの初期値 ($\varpi_{c0} = \varpi_{d0}, e_{c0} = 0.135, e_{d0} = 0.408$) を強制的に決めた数値積分の結果は図3a,3bである。図2bに比べ近星点経度の差($\delta\varpi_{cd}$) の振幅は小さいが $1/\sin i$ の増加につれて、振幅が大きくなる。$1/\sin i$ が1.9以上では惑星cdの近星点経度の差が180度になり、2惑星の近星点の連動が崩れ、軌道は不安定になっている。この状況は図2、図3共に同じ傾向である。

最大の近星点経度差が50°以下では惑星系は非常に安定である。cd2惑星の近星点の連動が崩れると非常に不安定になる。惑星の質量($1/\sin i$) が増加しても惑星cdの近星点の差が小さいと安定期間は永くなっている。

4.2 平均経度の変化と軌道の安定性

図4はAFOEデータで最内惑星(b)の近星点通過の時刻(JD=2450001.99)を元期とした3惑星

系の数値積分の結果で、図５は元期をJD=2440000.00とした結果である。各元期における中間と最外惑星ｃｄの惑星の位置はJD=2450001.99の時は衝（平均経度差180度）に近く、JD=2440000.00では合（平均経度差０度）に近い配置となっている。平均経度差が180度に近い惑星配置では、数値積分期間200万年の間３惑星ｂｃｄは安定な運動を繰り返し、図4aに示すように、惑星ｃｄの近星点経度差 ($\delta\varpi_{cd} = \varpi_c - \varpi_d$) は40度以下で、２惑星ｃｄの近星点が連動している。一方、平均経度差が０度に近い惑星配置では、惑星ｃｄの近星点経度差 ($\delta\varpi_{cd}$) は180度に達し、近星点の連動は崩れて、軌道は短期間（3.5万年）で不安定になっている（図5a)。この初期値では、図5bに示すように、惑星ｃｄは1:6平均運動共鳴に近い関係になっていて臨界引数 ($\sigma = \lambda_c - 6\lambda_d + \varpi_c + 4\varpi_d$) は０度の回りを秤動している。しかし、平均経度差が180度に近い惑星配置では、惑星ｃｄは1:6平均運動共鳴の関係にはなっていない（図4b)。

AFOEデータを用いｃｄ２惑星系で初期の平均経度差 ($\Delta\lambda_{cd}$) を０度から45度おきに強制的に変化させ、近星点経度差 ($\delta\varpi_{cd}$) と臨界引数 (σ) の変化を調べた結果が図6a,6bである。積分期間は１万年である。惑星ｃｄの近星点が連動する初期値のときは平均運動共鳴が崩れ、近星点の連動が崩れる初期値では1:6平均運動共鳴の関係が成立している。しかし、この平均運動共鳴は長期間安定に続かないので、短期間に共鳴関係が崩れ、軌道は不安定になる。

３惑星系について、惑星ｃｄの初期の平均経度差 ($\Delta\lambda_{cd} = \lambda_{c0} - \lambda_{d0}$) を $0, 30, \cdots, 330$ と変化させ惑星配置を強制的に変化させて550万年間数値積分を行った例を図７、図８に示す。図７はAFOEデータの結果で、 $\Delta\lambda_{cd}$ に対する軌道が安定な期間（惑星の離心率が１以下の期間）を対数で図7aに、惑星ｃｄの近星点経度の差 ($\delta\varpi_{cd}$) の最大振幅を図7bに示す。○印は計算期間(550万年)軌道が安定であったもの、矢付き○印は軌道が安定な期間が積分期間550万年より永いことを示す。● は550万年より短い期間で軌道が不安定になったことを示す。惑星ｃｄの初期の平均経度差 ($\Delta\lambda_{cd}$) が150度から270度の間だけで軌道は安定であった。図８はLick/AFOEデータの結果である。惑星ｃｄの初期の平均経度差 ($\Delta\lambda_{cd}$) をどのように決めても、軌道が安定な期間は全ての初期値で積分期間(550万年)より永く、近星点経度差 ($\delta\varpi_{cd}$) の最大値も40度以下であった。AFOEデータがLick/AFOEデータよりも一般に不安定性が大きいことがここでも表れている。

4.3 初期の近星点経度の差 ($\Delta\varpi_{cd}$) と軌道の安定性

Lick/AFOEデータ２惑星系で２惑星の初期の近星点経度差 ($\Delta\varpi_{cd} = \varpi_{c0} - \varpi_{d0}$) を $\Delta\varpi_{cd} = -180, -150, \cdots, 0, \cdots, 180$ 度となるように強制的に変化させ、2.2億年間数値積分した。惑星系が不安定になる期間を調べた結果が図9aで、数値積分期間の近星点経度差 ($\delta\varpi_{cd}$) の振幅の最大値を図9bに示している。初期の $\Delta\varpi_{cd}$ が -60度から $+30$度以内では積分期間2.2億年よりも永い期間軌道が安定であった(矢付き○印、○印)。その時の近星点経度差 ($\delta\varpi_{cd}$) の振幅の最大値は70度以下である。一方初期の $\Delta\varpi_{cd}$ が -60度から $+30$度以外では軌道が安定である期間が短く $\delta\varpi_{cd}$ の振幅の最大値は180度になっている(●印)。惑星ｃｄの近星点が連動している時は惑星軌道は安定である。

5 結論

種々の初期値で数値積分を行った結果、軌道が安定になるときは中間と最外側の惑星ｃｄの近星点が連動して運動することが重要で、その近星点経度の差の振幅が約60度以上になると近星点の連動が崩れ、軌道は不安定になる。近星点が連動する場合の惑星ｃｄの近星点経度の秤動の振幅は永年共鳴理論と数値積分の結果と良く一致する。永年共鳴により２惑星の近星点経度差は秤

動する。初期値が秤動中心に近いと軌道は安定になる。共鳴の境界付近では軌道はカオス的になり初期値依存性が非常に大きくなる。共鳴から離れ、近星点経度差が回転している状態では不安定になっている。惑星ｃｄの近星点の連動が崩れている場合でも、初期値によっては惑星ｃｄが平均運動共鳴（1:6）の関係になり、短期間軌道は安定に保たれる。しかし、平均運動共鳴は長期間安定に続かないために、υ Andormedae 惑星系の安定性には重要な働きをしない。

6 おわりに

惑星系が長期間安定である条件を検討するために、観測から決められた軌道要素とは必ずしも一致しない要素での数値シミュレーションも行った。多くの場合、外２惑星系の安定期間に比べ最内惑星を加えた３惑星系の安定期間は短い。しかし、中間惑星の平均経度を強制的に変化させたシミュレーションでは、３惑星系で550万年間安定であった初期値を用い、外２惑星系で数値シミュレーションを行った場合、550万年以前で軌道が不安定になる場合もあり、最内側の惑星ｂの存在が惑星系の安定性にどう影響するかを調べることは重要なことである。また、惑星ｃｄの近星点が連動しなくて、長期間惑星系が安定に存在できるか。これらを明らかにすることが今後の研究課題である。υ Andromedae 惑星系の安定性は初期値依存性が大きいので長期間の惑星系の安定性を議論するためにはより良い軌道要素が必要で、そのためにはより多くの精度良い観測が必要である。

7 参考文献

Butler R.P.,Marcy G.W.,Fischer D.A.,Brown T.W.,Contos A.R.,Korzennik S.G., Nisenson P. and Noyes R.W. : 1999, Evidence for Multiple Companions to Υ Andromedae, *Astrophys. J.*,**526**,pp.916-927.

Ito T. and Miyama S.M. : 2000, An estimation of upper limit masses of υ Andromedae planets, *Astrophys. J. lett.*,submitted.

Kozai Y. : 1983, Secular Perturbations of Asteroids with Commensurable Mean Motions, Celestial Mechanics of the International Symposium G. LEMAITRE, Louvain-la-Neuve, Belgique, pp.1-20.

Lissauer J.J. : 1999, Three planets for Upsilon Andromedae, *Nature*,**398**,pp.659-660.

Rivera E.J. and Lissauer J.J. : 2000, Stability Analysis of the Planetary System Orbiting υ Andromedae, *Astrophys. J.*,**530**,pp.454-463.

Table 1 Initial Orbital Parameters (Butler et al. 1999)

Parameters	Lick data	AFOE data	Combined Lick/AFOE
Companion b			
P(d)	4.6171 ± 0.0001	4.6171 ± 0.0003	4.6170 ± 0.0003
T_{peri}(JD)	2450315.34 ± 0.7	2450001.99 ± 0.51	2450002.24 ± 3.1
e	0.042 ± 0.030	0.042 ± 0.033	0.034 ± 0.15
ω (deg)	16.0 ± 139	63.8 ± 40	83.0 ± 243
$M_b \sin i (M_{JUP})$	0.72	0.74	0.71
Companion c			
P(d)	242.0 ± 0.7	243.5 ± 1.0	241.2 ± 1.1
T_{peri}(JD)	2451131.24 ± 23.4	2450140.4 ± 8.3	2450154.9 ± 20.8
e	0.23 ± 0.06	0.22 ± 0.06	0.18 ± 0.11
ω (deg)	261.0 ± 47	219.2 ± 14	243.6 ± 33
$M_c \sin i (M_{JUP})$	1.98	1.96	2.11
Companion d			
P(d)	1269.0 ± 8.5	1481.2 ± 35	1266.6 ± 30
T_{peri}(JD)	2453813.46 ± 32.0	2450046.8 ± 16.1	2451308.7 ± 40.5
e	0.36 ± 0.05	0.44 ± 0.05	0.41 ± 0.11
ω (deg)	236.0 ± 14.6	245.9 ± 5.9	247.7 ± 17.0
$M_d \sin i (M_{JUP})$	4.11	5.70	4.61

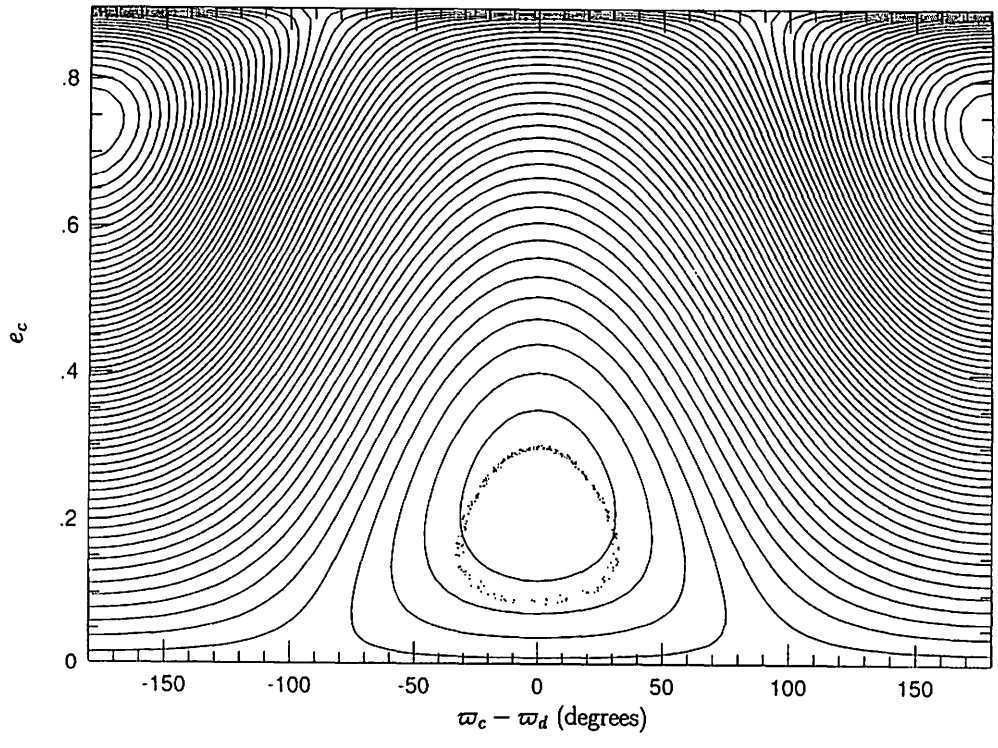

Fig.1 The planet c's equi–$\langle R \rangle$ value-curves,based on the fit to the AFOE data. The dots show the solutions by numerical integration.

Fig.2a

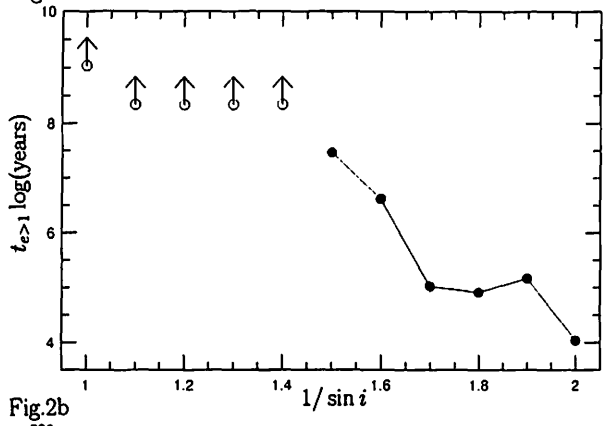

Fig.2b

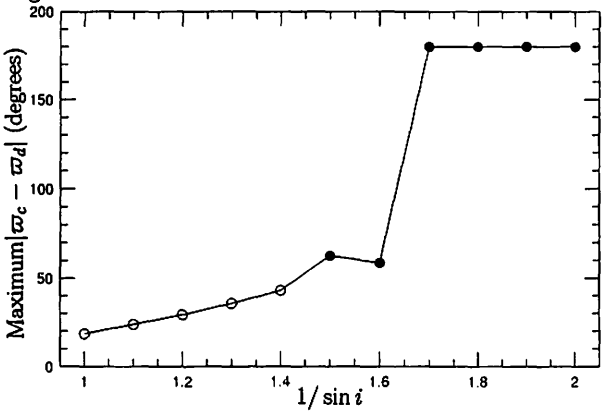

Fig.2a The instability time of various outer two-planet systems based on the fit to the AFOE data in the table 1.
The open circles mean the systems were still stable but the calculation was stopped to conserve CPU resources, and the filled circles indicate the time at which the eccentricity of one planet exceeds 1.

Fig.2b The maximum values of differences in the longitudes of periastron between outer two planets.

Fig.3a

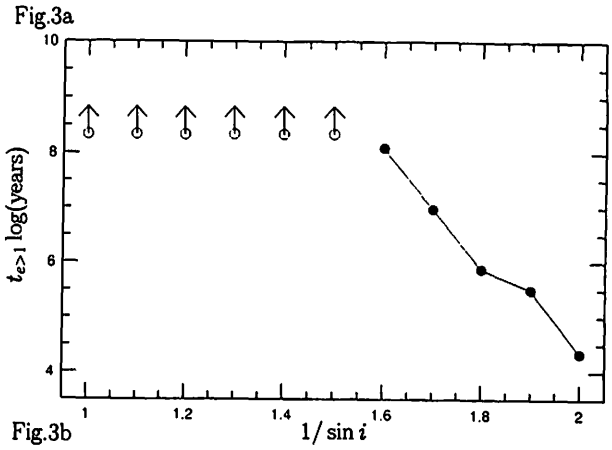

Fig.3b

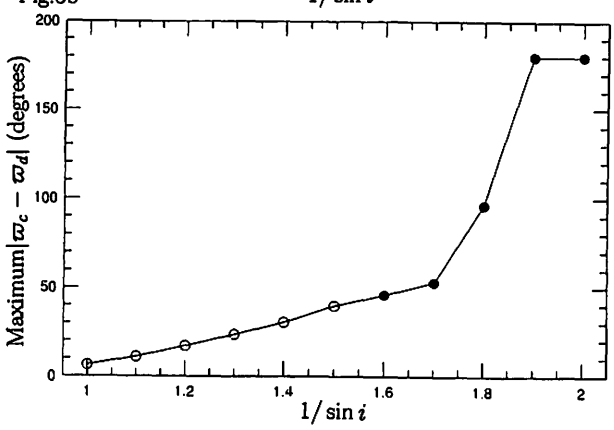

Fig.3a,3b Same as figure 2a,2b, but with different initial values. Initial eccentricities and longitudes of periastron are $e_c = 0.135, e_d = 0.408, \varpi_c = \varpi_d = 0°$.

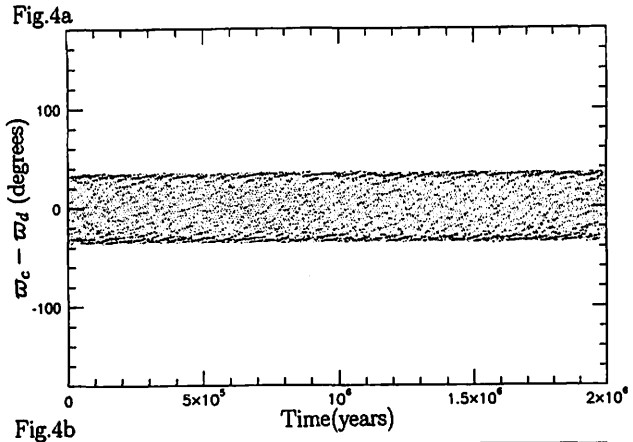

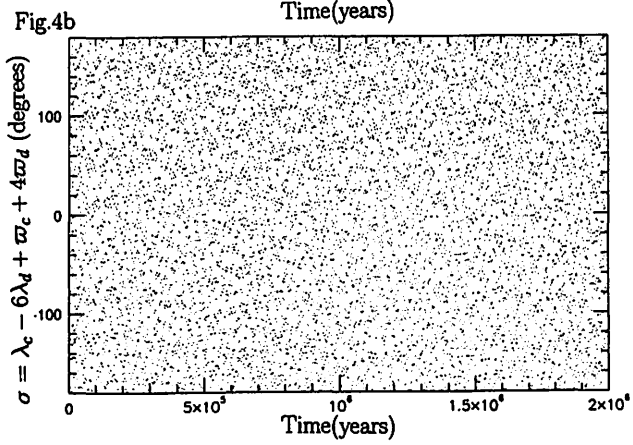

Fig.4a The differences in the longitudes of periastron ($\varpi_c - \varpi_d$) of the three-planet system based on the fit to the AFOE data and the epoch is JD=2450001.99.

Fig.4b The critical arguments ($\sigma = \lambda_c - 6\lambda_d + \varpi_c + 4\varpi_d$).

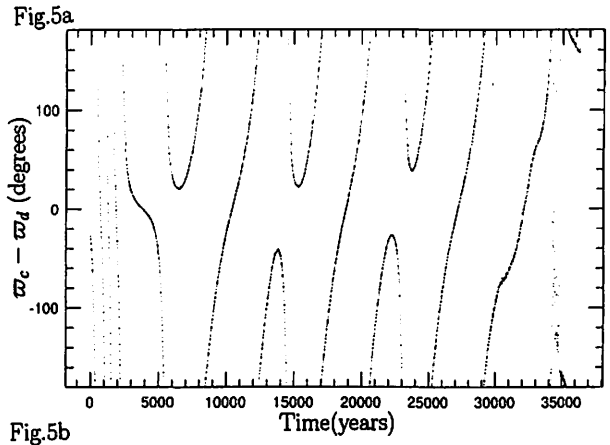

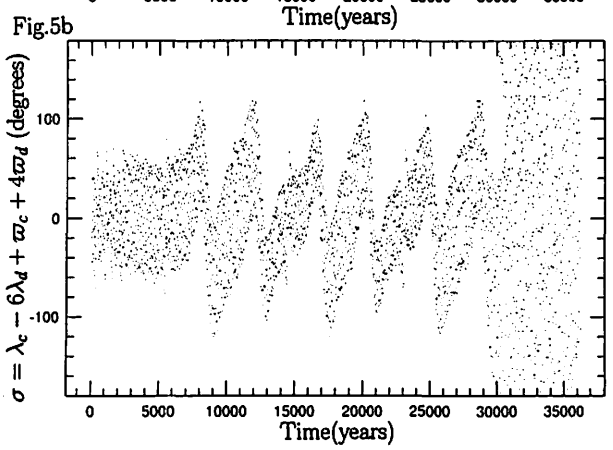

Fig.5 Same as figure 4, but the epoch is JD=2440000.00.

Fig.6a

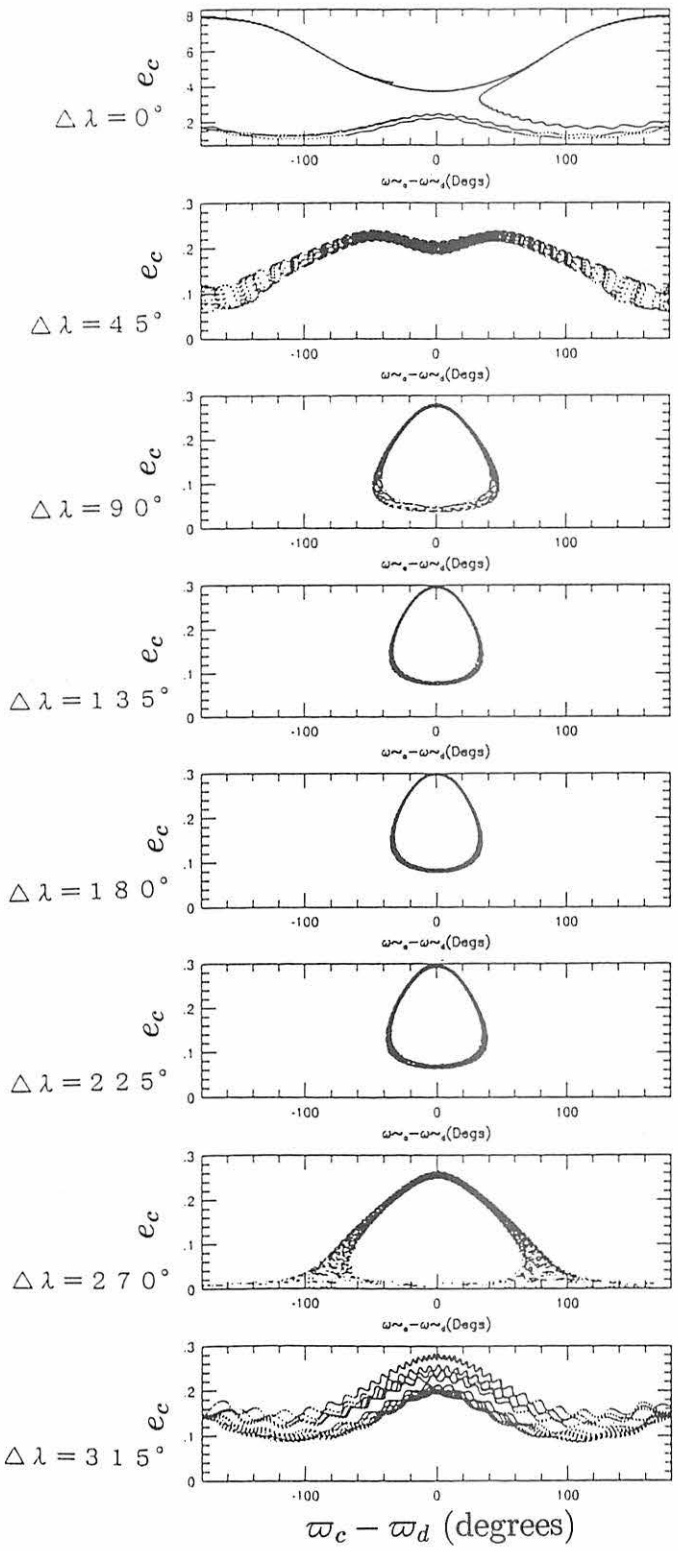

Fig.6a The relations between eccentricities of the planet c and differences in the longitudes of periastron ($\varpi_c - \varpi_d$).

Fig.6b

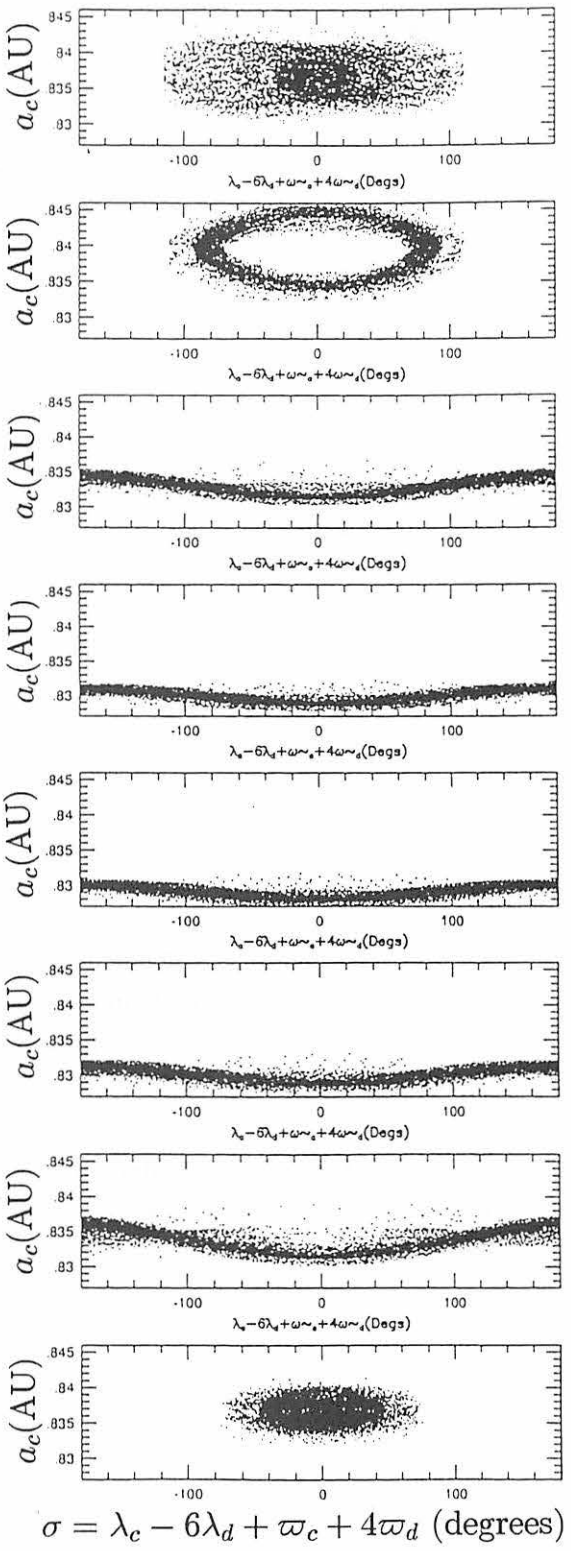

Fig.6b The relations between semi-major axes of the planet c and the critical arguments ($\sigma = \lambda_c - 6\lambda_d + \varpi_c + 4\varpi_d$).

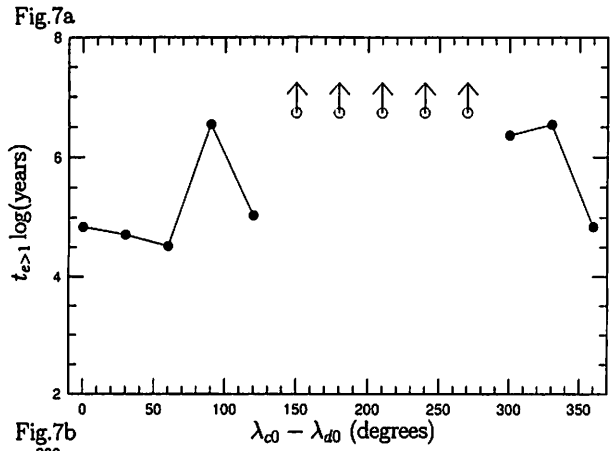

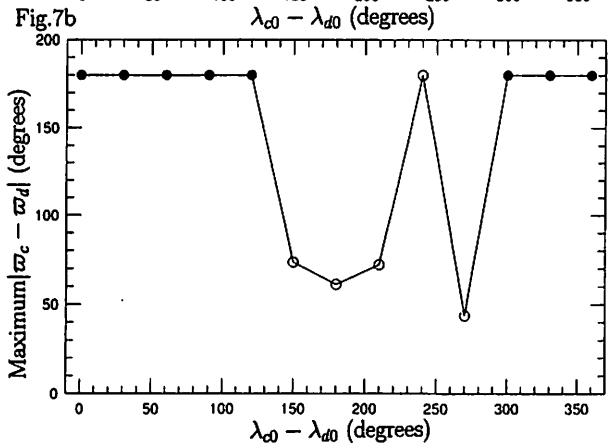

Fig.7a The instability time of various three-planet systems based on the fit to the AFOE data, but the initial mean longitudes of the planet c are changed. $\lambda_{c0} = \lambda_{d0} + 30° \cdot n$ $(n = 0, 1, \cdots, 11)$.

Fig.7b The maximum values of differences in the longitudes of periastron between outer two planets.

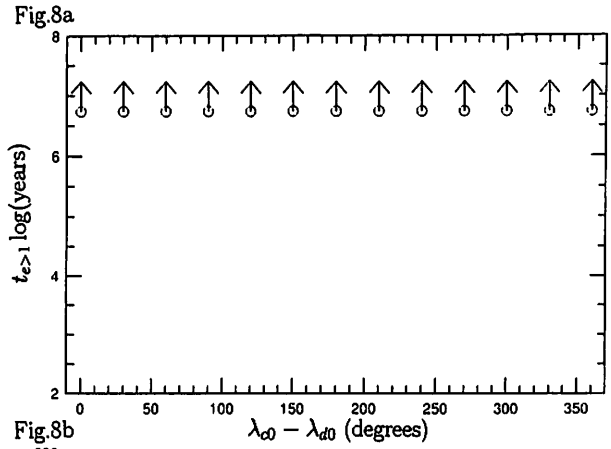

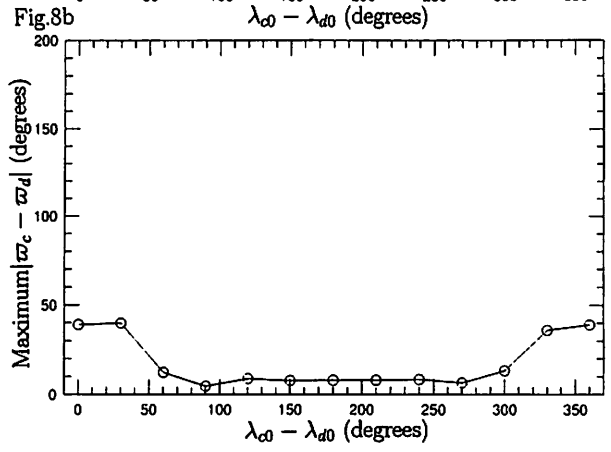

Fig.8 Same as figure 7, but for the Lick/AFOE data.

Fig.9a

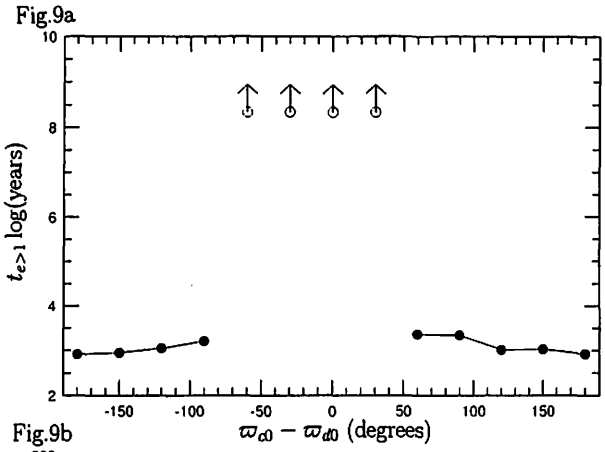

Fig.9b

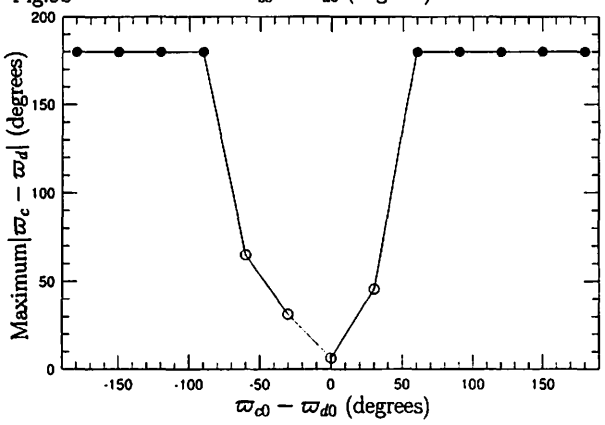

Fig.9a The instability time of various outer two-planet systems based on the fit to the Lick/AFOE data, but the initial longitudes of periastron of the planet c are changed. $\varpi_{c0} = \varpi_{d0} + 30° \cdot n$ $(n = -6, -5, \cdots, 0, \cdots, 6)$.

Fig.9b The maximum values of differences in the longitudes of periastron between outer two planets.

静止衛星の軌道解析に関する研究－VI.
－対流圏電波伝搬距離補正モデル－

河合雅司（富山商船高等専門学校）

A Study on the Orbital Analysis of Geosynchronous Satellites -VI.
- The Range Correction Model for Refraction in the Troposphere -

Masashi KAWAI

Toyama National College of Maritime Technology,
1-2 Neriya, Ebie, Shinminato, Toyama 933-0293, Japan

Abstract

The new range correction model for refraction in the troposphere was developed in this study. In this model, an increase of 20% in relative humidity increase the range correction of tropospheric refraction by one meter in case of elevation angle 49°. It is confirmed that post-fit range residuals in orbital analysis of geosynchronous satellite can be reduced to the noise level of observed ranges by considering three ideas. These ideas are as follows.

(1) Unknown force along track act on a spinning satellite.
(2) A tracking station moves horizontally and periodically with a lithosphere on the flows of asthenosphere which are generated by tidal generating forces.
(3) The range correction of tropospheric refraction varies with relative humidity.

These results are reported in this paper.

1．緒言

静止衛星の軌道解析において、軌道決定後の観測距離と計算距離の残差（O-C）に既存の軌道解析理論では説明することの出来ない、12時間周期及び24時間周期の変動が存在していることが分かっている。そして、月や太陽の潮汐力と強い相関のある12時間周期の変動については、海洋における海流や潮流に相当する流れがマントル内部にも存在しており、このマントル内部の流動と共に地殻が12時間周期、振幅 1～2m程度で動いていると考えることにより説明可能である。又、O-Cの24時間周期の変動については、相対湿度の変動と相関があることから、対流圏における電波伝搬遅延量が相対湿度により変動していると考えることにより説明出来ると思われる。[1] そこで、本研究では、相対湿度をパラメタとした新しい対流圏電波伝搬距離補正モデルを開発し、このモデルと潮汐力による地殻水平変動モデル及び慣性座標系における衛星速度ベクトルの方向（逆方向も含む）に作用する未知の力を考慮することにより、静止衛星の軌道を観測精度の範囲内で理論的に説明することを試みた。これらの結果について以下に報告する。

2．軌道計算システムの概要

ここでは、本研究で使用された軌道解析システム TOCS(Toyama Orbit Computation System) の衛星力学モデル等について簡単に紹介する。

[1] 衛星力学モデル

衛星運動方程式はJ2000.0赤道面座標系（慣性座標系）において次の力を考慮して積分した。

(1)地球万有引力による加速度
(2)地球重力乱れポテンシャルによる加速度（重力モデル：GEM-10B[2]，4次で打ち切り）
(3)月，太陽，惑星の引力による加速度（天体歴：DE200/LE200 JPL ephemerides [3]）
(4)太陽輻射圧による加速度
(5)地球潮汐による加速度（ラブモデル[4]，Lag Angleは2.5°，ラブ定数は0.25）
(6)一般相対性理論による加速度[5]
(7)未知の力による加速度[6]（衛星軌道に沿った方向に加速度を仮定）

[2] 電波伝搬補正モデル

電離層及び対流圏における補正を行った。電離層における補正については土屋モデルを用い[7]、対流圏における補正については、距離補正及び角度（仰角と方位角）補正共に一定値とし、距離補正値は4.0mで固定、衛星仰角と方位角の補正値は定誤差として推定した。（衛星角度補正を一定とする場合は、距離補正も一定とする必要がある。）

[3] 地球潮汐による観測局位置の変動

Wahrの理論によるモデル（２次の潮汐まで考慮）[5]を用いて補正を行った。

[4] 潮汐力による地殻の水平変動

静止衛星の軌道解析に関する研究－Ⅴ．で示されたモデルを用いた。そのモデルを以下に示す。

$$\Delta X=A\cdot\sin\theta_D\ ,\quad \Delta Y=A\cdot\cos\theta_D \tag{1}$$

$$A=D(T_F)\cdot\cos[2\cdot(L_O-L_D-\alpha_M)]$$

$$D(T_F)=C\cdot T_F=1.60\cdot T_F$$

$$L_D=18^\circ\cdot T_F+25^\circ$$

$$T_F=T_{FM}+\cos(2\cdot\theta_{MES})\cdot T_{FS}$$

$$T_{FM}=GM_M[1/(D_M-A_E)^2-1/D_M^2]\times10^6$$

$$T_{FS}=GM_S[1/(D_S-A_E)^2-1/D_S^2]\times10^6$$

ΔX:地殻変動量の東西方向成分（東が＋，西が－）[単位:m]
ΔY:地殻変動量の南北方向成分（北が＋，南が－）[単位:m]
A:地殻変動量[単位:m]
θ_D:地殻変動の方向（θ_D：北を0°として時計回りに360°まで測る。地域により値は異なり、日本周辺ではθ_D=315°と仮定）
L_O:観測局の経度
L_D:地殻変動の潮汐力に対する位相遅れ角度
θ_{MES}:地球から月へのベクトルと地球から太陽へのベクトルがなす角
$D(T_F)$:地殻変動の振幅[単位:m]（係数C は地域により異なった値をとると考えられる。本研究では日本周辺での値としてC=1.60を用いる。）
α_M:月の地位の経度（地球固定座標系における月位置の経度）
T_{FM}:月による潮汐力に10^6を乗じた値[単位:m/s^2]
T_{FS}:太陽による潮汐力に10^6を乗じた値[単位:m/s^2]
T_F:月と太陽による潮汐力の大きさを表わすパラメタ [単位:m/s^2]

G:万有引力定数，　M_M:月の質量，　M_S:太陽の質量
A_E:地球赤道半径，　D_M:地球と月の距離，　D_S:地球と太陽の距離

観測局の位置は地殻の周期変動により東西方向に ΔX、南北方向に ΔYだけ偏位しているので、上記の地殻変動モデルを用いて補正する。

3．対流圏電波伝搬補正モデル

本研究では対流圏電波伝搬距離補正値として4.0m（定数）を使用した。この場合は、実際の対流圏電波伝搬遅延量が変動する場合は、その変動が軌道決定後の O-Cにそのまま表れることになる。従って、この O-Cと本研究で開発されたモデルによる距離補正量とを比較することによりモデルの精度を評価することが可能である。対流圏電波伝搬遅延には、乾燥空気によるものと湿潤空気によるものとがあるが、静止衛星の場合乾燥空気による遅延量は一定値となり、本研究で使用された衛星データからこれを検出することは困難である。そこで、乾燥空気による伝搬遅延については無視した。本研究で開発されたモデル（ＫＲモデル）を次に紹介する。

$$\Delta R = N \sum_{i=1}^{9} \frac{\alpha_i r^i}{i} \qquad (2)$$

$r=((a_e+h)^2-(a_e\cdot\cos\theta)^2)^{0.5}-a_e\cdot\sin\theta$
$h=10Km$
$N=1.885\times10^{-5}\cdot E$

$\alpha_1=1$　　$\alpha_2=4\alpha$　　$\alpha_3=6\alpha^2+4b$
$\alpha_4=4\alpha(\alpha^2+3b)$　　$\alpha_5=\alpha^4+12\alpha^2b+6b^2$　　$\alpha_6=4\alpha b(\alpha^2+3b)$
$\alpha_7=b^2(6\alpha^2+4b)$　　$\alpha_8=4\alpha b^3$　　$\alpha_9=b^4$
$\alpha=-\sin\theta/h$　　$b=-\cos^2\theta/(2ha_e)$

ΔR :対流圏電波伝搬遅延量，h:対流圏の高さ
r :観測地点から対流圏の上限までの距離[m]
N:湿潤空気の屈折率－１（乾燥空気の屈折率は無視した。）
a_e:地球赤道半径[m]，E :相対湿度[%]，θ :衛星仰角

対流圏における距離補正モデルには、宇宙開発事業団（NASDA）で使用されているGSFC NONAME式（NASDAモデル）、[8]ザースタモイネンの式（ザースタモイネンモデル）、[9] NASAの軌道解析プログラムGEODYNⅡで使用されているモデル（GEODYNⅡモデル）[10]等がある。これら既存のモデル及び本研究のモデル（ＫＲモデル）により、気象庁の館山観測所で1991～1996年までの 7月に観測された時間毎の気象データ（気温，気圧，水蒸気分圧，相対湿度）の平均値を用いて、仰角49° の衛星に対する時間毎の対流圏電波伝搬距離補正値を計算した結果を Fig.1に示す。又、同じ観測所で同じ期間の 1月、 4月、 7月、10月に観測された時間毎の水蒸気分圧と相対湿度の平均値をFig.2、Fig.3に示す。これらの図から分かるように、既存のモデルによる補正値は水蒸気分圧等に依存していてほぼ一定値となり日変化していないのに対して、ＫＲモデルによる補正値は相対湿度に依存しているために大きく日変化していることが分かる。

4．解析データ

君津衛星管制センターで、1993年 6月～ 7月及び1994年 6月に観測された通信衛星(CS-3b) のデータを用いて軌道解析を行った。観測は、4GHzの電波を用いて毎週土曜～日曜にかけて48時間行われる。具体的には、約４分間１秒毎に衛星までの距離と角度を観測し、

Table 1. The Locations of Tracking Stations

TSCJ-C2 is station for observing ranges of CS-3b at Kimitu.

TSCJ-ANG is station for observing angles of CS-3b at kimitu.

Station	Coordinate	Latitude	Longitude	Height
TSCJ-C2	GEM-10B	35° 11' 35.795"N	140° 04' 29.486"E	189.742m
TSCJ-ANG	GEM-10B	35° 11' 36.822"N	140° 04' 31.221"E	200.836m

Table 2. CS-3b Tracking Data Observed at Kimitu

θ is the angle between the sun and the moon at the earth.

Data	Data Span (JST)	θ
Cb1	1993年06月05日08時～1993年06月07日07時	162°
Cb2	1993年06月12日08時～1993年06月14日07時	82°
Cb3	1993年06月19日08時～1993年06月21日07時	2°
Cb4	1993年06月26日08時～1993年06月28日07時	90°
Cb5	1993年07月03日08時～1993年07月05日07時	177°
Cb6	1993年07月10日08時～1993年07月12日07時	101°
Cb7	1993年07月17日08時～1993年07月19日07時	20°
Cb8	1994年06月04日08時～1994年06月06日07時	48°
Cb9	1994年06月11日08時～1994年06月13日07時	30°
Cb10	1994年06月18日08時～1994年06月20日07時	118°

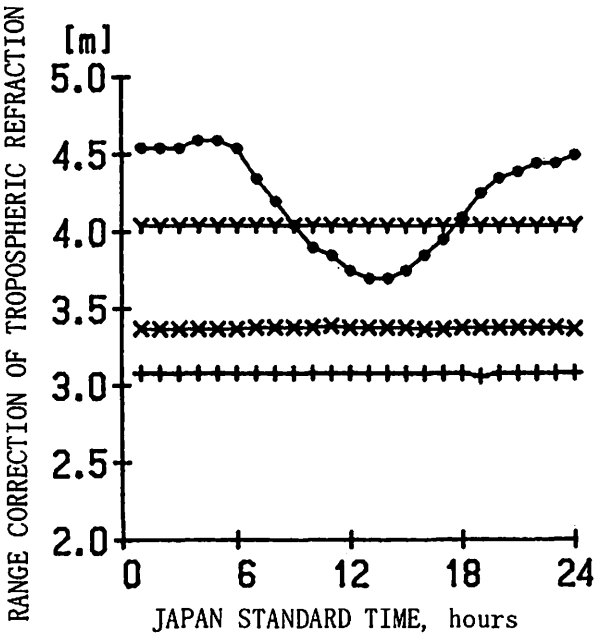

Fig. 1 The range corrections of tropospheric refraction with means of meteorologocal data observed at Tateyama station on July, 1991-1996.
・:New Model(KR Model), ＋:GEODYNⅡ Model
×:Saastamoinen Model, Y:NASDA Model

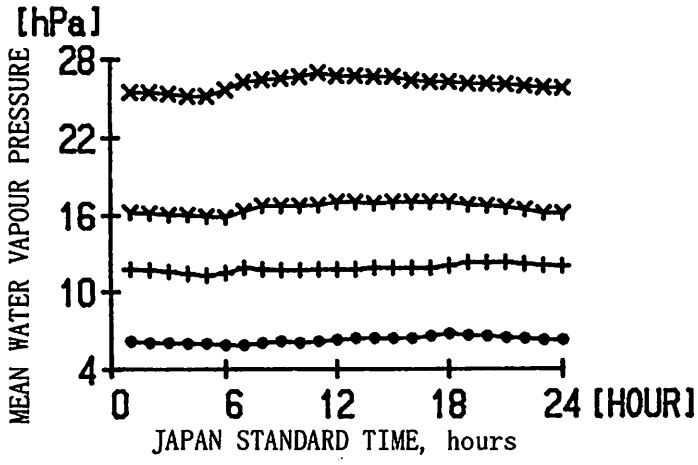

Fig. 2 The means of the water vapour pressure observed at Tateyama station on January, April, July and October, 1991-1996.
・:The means every houre for January, 1991-1996.
+:The means every houre for April, 1991-1996.
×:The means every houre for July, 1991-1996.
Y:The means every houre for October, 1991-1996.

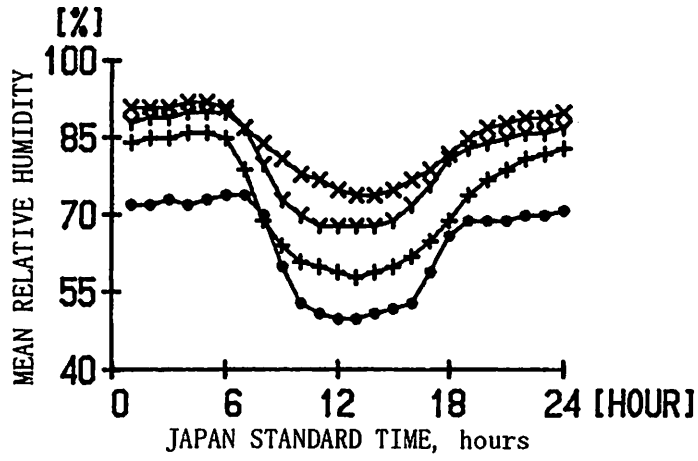

Fig. 3 The means of the relative humidity observed at Tateyama station on January, April, July and October, 1991-1996.
・:The means every houre for January, 1991-1996.
+:The means every houre for April, 1991-1996.
×:The means every houre for July, 1991-1996.
Y:The means every houre for October, 1991-1996.

Table 1.に、本研究で使用された衛星データをTable 2.に示す。Table 2.においてθは、観測期間のほぼ中央で太陽と月が地球においてなす角であり、潮汐力の大きさを表す指標である。θが0°又は180°に近い時は潮汐力が大きく、θが 90°に近い時は潮汐力が小さい。距離データの精度については、軌道決定後の O-Cの１時間毎の標準偏差で判断して、約0.4mである。角度データの精度は約0.002°（距離換算で約1000m）である。

又、本研究の軌道解析では、対流圏電波伝搬距離補正値を一定（4.0m）としているために、対流圏電波伝搬遅延量の変動が O-Cに表れる。そして、この O-Cと比較するための距離補正値をＫＲモデルにより計算した。ＫＲモデルの計算に用いた相対湿度は、気象庁により観測された君津衛星管制センター付近の平均的な時間毎の相対湿度（館山，勝浦，銚子，横浜の各気象庁観測所で１時間毎に観測された相対湿度の平均値）である。

５．解析結果

Table 2.に示された48時間アークのデータを用いて静止衛星の軌道を決定し、軌道決定後の観測距離と計算距離の残差（O-C） を求めた。

距離データの重みを１、角度データを距離に換算した量の重みを0.0001として重み付き最小自乗法によりパラメタを推定した。同時に推定されたパラメータは次の通りである。

(1) 衛星６軌道要素 (X, Y, Z, V_X, V_Y, V_Z)
(2) 太陽輻射圧における反射係数
(3) 慣性座標系における衛星速度ベクトル方向の加速度
　この加速度の符号は、速度ベクトルの方向が正、その逆方向が負。
(4) 定誤差
　角度データ（高度，方位角）の定誤差。

観測距離とは観測局から衛星に搭載されたトランスポンダーまでを電波が往復するのに要した時間に光速度を乗じた値の 1/2であり、計算距離とは軌道解析理論に基づいて計算された衛星の重心と観測局の距離である。トランスポンダーの位置と衛星重心とはずれているので観測距離に対してその補正を行う必要があるが、本研究ではこれを無視している。Table 1.に示された衛星観測データによる軌道決定後の O-Cと君津衛星管制センター周辺の平均相対湿度を用いてＫＲモデルで計算した対流圏電波伝搬距離補正値との比較をFig.4～Fig.11 に示す。これらの図において横軸は時間、左縦軸は O-Cの時間毎の平均値、右縦軸はＫＲモデルによる距離補正値である。 O-Cについては、対流圏遅延量4.0mを既に補正しているので、本研究における軌道解析理論が正しければ、 O-CとＫＲモデルによる補正値は完全に一致することになる。

Fig.4～Fig.5については、 O-Cと距離補正値が、ほぼ一致している。Fig.6とFig.7は、距離補正値の変動の位相が O-Cの変動の位相に対して 4時間程度遅れているが、これは上空の相対湿度の変動が地上の相対湿度の変動に対して、その位相が遅れているためと考えられる。

Fig.8とFig.9については、 O-Cよりも距離補正値の方が全体的に0.5m程度大きくなっている。これは、上空の相対湿度よりも地上の相対湿度の方が高かったためであると考えられる。そしてこれは、データCb7及びCb10の解析結果についてもほぼ同様である。

Fig.10とFig.11については、一部で O-Cと距離補正値との差が大きくなっている。これについては、 O-Cに含まれる12時間周期の変動がうまく除去されずに残っているためであり、潮汐力による地殻水平変動モデルに誤差があるものと考えられる。

これらの解析結果から分かるように、ＫＲモデルにおいて観測局周辺の地上で観測された平均相対湿度を用いて対流圏電波伝搬距離補正値を求めているために、その相対湿度が電波伝搬経路上の相対湿度と異なる場合は、それが補正誤差となる。又、潮汐力による地殻水平変動についても、実際には海洋における潮流の様に、一様な周期変動ではなく複雑な周期変動をしていると考えられるが、この変動を一つの余弦関数でモデル化しているために誤差が生じることは容易に想像出来る。この様な対流圏電波伝搬距離補正モデル及び

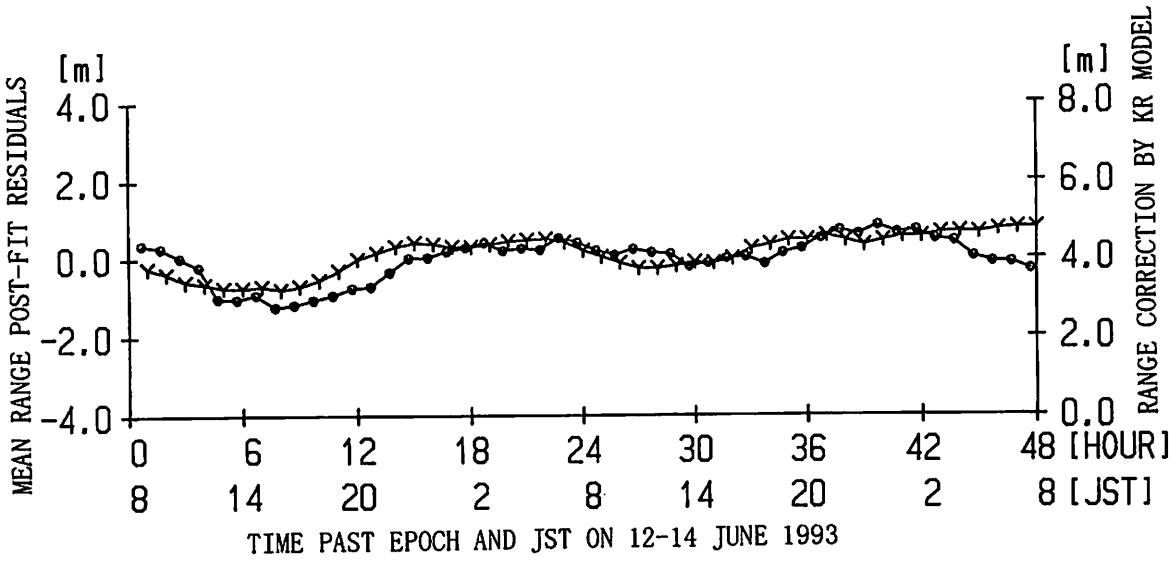

Fig. 4 Mean post-fit residuals of range data and range corrections of tropospheric refraction.
・ : Mean post-fit residuals of range data Cb2.
Y : Range corrections by KR Model with mean relative humidity observed around the tracking station.

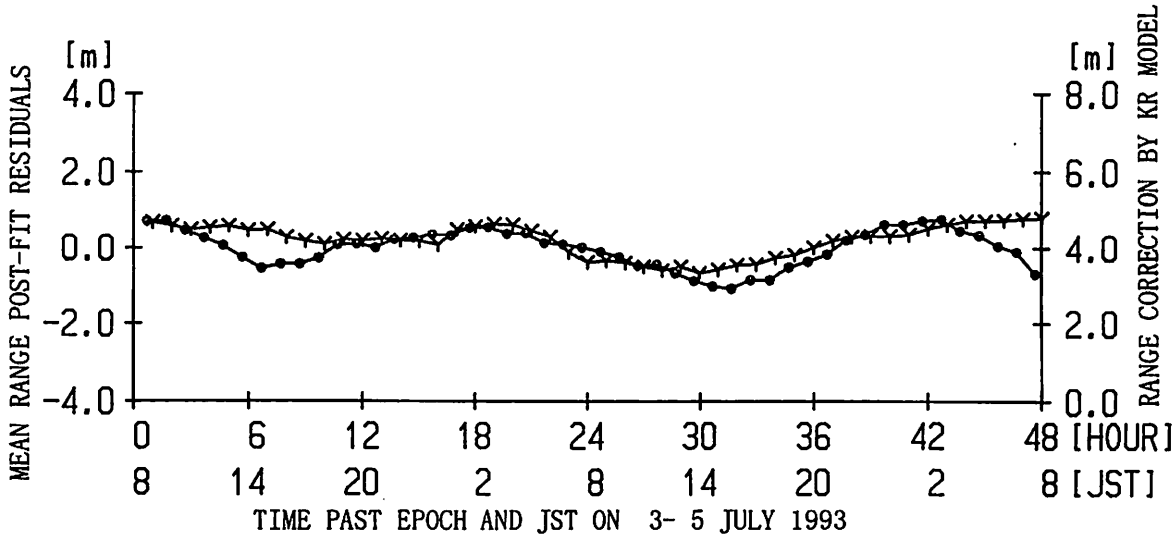

Fig. 5 Mean post-fit residuals of range data and range corrections of tropospheric refraction.
・ : Mean post-fit residuals of range data Cb5.
Y : Range corrections by KR Model with mean relative humidity observed around the tracking station.

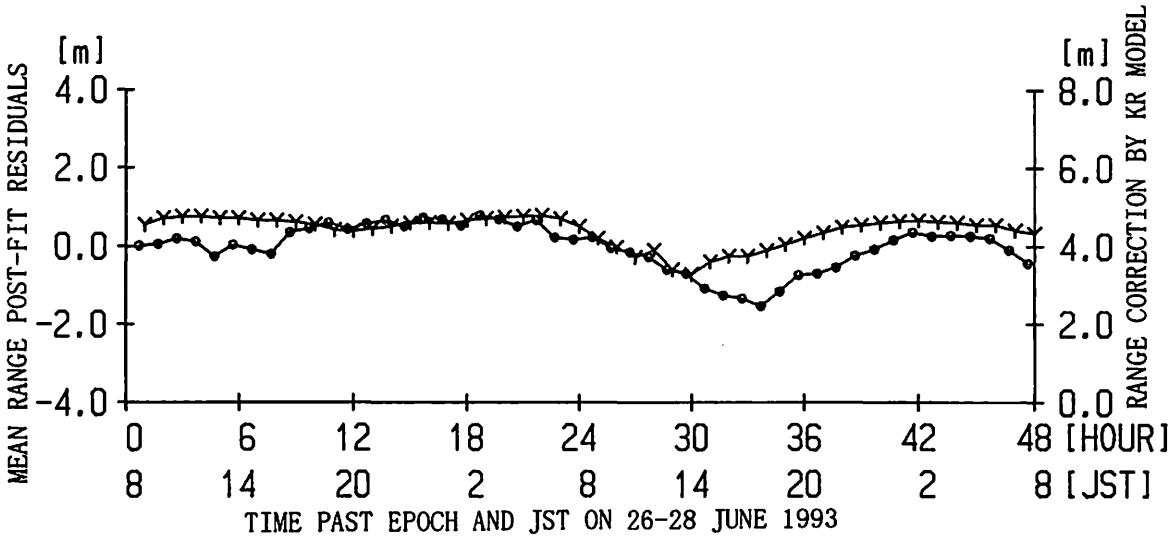

Fig. 6 Mean post-fit residuals of range data and range corrections of tropospheric refraction.
・ : Mean post-fit residuals of range data Cb4.
Y : Range corrections by KR Model with mean relative humidity observed around the tracking station.

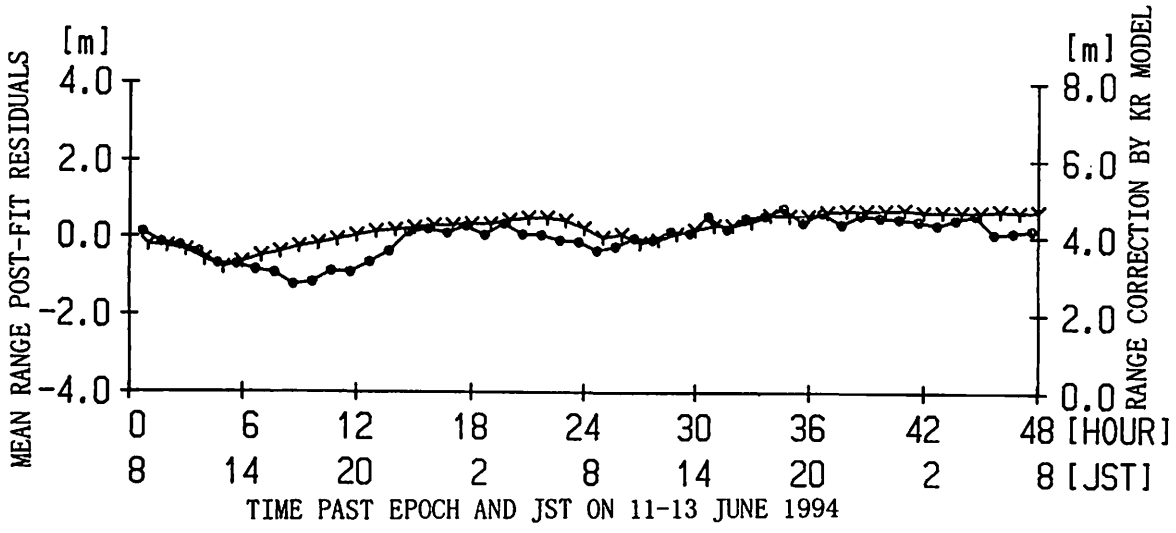

Fig. 7 Mean post-fit residuals of range data and range corrections of tropospheric refraction.
・ : Mean post-fit residuals of range data Cb9.
Y : Range corrections by KR Model with mean relative humidity observed around the tracking station.

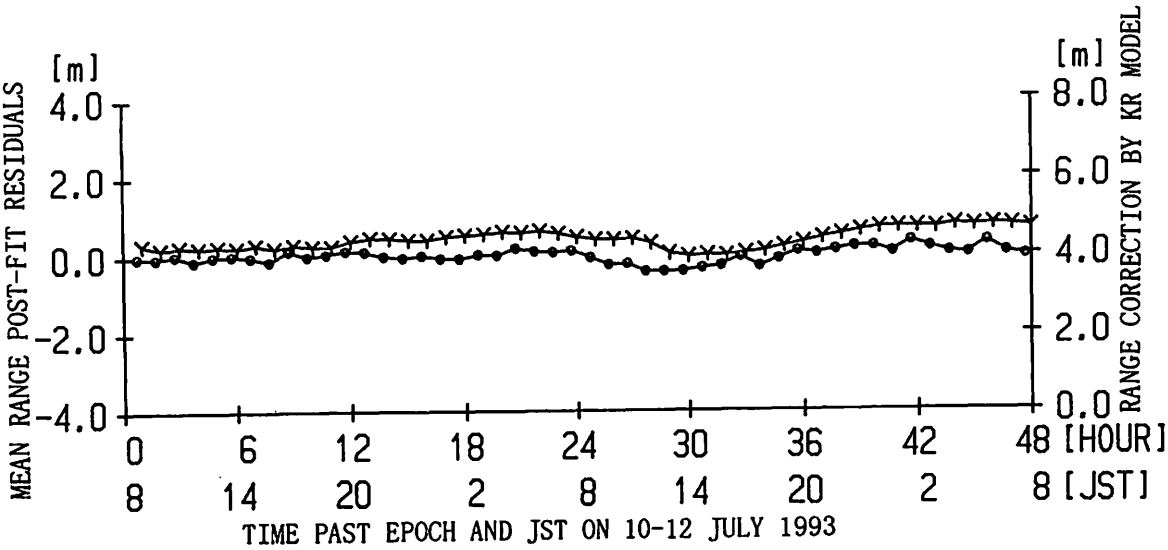

Fig. 8 Mean post-fit residuals of range data and range corrections of tropospheric refraction.
・ : Mean post-fit residuals of range data Cb6.
Y : Range corrections by KR Model with mean relative humidity observed around the tracking station.

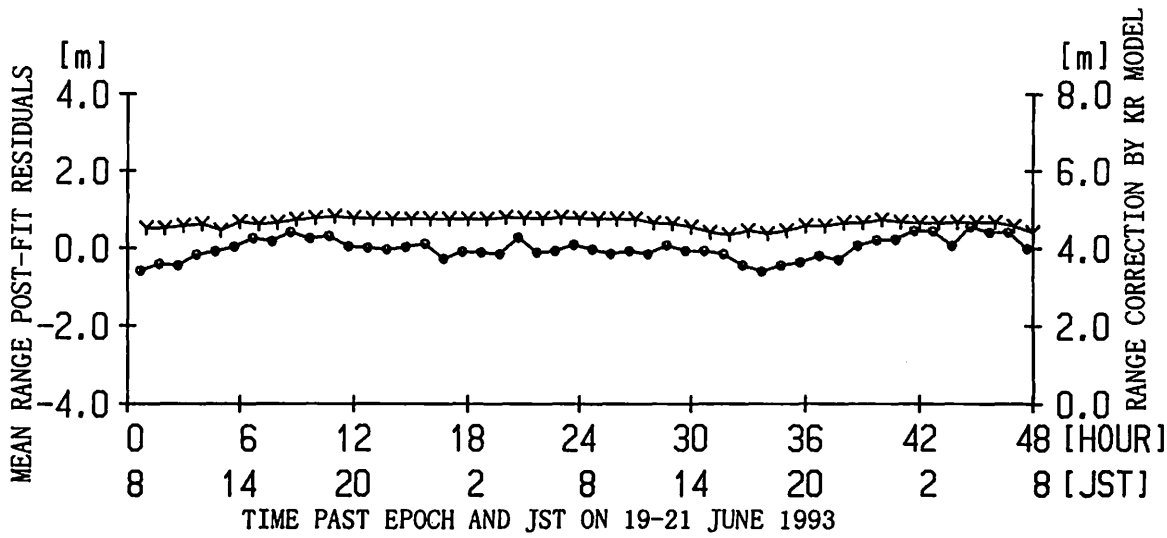

Fig. 9 Mean post-fit residuals of range data and range corrections of tropospheric refraction.
・ : Mean post-fit residuals of range data Cb3.
Y : Range corrections by KR Model with mean relative humidity observed around the tracking station.

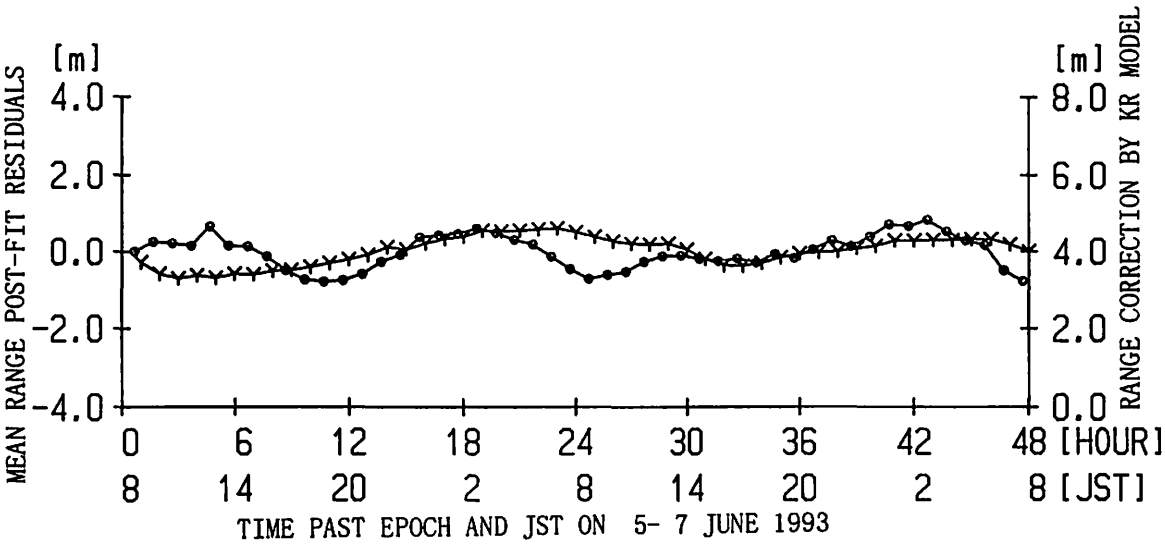

Fig. 10 Mean post-fit residuals of range data and range corrections of tropospheric refraction.
• : Mean post-fit residuals of range data Cb1.
Y : Range corrections by KR Model with mean relative humidity observed around the tracking station.

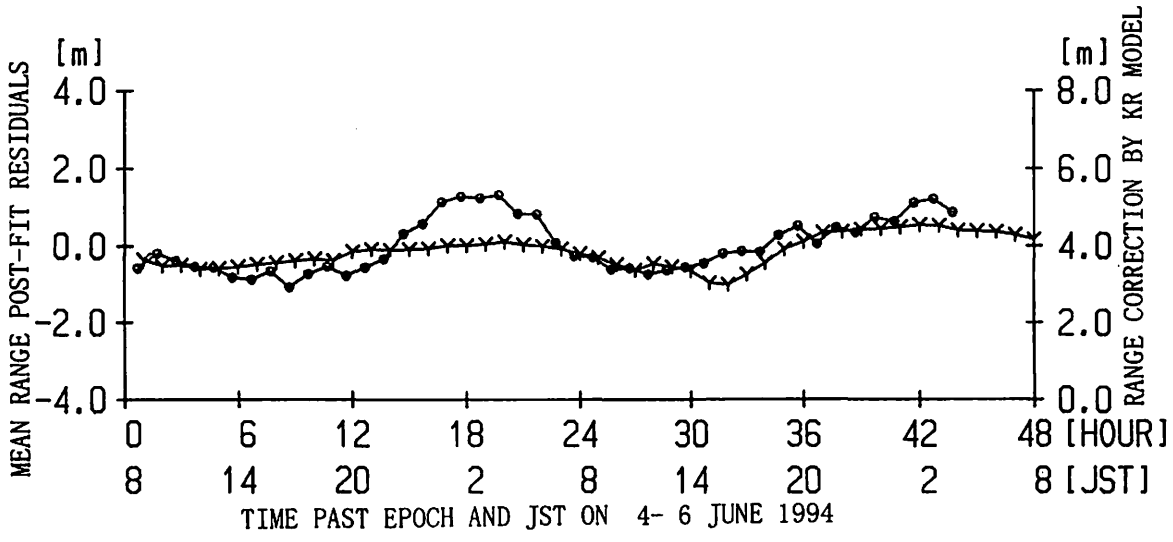

Fig. 11 Mean post-fit residuals of range data and range corrections of tropospheric refraction.
• : Mean post-fit residuals of range data Cb8.
Y : Range corrections by KR Model with mean relative humidity observed around the tracking station.

潮汐力による地殻水平変動モデルのモデル誤差を考慮すると、Fig.4～Fig.11 の解析結果は、本研究における軌道解析理論により、静止衛星の観測データがほぼ完全に説明可能であることを示していると考えることが出来る。

6．結言

本研究では、新しい対流圏電波伝搬距離補正モデル（ＫＲモデル）を開発した。このモデルは、仰角49° の衛星の場合、相対湿度が20%増加すると電波伝搬遅延が1m増加（仰角90° の場合は0.75m 増加）するようにモデル化されている。そして、このモデルによる距離補正値と対流圏距離補正を一定値（4.0m）として軌道決定した場合の O-Cとを比較した。

その結果、軌道解析理論において次の事項を考慮することにより、静止衛星の軌道を観測精度の範囲内でほぼ完全に説明することが可能であることを確認した。

(1) 衛星がスピンすることにより、衛星軌道に沿った方向に未知の力が作用すること。
(2) 潮汐力によりマントル内部に海流や潮流の様な流れが存在し、その流れと共に地殻が水平方向に動いていること。
(3) 相対湿度の変化により電波伝搬遅延量が変化すること。

対流圏電波伝搬伝搬角度補正モデルの開発、及び未知の力の解明については今後の課題である。

最後に通信衛星の貴重な観測データを提供して頂いた通信・放送機構に心から感謝の意を表する。更に、研究全般に渡って貴重な助言をして頂いた群馬天文台長の古在由秀氏、国立天文台の木下宙氏、磯部琇三氏、及び軌道解析プログラムの作成において色々指導して頂いた海上保安庁水路部の仙石新氏、国立天文台の福島登志夫氏、宇宙科学研究所の吉川真氏、又計算機の使用等において指導して頂いた国立天文台の平山智啓氏、富山商船高等専門学校の門村英城氏に心から感謝の意を表する。

参考文献

(1) 河合雅司:静止衛星の軌道解析に関する研究－Ｖ．　－観測距離と計算距離の残差と気象要素の関係－,日本航海学会論文集,第101号,pp.7-14,1999
(2) Francis J.Lerch,Barbara H.Putney,Carl A.Wagner and Steven M.Klosko:Goddard Earth Models for Oceanographic Applications(GEM10B and 10C),Marine Geodesy,Vol.5,No.2,pp.145-187,1981.
(3) E.M.Standish,Jr.:Orientation of the JPL Ephemerides,DE200/LE200,to the Dynamical Equinox of J2000,Astronomy and Astrophysics,114,pp.297-302,1982.
(4) 古在由秀:人工衛星による地球・海洋潮汐の検出,月刊海洋科学,地球と海洋潮汐,106号,pp.640-643,1978.
(5)Dennis D.McCarthy:IERS STANDARDS 1992,International Earth Rotation Service,1992.
(6)河合雅司:静止衛星の軌道解析に関する研究－Ⅱ,第27回天体力学研究会集録,pp.19-28,1995
(7)宇宙開発事業団:レンジとレンジレートの補正,宇宙開発事業団データベース,ABS No.2612.C.
(8) J.H.Berbert and H.C.Parker:GEOS Satellite Corrections for Refraction in the Troposphere,International Symposium on Electromagnetic Distance Measurement and Atmospheric Refraction,Boulder Colorado,1969.
(9) 日本測地学会:ＧＰＳ－人工衛星による精密測位システム－,日本測量協会,pp.228-229,1989
(10)William F.Eddy,et al.:GEODYNⅡ-Volume1,Systems Description Volume1,GSFC,1989

Relationship between the Subaru Telescope and Celestial Mechanics

Subaru Telescope, NAOJ
Tetsuharu Fuse
Tetsuharu.Fuse@SubaruTelescope.org

すばる望遠鏡と天体力学の関係

国立天文台ハワイ観測所　布施 哲治

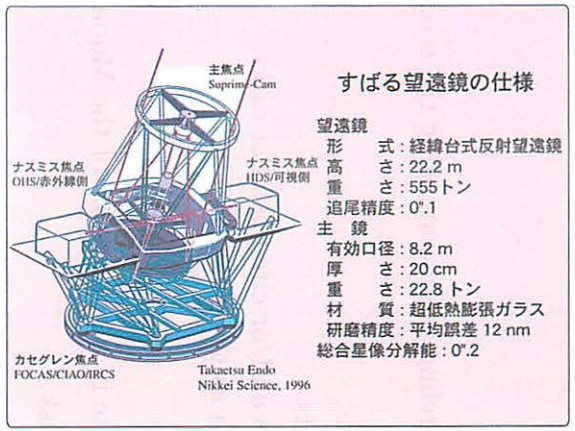

すばる望遠鏡の仕様

望遠鏡
- 形　　式：経緯台式反射望遠鏡
- 高　　さ：22.2 m
- 重　　さ：555トン
- 追尾精度：0".1

主　鏡
- 有効口径：8.2 m
- 厚　　さ：20 cm
- 重　　さ：22.8 トン
- 材　　質：超低熱膨張ガラス
- 研磨精度：平均誤差 12 nm

総合星像分解能：0".2

The Mauna Kea Observatories

Telescope	*Primary Use*	*Size*
1: Subaru Telescope	Opt/Infra	8.2 m
2: Keck Observatory	Opt/Infra	10 m x 2
3: NASA Infrared Telescope Facility (IRTF)	Infra	3.0 m
4: Canada-France-Hawaii Telescope (CFHT)	Opt/Infra	3.0 m
5: Gemini Northern 8-m Telescope	Opt/Infra	8.1 m
6: UH 2.2-m Telescope	Opt/Infra	2.2 m
7: United Kingdom Infrared Telescope (UKIRT)	Infra	3.8 m
8: UH 0.6-m Telescope	Opt	0.6 m
9: Caltech Submillimeter Observatory (CSO)	*1	10.4 m
10: James Clerk Maxwell Telescope (JCMT)	*1	15 m
11: Smithsonian Submillimeter Array	*2	6 m x 8

*1 Millimeter / Submillimeter, *2 Submillimeter

すばる望遠鏡の共同利用について

第一期共同利用期間
2000年10月～2001年３月中 の 36夜

2000年４月下旬　公募要項のアナウンス
↓
６月上旬　プロポーザル締め切り
↓
８月中旬　審査結果通知
↓
10月下旬　共同利用開始

第一期共同利用期間に行えること

- Suprime-Cam による撮像
- IRCS による分光＆撮像

【観測提案例】

Suprime-Cam による 新トロヤ群 探し
- 土星、天王星、海王星には力学的に存在してもよい
- 天王星と海王星の間の新しい小天体ベルトも?

CIAO による 小惑星の衛星探し
- CFHT による直接検出 (45 Eugenia, 軌道半径1200km)
- 小惑星＋衛星の質量がわかる →密度がわかる

CIAO による系外惑星探し
- 直接検出可能
- 本格観測には、波面補償光学装置 AO が必要

Suprime-Cam による EKBO 探し
- 現在の分布と実際の分布の関係
- 50AU～は何もないのか?

すばる望遠鏡 第一期観測装置

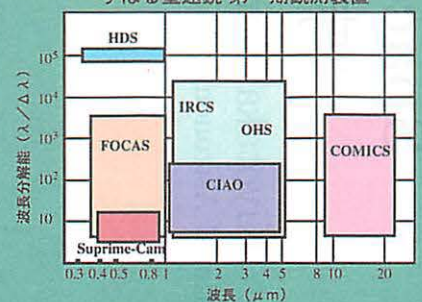

略　称	装　置　名	最大視野	限界等級
Suprime-Cam	すばる主焦点カメラ	30" x 24"	R = 28
FOCAS	微光天体分光撮像装置	6.4" x 6.4"	V = 24.5
HDS	高分散分光器	10" x 0.4"	V = 20
CIAO	コロナグラフ観測装置	25" x 25"	中心星依存
OHS	OH夜光除去分光器	20" x 1"	H = 24
IRCS	近赤外線分光撮像装置	1' x 1'	K = 23
COMICS	冷却中間赤外線分光撮像装置	42" x 31"	400 mJy

Space Occultation
宇宙空間掩蔽

Kiyotaka Tanikawa and Yoshitaka Mikami
National Astronomical Observatory, Mitaka, Tokyo, 181-8588 JAPAN

Abstract

The whole-sky-survey of multiple stars through a telescope on board a lunar satellite is proposed. The feasibility of the project is examined.

1. Introduction

The frequency of binaries and multiple stars in the general field and in open and globular clusters of Galaxy is one of the fundamental issues in astronomy. This is on one hand related to the initial mass function of star formation and on the other hand to the dynamics of star clusters. The determination of the frequency may well deserve of a target of a dedicated space mission.

In this short preliminary note, the author, as a first step, tries to see the possibility of detecting in a systematic way bright binaries via occultation in space. One serious comment comes from Hajime Kawakami(2000) of MSSL, UK that in the outer space conditions, occultation is not a necessary technique and it suffices to directly see the objects. If direct observations do not deteriorate the images and positions of objects, then these are far better than occultations since we can integrate radiations from objects. In addition, we can observe celestial objects from an earth satellite.

However, the author considers that it is of some value to study the feasibility of occultation observations because there may be some problems in direct observations related to pointing and tracking accuracies.

1.1 Purpose

A telescope on board a satellite encircling the moon, using the moon as an occulting disk, carry out the following observations:

(1) surveying multiple stellar systems,
(2) measuring the radii of supergiants,
(3) detecting circumstellar envelopes and/or circumstellar disks,
(4) observing other phenomena, such as the solar activity.

1.2. Specifications

(1) A small telescope on board a satellite in a polar orbit of the Moon,

(2) The moon is used as an occulting disk,

(3) Instruments used are Photo-intensifiers or CCD's,

(4) Measurement of the luminosity change,

(5) Observational wavelength: optical regime.

1.3. Advantages of the method

1. Active decision of observation program.
2. Repeated observation of the same objects.
3. The whole sky survey.
4. A large amount of data for a short time interval.

1.4. Expected results

1. Frequency of multiple stellar systems in the solar neighborhood and in nearby clusters,
2. Orbit determination of binary systems from multiple observations,
3. The upper limit of the magnitude of companions when not detected,
4. Mass-luminosity relation of supergiants when the radius is measured,
5. The upper limit of the luminosity of circumstellar material.

2. Observational Constraints

2.1. Image size(Born & Wolf, 1975; 吉田正太郎, 1988)

The image size is given by

$$\varepsilon_1 = 2''.5160 \times 10^6 \times \frac{\lambda}{\phi}$$

where λ, ϕ are the observational wavelength and the aperture of the telescope.

Table. Image size

wavelength nm	$\phi 50cm$ $''$	$\phi 1m$ $''$
300	0.151	0.075
400	0.201	0.100
500	0.252	0.126
600	0.302	0.151
700	0.352	0.176
800	0.402	0.201

2.2. Limiting magnitude and time resolution

Let us count the number of photons. The energy E per unit time(s), per unit area(m^2), per unit wave length(nm) at 550 nm for a star of visual magnitude $m_v = 0$ is given by $E = 3.64 \times 10^{-11}$J m^{-2} s^{-1}(nm)$^{-1}$ The number N of photons per unit time(s), per unit area(m^2), per unit wave length(nm) at 550 nm is $N = E/(hc/\lambda) = E\lambda/(hc)$. Substituting the necessary parameters $h = 6.626 \times 10^{-34}$J s, $c = 2.998 \times 10^8$m s^{-1}, $\lambda = 5.50 \times 10^{-7}$m into the above equations, we obtain

$$N = \frac{3.64 \times 5.50}{6.626 \times 2.998} \times 10^{-11-7+34-8}\mathrm{m}^{-2}\mathrm{s}^{-1}(\mathrm{nm})^{-1} = 1.01 \times 10^8\mathrm{m}^{-2}\mathrm{s}^{-1}(\mathrm{nm})^{-1}$$

Case(1) Radiation of 100 nm bandwidth with center at 550nm

The number N_{100} of photons is

$$N_{100} = 1.01 \times 10^{10}\mathrm{m}^{-2}\mathrm{s}^{-1}$$

Table. The number of photons with 10 % quantum efficiency

mag.	Number $m^{-2}s^{-1}$	Number $(0.5m)^{-2}s^{-1}$	Number $(0.5m)^{-2}(100s)^{-1}$	$\sqrt{\text{Number}}$	Number $(0.5m)^{-2}(1000s)^{-1}$
0	1.01×10^9	2.5×10^8	2.5×10^6		2.5×10^5
9	2.54×10^3	6.34×10^4	6.34×10^2	25.2	6.34×10
10	1.01×10^5	2.5×10^4	2.5×10^2	15.8	2.5×10
11	4.02×10^4	1.01×10^4	1.01×10^2	10.0	1.01×10
12	1.60×10^4	4.00×10^3	4.00×10	6.3	4.00
13	6.37×10^3	1.58×10^3	1.58×10		1.58
14	2.54×10^3	6.34×10^2	6.34		0.634

The number of stars(Rika-Nenpyo(理科年表), 2000) is $N_{<10} = 3.5 \times 10^5$, $N_{<11} = 8.7 \times 10^5$. We have a sufficiently large number of stars in this magnitude limit. The situation may be drastically improved in case of direct observations.

Time resolution may be limited by detectors. For CCD array, time resolution is as large as 1 sec. If we use a sophisticated technique("Time Delay"), the situation is better (Kawakami, 2000).

3. The Orbit of the Satellite

In the first part of this section, we consider a satellite encircling the moon in a circular orbit with semimajor axis 10^4km.

3.1. Effect of the finite distance of the occulting disk

1) The size of objects on the surface of the moon seen from the satellite

The size of the object with angular size $0''.1$ seen from 10^4km is

$$10^4 \times \frac{0.1}{3600} \times \frac{\pi}{180} km = \frac{\pi}{3.6 \times 1.8} \times 10^{4-1-3-2} km = 4.8m$$

Irregular surface geometry of the order 5m affects the observation. The corresponding size is 180m for the ground observation.

2) The size of the moon seen from distance 10^4km

The angular size of the radius 1740km of the moon is $\theta = \sin^{-1}(1.74/10) = .175$. Then the solid angle is $2\pi(1 - \cos\theta) = 0.00763 \times 4\pi$. This means that the moon occupies 7.63×10^{-3} of the whole sky. For reference, this values is 4.8×10^{-7} for the ground observation.

3) The velocity and period of the satellite with semimajor axis 10^4km

Neglecting the gravitational effect of the earth, we obtain the orbital velocity v from Kepler's law($n^2a^3 = GM_{moon}$) as

$$v = \sqrt{\frac{GM_{moon}}{a}} = 7.0 \times 10^2 \ m/s$$

The orbital period T is given as

$$T = 2\pi\sqrt{\frac{a^3}{GM_{moon}}} = 1.04 \text{ days}$$

3.2. Orbit change of the lunar satellite

A high altitude of the satellite is preferable because of the results in the preceding subsection. In order that the period of observation be as long as one year, the orbital stability is desirable. In this subsection, we estimate the relative importance of perturbations to the satellite(Kinoshita, 1998). For the earth satellite case, $J_2 = 1.08 \times 10^{-3}$, $J_3 = -2.54 \times 10^{-6}$, $J_4 - -1.62 \times 10^{-6}$, whereas for the moon satellite case, we have $J_2 = 2.02 \times 10^{-4}$, $J_3 = 1.21 \times 10^{-5}$. The effect of J_3 is relatively large. Elements a, e, and I do not change under the first order secular perturbation due to J_2. However, the pericenter and the node moves. e has a long-periodic(much longer than orbital period) variation due to J_3.

Perturbations from the earth and the sun is large compared with those for the earth satellite. The relative importance of the perturbations from the Earth and Sun, and J_2 of the moon with respect to the two-body main term are given by the ratios

$$\frac{m'}{m_{\text{moon}}}\left(\frac{a}{a'}\right)^3, \quad J_2\left(\frac{R_{moon}}{a}\right)^2$$

where a is the semimajor axis of the satellite, and m' and a' are the mass of the Earth(resp. Sun) and the distance from the Earth(resp. Sun). Then we get

$$1.43 \times 10^{-3}, \ 8.08 \times 10^{-6}, \ \ 6.12 \times 10^{-6}$$

for the Earth, Sun, and J_2 perturbations. Thus, the perturbation from the Earth is biggest. The orbital control might be necessary.

3.3. Orbital inclination and occultation

In this subsection, we will consider the observational schedule assuming the invariant elements of the orbit.

3.3.1. The condition for the inclination for the whole-sky-survey

We assume 10^4km for the semimajor axis of the orbit. The angular size of the moon is 0.175 radian = 10°.03. Therefore, if $I \geq 80°$, then the south and north polar sky region can be covered.

3.3.2. The relative velocity of celestial objects with respect to the moon

For reference, let us first consider the occultation observation from the Earth. For simplicity, we assume the moon's orbit around the Earth is circular. It goes around the Earth in about 27 days. The moon's mean motion relative to stars is

$$\frac{360^\circ}{27 \times 24 \times 3600\text{sec}} = \frac{360''}{27 \times 24\text{sec}} = 0.56''/sec$$

This gives the upper limit of the relative motion. For stars, moving non-perpendicular to the surface of the moon, the relative velocity is smaller.

Let us consider the observation from the lunar satellite of semimajor axis 10^4km. The period is 1 day. Then the mean motion is given by

$$\frac{360^\circ}{24 \times 3600\text{sec}} = \frac{360''}{24\text{sec}} = 15''/sec$$

In this case, in order to attain the angular accuracy of the order 0".15, we need to take data each 1/100 seconds. For stars crossing the lunar surface non-perpendicularly, the situation is better, i.e., the relative velocity is smaller.

Observational schedule should be constructed so as not to see the edge of the moon illuminated by the Sun or Earth.

3.4. Summary of orbital elements

a (km)	T (day)	I °	Area	Relative velocity ("/sec)	Size of the surface object m/0".1
5000	0.35	≥ 70	3.13×10^{-2}	42.9	2.4
10000	1.04	≥ 80	7.63×10^{-3}	15	4.8
15000	1.91	≥ 83.4	3.38×10^{-3}	7.9	7.2
20000	2.94	≥ 85.0	1.90×10^{-3}	5.1	9.6
Ground	27	–	4.8×10^{-7}	0.56	180

4. Detectable multiple stellar systems

We fix the aperture of the telescope to 50cm and suppose that we can separate two objects of angular distance 0".2. Then

Distance to binaries pc	Separation AU	Separation "
10	2	0.2
10^2	20	0.2
10^3	2×10^2	0.2
10^4	2×10^3	0.2

If we use a CCD array, we can determine to a certain degree the frequency of binaries in nearby clusters.

5. Comparison with existing surveys

1. Hipparcos – binaries with short periods

The accuracy of Hipparcos observation(at epoch 1991.25) is 1 mas for position and 1 mas/year for proper motion. However, only for a small number of binaries, the orbital elements have been determined due to the shortage of the observation period(3 years). Separation is $0''.3$ for binaries of magnitude difference 4^{mag} and $5''$ for 5^{mag}.

2. Spectroscopy – close binaries, advantageous for edge-on binaries.

3. Coronagraph – close binaries, advantageous for those with big difference in magnitude.

4. Occultation – visual binaries in the outer space with arbitrary $\sin i$.

Acknowledgments

The author expresses his thanks to Toshihiro Handa, Mituru Soma, Tadasi Nakajima, Wako Aoki, Hiromitsu Yokoo, Shinji Ukita, Satoshi Miyazaki, and especially to Hajime Kawakami(MSSL,UK) for useful suggestions.

References

Allen, C.W.: 1973, Astrophysical Quantities, The Athlone Press.

Born, M. and Wolf, E.: 1975, *Principles of Optics* Vol.II, Pergamon Press, Oxford.

Unsöld: 1978, 現代天文学 第2版 (小平桂一訳), 岩波書店.

Kawakami, H.: 2000, private communication.

Kinoshita, H.: 1998, *Dynamics of Celestial Objects and Orbits* (天体と軌道の力学), University of Tokyo Press(in Japanese).

Millennium Star Atlas Vol.I p.XIV.

Rika-Nenpyo(理科年表), 2000, (Ed. National Astronomical Observatory), Maruzen, Tokyo.

吉田正太郎: 1988, 望遠鏡光学・反射編, 誠文堂新光社; 1988, 望遠鏡光学・屈折編, 誠文堂新光社.

Thermal Relaxation in One-Dimensional Self-Gravitating Systems

Junichiro MAKINO*
Department of Astronomy, School of Science,
University of Tokyo, Tokyo 113-0033

May 8, 2000

Abstract

In this paper, we study the thermal relaxation in the one-dimensional self-gravitating system, or so-called sheet model. According to the standard argument, the thermal relaxation time of the sheet model is around Nt_c, where N is the number of sheets and t_c is the crossing time. It has been claimed that the system did not reach the thermal equilibrium in this thermal relaxation timescale, and that it takes much longer time for the system to reach true thermal equilibrium.

We demonstrate that this behavior is explained simply by the fact that the relaxation time is long. The relaxation time of sheets with average binding energy is $\sim 20Nt_c$, and that of sheets with high energy can exceed $1000Nt_c$. Thus, one needs to take the average over the relaxation timescale of high-energy sheets, if one wants to look at the thermal characteristic of these high energy sheets.

1 Introduction

The one-dimensional self-gravitating many-body system was originally introduced primarily as a simple toy model to understand the violent relaxation, [4] because the thermal relaxation timescale of its discrete realization, the sheet model, was believed to be long. Until 1980s, it had been generally accepted that the thermal relaxation time of the system of N equal-mass sheets is of the order of N^2t_c, where t_c is the crossing time of the system.

However, by means of numerical simulation Luwel *et al.*[3] have demonstrated that the relaxation time is of the order of Nt_c. Reidel and Miller [6, 7] reached a similar conclusion, though they reported the presence of systems which apparently did not relax for much longer timescale.

In a series of papers, Tsuchiya *et al.* [10, 11, 12] have studied the thermal relaxation process of one-dimensional self-gravitating systems in detail, by means of the numerical integration over very long timescale (some of their experiments covered $5 \times 10^8 t_c$). They claimed that the thermal relaxation of the sheet model proceeds in a highly complex manner. In the "microscopic relaxation timescale" of Nt_c, each sheet forgets its initial condition, and the system is well mixed. However, according to them, the system does not really reach the thermal equilibrium in this timescale, and the distribution function remains different from that of the isothermal state. They called this state a quasiequilibrium

By pursuing the time integration for much longer timescale, Tsuchiya *et al.* [12] found that the system exhibits the transition from one quasiequilibrium to another, and they claimed that the thermal equilibrium is only realized by averaging over the timescale longer

*E-mail address: makino@astron.s.u-tokyo.ac.jp

than the timescale of these transitions. Thus, they argued that there exists the timescale for "macroscopic" relaxation, which is much longer than the usual thermal relaxation (what they called "microscopic relaxation").

In this paper, we examine the nature of this "macroscopic" relaxation of the one-dimensional sheet model. In section 2, we describe the numerical model. In section 3, we present the result of the measurement of the relaxation time. It is shown that the relaxation time, defined as the timescale in which individual sheets change their energies, depends very strongly on the energy of individual sheet, and is very long for high energy sheets. This strong dependence of the relaxation timescale on the energy naturally explains the apparent "transient" phenomena observed by Tsuchiya *et al.*[12] Section 4 discusses the implication and relevance of our results.

2 The Model

2.1 Sheet model

The Hamiltonian of the sheet model is given by

$$H = \frac{m}{2}\sum_{i=1}^{N} v_i^2 + 2\pi G m^2 \sum_{i<j} |x_i - x_j|, \tag{1}$$

where x_i and v_i are the position and velocity of sheet i, m is the mass of the sheets, N is the number of the sheets and G is the gravitational constant. The crossing time is defined as

$$t_c = \frac{1}{4\pi G M}\sqrt{\frac{4E}{M}}, \tag{2}$$

where $M = mN$ is the total mass of the system. Following Tsuchiya *et al.*[12] and others, we use the system of units in which $M = 4E = 4\pi G = 1$. In this system, $t_c = 1$.

A unique nature of the one-dimensional gravitational system is that there exists the thermal equilibrium, unlike its counterpart in three dimensions. Rybicki [8] obtained the distribution function

$$f(\varepsilon) = \frac{1}{8}\left(\frac{1}{2\pi}\right)^{1/2}\left(\frac{3M}{2E}\right)^{3/2}\exp\left(-\frac{3M}{2E}\varepsilon\right), \tag{3}$$

where ε is the specific binding energy defined as

$$\varepsilon = \frac{v^2}{2} + \Psi(x) - \Psi(0). \tag{4}$$

Here, $\Psi(x)$ is the specific potential energy. This distribution function satisfies the relation

$$\exp\left(-\frac{3M}{2E}\varepsilon\right) = \mathrm{sech}^2\left(\frac{3x}{8E}\right). \tag{5}$$

We performed the time integration of the system with $N = 16$, 32, 64, 128 and 256. For all systems, the initial condition is a water-bag with the aspect ratio $x_{max}/v_{max} = 2.5$.

2.2 Numerical method

The important character of the sheet model is that one can calculate the exact orbit of each sheet until two sheets cross each other. Thus, we can integrate the evolution of the system precisely (except for the round-off error). This may sound like a great advantage, compared

to the systems in higher dimensions whose orbits can be calculated only numerically. Instead of numerically integrating the orbit of each sheet, we can calculate the exact orbit for any sheet, until it collides with the neighboring sheet. Thus, by arranging the pairs using heap, we can handle each collision in $\log N$ calculation cost.

Note, however, that typically each sheet collides with all other sheets in one crossing time. Thus, the calculation cost is $O(N^2 \log N)$ per crossing time. Our simulation with $N = 64$ for $2 \times 10^7 t_c$ took 8 hours on a VT-Alpha workstation with DEC Alpha 21164A CPU running at 533 MHz. For this run, the total energy of the system was conserved better than 3×10^{-12}.

3 Results

3.1 Approach to the thermal equilibrium

Figure 1 shows the time-averaged energy distribution function $N(\varepsilon)$, for different time periods and number of sheets. In all figures, the thin solid curve is the energy distribution of the isothermal distribution function of equation (3). What we see is quite clear. As we make the time interval longer, the time-averaged distribution function approaches to the isothermal distribution. Thus, the numerical result suggests the system is ergodic. However, it also shows that the time needed to populate the high-energy region is very long. The sampling time interval is 128 time units for $N = 16$, and 512 time units for $N = 64$ and 128. Thus, in the case of $T = 2^{18}$ and $N = 16$ (dash-dotted curve in figure 1a), total number of sample points is $2^{15} = 32768$.

If we can assume that the sample points are uncorrelated, the possibility that no sample exceeds energy level ε_0 is given simply by

$$P(\varepsilon_0, N) = P(\varepsilon < \varepsilon_0)^n, \tag{6}$$

where

$$P(\varepsilon < \varepsilon_0) = \int_0^{\varepsilon_0} N(\varepsilon) d\varepsilon, \tag{7}$$

and n is the number of sample points. Figure 2 shows $1 - P(\varepsilon)$ as a function of ε. For $\varepsilon = 1.25$, $P(\varepsilon) = 0.996$, and therefore the probability that none of 32768 samples does not exceed $\varepsilon = 1.25$ is practically zero ($< e^{-100}$). In other words, the numerical result seems to suggest that the system is not in the thermally relaxed state even after 2×10^5 crossing times.

Of course, this result is not surprising if the relaxation time is long. Samples taken with the time interval shorter than the relaxation time have a strong correlation, and therefore the effective number of freedom can be smaller than n. Roughly speaking, if the relaxation time is longer than 10^4, our numerical result is consistent with the assumption that the system is in the thermal equilibrium. In the next subsection, we investigate the relaxation time itself.

3.2 Relaxation timescale

We measured the following quantities:

$$D_1 = \frac{< \varepsilon_i(t_0) - \varepsilon_i(t_0 + \Delta t) >}{\Delta t}, \tag{8}$$

$$D_2 = \frac{< [\varepsilon_i(t_0) - \varepsilon_i(t_0 + \Delta t)]^2 >}{\Delta t}. \tag{9}$$

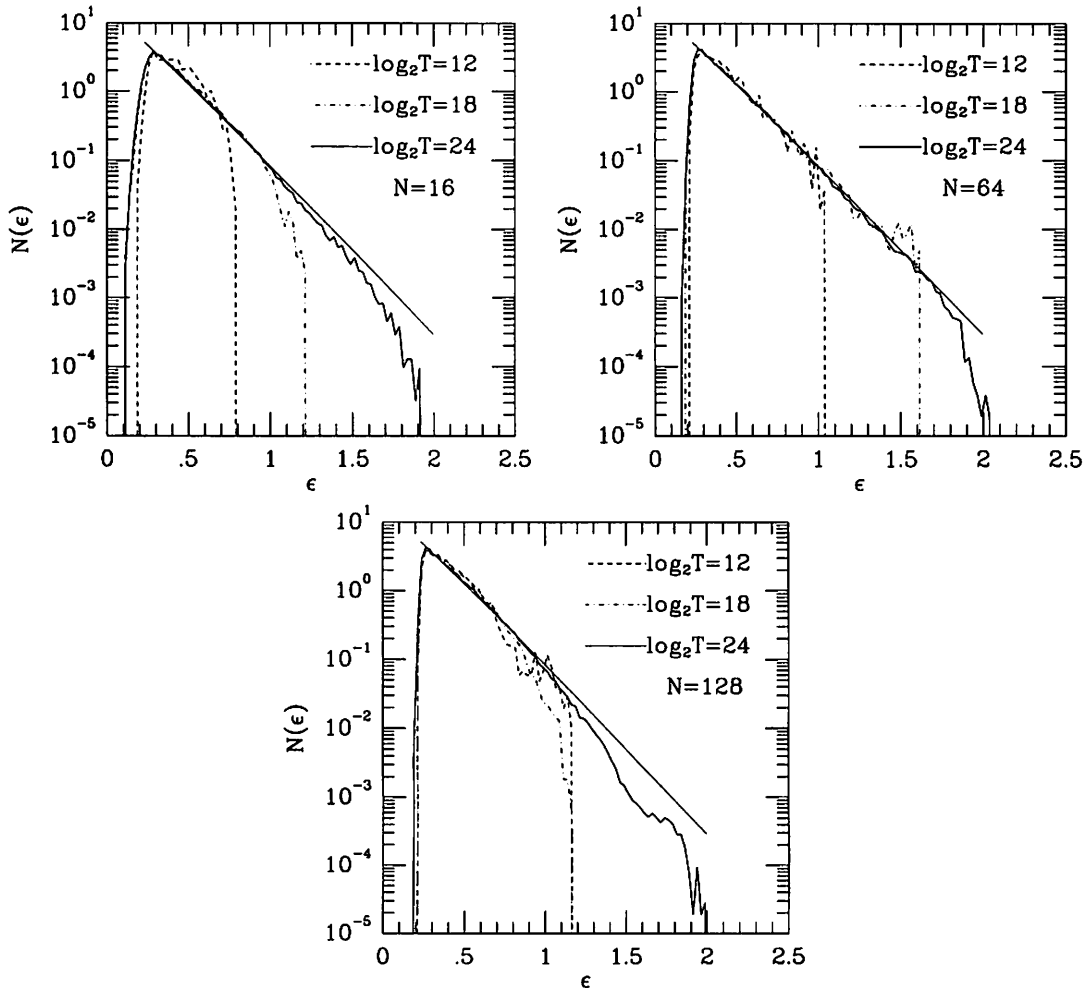

Figure 1: The time-averaged distribution function in the energy space $N(E)$; (a) $N = 16$, (b) $N = 64$, (c) $N = 128$.

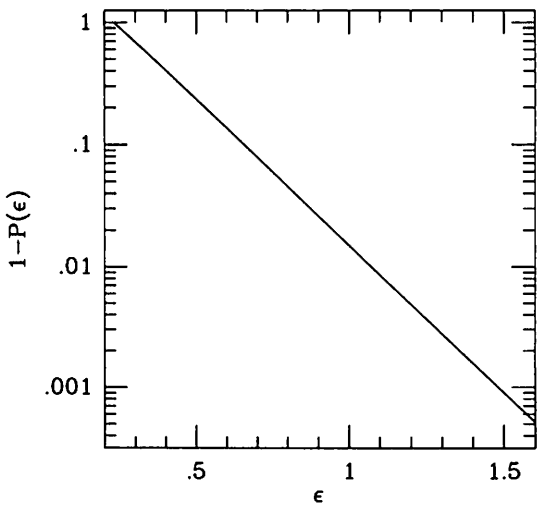

Figure 2: The compliment of the cumulative distribution function $1 - P(e)$ for the thermal equilibrium.

These quantities correspond to the coefficients of the first and second-order terms in the Fokker-Planck equation for the distribution function, and have been used as the measure of the relaxation in many studies (see, *e.g.*, Hernquist and Barnes,[1] Hernquist *et al.* [2]), for three-dimensional systems. However, to our knowledge this measure has not been used in the study of the sheet model.

In order to see the dependence of these diffusion coefficients on the energy, we calculated them for intervals of $\Delta\varepsilon = 0.15$. Figure 3 shows the results, for $N = 16, 64$ and 256. The time interval Δt was taken equal to Nt_c. We used smaller values for Δt and confirmed that the choice of Δt has negligible effect if Δt is larger than $10t_c$ and smaller than $4Nt_c$. Time average is taken over the whole simulation period. We can see that both the first- and second-order terms show very strong dependence on the energy of the sheets, and of the order of $1/100N$ for $e \sim 1.5$. Figure 3 suggests that the relaxation timescale grows exponentially as energy grows. This behavior is independent of the value of N.

We can define the relaxation timescale as

$$t_r = \varepsilon^2 / D_2, \tag{10}$$

that is, the timescale in which energy changes significantly. Figure 4 shows this relaxation timescale for different values of N and ε. The relaxation time shows very strong dependence on the energy and the relaxation of high-energy sheets is much slower than that of sheets with lower energies. This is partly because of the dependence of t_r on ε itself. However, as w can see in figure 3, the dependence of the diffusion coefficient is the main reason.

This result resolves the apparent contradiction between the fact that the relaxation timescale is of the order of Nt_c [5] and that the system reaches the true thermal equilibrium only in much longer timescale.[12] It is true that the relaxation timescale is $O(N)$, but the coefficient before N is quite large, in particular for sheets with high energies.

An important question is why the relaxation timescale depends so strongly on the energy. This is provably due to the fact that high-energy sheets have the orbital period significantly longer than the crossing time. Typical sheets have the period comparable to the crossing time, and therefore they are in strong resonance with each other. However, a high-energy sheet has the period longer than the crossing time, and thus it is out of resonance with the

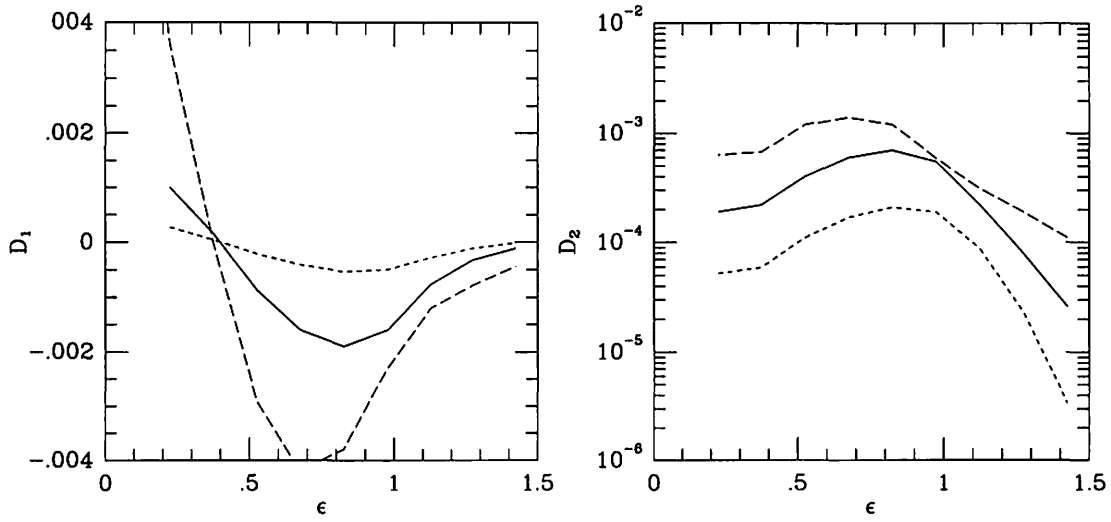

Figure 3: The diffusion coefficients (a) D_1 and (b) D_2 plotted against the energy e for three values of N. Long-dashed, solid, and short-dashed curves are the results for $N = 16$, 64 and 256, respectively.

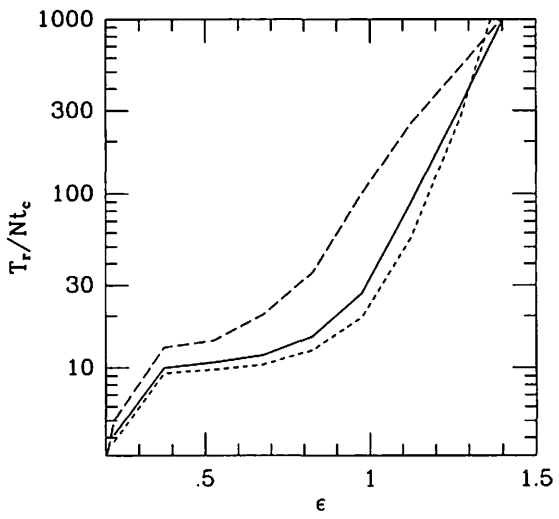

Figure 4: The relaxation time in unit of Nt_c plotted against the energy e for three values of N. Curves have the same meanings as in figure 3

rest of the system. Therefore, the coupling between high energy sheets and the rest of the system is much weaker than the coupling between sheets with average energy. This explains why the relaxation of high energy sheets is slow.

4 Summary and Discussion

In this paper, we studied the thermal relaxation process in one-dimensional self-gravitating systems. We confirmed the result obtained by Tsuchiya *et al.*[12] that the thermal relaxation takes place in the timescale much longer than Nt_c. However, we found that this is simply because the thermal relaxation timescale is much longer than Nt_c. Even for typical sheets, the relaxation timescale is around $10Nt_c$. In order to obtain good statistics, we need to take average over many relaxation times. Moreover, the relaxation time for sheets in the high-energy end of the distribution function is even longer, since the relaxation timescale grows exponentially as the energy grows. Thus, it is not surprising that we have to wait for more than $10^4 Nt_c$ to obtain good statistics.

Does this finding have any theoretical/practical relevance? Theoretically, there is nothing new in our result. What we found is simply that numerical simulation should cover the period much longer than the relaxation timescale to obtain statistical properties of the system, and that the relaxation timescale of a sheet depends on its energy. Both are obvious, but some of the previous studies neglected one or both of the above, and claimed to have found a complex behavior, which, in our view, is just a random walk.

Our finding of the long relaxation time by itself has rather little astrophysical significance, since in the large N limit, the relaxation time is infinite anyway. However, since any numerical simulation suffers some form of numerical relaxation, it is very important to understand how the relaxation effect changes the system. To illustrate this, we examine the claims by Tsuchiya *et al.*[12] in some detail here.

They argued that the evolution of the mass sheet model proceeds in the following four steps: (1) viliarization, (2) dynamical equilibrium, (3) quasiequilibrium, and (4) thermal equilibrium. According to them, the viliarization timescale is order of t_c, and the energy of each sheet is "conserved" in the dynamical equilibrium phase, which continues up to $t \sim Nt_c$. Then, "microscopic relaxation" takes place in the timescale of $t \sim Nt_c$, where the energy of each sheet is relaxed, but the whole system needs timescale much longer to reach the true equilibrium, because of some complex structure in the phase space.

Our numerical results are in good agreement with those of Tsuchiya *et al.*,[12] but our interpretation is much simpler: First system virializes, and then relaxation proceeds in the timescale of thermal relaxation, which depends on the energy of the individual sheets. Thus, the central region with short relaxation time relaxes to the distribution close to the thermal relaxation in less than $100Nt_c$, but the distribution in the high-energy tail takes much longer to settle. In addition, the small number statistics in the high-energy region makes it necessary to average over many relaxation times to obtain good statistics. In other words, there are no distinction between the "microscopic" and "macroscopic" relaxation, and the evolution of the system is perfectly understood in terms of the standard thermal relaxation.

Acknowledgments

I would like to thank Yoko Funato, Toshiyuki Fukushige and Daiichiro Sugimoto for stimulating discussions, and Shunsuke Hozumi for comments on the manuscript. This work is supported in part by the Research for the Future Program of Japan Society for the Promotion of Science (JSPS-RFTP97P01102).

References

[1] L. Hernquist and J. E. Barnes, Astrophys. J. **349** (1990), 562.

[2] L. Hernquist, P. Hut and J. Makino, Astrophys. J. Lett. **411** (1993), 248.

[3] M. Luwel, G. Severne, and P. J. Rousseeuw, Astrophys. Space Sci. **100** (1984), 261.

[4] D. Lynden-Bell, Mon. Not. Roy. Astron. Soc **136** (1967), 101.

[5] G. Severne, M. Luwel, and P. J. Rousseeuw, Astron. Astrophys. **138** (1984), 365.

[6] C. J. Reidl, Jr. and B. N. Miller, Astrophys. J. **318** (1987), 248.

[7] C. J. Reidl, Jr. and B. N. Miller, Astrophys. J. **332**, (1988) 619.

[8] G. B. Rybicki, Astrophys. Space Sci. **14**, (1971) 56.

[9] L. Spitzer and M. H. Hart, Astrophys. J. **164**, (1971) 399.

[10] T. Tsuchiya, T. Konishi, and N. Gouda, Phys. Rev. **E50** (1994), 2607.

[11] T. Tsuchiya, N. Gouda, and T. Konishi, Phys. Rev. **E53** (1996), 2210.

[12] T. Tsuchiya, N. Gouda, and T. Konishi, Ap. SS. **257** (1997), 319.

Phase transition and Fractal in self-gravitating ring model

Yasuhide Sota,* Osamu Iguchi, † Masahiro Morikawa, ‡

Department of Physics, Ochanomizu University,
Faculty of Science, 2-1-1 ohtuka, bunkyou-ku, Tokyo, Japan

Takayuki Tatekawa§

Department of Physics, Waseda University,
Shinjuku-ku, Tokyo 169, Japan

Abstract

Fractal and long-tail Lévy-type velocity distribution are well known characters in the self-gravitating viriallized system such as interstellar molecular clouds, so called, interstellar medium (ISM). Here we examined these characters from the viewpoint of the gravitational phase transition by using the one-dimensional ring model with large number of particles interacting with the three-dimensional gravitating force. We got the result that each particle shows Lévy-type random motion whose flight probability has the power-law tail at the critical point. We also examined the fractal dimension of particle distributions at the fixed constant time with the box-counting method. It shows no fractal nature if we allow the particles to rotate the ring many times, until it is captured by a cluster of particles. These results indicate that the fractal nature of self-gravitating system has no correlation with its non-Gaussian velocity natures. However, the nature of these results strongly depends on the fact that the configuration space of particle distribution is compact and the cutoff scale of gravitational force is finite. So in more ideal appropriate limit, we can still expect that both fractal and Lévy flight nature come from the property of phase transition.

I. INTRODUCTION

Self-gravitating system has the exotic statistical characters such as the nonextensivity of supposed-to-be extensive variables [1] and the negative specific heat in microcanonical situation [2]. The latter property makes the system strongly unstable in the canonical situation, that is, if it is immersed in the heat bath. Such a peculiar nature of gravito-statistics is expected to affect the behavior of the gravitationally viriallized system. For example, it is well known that observed ISM meets the viriallized condition and shows the scaling character called Larson's Law [3], which implies the scaling relation among molecular mass (M), molecular size (L) and velocity dispersion (σ^2) as follows,

$$\sigma \sim 1.1 \times L^{0.38}$$
$$\sigma \sim 0.42 \times M^{0.20}. \tag{1}$$

Each ISM also has the characters such as fractal boundary and non-Gaussian, long-tail velocity dispersion [4]. These characters have been explained mainly by the turbulence theory, since their observed Reynolds number is very large. Turbulence theory has succeeded in explaining the observed fractal and non-Gaussian velocity characters in some extents. However, the situation of ISM is quite different from that

*E-mail:sota@skyrose.phys.ocha.ac.jp
†E-mail:osamu@phys.ocha.ac.jp
‡E-mail:hiro@phys.ocha.ac.jp
§E-mail:tatekawa@gravity.phys.waseda.ac.jp

of fluid dynamics in the laboratory, mainly because gravitational interaction plays a key role in triggering the turbulence flow in the former.

There is another approach to explain such phenomena from the viewpoint of the statistics in self-gravitating system [5]. This approach is based on the fact that the main factor to cause turbulence is the gravitational interaction, since the observation indicates that the system is viriallized.

As we mentioned above, there is no stable state in self-gravitating system in the canonical situation. However, if we include the cutoff in the interaction in both large and small scale, we can produce the stationary free-particle state at high temperature and stationary collapsed state at low temperature [2]. In this case, we can regard the gravitationally bound state as the critical point in the phase transition between those two states.

In the case of ISM, the number of each cloud is not fixed, since some of the gas particles can evaporate against gravitational bound. In this sense, it is rather grand canonical as the approach of [5] or [6], especially when we allow for the statistics of ensembles of many different clouds with different numbers. However, if we pay attention to one of those clouds, we can see that it attains to the viriallized micro-canonical state in which all of the element particles are gravitationally bound, although it seems rather canonical after the long time-interval, according to the strength of the interaction with the heat bath. As for the case of ISM, the time scale of relaxation with heat bath seems quite long, since it is weakly interacted with the microwave blackbody radiation. In this sense, it could be fair to say that it is in microcanonical quasi-stable state in the intermediate time interval and finally collapses or diffuses in the long run.

From these considerations, we examine the dynamics of microcanoncial self-gravitating system in this paper, since it would indicate us the plenty of actual phenomena at the critical quasi-stable state in gravitationally viriallized objects such as ISM. In section 2, we introduce the one-dimensional ring model reflecting three dimensional self-gravitating system. In section 3, we will show our numerical results in microcanonical and canonical simulations. Finally, we will briefly comment on the conclusion in section 4.

II. GHMF MODEL ANALYSIS

In this section, we introduce the model of one dimensional self-gravitating system. In general, one-dimensional gravitating model has been analyzed in the context of relaxation [7]. In this context, they examine the model with the force whose potential meets the one-dimensional Poisson's equation and the free boundary condition. Since such a potential is linear and has no upper bound, there is no typical energy scale needed to make each particle escape against gravitational binding energy. This seems unsatisfactory, when it comes to treating the phase transition appearing in the three dimensional self-gravitating system with upper and lower cutoff.

Here we introduce another type of one-dimensional self-gravitating model which reflects the property of such a phase transition. First, we fix the movement of the element particle with the mass m along the one dimensional ring with the radius L and enforce the three dimensional gravitational interaction between each pair of those particles, whose distance is measured by the Euclid measure in the three dimensional Euclid space. The Hamiltonian of such a system becomes as follows,

$$\begin{aligned} H &= \sum_{i=1}^{N} \frac{p_i^2}{2m} - \sum_{i<j}^{N} \frac{Gm^2}{N|2L\sin(\theta_{ij}/2)|} \\ &= \sum_{i=1}^{N} \frac{p_i^2}{2m} - \sum_{i<j}^{N} \frac{Gm^2}{\sqrt{2}LN\sqrt{1-\cos\theta_{ij}}}, \end{aligned} \tag{2}$$

where $\theta_{ij} := \theta_i - \theta_j$ is the angle between i'th and j'th particle on the ring.

Here we divide the interaction term by the particle number N, to keep the extensibity of total energy and take the fluid limit as $N \to \infty$.

Secondly, we also include the lower scale cutoff, ϵ as

$$|2L\sin(\theta_{ij}/2)| \approx \sqrt{2}L\sqrt{1-\cos\theta_{ij}+\epsilon}, \tag{3}$$

since the potential and the force becomes infinite, at the moment that each particle crosses one of the other particles. Then the Hamiltonian and canonical equations of each particles finally become as follows,

$$H = \sum_{i=1}^{N} \frac{p_i^2}{2m} - \sum_{i<j}^{N} \frac{Gm^2}{\sqrt{2}LN\sqrt{1-\cos\theta_{ij}+\epsilon}}. \tag{4}$$

$$\dot{p}_i = -\frac{\partial H}{\partial \theta_i} = -\frac{Gm^2}{2\sqrt{2}LN} \sum_{i\neq j}^{N} \frac{\sin\theta_{ij}}{(1-\cos\theta_{ij}+\epsilon)^{3/2}}$$

$$\dot{\theta}_i = \frac{\partial H}{\partial p_i} = \frac{p_i}{m} \tag{5}$$

In this model, the particle interaction disappears, if the distance of the two particles, $L\delta\theta$, is smaller than the physical scale $\xi \equiv \sqrt{\epsilon}L$. If we take the Fourier expansion for the potential of this model and take only the smallest Fourier mode, we can derive a well-known one dimensional ring model, called Hamilton mean field (HMF) model [8]. Hence we call our model Gravitational HMF (GHMF) model, since it is the extension of HMF model to the case with the gravitational interaction. In the next section, we numerically examine the statistical aspects of GHMF system and compare it with the results of HMF.

III. NUMERICAL RESULTS

Here we numerically solved the canonical equations (5) with the symplectic integrator [9], which keeps the total Hamiltonian highly accurate, even after a long time-interval of numerical simulation. As well as such a microcanonical case, we also examined the canonical case by using Nose's method, where the above N-body system interacts with the heat bath and approaches the canonical equilibrium [10]. In our simulation, we fixed the value of ϵ as 0.01, since it is much harder to keep the total Hamiltonian an accurate value for smaller value of ϵ even with the symplectic method. For the simulation, we take the unit of $G = m = L = 1$.

A. T-U relation

Here, we examine the relation between the total energy U defined by H/N and the temperature T defined by the time averaged one-particle Kinetic energy averaged over all of the particles. This make it clear which type of phase-transition occurs in this system. For example, HMF model shows second-order phase transition, in which the first order derivative of partition function is continuous, while second one is not. This can be shown with the saddle point approximation in canonical system [8]. In the microcanonical numerical simulation, the system stays in the quasi-stable state with the negative specific heat during the long time interval, and then finally moves to the point on the canonical line in T-U plane.

We showed that in GHMF model, the things are more drastic, that is, the system shows the first order phase transition in canonical simulation, as we can see in three dimensional self-gravitating system (Fig.1). So although the state with a negative specific heat exists in GHMF as well as in HMF, we cannot see any counterpart on canonical T-U line in GHMF, which would be finally attained from the microcanonical quasi-stable state with negative specific heat in HMF.

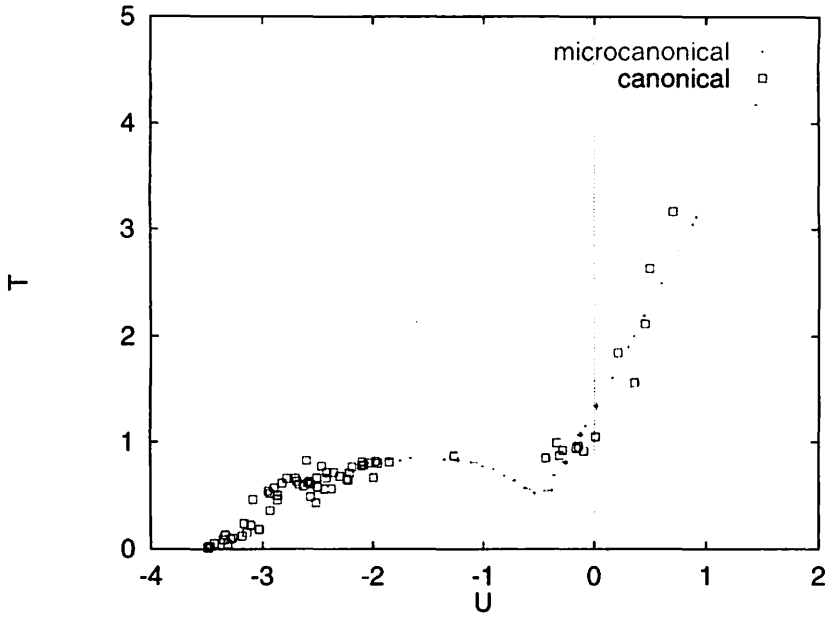

FIG. 1. Energy per one particle vs Temperature diagram (N=100, t=100 and 1000). Square shows the data in canonical simulation and plus shows the data in microcanomical simulation. The jump of the data points can be seen in canonical plot at the energy scale where the specific heat becomes negative in microcanonical plot.

B. Lévy motion and Fractal

Here we examined the particle motions at the state with the negative-specific heat in microcanonical simulation. We can expect some exotic statistical character around this critical state, since the fluctuation becomes large at a critical point, as is well known at phase transition. There are two sorts of flight motion for these particles. First one is the flight motion of the particle captured by gravitationally bounded cluster region. This motion can be expected, if the size of the cluster is much larger than the cutoff scale ξ. Second one is the flight motion of the particles moving along the ring so many times, until it is captured by a cluster of particles. This motion can be expected, if the perimeter of the ring, $2\pi L$, is not much larger than the size of the cluster. In our analysis, the size of the cluster is almost equal to L and ten times larger than ξ. So the second type of flight is more likely to occur than the first one.

It is shown that the second type of Lévy type motion and anomalous diffusion appear in HMF model at the state with the total energy almost equal to the critical one [11]. Here we took the same analysis to see if the Lévy motion occurs in GHMF. We also examined the jump probability to check if it really follows the power-law tail probability. At the energy level $U = U_{\rm cr} \approx -0.45$, we certainly got the result that the probability distribution has a non-Gaussian tail (Fig.2), as is seen in turbulent flow or in foreign exchange markets [12]. The averaged jump probability follows the power-law tail whose exponent is nearly equal to 1.0 between the time interval $dt = 10$ and $dt = 500$.

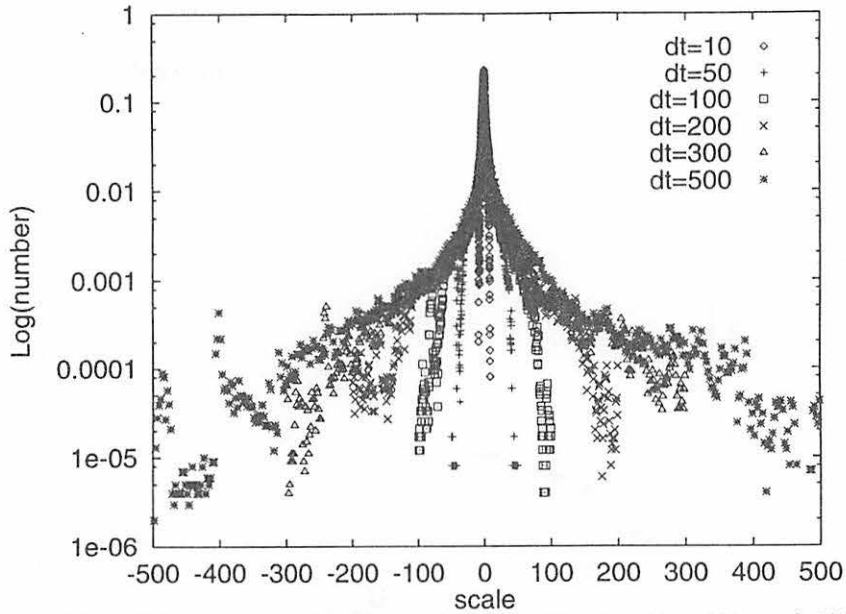

FIG. 2. Log-linear plot of for the time intervals : dt= 10, 50, 100, 200, 300, and 500 for the case of $N = 100, U = -0.45, t = 5000$.

We also compared it with the fractal dimension of the particle distribution at the constant time with the box-counting method [13], when the temperature almost attains to the relaxed value. The averaged distance between the two particles approximately becomes

$$L_{\rm av}(\xi) \approx \frac{L}{N_{\rm free}(\xi)}, \tag{6}$$

where $N_{\rm free}(\xi)$ is the number of the free particles which move independently of a cluster. If the box size r satisfies the condition $r > L_{\rm av}(\xi)$, we cannot expect the fractal dimension $D < 1.0$, since almost all of the boxes include at least one particle in this case. On the other hand, if $r < \xi$, we cannot see any gravitational nature, since the motions of particles become completely free within this box size. So we can expect to get fractal nature caused by the gravitational force only in the scale

$$\xi < r < L_{\rm av}(\xi). \tag{7}$$

In our simulation, $\xi = 0.1$ ($\epsilon = 0.01$) and $L_{\rm av}(\xi) \approx 0.56$ (Fig.3 and Fig.4). So the range (7) is too narrow to get the broad range of fractal region. (The scaling region can be seen only at $\theta \approx 0.056$ in Fig.4, which is much shorter than ξ.) So, we cannot see any fractal nature induced by gravitational interaction in our numerical results. This situation would be improved, if we took much smaller value of ϵ than the value 0.01 in our model.

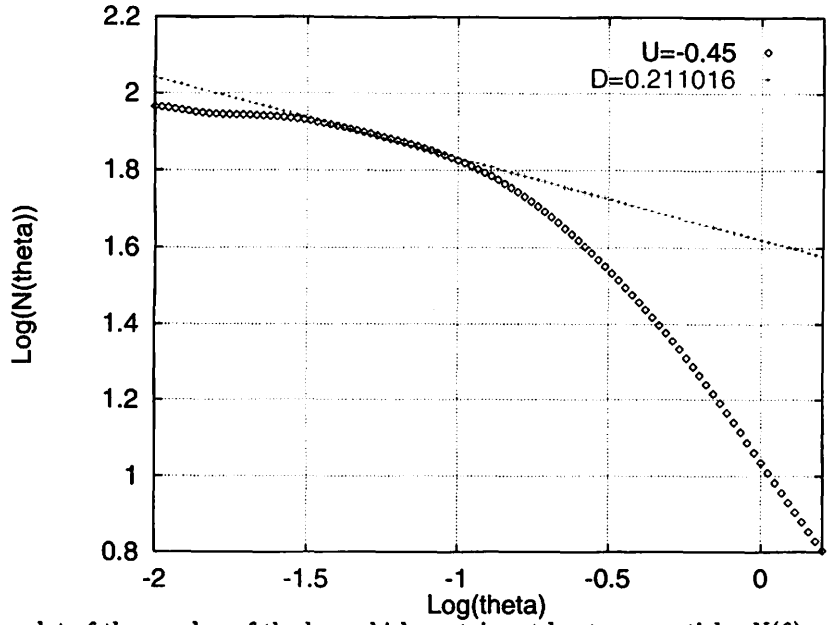

FIG. 3. Log-log plot of the number of the box which contains at least one particle, $N(\theta)$ vs the box size angle , $\theta = r/L$ for the case of $N = 100, U = -0.45, t = 5000$.

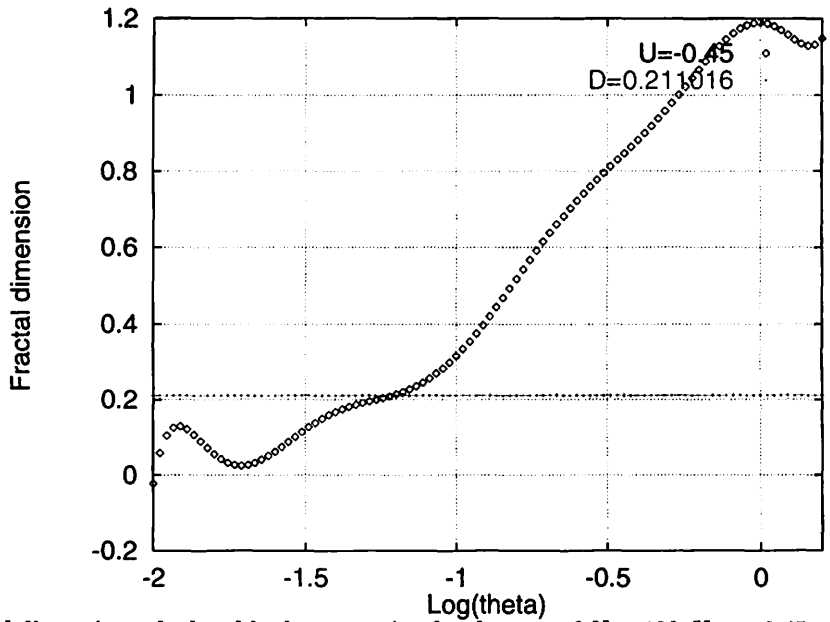

FIG. 4. Fractal dimension calculated by box-counting for the case of $N = 100, U = -0.45, t = 5000$. The curve shows the slope of the tangent line of $Log(N(\theta)) - Log(\theta)$ plot in Fig.3. Horizontal part of the curve can be seen at $\theta = 10^{-1.25} \approx 0.056$,which intersects with the horizontal line in the figure. Fractal dimension departs from one at the scale less than $\theta = 10^{-0.25} \approx 0.56$ corresponding to $L_{\rm av}(\xi)$.

IV. CONCLUSION

Here we got the result that the statistical state at the critical energy in GHMF is characterized by the Lévy motion. This motion is reasonable, from the viewpoint of phase transition, since the fluctuation of the physical variables become so large at the critical point. On the other hand, we cannot see any fractal nature in our model. This is mainly because the size of the configuration space is not much bigger than

that of cluster, which enables the free particle to visit the same cluster so many times. The periodicity of configuration space also prevents particles captured by a cluster from jumping within the cluster, since the particle departing from the cluster by chance is more likely to rotate along the ring. So the Lévy type motion in this model is not directly connected with the non-Gaussian motion and fractal nature in ISM, because the configuration space of the observed ISM has neither such a boundary nor periodicity. However, we can still expect that these natures are fulfilled in the limit of $\xi \to 0$ in our model, since the cluster size becomes much shorter than the perimeter of the ring in this limit. These analyzes should be our future challenge, although it is technically hard to accomplish such a limit in the simulation.

From these respects, our results could give the hint for the mechanism of the observed character of gravitationally viriallized objects such as ISM. These statistical approach characterized by the phase transition could be the alternative tactics to treat the highly non-linear large-number systems with the large fluctuations, compensating for the turbulence fluid approach. It is also interesting, in that it gives the hint for the statistics of self-gravitating system. It has been insisted that self-gravitating system do not follow the Maxwell-Boltzmann statistics, since the entropy is not extensive in the system with long-range force interactions [1]. Our results of Lévy motion at phase transition indicates that the variance of statistics diverges in such a highly jump probability. So the nonextensivity of self-gravitating system could be attributed to such a divergence.

V. ACKNOWLEDGMENTS

We thank: K. Maeda, A.Nakamichi, I. Joichi and K.Nakamura for useful discussions and comments on this subject.

---

[1] C. Tsallis, Braz. J. Phys. **29** (1999) 1.
[2] T. Padmanabhan, Phys. Rep. **188** (1990), 285.
[3] R. B. Larson, Mon. Not. R. astr. Soc. **194** (1981), 809.
[4] E. Falgarone, T. G. Phillips and C. K. Walker, ApJ **378** (1991), 186.
[5] H. J. de Vega, N. Sánchez and F. Combes, Phys. Rev. D **54** (1996), 6008.
[6] W. C. Saslaw and A. J. S. Hamilton, ApJ **276** (1984), 13.
[7] T. Tsuchiya, N. Gouda and T.Konishi, Phys.Rev.E **53** (1996),2210.
[8] M. Antoni and S. Ruffo, Phys. Rev. E **52** (1995),2361.
[9] M. Suzuki, Phys. Lett. A **146** (1990), 319.
[10] S. Nose, Molec. Phys. **52**(1984),255.
[11] V. Latora , A. Rapisarda and S. Ruffo, Phys.Rev.Lett. 83 (1999) 2104.
[12] S. Ghashghaie, W.Breymann, J.Peinke, P. Talkner and Y. Dodge, Nature **381** (1996),767.
[13] K. Falconer, Fractal Geometry (1990, John WileySons).

離散時間力学系の不安定(安定)多様体の漸近展開

後藤 振一郎[1]　　野崎一洋
名古屋大学　理学部・物理教室　R研

Asymptotic expansions of unstable (stable) manifolds in time-discrete systems

Shin-itiro GOTO and Kazuhiro NOZAKI
Department of Physics,Nagoya University,Nagoya 464-8602,Japan

abstract

By means of an updated renormalization method, we construct asymptotic expansions for unstable manifolds of hyperbolic fixed points in the double-well map and the dissipative Hénon map, both of which exhibit the strong homoclinic chaos. In terms of the asymptotic expansion , a simple formulation is presented to give the first homoclinic point in the double-well map. Even a truncated expansion of the unstable manifold is shown to reproduce the well-known many-leaved (fractal) structure of the strange attractor in the Hénon map.

1　はじめに

保存力学系におけるセパラトリクスの分裂によるホモ・ヘテロクリニック構造はよく知られているようにカオスを導く [1]. マップ系において不安定多様体を数値的に構成すると相空間中に複雑な構造を与えるが, それを解析的に導くことは難しい. 近可積分系において, この困難はボレル総和法を用いた特異摂動論により克服されてきた [2] [3] [4] [5] [6]. しかし, この方法は有限の大きさの差分間隔をもつ系などの可積分から遠い系では用いることができない.

近年, くりこみ群 (Renormalization Group) の方法は特異摂動論の一種として, その開発が進んでいる. このくりこみ群の方法は, 正則摂動解 (素朴な摂動パラメーターに関する摂動展開) から生じる永年項を非摂動解から生じる積分定数にくりこむことによって系統的に取り除く方法であり, 初めに Chen 等によって提案された [7]. その後, このくりこみ群の方法は包絡線による解釈による定式化 [8] や, リー群を基礎にした定式化などが現れた [9].

このくりこみ群の方法の離散系への応用はまず非カオス的な系で包絡線の解釈による方法で研究が行なわれた [10]. 我々はリー群によって定式化されたくりこみ群の方法をカオティックな離散系へ適用した. リー群を用いた解釈による方法は Chen 等によるアプローチ [7] や包絡線のアプローチ [8] より簡単であると考えられる. 今回この方法を用いて, 我々はダブルウェルマップにおける不安定多様体や安定多様体の双曲型不動点近傍での解析的な表式, 及びエノンマップにおけるストレンジアトラクター [11] を得たので報告する [12].

[1]e-mail: sgoto@allegro.phys.nagoya-u.ac.jp

2 漸近解析の道具としての “くりこみ群の方法” についての復習

ここでいう “くりこみ群の方法” とは漸近解析の道具の一種であり, 近年その開発が進んでいる. 与えられた微分方程式に対する予備的な考察がいらないという意味で強力な摂動論であるとともに, 与えられた微分方程式を縮約する道具として用いられる.

ここでは論文 [9] の解釈によるくりこみ群の方法の有効性を簡単な具体例をあげて説明する.

(微分方程式でのくりこみの例)

$$\frac{d^2q}{dt^2} + q = -\epsilon q, \qquad (0 < \epsilon \ll 1)$$

ここで ϵ は摂動パラメターである. この例は調和振動子そのものであり解が容易くだせるが, あえてこの系が解けないと思って摂動論的に解いてみる. その結果と厳密解とを比較して正則摂動論の破綻, およびくりこみ群の方法による正則摂動解の改善をみる. まず, 以下のように厳密解と正則摂動解が求まる.

厳密解

$$q = A\exp(\sqrt{1+\epsilon}\, t) + \text{c.c.}, \qquad [A \in \boldsymbol{C}\text{は積分定数}]$$

ここで c.c. は complex-conjugate を表す.

正則摂動論：(ϵ に関する素朴な摂動論)

$$\begin{aligned} q^{NE} &= q^{(0)} + \epsilon q^{(1)} + \cdots, \qquad \text{と展開して代入.} \\ \therefore \quad q^{NE}(t) &= A\Big(1 + \underbrace{i\epsilon t/2} + \cdots\Big)\exp(it) + \text{c.c.}. \end{aligned}$$

$\propto t$ より $t \to \infty$ で『発散』

ここで A は非摂動解から生じた積分定数で, 高次の摂動問題から生じる斉次解の振幅の自由度は非摂動解の振幅へと吸収させた. この例では永年項の存在により t の値が大きくなるにつれて正則摂動解が破れている. これを “くりこみ群の方法” により以下の様に改善する.

くりこみ群方程式の導出

正則摂動解を改善するために,$t \to \infty$ で発散する部分を $\widetilde{A}(t)$ と置く. この際, 非摂動解 $q^{(0)}$ から生じる積分定数 A を含む様に $\widetilde{A}(t)$ を定義する. すなわち,

正則摂動解： $q^{NE}(t) = \underbrace{A\Big(1 + it\epsilon/2 + \cdots\Big)}\exp(it) + \text{c.c.}$

発散する部分を $\widetilde{A}(t)$ とおく.

このように $\widetilde{A}(t)$ を定義する.

考え方

この方法の基本的な考え方は以下の通りである.

- 非摂動項の積分定数 (A) が摂動により変化 ($\widetilde{A}(t)$) する.

- 積分定数の変化 ($\widetilde{A}(t)$) に対する微分方程式をつくる.

このような手続きを見ると我々が提唱するリー群によるくりこみ群の方法の解釈は定数変化法に近いと言える. ここで上記の考え方に従い $\widetilde{A}(t)$ の満たす方程式を構成するわけであるが, それには以下の関係式を用いる.

くりこみ方程式 ($\widetilde{A}(t)$ が満たす方程式)

$$(*)\ \frac{d\widetilde{A}(t)}{dt} = \left.\frac{\partial}{\partial\tau}\right|_{\tau=0} \widetilde{A}(t+\tau) \qquad (:\text{自明な恒等式})\ \text{を使う.}$$

ここで (*) 式の使い方は以下の通りである. すなわち, $\widetilde{A}(t)$ のテイラー展開 ((*) 式左辺) と, $\widetilde{A}(t)$ の定義 ((*) 式右辺) とを両立させるのである. それぞれ式で表すと,

$$\begin{aligned}\widetilde{A}(t+\tau) &= \widetilde{A}(t) + \tau\frac{d\widetilde{A}(t)}{dt} + \cdots, \quad (\text{テイラー展開より}) \\ &\equiv A + (t+\tau)\frac{i\epsilon}{2}A + \cdots, \quad (\text{定義により})\end{aligned}$$

ここで両者を τ の一次で比較し,$\widetilde{A}(t)$ の満たす方程式を構成する. すなわち,

$$(\tau\text{の 1 次を比較}) \qquad \underbrace{\frac{d\widetilde{A}(t)}{dt}} = \frac{i\epsilon}{2}A = \underbrace{\frac{i\epsilon}{2}\{\widetilde{A}(t) + \mathcal{O}(\epsilon)\}},$$

ここで, 第 2 番目の等号で A を $\widetilde{A}(t)$ で書き直した. これにより, くりこみ群方程式と呼ばれる方程式が構成できたことになる.

$$\frac{d\widetilde{A}}{dt} = \frac{i\epsilon\widetilde{A}}{2} + \mathcal{O}(\epsilon^2) \quad \cdots(\text{くりこみ群方程式}).$$

このくりこみ群方程式を解くことによって $\widetilde{A}(t)$ を決定し, $q^{RG} = \widetilde{A}(t)\exp(it) + \text{c.c.}$ を構成すればくりこまれた解が得られる. 以下に正則摂動解とくりこまれた解の時間発展の様子をそれぞれ図 1,2 に示する.

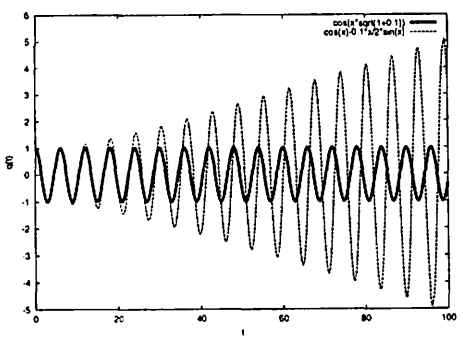

図 1: 摂動問題の厳密解と正則摂動解の比較. 太線は厳密解, 細線は正則摂動解を表す. Comparison of the exact solution and the regular perturbation result in the perturbation problem. Thick line denotes the exact solution, and thin line denotes the regular perturbation result.($\epsilon = 0.1$).

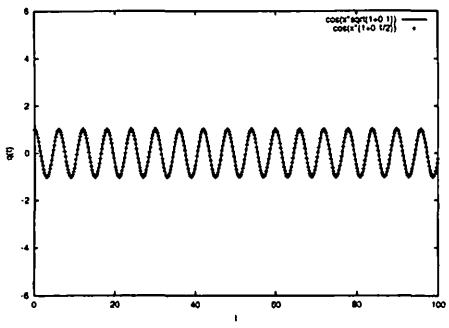

図 2: 摂動問題の厳密解とくりこまれた解の比較. 太線は厳密解,+ はくりこまれた解をそれぞれ表す.
Comparison of the exact solution and the renormalized solution in the perturbation problem. Solid line denotes the exact solution, and pluses (+) denote the renormalized solution. ($\epsilon = 0.1$).

この例で示されたように, くりこみ群の方法は正則摂動解さえ求められれば厳密解を知らなくても定性的に正しい解を構成することができる. もし, 更に近似の良い解が欲しい場合は正則摂動解を高次まで求めればよい.

3 本論：不安定 (安定) 多様体の構成

3.1 ダブルウェルマップ (シンプレクティックマップの例)

以下に今回の計算に用いたダブルウェルマップといわれるシンプレクティックマップを説明する. この系の発展方程式は以下で与えられ, 差分間隔 δ^2 が 0 の極限でセパラトリクスを持つが, $\delta^2 \neq 0$ であればホモクリニックカオスが生じる. 具体的な発展方程式 $(x_n, p_n) \mapsto (x_{n+1}, p_{n+1})$ は以下で与えられる.

$$\begin{cases} x_{n+1} - x_n = p_{n+1}, \\ p_{n+1} - p_n = \delta^2(x_n - 2{x_n}^3). \end{cases} \qquad (\delta^2 \ : \ \text{差分間隔})$$

$\delta^2 \to 0$ (連続極限)

差分間隔が無限小の時は, 次のような 1 自由度ハミルトン方程式と見ることができる. このハミルトン系は 2 重井戸型のポテンシャル (double well potential) 中の力学である. 不安定多様体と安定多様体が一致 (セパラトリクス) し, カオスは生じない. (図 3 参照).

$$\begin{cases} \dfrac{dx}{dt} = p, \quad \dfrac{dp}{dt} = x - 2x^3, \quad H = \dfrac{p^2}{2} + \dfrac{-x^2 + x^4}{2}. \end{cases}$$

$\delta^2 \neq 0$ (有限の値)

有限な差分間隔であるとき, このマップは不安定多様体と安定多様体が分裂し, ホモクリニック構造によるカオス生じる (図 4 参照).

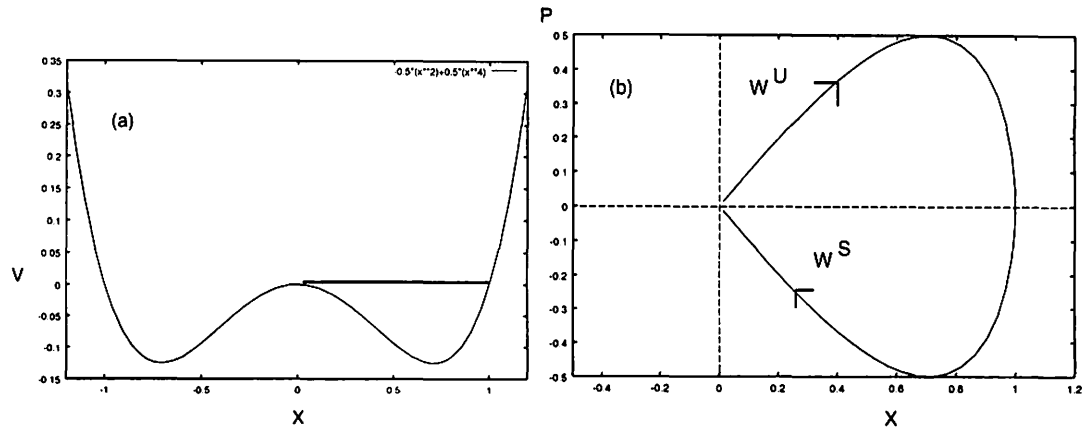

図 3: (a):ダブルウェルポテンシャル (b):セパラトリクス. (a):Double well potential. (b):Separatrix in the phase space.

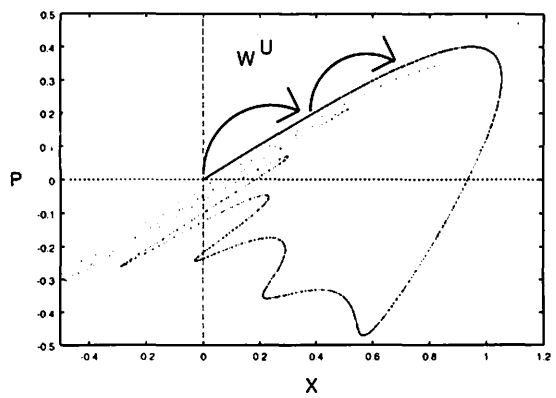

図 4: 差分間隔 $\delta^2 = 0.58$ のダブルウェルマップの数値的に構成した不安定多様体. Numerical construction of the unstable manifold for the Double well map with $\delta^2 = 0.58$.

3.2 不安定多様体 W^U の構成法の概要

この論文で行なう不安定多様体の構成は, 2階の差分方程式を1階差分方程式へと縮約することによって達成される. その縮約の方法としてくりこみ群の方法を用いる. 以下にこの手続きを示す.

1変数化したダブルウェルマップ 2階差分方程式

$$Lx_n \equiv x_{n+1} - (2+\delta^2)x_n + x_{n-1} = -2\delta^2 x_n^3$$

⇓(1)不動点からの正則摂動解を求める.

⇓(2)くりこみ方程式の導出.

W^U 上の 1 階差分方程式

$$x_{n+1} = g(x_n)$$

3.3 不安定多様体の具体的構成

摂動パラメーター

先程示した不安定多様体の構成法の概要に従って具体的計算を進める. まず, 正則摂動展開を構成する. 今考えている問題では差分間隔は小さくないので, 摂動パラメターは差分間隔に選ばない. 代わりに x_n 自身が小さいと思い, これを摂動パラメーターに選ぶ. すなわち $x_n \to \epsilon x_n$ という置き換えを行ったと思えばよい. これは, 双曲型不動点 (ダブルウェルマップの場合には原点に対応) からの展開に対応する.

- 摂動パラメーター： x_n 自身 $[x_n \to \epsilon x_n$. と思ってもよい.]
- $x_n = x_n^{(1)} + x_n^{(2)} + x_n^{(3)} + \cdots$. (原点からの展開に相当.)
- $x_n \to 0$ (不動点) as $n \to -\infty$ $\cdots (W^U$ の境界条件.)

正則摂動問題

正則摂動問題は x_n の展開形を発展方程式へ代入することにより以下で与えられるような方程式系が得られる.

$$Lx_n^{(1)} = 0, \qquad Lx_n^{(2)} = 0, \qquad Lx_n^{(3)} = -2\delta^2 x_n^{(1)3}, \cdots.$$

正則摂動解

リーディングオーダーの解の形を $x_n^{(1)} = AK^n$ とおき, K を決定すると K は差分間隔 δ^2 によって具体的に書き表される. K のとりうる値は 2 通りあるが, 不安定多様体の境界条件を満たすように選ぶ. また, A は未定な定数である. この定数はリーディングオーダーの摂動問題が線形問題であることに起因する. このようにして各オーダー毎に摂動問題を解くことにより以下のような正則摂動解が求まる. なおここでも調和振動子の例と同様, 高次の摂動問題から生じる積分定数は全てリーディングオーダーの積分定数 A に吸収させた.

$$\begin{aligned} x_n &= \underbrace{A\Big(1 - c_2A^2K^{2n} + c_4A^4K^{4n} - c_6A^6K^{6n} + \cdots\Big)}K^n, \\ &= \widetilde{A}(n)K^n, \qquad \boxed{K > 1 \text{ より発散 , } \widetilde{A}(n) \text{ と置く.}} \end{aligned}$$

ここで, A は積分定数, $K = \frac{1}{2}[(2+\delta^2) + \sqrt{(2+\delta^2)^2 - 4}] > 1$ c_2, c_4, c_6 は K に依存する定数[2]である.

[2]詳細はプレプリント [12] を参照.

くりこみ

先程定義した $\widetilde{A}(n)$ が満たす 1 階の差分方程式を構成することによりくりこみ群方程式を導出する.$\widetilde{A}(n)$ の定義により

$$\widetilde{A}(n+1)-\widetilde{A}(n)=-c_2(K^2-1)K^{2n}A^3+c_4(K^4-1)K^{4n}A^5+\cdots,$$

である.$\widetilde{A}(n)$ の満たす方程式を構成するために, 右辺の A を $\widetilde{A}(n)$ で書き直す. 具体的に A を $\widetilde{A}(n)$ で書き表すと,

$$A=\widetilde{A}(n)\{1+c_2\widetilde{A}(n)^2K^{2n}+(3c_2^2-c_4)\widetilde{A}(n)^4K^{4n}+\cdots\},$$

と計算される. これを $\widetilde{A}(n+1)-\widetilde{A}(n)$ へ代入して以下のくりこみ群方程式を得る.

$$\begin{aligned}\widetilde{A}(n+1)-\widetilde{A}(n) &= -c_2(K^2-1)K^{2n}\widetilde{A}(n)^3\\ &\quad+\{c_4(K^4-1)-3c_2^2(K^2-1)\}K^{4n}\widetilde{A}(n)^5\\ &\quad-\{c_6(K^6-1)-5c_2c_4(K^4-1)\\ &\quad+3c_2(K^2-1)(4c_2^2-c_4)\}K^{6n}\widetilde{A}(n)^7+\cdots,\end{aligned}$$

これは非自励系の方程式である. 位置座標とくりこみ群方程式との関係 $x_n=\widetilde{A}(n)K^n$ を用いて x_n の方程式へと書き直すと以下の自励方程式が得られる.

くりこみ群方程式 ($x_{n+1}=g(x_n)$: 1 階差分方程式)

$$\begin{aligned}x_{n+1} &= Kx_n-Kc_2(K^2-1)x_n^3\\ &\quad+K\{c_4(K^4-1)-3c_2^2(K^2-1)\}x_n^5\\ &\quad-K\{c_6(K^6-1)-5c_2c_4(K^4-1)\\ &\quad+3c_2(K^2-1)(4c_2^2-c_4)\}x_n^7+\cdots\\ &\equiv g_1(x_n),\quad(\cdots x_n\text{の巾展開型})\end{aligned}$$

これは不安定多様体上の一階の差分方程式である. この 1 階方程式により x_n が与えられれば x_{n+1} が決まる式であるので横軸に x_n, 縦軸に x_{n+1} をとり数値的に得られた不安定多様体と比較した結果を図 5 に示す.

数値的に構成した多様体とくりこみによって得られた多様体の比較

図 5 を見ると原点 (双曲型不動点) の近くでは数値的に構成した多様体と解析的に得られた多様体の一致は良いが $x_n\approx 1$ の辺りでその一致は悪くなる. この原因は $x_{n+1}=g_1(x_n)$ の x_n に対する傾きが発散しているからであると考えられる. ここで得られた多様体の解析的な表式は x_n の巾展開型であるので, そのような微分の発散する地点を越えて多様体を構成することは難しいからである. 一般に, より高次の正則問題を解けば, $x_{n+1}=g_1(x_n)$ が x_n の微分が発散する地点までは多様体の近似はどんどん良くなっていくと考えられる. また, 数値的に得られた不安定多様体を見ると, x_n を決めても x_{n+1} は一意に決まらないことがわかる. すなわち, 不安定多様体を $x_{n+1}=g(x_n)$ の形で書いた時には $g(x_n)$ は x_n の多価関数になっていることが読みとれる. 今回得られた多様体の解析的な形は, この多価関数の双曲型不動点につながる一つの分岐を構成したことになる.

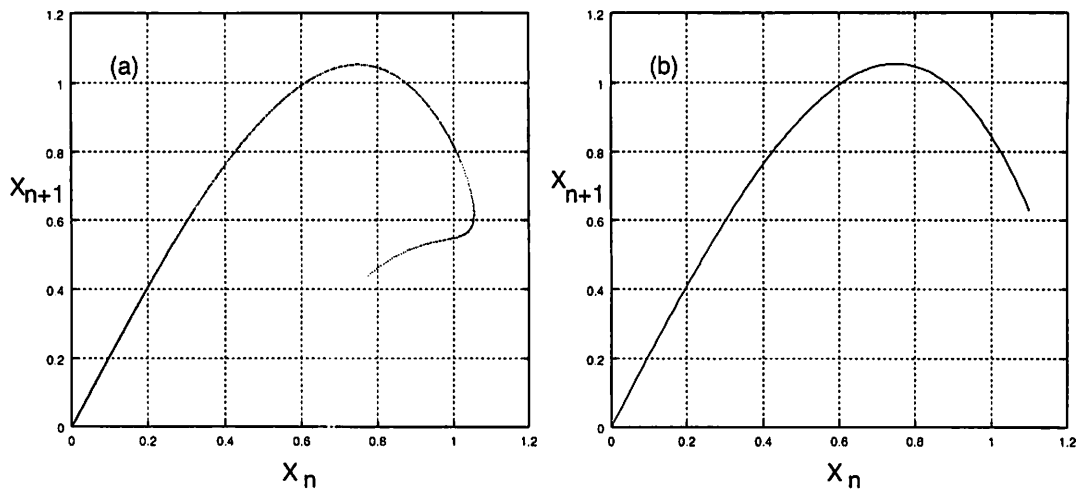

図 5: ダブルウェルマップの不安定多様体 W^U の一部. (a) : 数値的に得られた W^U. (b) : くりこみで得られた W^U. A part of the unstable manifolds for the double well map. (a): W^U plotted by means of the numerical simulation. (b): W^U plotted by means of the renormalization method. $(K = 2.1,\ \delta^2 = 0.58)$.

以上をまとめておく.

$x_{n+1} = g(x_n)$ は x_n の巾展開型になっている. くりこみと数値解は多様体の傾きが発散する地点までよい一致. $x_{n+1} = g(x_n)$ の一価のところまでを "くりこみ" によって解析的に構成できた.

不安定多様体の他の分岐の構成法

くりこみ群の方法で多様体の一価のところを解析的に構成したわけであるが, 他の分岐の構成は分岐間をつなぐ関数マップを構成することによって達成される. この関数マップを構成することにより, 解析的には不可能でも数値的には第一分岐 (不動点につながる分岐) の不安定多様体を延長することが可能となる. その関数マップは以下で与えられる.

[分岐 (j) から分岐 $(j+1)$ へのマップ] "$\tilde{g}_j \mapsto \tilde{g}_{j+1}$" (; 関数マップ)

- $\tilde{g}_{j+1}(x_n) = 2x_n - \tilde{g}_j^{-1}(x_n) + \delta^2(x_n - 2x_n^3)$.

以下に数値的に構成した不安定多様体とくりこみで得られた多様体とその関数マップによる延長によって合成された多様体[3] を比較した図を示す (図 6 参照). 数値的に得られた多様体とくりこみとその延長によって得られた多様体の一致はよい.

[3]合成された多様体とは以下の操作で得られる : くりこみの操作で得られた多様体を, 数値的に得られた多様体との近似が良い部分までに制限し, それを関数マップで延長する.

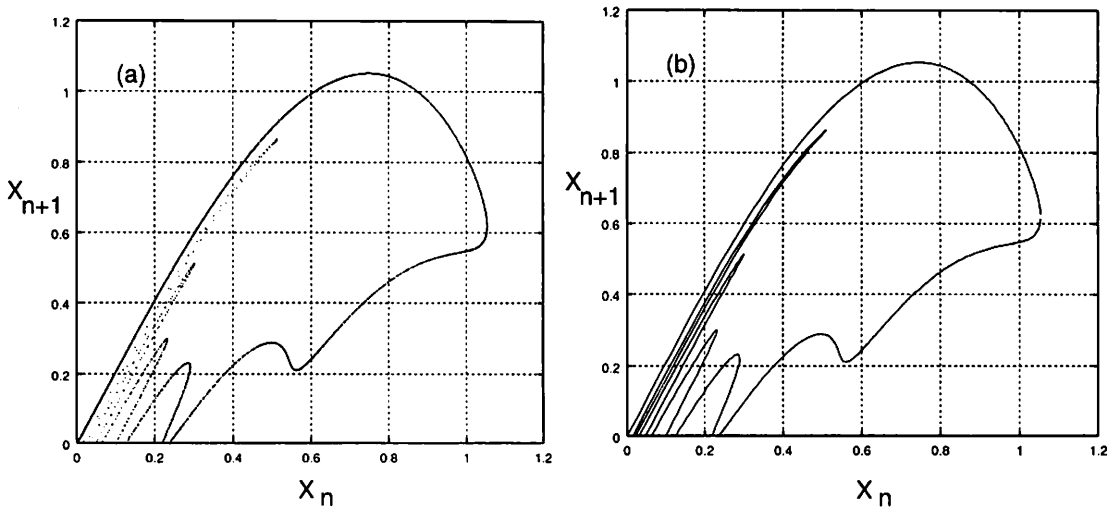

図 6: ダブルウェルマップの不安定多様体 W^U. (a):数値的に得られた W^U (b):くりこみの延長, 及び合成によって構成した W^U. Unstable manifolds W^U for the double well map. (a):W^U plotted by means of the numerical simulation. (b):W^U plotted by means of the matching the some of the $\tilde{g}_j$. ($K = 2.1$, $\delta^2 = 0.58$).

3.4 シンプレクティックマップ系での不安定多様体の構成の応用

ここでは, 前小節までの結果を応用することによりホモクリニック点の座標検出公式を導出する. 基本的なアイデアとしてダブルウェルマップなどの系で知られている以下の対称性を用いる.

ダブルウェルマップの対称性

$$W^U \ni \begin{pmatrix} x_n \\ p_n \end{pmatrix} \text{に対して } W^S \ni \begin{pmatrix} x'_n \\ p'_n \end{pmatrix} \equiv \begin{pmatrix} x_n - p_n \\ -p_n \end{pmatrix}$$

($\cdots$鏡映写像 R より.
R とは, 可逆写像 M に対して $M^{-1} = RMR, R^2 = 1$ を満たすもの.)

これにより, 不安定多様体の表式を知っている時には安定多様体の表式がわかる. 更に, 不安定多様体と安定多様体を知っていればその共通集合であるホモクリニック点の座標がわかる. ホモクリニック点を知っていれば, 特に空相間構造に重要な役割をはたす P.I.P.(; Principal Intersection Point)[5] の座標がわかる. 結果のみ記述すると, ホモクリニック点の x 座標 x^h,P.I.P. の x 座標 x^* はそれぞれ以下で与えられる [12].

$$\begin{aligned} x^h &= \tilde{g}_j \tilde{g}_k(x^h), \qquad (j,k \text{ は分岐の番号を表す.}) \\ x^* &= \tilde{g}_j(x^*), \quad p^* = 0. \end{aligned}$$

3.5 エノンマップ (散逸系のマップの例)

次に散逸的なマップ系における不安定多様体の構成を試みる [13]. ここでは代表的な系としてエノンマップを用いる. 散逸系においても不安定多様体の構成法は先程のシンプレクティックマップの場合と同様にして行われる 先程の不安定多様体の計算ではシンプレクティック性は全く用いていないので, 先程の方法がそのまま使えるのである.

エノンマップとは以下の発展方程式 $(x_n, p_n) \mapsto (x_{n+1}, p_{n+1})$ のことである. 特にここではパラメーター a, b をそれぞれ 1.4, 0.3 に固定しておく.

$$\begin{cases} x_{n+1} = 1 - ax_n^2 + y_n, \\ y_{n+1} = bx_n. \end{cases} \qquad (a = 1.4\ ,\ b = 0.3\ ).$$

くりこみ群の方法による不安定多様体の構成結果

マップの 2 つの不動点のうち、

$$\bar{x} = \frac{b - 1 + \sqrt{(b-1)^2 + 4a}}{2a}, \quad \bar{y} = b\bar{x}.$$

の不動点に付随する不安定多様体 (W^U) を構成する.
ダブルウェルマップの場合と同様に, 数値的に構成した不安定多様体とくりこみにより得られた不安定多様体を以下のように図で比較する (図 7 参照). くりこみの方法では不動点から多様体を構成しているので, 不動点を原点にする座標系 $\hat{x} = x - \bar{x}$ を用いて多様体を観察する. なお, くりこみによる不安定多様体の構成は摂動パラメターの 5 次まで計算した結果である.

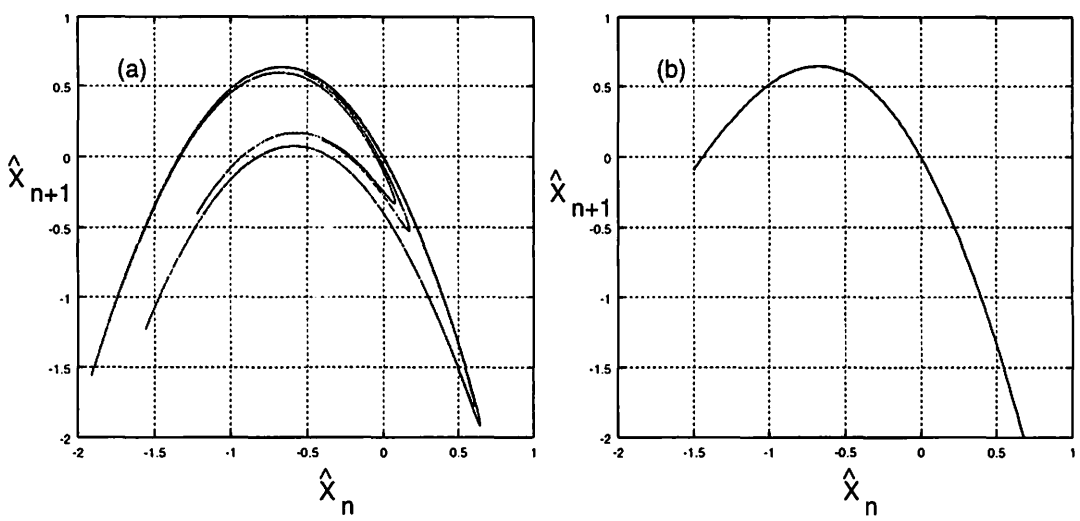

図 7: エノンマップの不安定多様体 W^U (a) : 数値的に得られた W^U. (b) : くりこみで得られた W^U. Unstable manifolds W^U for the Hénon map. (a):W^U plotted by means of the numerical simulation. (b):W^U plotted by means of the renormalization method.

くりこみによる不安定多様体の適用範囲等はダブルウェルマップの場合と同じである.
すなわち、$x_{n+1} = g(x_n)$ とくりこみ群方程式を書いた時, その有効範囲は $g(x_n)$ の x_n で微分が発散する地点までである.

3.6 エノンマップ系での不安定多様体の構成の応用

ここではくりこみ群の方法と分岐間の関数マップによって得られる多様体の構成法を応用することにより, ストレンジアトラクターの構成を行った. ストレンジアトラクターは不安定多様体を延長することによって構成できるので, 不安定多様体を構成すれば自然にアトラクターが構成できる. 以下に数値的に構成したアトラクターとくりこみ群の方法とその延長によって得られたアトラクターを図で比較する (図 8 参照).

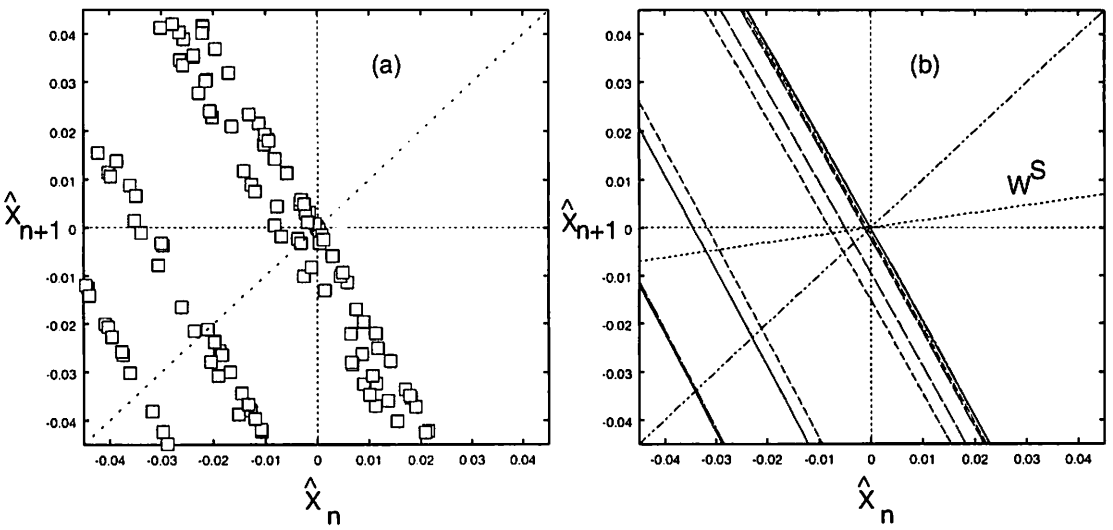

図 8: エノンマップの不動点近傍のリターンマップの様子. (a):数値的に (: □) 得られた W^U (b):くりこみで得られた W^U. Retrun map near the fixed point for the Hénon map. (a):W^U plotted by means of the numerical simulation.(: □). (b):W^U plotted by means of the renormalization method.

図 8 は原点が双曲型不動点である. 従ってこの近傍では安定多様体の近似は線形の近似が十分に使える領域である. 不安定多様体と安定多様体の交わりがホモクリニック点である. ことからリターンマップの図において傾き 4 5 ° のラインを用いることにより, ホモクリニック点の座標とその時間発展が理解できる.

4 まとめ

今回の研究により双曲型不動点における不安定多様体の漸近展開を漸近解析の道具としてのくりこみ群の方法によって構成することができた. 今回多様体の構成を行った例はシンプレクティックマップの例としてダブルウェルマップ, 散逸系のマップのエノンマップの 2 つである. くりこみ群の方法によって解析的に多様体が構成できた領域は不安定多様体 $x_{n+1} = g(x_n)$ の関数形の第一分岐までである. それ以外の分岐はその具体的な関数形は知ることができないが, 分岐から分岐への関数マップを構成することによって第一分岐の多様体を延長することができた.

その不安定多様体の構成の応用としてダブルウェルマップに対しては, ホモクリニック点の座標検出公式を与え, エノンマップに対しては, ストレンジアトラクターを構成した.

参考文献

[1] H. Poincaré, Acta math. 13 (1890). 1

[2] V. Hakkim and K. Mallic Nonlinearlity 6-1 (1993) 57.

[3] K. Nakamura and M. Hamada J. Phys. A29 (1996) 7315.

[4] A. Tobvis, M. Tsuchiya and C. Jaffe Chaos 8-3 (1998) 665.

[5] V. G. Gelfreich, V. F. Lazutkin and N. V. Svanidze, Physica 71D (1994) 82.

[6] Y. Hirata, K. Nozaki and T. Konishi, Prog. Theo. Phys. 102-3 (1999) 701.

[7] L. Y. Chen, N. Goldenfeld and Y. Oono, Phys. Rev. E 54 (1996) 376.

[8] T. Kunihiro, Prog. Theo. Phys. 94-4 (1995) 503.

[9] S. Goto, Y. Masutomi, and K. Nozaki, Prog. Theo. Phys. 102-3 (1999) 471.

[10] T. Kunihiro,and J. Matsukidaira, Phys. Rev. E 57 (1998) 4817.

[11] For example, H. G. Schuster, *Deterministic Chaos (An Introduction)*, Physik-Verlag, 1984.

[12] S. Goto, and K. Nozaki, chao-dyn/9910025, (http://xxx.lanl.gov/list/nlin.CD/9910).

[13] H.Daido, Prog. Theo. Phys. 63-4 (1980) 1190.

A condition for the existence of homoclinic intersection in the C^2 standard-like mappings

Yoshihiro YAMAGUCHI[1] and Kiyotaka TANIKAWA[2]

[1] *Teikyo Heisei University, Ichihara, Chiba 290-0193, Japan*

[2] *National Astronomical Observatory, Mitaka, Tokyo 181-8588, Japan*

Abstract

A sufficent condition for the existence of homoclinic intersection in the doubly reversible C^2 standard-like mappings is obtained. To derive the condition, we only use the geometrical structure of stable and unstable manifolds and the information on the first and second derivatives of the mapping function. Then the obtained result can be applicable to many mapping systems.

§1. Statement of the problem and result

Area-preserving twist mappings[1-3] on the cylinder show many important properties. We are interested in the structure of stable and unstable manifolds of Birkhoff saddles.[4] Chaotic behavior appears due to the existence of Smale horseshoes[5] produced by the transversal intersection of stable and unstable manifolds. The proof of existence of homoclinic intersection is one of the most fundamental issues in this field. If the analytical form of the mapping is given, we can apply several mothods to prove the existence of the homoclinic intersection of stable and unstable manifolds of the fixed point.[6-10] Without using the explicit expression of the function in the mapping, can we prove the existence of homoclinic intersection? In order to consider this problem, we study C^2 mappings. In C^2 mappings, we can use information on the first and second derivatives of the mapping function. We shall give a simple sufficient condition for the existence of the homoclinic intersection of stable and unstable manifolds of the fixed point.

We use the method developed by Brown[11] who proved the existence of homoclinic intersection of the conservative Hénon mapping.[12] He used the mapping of curvature of unstable manifold. In this paper, we use the mappings of the first and the second derivatives of unstable manifold since these mappings are simpler than that of curvature. We also use the symmetrical structure of stable and unstable manifolds.[13] In §1.1, we introduce the system and state a theorem. The discussion is in §1.2. We give the proof of the theorem in §2.

1.1. *System and theorem*

We are interested in the homoclinic intersection for doubly reversible C^2 twist standard-like mappings on the cylinder. Let $A = S^1 \times \mathbf{R}$ be the cylinder with coordinate (x, y) where $x \in S^1$ and $y \in \mathbf{R}$. Let $T : A \to A$ be an orientation preserving and measure preserving C^2 diffeomorphism expressed in the form

$$T : y_{n+1} = y_n + f(x_n), \quad x_{n+1} = x_n + y_{n+1}(\text{Mod } 2\pi). \tag{1}$$

where C^2 function $f(x)$ is assumed to satisfy the following properties.
[p1] $f(x)$ is an odd function.
[p2] $f(x)$ is a periodic function with period 2π.
[p3] $f(x) > 0$ $(x \in (0, \pi))$.
[p4] $\dfrac{\mathrm{d}^2 f(x)}{\mathrm{d}x^2} < 0$ $(x \in (0, \pi))$.

The double reversibility[14] requires the first property [p1]. According to [p1] and [p2], we have $f(0) = f(\pi) = 0$ and $f''(0) = f''(\pi) = 0$. [p4] is an additional property for the discussion of the existence of homoclinic intersection. Here we define two positive constants α and β.

$$\frac{\mathrm{d}f(0)}{\mathrm{d}x} = \alpha > 0, \quad \frac{\mathrm{d}f(\pi)}{\mathrm{d}x} = -\beta < 0. \tag{2}$$

In the region $x \in (0, \pi)$, there exists only one point$(x = \Omega)$ with $\mathrm{d}f(x)/\mathrm{d}x = 0$ due to [p4]. There exist two fixed points $p = (0, 0)$ and $q = (\pi, 0)$. Point p is a saddle, and point q is an elliptic point for $0 < \beta < 4$, and is a saddle with reflection for $\beta > 4$.

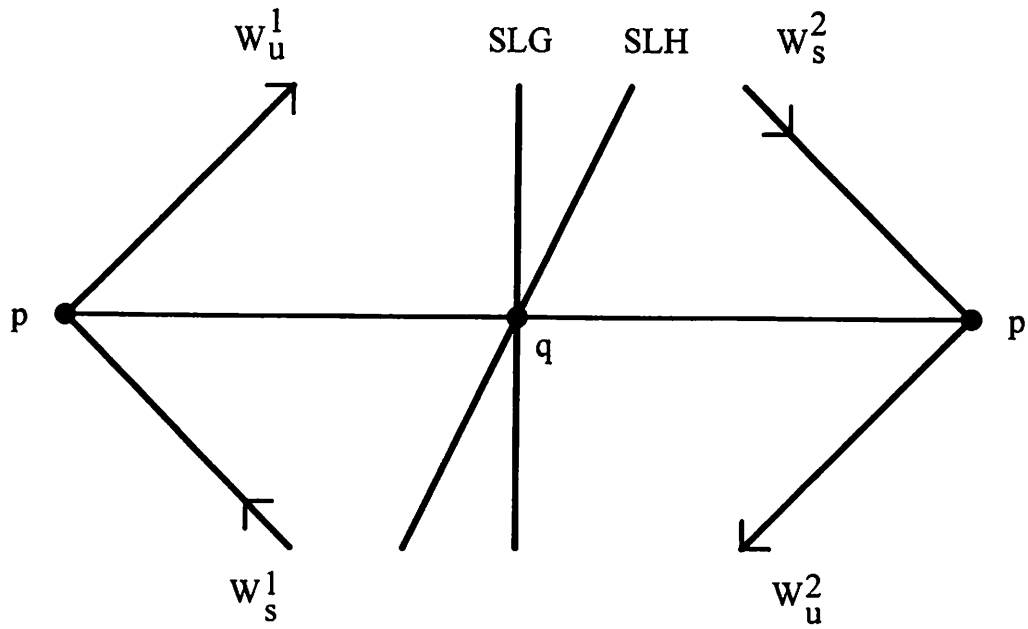

Fig.1: Names of stable and unstable manifolds of p and two symmetry lines SLG and SLH. The upper part$(y > 0)$ of SLG(SLH) is written by $\mathrm{SLG}^+(\mathrm{SLH}^+)$.

Hereafter the homoclinic intersection of the stable manifold W_s and the unstable manifold W_u of p is studied. The stable(unstable) manifold has two branches. In Fig.1, the geometry is illustrated with names of stable and unstable manifolds. The symmetry lines are also shown in Fig.1. The detailed explanations of symmetry lines are in §2.1. We state our result on the existence of homoclinic intersection of $W_u^{1,2}$ and $W_s^{2,1}$.

Theorem: The transversal homoclinic intersection points of $W_u^{1,2}$ and $W_s^{2,1}$ exist if the conditions $\sqrt{4\alpha+\alpha^2}-\alpha \leq \beta$ and $0 < \beta < 2$ hold or if the condition $\beta \geq 2$ holds.

Combining the result proved by Birkhoff-Smith[15] and this theorem, we have a corollary:

Corollary: Under the same conditions in Theorem, the transversal homoclinic intersection points of $W_u^{1,2}$ and $W_s^{1,2}$ exist.

1.2. *Discussion*

First we consider the case with $\beta \geq 2$. If the bifurcation of the fixed point(q) into a saddle with reflection occurs, this condition holds. This implies that the bifurcation of q into a saddle with reflection does not occur in the integrable mappings.

Homoclinic intersection points of stable(W_s) and unstable(W_u) manifolds of p exist if the condition $\alpha = \beta \geq \alpha_c = 4/3$ holds. This theorem implies that the homoclinic intersection points exist at $\alpha \geq \alpha_c$ for every mapping with symmetry $f(x) = f(\pi - x)(x \in [0, \pi])$. Decreasing the value of α from α_c, homoclinic intersection points do not disappear since the intersection is transversal and the homoclinic tangency situation is inhibited in the conservative systems. However, our result does not exclude the possibility that the system reduces to an integrable state at another critical value α_i less than α_c. If this reduction occurs, the stable and unstable manifolds form a saddle connection(also called a separatrix) and the transversal homoclinic intersection points disappear. If the mapping is integrable in every parameter region, the function does not have the symmetry relation $f(x) = f(\pi - x)(x \in [0, \pi])$.

Examples. First two examples satisfy the symmetry relation $f(x) = f(\pi - x)(x \in [0, \pi])$, whereas the latter two do not.

1. The standard mapping $f(x) = f_s(x)$ with

$$f_s(x) = \alpha \sin(x). \tag{3}$$

Nonintegrability of the standard mapping is well known.[7]

2. The mapping[16] $f(x) = f_{as}(x)$ with

$$f_{as}(x) = \alpha\sqrt{1+\epsilon}\arcsin\left(\frac{\sin(x)}{\sqrt{1+\epsilon}}\right) \tag{4}$$

where $f'_{as}(0) = -f'_{as}(\pi) = \alpha$. In Fig.2, the homoclinic intersection of this mapping is shown where $\alpha = 1$ and $\epsilon = 0.1$. Then this mapping is not integrable even if $\alpha < \alpha_c$.

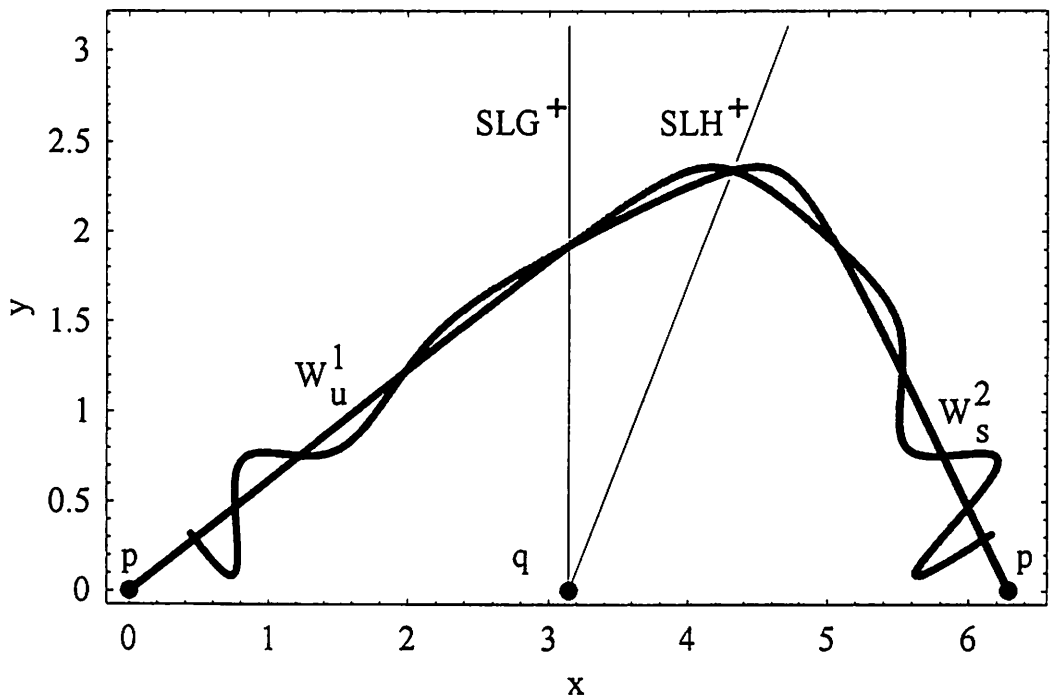

Fig.2: The stable and unstable manifolds of the fixed point of the mapping defined by Eq.(4) with $\alpha = 1$ and $\epsilon = 0.1$.

3. Suris mapping[17] with a positive parameter $a(\neq 1)$. This is an example of integrable mapping.

$$f_{su}(x) = g_{su}(x) + g_{su}^{-1}(x) - 2x, \tag{5}$$

where

$$g_{su}(x) = 4\arctan\left(\frac{\tan(x/4)}{a}\right). \tag{6}$$

For this mapping, we have $\alpha = a + 1/a - 2$ and $\beta = 2(a-1)^2/(1+a^2)$. It is easy to prove that the conditions in Theorem and the relation $f(x) = f(\pi - x)$ do not hold in the case $a \neq 1$.

4. The mapping defined by sine- and arcsine-functions

$$f_{ss}(x) = g_{ss}(x) + g_{ss}^{-1}(x) - 2x, \tag{7}$$

with

$$g_{ss}(x) = a\sin(x)(0 \leq x \leq x_c), \tag{8}$$

$$g_{ss}(x) = \frac{\arcsin((x-2\pi)/a)}{k} + 2\pi(x_c < x < 2\pi) \tag{9}$$

where three constants satisfy the following two relations:

$$x_c = 2\pi - a\sqrt{1-1/(ak)^2}, \tag{10}$$

$$1 = ak\cos kx_c. \tag{11}$$

The function $f_{ss}(x)$ is of C^2. According to the construction of $f_{ss}(x)$, the stable and unstable manifolds of p form a separatrix. We have $\alpha = ak + 1/(ak) - 2$ and $\beta = 2 - 2/(ak\sqrt{1-\pi^2/a^2})$, for example, $a = 5.013$, $x_c = 1.370$, $\alpha = 3.213$ and $\beta = 1.488$ for the case with $k = 1$. Two constants α and β do not satisfy the conditions in Theorem. In spite of the non-existence of homoclinic intersection of stable and unstable manifolds of the fixed point, this mapping is not integrable(see Fig.3) since there exists the chaotic motion around saddles with period-2. The chaotic motion is induced by the existence of homoclinic intersection of stable and unstable manifolds of saddles with period-2.

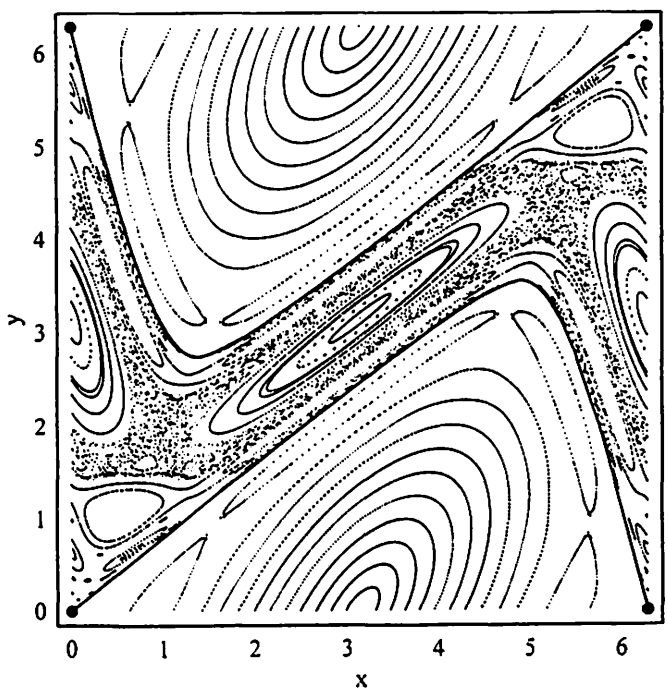

Fig.3: The separatix of p and the chaotic motion in the mapping defined by Eq.(7) with $k = 1, a = 5.013$ and $x_c = 1.370$.

§2. Proof of Theorem

2.1. *Basic tools*

Let us first introduce symmetry lines of T. The reversible mapping T can be expressed in the form

$$T = H \circ G, \tag{12}$$

where G and H are involutions, i.e., $G \circ G = H \circ H = Id$, the Jacobian determinant of G and of H being -1. Our mapping T has double reversibility, i.e., it has two pairs of involutions. We take the following pair showing the left-right symmetry.

$$H : y_{n+1} = y_n, \quad x_{n+1} = -x_n + y_n (\text{Mod } 2\pi), \tag{13}$$

$$G : y_{n+1} = y_n + f(x_n), \quad x_{n+1} = -x_n (\text{Mod } 2\pi). \tag{14}$$

The set of the fixed points of G and H are called the symmetry lines.

$$H : y = 2x, \quad y = 2(x - \pi) \text{ (referred to as SLH)}, \tag{15}$$

$$G : x = 0, \quad x = \pi \text{ (referred to as SLG)}. \tag{16}$$

Two fixed points p and q are also fixed points of H and G.

Property 1: $H(W_u^1) = W_s^2, H(W_s^2) = W_u^1, G(W_u^1) = W_s^2$, and $G(W_s^2) = W_u^1$.

This property is a different representation of reversibilty. The proof is easy(see Ref.11).

Let $z(t) = (z_1(t), z_2(t))$ be the parametrization of W_u^1 with t the arc length along W_u^1 from p. We denote the order relation on W_u^1 by $z(t_1) \preceq z(t_2)$ if $t_1 \leq t_2$ and by $z(t_1) \prec z(t_2)$ if $t_1 < t_2$. The unstable manifold W_u^1 is a C^2 curve and it starts from p toward the upper-right direction. So, for small $t > 0$, we have $\mathrm{d}z_1(t)/\mathrm{d}t > 0$ and $\mathrm{d}z_2(t)/\mathrm{d}t > 0$. As long as its slope is finite, it can be expressed by a graph of a C^2 function

$$y = F(x). \tag{17}$$

We call z the first turning point(FTP) of W_u^1 if it is the smallest point in the sense of order($\prec$) such that $\mathrm{d}z_1/\mathrm{d}t = 0$, and denote the point by z^{FTP}. Note the existence of situation that the unstable manifold W_u^1 does not turn back even if $\mathrm{d}z_1/\mathrm{d}t = 0$ holds at z^{FTP}. In the following proof, we only use information on W_u^1 at $z \prec z^{FTP}$. Expression (17) holds at least in the region $z_1 \in (0, z_1^{FTP})$. Let us denote the arc of W_u^1 in this region by Γ_u. We have the functional equation for $F(x)$.

$$F(x_{n+1}) = F(x_n) + f(x_n). \tag{18}$$

We use the abbreviations for the slope $\xi(x) = \mathrm{d}F(x)/\mathrm{d}x$ and the second derivative $\eta(x) = \mathrm{d}^2F(x)/\mathrm{d}x^2$. Suppose that w is the image of z under T. Then we can derive the following mappings for ξ and η.

$$\xi(w_1) = \frac{\xi(z_1) + f'(z_1)}{1 + \xi(z_1) + f'(z_1)}, \tag{19}$$

$$\eta(w_1) = \frac{\eta(z_1) + f''(z_1)}{(1 + \xi(z_1) + f'(z_1))^3}. \tag{20}$$

where $f'(z_1) = \mathrm{d}f(z_1)/\mathrm{d}z_1$, and so on.

The curvature $\kappa(z_1)$ in the region $0 \preceq z \preceq z^{FTP}$ is

$$\kappa(z_1) = \frac{\eta(z_1)}{(1 + \xi(z_1)^2)^{3/2}}. \tag{21}$$

Equations (19) and (20) give the slope and the second derivative of W_u^1 at p.

$$\xi(0) = \frac{\sqrt{4\alpha + \alpha^2} - \alpha}{2} (< 1), \tag{22}$$

$$\eta(0) = 0. \tag{23}$$

The first maximum point(FMP) z^{FMP} is the smallest point in the sense of order($\prec$) such that $\xi(z_1^{FMP}) = 0$ and $\eta(z_1^{FMP}) < 0$. Note that $\mathrm{d}z_2(t)/\mathrm{d}t = 0$ at FMP.

For later convenience, let us define three domains D_1, D_2 and D_3.

$$\begin{aligned} D_1 &= \{0 \le x \le \Omega, y > 0\}, \\ D_2 &= \{\Omega < x < \pi, y > 0\}, \\ D_3 &= \{\pi < x < 2\pi, y > 0\}. \end{aligned} \tag{24}$$

2.2. *Proof*

Lemma 1: The curvature of W_u^1 in D_1 is negative.

Proof: We have $\kappa(0) = 0$ from Eqs.(21) and (23). Take $w \in D_1$. The order relation $p \prec z = T^{-1}(w) \prec w$ holds. The relations $f''(x) < 0$ in $x \in (0, \pi)$ and $\kappa(0) = 0$ give $\kappa(w_1) < 0$ in $w \in D_1$.(Q.E.D.)

Lemma 2: FMP is not in D_1.

Proof: The point $z = T^{-1}w$ is in D_1 as long as $w \in D_1$. Since $f'(z_1) > 0$ in $z \in D_1$ and $\xi(0) > 0$, the right-hand side of Eq.(19) is positive.(Q.E.D.)

Next we shall discuss the curvature of Γ_u in $D_2 \cup \mathrm{SLG}^+$. The slope of the preimage of FMP satisfies the relation $\xi(x_m) + f'(x_m) = 0$ where x_m is the

x-coordinate of the preimage. The slope at the preimage of FTP satisfies the relation $1+\xi(x_t)+f'(x_t)=0$ where x_t is the x-coordinate of the preimage. It is easy to show the relation $x_m < x_t$. This means the order relation $z^{FMP} \prec z^{FTP}$ and the slope of W_u^1 changes from $-\infty$ to $+\infty$ around FTP.

There are two origins of the change of sign$(\eta(w_1))$ from a negative value to a positive one. The first origin is that the sign$(\eta(z_1)+f''(z_1))$ is negative and the sign$(1+\xi(z_1)+f'(z_1))$ changes from a positive value to a negative one. The second origin is that the the sign$(\eta(z_1)+f''(z_1))$ changes from a negative value to a positive one and the sign$(1+\xi(z_1)+f'(z_1))$ is positve. If x_t is in $D_2 \cup \mathrm{SLG}^+$, the first origin induces the change of sign$(\eta(w_1))$ since $f''(z_1) \leq 0$ in $D_2 \cup \mathrm{SLG}^+$. In this case, the change of sign$(\eta(w_1))$ occurs at FTP and then Γ_u has a negative value of η. This means that there are no maximum nor minimum points between FMP and FTP in Γ_u. If x_t is in $(\pi, 2\pi)$, we can not deny the possibility that the second origin induces the change of sign(η). But in this situation, the arc of Γ_u in $D_2 \cup \mathrm{SLG}^+$ has a negative value of η. In this case, the possibility of the existence of maximum or mimimum points between FMP and FTP can not be denied. These results are summarized as Lemma 3.

Lemma 3: The curvature of Γ_u in $D_2 \cup \mathrm{SLG}^+$ is negative.

According to Lemmas 1-3, the slope of Γ_u decreases in $D_1 \cup D_2 \cup \mathrm{SLG}^+$. In order to make clear the structure of Γ_u in $D_2 \cup \mathrm{SLG}^+$, we shall introduce several tools used in the following lemmas.

Under the operation of H or G, W_u^1 is mapped to W_s^2 and *vice versa*(see Property 1). The slope and the second derivatives of W_u^1 are mapped to those of W_s^2.

$$H : \xi_{n+1} = \frac{\xi_n}{\xi_n - 1}, \tag{25}$$

$$H : \eta_{n+1} = \frac{\eta_n}{(1-\xi_n)^3}, \tag{26}$$

$$G : \xi_{n+1} = -\xi_n - f'(x_n), \tag{27}$$

$$G : \eta_{n+1} = \eta_n + f''(x_n). \tag{28}$$

If ξ_n, η_n and x_n refer to W_u^1, then ξ_{n+1}, η_{n+1} and x_{n+1} refer to W_s^2, and *vice versa*. These relations give Lemmas 4-7.

Lemma 4: Let $z \in W_u^1$(or W_s^2) be a point such that $\xi(z_1)=0$. Then the slope at $H(z)$ in W_s^2(or W_u^1) is also 0. If $\eta(z) > 0 (=0, <0)$, then the second derivative at $H(z)$ in W_s^2(or W_u^1) is also positive(0, negative).

Lemma 5: The following relations hold at the intersection point($x=\pi$) of $W_u^1(W_s^2)$ and SLG^+.

$$\xi_u(\pi) + \xi_s(\pi) = \beta, \tag{29}$$

$$\eta_u(\pi) = \eta_s(\pi). \tag{30}$$

where the suffix $u(s)$ refers to $W_u^1(W_s^2)$.

Lemma 6: Let γ_u be the subarc of Γ_u in D_1. The mapped image $G(\gamma_u) \subset W_s^2$ is a strictly decreasing function in the region $x \in [2\pi - \Omega, 2\pi]$.

Proof: The signs of $f'(x)$ and ξ in D_1 are positive. Then the slope of the image point is negative due to Eq.(27).(Q.E.D.)

Lemma 7: Let γ_u be the subarc of Γ_u in $D_2 \cup \mathrm{SLG}^+$. Then $G(\gamma_u)(\subset W_s^2)$ has at most one point whose slope is zero.

Proof: Let z be a point of γ_u. The slope $\xi(z_1)$ is a decreasing function of z_1 due to Lemma 3. On the other hand, the function $-f'(z_1)$ is an increasing function of z_1 in $D_1 \cup D_2 \cup \mathrm{SLG}^+$. Then there exists at most one root z_1^* of the equation

$$-\xi(z_1) - f'(z_1) = 0. \tag{31}$$

Then Lemma 7 is proved.(Q.E.D.)

Using Lemma 7, we shall prove Lemma 8.

Lemma 8: FMP is not in $D_2 \cup \mathrm{SLG}^+$.

Proof: Assume that FMP is in D_2. We shall derive a contradiction. According to Eq.(26), we have

$$\eta(H(z^{FMP})) = \eta(z^{FMP}). \tag{32}$$

Since FMP is a local maximum point($\eta(z^{FMP}) < 0$), the mapped point $H(z^{FMP})$ is also a local maximum point. Combining the fact $f(z_1^{FMP}) > 0$ and the symmetrical transformations(Eqs.(13) and (14)), we have that y-coordinate of $G(z^{FMP})$ is larger than that of $H(z^{FMP})$, and x-coordinate of $G(z^{FMP})$ is less than that of $H(z^{FMP})$. Since FMP is in D_2, $f'(z^{FMP})$ has a negative value. Equation (27) means that the slope($\xi_s = -f'(z^{FMP})$) of W_s^2 at $G(z^{FMP})$ is positive. Then there exists at least one local maximum point and one local minimum point in the arc of W_s^2 connecting $G(z^{FMP})$ and $H(z^{FMP})$. This contradicts Lemma 7.

Next assume that FMP exists in SLG^+, and derive a contradiction. From Eq.(27), the slope of W_S^2 at the intersection point($x = \pi$) is equal to $\beta(> 0)$. The slope at the mapped point $H(z^{FMP})$ is zero due to Eq.(25) and $H(z^{FMP})$ is the maximum point since Eq(32) holds in this situaiton. This implies that the arc of W_s^2 connecting z^{FMP} and $H(z^{FMP})$ has at least one local maximum point and one mimimum point. This contradicts Lemma 7.(Q.E.D.)

Next we give the structure of W_s^2 in D_3.

Lemma 9: Let γ_u be the arc of Γ_u in $D_1 \cup D_2 \cup \mathrm{SLG}^+$ and s be the intersection point of γ_u and SLG^+. The slope and the second derivative of the arc $H(\gamma_u)$ of W_s^2 are negative. The second derivative of the arc $G(\gamma_u)$ of W_s^2 is negative and has one maximum point between s and $T(s)$.

Proof: Let z be a point in γ_u. Then the relation $0 < \xi(z) < \xi(0) < 1$ holds. Lemma 3 shows that the second derivative of γ_u is negative. Equations (25) and (26) give the claim for $H(\gamma_u)$. Equation (28) gives the first claim for $G(\gamma_u)$. The y coordinate of s is equal to that of $T(s)$. Combining this fact and Lemma 7, the second claim for $G(\gamma_u)$ is obtained.(Q.E.D.)

Lemmas 1-9 hold for the general situations for C^2 mappings. Using these results, we study the possibility of existence of separatrix constructed by W_u^1 and W_s^2.

Lemma 10: The separatrix constructed by W_u^1 and W_s^2 does not exist at $\beta \geq 2$.

Proof: If the separatrix exists, we have the relation.

$$\xi_u(s) = \xi_s(s) = \frac{\beta}{2}, \tag{33}$$

$$\xi_u(v) = \xi_s(v) = 0 \tag{34}$$

where v is the intersection point of separatrix and SLH^+. Combining Lemma 9 and Eq.(34), we find that v is FMP. Then the slope of separatrix in $v \prec z \preceq p$(at $x = 2\pi$) is finite and is negative.

The slope at $T(s)$ is obatined

$$\xi_u(T(s)) = \xi_s(T(s)) = \frac{\beta}{\beta - 2}. \tag{35}$$

If the condition $\beta \geq 2$ holds, we have that $\xi_u(T(s)) = \xi_s(T(s)) > 0$ or the slope diverges. This contradicts the property of the separatrix mentioned above.(Q.E.D.)

Lemma 11: At $\beta \geq 2$, W_u^1 and W_s^2 intersect transversely.

Proof: At $\beta \geq 2$, there is no separatrix. We know that W_u^1 intersects SLG^+ at s. The reversibility guarantees the intersection of W_s^2 and SLG^+ at s. This fact does not directly imply the transversal intersection of W_u^1 and W_s^2. Assume the nontransversal intersection situation at s with the relation $\xi_u(s) = \xi_s(s) = \beta/2$. Then the nontransversal intersection exists at $T(s)$. We shall derive a contradiction. Suppose that s is a point in W_u^1. The slope of $T(s)$ diverges or has a positive value(see the proof in Lemma 10). Next suppose that s is the point in W_s^2. Lemma 9 means that the slope of W_s^2 is negative. These facts imply the transversal intersection at $T(s)$.(Q.E.D.)

Proof of Theorem: Lemma 11 gives the proof in the case with $\beta \geq 2$. Let us consider the case with $0 < \beta < 2$. If the relation

$$\frac{\beta}{2} \geq \xi_u(0) \tag{36}$$

holds, we have

$$\xi_s(\pi) > \frac{\beta}{2} > \xi_u(\pi). \tag{37}$$

Here we used Eq.(29) to derive Eq.(36). This relation shows the transversal intersection of W_u^1 and W_s^2 at $x = \pi$. Then Eq.(36) gives the condition of Theorem.(Q.E.D.)

References

1) K.R.Meyer and G.R.Hall, *Introduction to Hamiltonian Dynamical Sytems and the N-Body Problem* (Springer-Verlag,1991).
2) L.E.Reichl, *The Transition to Chaos* (Springer-Verlag,1992).
3) R.S.Mackay, *Renormalisation in Area-Preserving Maps* (World Scientific,1993).
4) G.D.Birkhoff, Acta. Math. **43** (1920),44.
5) S.Smale, Bull. Am. Math. Soc. **73** (1967),747.
6) V.K.Melnikov, Trans. Moscow Math. Soc. **12** (1963),3.
7) V.F.Lazutkin, I.G.Schachmannski and M.B.Tabanov, Physica D **40** (1989),235.
8) V.Hakim and K.Mallick, Nonlinearity **6** (1993),57.
9) K.Nakamura and M.Hamada, J. Phys. A **29** (1996),7315.
10) Y.Hirata, K.Nozaki and T.Konishi, Prog. Theor. Phys. **102** (1999),701.
11) R.Brown, Ergod. Th. & Dynam. Sys. **15** (1995),1045.
12) M.Hénon, Quart. Appl. Math. **XXVII(3)** (1969),291. R.Devaney, J. Diff. Equ. **51** (1984),254.
13) Y.Yamaguchi and K.Tanikawa, Prog. Theor. Phys. **101** (1999),1.
14) K.Tanikawa and Y.Yamaguchi, J. Math. Phys. **28** (1987),921. R.De Vogelaere, in *Contributions to the Theory of Oscillations, Vol.IV. Ann. Math. Studies* **No.41**, Princeton University Press(1953). p.53.
15) G.D.Birkhoff and P.A.Smith, J. de Math.(Liouville). S.9 **7** (1928),345.
16) J.Wilbrink, Physica D **26** (1987),358.
17) Y.B.Suris, Functional Anal. Appl. **23** (1989),74.

Symmetrical Non-Birkhoff Period-3 Orbits in the Standard-like Mappings

Yoshihiro YAMAGUCHI[1] and Kiyotaka TANIKAWA[2]

[1] Teikyo Heisei University, Ichihara, Chiba 290-0193, Japan.

[2] National Astronomical Observatory, Mitaka, Tokyo 181-8588, Japan.

Abstract

A necessary condition for the existence of non-Birkhoff period-3 orbits is derived in the C^0 standard-like mappings. The symmetical *non-Birkhoff* period-3 orbits of pseudo-Anosov braid-type are found. Then the standard-like mapping is a pseudo-Anosov system at a certain parameter range. The braid types of all period-3 orbits are derived. Using these braids, the lower bound of the topological entropy is estimated. These orbits do not exist in a horseshoe.

1 Introduction

For one dimensional mappings, there exist two beautiful and powerful theorems, namely, theorems proved by Sharkovskii,[1)] and Li and Yorke.[2)] The period-3 orbit plays an essential role in both theorems. Extended version of these theorems for two dimensional mappings is obtained by Matsuoka[3)](see also Ref.4). The theorem is expressed in terms of the generator σ_i of braid.[5)]

Theorem 1(Matsuoka): A period-3 orbit with the alternate braid $\theta_3^m \sigma_1^{i_1} \sigma_2^{-j_1} \cdots \sigma_1^{i_d} \sigma_2^{-j_d}$ implies chaos where $\theta_3 = (\sigma_1\sigma_2)^3, m \in \mathbf{Z}$ and $i_k, j_k > 0 (k = 1, \cdots, d)$.

The term "chaos" in Theorem 1 means the existence of orbits with positive topological entropy. Theorem 1 is based on the theorem proved by Thurston.[6)] The simplest alternate braid is $\sigma_1\sigma_2^{-1}$, and this has the so-called pseudo-Anosov(pA) property.[7)]

It is natural to ask the following question: Does a period-3 orbit of braid type $\sigma_1\sigma_2^{-1}$ exist in two dimensional mappings? We know the famous example of period-5 orbit of braid type pA. This orbit exists in the horseshoe. But we do not know a period-3 or -4 orbit of braid type pA in the two dimensional mappings. We want to find these orbits in the two dimensional twist mappings.[8)] In the twist mappings, we know the eixstence of the order preserving orbits with period-3(called *Birkhoff orbit*).[9)] These orbits are of braid type $\sigma_1\sigma_2$ which corresponds to a cyclic permutation of the trivial braid. In order to attain our purpose, we have to find the orbits which do not preserve the order. These are called *non-Birkhoff orbits.*[10)] Using the non-Birkhoff orbits, Boyland and Hall[11)] proved a theorem which gives the criterion for the existence of invariant curves(KAM curves). Leage and Mackay[12)] tested out their criterion on the standard mapping. They found non-Birkhoff orbits whose rotation numbers accumulate to the golden ratio. Olvera and Simó[13)] found non-Birkhoff orbits in the horseshoe. The braid type of non-Birkhoff orbits has not been studied. Using the topological entropy of braid, we can judge whether or not the non-Birkhoff orbit exists in the horseshoe.

In this paper, we use the standard-like mappings as a typical model of twist mappings. The standard-like mapping T defined in the cylinder$(0 \leq x_n < 2\pi, -\infty < y_n < \infty)$ is given by

$$y_{n+1} = y_n - af(x_n), \tag{1}$$
$$x_{n+1} = x_n + y_{n+1} \ (\text{Mod } 2\pi) \tag{2}$$

where a is a positive parameter and the C^0 function $f(x)$ has the following properties.

[1] $f(x)$ is odd.

[2] $f(x)$ is periodic with period 2π.

[3] $f(x) > 0$ for $0 < x < \pi$ and $f(x) < 0$ for $\pi < x < 2\pi$.

[4] $\max f(x) = 1$.

Note that the unimodality of $f(x)$ in $0 \leq x < \pi$ is not assumed. The reversibility of the mapping is assured by [1]. We have $f(0) = f(\pi) = 0$ from properties [2] and [3]. Then there are two fixed points $P = (0, 0)$ and $Q = (\pi, 0)$ in T. In the following discussion, we use four symmetry axes of T.[14),15)]

$$x = 0, \pi \ (\text{Mod } 2\pi), \tag{3}$$
$$y = 2x, 2(x - \pi) \ (\text{Mod } 2\pi). \tag{4}$$

Here we fix the notation for period-3 orbits with rotation number $\nu = p/3(p = 1, 2, \cdots)$ in the universal cover$(-\infty \leq x_n < \infty, -\infty < y_n < \infty)$.

$$p_1 = (x_1, y_1),\ p_2 = (x_2, y_2),\ p_3 = (x_3, y_3),\ p_4 = (x_4, y_4), \tag{5}$$
$$0 \leq x_1 < 2\pi,\ y_1 > 0, \tag{6}$$
$$x_4 = x_1 + 2\pi p,\ y_4 = y_1. \tag{7}$$

In this paper, we consider the following type of the non-Birkhoff period-3 orbit.

$$x_1 < x_2,\ x_3 < x_2,\ x_3 < x_4. \tag{8}$$

In this orbit, the turning back of orbital points occurs once. The period-3 orbit in the universal cover is determined by the following six equations.

$$y_2 = y_1 - af(x_1), \tag{9}$$
$$x_2 = x_1 + y_2, \tag{10}$$
$$y_3 = y_2 - af(x_2), \tag{11}$$
$$x_3 = x_2 + y_3, \tag{12}$$
$$y_1 = y_3 - af(x_3), \tag{13}$$
$$x_1 + 2\pi p = x_3 + y_1. \tag{14}$$

From Eqs.(9)-(14), two relations are obtained.

$$f(x_1) + f(x_2) + f(x_3) = 0, \tag{15}$$
$$y_1 + y_2 + y_3 = 2\pi p. \tag{16}$$

In §2, we shall give the necessary condition for the existence of the non-Birkhoff period-3 orbit. In §3, the pseudo-Anosov property of symmetrical non-Birkhoff orbits is discussed. We give the concluding remarks in §4.

2 Search for Non-Birkhoff Period-3 Orbits

In this section, we first formulate the necessary condition for the existence of the non-Birkhoff period-3 orbits(Theorem 2) and then numerically search these.

2.1 *Non-Birkhoff period-3 orbit: General situation*

Theorem 2: The necessary condition for the existence of non-Birkhoff period-3 orbits with rotation number $\nu = p/3 (p = 1, 2, \ldots)$ is $a > 2\pi p/3$.

Proof of Theorem 2

First we consider the situation that $0 \leq x_1 < \pi$ holds.

Property 1

[P1] $0 < y_2 < a$.
[P2] $-a < y_3 < 0$.
[P3] $0 < y_2 \leq y_1$.
[P4] $f(x_2) > 0$.
[P5] $f(x_3) < 0$.
[P6] $\pi p < y_1 < \pi p + a/2$.

Proof of Property 1

The first inequality in [P1] is derived from the condition $x_1 < x_2$ and Eq.(10). The second inequality in [P2] is derived from the condition $x_3 < x_2$ and Eq.(12). The second inequality in [P3] is derived from the condition $0 \leq x_1 < \pi$ and Eq.(9).

Using the relation $y_3 < 0$, we have

$$y_3 = y_2 - af(x_2) < 0. \tag{17}$$

Using the relation $y_2 > 0$, we have

$$0 < y_2 < af(x_2) \leq a. \tag{18}$$

This relation gives [P4] and the second inequality in [P1].

Since $y_1 > 0$, the sign of the right hand side in Eq.(13) is positive. Since $y_3 < 0$, we have $f(x_3) < 0$, that is, [P5].

Using relations $y_1 > 0$, $y_3 < 0$ and Eq.(13), we have

$$0 > y_3 > af(x_3) > -a. \tag{19}$$

This is the first inequality in [P2].

Rewriting Eq.(16), we have the relation.

$$2\pi p = 2y_1 - af(x_1) + y_3. \tag{20}$$

The second and third terms in Eq.(20) are negative. Then the first inequality in [P6] is proved.

We rewrite Eq.(15).

$$f(x_1) + f(x_2) = -f(x_3). \tag{21}$$

According to [P5], we have the relation.

$$0 < a(f(x_1) + f(x_2)) \leq a. \tag{22}$$

Rewriting Eq.(20) and using the previous result, we obtain the relation:

$$\begin{aligned} 2\pi p &= 2y_1 + y_2 - a(f(x_1) + f(x_2)), & (23) \\ 0 &< 2y_1 + y_2 - 2\pi p \leq a. & (24) \end{aligned}$$

The first inequality does not give new condition. The second inequality gives the relation:

$$y_2 \leq 2\pi p + a - 2y_1. \tag{25}$$

Using $y_2 > 0$, we have the relation:

$$0 < y_2 \leq 2\pi p + a - 2y_1. \tag{26}$$

This gives the second inequality in [P6].

Lemma 1: The necessary condition for the existence of the period-3 orbits of non-Birkhoff type with rotation number $\nu = p/3$ satifying $0 \leq x_1 < \pi$ is $a > 2\pi p/3$.

Proof: Using Eq.(16) and [P6], we have the following relation.

$$\pi p > y_2 + y_3 > \pi p - \frac{a}{2}. \tag{27}$$

Using the second inequality and [P1], we have

$$a > y_2 > \pi p - \frac{a}{2} - y_3. \tag{28}$$

Using [P2], we have a final relation.

$$0 > y_3 > \pi p - \frac{3a}{2} \tag{29}$$

This gives Lemma 1.(Q.E.D.)

Next we study the situation that $\pi \leq x_1 < 2\pi$ holds. In this situation, [P2],[P4] and [P5] hold. The following Property 2([P7],[P8] and [P9]) holds instead of [P1],[P3] and [P6].

Property 2

[P7] $0 < y_1 < a$.

[P8] $0 < y_1 \leq y_2$.

[P9] $\pi p < y_2 < \pi p + \frac{a}{2}$.

We can easily prove Property 2, then we omit it.

Lemma 2: The necessary condition for the existence of the period-3 orbits of non-Birkhoff type with rotation number $\nu = p/3$ satifying $\pi \leq x_1 < 2\pi$ is $a > 2\pi p/3$.

Proof: Using Eq.(16) and [P9], we have the following relation.

$$\pi p - \frac{a}{2} \leq y_1 + y_3 < \pi p. \tag{30}$$

Using [P2] and [P7], we have two relations.

$$\pi p - \frac{a}{2} - y_1 \leq y_3 < 0, \tag{31}$$

$$\pi p - \frac{a}{2} < y_1 < a. \tag{32}$$

These give Lemma 2.(Q.E.D.)

Combining Lemmas 1 and 2, Theorem 2 is proved.(Q.E.D.)

2.2 *Symmetrical non-Birkhoff period-3 orbits*

First we consider the period-3 orbits with $\nu = p/3 (p = 1, 2, 3)$ having a point on the $x = 0$ axis. The equation for determining y_1 reduces to

$$2\pi p = 3y_1 - af(y_1). \tag{33}$$

The graph of the function in the right hand side of Eq.(33) is illustrated in Figs.1a-c. New orbits with $\nu = 1/3$ and $2/3$ appear in the region $2\pi < y_1 < 3\pi$(see Figs.1a and b) due to the tangent bifurcation. The orbits with $\nu = 3/3$ appear in the region $4\pi < y_1 < 5\pi$(see Fig.1c). These solutions for y_1 satisfy [P6] and then these correspond to the non-Birkhoff period-3 orbits. The typical orbits are illustrated in Figs.2a-c. Increasing a, new non-Birkhoff periodic point with $\nu = 1/3$ and $2/3$ appear in the region $4\pi < y_1 < 5\pi$ and non-Birkhoff periodic points with $\nu = 3/3$ appear in the region $6\pi < y_1 < 7\pi$ and so on.

Next we search for non-Birkhoff period-3 orbits having a point on the symmetry axis $x = \pi$. The equation for determining the y-position of the point is

$$2\pi p = 3y_1 - af(\pi + y_1). \tag{34}$$

The appearance of non-Birkhoff periodic points on the $x = \pi$-axis is illustrated in Fig.1d-f. The typical orbits are illustrated in Fig.2d-f. In Table I, we summarize these results.

Table I: Birth of non-Birkhoff orbits

ν	x_1	The m-th Interval($m \geq 1$)
1/3	0	$2m\pi < y_1 < (2m+1)\pi$
2/3	0	$2m\pi < y_1 < (2m+1)\pi$
3/3	0	$(2m+2)\pi < y_1 < (2m+3)\pi$
1/3	π	$(2m-1)\pi < y_1 < 2m\pi$
2/3	π	$(2m+1)\pi < y_1 < (2m+2)\pi$
3/3	π	$(2m+1)\pi < y_1 < (2m+2)\pi$

We call the non-Birkhoff orbits born in the $m-$th interval in Table I "the m-th non-Birkhoff orbits".

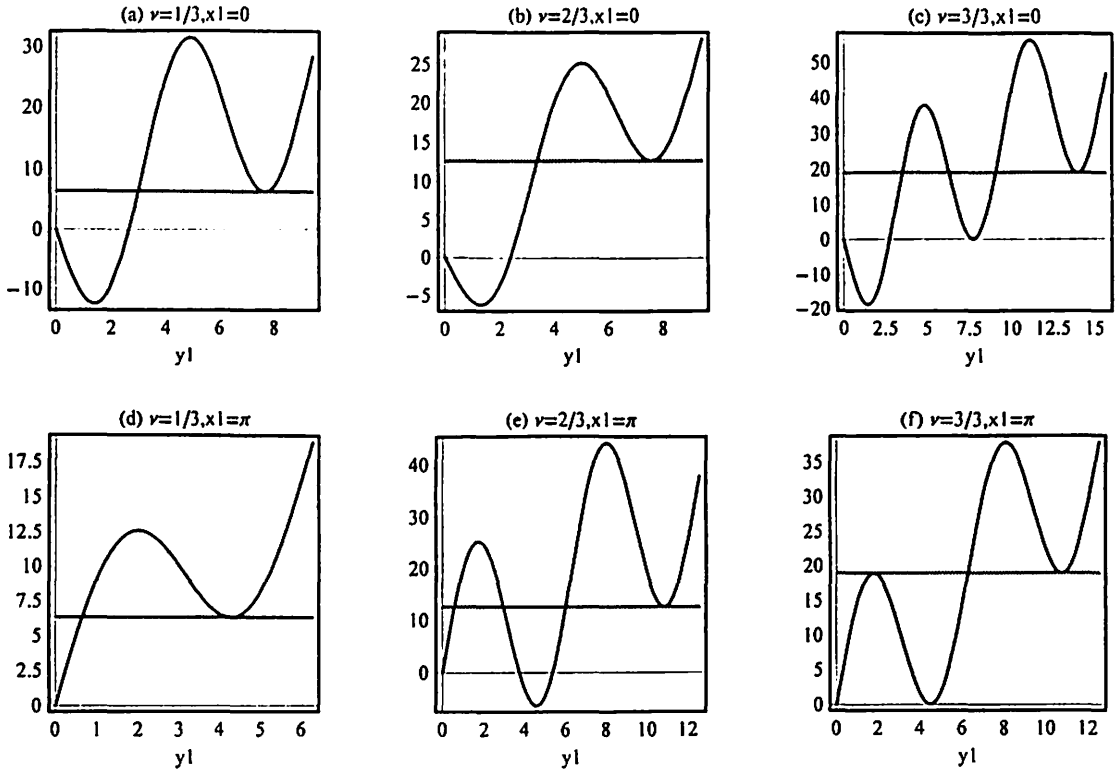

Fig.1: We use the standard mapping with $f(x) = \sin x$. A horizontal line(sine-like curve) means the left(right) hand side of Eq.(33) or Eq.(34). Figs.a-c(d-f) show the appearance of non-Birkhoff periodic points on the $x = 0(x = \pi)$ axis. (a) $a = 17.014$,(b) 10.567,(c) 23.370, (d) 7.222, (e) 20.198 and (f)13.811.

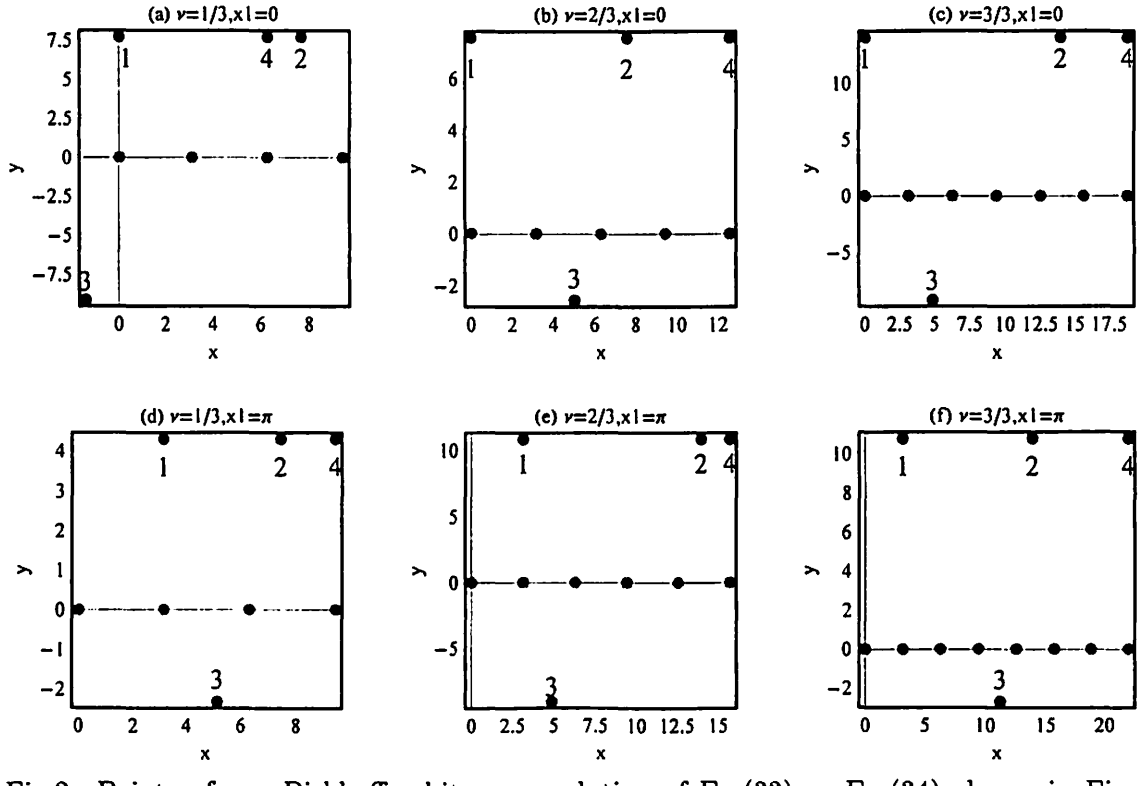

Fig.2: Points of non-Birkhoff orbits as a solution of Eq.(33) or Eq.(34) shown in Figs.1a-f. Circles on the x-axis are the fixed points. Symbol 'i' stands for p_i.

3 Pseudo-Anosov Property

In this section we construct the braid for the first non-Birkhoff period-3 orbit with $\nu = 1/3$ having a point on the $x = \pi$ axis. This period-3 orbit goes around the fixed point P and the cylinder once since the rotation number is $\nu = 1/3$. The construction of the braid is divided into two steps. The essential tool is the isotopy. The procedure is illustrated in Fig.3. There a symbol i stands for x_i. We use this convention in what follows.

The first step is shown in Fig.3a. We draw two threads from 1 to 2 and from 3 to 4. These represent the order preserving segment of the orbit. We have to draw these two threads so that they do not intersect each other. We draw the thread for the backward moving segment of orbit in front of the threads for the forward moving segment of the orbit. According to this rule, we draw the thread from 2 to 3 in front of the remaining two at their intersection point. In the second step, we go from the universal cover to the cylinder, that is, we project the braid on the surface of cylinder. In this projection, the thread from 4 to 1 passes behind the other threads. This is illustrated in the lower part of broken line in Fig.3b. Finally we have the required braid.

$$\sigma_2^{-1}\sigma_1^{-1}\sigma_2\sigma_1 = \sigma_1\sigma_2^{-1}\sigma_1^{-1}\sigma_1 = \sigma_1\sigma_2^{-1}. \tag{35}$$

Accoding to Theorem 1, T is a pseudo-Anosov system and has a chaotic orbit with a positive topological entropy $h(\geq \ln(3+\sqrt{5})/2)$. The topological entropy is calculated from the eigenvalue of Burau matrix$(M(t))$ with $t = \cos\theta + i\cos\theta (0 \leq \theta < 2\pi)$(see Table II). The Burau matrices for $\sigma_{1,2}$ and $\sigma_{1,2}^{-1}$ are given in Appendix I. It is easy to prove that the maximum absolute value of eigenvalues is obtained at $t = -1$. This property holds for other braids listed in Table III.

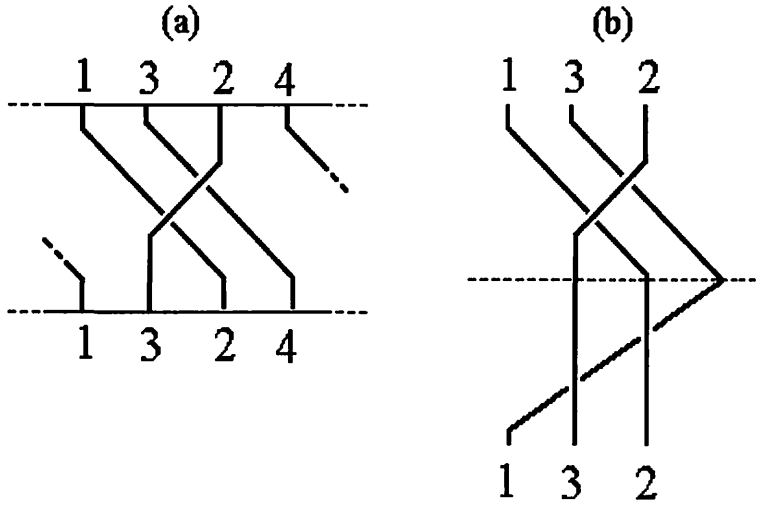

Fig.3: Construction of a braid. Symbol 'i' stands for x_i.

Here we show the simplified method combining two steps described above.
[1] Prepare a cylinder.
[2] Put three orbital points in the front side of the upper and bottom circles.
[3] For the orbit with $\nu = p/3$, the thread connecting $1 \to 2, \cdots, 3 \to 1$ revolves round the cylinder p times.
[4] If the movement from n to $n+1$ is the backward one, the thread connecting n and $n+1$ passes in front of other braids. If the movement from n to $n+1$ is faster than other movement from n' to $n'+1$, the thread connecting n and $n+1$ passes behind the thread connecting n' and $n'+1$.
[5] The intersections of threads in the rear side of the cylinder are inhibited. At this step, the orbit gains the rotation number.
[6] Using Reidemeister move($\sigma_1\sigma_2\sigma_1 = \sigma_2\sigma_1\sigma_2$) and Markov move($\sigma_i \leftrightarrow \sigma_j\sigma_i\sigma_j^{-1}$), reduce the braid to a simpler form and then express the braid type with generators.

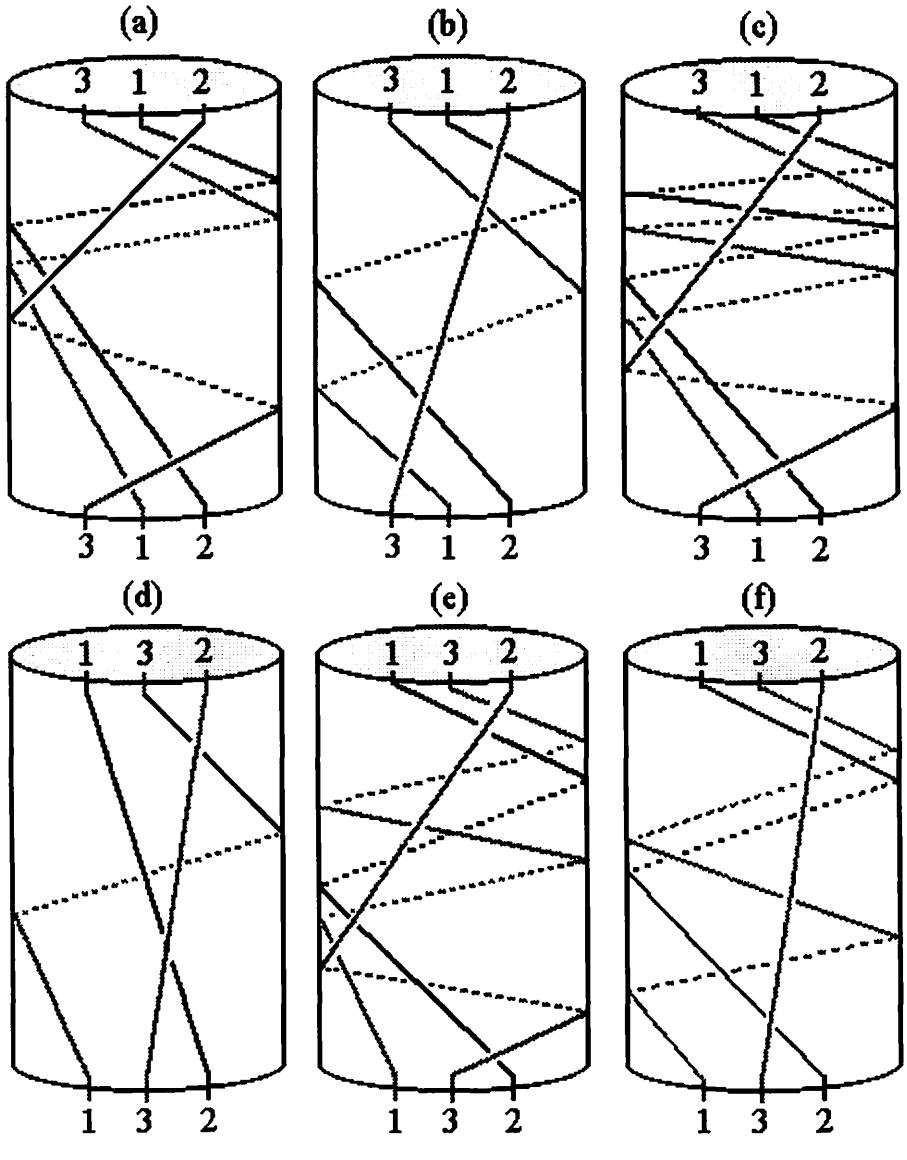

Fig.4 Braids for the first non-Birkhoff period-3 orbits.(a) $\nu = 1/3(x = 0)$, (b) $2/3(x = 0)$,(c) $3/3(x = 0)$, (d) $1/3(x = \pi)$, (e) $2/3(x = \pi)$ and (f) $3/3(x = \pi)$.

Using this procedure, we obtain the same braid type for the non-Birkhoff orbit with $\nu = 1/3$ having a point on the $x = \pi$ axis(compare Fig.3 and Fig.4d). We construct the braids for other three orbits(see Fig.4). We summarize our results in Tables II and III.

Table II: Examples of Burau Matrix

ν	Axis	$M(t)$
1/3	$x = \pi$	$\begin{pmatrix} 1-t & -1/t \\ 1 & -1/t \end{pmatrix}$
2/3	$x = \pi$	$\begin{pmatrix} -1+1/t^3-1/t^2+1/t+t-t^2 & (-1+t-t^2+t^3-t^4)/t^4 \\ 1/t^3 & -1/t^4 \end{pmatrix}$
3/3	$x = \pi$	$\begin{pmatrix} 1-t+t^2-t^3 & 1-1/t-t \\ 1 & -1/t \end{pmatrix}$

Table III: Braid Type and Topological Entropy

ν	Axis	Braid Type	Topological Entropy
1/3	$x = 0$	$\theta_3^{-1}\sigma_1^3\sigma_2^{-1}$	$\geq \ln((5+\sqrt{21})/2)$
1/3	$x = \pi$	$\sigma_1\sigma_2^{-1}$	$\geq \ln((3+\sqrt{5})/2)$
2/3	$x = 0$	$\sigma_1\sigma_2^{-1}$	$\geq \ln((3+\sqrt{5})/2)$
2/3	$x = \pi$	$\theta_3^{-1}\sigma_1^5\sigma_2^{-1}$	$\geq \ln((7+3\sqrt{5})/2)$
3/3	$x = 0$	$\theta_3^{-1}\sigma_1^5\sigma_2^{-1}$	$\geq \ln((7+3\sqrt{5})/2)$
3/3	$x = \pi$	$\sigma_1^3\sigma_2^{-1}$	$\geq \ln((5+\sqrt{21})/2)$

Using the procedure, we also obtain the braid types of the m-th non-Birkhoff orbits with $\nu = p/3(p \geq 1)$. The results are shown in Table IV.

Table IV: Classification of Braid Types

$\nu(n \geq 0)$ Axis$(x = 0)$	$\nu(n \geq 0)$ Axis$(x = \pi)$	Braid Type$(m \geq 1)$
$(3n+1)/3$		$\theta_3^{-2m-n+1}\sigma_1^{6(m+n)-3}\sigma_2^{-1}$
	$(3n+3)/3$	$\theta_3^{-2m-n+2}\sigma_1^{6(m+n)-3}\sigma_2^{-1}$
$(3n+2)/3$	$(3n+1)/3$	$\theta_3^{-2m-n+2}\sigma_1^{6(m+n)-5}\sigma_2^{-1}$
$(3n+3)/3$	$(3n+2)/3$	$\theta_3^{-2m-n+2}\sigma_1^{6(m+n)-1}\sigma_2^{-1}$

Since the inverse full twist θ_3^{-1} does not contribute the topologicalentropy, we can delete it from the expressions of braids in Table IV. Then all braid types are expressed in the form.

$$\beta_3^{(2k+1)} = \sigma_1^{2k+1}\sigma_2^{-1}(k \geq 0) \tag{36}$$

where we take a suitable series in $\{\beta_3^{(2k+1)}\}$. The maximum absolute value of eigenvalues is obtained at $t = -1$ for the braid in Eq.(36). This fact is proven in Appendix II. The Burau matrix $M(t)$ for $\beta_3^{(2k+1)}$ with $t = -1$ takes the following form.

$$M(-1) = \begin{pmatrix} 2k+2 & 2k+1 \\ 1 & 1 \end{pmatrix}. \tag{37}$$

Then the topological entropy $h(\beta_3^{(2k+1)})$ is obtained.

$$h(\beta_3^{(2k+1)}) \geq \ln\left(\frac{2k+3+\sqrt{4k^2+12k+5}}{2}\right). \tag{38}$$

In the limit $k \gg 1$, the topological entropy diverges as $\ln k$. The braid $\sigma_1\sigma_2^{-1}$ gives the lower bound of topological entropy. This value is larger than $\log 2$. Then all symmetrical non-Birkhoff period-3 orbits are not embedded in the horseshoe.

4 Concluding Remarks

We give remarks corresponding to the non-Birkhoff period 3 orbits not on the symmetry axes. There are two types of them. The first type was born due to the equi-period bifurcation of the elliptic point(named the mother SNB) on the symmetry axis. The braid type of this type is identical to that of the mother SNB. The second one was born due to the tangent bifurcation. It is difficult to find the second type orbits and to construct its braid type, systematically.

Consider $f(x)$ with two maxima in $0 < x < \pi$. We study the birth of the first non-Birkhoff orbit with $\nu = 1/3$ starting from the $x = \pi$-axis. Since $f(x)$ has two maxima, the tangent bifurcation occurs in the interval $\pi < y_1 < 2\pi$ twice. The braids of two orbits born at the first and second bifurcations are $\sigma_1\sigma_2^{-1}$ since these orbits go around P once and rotate the cylinder once. Then the results mentioned above hold for $f(x)$ with multiple maxima.

Finally we give a comment on the non-Birkhoff period-4 orbit. We find it with the braid type with $\sigma_1\sigma_2\sigma_3^{-1}$, whose topological entropy is larger than $\ln 2.174\ldots > \ln 2$. Then this orbit is not embedded in the horseshoe.

Acknowledgement

Authors would like to thank Dr.T.Matsuoka for helpful discussions and comments.

References

1) A.N.Sharkovskii, Ukrain. Math. Zh. **16** (1964), p.61.
2) T.-Y.Li and J.Yorke, Ammer. Math. Monthly **82** (1975), p.985.
3) T.Matsuoka, in *Dynamical Systems* **1**, World Scientific (1986). p.58. Comtemp. Math. **152** (1993), 21. See also Lecture Note(in Japanese), *Bussei Kenkyu* 67-1 (1996) pp.1-56.
4) P.Boyland, Topology and its Appl. **58** (1994), 223.
5) K.Murasugi,*Knot Theory & Its Applications*(Birkhäuser,1996).
6) W.P.Thurston, Bull. Amer. Math. Soc. **6** (1982), 357.
7) A.J.Casson and S.A.Bleiler, *Automorphisms of Surfaces after Nielsen and Thurston*, London Math. Society Student Texts 9 (Cambridge Univ. Press,1988).
8) K.R.Meyer and G.R.Hall, *Introduction to Hamiltonian Dynamical Sytems and the N-Body Problem* (Springer-Verlag,1991).
9) G.D.Birkhoff, Acta. Math. **43** (1920),44.
10) G.R.Hall, Ergod. Th. & Dynam. Sys. **4** (1984), 585.

11) P.L.Boyland and G.R.Hall, Topology **26** (1987), 21.
12) I.Leage and R.S.Mackay, Phys. Lett. **A118** (1986),274.
13) A.Olvera and C.Simó, Int. J. Bifurcation and Chaos **3** (1993),165.
14) Y.Yamaguchi and K.Tanikawa, Prog. Theor. Phys. **101** (1999),1.
15) K.Tanikawa and Y.Yamaguchi, J. Math. Phys. **28** (1987),921. R.De Vogelaere, in *Contributions to the Theory of Oscillations*, Vol.IV. *Ann. Math. Studies* **No.41**, Princeton University Press (1953). p.53.

Appendix I

We give Burau matrix representations for $\sigma_{1,2}$ and $\sigma_{1,2}^{-1}$.

$$\sigma_1 = \begin{pmatrix} -t & 1 \\ 0 & 1 \end{pmatrix},\ \sigma_1^{-1} = \begin{pmatrix} -1/t & 1/t \\ 0 & 1 \end{pmatrix}, \sigma_2 = \begin{pmatrix} 1 & 0 \\ t & -t \end{pmatrix},\ \sigma_2^{-1} = \begin{pmatrix} 1 & 0 \\ 1 & -1/t \end{pmatrix}.$$

Appendix II

In this Appendix, we prove that the maximum absolute value of eigenvales is obtained at $t = -1$ for the braid type with $\sigma_1^{2k+1}\sigma_2^{-1}$. For the Burau matrix $M(t)$ of this braid, we have the following properties:

$$\mathrm{Tr}M(t) = \sum_{i=-1}^{2k+1}(-t)^k, \tag{39}$$

$$\mathrm{Det}M(t) = t^{2k}. \tag{40}$$

We have the absolute eigenvalues of $M(t)$ with $t = \exp(i\theta)$.

$$|\lambda_\pm(\theta)|^2 = \frac{1}{4}\left(p(\theta) \mp \sqrt{p^2(\theta) - 4}\right)^2, \tag{41}$$

where

$$p(\theta) = \frac{\cos(n + 3/2)\theta}{\cos\theta/2}. \tag{42}$$

Here $|p(\theta)| > 2$ is assumed. If the relation $|p(\theta)| \leq 2$ holds, we have $|\lambda_\pm|^2 = 1$. As a result, we obtain the maximum absolute value $|\lambda_{\max}(\theta)|$ of two eigenvalues.

$$|\lambda_{\max}(\theta)|^2 = \frac{1}{4}\left(|p(\theta)| + \sqrt{p^2(\theta) - 4}\right)^2. \tag{43}$$

If the relation $p(\pi)(= 2k + 3) \geq |p(\theta)|$ holds, we have the relation $|\lambda_{\max}(\pi)| \geq |\lambda_{\max}(\theta)|$. In the following, we prove the relation $2k + 3 \mp p(\theta) \geq 0$:

$$\begin{aligned} 2k + 3 \mp p(\theta) = & \sum_{i=-1}^{k-1}\left(1 \pm (-1)^i \cos(k - i)\theta \sin^{2i+2}\theta/2\right) \\ & + \sum_{i=-1}^{k-1}\left(1 \mp (-1)^i \sin(k - i - 1/2)\theta \sin^{2i+3}\theta/2\right) \\ & + \left(1 \pm \sin^{2k+2}\theta/2\right) \geq 0. \end{aligned} \tag{44}$$

Kicked Harper Map における大域的カオスの発生
Transition to Global Chaos in the Kicked Haper Map

篠原 晋*
早稲田大学理工学部 応用物理学科

Susumu SHINOHARA*
Department of Applied Physics, Waseda University, Tokyo 169-8555

Abstract

The Kicked Haper map is studied by defining the indicator points in the phase space. Along the torus on which the indicator points are located, the twist condition is violated. By using the indicator points, the critical parameter values at which the transition to global chaos occurs are numerically determined.

1 Introduction

ハミルトン力学系のトーラスの摂動に対する頑丈さ (robustness) は、トーラスの回転数の数論的性質によって決まると考えられている. たとえば標準写像では、有理数で最も "近似しにくい" 黄金比の回転数をもつトーラスが最も頑丈 (most robust) であり、黄金比と対等な無理数を回転数にもつトーラスは、相対的に頑丈 (locally most robust) であることが数値的に示されている [1, 2]. その一方、ノンツイスト写像と呼ばれる二次元保測写像では、標準写像などで得られているトーラス崩壊過程の描像は成り立たず、shearless トーラスと呼ばれるトーラスが、その回転数の数論的性質に依らず摂動に対して常に最も頑丈であることが分かってきた. ある対称性をもったノンツイスト写像では、shearless トーラスの正確な位置を求めることが出来る [3]. ここでは、ノンツイスト写像 Kicked Haper (KH) map について、shearless トーラスが通る点の座標を導出し、KH map における大域的カオス発生の臨界パラメータ値を決定する.

KH map は、次式で定義される二次元保測写像である: $T_{K,L} : \mathbf{T}^2 \mapsto \mathbf{T}^2$,

$$\begin{pmatrix} p' \\ x' \end{pmatrix} = T_{K,L} \begin{pmatrix} p \\ x \end{pmatrix} = \begin{pmatrix} p + K \sin x \\ x - L \sin p' \end{pmatrix}.$$

ここで、$K, L \in \mathbf{R}$, $\mathbf{T} = \mathbf{R}/2\pi\mathbf{Z}$ である. KH map は、二次元保測写像の具体的モデルとして、標準写像と並んでよく研究され、とくに stochastic web 上の拡散の性質が詳しく研究されている [4]. KH map は、$K = 0$ または $L = 0$ のとき可積分である. K を摂動パラメータと考えると、$-L \sin(p')$ の項がツイスト関数となるが、このツイスト関数は非単調なので KH map はノンツイスト写像である [5].

2 Symmetry of the KH Map

KH map は以下に挙げる対称性をもつ:

*E-mail address: susumu@aizawa.phys.waseda.ac.jp

(i) Symmetry of the parameter space

座標変換 $U, V, W : \mathbf{T}^2 \mapsto \mathbf{T}^2$ を

$$U\begin{pmatrix} p \\ x \end{pmatrix} = \begin{pmatrix} p \\ x+\pi \end{pmatrix}, \quad V\begin{pmatrix} p \\ x \end{pmatrix} = \begin{pmatrix} p+\pi \\ x \end{pmatrix}, \quad W\begin{pmatrix} p \\ x \end{pmatrix} = \begin{pmatrix} -x \\ -p \end{pmatrix}.$$

と定義すると、KH map $T_{K,L}$ は次式を満たす:

$$T_{-K,L} = U^{-1} \circ T_{K,L} \circ U, \quad T_{K,-L} = V^{-1} \circ T_{K,L} \circ V, \quad T_{L,K} = W^{-1} \circ T_{K,L}^{-1} \circ W.$$

したがって、パラメータ平面 (K-L 平面) は次の三つの変換のもとで不変である.

$$(K, L) \mapsto (-K, L), \quad (K, L) \mapsto (K, -L), \quad (K, L) \mapsto (L, K).$$

ここでは、次のパラメータ領域に注目する:

$$0 \leq K \leq \infty, \quad 0 \leq L \leq K.$$

(ii) Reversibility

$$^{\exists} M_1, M_2 : \mathbf{T}^2 \mapsto \mathbf{T}^2 \quad s.t. \quad T_{K,L} = M_2 \circ M_1 \quad and \quad M_1^2 = M_2^2 = 1.$$

KH map では、M_1, M_2 を次のようにとることが出来る:

$$M_1\begin{pmatrix} p \\ x \end{pmatrix} = \begin{pmatrix} -p - K\sin x \\ x \end{pmatrix}, \quad M_2\begin{pmatrix} p \\ x \end{pmatrix} = \begin{pmatrix} -p \\ x + L\sin p \end{pmatrix}.$$

(iii) Symmetry of the phase space

KH map $T_{K,L}$ は次式で定義される写像 $S : \mathbf{T}^2 \mapsto \mathbf{T}^2$ と可換である. *i.e.*, $S \circ T_{K,L} = T_{K,L} \circ S$,

$$S\begin{pmatrix} p \\ x \end{pmatrix} = \begin{pmatrix} p-\pi \\ -x-\pi \end{pmatrix}.$$

3 The Indicator Points of the KH Map

次の方程式の解 $\boldsymbol{x}_1, \boldsymbol{x}_2 \in \mathbf{T}^2$ を indicator points と呼ぶ.

$$\begin{aligned} M_1\boldsymbol{x}_1 &= S\boldsymbol{x}_1, \\ M_2\boldsymbol{x}_2 &= S\boldsymbol{x}_2. \end{aligned}$$

これらの方程式の解は、それぞれ以下のように与えられる:

$$\boldsymbol{x}_1 = \boldsymbol{x}_1(K) = \left(\mp\frac{\pi}{2},\ \mathcal{P}\left(+\frac{\pi}{2} \pm \frac{K}{2}\right)\right),\ \left(\mp\frac{\pi}{2},\ \mathcal{P}\left(-\frac{\pi}{2} \pm \frac{K}{2}\right)\right),$$

$$\boldsymbol{x}_2 = \boldsymbol{x}_2(L) = \left(\mathcal{P}\left(+\frac{\pi}{2} \pm \frac{L}{2}\right),\ \mp\frac{\pi}{2}\right),\ \left(\mathcal{P}\left(-\frac{\pi}{2} \pm \frac{L}{2}\right),\ \mp\frac{\pi}{2}\right).$$

ここで、$\mathcal{P}$ は $\mathbf{R}$ から $\mathbf{T}$ への射影である. *i.e.*, $\mathcal{P} : x + 2k\pi \mapsto x$, $x \in [-\pi, \pi)$, $k \in \mathbf{Z}$.

Figs.1,2 はそれぞれ、$K = 2.1, L = 1.1$ の時の KH map の相空間、$p \equiv -\pi/2, x \approx 2$ での回転

数プロファイルである. シアー dR/dx がゼロになるトーラスを shearless トーラスという [6]. KH map では、ツイスト関数が二つの極値を持つので、二本の shearless トーラスが存在する. 前節で挙げた対称性 *(ii)* と *(iii)* を持つ写像では、indicator point を通るトーラスは shearless トーラスであることが示される [3].

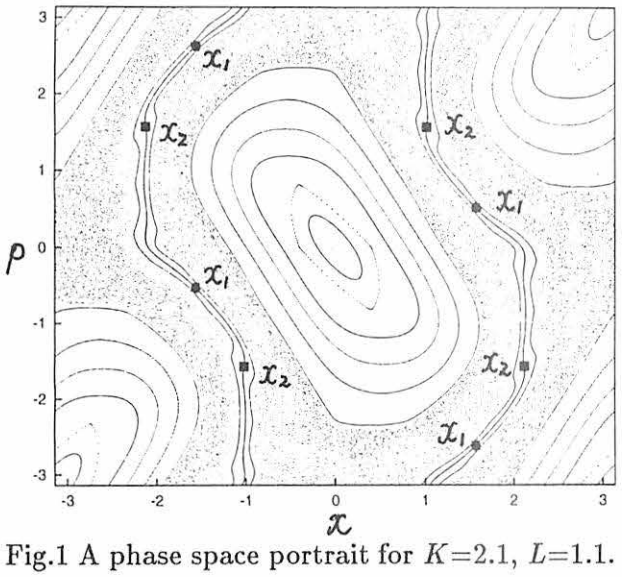

Fig.1 A phase space portrait for K=2.1, L=1.1.

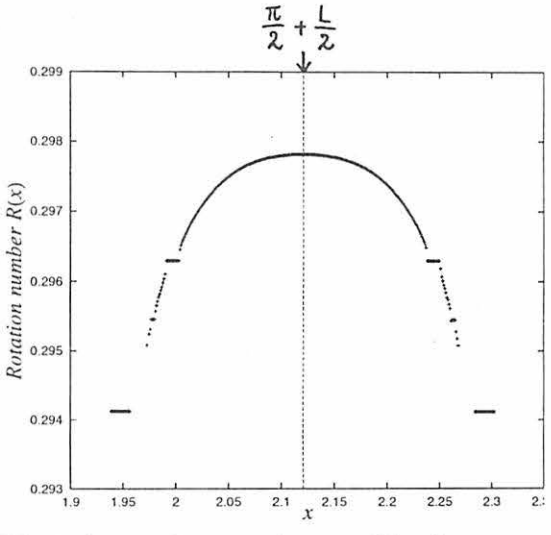

Fig.2 A rotation number profile along $p \equiv -\pi/2$.

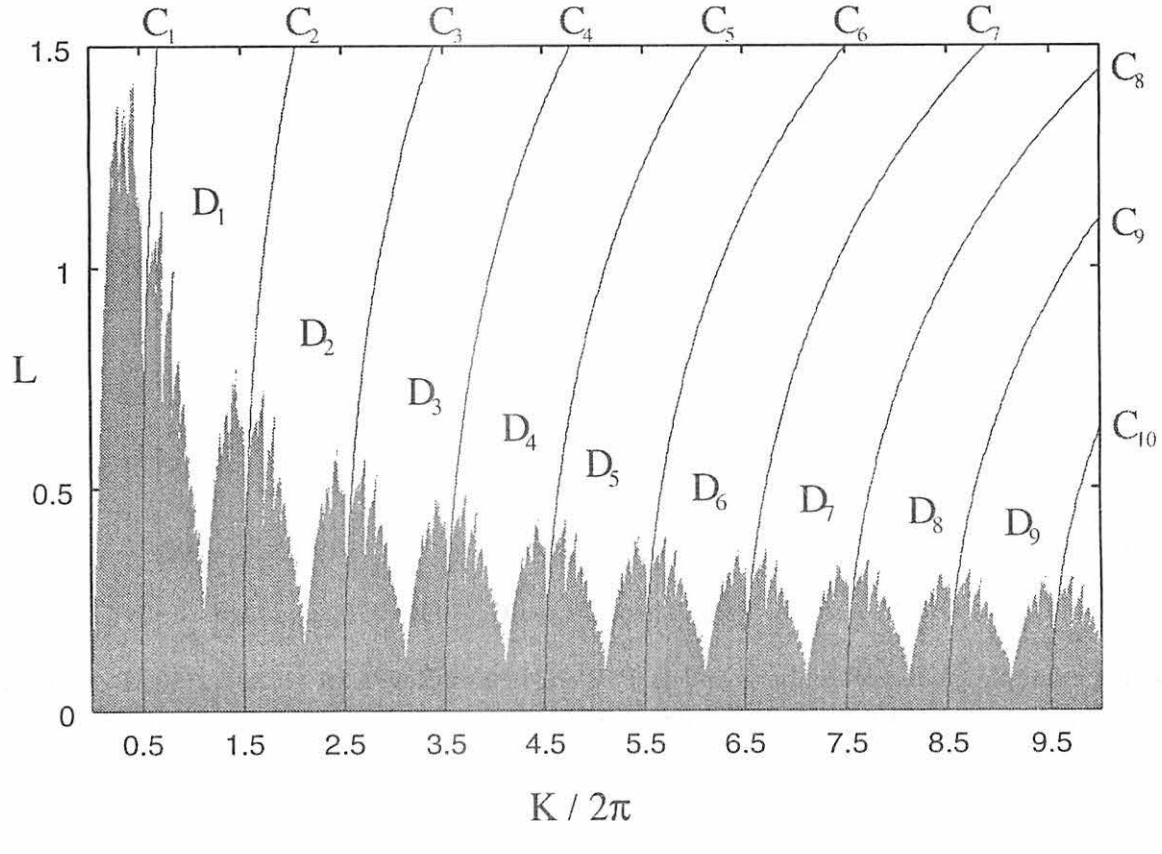

Fig.3 Phase diagram of the KH map. The trajectory of an indicator point remains bounded for the gray region, but unbounded for the white region.

4 The Critical Boundary of the KH Map

Fig.1 に示したように、shearless トーラス周辺は、他のトーラスに比べて頑丈である. したがって、$\boldsymbol{x}_1$と $\boldsymbol{x}_2$の軌道の振舞が拡散的であるか否かを調べることにより、相空間にトーラスが存在するかどうかを判定できる. もし拡散的であれば、トーラスは全く存在せず、非拡散的であれば、すくなくとも一本のトーラスが存在するはずである. パラメータ平面の各点について、$\boldsymbol{x}_1$と $\boldsymbol{x}_2$の軌道の振舞を数値的に調べた結果を Fig.3 に示す. Fig.3 の灰色領域では $\boldsymbol{x}_1$と $\boldsymbol{x}_2$の軌道がともに有界領域に留まり、白色領域ではどちらか一方あるいは両方が拡散的となる. 灰色領域と白色領域の境界のパラメータ値は、last KAM が崩壊し大域的カオスが発生する臨界パラメータ値に相当することから、この境界を critical boundary とよぶ. critical boundary の形状は、indicator point が周期点またはヘテロクリニック点になるようなパラメータ曲線の形状によって決まる [3]. Fig.3 には、$\boldsymbol{x}_2$が 2 周期点となるようなパラメータ曲線 C_jが描かれている. ここで、C_jは次のように与えられる:

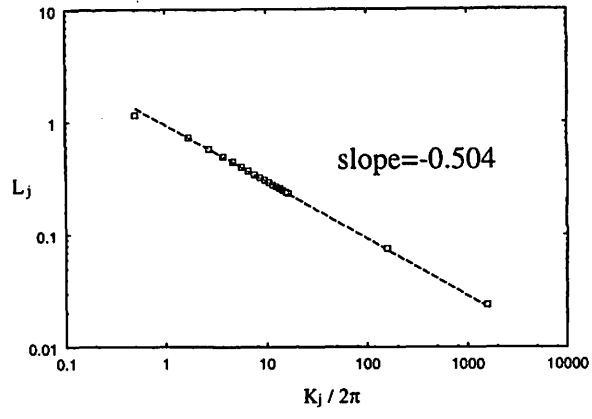

Fig.4 L_j vs. $K_j/2\pi$

$$\mathrm{C}_j = \left\{(K,L)\,\middle|\,T_{K,L}^2\boldsymbol{x}_2 = \boldsymbol{x}_2\right\} = \left\{(K,L)\,\middle|\,K\cos\left(\frac{L}{2}\right) = (2j-1)\pi\right\}. \quad (j=1,2,\cdots)$$

曲線 C_jと曲線 C_{j+1}によって挟まれる領域を D_jとおくと、各 D_j内での critical boudary の構造は定性的にほぼ等しい. 各 D_jにおける critical boundary の点のなかで、L の値が最大となる点の座標を (K_j, L_j) とおくと、次の関係式が成り立つことが分かった (Fig.4 参照):

$$L_j \propto K_j^{-\beta}, \quad \beta \simeq 0.504$$

References

[1] J. M. Greene, J. Math. Phys. **20** (1979) 1183.

[2] R. S. MacKay and J. Stark, Nonlinearity **5** (1992) 867.

[3] S. Shinohara and Y. Aizawa, Prog. Theor. Phys. **97** (1997) 379; *ibid.* **100** (1998) 219.

[4] for example, A. J. Lichtenberg and B. P. Wood, Phys. Rev. **A39** (1989) 2153; R. Lima and D. Shepelyansky, Phys. Rev. Lett. **67** (1991) 1377; R. Artuso et al. Int. J. Mod. Phys. **B8** (1994) 207.

[5] S. Saito, Y. Nomura, K. Hirose and Y. H. Ichikawa, Chaos **7** (1997) 245.

[6] D. del-Castillo-Negrete, J. M. Greene and P. J. Morrison, Physica **D91** (1996) 1; *ibid.* **D100** (1997) 311.

Effects of Interaction between Heat Reservoir and Cluster on Spontaneuos Alloying Phenomenon II

T.R. Kobayashi,* K.S. Ikeda *, S. Sawada†, Y. Shimizu‡

Abstract

"Spontaneuos alloying phenomena" for nanometer size metal clusters was observed by Yasuda, Mori et al. [4] and simulated with classical Hamiltonian dynamics by Ikeda, Sawada,Shimizu. However they confirmed very rapid allowing, detail of dynamics was concealed under heat up problem yet. Therefor we simulate under isothermal conditions using classical molecular dynamics with Langevin dynamics and velocity scaling method. Furthermore, all physical quantities are processed on ensemble average. In this paper we show gross features of spontaneuos alloying phenomena.

1 はじめに

原子数が 10^3 程度の微粒子の物性はバルクのそれとは著しく異なる事が予想される。室温下で、炭素膜上に支持した Au 微粒子 (host) に対して Cu(guest) 原子を蒸着させ、電子顕微鏡でその場観察する実験において、事実、粒径が数ナノメートル程度の金属超微粒子がバルク固体よりも速く合金化する現象が、大阪大学の保田-森らによって観測された。[4][1] この現象を自発的合金化現象 (Spontaneous Alloying Phenomenon) と云う。

保田-森らの実験から結論づけられる自発的合金化現象の特徴は以下に纏められる。

1. バルクに比べて 9 桁速く合金化する。(table 1)
2. host クラスター径が臨界値より大きい場合、クラスター表面上で薄皮状に合金を作り、中心部には host 原子のみからなる核が残される。
3. 合金の生成熱により左右される。
   合金生成熱が大きな正の値を持つ組合わせの場合、自発的合金化は起こらない。合金生成熱が負の値を持つ組合わせの場合、値が大きい程臨界径は大きくなる。

*Department of Physics, Faculty of Science and Engineering, Ritsumeikan University, Nojihigashi 1-1-1, Kusatsu 525-8577, Japan
†Department of Physics,Kwansei Gakuin University, 1-1-155, Uegahara, Nishinomiya 662-0891, Japan
‡Institute for Fundamental Chemistry, Takano-Nishihiraki-cho 34-4, Sakyou-ku, Kyoto 606-8103, Japan

4. 合金化の過程は固相状態で起きる。
双晶構造を持つクラスターは合金化前後でその構造を変えない観測事実がある。

この事実を受け、京大基礎化学研究所の清水、関西学院大学の澤田、立命館大学の池田らによって理論的な解明を目指す研究が為されている。[2] これまでは現象を再現する事に主眼が置かれていた為に全エネルギーが保存する孤立系で為されて来たが、本研究は MD シミュレーションに温度制御を組み込む事により、温度上昇によって隠蔽されてしまっていた種々の動力学的特徴を抜きだし、更に、シミュレーションの集団平均を取る事により少数多体系特有の大きな揺らぎを押え込む事に成功した。

本稿ではこれらのシミュレーションにより明らかになった自発的合金化現象の動力学的特徴を報告する。

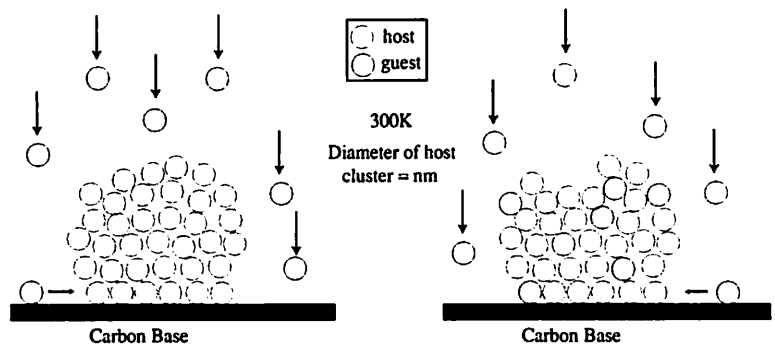

Figure 1: Conceptual illustration of spontaneuse alloying. Copper atoms (guest) are vapor-deposited onto nm-size gold clster (host) on base of carbon graphite film (left). Then a rapid dissolution of guest atoms into host cluster takes place (right).

2 モデルと条件

2.1 2次元2体力モデル

シミュレーションは2次元2体力モデルを用いている。より実験に即した状況を再現するには3次元でシミュレーションするべきであるが、以下の理由により2次元を採用している。

計算コストの削減

計算機上で現象を再現するに当たり基準に置いている実験は金の微粒子に銅をまぶすものであり、クラスター径はほぼ 4nm で原子数にして 1000 個のオーダー、クラスター中の原子を球殻構造の観点で捉えて層数を考えると 6 乃至は 7 層程度である。現象を計算機上で再現する際に考えなければならない事は、自発的合金

Table 1: A comparison of diffusion coefficient between bulk system and cluster. (Temperature = 300K)

$(Cu \rightarrow Au)$	diffusion coefficient
Bulk	$2.4 \times 10^{-28}[m^2/s]$
Cluster	$2.0 \times 10^{-19}[m^2/s]$

化現象に於いて粒子の個数とサイズ或は層の数のどちらが本質的に重要であるか、と云う事である。容易に想像できる事はクラスター表面での振舞いが合金化現象に大きく寄与している事である。従って表面に存在する原子と内部に存在する原子の比率、或は層の数を最も重要な項目に据えた。2次元で6層程度のクラスターを準備するには100個程度の原子数で済、延いてはクラスターサイズを調べる際の計算コストを大幅に圧縮できる。

クラスター合金化現象に於ける解析手法の確立

今一つの理由は微小クラスターのダイナミクスを解析する手法を整える事である。現状では確立された方法は何もなく、その様な状況下ではMDシミュレーションが示す様相を備に観察する事が唯一の方法であり、系のスナップショットやアニメーションを観る事が多いに役立つ。その際に平面上に限定される2次元の方が3次元の動画よりも遥に集中する点を絞りやすい。2次元で解析手法を確立した後に3次元の系に研究対象を移す計画である。

MDの時間積分法はVerlet法を用い、時間刻みは $1.0 \times 10^{-14}[s]$ である。

2.2 host-guest原子の差異の表現

2体力ポテンシャルの一つとして採用しているMorseポテンシャル[3]は i 番目の原子では

$$V_i = \sum_{i \neq j} \epsilon_{i,j}[\exp(-2\beta(r_{ij} - \sigma)) - 2\exp(-\beta(r_{ij} - \sigma))] \tag{1}$$

である。但し σ は平均原子間距離を、β はポテンシャルの有効距離を、ϵ はポテンシャルの深さを各々決定する係数である。ここでhost原子とguest原子の違いは異種原子間のみ反応生成熱に相当するエネルギー分をポテンシャルに上乗せすることで反映させている。

$$\epsilon_{i,j} = \begin{cases} \alpha\epsilon & i,j \text{原子が異種の時 } (\alpha \neq 1) \\ \epsilon & ij \text{原子が同種の時} \end{cases} \tag{2}$$

2.3 初期配置の条件

孤立系であるが故に懸念される事項の一つに「不自然な系の温度変化」が挙げられる。実験はほぼ室温の一定温度条件下で為されているが、シミュレーションを実験に似せてguest原子がクラスターに蒸着するところから再現すると、クラスターに温度が溜まりすぐさま融解してしまう。この困難は、クラスターに付着したguest原子はある程度層を成すまでクラスター表面に留まることを理由に、始めからクラスターの周辺にguest原子を置いた配置を採用することで回避した。図2に初期配置を挙げる。

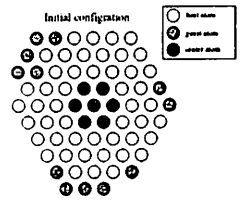

Figure 2: initial configuration of cluster

2.4 温度の定義

温度は熱力学的な概念の物理量であり、クラスターのシミュレーションにその侭で用いる事は出来ない。従ってここでは運動エネルギーを温度と同一視することにした。

温度 T は運動エネルギーを E_k、クラスター原子数を N、ボルツマン定数を k_B として

$$T = \frac{2E_k}{(2N-3)k_B} \tag{3}$$

で与えられる。$(2N-3)$ は生きている系の自由度である。

2.5 Langevin ダイナミクス法

外界からの揺動力として、Brown 運動から導かれる Langevin 方程式

$$\dot{v}(t) = -\gamma_L v + \frac{R(t)}{m} \tag{4}$$

を差分化したもの

$$v(t+dt) - v(t) = -\gamma_L v(t) + \sqrt{\frac{2\gamma_L k_B T}{mdt}} R_{Gauss}(t) \tag{5}$$

を使う方法である。ここで $R_{Gauss}(t)$ はガウス分布に則った乱数であり、$v(t)$ は原子の速度である。Langevin ダイナミクス法は、系をカノニカル集団として振舞わせる。即ち、温度の制御と外部の系との動力学的な相互作用を系に持ち込む事が出来る。

2.6 速度スケーリング法

目的の温度になるように強制的に運動エネルギーをスケールする方法である。ある時間（短時間平均）間隔で速度を

$$v'(t) = (1 + \gamma_v(1 - \frac{T_{ShortTimeAve}(t)}{T_{setting}}))v(t) \tag{6}$$

と修正する。

速度スケーリング法は以下の特徴を有する。

- **的確な温度制御**
  直に系のエネルギーを制御するので、設定温度からの揺らぎが非常に小さく 100ns の緩和時間で 3%以内である。
- **動力学的特徴の保存**
  系の温度を時々刻々の運動エネルギーから求めるのではなく、前 1000 ステップ分の短時間平均を用いる事によりクラスター固有振動の影響を排除し、且つ長い緩和時間を設定する事で 1 ステップ当たりで系に与える動力学的な影響を最小限にしている。
- **設定温度到達後はほぼ孤立系である**
  式 6 から明らかなように、系が設定温度にある時は系に対して実質何もしない。

Langevin ダイナミクス法を用いた場合と比較する事によって、合金化機構に支配的な影響を持つものが温度かダイナミクスかを同定することが期待できる。

2.7 温度設定

合金化が固相で起こる事実を踏まえ、系が固相に在る事を証拠立てる評価基準を設ける必要が在る。良く使われる方法は、式 7 で表される各粒子配置の二乗揺らぎ (RMS, Lindemann Index) を調べ、δ が 1 を越える温度を融点と解釈するものである。

$$\delta = \frac{2}{N(N-1)} \sum_{i<j} \frac{\sqrt{\langle r_{ij}^2 \rangle_t - \langle r_{ij} \rangle_t^2}}{\langle r_{ij} \rangle_t} \tag{7}$$

今一つの方法は、潜熱を判定するものである。温度の低い固相からシミュレーションを始め徐々に系にエネルギーを与えて行くと、丁度融点では系の総エネルギーは増加しているのにも関わらず温度が上昇しない現象が現れる。その温度を融点と解釈する。(Fig. 3).

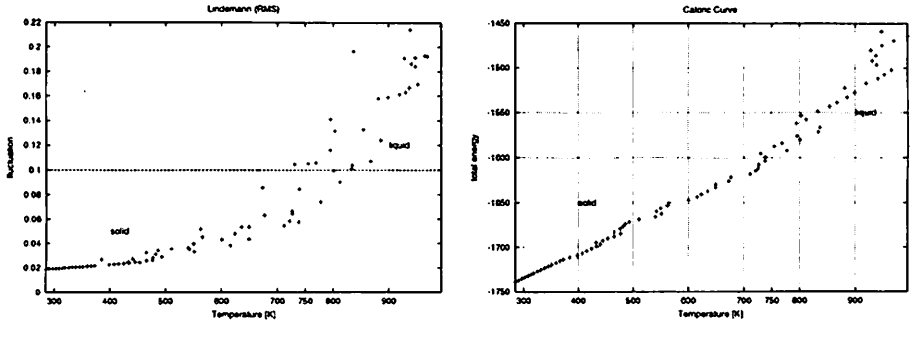

(a) Lindemann Index　　(b) Caloric curve

Figure 3: These results indicate melting temperature at 750 K. System parameters are Cu55(host)+12(guest) $\alpha = 1.0$. Each point is average of 10^5 steps.

3 解析の視点と物理量

3.1 解析視点

複雑な合金化現象のダイナミクスを解明するために、少しずつ条件を変えたシミュレーションを並べて互いの比較を試みる。ここでは実験で明らかにされた特徴である**温度依存性** と **生成熱依存性**に注目する。

直接実験結果との比較議論が可能なクラスターサイズ依存性や、実験では時間的或は空間的解像度が低い為に純粋にシミュレーションの範囲内での議論になるもののダイナミクスの詳細を把握する為に有用な異原子間の原子比率依存性なども考えられ、現在研究が進められている。

- **温度依存性**
  500,550,600,650K の各温度に設定。条件は host:guest = 55:12, $\alpha = 1.2$

- **生成熱依存性**
  生成熱変数である α を 0.95 (生成熱正) 1.0 (同種) 1.1 (生成熱負) 1.2 1.3 1.4 に設定。生成熱が合金化の推進力になっているか否か、或はその他の役割を調べる。条件は host:guest = 47:20, 600K

孤立系では合金化前後で 100K のオーダーで温度上昇し、亦、温度上昇率は生成熱と結び付いており、これらの依存性は正確な温度制御を用いてはじめて議論可能になる。尚、少数多体問題に特有な大きな揺らぎを排除するために、全ての解析量は 6 本のシミュレーションの集団平均を用いている。

3.2 考慮する物理量

合金化現象の特徴を抽出する為の物理量を議論する。

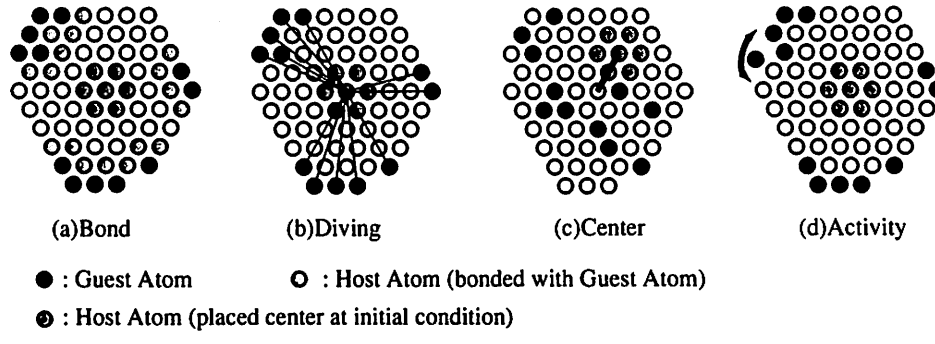

Figure 4: Illustrations of considering physical quantities.

1. **最近接異種原子数 (Bond)**
   Guest 原子の Host への親和度を表現する指標の一つ。ほぼポテンシャル・エネルギー変化を追随し、且つ、電子線回折を根拠に合金化を判断する実験の状況に即した量である。Figure 4-(a)
2. **クラスター重心と guest 原子間平均距離 (Diving)**
   Guest 原子の Host への親和度を表現する指標の一つ。Guest 原子がクラスター内部へ潜り込む様子を抽出する。Figure 4-(b)
3. **クラスター重心と初期中心原子団距離 (Center)**
   初期状態でクラスターの中心部に位置した 7 個の原子の遍歴。主に Host 側の動きを観るのに役立つ。Figure 4-(c)
4. **活性度 (Activity)**
   最近接原子の組み換え数を累積したもの。原子の実際の移動を定量化している。Figure 4-(d)

その他、ダイナミクスの詳細として集団運動を考慮すべきであり、研究が進められている。

4 結果と課題

ここでは温度依存性と生成熱依存性の観点からシミュレーション結果を纏めて議論する。

4.1 温度依存性

最近接異種原子数 (Bond) (Figure 5-(a)) は下の曲線から順に 500,550,600,650K である。クラスター重心と guest 原子間平均距離 (Diving) (Figure 5-(b)) は上の曲線から順に温度が上がる。クラスター重心と初期中心原子団距離 (Center) (Figure 5-(c)) は下の曲線から順に温度が上がる。以上 3 つの時系列と $1\mu s$ の時点でのクラスター各層での累積活性度 (Activity) (Figure 5-(d)) を示す。

これらのグラフは温度が上がるにつれて合金化速度が上がっている事を示している。先に述べたように実験との対応が最も良いと考えられる物理量は Bond であり、500K でも $3\mu s$ の後には理想混入値 [1] 4.9 に到達している。而し、Diving, Center の両物理量は温度が低いとクラスターの中心部は殆ど動かない事を示している。

尚、Langevin ダイナミクスによるシミュレーションも全く同じ特徴を示し、速度スケール法との差は数倍程度に収まっている事を添えておく。

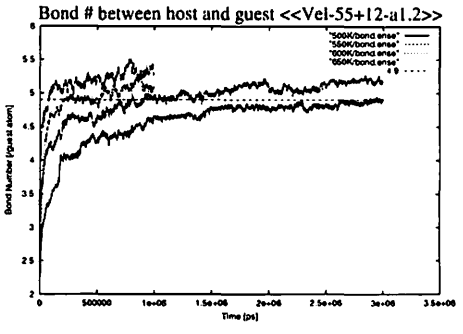

(a) Bond number between differnt species

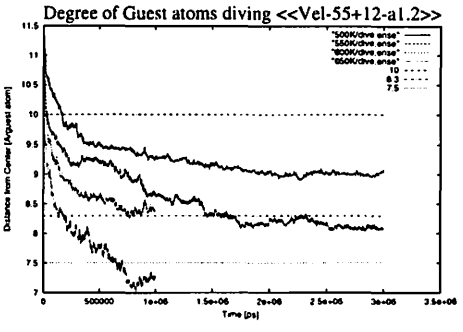

(b) Average of distance from center to guest atoms

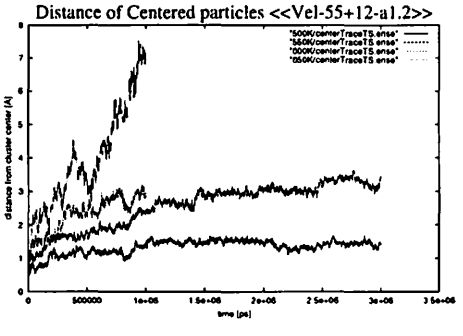

(c) Distance of centered particles

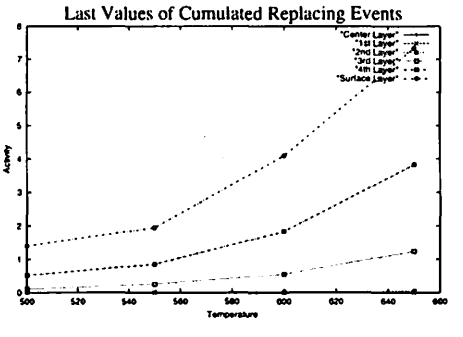

(d) Activity of enach layer

Figure 5: three time serieases and a cumulated replacing events at each layer at $1\mu s$. Obviously along with the increase of temperature, alloying time become short.(See (a)(b)(c)) Activities also same trend.(See (d))

[1] 理想混入値 r は Guest 原子が均等に拡散した状態をさし、$r = 6N_{host}/(N_{host} + N_{guest})$ で表される。6 は配位数である。

4.2 生成熱依存性

最近接異種原子数 (Bond) (Figure 6-(a)) は 3 パートに別れており、最下の曲線が $\alpha = 0.95$ 中が $\alpha = 1.0$ 最上の集団が $\alpha = 1.1 \sim 1.4$ である。クラスター重心と guest 原子間平均距離 (Diving) (Figure6-(b)) は最も深く潜り込んでいる曲線が $\alpha = 1.1$ 、ほぼ同じ潜り込みを示しているのが $\alpha = 1.0$ で値 8 に落ちついている。$\alpha = 0.95, 1.2 \sim 1.4$ は値 $8.5 \sim 9$ に集まっている。クラスター重心と初期中心原子団距離 (Center) (Figure 6-(c)) は下から順に $\alpha = 1.4, 1.3, 1.2$ となり、$\alpha = 0.95 \sim 1.1$ はほぼ同じ様相を示している。以上 3 つの時系列と $1\mu s$ の時点でのクラスター各層での累積活性度 (Activity) (Figure 6-(d)) を示す。

Bond は生成熱が負の値に大きくなるにつれて合金化速度が上がっている様に見えるので生成熱が合金化の推進力を担っていると考えたいが、他の物理量が奇妙な特徴を示しており一概に断定はできない。

Bond を観ると生成熱が負であれば殆ど同じ様相を示しているので実験で観測される意味での差異は無いかも知れないが、Diving, Center の両グラフは $\alpha = 1.1$ が最も深層まで Guest 原子が潜り込み、且つ中心が動いており、α が 1.2 を越えると中心部の動きは段々鈍くなり、Guest 原子も深層部までは潜り込まなくなる事を示している。

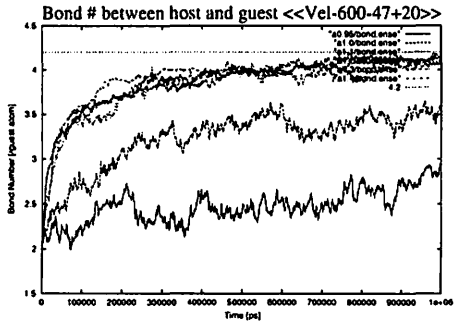

(a) Bond number between differnt species

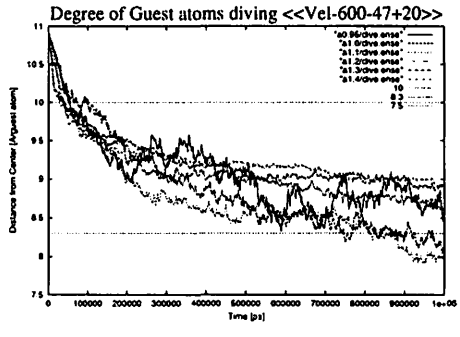

(b) Average of distance from center to guest atoms

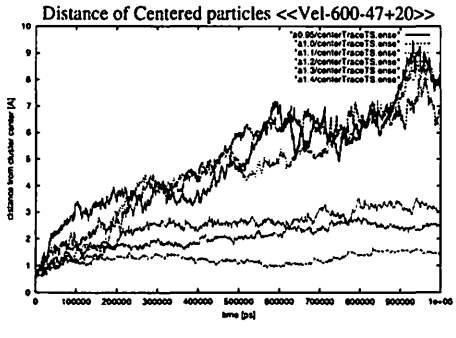

(c) Distance of centered particles

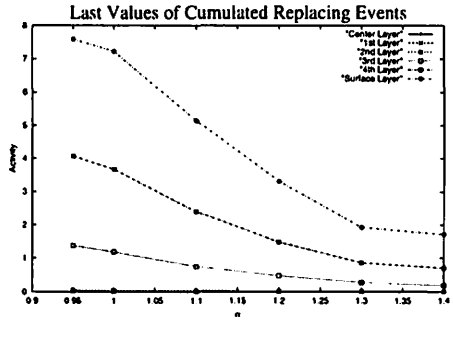

(d) Activity of each layer

Figure 6: Along with the increase α, acitivities are decrease. These physical quantities seem to show inconsistent feature.

生成熱が負の値に大きくなればそれだけ異種原子間の結合が増えた際に開放されるエネルギーが大きくなるのが、同時に異種原子間の結合を切るのに必要なエネルギーも大きくなっており、一度獲得した異種原子間の結合は切られにくくなると考えられる。従って組み換え事象の累積数 (Activity) も生成熱が大きくなるに従って小さくなる筈であり、Activity のグラフは確かにその特徴を示している。

4.3 結論並びに課題

MD に温度制御を持ち込む事で温度変化の影に隠れた様々な現象が確認されて来ている。温度依存性に関しては全ての物理量が温度の上昇につれて合金加速度が上がっている事を示しており一貫した理解が可能であるが、生成熱依存性に関しては以下の見解と問題をもたらした。

- **合金化の推進力になるが枷にもなる**
  $\alpha = 1.1$ 迄は Figure 6 が示すように全ての物理量が合金化効率が上がっているが、1.1 よりも大きくなるとクラスター活性度の低下が著しくなる。

- **クラスター活性度が低下しても Bond で観る合金化速度は変化していない**
  この結果は生成熱の違いによる合金化過程のダイナミクスが質的に変化している事を示唆していると考えられ、ダイナミクスの詳細を整理するために原子が移動する様相を集団運動の観点から分類するべく現在研究が進められている。

特に生成熱依存性の示す結果は現状では首尾一貫した理解を許さず金属微粒子の自発的合金化のダイナミクスを明らかにする鍵を内包していると思われる。これまでは合金化現象の相対的な特徴に焦点を当てて研究が進められて来たが、今後はよりダイナミクスの詳細を解明する段階に進まなければならない。

亦、微粒子のサイズ依存性に関連して、クラスターの表面拡散とクラスターの動径方向の拡散 (垂直拡散) と活性化エネルギーの関係、合金化のエントロピック、或はエンタルピックな理解の試みが始められている。

References

[1] 保田英洋、森博太郎. ナノメートルサイズのアモルファス sb クラスターの au 原子蒸着の際の合金化過程. 日本金属学会誌, 59(7):681–685, 1995.

[2] 清水　寧、池田　研介、澤田　信一、里子　允敏. 自発的合金化の解明に向けて. 表面, 19:479–493, 1997.

[3] L. A. Girifalco and V. G. Weizer. Application of the morse potential function to cubic metals. *Phys. Rev.*, 114(3):687–690, 1959.

[4] H. Yasuda, H. Mori, M. Komatsu, K. Takeda, and H. Fujita. In situ observation of spontaneous alloying in atom clusters. *J. Electron Microsc.*, 41:267+, 1992.

MULTIPLE COLLISIONS IN THE ONE-DIMENSIONAL FREE-FALL FOUR-BODY PROBLEM

KIYOTAKA TANIKAWA[1] and SEPPO MIKKOLA[2]

[1]National Astronomical Observatory, Mitaka, Tokyo, 181 Japan
Email: tanikawa@cc.nao.ac.jp
[2]Tuorla Observatory, University of Turku, 21500 Piikkiö, Finland
Email: seppo.mikkola@astro.utu.fi

Abstract

The motion of particles in the one-dimensional free-fall four-body problem is numerically studied. The equal mass case $(m_1, m_2, m_3, m_4) = (1, 1, 1, 1)$ is studied. An orbit is expressed as a symbol sequence. Quadruple collisions, triple collisions, and simultaneous binary collisions are systematically obtained. It turns out that triple and simultaneous binary collisions form curves in the initial value space and quadruple collisions are obtained as cross-points of these curves. Due to the symmetry of the problem, there is an infinite number of finite orbits. Relationship between the collision and escape is briefly discussed.

1 Introduction

The one-dimensional four-body problem is a special kind of the general four-body problem, in which four mass points are aligned in a fixed line. The problem is of three degrees of freedom. The term 'free-fall' means that four mass points are initially at rest. In the one-dimensional four-body problem, Mather & McGehee(1975) proved the existence of the solutions which become unbounded in finite time. Sergysels & Loks(1987), using the energy and angular momentum integrals in the general four-body problem, obtained the conditions limiting the regions where motion cannot occur. Lacomba & Perez-Chavela(1992, 1993) studied the flow on the total collision manifold and the global flow, and escape and capture orbits in the rhomboidal four-body problem. Vidal(1999) studied the singularities and the flow on the total collision manifold in the rotating tetrahedral four-body problem. Mikkola(1983, 1984) numerically investigated the binary-binary close encounters for a wide parameter range.

The present work is an extension of Tanikawa & Mikkola(2000a, 2000b) who studied the one-dimensional three-body problem via symbolic dynamics. By restricting ourselves to the free-fall problem, we are able to systematically study the structure of the initial value space of our four-body problem.

In this paper we use a simple idea to map the initial values, in the one-dimensional four-body problem, which lead to quadruple-, triple- or simultaneous binary collision. Due to the symmetry of the problem, all the orbits experience collision in both directions of time. It turns out, indeed, that there are numerous (presumably infinitely many) curves, the points of which are initial conditions for orbits leading to the above three types of collision.

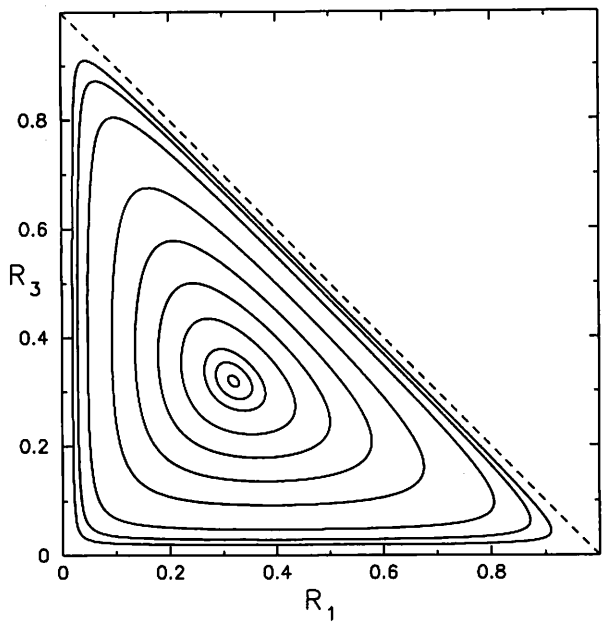

Figure 1: Equi-energy contours in the initial value space

2 Outline of the problem and the numerical method

We put four mass points m_1, m_2, m_3 and m_4 in this order on a line and fix the the gravitational constant G to one. Then the Hamiltonian of the problem is given by

$$H = T - U; \quad T = \frac{1}{2}\sum_{i=1}^{4}\frac{w_i^2}{m_i}; \qquad U = \sum_{i<j}\frac{m_i m_j}{|x_i - x_j|}. \tag{1}$$

where w_i are momenta conjugate to the coordinates x_i on the line.

2.1 Regularization of the problem

To integrate this system numerically we use a one-dimensional version of the chain method (Mikkola & Aarseth 1993). First the differences of the coordinates (=distances of consecutive bodies)

$$X_k = x_{k+1} - x_k \tag{2}$$

are introduced as new coordinates. The corresponding momenta are designated by W_k and the old momenta are obtained using the generating function

$$S = \sum_{k=1}^{3} W_k(x_{k+1} - x_k), \tag{3}$$

as

$$w_j = \frac{\partial S}{\partial x_j} = W_{j-1} - W_j, \tag{4}$$

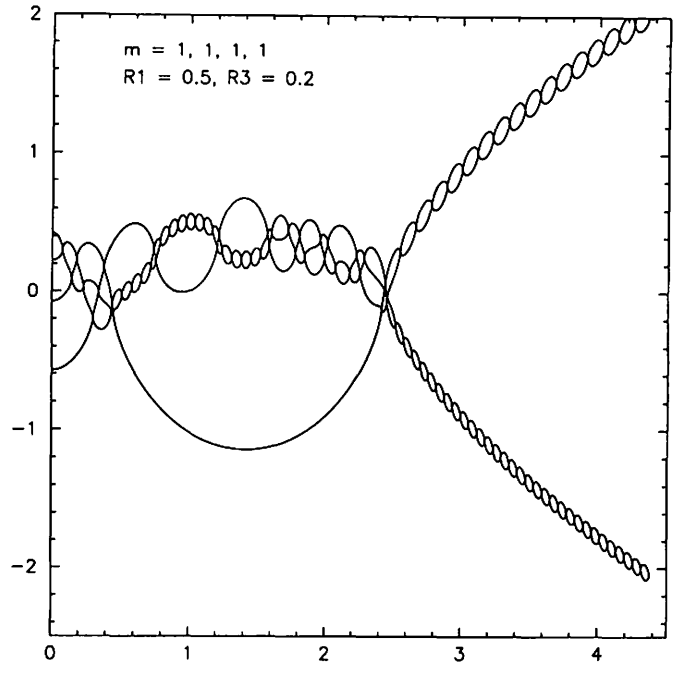

Figure 2: An example of orbits

which applies if we define $W_0 = W_4 = 0$. After this the second canonical transformation

$$X_k = Q_k^2; \;\; W_k = P_k/(2Q_k), \tag{5}$$

accompanied with a Poincare time transformation, gives our regularized Hamiltonian in the form

$$\Gamma = (H(\mathbf{P},\mathbf{Q}) + P_t)/L(\mathbf{P},\mathbf{Q}) \tag{6}$$

Here $H = T - U$ is the original Hamiltonian expressed in terms of the new variables, P_t is the momentum of time ($P_t = -E$, E is the (initial) numerical value of the Hamiltonian), and $L = T + U$ is the Lagrangian.

The equations of motion for the momenta P_k, coordinates Q_k and time t

$$P_k' = -\frac{\partial \Gamma}{\partial Q_k}; \qquad Q_k' = \frac{\partial \Gamma}{\partial P_k}; \qquad t' = \frac{\partial \Gamma}{\partial P_t}, \tag{7}$$

following from this Hamiltonian, are regular for two-particle collisions and can be integrated numerically with conventional methods, such as the Bulirsch-Stoer integrator (Bulirsch & Stoer 1966).

2.2 Initial conditions

The initial distance between m_1 and m_4 is set to one. The initial velocities are set to zero. Denoting $R_1 = x_2 - x_1$ and $R_3 = x_4 - x_3$, we get $x_3 - x_1 = 1 - R_3$, $x_3 - x_2 = 1 - R_1 - R_3$, and $x_4 - x_2 = 1 - R_1$. Then we obtain the expression for the initial Energy E as

$$E = -\frac{m_1 m_2}{R_1} - \frac{m_1 m_3}{1 - R_3} - m_1 m_4 - \frac{m_2 m_3}{1 - R_1 - R_3} - \frac{m_2 m_4}{1 - R_1} - \frac{m_3 m_4}{R_3} \tag{8}$$

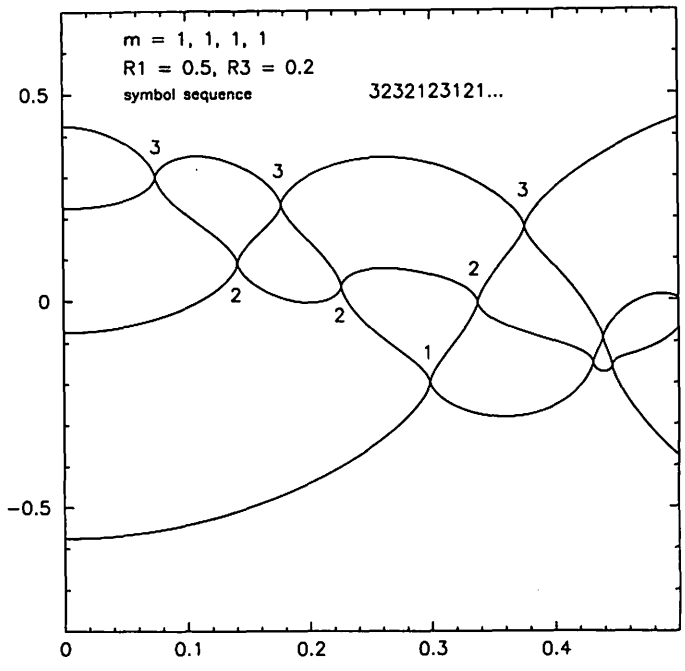

Figure 3: A symbol sequence and an orbit. The orbit is an initial part of the orbit in Fig.1.

with

$$0 < R_1 < 1, \quad 0 < R_3 < 1, \quad 0 < R_1 + R_3 < 1 \tag{9}$$

For given R_1 and R_3, the system is completely determined. The initial value space is given by Eq.(9). This is a triangular region in the (R_1, R_3) space as shown in Fig.1. In the figure, the equi-energy contours are shown for our case $m_1 = m_2 = m_3 = m_4 = 1$. The energy decreases to negative infinity when approaching the edges of the triangle which correspond to binary collisions. Three vertices correspond to initial triple collisions. The initial value space is symmetric with respect to the line $R_1 = R_3$. This is because the system conserves when we make a change $x \to -x$.

In the present study a 1000×1000 grid is adopted. The total number of orbits considered here is 0.5 million. To obtain particular local structures of the surface, additional orbit integrations have been carried out.

3 Orbits and Symbol Sequences

Particles in the one-dimensional four-body system with negative energy inevitably repeat binary collisions. This makes it possible to classify the history of the motion of four particles referring to the itinerary of two-particle collisions along orbits. A (one-sided) symbol sequence can be constructed in such a way that when particles 1 and 2 collide, the symbol '1' is added to the sequence, when particles 2 and 3 collide, the symbol '2' is added, and when particles 3

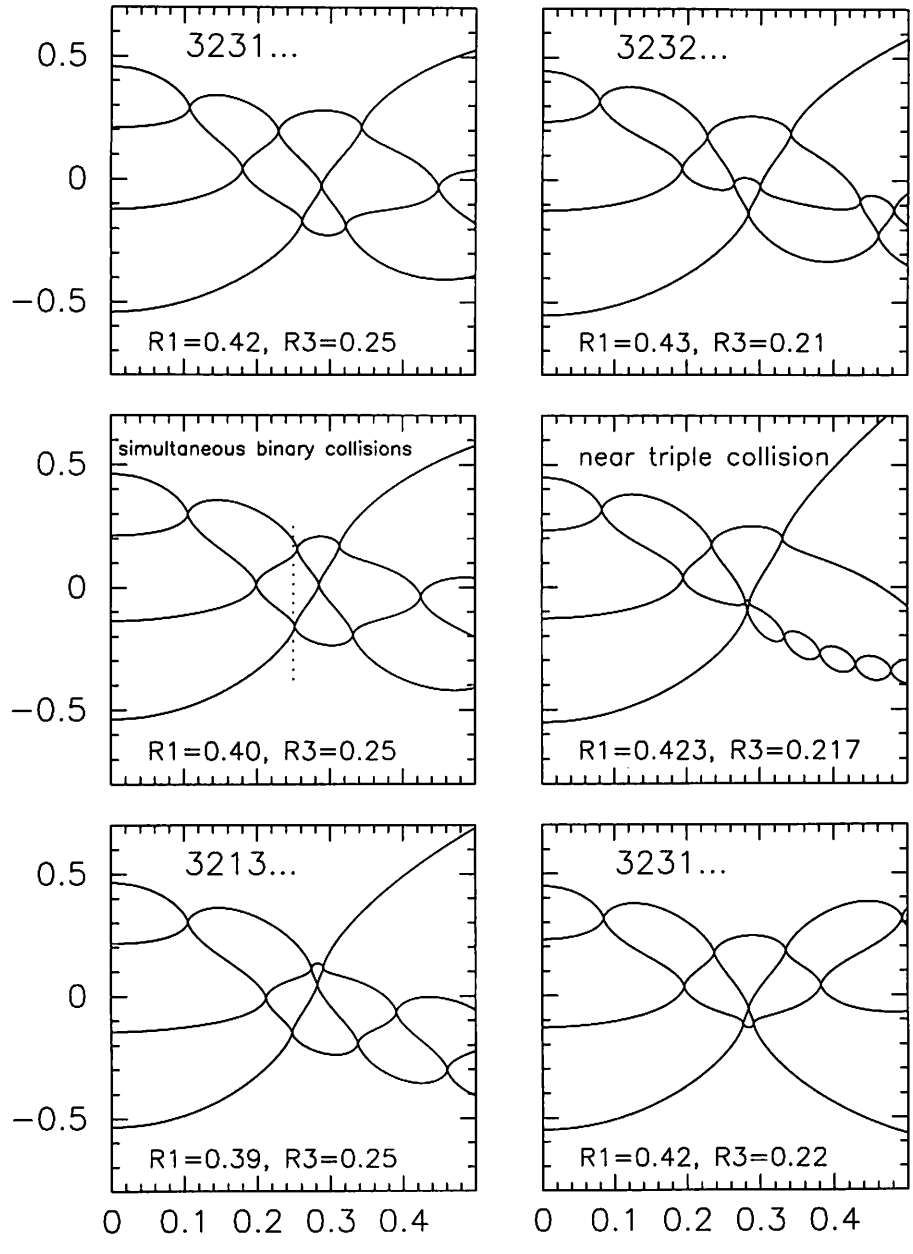

Figure 4: An orbit experiencing a simultaneous binary collision and the one experiencing a triple collision.

and 4 collide, the symbol '3' is concatenated. We can classify the orbits up to the same sequence of binary collisions.

A typical example of orbits is shown in Fig.2. The abscissa denotes the time and the ordinate denotes the x-coordinates of particles. Four curves represent the trajectories of particles, i.e., variations of the x-coordinate as a function of time. We enlarge the initial part of these trajectories in Fig.3. The figure shows how we construct symbol sequences from a given orbit. As is shown in the figure, the chronological order of binary collisions in this particular orbit is 3232123.... We write this as .3232123... and call this sequence of symbols '1', '2', and '3' the *future* symbol sequence of the orbit. The initial dot '.' indicates the present. Integrating an orbit backward in time, we could obtain the *past* symbol sequence $\ldots s_{-3}s_{-2}s_{-1}.$ for the orbit where s_i is one of 1, 2 and 3. Concatenating the past and future symbol sequences of an orbit, we would obtain the symbol sequences $\ldots s_{-3}s_{-2}s_{-1}.s_1s_2s_3\ldots$ of the orbit. In the present work, however, we only consider the future symbol sequences because the past symbol sequence is a mirror image of the future sequence due to the free-fall condition. We frequently omit the first 'period' in the sequence.

4 Collision Orbits in the Initial Value Space

There can be three types of multiple collision along an orbit: a simultaneous binary collision, a triple collision, and a quadruple collision. It is well known that a simultaneous binary collision is regularizable. We show in Fig.4 how simultaneous binary collision orbits and triple collision orbits are embedded in general orbits. The figures in the left three panels show the situation for the former. In the top panel, an orbit has symbol sequence 323.... This orbit experiences a binary collision between particles 3 and 4 at the third collision. In the bottom panel, an orbit has symbol sequence 321.... This orbit experiences a binary collision between particles 1 and 2 at the third collision. The middle panel shows an orbit with initial conditions on the midway between orbits of the top and bottom panels. the dotted vertical line in the figure shows that a collision between particles 3 and 4 and a collision between particles 1 and 2 occur simultaneously. These facts suggest that an orbit experiencing a simultaneous binary collision stays at a boundary of orbits which experience, respectively, a binary collision between 1 and 2 and the one between 3 and 4. This will be actually observed in the next section.

The figures in the right three panels of Fig.4 show the transition of the form of orbits through the state of triple collision. In the top panel, an orbit has symbol sequence 3232.... The orbit experiences a binary collision between particles 2 and 3 at the fourth binary collision. In the bottom panel, an orbit has symbol sequence 3231.... The orbit experiences a binary collision between particles 1 and 2 at the fourth binary collision. The middle panel shows an orbit with initial conditions on the midway between orbits of the top and bottom panels. This orbit is very close to the one which experiences a triple collision among particles 1, 2, and 3. This allows us an interpretation that between orbits experiencing binary collisions, respectively between 1 and 2

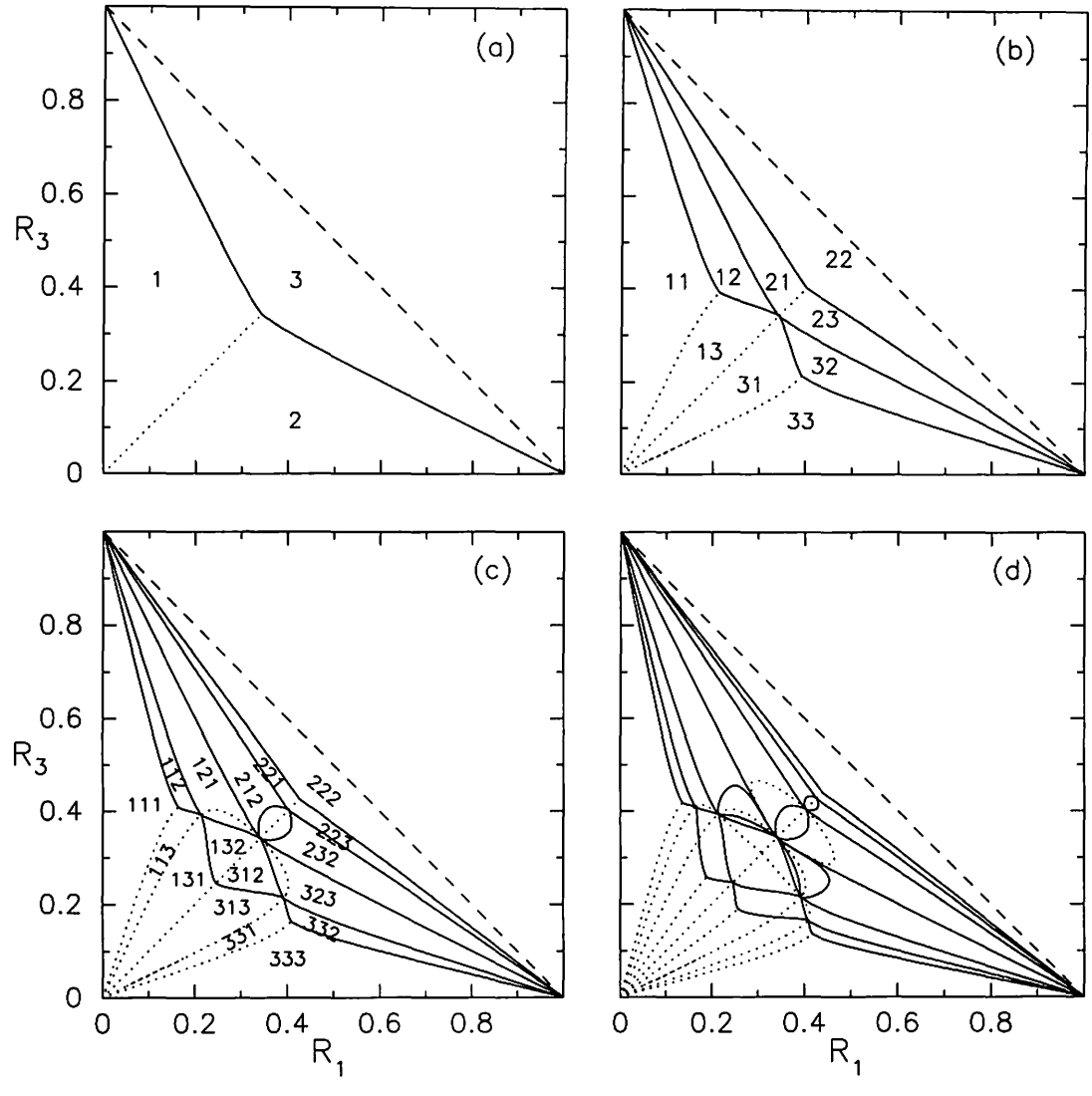

Figure 5: Quadruple-, triple-, and simultaneous binary-collisions. Solid curves are triple collision curves and dotted curves are simultaneous binary collision curves. Cross-points are quadruple collision points. Symbols sequences until length 4.

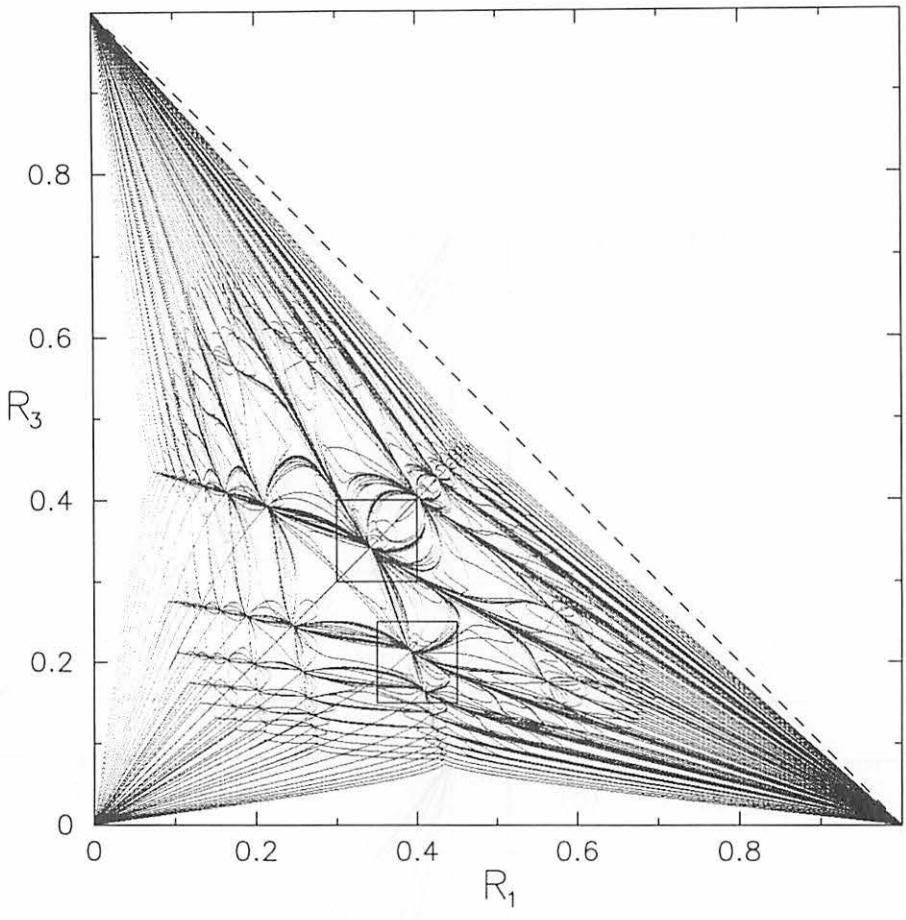

Figure 6: Collision curves arising from symbol sequences of length ≤ 10.

and between 2 and 3 sits an orbit which experiences a triple collision among 1, 2, and 3. This situation is similar to that in the one-dimensional three-body problem(Tanikawa & Mikkola, 2000a, b).

Now let us map symbol sequences on the initial value space. Figure 5 shows the evolution of the divisions of the initial value space with the length of symbol sequences. In Fig.5(a), the space is divided into three parts with the first symbols '1', '2', and '3' in symbol sequences. Boundaries of regions are initial conditions for orbits with multiple collisions. The dotted curve between '1' and '3' is the one for simultaneous binary collisions. Solid curves between '1' and '2' and between '2' and '3' are the ones for triple collisions. Finally, the crosspoint is the initial position of the orbit which ends in quadruple collision, the quadruple collision point in short. The figure tells us the following important facts to us. First, orbits experiencing a simultaneous binary collision form a curve on the initial value space. Second, orbits experiencing a triple collision form a curve on the initial value space. Third, an orbit experiencing a quadruple collision is found as a crosspoint of these three collision curves. It is to be noted that the quadruple collision point in the figure is not at the highest energy point in Fig.1.

Figure 5(b) shows the division of the initial value space by the regions with symbol sequences of length two. It is seen that each region in Fig.5(a)

is divided into three. We note three facts. First, all possible combinations of symbols appear for symbol sequences with length two. Second, there are additionally three quadruple collision points. This is related to the first fact. Third, simultaneous binary collision curves appear close to the origin. This is reasonable because if the distance between particle 2 and 3 are large, binary collisions between 1 and 2 and between 3 and 4 is apt to take place. We also note that additional collision curves pass through the quadruple collision point found in Fig.1(a).

Figure 5(c) shows the division of the initial value space by the regions with symbol sequences of length three. It is seen that now there are not all combinations of symbols. There are 23 symbol sequences. $3^3 = 27$ is the possible number of combinations. We do not have 122, 211, 233, and 322. Corresponding to this, the number of new quadruple collision points is three instead of five.

In Fig.5(d), we do not write symbol sequences because the structure is too fine.

Figure 6 shows the collision curves corresponding to symbol sequences of length ≤ 10. We observe an ever increasing complexity of the structure. There are areas where density of collision curves are high. In other words, the distribution of collision curves are not uniform. In the central area, collision curves fill the space slower than in other places. We see a sequence of quadruple collision points tending toward the boundary of the space.

We enlarge two areas in Figs.7 and 8. Figure 7 shows the enlargement of the upper box in Fig.6. Six figures represent the distribution of collision curves arising from symbol sequences of length $\leq 7, 8, 9, 10, 15$, and 20, respectively. In each figure, the central quadruple collision point is the one seen in Fig.5(a). Here we do not make a difference for diffirent collision curves. The number of collision curves increases very quickly. Also the number of collision curves emanating from the central quadruple collision point increases quickly. We see that a lot of collision curves pass through newly born quadruple collision points.

Figure 8 shows the enlargement of the lower box in Fig.6. The figure also shows that quadruple collision points for shorter symbol suqeunces dominate the local structure of the initial value space.

5 Escape and collision

There are three types of escape: 1) an escape of m_1, 2) an escape of m_4, and 3) an escape of two binaries $m_1 - m_2$ and $m_3 - m_4$. In the case 1), symbol '1' never appears in symbol sequences after some instant. In the case 2), symbol '3' never appears after some instant. Finally, in the case 3), symbol '2' never appears after some instant. Numerically escape is judged as follows. We take a fixed length of symbol sequences(e.g., 100). Let us consider the case 1). Symbol '1' necessarily appears, i.e., there is a collision between particles 1 and 2 at some instant since the initial velocities are zero. After the first appearance of symbol '1', if there exists $k < 100$ such that symbol '1' does not appear for

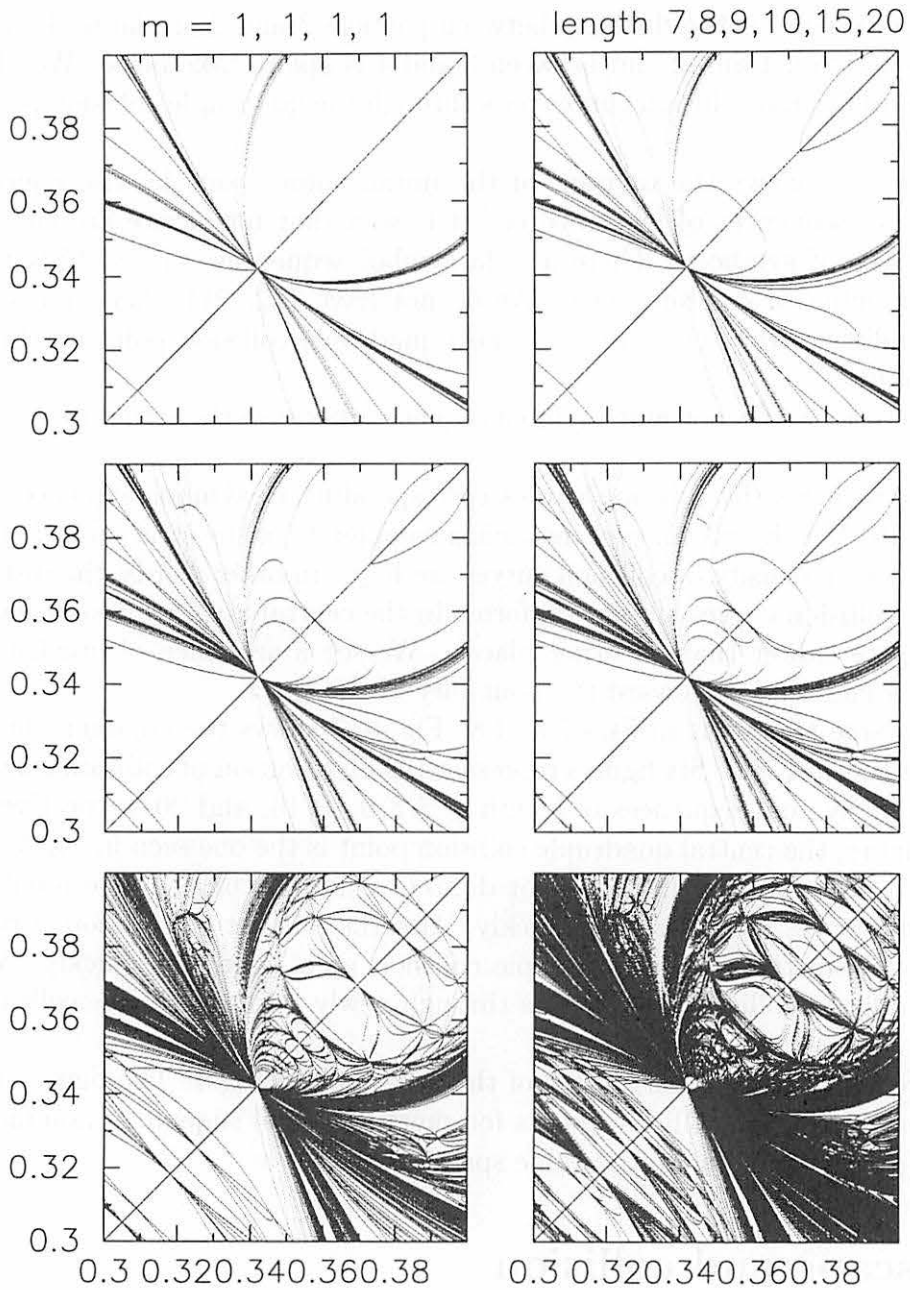

Figure 7: Enlargement of the upper box in Fig.6. Collision curves of symbol sequences of lengths 6,7,8,10,15,20.

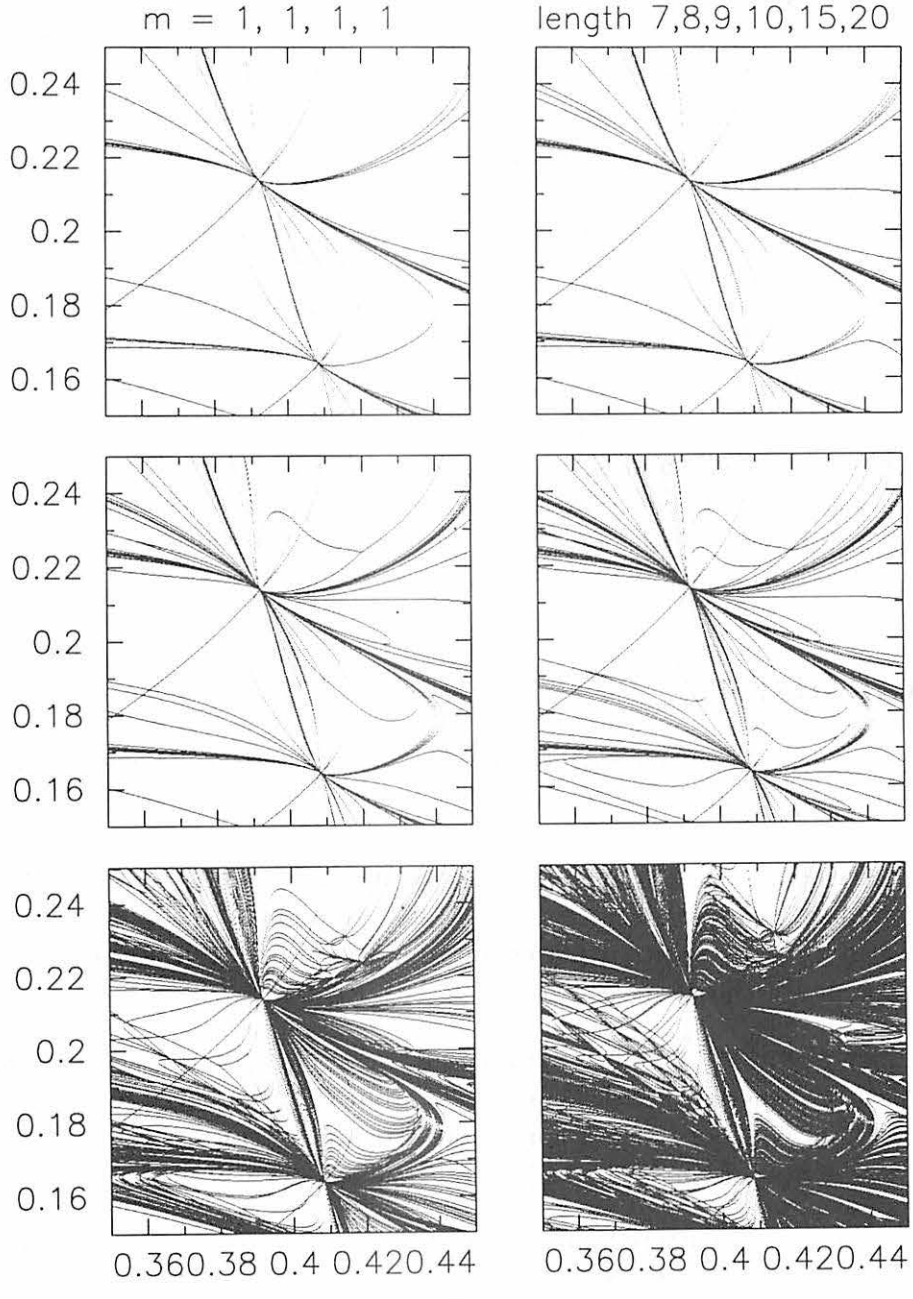

Figure 8: Enlargement of the lower box in Fig.6. Collision curves of symbol sequences of lengths 6,7,8,10,15,20.

the digit higher than or equal to k, then the particle 1 is judged to escape at length k. A long ejection orbit is not excluded by this procedure. However, we use this as an working criterion since escape orbits are obtained through this procedure.

In the one-dimensional three-body problem with initial non-zero velocities, there are large areas for escape orbits. Triple collision curves do not pass through the area. In other words, there remain large empty areas when we increase the length of symbol sequences and map the corresponding triple collision curves. In contrast to this, multiple collision curves rather uniformly fill the initial value space in our problem, i.e., escape orbits seems not globally localized.

In order to confirm this, we compare the distribution of escape orbits and collision curves. Figure 9 shows an example of correspondence between collision and escape. The left three panels show the collision curves coming from symbol sequence of length $\leq$ 2, 3, and 4 and the right three panels show the escape orbits at the fifth, sixth and seventh binary collisions. It is apparent that escape orbits are along triple collision curves and simultaneous binary collision is not responsible for escape. From this observation, we can say that orbits starting from empty space in Fig.6 escape late.

6 Conclusion

We obtain numerical evidence with respect to the dynamics of the one-dimensional free-fall four-body problem.

Orbits esperiencing a simultanenous binary collision form curves in the initial value space. The same is true for orbits experiencing a triple collision. Initial points for orbits experiencing quadruple collision is obtained as crosspoints of these curves(Fig.5).

The number of multiple collision curves increase rapidly with the length of symbol sequences taken into account. From the symmetry of the problem, triple collision curves correspond to finite orbits with respect to both direction of time. (Fig. 6).

Escape regions are scattered in various places. This resembles the one-dimensional free-fall three-body three-body problem. escape points distribute along collision curves(Fig.9).

Orbital behavior in the four-body problem is sensitive to the initial conditions.

References

[1] Bulirsch, R. and Stoer, J.: 1966, Numerical Treatment of Differential Equations by Extrapolation Methods, *Num. Math.*, **8**, 1–13.

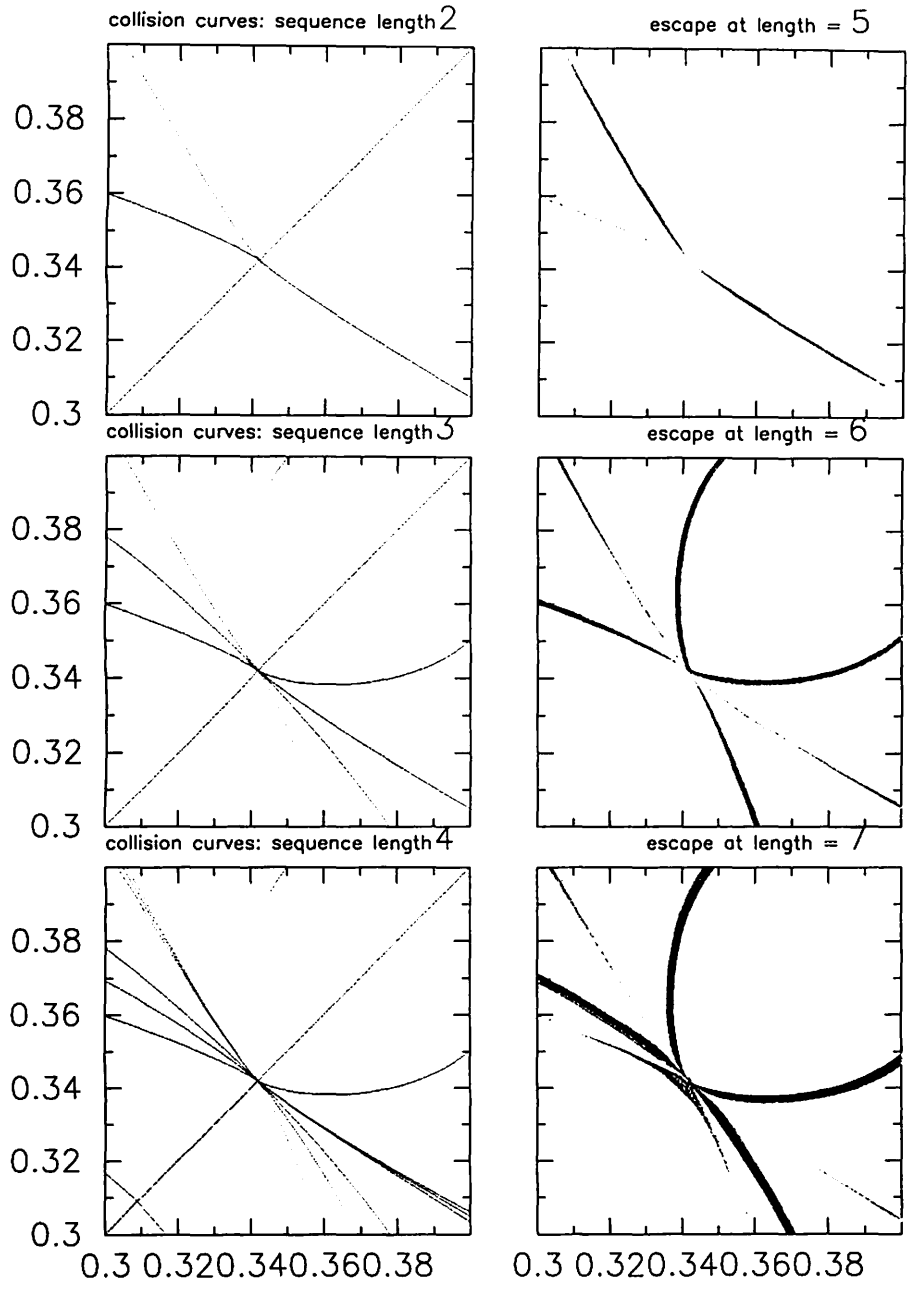

Figure 9: collision and escape. Collision curves of symbol sequences of lengths 2,3,4 and escape after length 5,6,7.

[2] Mather, J.N. and McGehee, R.: 1975, Solutions of the collinear four body problem which becomes unbounded in finite time, *Lecture Notes in Physics* **38**, 573-597.

[3] Lacomba, E.A. and Perez-Chavela, E.:(1992), A compact model for the planar rhomboidal 4-body problem, *Celest. Mech. & Dyn. Astr.* **54**, 343-355.

[4] Lacomba, E.A. and Perez-Chavela, E.:(1993), Motions close to escapes in the rhomboidal four-body problem, *Celest. Mech. & Dyn. Astr.* **57**, 411-437.

[5] Mikkola, S.: 1983, Encounters of binaries - I. Equal energies, *Mon. Not. R. astr. Soc.* **203**, 1107-1121.

[6] Mikkola, S.: 1984, Encounters of binaries - II. Unequal energies, *Mon. Not. R. astr. Soc.* **207**, 115-126.

[7] Mikkola, S. and Aarseth, S.: 1993, A chain regularization method for the few-body problem, *Celest. Mech. & Dyn. Astr.* **57**, 439-459.

[8] Sergysels, R. and Loks, A.: 1987, Restrictions on the motion in the general four-body problem, *Astron. & Astrophys.* **182**, 163-166.

[9] Tanikawa, K. and Mikkola, S.:(2000a), Triple collisions in one-dimensional three-body problem, *Celest. Mech. & Dyn. Astr.*(in press).

[10] Tanikawa, K. and Mikkola, S.:(2000b), One-dimensional three-body problem via symbolic dynamics, *Chaos*(in press).

[11] Vidal, C.:(1999), The tetrahedral 4-body problem with rotation, *Celest. Mech. & Dyn. Astr.* **71**, 15-33.

On Escape Orbits in the Symmetric Collinear Four-Body Problem

Masayoshi Sekiguchi,
Kisarazu National College of Technology,
E-mail : masa@yana.kisarazu.ac.jp
March 15, 2000

Abstract In this paper we study escape orbits in the symmetric collinear 4-body problem by using a set of McGehee-like variables which is universal for different energy levels, i.e., negative, zero and positive levels. This set of variables enables us to review the behavior of escape orbits easily.

1 Introduction

The symmetric collinear 4-body problem is a particular case of the general newtonian 4-body problem. There are two different pairs of equi-mass particles (two m_1's and two m_2's) collinearly and symmetrically with respect to the origin. They attract each other by newtonian gravitation law. We give them initial conditions such that they keep symmetric configurations through the motion. There occurs naturally a binary collision between m_1's or simultaneous binary collisions between m_1's and m_2's, but occasionally a quadruple collision. We continue solutions beyond binary collisions as many authors did. Therefore, particles in our system experience binary collisions many times. Some solutions remain in a bounded region of the configuration space or end up with a quadruple collision, but others become unbounded in the configuration space(hereafter referred to as "escape orbits").

We are interested in determining the initial conditions leading to escape and investigating their distribution. In this paper, we give a set of new variables which blows up infinity as well as collision singularity and compactifies the phase space. It also can be applied for different levels of energy. As a result, we easily obtain the overview of escape orbits.

2 Blowing-up Singularities and Compactification

We put four masses m_2, m_1, m_1, m_2 in this order collinearly with their coordinates $-q_2$, $-q_1$, q_1, q_2 and velocities $-\dot{q}_2$, $-\dot{q}_1$, $\dot{q}_1$, $\dot{q}_2$, respectively, where $0 < q_1 < q_2$. These initial conditions keep them symmetric with respect to the origin for all time. If the center of masses is fixed at the origin, this system has only two degrees of freedom. Thus, we obtain Lagrangian function of this system, i.e.,

$$L = m_1\dot{q}_1^2 + m_2\dot{q}_2^2 + U(q),$$

where

$$U(q) = \frac{m_1^2}{2q_1} + \frac{m_2^2}{2q_2} + \frac{2m_1m_2}{q_1+q_2} + \frac{2m_1m_2}{q_2-q_1}.$$

We blow up all singularities in this system with the aid of the McGehee's excellent idea. At first, we introduce an anisotropic polar-coordinate system (r, θ) where r^2 is a half of

the moment of inertia, i.e.,

$$r = \sqrt{m_1 q_1^2 + m_2 q_2^2}\ ,$$

$$q_1 = \frac{r}{\sqrt{m_1}} \cos\theta,$$

$$q_2 = \frac{r}{\sqrt{m_2}} \sin\theta.$$

Then we have the new Lagrangian function as follows.

$$L' = \dot{r}^2 + r^2\dot{\theta}^2 + \frac{V(\theta)}{r}\ .$$

If we assume $m_1 + m_2 = 1$, then we can set

$$\sqrt{m_1} = \cos\varphi,$$

$$\sqrt{m_2} = \sin\varphi,$$

where $\varphi \in (0, \frac{\pi}{2})$. We call φ "mass angle". Then we obtain an expression

$$V(\theta) = \frac{1}{2}\Big(\frac{\cos^5\varphi}{\cos\theta} + \frac{\sin^5\varphi}{\sin\theta} + \frac{\sin^3 2\varphi \cos\varphi \sin\theta}{\sin(\theta+\varphi)\sin(\theta-\varphi)}\Big)$$

Since $U(q)$ is defined on a region $\{(q_1, q_2) \mid 0 < q_1 < q_2\}$, $V(\theta)$ is defined on an open interval $(\varphi, \frac{\pi}{2})$. We derive a Hamiltonian function H from L', i.e.,

$$p_r \equiv \frac{\partial L'}{\partial \dot{r}} = 2\dot{r}$$

$$p_\theta \equiv \frac{\partial L'}{\partial \dot{\theta}} = 2r^2\dot{\theta}$$

$$H = \frac{1}{4}(p_r^2 + \frac{p_\theta^2}{r^2}) - \frac{V(\theta)}{r}$$

There are three types of collision in our system; quadruple collision when $r = 0$, binary collision when $\theta = \frac{\pi}{2}$ and simultaneously binary collisions when $\theta = \varphi$, where the potential function $U(q)$ becomes singular in these cases, as well as $\frac{V(\theta)}{r}$. The Hamiltonian equations also become singular at these points. We blow up these singularities by introducing new variables u_1, u_2 and s instead of p_r, p_θ and t, respectively, via the following definitions,

$$u_1 = \frac{p_r}{2}\sqrt{r\cos\theta\sin(\theta-\varphi)}$$

$$u_2 = \frac{p_\theta}{2}\sqrt{\frac{\cos\theta\sin(\theta-\varphi)}{r}}$$

$$ds = \frac{dt}{\sqrt{r\cos\theta\sin(\theta-\varphi)^3}}$$

Hence, one can see this transformation provides us with equations as follows,

$$\frac{dr}{ds} = r u_1 \cos\theta \sin(\theta-\varphi), \tag{1.1}$$

$$\frac{d\theta}{ds} = 2u_2 \cos\theta \sin(\theta - \varphi), \tag{1.2}$$

$$\frac{du_1}{ds} = (u_1^2 + 2u_2^2 - W(\theta)\cos\theta\sin(\theta - \varphi) + u_1 u_2 \cos(2\theta - \varphi), \tag{1.3}$$

$$\frac{du_2}{ds} = (\frac{dW(\theta)}{d\theta} - u_1 u_2)\cos\theta\sin(\theta - \varphi) + (u_2^2 - W(\theta))\cos(2\theta - \varphi). \tag{1.4}$$

This system of equations is non-singular, however, no longer constitutes any Hamiltonian system. We have a new energy relation induced from the Hamiltonian H, i.e.,

$$u_1^2 + u_2^2 - W(\theta) = hr\cos\theta\sin(\theta - \varphi), \tag{2}$$

where h is a value of energy and $W(\theta) \equiv V(\theta)\cos\theta\sin(\theta - \varphi)$. This equation (2) implies equi-energy manifolds when the value of energy h is fixed. One can define additional three manifolds by substituting $r = 0$ or $\theta = \varphi, \frac{\pi}{2}$ in (2). These are all invariant manifold. One can extend the system (1.1) to (1.4) to the boundary $r = 0$, $\theta = \varphi$ and $\theta = \frac{\pi}{2}$.

Let the phase space be bounded by introducing three new variables $\psi \in [0, \frac{\pi}{2})$, $\xi \in [0, \frac{\pi}{2})$ and $\eta \in S^1$ which satisfy the following equations,

$$r = \tan\psi,$$

$$u_1 = \tan\xi\cos\eta,$$

$$u_2 = \tan\xi\sin\eta.$$

If we change the independent variable "s" to "τ" with

$$d\tau = \frac{ds}{\sin\xi\cos\xi},$$

then we have a system of differential equations without any singularity, i.e.,

$$\frac{d\psi}{d\tau} = F\sin\psi\cos\psi\sin^2\xi\cos\eta, \tag{3.1}$$

$$\frac{d\theta}{d\tau} = 2F\sin^2\xi\sin\eta, \tag{3.2}$$

$$\frac{d\xi}{d\tau} = \sin\xi\cos\xi\Big[F\frac{dW(\theta)}{d\theta}\sin\eta\cos^2\xi + (F\cos\eta + G\sin\eta)(\sin^2\xi - W(\theta)\cos^2\xi)\Big], \tag{3.3}$$

$$\frac{d\eta}{d\tau} = \{\frac{dW(\theta)}{d\theta}F - W(\theta)G\}\cos\eta\cos^2\xi + (W(\theta)\cos^2\xi - 2\sin^2\xi)F\sin\eta, \tag{3.4}$$

where $F \equiv \cos\theta\sin(\theta - \varphi)$ and $G \equiv \cos(2\theta - \varphi)$. Similarly, (2) becomes

$$(\sin^2\xi - W(\theta)\cos^2\xi)\cos\psi = h\sin\psi\cos^2\xi\cos\theta\sin(\theta - \varphi). \tag{4}$$

Thereby, we can extend the domain of our system of differential equations (1.1) to (1.4) to the boundaries: $\psi = \frac{\pi}{2}$ and $\xi = \frac{\pi}{2}$. This enable us to paste two manifolds on the equi-energy manifold, which are defined by substituting $\psi = \frac{\pi}{2}$ or $\xi = \frac{\pi}{2}$ in (4). We call the former set 'inifinity manifold'(we do not name the latter set). These are also invariant manifold. Thus, we complete to compactificate the phase space.

Consequently, we obtain additional five manifolds paste on the original equi-energy manifold, where continuous flow exists. These flows on the pasted manifolds are fictitious but reflect real flow near the boundaries.

3 Discussion

In this section, we observe behaviors of variables of escape orbits where r goes to infinity or ψ tends to $\frac{\pi}{2}$. As we mentioned above, flows on the infinity manifold reflect real flow of escape orbits. Expression of the infinity manifold is

$$h\cos^2\xi\cos\theta\sin(\theta-\varphi)=0. \tag{5}$$

The flow is given by the system of equations (3.2) to (3.4). We omit (3.1) because $\psi=\frac{\pi}{2}$ is a constant of motion. Equation (5) indicates that the infinity manifold is a union of sets: $\{(\psi=\frac{\pi}{2})\wedge(\theta=\varphi,\frac{\pi}{2})\}$, $\{(\psi=\frac{\pi}{2})\wedge(\xi=\frac{\pi}{2})\}$ and $\{(\psi=\frac{\pi}{2})\wedge(h=0)\}$. We call them 'binary collision set', 'unbounded velocity set' and 'parabolic motion set', respectively. We divide our discussion into these three cases.

3.1 Binary collision set

When h is negative, velocity $\sqrt{u_1^2+u_2^2}$ remains bounded. This means $\xi<\frac{\pi}{2}$. Therefore, escape orbits necessarily approach to binary collision set. When h is not negative, escape orbits are not forbidden to get close to binary collision set.

3.2 Unbounded velocity set

Value of ξ is able to reach $\frac{\pi}{2}$ only if $h>0$. Substituting $\xi=\frac{\pi}{2}$ in (3.2) and (3.4) give us

$$\frac{d\theta}{d\tau}=2F\sin\eta, \tag{6.1}$$

$$\frac{d\eta}{d\tau}=-2F\sin\eta. \tag{6.2}$$

One of fixed points of this system is $\eta=0$ and θ arbitrary. $\eta=0$ leads to $p_\theta=0$ and $p_r\neq 0$. This implies that escape orbits keep their proportion of distances almost constant and increase their diameters to infinity. Their proportion is also arbitrary as well as θ.

Other fixed points are intersections with binary collision set, where η can take any value.

3.3 Parabolic motion set

Expression $h=0$ also indicates a special shell of the equi-energy manifold, which derives

$$\sin^2\xi-W(\theta)\cos^2\xi=0. \tag{7}$$

This relation between θ and ξ is fixed for every values of $\psi\in[0,\frac{\pi}{2})$. It should be kept at $\psi=\frac{\pi}{2}$ as well for continuity. Therefore, $\xi=\tan^{-1}\sqrt{W(\theta)}<\frac{\pi}{2}$ even if $\psi=\frac{\pi}{2}$. Using condition (7), we reduce the system (3.1) to (3.4).

$$\frac{d\psi}{d\tau}=W(\theta)F\cos^2\xi\sin\psi\cos\psi\cos\eta, \tag{8.1}$$

$$\frac{d\theta}{d\tau}=2W(\theta)F\cos^2\xi\sin\eta, \tag{8.2}$$

$$\frac{d\xi}{d\tau} = F\frac{dW(\theta)}{d\theta}\sin\xi\cos^3\xi\sin\eta, \tag{8.3}$$

$$\frac{d\eta}{d\tau} = \cos^2\xi\{(\frac{dW(\theta)}{d\theta}F - W(\theta)G)\cos\eta - W(\theta)F\sin\eta\}, \tag{8.4}$$

There are fixed points at $\psi = \frac{\pi}{2}$, which are $(\theta,\eta) = (\theta_0, 0)$ and $(\varphi, \pm\frac{\pi}{2})$, $(\frac{\pi}{2}, \pm\frac{\pi}{2})$. θ_0 is a value of θ when a solution is homothetic. Escape orbits become close to these fixed points.

Reference

1 McGehee,R.:1974,'Triple Collision in the Collinear Three-Body Problem', *Inventiones mathematicae*,**27**,191-227.

2 Devaney,R.L.:1980,'Triple Collision in the Planar Isosceles Three-Body Problem', *Inventiones mathematicae*,**60**,249-267.

3 Lacomba,E.A. and Simó,C.:1982,'Boundary Manifolds for Energy Surfaces in Celestial Mechanics',*Celestial Mechanics*,**28**,37-48.

4 Simó,C. and Lacomba,E.A.:1982,'Analysis of Some Degenerate Quadruple Collisions', *Celestial Mechanics*,**28**,49-62.

5 Lacomba,E.A. and Pérez-Chavela.E.:1992,'A Compact Model For the Rhomboidal 4-Body Problem',*Celestial Mechanics and Dynamical Astronomy*,**54**,343-355.

6 Lacomba,E.A. and Pérez-Chavela.E.:1993,'Motions Close To Escapes in the Rhomboidal Four Body Problem',*Celestial Mechanics and Dynamical Astronomy*,**57**,411-437.

運動量について4次の多項式第一積分を持つ2次元同次多項式ポテンシャル系

Polynomial first integrals of order 4 in the momenta for Hamiltonian systems with a 2D homogeneous polynomial potential

中川 克也（総研大／国立天文台）
Katsuya Nakagawa
e-mail:k.nakagawa@nao.ac.jp

概要：運動量について4次の多項式第一積分を持つ2次元同次多項式ポテンシャル系は，極座標・放物線座標・直交座標で変数分離可能な系，および既知の変数分離可能でない3つの系に限ることを示した．

Abstract. It is shown that if a Hamiltonian system with a 2D homogeneous polynomial potential admits polynomial first integrals of order 4 in the momenta, then the system must be one of
- separable ones (in polar, parabolic, and Cartesian coordinates), and
- three non-separable ones discovered in the 1980's.

1 はじめに ～ ハミルトン系の可積分性と第一積分 ～

微分方程式系において，任意の一般解に沿って値が一定になるような関数を系の**第一積分**という．ハミルトン系において自由度の数だけの独立な第一積分が存在するとき，運動方程式の解を求積的に求めることができる．このとき，系は**可積分**であるという．本研究では自由度2のハミルトン系

$$H = \frac{1}{2}(p_x^2 + p_y^2) + V(x, y) \tag{1}$$

の可積分性について考える．系 (1) の可積分性はポテンシャル $V(x, y)$ によって決まる．ポテンシャルとしてはどのような関数を考えてもよいが，ここでは特に同次多項式ポテンシャルを考える．

問題

ポテンシャルが具体的に与えられたときに，系が可積分か否かを判定せよ．もし可積分ならば，運動方程式の一般解またはハミルトニアンと独立な第一積分の表式を示せ．

この問題に答えてくれる万能の判定方法は未だない．最先端の非可積分性証明は，微分ガロア理論に基づく可積分性の必要条件による [6, 7, 10]．もし考えているポテンシャルがこの必要条件を満たさないことが分かれば，系は非可積分である．

一方，系の可積分性を証明するには，運動方程式を解いて一般解を求めるか，あるいはハミルトニアンと独立な第一積分を1個見つけるかすればよい．本稿では，第一積分を見つけるということに注目する．第一積分を求めるための一般的な方法は知られていないが，もし多項式で表される第一積分を考えているなら，次節で述べる方法を採用するのがよい．

2　多項式第一積分

本節の内容は基本的にレビュー論文 [2] に基づいている.

2.1　多項式第一積分に関する 2 つの仮定

多項式第一積分 Φ に対して一般性を失うことなく次のような性質を持つと仮定することができる.

性質 1　Φ は運動量 (p_x, p_y) について偶関数，または奇関数である.

性質 2　Φ は同次多項式ポテンシャルの次数によって決まる量をウエイトとする同次式である.

性質 1 は系 (1) の時間反転対称性から導かれる．系 (1) は，時間反転の変換

$$t \to -t,\ x \to x,\ y \to y,\ p_x \to -p_x,\ p_y \to -p_y$$

により不変である．系が第一積分 $\Phi(x, y, p_x, p_y)$ を持つとすると，系の時間反転不変性より $\Phi(x, y, -p_x, -p_y)$ も第一積分となる．したがって

$$\Phi^+ = \frac{1}{2}\{\Phi(x, y, p_x, p_y) + \Phi(x, y, -p_x, -p_y)\},\quad \Phi^- = \frac{1}{2}\{\Phi(x, y, p_x, p_y) - \Phi(x, y, -p_x, -p_y)\}$$

も，ともに第一積分である．ここで，任意の第一積分 Φ は $\Phi = \Phi^+ + \Phi^-$ と書けることに注意しよう．Φ^+ は (p_x, p_y) について偶関数の第一積分，Φ^- は (p_x, p_y) について奇関数の第一積分になっている．したがって，第一積分として最初から Φ^+ または Φ^- を考えてもよい．つまり，第一積分は運動量 (p_x, p_y) について偶関数か奇関数のどちらかであると仮定してもよい.

性質 2 は系 (1) のスケール変換に対する不変性から導かれる．一般に N 階の微分方程式系

$$\frac{dx_i}{dt} = F(x_1, x_2, \ldots, x_N),\quad (i = 1, 2, \ldots, N)$$

が，$g_1, g_2, \ldots, g_N$ を適当な定数とするスケール変換（相似変換）

$$t \to \alpha^{-1}t,\ x_1 \to \alpha^{g_1}x_1,\ x_2 \to \alpha^{g_2}x_2, \ldots, x_N \to \alpha^{g_N}x_N$$

によって不変であるとき，この系を**相似不変系**という．ここで，パラメーター α は任意である．また，相似変換によって α^M 倍される，つまり

$$\phi(\alpha^{-1}t, \alpha^{g_1}x_1, \ldots, \alpha^{g_N}x_N) = \alpha^M\phi(t, x_1, \ldots, x_N)$$

を満たす関数 $\phi(t, \boldsymbol{x})$ を M をウエイトとする**同次式**という.

いま，ある相似不変系が多項式第一積分 Φ を持つとする．この多項式第一積分を

$$\Phi = \sum_m \Phi_m$$

のような和に表す．ここで，Φ_m は m をウエイトとする同次多項式である．これにスケール変換を行なった

$$\Phi' = \sum_m \alpha^m \Phi_m$$

は再び元の系の第一積分になる．ここで，パラメーター α は任意であるから，結局すべての Φ_m が第一積分になっていることが分かる．したがって，相似不変系における多項式第一積分は相似変換によって決まる量をウエイトとする同次式であると仮定してもよい.

実際，ポテンシャルが k 次の同次多項式のとき，ハミルトン系 (1) はスケール変換

$$t \to \alpha^{-1}t, \quad x \to \alpha^{2/(k-2)}x, \quad y \to \alpha^{2/(k-2)}y, \quad p_x \to \alpha^{k/(k-2)}p_x, \quad p_y \to \alpha^{k/(k-2)}p_y \tag{2}$$

によって不変である．したがって，第一積分は同次多項式ポテンシャルの次数によって決まる量をウエイトとする同次式であると仮定してもよい．例えば，ハミルトニアンに対してスケール変換 (2) を行なうと

$$H \to \alpha^{2k/(k-2)}H$$

となる．これより，ハミルトニアンは $2k/(k-2)$ をウエイトとする同次式である．

2.2 多項式第一積分の求め方

多項式第一積分の性質 1 より，運動量について N 次の多項式第一積分は

$$\Phi = \sum_{n=0}^{[N/2]} \sum_{m=0}^{N-2n} A^{m,N-2n}(x,y)p_x^m p_y^{N-2n-m}$$

と書ける．ハミルトニアンとのポアソン括弧が 0 に等しいとおく．これを運動量 (p_x, p_y) についての恒等式とみて，$p_x^m p_y^{l-m}$ の係数が 0 に等しいとおくと

$$A_x^{m-1,l-1} + A_y^{m,l-1} = (m+1)A^{m+1,l+1}V_x + (l-m+1)A^{m,l+1}V_y \tag{3}$$

を得る．ただし，

$$m = 0,\ldots,l;\ l = N+1, N-1, N-3, \ldots, \begin{cases} 0 & (N \text{が奇数}) \\ 1 & (N \text{が偶数}) \end{cases}$$

で，$s<0, t<0, s>N$, または $t>N$ のときは $A^{s,t}=0$ とする．また，下付きの x, y は偏微分を表す．

$l = N+1$ に対して，(3) は

$$A_x^{m-1,N} + A_y^{m,N} = 0, \quad (m = 0,1,\ldots,N+1)$$

となる．これを解いて

$$A^{m,N}(x,y) = \sum_{v=0}^{m} \sum_{u=0}^{N-m} (-1)^v \binom{u+v}{v} a_{u+v,m-v} x^u y^v, \quad (m = 0,1,\ldots,N)$$

を得る．ここで，$a_{u+v,m-v}$ は積分定数である．多項式第一積分の性質 2 より，$N+1$ 個の多項式 $A^{m,N}$ は次数の等しい同次多項式でなければならない．したがって，問題は和 $u+v$ によってラベル付けされる $N+1$ 通りの場合に分けられる $(u+v = N, N-1, \ldots, 1, 0)$．各々の場合に，第一積分の運動量について N 次の項は次のような形になる．

$u+v$	第一積分の運動量について N 次の項
N	$a_{N,0}(yp_x - xp_y)^N$
$N-1$	$(a_{N-1,0}p_x + a_{N-1,1}p_y)(yp_x - xp_y)^{N-1}$
$N-2$	$(a_{N-2,0}p_x^2 + a_{N-2,1}p_xp_y + a_{N-2,2}p_y^2)(yp_x - xp_y)^{N-2}$
$\vdots$	$\vdots$
0	$a_{0,0}p_x^N + a_{0,1}p_x^{N-1}p_y + \cdots + a_{0,N}p_y^N = \sum_{j=0}^{N} a_{0,j}p_x^{N-j}p_y^j$

$A^{m,N}$ が $u+v$ 次の同次多項式であるとき，スケール変換 (2) に対する第一積分の運動量について N 次の項のウエイトは

$$(u+v)\frac{2}{k-2}+N\frac{k}{k-2}=\frac{2(u+v)+Nk}{k-2}$$

である．多項式第一積分の性質 2 より，第一積分の運動量について $N-2n$ 次の項のウエイトもこれに等しくなければならない．よって，同次多項式 $A^{m,N-2n}$ の次数は $u+v+nk$ となる．

$l=N-1$ に対して，(3) は

$$A_x^{m-1,N-2}+A_y^{m,N-2}=(m+1)A^{m+1,N}V_x+(N-m)A^{m,N}V_y,\quad (m=0,1,\ldots,N-1) \tag{4}$$

となる．(4) の $(m+1)$ 番目の式の両辺に偏微分演算子 $(-1)^m\partial^{N-1}/\partial x^{N-m-1}\partial y^m$ を作用させて，$m=0$ から $m=N-1$ までの和をとると，ポテンシャルについての偏微分方程式

$$\sum_{m=0}^{N-1}(-1)^m\frac{\partial^{N-1}}{\partial x^{N-m-1}\partial y^m}\left[(m+1)A^{m+1,N}V_x+(N-m)A^{m,N}V_y\right]=0$$

を得る．$l=N-3,N-5,\ldots$ に対しても，同様の操作によってポテンシャルについての偏微分方程式を導くことができる．これにより，N が奇数のときは $(N+1)/2$ 個，N が偶数のときは $N/2$ 個の偏微分方程式を得る．

さて，k 次の同次多項式ポテンシャルを

$$V(x,y)=V_k=\sum_{j=0}^{k}\alpha_j x^{k-j}y^j=\alpha_0x^k+\alpha_1x^{k-1}y+\cdots+\alpha_ky^k \tag{5}$$

とおく．これを上で得られた偏微分方程式に代入したものは，(x,y) についての恒等式にならなければならない．係数がすべて 0 に等しいとおくことにより，連立代数方程式が得られる．よって問題は，N が奇数のときは $(N+1)/2$ 組，N が偶数のときは $N/2$ 組の連立代数方程式を解くことに帰着する．

2.3 座標回転による自由度

可積分なポテンシャルを座標回転して得られるポテンシャルはまた可積分である．したがって，可積分なポテンシャルを座標回転することによって，見かけ上は異なる可積分なポテンシャルを無数に作ることができる．このようなポテンシャルは同一視しなければならない．そこで，適当な座標回転を考えることにより同次多項式ポテンシャル (5) の $x^{k-1}y$ の項を消去する．一般に，k 次の同次多項式ポテンシャルの場合，これを実現する座標回転の数は高々 k 個である．つまり，最初から $\alpha_1=0$ とすることによって，同一視すべきポテンシャルの数は高々 k 個になる．

3 既知のこと・未知のこと

現在のところ，前節で得られたポテンシャル $V(x,y)$ についての偏微分方程式が完全に解かれているのは $N=1,2$ のときだけである [2].

$N=1$ のとき

運動量について 1 次の多項式第一積分を持つ 2 次元同次多項式ポテンシャルは次の 2 つのポテンシャル，およびそれらを座標回転して得られるものに限る．

ポテンシャル	ハミルトニアンと独立な第一積分
$V_k = r^k = (x^2+y^2)^{k/2}$, k は偶数	$\Phi = yp_x - xp_y$
$V_k = x^k$	$\Phi = p_y$

$N=2$ のとき

運動量について 2 次の（必ずしも多項式でない）第一積分については，次の定理が知られている．

Bertrand-Darboux の定理（抜粋）([5])

自由度 2 のハミルトン系 (1)（ポテンシャルは任意の関数）が，ハミルトニアンと独立な運動量について 2 次の第一積分を持つための必要十分条件は，系が楕円座標・極座標・放物線座標・直交座標のいずれかで変数分離可能なことである．

運動量について 2 次の多項式第一積分を持つ 2 次元同次多項式ポテンシャルは下に示す 3 つのポテンシャル，およびそれらを座標回転して得られるものに限る．それぞれ，極座標，放物線座標，直交座標で変数分離可能となっている．上の Bertrand-Darboux の定理の楕円座標で変数分離可能な場合は，ポテンシャルが同次多項式であるという制限によって姿を消している．

ポテンシャル	ハミルトニアンと独立な第一積分
$V_k = r^k = (x^2+y^2)^{k/2}$, k は偶数	$\Phi = (yp_x - xp_y)^2$
$V_k = \dfrac{1}{r}\left[\left(\dfrac{r+x}{2}\right)^{k+1} + (-1)^k\left(\dfrac{r-x}{2}\right)^{k+1}\right]$	$\Phi = p_y(yp_x - xp_y) + \dfrac{1}{2}y^2V_{k-1}$
$V_k = Ax^k + By^k$	$\Phi = p_x^2 + 2Ax^k,\ p_y^2 + 2By^k$

ここでは，運動量について 2 次の多項式第一積分を持つ 2 次元同次多項式ポテンシャル系が，極座標，放物線座標，直交座標のいずれかで変数分離可能となること証明する．

証明　第一積分は運動量について偶関数と仮定できるから

$$\Phi = A_0(x,y)p_x^2 + A_1(x,y)p_xp_y + A_2(x,y)p_y^2 + B_0(x,y)$$

とおく．ハミルトニアンとのポアソン括弧の値が 0 になるための条件 (3) を書き下すと，

$$\begin{cases} A_{0x} = 0 \\ A_{0y} + A_{1x} = 0 \\ A_{1y} + A_{2x} = 0 \\ A_{2y} = 0 \end{cases} \tag{6}$$

$$\begin{cases} B_{0x} = 2A_0V_x + A_1V_y \\ B_{0y} = A_1V_x + 2A_2V_y \end{cases} \tag{7}$$

(6) から運動量について 2 次の項が決まり，場合分けは次の 3 通りになる．

(i) $\Phi = a_2(yp_x - xp_y)^2 + B_0(x,y)$

(ii) $\Phi = (a_1p_x + b_1p_y)(yp_x - xp_y) + B_0(x,y)$

(iii) $\Phi = a_0p_x^2 + b_0p_xp_y + c_0p_y^2 + B_0(x,y)$

(7) から得られる偏微分方程式は

$$A_1(V_{xx} - V_{yy}) + 2(A_2 - A_0)V_{xy} + (A_{1x} - 2A_{0y})V_x + (2A_{2x} - A_{1y})V_y = 0 \tag{8}$$

である．3 つの場合 (i), (ii), (iii) それぞれに対して，ポテンシャル (5) を (8) に代入して (x,y) についての恒等式を得る．ただし，$\alpha_1 = 0$ としておく．得られた恒等式から導かれる連立代数方程式が，(i) $a_2 \neq 0$, (ii) $(a_1,b_1) \neq (0,0)$, (iii) $(a_0,b_0,c_0) \neq (0,0,0)$ を満足する解を持つようにポテンシャルの係数 α_j を定めればよい．

場合 (i)　$a_2 \neq 0$ であるから，$a_2 = 1$ とする．偏微分方程式 (8) は

$$xy(V_{xx} - V_{yy}) - (x^2 - y^2)V_{xy} + 3yV_x - 3xV_y = 0$$

となる．これは

$$(x\partial_x + y\partial_y + 2)(yV_x - xV_y) = 0$$

と書け，更に同次式に関するオイラーの定理を用いることによって

$$(k+2)(yV_x - xV_y) = 0$$

となる．結局，

$$yV_x - xV_y = 0$$

を得る．これにポテンシャル (5) を代入して得られる連立代数方程式から，係数 α_j についての漸化式

$$\alpha_1 = \alpha_{k-1} = 0, \quad \alpha_{j+1} = \frac{k-j+1}{j+1}\alpha_{j-1}, \quad (j = 1,2,\ldots,k-1) \tag{9}$$

を得る．漸化式 (9) より，k が奇数のときは $\alpha_0 = \alpha_1 = \cdots = \alpha_k = 0$，つまりポテンシャルは恒等的に 0 となることが分かる．また，k が偶数のときは $\alpha_{2m+1} = 0$,

$$\alpha_{2m} = \frac{k-2m+2}{2m}\alpha_{2m-2} = \frac{k/2-m+1}{m}\alpha_{2m-2} = \frac{\binom{k/2}{m}}{\binom{k/2}{m-1}}\alpha_{2m-2}$$
$$= \frac{\binom{k/2}{m}}{\binom{k/2}{m-1}} \cdot \frac{\binom{k/2}{m-1}}{\binom{k/2}{m-2}}\alpha_{2m-4} = \cdots = \binom{k/2}{m}\alpha_0$$

と求められる．$\alpha_0 = 1$ とおいて，

$$V_k = \sum_{m=0}^{k}\binom{k/2}{m}x^{k-2m}y^{2m} = (x^2+y^2)^{k/2}$$

を得る．これは極座標 (r,θ) で変数分離可能である．ここで，

$$r = (x^2+y^2)^{1/2}, \quad \theta = \tan^{-1}\frac{y}{x}$$

である．また，第一積分は

$$\Phi = (yp_x - xp_y)^2$$

となるが，これは運動量について 1 次の第一積分 $\Phi = yp_x - xp_y$ を自乗したものであるから自明な第一積分である．

場合 (ii)　偏微分方程式 (8) は

$$a_1(xV_{xx} + 2yV_{xy} - xV_{yy} + 3V_x) + b_1(yV_{xx} - 2xV_{xy} - yV_{yy} - 3V_y) = 0$$

となる．ポテンシャル (5) を代入して漸化式

$$\begin{aligned}&\{(k-j+1)(k+j+1)\alpha_{j-1} - j(j+1)\alpha_{j+1}\}a_1\\ &+ \{j(2k-j+2)\alpha_j - (k-j+1)(k-j+2)\alpha_{j-2}\}b_1 = 0, \quad (j = 1,2,\dots,k)\end{aligned} \tag{10}$$

を得る．$j = 1,2$ を代入すると，

$$\begin{cases} \{k(k+2)\alpha_0 - 2\alpha_2\}a_1 = 0 \\ -6\alpha_3 a_1 + \{4k\alpha_2 - k(k-1)\alpha_0\}b_1 = 0 \end{cases} \tag{11}$$

$(a_1, b_1) \neq (0,0)$ だから，連立方程式 (11) の係数行列の行列式の値が 0，つまり

$$\alpha_2 = \frac{k-1}{4}\alpha_0, \quad \text{または} \quad \alpha_2 = \frac{k(k+2)}{2}\alpha_0$$

でなければならない．

• $\alpha_2 = (k-1)\alpha_0/4$ のとき，$\alpha_0 = 0$ と仮定すると，$\alpha_0 = \alpha_1 = \alpha_2 = 0$．このとき，$\alpha_0 = \alpha_1 = \cdots = \alpha_k = 0$ となることが次のようにして分かる．

いま，$\alpha_0 = \alpha_1 = \cdots = \alpha_j = 0$ になった仮定する．ただし，$j \geq 2$ である．このとき，漸化式 (10) で j に $j, j+1$ を代入すると

$$\begin{cases} -j(j+1)\alpha_{j+1}a_1 = 0 & (j \leq k) \\ -(j+1)(j+2)\alpha_{j+2}a_1 + (j+1)(2k-j+1)\alpha_{j+1}b_1 = 0 & (j \leq k-1) \end{cases}$$

$(a_1, b_1) \neq (0,0)$ だから，$\alpha_{j+1} = 0$ でなければならない．これより，帰納的に $\alpha_0 = \alpha_1 = \cdots = \alpha_k = 0$ となる．つまり，ポテンシャルが恒等的に 0 になってしまう．よって，$\alpha_0 \neq 0$ とする．すると，(11) の第 1 式から $a_1 = 0$ となる．$(a_1, b_1) \neq (0,0)$ だから，$b_1 \neq 0$ でなければならない．$b_1 = 1$ とすると，漸化式 (10) は

$$\alpha_j = \frac{(k-j+1)(k-j+2)}{j(2k-j+2)}\alpha_{j-2}, \quad (j = 2,3,\dots,k) \tag{12}$$

となる．$\alpha_1 = 0$ に注意すると，$\alpha_{2m+1} = 0$ となることが分かる．また，

$$\begin{aligned}\alpha_{2m} &= \frac{(k-2m+1)(k-2m+2)}{2m(2k-2m+2)}\alpha_{2m-2} = \frac{\binom{k-m}{m}}{2\binom{k-m+1}{m-1}}\alpha_{2m-2} \\ &= \frac{\binom{k-m}{m}}{2\binom{k-m+1}{m-1}} \cdot \frac{\binom{k-m+1}{m-1}}{2\binom{k-m+2}{m-2}}\alpha_{2m-4} = \cdots = 2^{-2m}\binom{k-m}{m}\alpha_0\end{aligned}$$

と求められる．$\alpha_0 = 1$ とおいて，

$$V_k = \sum_{m=0}^{[k/2]} 2^{-2m}\binom{k-m}{m}x^{k-2m}y^{2m} = \frac{1}{r}\left[\left(\frac{r+x}{2}\right)^{k+1} + (-1)^k\left(\frac{r-x}{2}\right)^{k+1}\right]$$

を得る．これは放物線座標 (ξ,η) で変数分離可能である．ここで，

$$\xi=\frac{r+x}{2},\quad \eta=\frac{r-x}{2}$$

である．また，第一積分は

$$\Phi=p_y(yp_x-xp_y)+\frac{1}{2}y^2V_{k-1}$$

である．

• $\alpha_2=k(k+2)\alpha_0/2$ のとき，$\alpha_0=0$ ならば上で見たようにポテンシャルが恒等的に 0 になってしまうので $\alpha_0\neq 0$ の場合を考える．$\alpha_0=1$ とおくと，(11) の第 2 式から

$$b_1=\frac{6\alpha_3}{k(k+1)(2k+1)}a_1.$$

したがって，第一積分は

$$\Phi=a_1\left(p_x+\frac{6\alpha_3}{k(k+1)(2k+1)}p_y\right)(yp_x-xp_y)+B_0(x,y)$$

となる．ここで，

$$a_1=\frac{k(k+1)(2k+1)}{\sqrt{k^2(k+1)^2(2k+1)^2+36\alpha_3^2}}$$

とおいて，座標回転

$$x\to x\cos\varphi-y\sin\varphi,\quad y\to x\sin\varphi+y\cos\varphi;\quad \tan\varphi=-\frac{k(k+1)(2k+1)}{6\alpha_3}$$

を行なうと，第一積分は

$$\Phi=p_y(yp_x-xp_y)+B_0(x,y)$$

という形になる．これは $a_1=0, b_1=1$ であることを示している．したがって，再び漸化式 (12) を得，ポテンシャルは放物線座標で変数分離可能となる．

場合 (iii)　第一積分 Φ から明らかな第一積分 $2c_0H$ を引くことにより $c_0=0$ とする．これにより，ハミルトニアン自身を除外できる．このとき，偏微分方程式 (8) は

$$2a_0V_{xy}+b_0(V_{xx}-V_{yy})=0$$

となる．ポテンシャル (5) を代入して漸化式

$$2j(k-j)\alpha_ja_0+\{j(j+1)\alpha_{j+1}-(k-j)(k-j+1)\alpha_{j-1}\}b_0=0,\quad (j=1,2,\dots,k-1)\tag{13}$$

を得る．$j=1,2$ を代入すると

$$\begin{cases}\{2\alpha_2-k(k-1)\alpha_0\}b_0=0\\ 4(k-2)\alpha_2a_0+6\alpha_3b_0=0\end{cases}\tag{14}$$

$(a_0,b_0)\neq(0,0)$ だから，

$$\alpha_2=0\quad\text{または}\quad \alpha_2=\frac{k(k-1)}{2}$$

でなければならない．

• $\alpha_2 = 0$ のとき，(14) の第 1 式から

$$-k(k-1)\alpha_0 b_0 = 0.$$

ここで，$b_0 \neq 0$ であると仮定すると，$\alpha_0 = 0$ となる．つまり，$\alpha_0 = \alpha_1 = \alpha_2 = 0$ である．このとき，漸化式 (13) から $\alpha_3 = \alpha_4 = \cdots = \alpha_k = 0$，つまり，ポテンシャルが恒等的に 0 になることが分かる．よって，$b_0 = 0$ とする．すると $(a_0, b_0) \neq (0,0)$ だから，$a_0 \neq 0$ でなければならない．$a_0 = 1$ とおくと，漸化式 (13) は

$$2j(k-j)\alpha_j = 0, \quad (j = 1, 2, \ldots, k-1) \tag{15}$$

となる．これより，$\alpha_1 = \alpha_2 = \cdots = \alpha_{k-1} = 0$ となり，ポテンシャルは

$$V_k = \alpha_0 x^k + \alpha_k y^k.$$

これは直交座標 (x, y) で変数分離可能である．また，第一積分は

$$\Phi = p_x^2 + 2\alpha_0 x^k, \quad \text{あるいは} \quad \Phi = p_y^2 + 2\alpha_k y^k$$

である．

• $\alpha_2 = k(k-1)\alpha_0/2$ のとき，$\alpha_0 = 0$ とすると，$\alpha_0 = \alpha_1 = \alpha_2 = 0$．このとき，$b_0 \neq 0$ ならば，上で見たようにポテンシャルは恒等的に 0 になってしまう．よって，$b_0 = 0$ とする．このとき，漸化式 (13) から $\alpha_1 = \alpha_2 = \cdots = \alpha_{k-1} = 0$ となることが分かるので，ポテンシャルは

$$V_k = y^k$$

である．ここで，$\alpha_k = 1$ とおいた．また，第一積分は

$$\Phi = p_x^2$$

となるが，これは運動量について 1 次の第一積分 $\Phi = p_x$ の自乗だから，自明な第一積分である．

次に，$\alpha_0 \neq 0$ とする．$\alpha_0 = 1$ とおくと (14) の第 2 式より，

$$a_0 = \frac{3\alpha_3}{k(k-1)(k-2)} b_0.$$

よって，第一積分は

$$\Phi = b_0 \left\{ -\frac{3\alpha_3}{k(k-1)(k-2)} p_x^2 + p_x p_y \right\} + B_0(x, y)$$

となる．ここで，

$$x \to x\cos\varphi - y\sin\varphi, \quad y \to x\sin\varphi + y\cos\varphi, \quad \tan 2\varphi = -\frac{k(k-1)(k-2)}{3\alpha_3}$$

で与えられる座標回転を行なうと，第一積分は

$$\Phi = a_0 p_x^2 + c_0 p_y^2 + B_0(x, y)$$

という形になる．これは，$b_0 = 0$ であることを示している．ここで，再び $\Phi - 2c_0 H$ を考えることにより，$c_0 = 0$ とする．これにより，再び漸化式 (15) を得，ポテンシャルは直交座標で変数分離可能となる． ∎

$N = 3, 4$ のとき

自明な例として，運動量について 1 次または 2 次の多項式第一積分の積によって作られる第一積分がある．これに対して，自明でない第一積分，つまり運動量についてより低次の多項式第一積分に帰着できない第一積分の例として，以下の 3 つのポテンシャルが運動量について 4 次の多項式第一積分を持つことが知られている．

$$\begin{cases} V_3 = x^3 + \dfrac{3}{16}xy^2 \\ \Phi = p_y^4 - \dfrac{1}{4}y^3 p_x p_y + \dfrac{3}{4}xy^2 p_y^2 - \dfrac{3}{64}x^2 y^4 - \dfrac{1}{128}y^6 \end{cases} \tag{16}$$

$$\begin{cases} V_3 = x^3 + \dfrac{1}{2}xy^2 + \dfrac{\sqrt{3}\,i}{18}y^3 \\ \Phi = p_x p_y^3 - \dfrac{\sqrt{3}i}{2}p_y^4 + \dfrac{1}{2}y^3 p_x^2 - \left(\dfrac{3}{2}xy^2 - \dfrac{\sqrt{3}i}{2}y^3\right)p_x p_y + \left(3x^2 y - \sqrt{3}ixy^2 + \dfrac{1}{2}y^3\right)p_y^2 \\ \qquad + \dfrac{1}{2}x^3 y^3 + \dfrac{\sqrt{3}i}{8}x^2 y^4 - \dfrac{1}{4}xy^5 + \dfrac{5i}{24\sqrt{3}}y^6 \end{cases} \tag{17}$$

$$\begin{cases} V_4 = x^4 + \dfrac{3}{4}x^2 y^2 + \dfrac{1}{8}y^4 \\ \Phi = p_y^4 + \dfrac{1}{2}y^4 p_x^2 + \left(3x^2 y^2 + \dfrac{1}{2}y^4\right)p_y^2 - 2xy^3 p_x p_y + \dfrac{1}{4}x^4 y^4 + \dfrac{1}{4}x^2 y^6 + \dfrac{1}{16}y^8 \end{cases} \tag{18}$$

これら 3 つのポテンシャルは，もともとは，特異点解析とよばれる手法によって発見されたものである [3, 4, 8]．特異点解析の詳細については [9] を参照のこと．更に，Hietarinta [1] によると同次多項式ポテンシャルの次数が 5 次以下の場合は，自明でない多項式第一積分を持つ例は (16), (17), (18) に限る．では，同次多項式ポテンシャルの次数を 6 以上にしたらどうなるか？これが本研究で扱う問題である．

$N \geq 5$ のとき

現在のところ，運動量について 5 次以上の自明でない多項式第一積分を持つ 2 次元同次多項式ポテンシャル系は知られていない．

4 運動量について 3 次の多項式第一積分 ($N = 3$)

第一積分は運動量について奇関数であると仮定してよいので，

$$\Phi = A_0(x,y)p_x^3 + A_1(x,y)p_x^2 p_y + A_2(x,y)p_x p_y^2 + A_3(x,y)p_y^3 + B_0(x,y)p_x + B_1(x,y)p_y$$

とおける．ハミルトニアンとのポアソン括弧の値が 0 になるための条件 (3) を書き下すと，

$$\begin{cases} A_{0x} = 0 \\ A_{0y} + A_{1x} = 0 \\ A_{1y} + A_{2x} = 0 \\ A_{2y} + A_{3x} = 0 \\ A_{3y} = 0 \end{cases} \tag{19}$$

$$\begin{cases} B_{0x} = 3A_0 V_x + A_1 V_y \\ B_{0y} + B_{1x} = 2A_1 V_x + 2A_2 V_y \\ B_{1y} = A_2 V_x + 3A_3 V_y \end{cases} \tag{20}$$

$$B_0V_x + B_1V_y = 0 \tag{21}$$

(19) から運動量について 3 次の項が決まり，場合分けは次の 4 通りになる．

(i) $\Phi = a_3(yp_x - xp_y)^3 + B_0p_x + B_1p_y$

(ii) $\Phi = (a_2p_x + b_2p_y)(yp_x - xp_y)^2 + B_0p_x + B_1p_y$

(iii) $\Phi = (a_1p_x^2 + b_1p_xp_y + c_1p_y^2)(yp_x - xp_y) + B_0p_x + B_1p_y$

(iv) $\Phi = a_0p_x^3 + b_0p_x^2p_y + c_0p_xp_y^2 + d_0p_y^3 + B_0p_x + B_1p_y$

(20) から得られる偏微分方程式は

$$\begin{aligned}&A_2V_{xxx} + (3A_3 - 2A_1)V_{xxy} + (3A_0 - 2A_2)V_{xyy} + A_1V_{yyy}\\ &+ 2(A_{2x} - A_{1y})(V_{xx} - V_{yy}) + 2(3A_{0y} - A_{1x} - A_{2y} + 3A_{3x})V_{xy}\\ &+ (3A_{0yy} - 2A_{1xy} + A_{2xx})V_x + (A_{1yy} - 2A_{2xy} + 3A_{3xx})V_y = 0.\end{aligned} \tag{22}$$

2 つの偏微分方程式 (22), (21) にポテンシャル (5) を代入したものを (x, y) についての恒等式とみる．2 つの恒等式において係数がすべて 0 に等しいとおくことによって得られる 2 組の連立代数方程式が，(i) $a_3 \neq 0$, (ii) $(a_2, b_2) \neq (0, 0)$, (iii) $(a_1, b_1, c_1) \neq (0, 0, 0)$, (iv) $(a_0, b_0, c_0, d_0) \neq (0, 0, 0, 0)$ となる解を持つようにポテンシャルの係数 α_j を定める．結果は次の表のようになる (証明は本論文（予定）を参照して下さい)．

場合	ポテンシャル	ハミルトニアンと独立な多項式第一積分
(i)	$V_k = (x^2 + y^2)^{k/2}$	$\Phi = (yp_x - xp_y)^3$
(ii)	解なし ($V_k \equiv 0$)	
(iii)	$V_k = (x^2 + y^2)^{k/2}$	$\Phi = (yp_x - xp_y)H$
(iv)	$V_k = x^k$	$\Phi = b_0p_y(p_x^2 + 2x^k) + d_0p_y^3$

上表の第一積分は，運動量について 1 次あるいは 2 次の多項式第一積分に帰着するので自明な第一積分である．

5 運動量について 4 次の多項式第一積分 ($N = 4$)

第一積分は運動量について偶関数と仮定してよいので，

$$\begin{aligned}\Phi = {} & A_0(x,y)p_x^4 + A_1(x,y)p_x^3p_y + A_2(x,y)p_x^2p_y^2 + A_3(x,y)p_xp_y^3 + A_4(x,y)p_y^4\\ & + B_0(x,y)p_x^2 + B_1(x,y)p_xp_y + B_2(x,y)p_y^2 + C_0(x,y)\end{aligned}$$

とおける．ハミルトニアンとのポアソン括弧の値が 0 になるための条件 (3) を書き下すと，

$$\begin{cases} A_{0x} = 0\\ A_{0y} + A_{1x} = 0\\ A_{1y} + A_{2x} = 0\\ A_{2y} + A_{3x} = 0\\ A_{3y} + A_{4x} = 0\\ A_{4y} = 0 \end{cases} \tag{23}$$

$$\begin{cases} B_{0x} = 3A_0V_x + A_1V_y \\ B_{0y} + B_{1x} = 3A_1V_x + 2A_2V_y \\ B_{1y} + B_{2x} = 2A_2V_x + 3A_3V_y \\ B_{2y} = A_3V_x + 4A_4V_y \end{cases} \tag{24}$$

$$\begin{cases} C_{0x} = 2B_0V_x + B_1V_y \\ C_{0y} = B_1V_x + 2B_2V_y \end{cases} \tag{25}$$

(23) から運動量について 4 次の項が決まり，場合分けは次の 5 通りになる．

(i) $\Phi = a_4(yp_x - xp_y)^4 + B_0p_x^2 + B_1p_xp_y + B_2p_y^2 + C_0$

(ii) $\Phi = (a_3p_x + b_3p_y)(yp_x - xp_y)^3 + B_0p_x^2 + B_1p_xp_y + B_2p_y^2 + C_0$

(iii) $\Phi = (a_2p_x^2 + b_2p_xp_y + c_2p_y^2)(yp_x - xp_y)^2 + B_0p_x^2 + B_1p_xp_y + B_2p_y^2 + C_0$

(iv) $\Phi = (a_1p_x^3 + b_1p_x^2p_y + c_1p_xp_y^2 + d_1p_y^3)(yp_x - xp_y) + B_0p_x^2 + B_1p_xp_y + B_2p_y^2 + C_0$

(v) $\Phi = a_0p_x^4 + b_0p_x^3p_y + c_0p_x^2p_y^2 + d_0p_xp_y^3 + e_0p_y^4 + B_0p_x^2 + B_1p_xp_y + B_2p_y^2 + C_0$

(24) から得られる偏微分方程式は

$$\begin{aligned} &A_3V_{xxxx} - 2(A_2 - 2A_4)V_{xxxy} + 3(A_1 - A_3)V_{xxyy} - 2(2A_0 - A_2)V_{xyyy} - A_1V_{yyyy} \\ &- (2A_{2y} - 3A_{3x})V_{xxx} + (6A_{1y} - 4A_{2x} - 3A_{3x} + 12A_{4x})V_{xxy} \\ &- (12A_{0y} - 3A_{1x} - 4A_{2y} + 6A_{3x})V_{xyy} - (3A_{1y} - 2A_{2x})V_{yyy} \\ &+ (3A_{1yy} - 4A_{2xy} + 3A_{3xx})(V_{xx} - V_{yy}) \\ &- (12A_{0yy} - 6A_{1xy} + 2A_{2xx} - 2A_{2yy} + 6A_{3xy} - 12A_{4xx})V_{xy} \\ &- (4A_{0yyy} - 3A_{1xyy} + 2A_{2xxy} - A_{3xxx})V_x \\ &- (A_{1yyy} - 2A_{2xyy} + 3A_{3xxy} - 4A_{4xxx})V_y = 0. \end{aligned} \tag{26}$$

また，(25) から得られる偏微分方程式は

$$B_1(V_{xx} - V_{yy}) + 2(B_2 - B_0)V_{xy} + (B_{1x} - 2B_{0y})V_x + (2B_{2x} - B_{1y})V_y = 0. \tag{27}$$

2 つの偏微分方程式 (26), (27) にポテンシャル (5) を代入したものを (x, y) についての恒等式とみる．2 つの恒等式において係数がすべて 0 に等しいとおくことによって得られる 2 組の連立代数方程式が，(i) $a_4 \neq 0$, (ii) $(a_3, b_3) \neq (0,0)$, (iii) $(a_2, b_2, c_2) \neq (0,0,0)$, (iv) $(a_1, b_1, c_1, d_1) \neq (0,0,0,0)$, (v) $(a_0, b_0, c_0, d_0, e_0) \neq (0,0,0,0,0)$ となる解を持つようにポテンシャルの係数 α_j を定める．結果は次の表のようになる．

場合	ポテンシャル	ハミルトニアンと独立な多項式第一積分
(i)	$V_k = (x^2 + y^2)^{k/2}$	$\Phi = (yp_x - xp_y)^4$
(ii)	解なし ($V_k \equiv 0$)	
(iii)	$V_k = (x^2 + y^2)^{k/2}$	$\Phi = (yp_x - xp_y)^2 H$
	$V_k = \frac{1}{r}\left[\left(\frac{r+x}{2}\right)^{k+1} + (-1)^k\left(\frac{r-x}{2}\right)^{k+1}\right]$	$\Phi = \left(p_y(yp_x - xp_y) + \frac{1}{2}y^2V_{k-1}\right)^2$
(iv)	$V_k = \frac{1}{r}\left[\left(\frac{r+x}{2}\right)^{k+1} + (-1)^k\left(\frac{r-x}{2}\right)^{k+1}\right]$	$\Phi = \left(p_y(yp_x - xp_y) + \frac{1}{2}y^2V_{k-1}\right) H$
(v)	$V_k = Ax^k + By^k$	$\Phi = a_0(p_x^2 + 2Ax^k)^2 + e_0(p_y^2 + 2By^k)^2$

上表の第一積分は，運動量について 1 次あるいは 2 次の多項式第一積分に帰着するので自明な第一積分である．ただし，第 3 節で述べたように $k=3,4$ の場合には自明でない第一積分を持つ例 (16), (17), (18) が知られている．Hietarinta [1] の研究によって，$k \leq 5$ の範囲ではこの 3 例以外には，自明でない運動量について 4 次の多項式第一積分を持つ例は存在しないことが分かっている．本研究の主結果は，$k \geq 6$ としても新しい例は出てこないことを証明したことである．3 つの例 (16), (17), (18) は，すべて場合 (v) に属している．以下の Appendix で，この場合 (v) の証明を述べる．

以上の結果より，次の定理を得る．

定理

運動量について高々 4 次の多項式第一積分を持つ 2 次元同次多項式ポテンシャル系は，極座標・放物線座標・直交座標のいずれかで変数分離可能な系と以下に挙げる既知の変数分離可能でない系に限る．

$$V_3 = x^3 + \frac{3}{16}xy^2, \quad V_3 = x^3 + \frac{1}{2}xy^2 + \frac{\sqrt{3}\,i}{18}y^3, \quad V_4 = x^4 + \frac{3}{4}x^2y^2 + \frac{1}{8}y^4$$

Appendix

$N=4$：場合 (v)：自明でない第一積分の非存在証明

ここでは，運動量について 4 次の多項式第一積分の場合 (v) において，$k \geq 6$ ならば，ポテンシャルは直交座標で変数分離可能なものに限ることを証明する．

証明　第一積分は

$$\Phi = a_0p_x^4 + b_0p_x^3p_y + c_0p_x^2p_y^2 + d_0p_xp_y^3 + e_0p_y^4 + B_0p_x^2 + B_1p_xp_y + B_2p_y^2 + C_0.$$

自明な第一積分であるハミルトニアンの自乗を除外するために Φ の代わりに $\Phi - 2c_0H^2$ を考える．これにより，最初から $c_0 = 0$ となる．このとき，偏微分方程式 (26) は

$$4a_0V_{xyyy} - b_0(3V_{xxyy} - V_{yyyy}) - d_0(V_{xxxx} - 3V_{xxyy}) - 4e_0V_{xxxy} = 0 \tag{28}$$

となる．ポテンシャル (5) を代入すると漸化式

$$\begin{aligned}
&4(j-1)j(j+1)(k-j-1)\alpha_{j+1}a_0 \\
&+ j(j-1)\{(j+1)(j+2)\alpha_{j+2} - 3(k-j)(k-j-1)\alpha_j\}b_0 \\
&+ (k-j)(k-j-1)\{3j(j-1)\alpha_j - (k-j+1)(k-j+2)\alpha_{j-2}\}d_0 \\
&- 4(j-1)(k-j-1)(k-j)(k-j+1)\alpha_{j-1}e_0 = 0, \quad (j = 2, 3, \ldots, k-2)
\end{aligned} \tag{29}$$

が得られる．一方，偏微分方程式 (27) から得られる恒等式において，x^{2k-2}, $x^{2k-3}y$, $x^{2k-4}y^2$, $x^{2k-5}y^3$ の係数がそれぞれ 0 に等しいとおいた式から

$$\begin{cases}
M_{11}b_0 = 0 \\
M_{21}b_0 + M_{22}a_0 = 0 \\
M_{31}b_0 + M_{32}a_0 + M_{33}d_0 = 0 \\
M_{41}b_0 + M_{42}a_0 + M_{43}d_0 + M_{44}e_0 = 0
\end{cases} \tag{30}$$

を得る．ここで，

$$M_{11}=\frac{\{k(k-1)\alpha_0-2\alpha_2\}\{3k(2k-1)\alpha_0-2\alpha_2\}}{k(k-1)},$$

$$M_{21}=\frac{-6(7k-6)\alpha_0\alpha_3}{k-2}+\frac{12(7k-6)\alpha_2\alpha_3}{k(k-1)(k-2)},\quad M_{22}=-\frac{16(3k-2)\{k(k-1)\alpha_0-2\alpha_2\}\alpha_2}{k(k-1)},$$

$$M_{31}=6(k-1)(2k-3)\alpha_0\alpha_2-\frac{2(17k^2-28k+6)\alpha_2^2}{k(k-1)}+\frac{18(7k-6)\alpha_3^2}{k(k-1)(k-2)}$$
$$-\frac{12(7k^2-22k+18)\alpha_0\alpha_4}{(k-2)(k-3)}+\frac{48(2k^2-4k+3)\alpha_2\alpha_4}{k(k-1)(k-2)(k-3)},$$

$$M_{32}=\frac{-12(2k-3)(3k-4)\alpha_0\alpha_3}{k-2}+\frac{24(2k-3)(5k-4)\alpha_2\alpha_3}{k(k-1)(k-2)},\quad M_{33}=4k(2k-3)\alpha_0\alpha_2,$$

$$M_{41}=6(k-2)(2k-3)\alpha_0\alpha_3-\frac{4(29k^2-44k+6)\alpha_2\alpha_3}{k(k-1)}+\frac{48(7k-12)\alpha_3\alpha_4}{k(k-2)(k-3)}$$
$$-\frac{20(7k^2-31k+36)\alpha_0\alpha_5}{(k-3)(k-4)}+\frac{40(5k^2-11k+12)\alpha_2\alpha_5}{k(k-1)(k-3)(k-4)},$$

$$M_{42}=\frac{-16(k-2)(3k-4)\alpha_2^2}{k-1}+\frac{144\alpha_3^2}{k-2}-\frac{96(k-2)^2\alpha_0\alpha_4}{k-3}+\frac{384(k-2)\alpha_2\alpha_4}{k(k-3)},$$

$$M_{43}=12k(k-2)\alpha_0\alpha_3,\quad M_{44}=32(k-2)\alpha_2^2$$

である．ただし，$k\geq 5$ である．$(a_0,b_0,d_0,e_0)\neq(0,0,0,0)$ であるから，$M_{11}M_{22}M_{33}M_{44}=0$ でなければならない．すなわち，

$$\alpha_0=0,\quad \alpha_2=0,\quad \alpha_2=\frac{k(k-1)}{2}\alpha_0,\quad \text{または}\quad \alpha_2=\frac{3k(2k-1)}{2}\alpha_0$$

である．

• $\alpha_0=0$ のとき，$\alpha_2=\alpha_3=\cdots=\alpha_{k-1}=0$ となることが次のようにして分かる．

(30) の第 1, 2 式から

$$\begin{cases}\dfrac{4\alpha_2^2}{k(k-1)}b_0=0\\ \dfrac{12(7k-6)\alpha_2\alpha_3}{k(k-1)(k-2)}b_0+\dfrac{32(3k-2)\alpha_2^2}{k(k-1)}a_0=0\end{cases}$$

ここで，$\alpha_2\neq 0$ と仮定すると，上の 2 式から $b_0=a_0=0$ となる．このとき，漸化式 (29) で $j=2,3$ を代入すると

$$\begin{cases}6(k-2)(k-3)\alpha_2d_0=0,.\\ 18(k-3)(k-4)\alpha_3d_0-8(k-2)(k-3)(k-4)\alpha_2e_0=0\end{cases}$$

これより，$\alpha_2\neq 0$ ならば $d_0=e_0=0$ である．よって，$\alpha_2=0$ でなければならない．

(30) の第 3 式から

$$\frac{18(7k-6)\alpha_3^2}{k(k-1)(k-2)}b_0=0.$$

ここで，$\alpha_3\neq 0$ と仮定すると，上式から $b_0=0$ となる．このとき，漸化式 (29) で $j=2,3,4$ を代入すると

$$\begin{cases}24(k-3)\alpha_3a_0=0\\ 96(k-4)\alpha_4a_0+18(k-3)(k-4)\alpha_3d_0=0\\ 240(k-5)\alpha_5a_0+36(k-4)(k-5)\alpha_4d_0-12(k-3)(k-4)(k-5)\alpha_3e_0=0.\end{cases}$$

これより，$\alpha_3 \neq 0$ ならば $a_0 = d_0 = e_0 = 0$ である．よって，$\alpha_3 = 0$ でなければならない．

いま，$\alpha_0 = \alpha_1 = \cdots = \alpha_j = 0$ になったと仮定する．ただし，$j \geq 3$ である．このとき，漸化式 (29) で j に $j-1, j, j+1, j+2$ を代入すると

$$
\begin{cases}
(j-2)(j-1)j(j+1)\alpha_{j+1}b_0 = 0, \\
4(j-1)j(j+1)(k-j+1)\alpha_{j+1}a_0 + (j-1)j(j+1)(j+2)\alpha_{j+2}b_0 = 0, \\
4j(j+1)(j+2)(k-j)\alpha_{j+2}a_0 \\
\quad + j(j+1)\{(j+2)(j+3)\alpha_{j+3} - 3(k-j-1)(k-j-2)\alpha_{j+1}\}b_0 \\
\quad + 3j(j+1)(k-j-1)(k-j-2)\alpha_{j+1}d_0 = 0 \quad (j \leq k-3) \\
4(j+1)(j+2)(j+3)(k-j-1)\alpha_{j+3}a_0 \\
\quad + (j+1)(j+2)\{(j+3)(j+4)\alpha_{j+4} - 3(k-j-2)(k-j-3)\alpha_{j+2}\}b_0 \\
\quad + 3(j+1)(j+2)(k-j-2)(k-j-3)\alpha_{j+2}d_0 \\
\quad - 4(j+1)(k-j-3)(k-j-2)(k-j-1)\alpha_{j+1}e_0 = 0 \quad (j \leq k-4)
\end{cases}
\tag{31}
$$

ここで，$\alpha_{j+1} \neq 0$ と仮定すると，$b_0 = a_0 = d_0 = e_0 = 0$ となってしまう．よって，$\alpha_{j+1} = 0$ でなければならない．ただし，$j \leq k-4$ である．ここまでで，$\alpha_0 = \alpha_1 = \cdots = \alpha_{k-3} = 0$ が示された．

$\alpha_{k-2} \neq 0$ と仮定すると，(31) より $b_0 = a_0 = d_0 = 0$ となる．このとき，偏微分方程式 (27) から得られる恒等式において，x^3y^{2k-5} の係数が 0 に等しいとおいた式から

$$
\frac{16(k-2)(3k-4)\alpha_{k-2}^2}{k-1}e_0 = 0.
$$

これより，$\alpha_{k-2} \neq 0$ ならば $e_0 = 0$ である．よって，$\alpha_{k-2} = 0$ でなければならない．

$\alpha_{k-1} \neq 0$ と仮定すると，(31) より $b_0 = a_0 = 0$ となる．このとき，偏微分方程式 (27) から得られる恒等式において，x^2y^{2k-4}, xy^{2k-3} の係数が 0 に等しいとおいた式から

$$
\begin{cases}
-3(k-1)(2k-3)\alpha_{k-1}^2 d_0 = 0 \\
-6(k-1)(2k-1)\alpha_{k-1}\alpha_k d_0 + \dfrac{8(k-1)(3k-1)\alpha_{k-1}^2}{k}e_0 = 0
\end{cases}
$$

これより，$\alpha_{k-1} \neq 0$ ならば $d_0 = e_0 = 0$ である．よって，$\alpha_{k-1} = 0$ でなければならない．以上で，$\alpha_0 = \alpha_1 = \cdots = \alpha_{k-1} = 0$ が示された．
さて，このとき偏微分方程式 (27) から得られる恒等式において，x^2y^{2k-4}, y^{2k-2} の係数が 0 に等しいとおいた式から

$$
\begin{cases}
\dfrac{1}{2}k^2(k-1)(2k-3)\alpha_k^2 b_0 = 0 \\
-3k(2k-1)\alpha_k^2 d_0 = 0
\end{cases}
$$

これより，$\alpha_k \neq 0$, $b_0 = d_0 = 0$ とすればよいことが分かる．$\alpha_k = 1$ とおいて，ポテンシャル

$$
V_k = y^k
$$

を得る．また，第一積分は

$$
\Phi = a_0 p_x^4 + e_0(p_y^2 + 2y^k)^2.
$$

しかし，これは運動量について 1 次の第一積分 $\Phi = p_x$ と運動量について 2 次の第一積分 $\Phi = p_y^2 + 2y^k$ に帰着するので自明な第一積分である．

• $\alpha_2 = 0$ のとき，もし $\alpha_0 = 0$ ならば上の場合に帰着する．よって，$\alpha_0 \neq 0$ の場合を考える．$\alpha_0 = 1$ と固定すると，(30) の第 1, 2, 3 式から

$$\begin{cases} 3k(2k-1)b_0 = 0 \\ -\dfrac{6(7k-6)\alpha_3}{k-2}b_0 = 0 \\ -\dfrac{12(2k-3)(3k-4)\alpha_3}{k-2}a_0 + \left\{ \dfrac{18(7k-6)\alpha_3^2}{k(k-1)(k-2)} - \dfrac{12(7k^2-22k+18)\alpha_4}{(k-2)(k-3)} \right\} b_0 = 0 \end{cases}$$

これより，$b_0 = 0, \alpha_3 a_0 = 0$ となることが分かる．また，漸化式 (29) に $j = 2$ を代入すると

$$24(k-3)\alpha_3 a_0 - k(k-1)(k-2)(k-3)d_0 = 0.$$

$\alpha_3 a_0 = 0$ であるから，$d_0 = 0$ となる．このとき，$\alpha_1 = \alpha_2 = \cdots = \alpha_{k-1} = 0$ であることが次のようにして分かる．

いま，$\alpha_1 = \alpha_2 = \cdots = \alpha_j = 0$ になったと仮定する．ただし，$j \geq 2$ である．このとき，漸化式 (29) で j に $j, j+2$ を代入すると

$$\begin{cases} 4(j-1)j(j+1)(k-j+1)\alpha_{j+1}a_0 = 0 \\ 4(j+1)(j+2)(j+3)(k-j-1)\alpha_{j+3} - 4(j+1)(k-j-3)(k-j-2)(k-j-1)\alpha_{j+1}e_0 = 0 \end{cases}$$

$(a_0, e_0) \neq (0,0)$ であるから，$\alpha_{j+1} = 0$ でなければならない．ただし，$j \leq k-4$ である．ここまでで，$\alpha_1 = \alpha_2 = \cdots = \alpha_{k-3} = 0$ が示された．

漸化式 (29) に $j = k-3$ を代入すると

$$16(k-4)(k-3)(k-2)\alpha_{k-2}a_0 = 0.$$

ここで，$\alpha_{k-2} \neq 0$ と仮定すると $a_0 = 0$ となる．このとき，偏微分方程式 (27) から得られる恒等式において，$x^{k-1}y^{k-1}$ の係数が 0 に等しいとおいた式から

$$-\frac{8k(k+2)\alpha_{k-2}}{k-1}e_0 = 0.$$

これより，$\alpha_{k-2} \neq 0$ ならば $e_0 = 0$ である．よって，$\alpha_{k-2} = 0$ でなければならない．

漸化式 (29) に $j = k-2$ を代入すると

$$12(k-3)(k-2)(k-1)\alpha_{k-1}a_0 = 0.$$

ここで，$\alpha_{k-1} \neq 0$ と仮定すると $a_0 = 0$ となる．このとき，偏微分方程式 (27) から得られる恒等式において，$x^{k-2}y^k$ の係数が 0 に等しいとおいた式から

$$-4(k-1)\alpha_{k-1}e_0 = 0.$$

これより，$\alpha_{k-1} \neq 0$ ならば $e_0 = 0$ である．よって，$\alpha_{k-1} = 0$ でなければならない．以上で，$\alpha_1 = \alpha_2 = \cdots = \alpha_{k-1} = 0$ が示された．したがって，ポテンシャルは

$$V_k = x^k + \alpha_k y^k$$

となる．また，第一積分は

$$\Phi = a_0(p_x^2 + 2x^k)^2 + e_0(p_y^2 + 2\alpha_k y^k)^2$$

これは，運動量について 2 次の第一積分 $\Phi = p_x^2 + 2x^k$ と $\Phi = p_y^2 + 2\alpha_k y^k$ に帰着するので自明な第一積分である．

• $\alpha_2 = k(k-1)\alpha_0/2$ のとき，もし $\alpha_0 = 0$ ならば上の場合に帰着する．よって，$\alpha_0 \neq 0$ の場合を考える．$\alpha_0 = 1$ と固定すると，(30) の第 3, 4 式から順に

$$d_0 = -\frac{12\alpha_3}{k(k-1)(k-2)}a_0 + \left\{\frac{5k^2+2k-12}{4k(2k-3)} - \frac{9(7k-6)\alpha_3^2}{k^3(k-1)^2(k-2)(2k-3)} + \frac{6(3k^2-14k+12)\alpha_3^2}{k^2(k-1)(k-2)(k-3)(2k-3)}\right\}b_0,$$

$$e_0 = \left\{\frac{3k-4}{8(k-1)} - \frac{18\alpha_3^2}{k^2(k-1)^3(k-2)^2} - \frac{12\alpha_4}{k(k-1)^2(k-3)}\right\}a_0 + \left\{\frac{(77k^2-206k+138)\alpha_3}{8k(k-1)^2(k-2)(2k-3)} + \frac{27(7k-6)\alpha_3^2}{2k^4(k-1)^4(k-2)(2k-3)} - \frac{3(37k^3-178k^2+282k-144)\alpha_3\alpha_4}{k^3(k-1)^3(k-2)^2(k-3)(2k-3)} + \frac{5(k^2-10k+12)\alpha_5}{k^2(k-1)^2(k-2)(k-3)(k-4)}\right\}b_0$$

を得る．このとき，漸化式 (29) から

$$\alpha_4 = \frac{(k-3)\{k^2(k-1)^2(k-2)^2+36\alpha_3^2\}}{24k(k-1)(k-2)},\quad \alpha_5 = \frac{(k-3)(k-4)\{k^2(k-1)^2(k-2)^2+18\alpha_3^2\}\alpha_3}{10k^2(k-1)^2(k-2)^2}.$$

これにより，d_0, e_0 は

$$d_0 = -\frac{12\alpha_3}{k(k-1)(k-2)}a_0 + \frac{k^2(k-1)^2(k-2)^2-18\alpha_3^2}{k^2(k-1)^2(k-2)^2}b_0,$$

$$e_0 = \frac{k^2(k-1)^2(k-2)^2-18\alpha_3^2}{k^2(k-1)^2(k-2)^2}a_0 + \frac{3k^2(k-1)^2(k-2)^2\alpha_3-27\alpha_3^3}{k^3(k-1)^3(k-2)^3}b_0$$

となる．このとき，第一積分は

$$\Phi = a_0\left\{p_x^4 - \frac{12\alpha_3}{k(k-1)(k-2)}p_xp_y^3 + \frac{k^2(k-1)^2(k-2)^2-18\alpha_3^2}{k^2(k-1)^2(k-2)^2}p_y^4\right\} + b_0\left\{p_x^3p_y + \frac{k^2(k-1)^2(k-2)^2-18\alpha_3^2}{k^2(k-1)^2(k-2)^2}p_xp_y^3 + \frac{3k^2(k-1)^2(k-2)^2\alpha_3-27\alpha_3^3}{k^3(k-1)^3(k-2)^3}p_y^4\right\} + B_0p_x^2 + B_1p_xp_y + B_2p_y^2 + C_0$$

となる．ここで，座標回転

$$x \to x\cos\varphi - y\sin\varphi,\quad y \to x\sin\varphi + y\cos\varphi,\quad \tan 2\varphi = -\frac{k(k-1)(k-2)}{3\alpha_3}$$

を行なうと，第一積分は

$$\Phi = a_0(p_x^4+p_y^4) + c_0p_x^2p_y^2 + B_0p_x^2 + B_1p_xp_y + B_2p_y^2 + C_0$$

という形になる．再び，第一積分から $2c_0H^2$ を引くことにより，$c_0 = 0$ とする．このとき，第一積分は

$$\Phi = p_x^4 + p_y^4 + B_0p_x^2 + B_1p_xp_y + B_2p_y^2 + C_0$$

の形になる．漸化式 (29) は

$$4(j-1)j(j+1)(k-j-1)\alpha_{j+1} - 4(j-1)(k-j-1)(k-j)(k-j+1)\alpha_{j-1} = 0,$$

となる．ただし，$j=2,3,\dots,k-2$ である．両辺を $4(j-1)(k-j-1)$ で割ると，

$$j(j+1)\alpha_{j+1}-(k-j+1)(k-j)\alpha_{j-1}=0.$$

この漸化式より，k が偶数のとき，

$$V_k=\alpha_0\sum_{m=0}^{[k/2]}\binom{k}{2m}x^{k-2m}y^{2m}+\alpha_1\sum_{m=0}^{[k/2]-1}\frac{1}{2m+1}\binom{k-1}{2m}x^{k-2m-1}y^{2m+1},$$

k が奇数のとき，

$$V_k=\alpha_0\sum_{m=0}^{[k/2]}\binom{k}{2m}x^{k-2m}y^{2m}+\alpha_1\sum_{m=0}^{[k/2]}\frac{1}{2m+1}\binom{k-1}{2m}x^{k-2m-1}y^{2m+1}$$

を得る．ともに $\pi/4$ の回転によって直交座標で変数分離可能な形になる．

• $\alpha_2=3k(2k-1)\alpha_0/2$ のとき，もし $\alpha_0=0$ ならば上の場合に帰着する．よって，$\alpha_0\neq 0$ の場合を考える．$\alpha_0=1$ と固定すると，(30) の第 2, 3, 4 式から順に

$$a_0=-\frac{(7k-6)\alpha_3}{4k(k-2)(2k-1)(3k-2)},$$

$$\begin{aligned}d_0=&\frac{3(30k^2-59k+24)}{4(k-1)(2k-3)}+\frac{(7k-6)(18k^2-31k+16)\alpha_3^2}{2k^2(k-1)(k-2)^2(2k-1)^2(2k-3)(3k-2)}\\&-\frac{2(17k^2-31k+20)\alpha_4}{k(k-1)(k-2)(k-3)(2k-1)(2k-3)},\end{aligned}$$

$$\begin{aligned}e_0=&\frac{(150k^3-295k^2+128k-12)\alpha_3}{24k(k-2)(2k-1)^2(2k-3)(3k-2)}+\frac{(7k-6)(6k^3-5k^2-12k+14)\alpha_3^3}{12k^3(k-1)(k-2)^3(2k-1)^4(2k-3)(3k-2)}\\&+\frac{(37k^4-206k^3+417k^2-382k+128)\alpha_3\alpha_4}{3k^2(k-1)(k-2)^2(k-3)(2k-1)^3(2k-3)(3k-2)}\\&-\frac{5(23k^2-43k+38)\alpha_5}{18k(k-1)(k-2)(k-3)(k-4)(2k-1)^2}.\end{aligned}$$

ここで，$b_0=1$ とおいた．このとき，漸化式 (29) より，

$$\begin{aligned}\alpha_4=&\frac{3k(k-2)(k-3)(2k-1)(11k-6)(42k^2-77k+26)}{8(241k^3-519k^2+456k-124)}\\&+\frac{2(k-3)(7k-6)(258k^3-527k^2+388k-92)\alpha_3^2}{8k(k-2)(2k-1)(3k-2)(241k^3-519k^2+456k-124)},\end{aligned}$$

$$\begin{aligned}\alpha_5=&\frac{3(k-3)(k-4)(43790k^5-179247k^4+285460k^3-221960k^2+83760k-12208)\alpha_3}{10(95k^2-151k+74)(241k^3-519k^2+456k^2-124)}\\&+\frac{3(k-1)(k-3)(k-4)(7k-6)(29910k^5-102733k^4+143546k^3-101604k^2+36376k-5216)\alpha_3^3}{10k^2(k-2)^2(2k-1)^2(3k-2)^2(95k^2-151k+74)(241k^3-519k^2+456k^2-124)}.\end{aligned}$$

これにより，a_0, b_0, d_0, e_0 は k の有理式を係数とする α_3 の多項式になる．漸化式 (29) から，$\alpha_6, \alpha_7, \dots, \alpha_k$ も k の有理式を係数とする α_3 の多項式として表せることが分かる．このとき，偏微分方程式 (27) から得られる恒等式の $x^{2k-6}y^4, x^{2k-7}y^5, \dots, y^{2k-2}$ の係数から，$2k-5$ 個の代数方程式が得られることになる．これらは k の有理式を係数とする α_3 についての代数方程式で，次数は順に $4, 5, \dots, 2k-2$ となる．よって，これら $2k-5$ 個の代数方程式が共通解を持つかどうかという問題に帰着する．

終結式

複数の代数方程式が共通解を持つかどうかを判定する手段として終結式とよばれる量を計算する方法がある．

2つの多項式

$$f(x) = a_0x^n + a_1x^{n-1} + \cdots + a_n, \quad g(x) = b_0x^m + b_1x^{m-1} + \cdots + b_m$$

に対して，次のような $m+n$ 次の行列式を $f(x), g(x)$ の**終結式**という．

$$R(f,g) = \begin{vmatrix} a_0 & a_1 & \cdots & a_n & & & \\ & a_0 & a_1 & \cdots & a_n & & \\ & & \cdots & \cdots & \cdots & & \\ & & & a_0 & a_1 & \cdots & a_n \\ b_0 & b_1 & \cdots & \cdots & b_m & & \\ & & \cdots & \cdots & \cdots & & \\ & & b_0 & b_1 & \cdots & \cdots & b_m \end{vmatrix}$$

定理

$a_0b_0 \neq 0$ のとき，2つの方程式 $f(x) = 0, g(x) = 0$ が少なくとも1つの共通解を持つための必要十分条件は，$R(f,g) = 0$ となることである．

必要性の証明　共通解 α があったとすると

$$\begin{cases} \alpha^{m-1}f(\alpha) &= a_0\alpha^{m+n-1} + a_1\alpha^{m+n-2} + \cdots + a_n\alpha^{m-1} = 0 \\ \alpha^{m-2}f(\alpha) &= a_0\alpha^{m+n-2} + a_1\alpha^{m+n-3} + \cdots + a_n\alpha^{m-2} = 0 \\ & \vdots \\ f(\alpha) &= a_0\alpha^n + a_1\alpha^{n-1} + \cdots + a_n = 0 \\ \alpha^{n-1}g(\alpha) &= b_0\alpha^{m+n-1} + b_1\alpha^{m+n-2} + \cdots + b_m\alpha^{n-1} = 0 \\ \alpha^{n-2}g(\alpha) &= b_0\alpha^{m+n-2} + b_1\alpha^{m+n-3} + \cdots + b_m\alpha^{n-2} = 0 \\ & \vdots \\ g(\alpha) &= b_0\alpha^m + b_1\alpha^{m-1} + \cdots + b_m = 0 \end{cases}$$

が成り立つ．ここで，終結式の第 $1, 2, \ldots, m+n-1$ 列に，それぞれ $\alpha^{m+n-1}, \alpha^{m+n-2}, \ldots, \alpha$ を掛けて，第 $m+n$ 列に加えると，上の連立方程式より第 $m+n$ 列の要素はすべて0になる．したがって，終結式 $R(f,g)$ の値は0である．∎

十分性の証明　終結式 $R(f,g)$ の値が0になったとすると，終結式を構成する $m+n$ 個の行ベクトルは一次従属である．第 $1, 2, \ldots, m+n$ 行ベクトルをそれぞれ $\boldsymbol{a}_1, \boldsymbol{a}_2, \ldots, \boldsymbol{a}_m, \boldsymbol{b}_1, \boldsymbol{b}_2, \ldots, \boldsymbol{b}_n$ とおくと

$$\sum_{i=1}^{m} c_i\boldsymbol{a}_i + \sum_{j=1}^{n} d_j\boldsymbol{b}_j = 0, \quad (c_1, \ldots, d_n) \neq (0, \ldots, 0)$$

という関係が成り立つ．このベクトル式の第 $1, 2, \ldots, m+n$ 成分にそれぞれ $x^{m+n-1}, x^{m+n-2}, \ldots, 1$ を掛けて辺々加えると

$$\sum_{i=1}^{m} c_ix^{m-i}f(x) + \sum_{j=1}^{n} d_jx^{n-j}g(x) = 0$$

を得る．ここで，$\sum_{i=1}^{m} c_i x^{m-i} = h(x)$, $\sum_{j=1}^{n} d_j x^{n-j} = k(x)$ とおくと

$$h(x)f(x) = -k(x)g(x)$$

となる．多項式 $f(x)$ の次数を $\deg f(x)$ と表すことにすると，

$$\deg k(x) \leq n-1 < n = \deg f(x).$$

ここで，$f(x)$ と $g(x)$ が共通因子を持たないと仮定すると，$k(x)$ がより次数の高い $f(x)$ で割り切れることになり矛盾を生ずる．したがって，$f(x)$ と $g(x)$ は共通因子を持つ．つまり，$f(x)=0$ と $g(x)=0$ は共通解を持つ． ∎

終結式の計算

α_3 についての $2k-5$ 個の代数方程式のうち最も次数の低いもの 2 つに対する終結式を計算してみる．それらは 4 次方程式と 5 次方程式で，以下のような方程式である．

$$-\frac{9(k-2)k^2(k+2)(2k-1)(5k-2)G_1(k)}{4(k-1)S(k)^2} + \frac{3(k+2)(5k-2)(7k-6)G_2(k)\alpha_3^2}{4(k-2)(k-1)(2k-1)(3k-2)R(k)S(k)^2}$$
$$+\frac{2(k+2)(5k-2)(7k-6)G_3(k)\alpha_3^4}{(k-2)^3(k-1)k^2(2k-1)^3(3k-2)^3R(k)S(k)^2} = 0. \tag{32}$$

$$-\frac{9(k-3)k(k+2)(5k-2)G_4(k)\alpha_3}{20(k-1)(3k-2)R(k)S(k)^2} + \frac{3(k-3)(k+2)(5k-2)(7k-6)G_5(k)\alpha_3^3}{20(k-2)^2(k-1)k(2k-1)^2(3k-2)^2R(k)S(k)}$$
$$+\frac{(k-3)(k+2)(5k-2)(7k-6)G_6(k)\alpha_3^5}{5(k-2)^4(k-1)k^3(2k-1)^4(3k-2)^4R(k)S(k)^2} = 0. \tag{33}$$

ただし，

$$R(k) = 74 - 151\,k + 95\,k^2,$$
$$S(k) = -124 + 456\,k - 519\,k^2 + 241\,k^3,$$
$$G_1(k) = 29952 - 260400\,k + 932160\,k^2 - 1727456\,k^3 + 1706012\,k^4 - 810861\,k^5 + 118529\,k^6 + 16870\,k^7,$$
$$G_2(k) = -3170144 + 37193808\,k - 190561760\,k^2 + 553816792\,k^3 - 998755638\,k^4 + 1151765545\,k^5 - 843129587\,k^6 + 371783811\,k^7 - 86588015\,k^8 + 7446900\,k^9,$$
$$G_3(k) = -1361952 + 20130192\,k - 133944304\,k^2 + 527295832\,k^3 - 1360307178\,k^4 + 2408313485\,k^5 - 2978361002\,k^6 + 2565200757\,k^7 - 1500811081\,k^8 + 563283562\,k^9 - 120201105\,k^{10} + 10736550\,k^{11},$$
$$G_4(k) = -54723072 + 687806528\,k - 3817158400\,k^2 + 12223132176\,k^3 - 24787677856\,k^4 + 32872864764\,k^5 - 28351948208\,k^6 + 15180036291\,k^7 - 4446138980\,k^8 + 454376975\,k^9 + 40055750\,k^{10},$$
$$G_5(k) = 68988096 - 912699392\,k + 5346987920\,k^2 - 18143124368\,k^3 + 39260441572\,k^4 - 56288554120\,k^5 + 53780522743\,k^6 - 33457433369\,k^7 + 12720106145\,k^8 - 2562547775\,k^9 + 186064500\,k^{10},$$
$$G_6(k) = 56393856 - 913712256\,k + 6725558432\,k^2 - 29645084416\,k^3 + 86929567784\,k^4 - 178232080840\,k^5 + 261364852406\,k^6 - 275416174516\,k^7 + 206176050353\,k^8 - 106294583086\,k^9 + 35472298955\,k^{10} - 6761687100\,k^{11} + 538285500\,k^{12}$$

である．代数方程式 (32), (33) に対する終結式を計算すると

$$\frac{-2893401(k-4)^2(k-3)^4(k+2)^9(2k-3)^4(3k-4)^4(3k-1)^4(5k-6)^2(5k-2)^{29}(7k-6)^4}{4096(k-2)^{11}(k-1)^9k^2(2k-1)^{11}(3k-2)^{16}R(k)^6S(k)^{10}}$$
$$\times(29952-260400k+932160k^2-1727456k^3+1706012k^4-810861k^5+118529k^6+16870k^7)$$
$$\times(-2787216+23021920k-82567904k^2+167598204k^3-211881739k^4+173025983k^5$$
$$-91304549k^6+30037885k^7-5594600k^8+450000k^9)^2$$

となる．これは，$k\geq 6$ のときは 0 にならない．したがって，代数方程式 (32), (33) は共通解を持たない．つまり，$2k-5$ 個の代数方程式を同時に満足する α_3 の値は存在しない．したがって，この場合は解なしである．

以上より，$k\geq 6$ のとき運動量について 4 次の多項式第一積分を持つのは直交座標で変数分離可能な系に限る． ∎

ちなみに $k=3,4$ の場合

$k=3$ のとき，連立代数方程式 (30) の係数は次のようになる．

$$M_{11}=\frac{1}{3}(3\alpha_0-\alpha_2)(45\alpha_0-2\alpha_2),$$
$$M_{21}=-30\alpha_3(3\alpha_0-\alpha_2),\quad M_{22}=-\frac{112}{3}\alpha_2(3\alpha_0-\alpha_2),$$
$$M_{31}=-9\alpha_0\alpha_2-7\alpha_2^2+45\alpha_3^2,\quad M_{32}=60\alpha_2\alpha_3,\quad M_{33}=-9(\alpha_0-2\alpha_2)(5\alpha_0-\alpha_2),$$
$$M_{41}=-30\alpha_2\alpha_3,\quad M_{42}=-40\alpha_2^2,\quad M_{43}=30\alpha_3(3\alpha_0-2\alpha_2),\quad M_{44}=-\frac{8}{3}\alpha_2(3\alpha_0-16\alpha_2).$$

$(b_0,a_0,d_0,e_0)\neq(0,0,0,0)$ であるから，$M_{11}M_{22}M_{33}M_{44}=0$ でなければならない．すなわち，

$$\alpha_2=0,\quad \alpha_2=3\alpha_0,\quad \alpha_2=\frac{45}{2}\alpha_0,\quad \alpha_2=\frac{1}{2}\alpha_0,\quad \alpha_2=5\alpha_0,\quad \text{または}\quad \alpha_2=\frac{3}{16}\alpha_0$$

である．それぞれの場合にポテンシャルを求めて，適当な座標回転とスケール変換によって互いに移り合うものを同一視すると，次の 3 つが残る．

- $V_3=\alpha_0x^3+\alpha_3y^3,\quad (V_3=x^3+3xy^2+\alpha_3y^3)$
- $V_3=x^3+\frac{3}{16}xy^2,\quad \left(V_3=x^3+\frac{45}{2}xy^2\pm\frac{17\sqrt{14}\,i}{2}y^3\right)$
- $V_3=x^3+\frac{1}{2}xy^2\pm\frac{\sqrt{3}\,i}{18}y^3,\quad \left(V_3=x^3+\frac{45}{2}xy^2\mp\frac{27\sqrt{3}\,i}{2}y^3,\quad V_3=x^3+5xy^2\pm\frac{22\sqrt{3}\,i}{9}y^3\right)$

$k=4$ のとき，連立代数方程式 (30) の係数は次のようになる．

$$M_{11}=\frac{1}{3}(6\alpha_0-\alpha_2)(42\alpha_0-\alpha_2),$$
$$M_{21}=-11\alpha_3(6\alpha_0-\alpha_2),\quad M_{22}=-\frac{80}{3}\alpha_2(6\alpha_0-\alpha_2),$$
$$M_{31}=\frac{1}{6}(540\alpha_0\alpha_2-16\alpha_2^2+99\alpha_3^2-1512\alpha_0\alpha_4+228\alpha_2\alpha_4),$$
$$M_{32}=-80\alpha_3(3\alpha_0-\alpha_2),\quad M_{33}=80\alpha_0\alpha_2,$$
$$M_{41}=-2\alpha_3(6\alpha_0+37\alpha_2-48\alpha_4),\quad M_{42}=-\frac{8}{3}(32\alpha_2^2-27\alpha_3^2-24\alpha_2\alpha_4),$$
$$M_{43}=24\alpha_3(7\alpha_0-\alpha_2),\quad M_{44}=-\frac{64}{3}\alpha_2(3\alpha_0-4\alpha_2).$$

$(b_0, a_0, d_0, e_0) \neq (0,0,0,0)$ であるから，$M_{11}M_{22}M_{33}M_{44} = 0$ でなければならない．すなわち，

$$\alpha_0 = 0, \quad \alpha_2 = 0, \quad \alpha_2 = 6\alpha_0, \quad \alpha_2 = 42\alpha_0, \quad \text{または} \quad \alpha_2 = \frac{3}{4}\alpha_0$$

である．それぞれの場合にポテンシャルを求めて，適当な座標回転とスケール変換によって互いに移り合うものを同一視すると，次の2つが残る．

- $V_4 = \alpha_0 x^4 + \alpha_4 y^4, \quad \left(V_4 = x^4 + 6x^2y^2 + \alpha_3 xy^3 + \dfrac{16+\alpha_3^2}{16} y^4\right)$
- $V_4 = x^4 + \dfrac{3}{4}x^2y^2 + \dfrac{1}{8}y^4, \quad \left(V_4 = x^4 + 6x^2y^2 + 8y^4, \quad V_4 = x^4 + 42x^2y^2 \pm 28\sqrt{10}\, ixy^3 - 48y^4\right)$

参考文献

[1] J. Hietarinta, "A search for integrable two-dimensional Hamiltonian systems with polynomial potential," *Physics Letters* **96A** (1983) 273–278.

[2] J. Hietarinta, "Direct methods for the search of the second invariant," *Physics Reports* **147** (1987) 87–154.

[3] L. S. Hall, "A theory of exact and approximate configurational invariants," *Physica* **8D** (1983) 90–116.

[4] B. Grammaticos, B. Dorizzi, R. Padjen, "Painlevé property and integrals of motion for the Hénon-Heiles system," *Physics Letters* **89A** (1982) 111–113.

[5] I. Marshall, S. Wojciechowski, "When is a Hamiltonian system separable?," *J. Math. Phys.* **29** (1988) 1338–1346.

[6] J.J. Morales-Ruiz, J.P. Ramis, "A note on the non-integrability of some Hamiltonian systems with a homogeneous potential," *Preprint* (1997).

[7] J.J. Morales-Ruiz, J.P. Ramis, "Galoisian obstruction to integrability of Hamiltonian systems," *Preprint* (1998).

[8] A. Ramani, B. Dorizzi, B. Grammaticos, "Painlevé conjecture revisited," *Physics Review Letters* **49** (1982) 1539–1541.

[9] A. Ramani, B. Grammaticos, T. Bountis, "The Painlevé property and singularity analysis of integrable and non-integrable systems," *Physics Reports* **180** (1989) 159–245.

[10] H. Yoshida, "A new necessary condition for the integrability of Hamiltonian systems with a two dimensional homogeneous potential," *Physica* **D128** (1999) 53–69.

微分ガロア理論にもとづくHamilton系の可積分性の必要条件
Necessary Condition for the Integrability of Hamiltonian Systems based on Differential Galois Theory

吉田春夫 (国立天文台)
H. Yoshida (National Astronomical Observatory)

abstract

同次式ポテンシャルを持つHamilton系の直線解の周りの変分方程式は独立変数の変換によってGaussの超幾何方程式に変換される．そしてもとのHamilton系が可積分なら超幾何方程式は微分Galois理論の意味で可解となる，つまり解が四則演算・微分演算に加え代数方程式を解く演算，不定積分演算，指数関数演算という初等的な演算のみで得られる（初等的に解ける）ことが示される．一方，超幾何方程式が微分Galois理論の意味で可解となるための必要条件は木村俊房 (1969) によって得られており，それを適用することによって可積分性の強力な必要条件が得られる．既知の可積分ポテンシャルをこの必要条件に照らして分類すると元素の周期律表のようなものが構成でき，未知の可積分系の存在をも暗示する．

1 はじめに

5次方程式以上の一般の代数方程式にはべき根のみで表される解の公式が存在しない．このことを示したAbelの定理は後にGaloisによって一般5次方程式のGalois群G（5次の対称群）が可解群でないということの論理的帰結として示されるに至った．可解群という名自身，この偉大な歴史的事実に基づいて付けられたようである．微分Galois理論とは一言で言えばこの代数方程式に対するGalois理論の微分方程式版である．与えられた微分方程式が「解析的」に解けるか否かを何らかの群論的な手法で判定したいと願うのは全く自然な欲求である．そして特に線形微分方程式における微分Galois理論であるPicard-Vessiot理論は十分に確立されていると考えて良い．

今，$p(z), q(z)$ を有理関数とする2階の線形常微分方程式

$$\frac{d^2\xi}{dz^2} + p(z)\frac{d\xi}{dz} + q(z)\xi = 0 \tag{1}$$

を考える．そしてその2つの1次独立な解が，有理関数から始めて

- 四則演算 + 微分演算
- 不定積分演算 + 指数関数演算
- 代数方程式を解く

という操作のみで求められるか否かを問題とする．これは与えられた微分方程式が「初等的に解ける」という状況の精密化である．Picard-Vessiot 理論によれば，これは微分方程式 (1) に対する微分 Galois 群 G の単位元成分 G_0が可解群 (solvable group) となることと同値であり，さらに微分 Galois 群 G が $SL(2,\mathbf{C})$ の部分群となる場合，

- G は同時 3 角化可能, or
- G は有限群, or
- G_0が対角化可能で $[G:G_0]=2$

と同値であることが知られている．Picard-Vessiot 理論については [2] や [5] を参照せよ．[2] には例として Airy の微分方程式

$$\frac{d^2\xi}{dz^2}+z\xi=0 \tag{2}$$

の解が上に述べた意味で初等的には表し得ないことが示されている．

今，一般に非線形な Hamilton 系が可積分な部分系を持つとする．例えばポテンシャル系が直線解を持てば，その直線解自身は自由度 1 の Hamilton 系の解となっているから可積分な部分系である．そこでもとの非線形な Hamilton 系の運動方程式をこの可積分な部分系の周りで線形化して得られる変分方程式を考える．Morales and Ramis[6] は比較的ゆるい仮定の下で，もとの非線形な Hamilton 系の可積分性が，この変分方程式の，Picard-Vessiot 理論の意味での可解性を導くことを示した．つまり元の Hamilton 系が Liouville の意味で積分可能（十分な数の独立な第一積分を持つ）ならば，変分方程式も「解ける」ということである．特に元の Hamilton 系が同次式ポテンシャル系ならば常に可積分な部分系としての直線解が存在し，さらに直線解のまわりの変分方程式が Gauss の超幾何方程式に変換されることがわかっている．一方で Gauss の超幾何方程式が可解となるための必要十分条件は木村 [3] によって得られている．よってこの Morales and Ramis[6] の結果から，具体的に与えられたポテンシャルが可積分となるための必要条件が簡単に導かれることになる [6]．以下ではこの必要条件を 2 次元の同次式ポテンシャル系の場合に限定して具体的に見ていくことにする．より詳細な内容は [9], [10], [11] などを参照されたい．

2 変分方程式として得られる Gauss の超幾何方程式の可解性

$V(q_1,q_2)$ を k次の同次式ポテンシャルとする Hamilton 系

$$H=\frac{1}{2}(p_1^2+p_2^2)+V(q_1,q_2) \tag{3}$$

を考える．この系は常に直線解

$$\boldsymbol{q}=\boldsymbol{c}\phi(t),\quad \boldsymbol{p}=\boldsymbol{c}\dot{\phi}(t) \tag{4}$$

を持つ．ここで$\phi(t)$ は

$$\frac{d^2\phi}{dt^2}+\phi^{k-1}=0 \tag{5}$$

を満たす時間 t の関数であり，定数ベクトル$\boldsymbol{c}$は代数方程式

$$\nabla V(\boldsymbol{c})=\boldsymbol{c} \tag{6}$$

の1つの解である．今，代数方程式 (6) の解$\boldsymbol{c}$を1つ固定する．運動方程式を直線解 (4) の周りで線形化して得られる変分方程式は ($\boldsymbol{\xi} := \delta \boldsymbol{q}$)

$$\frac{d^2\boldsymbol{\xi}}{dt^2} + \phi(t)^{k-2}\partial^2 V(\boldsymbol{c})\boldsymbol{\xi} = 0 \tag{7}$$

となる．ここで$\partial^2 V(\boldsymbol{c})$ は $V(\boldsymbol{q})$ のヘッシアン行列を点$\boldsymbol{q} = \boldsymbol{c}$で評価したものである．適当な座標回転 $(\xi_1, \xi_2) \to (\xi_1', \xi_2')$ によってヘッシアン行列$\partial^2 V(\boldsymbol{c})$ は対角化される．さらに $(k-1)$ は$\partial^2 V(\boldsymbol{c})$ の，$\boldsymbol{c}$を固有ベクトルとする固有値なので，他の固有値をλとして，対角化後の変分方程式は

$$\frac{d^2\boldsymbol{\xi}'}{dt^2} + \phi(t)^{k-2}\begin{pmatrix}\lambda & 0\\ 0 & k-1\end{pmatrix}\boldsymbol{\xi}' = 0 \tag{8}$$

となる．この第1の成分

$$\frac{d^2\xi_1'}{dt^2} + \lambda\phi(t)^{k-2}\xi_1' = 0 \tag{9}$$

は直線解 (4) に直交する変分を記述するので，**直交変分方程式** (Normal Variational Equation, NVE) と呼ばれる．今，適当な座標回転によって最初から直線解が $q_1 = p_1 = 0$ で与えられているとする．この時，NVE は

$$\frac{d\xi_1}{dt} = \eta_1, \quad \frac{d\eta_1}{dt} = -\lambda q_2^{k-2}\xi_1 \tag{10}$$

と書ける．ここで $q_2 = q_2(t)$ は

$$\frac{dq_2}{dt} = p_2, \quad \frac{dp_2}{dt} = -q_2^{k-1} \tag{11}$$

の解で，この直線解のエネルギーを

$$\frac{1}{2}p_2^2 + \frac{1}{k}q_2^k = \text{const.} = \frac{1}{k} \tag{12}$$

に固定しておく．独立変数の変換 $t \to z$を

$$z = [q_2(t)]^k \tag{13}$$

によって行えば，(10) は

$$z(1-z)\frac{d^2\xi_1}{dz^2} + \left(\frac{k-1}{k} - \frac{3k-2}{2k}z\right)\frac{d\xi_1}{dz} + \frac{\lambda}{2k}\xi_1 = 0 \tag{14}$$

に変換される [8]．これは **Gauss の超幾何方程式**

$$z(1-z)\frac{d^2\xi}{dz^2} + [c-(a+b+1)z]\frac{d\xi}{dz} - ab\xi = 0 \tag{15}$$

でパラメータを

$$a+b = \frac{1}{2} - \frac{1}{k}, \quad ab = -\frac{\lambda}{2k}, \quad c = 1 - \frac{1}{k} \tag{16}$$

としたものである．この時次の定理が主張できる．

定理 1

Hamilton 系 (3) が積分可能とする．このとき全ての直線解 (4) に対して，変分方程式として得られる Gauss の超幾何方程式 (14) は Picard-Vessiot の意味で可解である，つまりその解が有理関数から出発して四則演算・微分演算に加え代数方程式を解く演算，不定積分演算，指数関数演算，という初等的な演算の合成のみで得られる．

定理 1 は Morales-Ruiz and Ramis [6] で微分 Galois 理論の言葉を用いたより一般的な結果として主張されているものだが，筆者の理解をはるかに越えているため自家製の比較的初等的な証明を [10] において与えておいた．

3 Gauss の超幾何方程式の可解性に関する木村の定理

Gauss の超幾何方程式 (15) は $z = 0, 1, \infty$ を確定特異点とするが，各特異点の周りで解を Frobenius 展開して得られる**指数** (exponent) は基本的な量である．例えば $z = 0$ の周りでの展開は

$$\xi(z) = z^{\rho} \sum_{j=0}^{\infty} a_j z^j \tag{17}$$

の形となるが，zのベキとして表れるρが exponent に他ならず，**決定方程式**と呼ばれる 2 次方程式の解として決められる．0 及び $1-c$ が 2 つの exponent である．同様に $z = 1$ における exponent は 0 及び $c-a-b$，そして $z = \infty$ における exponent は a 及び b であることが容易に確認できる．ここではその差 (exponent difference)

$$\hat{\lambda} = 1 - c, \quad \hat{\mu} = c - a - b, \quad \hat{\nu} = b - a \tag{18}$$

が重要な役割を果たす [3].

定理 2 （木村俊房）

一般に Gauss の超幾何方程式 (15) が Picard-Vessiot の意味で可解であるための必要かつ十分な条件は，$\hat{\lambda}, \hat{\mu}, \hat{\nu}$ をそれぞれ確定特異点 $z = 0, 1, \infty$ における exponent の差 (18) として

- $\hat{\lambda} \pm \hat{\mu} \pm \hat{\nu}$ の少なくとも 1 つが奇整数である，または
- $\pm\hat{\lambda}, \pm\hat{\mu}, \pm\hat{\nu}$ が勝手な順序で **Schwarz-福原-大橋の表**の値をとる，

ことである．

定理 2 の第 1 の条件，つまり$\hat{\lambda} \pm \hat{\mu} \pm \hat{\nu}$の少なくとも 1 つが奇整数であるという条件は Gauss の超幾何方程式が可約である場合に対応している．ここで一般に 2 階の線形微分方程式 (1) が，$r(z)$ を有理関数とする 1 階の線形微分方程式

$$\frac{d\xi}{dz} + r(z)\xi = 0 \tag{19}$$

を満たす解を持つとき，(1) は**可約** (reducible) であるという．(19) および (19) を zで微分して得られる $d^2\xi/dz^2 = (r^2 - dr/dz)\xi$ を (1) に代入すれば $r(z)$ についての非線形微分方程式

$$\frac{dr}{dz} - r^2 + p(z)r - q(z) = 0 \tag{20}$$

が得られる．そして特に (1) が Gauss の超幾何方程式の時，実際にある有理関数 $r(z)$ が (20) を満たすことを要請することによって，定理 2 の第 1 の条件が導出される．

一方，第 2 の条件は 1 つの場合を除いて，Gauss の超幾何方程式の解が代数関数となる条件を求めた Schwarz(1872) の結果と等しい．解自身が代数関数となれば当然 Picard-Vessiot の意味で可解である．以下の **Schwarz の表**において 1 行目を $(\frac{1}{2}, \frac{1}{2}, \text{任意})$ と書き換えることによって **Schwarz-福原-大橋の表**は得られる．いずれの場合も表の値に任意の整数 (l, m, n) を加えてかま

1	$\frac{1}{2}$	$\frac{1}{2}$	$\frac{1}{N}$	正2面体
2	$\frac{1}{2}$	$\frac{1}{3}$	$\frac{1}{3}$	正4面体
3	$\frac{2}{3}$	$\frac{1}{3}$	$\frac{1}{3}$	
4	$\frac{1}{2}$	$\frac{1}{3}$	$\frac{1}{4}$	正8面体
5	$\frac{2}{3}$	$\frac{1}{4}$	$\frac{1}{4}$	
6	$\frac{1}{2}$	$\frac{1}{3}$	$\frac{1}{5}$	正20面体
7	$\frac{2}{5}$	$\frac{1}{3}$	$\frac{1}{3}$	
8	$\frac{2}{3}$	$\frac{1}{5}$	$\frac{1}{5}$	
9	$\frac{1}{2}$	$\frac{2}{5}$	$\frac{1}{5}$	
10	$\frac{3}{5}$	$\frac{1}{3}$	$\frac{1}{5}$	
11	$\frac{2}{5}$	$\frac{2}{5}$	$\frac{2}{5}$	
12	$\frac{2}{3}$	$\frac{1}{3}$	$\frac{1}{5}$	
13	$\frac{4}{5}$	$\frac{1}{5}$	$\frac{1}{5}$	
14	$\frac{1}{2}$	$\frac{2}{5}$	$\frac{1}{3}$	
15	$\frac{3}{5}$	$\frac{2}{5}$	$\frac{1}{3}$	

表 1: Schwarz の表

わない．ただし 1, 2, 4, 6 行以外では $l+m+n=$ 偶数という制限がつく．Schwarz の表およびその周辺については，筆者の知る限りで現存するベストの解説が [4] にある．Schwarz の表は正多面体の存在と密接に関係しているがこれについては [9], [11] なども参照せよ．

4 同次式ポテンシャル系の可積分性の新しい必要条件

同次式ポテンシャル系において直線解の周りの直交変分方程式として得られた Gauss の超幾何方程式 (14) における exponent の差 (18) は

$$\hat{\lambda}=\frac{1}{k},\quad \hat{\mu}=\frac{1}{2},\quad \hat{\nu}=\frac{\sqrt{(k-2)^2+8k\lambda}}{2k} \tag{21}$$

である．これから定理 2 の第 1 の条件，つまり $\hat{\lambda}\pm\hat{\mu}\pm\hat{\nu}$ の少なくとも 1 つが奇整数である，という条件は

$$\lambda=j+j(j-1)k/2=\{0,1,k-1,k+2,3k-2,\ldots\} \tag{22}$$

という条件に翻訳される．また Schwarz-福原-大橋の表の第 1 行から，$k=\pm 2$ ならば任意の λ が許されることがわかる．さらに任意の次数 k において，$\hat{\nu}=1/2+$ 整数, となるような λ が許される値であることが分かるが，これは

$$\lambda=\frac{k-1}{2k}+j(j-1)k/2=\left\{\frac{k-1}{2k},\frac{k-1}{2k}+k,\frac{k-1}{2k}+3k,\ldots\right\} \tag{23}$$

という条件を与える．$k=\pm 3,\pm 4,\pm 5$ の場合を除けばこれ以外の可能性はない．

$k=\pm 3,\pm 4,\pm 5$ のときは Schwarz の表に適合する λ の値はより多くなる．例えば $k=4$ の時，一般の k で許される

$$\lambda=\{0,1,3,6,10,\ldots\}\cup\left\{\frac{3}{8},\frac{35}{8},\frac{99}{8},\frac{195}{8},\ldots\right\} \tag{24}$$

に加えて Schwarz の表の第 4 行から

$$\lambda = -\frac{1}{8} + \frac{1}{8}\left(\frac{4}{3} + 4j\right)^2 = \left\{\frac{7}{72}, \frac{55}{72}, \frac{247}{72}, \frac{391}{72}, \cdots\right\} \tag{25}$$

が可能な値となる．このようにして得られた可積分性の新しい必要条件は，全く同じ仮定の下で [8] で得られた必要条件をはるかに強くしている．

得られた必要条件を 4 次の同次式ポテンシャル

$$V(q_1, q_2) = \frac{1}{4}(q_1^4 + q_2^4) + \frac{e}{2} q_1^2 q_2^2 \tag{26}$$

に適用すると，可積分となるためには $e = 0, 1, 3$ となるべきことが導かれるが，それらは実際に可積分であることが簡単に確認できる．一方，3 次の同次式ポテンシャル

$$V(q_1, q_2) = q_1^2 q_2 + \frac{e}{3} q_2^3 \tag{27}$$

に適用すると，$e = 1, 2, 6, 16$ のみが生き残る．$e = 1, 2, 16$ の 3 つの場合は実際に可積分であることが示される．しかし $e = 2$ の場合は（おそらく）非可積分であろうが，現在の解析ではそれを示すことはできない [10]．これは線形解析の致命的な限界である．

5 既知の可積分な 2 次元同次多項式ポテンシャルの分類と予想

可積分なポテンシャルで最も簡単なものは変数分離可能なポテンシャルで，この変数分離可能性は，運動量について 2 次の第一積分の存在と密接に関係している．直交座標で変数分離可能な同次多項式ポテンシャルは A, B を任意の定数パラメータとした

$$V_k = A q_1^k + B q_2^k \tag{28}$$

である．$A = B$ の簡単な場合でも角度 $\pi/4$ の座標回転すると非自明な

$$V_3 = 3q_1^2 q_2 + q_2^3 \tag{29}$$
$$V_4 = q_1^4 + 6q_1^2 q_2^2 + q_2^4 \tag{30}$$
$$V_5 = q_1^5 + 10q_1^3 q_2^2 + 5q_1 q_2^4 \tag{31}$$

の形となる．また極座標で変数分離可能な同次多項式ポテンシャルは

$$V_2 = q_1^2 + q_2^2 \tag{32}$$
$$V_4 = q_1^4 + 2q_1^2 q_2^2 + q_2^4 \tag{33}$$
$$V_6 = q_1^6 + 3q_1^4 q_2^2 + 3q_1^2 q_2^4 + q_2^6 \tag{34}$$

である．最後の可能性として放物線座標で変数分離可能な同次多項式ポテンシャル

$$V_3 = 4q_1^2 q_2 + 8q_2^3 \tag{35}$$
$$V_4 = q_1^4 + 12q_1^2 q_2^2 + 16q_2^4 \tag{36}$$
$$V_5 = 6q_1^4 q_2 + 32q_1^2 q_2^3 + 32q_2^5 \tag{37}$$

がある．この系列の発見は比較的新しい．以上の変数分離可能な系列以外に次の３つの可積分な同次多項式ポテンシャルが知られている．それらはすべて運動量について４次の第一積分を持つ．

$$V_3 = q_1^2 q_2 + \frac{16}{3} q_2^3 \tag{38}$$

$$V_3 = \frac{i\sqrt{3}}{9} q_1^3 + q_1^2 q_2 + 2 q_2^3 \tag{39}$$

$$V_4 = q_1^4 + 6 q_1^2 q_2^2 + 8 q_2^4 \tag{40}$$

J. Hietarinta [1] によれば運動量について高々４次の第一積分を持つ５次式以下の２次元同次多項式ポテンシャルは以上のものにつきる．また中川克也 [7] は運動量について高々４次の第一積分を持つ任意次数の同次多項式ポテンシャルも以上のものしかないことを示している．以上の既知の可積分な同次式ポテンシャルでの固有値λの値（取りうる異なる値を列挙）は以下のように計算される．

- 直交座標分離：$V_k = A q_1^k + B q_2^k$

$$\lambda = (0, k-1) \tag{41}$$

- 極座標分離：$V_k = (q_1^2 + q_2^2)^{k/2}$

$$\lambda = (1) \tag{42}$$

- 放物線座標分離：$V_k = \sum_{m=0}^{[k/2]} 2^{k-2m} \frac{(k-m)!}{m!(k-2m)!} q_1^{2m} q_2^{k-2m}$

$$\lambda = \left(\frac{k-1}{2k}, k+2 \right) \tag{43}$$

- $V_3 = q_1^2 q_2 + \frac{16}{3} q_2^3$

$$\lambda = \left(\frac{1}{8}, 15 \right) \tag{44}$$

- $V_3 = \frac{i\sqrt{3}}{9} q_1^3 + q_1^2 q_2 + 2 q_2^3$

$$\lambda = \left(\frac{1}{3}, \frac{10}{3}, 15 \right) \tag{45}$$

- $V_4 = q_1^4 + 6 q_1^2 q_2^2 + 8 q_2^4$

$$\lambda = \left(\frac{3}{8}, 3, 21 \right) \tag{46}$$

以上の可積分なポテンシャルを対応する Gauss の超幾何方程式が全て可約となる場合，および Schwarz の表に適合する場合に応じて分類することは意味があるだろう．直交座標分離および極座標分離されるポテンシャルはすべて可約，そして放物線座標分離されるポテンシャルは正２面体の系列に対応し，いずれも無限系列を構成する．３次の同次式ポテンシャル (38) は正４面体に対応する．正４面体，正８面体，正２０面体は $k = 3, 4, 5$ 次の同次式ポテンシャルでのみ現れうるが，正８面体および正２０面体に関連するポテンシャルは見つかっていない．また残された (39) および (40) での固有値λの値は正２面体のそれである．今のところこれらは孤立した可積分系のような印象を与えるが，実は正２面体に対応する新たな可積分系の無限系列の例であると考えるに足る十分な状況証拠がある．残念ながらその予想される新系列での $k = 5, 6, 7, \ldots$での例は未発見である．以上の考察をまとめると以下のような可積分な同次多項式ポテンシャルの「周期律表」が得られる．この周期律表の未発見な箇所を埋めていくのが今後の課題である．

無限系列

	可約	正2面体	正2面体a
$k=3$	$Aq_1^3+Bq_2^3$	$q_1^2q_2+2q_2^3$	$\frac{i\sqrt{3}}{9}q_1^3+q_1^2q_2+2q_2^3$
$k=4$	$Aq_1^4+Bq_2^4$ $(q_1^2+q_2^2)^2$	$q_1^4+12q_1^2q_2^2+16q_2^4$	$2q_1^4+12q_1^2q_2^2+16q_2^4$
$k=5$	$Aq_1^5+Bq_2^5$	$3q_1^4q_2+16q_1^2q_2^3+16q_2^5$	未発見
$k=6$	$Aq_1^6+Bq_2^6$ $(q_1^2+q_2^2)^3$	$q_1^6+24q_1^4q_2^2+80q_1^2q_2^4+64q_2^6$	未発見
$\vdots$	$\vdots$	$\vdots$	$\vdots$

例外型

	正4面体	正8面体	正20面体
$k=3$	$q_1^2q_2+\frac{16}{3}q_2^3$	未発見	未発見
$k=4$	-	未発見	-
$k=5$	-	-	未発見

参考文献

[1] J. Hietarinta, A search for integrable two-dimensional Hamiltonian systems with polynomial potential, *Phys. Lett. A* **96** (1983) 273–278.

[2] I. Kaplansky, *An Introduction to Differential Algebra*, Hermann (1976).

[3] T. Kimura, On Riemann's equations which are solvable by quadratures, *Funkcialaj Ekvacioj* **12** (1969) 269–281.

[4] 河野實彦, 微分方程式と数式処理, 森北出版 (1998).

[5] J.J. Kovacic, An algorithm for solving second order linear homogeneous differential equations, *J. Symbolic Computation* **2** (1986) 3–43.

[6] J.J. Morales-Ruiz, and J.P. Ramis, A Note on the non-integrability of some Hamiltonian systems with a homogeneous potential, *Preprint* (1997).

[7] 中川克也, 運動量について4次の多項式第一積分を持つ2次元同次多項式ポテンシャル系, 本集録 (2000).

[8] H. Yoshida, A criterion for the non-existence of an additional integral in Hamiltonian systems with a homogeneous potential, *Physica D* **29** (1987) 128–142.

[9] 吉田春夫, 積分可能な同次式ポテンシャル系と Schwarz の3角形, 京都大学数理解析研究所講究録 **1070** (1998) 69–84.

[10] H. Yoshida, A new necessary condition for the integrability of Hamiltonian systems with a two dimensional homogeneous potential, *Physica D* **128** (1999) 53–69.

[11] 吉田春夫, 微分ガロア理論による可積分性の必要条件, 数理科学8月号 (1999) 41–49.

力学系における第1積分の非退化性の証明と特異点解析

A Proof of Non-degeneration of First Integrals in Dynamical System and the Singular Point Analysis.

2000.3.15

梅山女学園大学 生活科学部 生活社会科学科

石井雅治　Masaharu ISHII

Abstract

Here we considerd a dynamical system represented by ordinary differential equation in complex time domain,

$$\frac{dx(t)}{dt} = f(x(t)) \quad (x : \mathbf{C}-S_0 \to \mathbf{C}^n,\ f : \mathbf{C}^n - S_1 \to \mathbf{C}^n).$$

We showed that if n-1 first integrals exist, non-degenerative ones can be always chosen on the neighborhood of the singular points. From this result we can say that weak Painleve property is necesarry and sufficient condition of integrability on the neighborhood of the singular points without non-degeneration condition, and that infinitely many valuedness of first integral is classified into topological many-valuedness which is compatible with weak Painleve property and point many-valuedness which is not. Furthermore we show a possibility that topological many-valuedness brings non-chaotic behavior of the solution.

ここでは複素時間 t について定義された常微分方程式

$$\frac{dx(t)}{dt} = f(x(t)) \quad (x : \mathbf{C}-S_0 \to \mathbf{C}^n,\ f : \mathbf{C}^n - S_1 \to \mathbf{C}^n)$$

で表される力学系を対象とし、系の可積分性を通じて、解の特異点近傍での展開と、その挙動との関係を見ていく。1.で必要な基本的概念を説明し、2.,3.で得られた結果を示す。

1. 常微分方程式で表される力学系の可積分性

1.-1. 可積分性とは？

系が$U(\subset \mathbf{C}^n)$で“完全可積分”であるとは、U上で定義された1価または有限多価の解析関数で表される保存量（第1積分）が$n-1$個存在することとする。以下この第1積分を$\Phi_i\ (i=1,2,\cdots,n-1)$で表す。

可積分性は系の挙動を大きく制約する。**例**：流れがコンパクトな保存系では、通常、大域的に完全可積分な場合、周期運動が生じ、非可積分な場合、準周期運動やカオスが生じる。

Hamilton系については上記に加え、$\mathbf{C}^{n/2}-S$上で定義された1価または有限多価の解析関数で表される保存量（第1積分）が$n/2$個（$\Phi_i\ (i=1,2,\cdots,n/2)$）存在し、これらが$[\Phi_i,\Phi_j]_{PB}=0$を満たすとき、“Liouvilleの意味で可積分”であるという。このとき、$\Phi_i=c_i$が定める解析多様体上での積分演算によって、角積分とよばれる独立な保存量$\Phi_j\ (j=n/2+1,n/2+2,\cdots,n-1)$が得られる。

＊注意！：角積分は通常、無限多価となるので、大域的完全可積分性とLiouvilleの意味での可積分性はしばしば異なる。

1.-2. Painleve特性

系の解$x(t)$が複素平面上にもつ動く特異点(自励起系の場合、無限遠点以外の特異点)が全て極であるとき、系はPainleve特性をもつという。動く特異点が全て高々代数的であるとき、系は弱いPainleve特性をもつという。

極(代数的特異点)近傍での解の有理型(Puiseux)展開を(弱い)Painleve展開という。一般に高々代数的極から始まる解の展開において、任意定数の表れるtのべき次数に極の位数を加えた次数(すなわち最低次からの相対的次数)をKovalevskaja指数またはレゾナンス(通常両者は一致する)という。弱いPainleve展開が可能な場合、当然、Kovalevskaja指数は有理数となる。

(弱い)Painleve特性をもつ系が、しばしば可積分であることが知られている。実際、この特性を用いて多数の可積分系が発見されている。

例 :Kovalevskaja のコマ。

1.-3. 可積分性の非退化条件

相似不変系について、極あるいは代数的特異性をもつ特解の近傍 U (**Fig.1** 参照)で、積分が非退化条件

$$rank[\frac{\partial\Phi_1}{\partial x},\frac{\partial\Phi_2}{\partial x},\cdots,\frac{\partial\Phi_{n-1}}{\partial x}]\Big|_U = n-1$$

を満足するとき、弱い Painleve 展開が可能であり、Kovalevskaja 指数が有理数になることが知られている(吉田 1982)。逆に、弱い Painleve 展開が $n-1$ 個の任意定数を含むとき、これらの任意定数は U 上での 1 価解析的積分になることが分かっている(石井)。

Fig.1

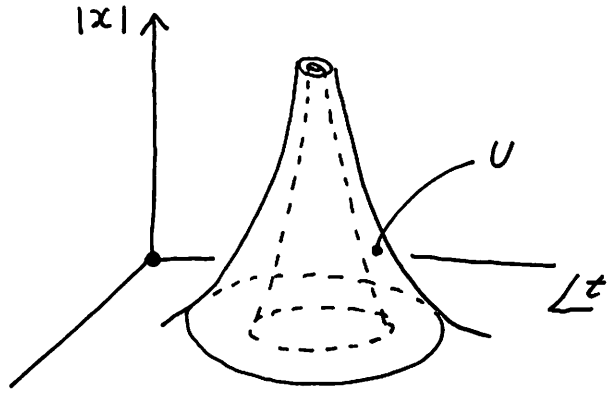

しかしこれらの結果を使って、系の可積分性を判定することはできない。解の弱い Painleve 展開が不可能な場合であっても、第 1 積分が存在しないのか、単に第 1 積分が退化しているのか、を区別できないからである。

1.-4. Painleve 特性をもたない可積分系

Liouville の意味で可積分な Hamilton 系はほとんど、弱い Painleve 特性をもつ。しかし例外的に、もたない系が見つかっている。

例 : Hamiltonian が

$$H=\frac{1}{2}(p_1^2+p_2^2)-\frac{1}{\varepsilon_1 q_1^2+\varepsilon_2 q_2^2}$$

である力学系は、第1積分

$$\Phi=(q_1p_2-q_2p_1)^2-\frac{2(q_1^2+q_2^2)}{\varepsilon_1q_1^2+\varepsilon_2q_2^2}$$

をもつ、すなわちLiouvilleの意味で可積分であるにも関わらず、
$\varepsilon_1/\varepsilon_2\le 1$のとき特解

$$(q,p)=(\sqrt[4]{2/\varepsilon_1}\,t^{1/2},0,\frac{1}{2}\sqrt[4]{2/\varepsilon_1}\,t^{-1/2},0)$$

の近傍で、Kovalevskaja指数に虚数のものが表れることが知られている。この系は弱いPainleve展開が不可能な可積分系である。
この特解上では非退化条件が成立しないことに注意。

結局、弱いPainleve展開の不可能性は、非退化条件のせいで可積分性の情報を与えないのであろうか？しかしこの特解の近傍で $\mu_1=\mu_2=1$
とおいて、角積分の漸近形を計算してみると、

$$\approx\log q_1^{-1}\pm\frac{1}{2i}\log q_2$$

となっていて、角積分が無限多価性をもつこと、すなわち系がこの近傍で完全可積分でないことが分かる。

2. 非退化条件

2.-1. 条件の成立

定理：極あるいは代数的特異性をもつ特解の近傍で系が完全可積分であれば、その近傍で非退化条件を満足するような第1積分を選ぶことができる。
(New !)

証明の概要：特異点の解の断片の近傍で非退化な局所的な積分$\phi_1,\phi_2,\cdots,\phi_{n-1}$をとる(必ず非退化に取れる)。これを解を含むループに沿って解析接続し出発した近傍に戻し、$\Gamma\phi_1,\Gamma\phi_2,\cdots,\Gamma\phi_{n-1}$とおく。元の積分を局所座標$\phi_1,\phi_2,\cdots,\phi_{n-1}$で表したものを、$\Phi_i'(\phi)$ $(i=1,2,\cdots,n-1)$とおくと、$\Phi_i'(\phi)=\Phi_i'(\Gamma\phi)$が成立する。これからほとんど至るところで、$\phi=\Gamma\phi$であることがいえる。さらに積分の関数としての連続性から、全体で$\phi=\Gamma\phi$が成立し、ゆえに積分$\phi_1,\phi_2,\cdots,\phi_{n-1}$は特解の近傍で定義された非退化な積分である。

結局、非退化条件は自動的に成り立ち、弱い Painleve 展開は常に系の可積分性の情報を与えていることが分かる。また次に述べるように、そもそも非退化条件なしで、完全可積分系は弱い Painleve 展開を許すのである。

2. -2. 条件の除去(代数的場合と解析的場合)

代数的場合の定理:完全可積分系の第 1 積分が代数関数であれば、解は弱い Painleve 展開が可能である。(さらに、この代数的に完全可積分であることと、適当な時間の変換の下で解が $n-1$ 個の任意定数を含む代数関数で表されることとは必要十分になる)(石井 1993)

この定理は非退化条件を仮定しないものの、第 1 積分が代数関数に限られ、Hamilton 系の解析には事実上利用できない。角積分は一般に代数関数では表せないからである。

解析的的場合の定理: 系が特解の近傍で完全可積分であれば、解は弱い Painleve 展開が可能である。(New !)

証明の概要:まず、特異点近傍での解の挙動を $\mathbf{P}''(\mathbf{C})$ の通常点近傍での 1 次元多様体と見て、この多様体近傍で積分を Weierstrass 多項式で表し、代数的手法により元の常微分方程式を 1 変数の代数型常微分方程式にリダクションする。この変数に関する分岐べき級数展開を用いて、リダクションされた微分方程式における動く特異点の型が代数的であることを示す。

この定理では、非退化条件を仮定せず、また第 1 積分の型にも制限がないので、Hamilton 系を含む広いクラスの系について、弱い Painleve 展開から可積分性の情報を得ることができる。さらに、この定理は、続く 3.で述べるように無限多価第 1 積分を分類する原理となる。

2.-3. Painleve 展開の必要十分条件

以上から、あらかじめ非退化条件を仮定することなしに、一般に、解が特解の近傍で $n-1$ 個の独立な任意定数を含んで弱い Painleve 展開可能であることと、その近傍で系が完全可積分であることとは必要十分になる。結局、弱い Painleve 展開可能性とは特解近傍での完全可積分性のことなのである。

3. 点無限多価性とトポロジカル無限多価性

3.-1. 無限多価性の分類

点無限多価性:解析的場合の定理の対偶から、系が弱い Painleve 特性をもたないとき、代数的特異点を持つ特解の近傍で、少なくとも1つの第1積分は無限多価になっていることがいえる。このような近傍での無限多価性を、以下“点無限多価性”とよぶ。

例示した Hamilton 系は、実際に点無限多価性をもち、そのため弱い Painleve 特性をもたなかったのである。非退化条件が成立しなかったのがその理由ではない。

トポロジカル無限多価性:代数的特異点を持つ特解の近傍では、第1積分が解析的または代数型であるにも関わらず、例えば **Fig.2** の例のように大域的な定義域のトポロジーから無限多価性が生じる場合がある。このような、点無限多価ではない無限多価性を、以下“トポロジカル無限多価性”とよぶ。 **例**:楕円積分(**Fig.2** 参照)

Fig.2

$$f(x)=\int_{x_0}^{x}\frac{dx}{\sqrt{1-x^3}}$$

積分路として Γ_1,Γ_2 のどちらを選ぶかで値が異なるにも関わらず、特異性は代数的。

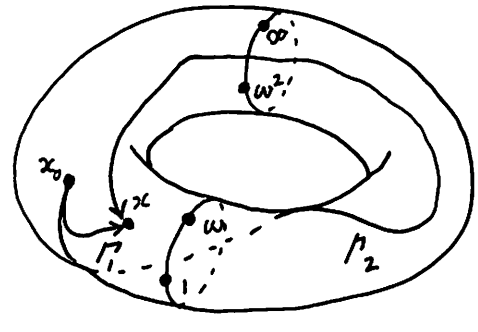

準周期運動は第1積分のトポロジカル無限多価性によって生じるが、この無限多価性は弱い Painleve 展開を許容する。そのため、通常、Liouville の意味で可積分な Hamilton 系は弱い Painleve 特性をもつのである。

3.-2.特異点配置と挙動

特異点の近傍での解の展開を使って、複素t平面上で特異点を区別して目印を付け、その配置を表すことができる。特異点配置は系の可積分性に応じて制約されるので、特異点配置を通して系の可積分性と系の挙動をある程度結びつけることができる。特異点配置とは例えば次の **Fig.3** に示す配置であって、△、○、×、□ の各記号は、異なった解の展開に対応する特異点を示す。

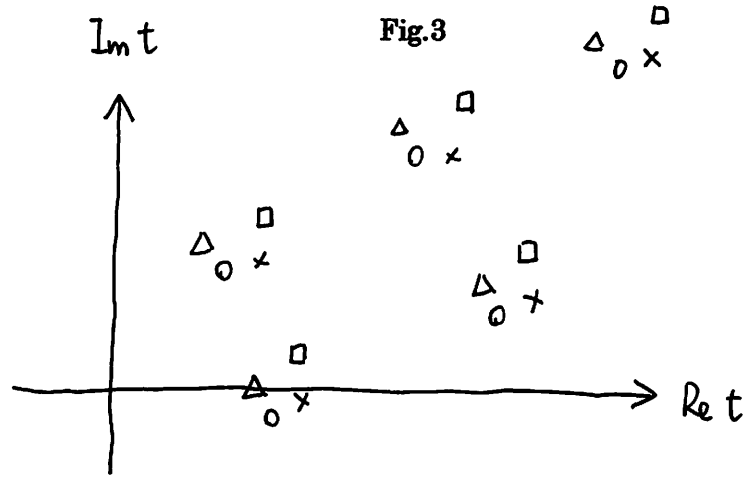

Fig.3

命題：系が特異点近傍だけでなく、大域的に、すなわち$\mathbf{C}''$のほとんど至るところで、完全可積分であるとき、特定の解の展開に対応する特異点が2個以上あれば、全体的な特異点配置は周期的(2次元的な場合もある)である。従って系の挙動は周期的である。
(New ?)

特定の解の展開が含む任意定数$c_1, c_2, \cdots, c_{n-1}$は第1積分の大域性から常に同一である。原点近傍$U(0)$での、その解の展開を、$x(t; c_1, c_2, \cdots, c_{n-1})|_{U(0)}$で表せば、2つの特異点$t = t_1$と$t = t_2$の近傍$U(t_1)$と$U(t_2)$上での展開は、$x(t - t_1; c_1, c_2, \cdots, c_{n-1})|_{U(t_1)}$、$x(t - t_2; c_1, c_2, \cdots, c_{n-1})|_{U(t_2)}$と表せる。すなわちそれらは$U(t_1)$と$U(t_2)$上で同一の関数を与える。従って、その2つの特異点を結ぶ直線方向に解を解析接続して行けば、$t = t_2 + (t_2 - t_1)$が特異点と

なってまた同じ展開 $x(t-(t_2+(t_2-t_1));c_1,c_2,\cdots,c_{n-1})|_{U(t_2+(t_2-t_1))}$

が表れる。他の特異点は、$t=t_2+(t_2-t_1)$ の特異点から派生的に同一配置で生じるので、全体的な特異点配置は周期的になる。

3.-3. トポロジカル無限多価系の特異点配置と挙動

トポロジカル無限多価性をもつ完全可積分系は、大域的に完全可積分な系とは異なり、特定の解の展開が含む任意定数が、その解の展開が位置する複素 t 平面上の場所によって異なり得る。すなわち、特異点 $t=t_1$ の近傍 $U(t_1)$ の解の展開 $x(t-t_1;c_1,c_2,\cdots,c_{n-1})|_{U(t_1)}$ を解析接続して行き同じ解の展開が表れるとしても、第1積分の無限多価によって任意定数が一般に $c_1,c_2,\cdots,c_{n-1}$ から $c_1',c_2',\cdots,c_{n-1}'$ へと変化し、$U(t_2)$ 上の解の展開は $x(t-t_2;c_1',c_2',\cdots,c_{n-1}')|_{U(t_2)}$ となってしまうのである。この場合にも第1積分が次の条件を満足すれば、特異点配置が分かるものと思われる。

$U(t_1)$ 上の解の展開の近傍 $V(x(t_1))(\subset \mathbf{C}^n)$ で定義された第1積分 ϕ を、解に沿って解析接続して行き、解が再び同じ解の展開の近傍に到達したときに、そこまで接続された第1積分を $\Gamma\phi$ とおく(このような接続は必ずできる)。ϕ と $\Gamma\phi$ が定義域をずらしただけの同一の関数であるとき、ここでは解析接続が推移的であるとよぶ。明らかに大域的第1積分の解析接続は推移的である。

命題：トポロジカル無限多価性をもつ完全可積分系の第1積分の解析接続が推移的であるとき、特定の解の展開に対応する特異点が2個以上あれば、この特異点の配置は周期的(2次元的な場合もある)である。従って全体的な特異点配置は準周期的になり、系の挙動は準周期的である。

解析接続の推移性によって、特定の解の展開に対応する特異点の近傍での解の1次元多様体としての形状が同一であるので、この命題が成立するものと思われるが、証明はまだできていない。

Liouville の意味で可積分な Hamilton 系では、しばしば準周期

運動が生じるが、この場合は明らかに第1積分の解析接続は
推移的であり、命題が成立している。

一般に体積保存系であって、トポロジカル無限多価性をもつ完
全可積分系では、解析接続の推移性か、それに近い事態が生じ、
その挙動は準周期運動に近いものになると思われるが、まだ
はっきりしない。

4. 結論と課題

結論

A. 第1積分の非退化条件は自動的に成立する。
B. 第1積分の非退化条件なしに、弱い Painleve 展開が特異点回りの可積分性の必要条件になる
C. 解が特解の近傍で十分な数の任意定数を含んで弱い Painleve 展開可能であることと、系がその近傍で完全可積分であることとは必要十分である。
D. 系が弱い Painleve 特性をもたないとき、代数的特異点を持つ特解の近傍で第1積分は無限多価になっている。
E. 第1積分の多価性は点無限多価性とトポロジカル無限多価性に分類される。

F. 体積保存系であって、トポロジカル無限多価性をもつ完全可積分系では、その挙動は準周期運動に近いものになると思われるが、まだはっきりしない。

課題

A. トポロジカル無限多価系の挙動が非カオス的であることを一般的に示す。
B. A.から、点無限多価性がカオスの必要条件になっていることが導かれるはずであり、カオスを特異点回りの現象として解析する。

多自由度ハミルトン系における共鳴近傍の力学

Dynamics near Resonance in Hamiltonian Systems with Many Degrees of Freedom

平田 吉博*
名古屋大学大学院理学研究科
Yoshihiro Hirata
Department of Physics, Nagoya University

概 要

Newton に始まる運動方程式の研究の大きな流れは，今世紀，正確にいうと前世紀の末から解析学的なアプローチから幾何学的なアプローチへと手法を変えつつある．本稿では，ハミルトン力学系の非線形共鳴近傍の力学を解析する幾何学的方法と，その多次元化の試みについて紹介する．この多次元化は 20 世紀の力学研究の重要な積み残しであり，20 世紀最後の年である今年中にどこまで解決できるか，今後の動向に注目である．

1 はじめに

マクロなスケールにおける運動法則を記述する方法として，Newton 力学を用いるのは現在では当たり前のことである．Newton の運動方程式は，もはや実験精度の中で間違いのないものとされており，またその取り扱いの方法として，Lagrange, Euler, Hamilton, Poisson, Jacobi らによる現代的な解析力学も完成されたものといってよいだろう．

では，与えられた物理現象を記述する方程式が得られれば，それは運動がすべて理解されたことになるのであろうか？ もちろん運動方程式を見るやいなやその一般解が得られる場合もある．簡単に一般解が得られなくとも，ある種の特殊な能力を持つ人は，頭の中で運動方程式を長時間にわたって数値積分できたりするかも知れない．しかし，大多数の人にとってそれは不可能であろう．つまり運動方程式を書き下してそれで終わり，ということでは物理としてはやりっぱなし，ということになる．物理屋としては運動方程式を書いたら，そこから実際の運動を論じる必要があろう．

もちろん，運動方程式の一般解が得られるような場合は問題ない．解く方法としては，Hamilton–Jacobi の方法 [1] が有名である．初等関数で解が得られてしまえば，あとはプロットするなり眺めるなりすれば，長時間の運動も理解できる．運動方程式が初等演算の有限回の反復により解ける場合，その系は可積分系と呼ばれる．

問題は，初等演算によって解けない場合である．そのような系が存在することは，実は前世紀に Liouville, Poincaré によって示されている．しかもその後の研究により，解けない系，つまり非可積分系がほとんどである，と考えられている．さらに今世紀の電子計算機の発達により，非可積分

*E-mail: yhirata@allegro.phys.nagoya-u.ac.jp

系は微分方程式で記述される決定論的な法則に従うにも拘らず，長時間後の振舞いは予測不可能で，確率的でさえあることもわかってきた．これが力学系のカオス現象である．

力学系がカオスになっているとき，一般にすぐ近くの初期値からスタートした2つの軌道は，時間と共に指数的に遠ざかっていく．つまり，1つのカオス軌道を追いかけただけでは，すぐ隣りの軌道について長時間後の振舞いは何もわからないといっていい．そして我々はすべての初期値についてくまなく相空間内をサーチすることはできないので，例えどんなに速い計算機を使ったところで，相空間の全域の状態を知ることはできないことになる．

そのため力学系がカオスである場合，幾何学的な取り扱いが重要である．つまり解軌道を解析学的に構成することは不可能であるため，相空間の幾何学的構造から定性的に力学を理解するという方法である．このアプローチは Poincaré に始まり，かの Arnold はその著書 [2] に「ハミルトン力学—それは相空間の幾何学である」と記している[1]．そして今世紀の力学研究は，ほとんどといっていいほどこの流れにある [3].

しかし数多くの研究論文が産まれる中で，意外に基本的なことが知られていないということも事実である．ハミルトン系カオスの研究者は，普段当然のような顔をして N 自由度ハミルトン系のかわりに $(2N-2)$ 次元シンプレクティック写像を使っている．しかし，ハミルトン系の Poincaré 写像はシンプレクティック写像になる，ということ以上のことを知らない[2]．多自由度系の Poincaré 写像は，2 自由度系の Poincaré 写像（すなわち面積保存写像）の直積に小さな摂動が加わったもの，と安易に考えがちである．例えば，3 自由度ハミルトン系の Poincaré 写像のモデルとして，Froeschlé 写像

$$
\begin{cases}
I_1' &= I_1 + a\sin\theta_1 + c\sin(\theta_1+\theta_2), \\
\theta_1' &= \theta_1 + I_1', \\
I_2' &= I_2 + a\sin\theta_2 + c\sin(\theta_1+\theta_2), \\
\theta_2' &= \theta_2 + I_2',
\end{cases}
\tag{1}
$$

$c \ll a \ll 1$ はよく用いられるが，この写像を考える根拠は今一つはっきりしない[3].

以上の反省を踏まえ，来たるべき 21 世紀に備えるべくこの問題にとりかかる．**N 自由度ハミルトン系と $(2N-2)$ 次元シンプレクティック写像の関連を明らかにする**，ということだ．Poincaré 写像を解析的構成することは一般にはできない[4]が，これを近似的に行なう．このために非線形共鳴近傍を考える．非線形共鳴近傍では遅い運動と速い運動がよい近似で分離できる．このことを用いて，ある自由度に対して運動方程式を積分し，近似 Poincaré 写像を構成する．よしんば，これまでの多自由度ハミルトン系の研究を正当化しよう，という試みである．またこのことにより，非線形共鳴近傍のダイナミクスを系統的に調べることができ，一石二鳥である．

本節の最後に，本稿の構成について述べる．次節において，ハミルトン系の基本的な内容について復習し，問題を提起する．3 節が本稿のメインである．非線形共鳴の定義と意味について述べたあと，具体的な計算をお見せする．自由度 3 の場合については単純な例を示し，Froeschlé 写像(1)は決して自由度 3 のダイナミクスを代表しないことをみる．最後に 4 節において内容をまとめ，今後の方針についても議論する．内容はこの分野の素人の方にも読めるよう努力したが，もし不十分な点などがあったら文献を参照されたい．

---

[1] Arnold はそういうつもりで書いたのではないかも知れない．ここでは都合のいいように拡大解釈させて頂く．

[2] もちろんこれは筆者の反省の弁である．尚，カオスが生じる上で最も簡単な $N=2$ の場合は 1979 年に Chirikov の論文 [4] がある．

[3] Froeschlé は原論文 [5] で Arnold の提案であるといっているが，そこに引かれている参考文献は Hénon への私信であり，手に入れることは困難であると思われる．

[4] もしそんなことができるなら，Poincaré 写像をとる自由度は変数分離可能ということになる．それならその自由度は始めから考えなければよい．

2 ハミルトン系の復習

本節では，ハミルトン系の初等的な性質について復習する．ただし全般的なレビューではなく，次節以降で必要となる内容のみに限らせて頂く．不十分な点は，文献 [1] を参考にして頂きたい．

2.1 ハミルトン系と正準変換

N 自由度ハミルトン系は，ハミルトニアン $H = H(q,p)$, $q,p \in R^N$ を用いて，

$$\frac{dq}{dt} = \frac{\partial H}{\partial p}, \quad \frac{dp}{dt} = -\frac{\partial H}{\partial q} \tag{2}$$

によって定義される．各成分を書くときには $q = (q_1, \ldots, q_N)$ 等，下付き添字を用いる．相空間上の関数 F, G に対する Poisson 括弧を，$\{F,G\} = \sum_{j=1}^{N} \left(\frac{\partial F}{\partial q_j}\frac{\partial G}{\partial p_j} - \frac{\partial F}{\partial p_j}\frac{\partial G}{\partial q_j} \right)$ により定義する．

ハミルトン系の性質の内で最も基本的なものはシンプレクティック性である．運動方程式(2) の解軌道を $(q(t),p(t))$ とする．このとき，

$$\sum_{j=1}^{N} dq_j(t) \wedge dp_j(t) = \sum_{j=1}^{N} dq_j(0) \wedge dp_j(0) \tag{3}$$

が従う．これは $(q(0),p(0))$ から $(q(t),p(t))$ への時間発展（すなわち任意の時間発展）が正準変換になっていることを表す．

2.2 可積分系

以上の準備の下，可積分系を定義する．

定理 1 (Liouville) ハミルトン系(2) にハミルトニアン以外に $(N-1)$ 個の独立な一価解析的第一積分[5] $\Phi_1, \ldots, \Phi_{N-1}$ が存在したとする．$\Phi_N = H$ とかく．これら N 個の第一積分は包合系をなすとする．すなわち，$\{\Phi_i, \Phi_j\} = 0, \forall i,j$．このときハミルトン系(2) は求積操作[6]により求積可能である．

ハミルトン系とは限らない一般の力学系の場合，$(n-1)$ 個の第一積分の存在により n 階微分方程式が求積される．ハミルトン系においては，ハミルトニアンを含め $(2N-1)$ 個の積分が必要であるが，シンプレクティック性からそれよりも少ない数の第一積分が求積可能性を保証するのである．証明は，N 個の包合的積分を用いて残りの $(N-1)$ 個の積分を構成することによりなされる．

定理 1 を用いて以下の定義をする：

定義 1 ハミルトン系(2) に N 個の包合的一価解析的積分 $\Phi_1, \ldots, \Phi_{N-1}, \Phi_N (= H)$ が存在するとき，このハミルトン系は**可積分**[7]であるという．

$N = 1$ の場合はハミルトニアンが第一積分であるためいつも可積分である．よって我々カオスの研究者が問題にするのは $N \geq 2$ の場合である．

---

[5] 第一積分とはいわゆる保存量のこと．すなわち，$\frac{dF}{dt} = 0$ なる定数でない関数．ちなみに，第一積分以外に，積分，保存量，運動の恒量などとも呼ばれる．

[6] 四則演算，微分演算，不定積分演算，逆関数演算，超越方程式も含め微分方程式以外の方程式を解く演算，およびそれらの有限回の反復．

[7] より正確には，Liouville の意味での可積分と呼ばれる．

定義1により可積分ハミルトン系が定義されたが，この定義の幾何学的意味を与えるのがArnold–Jostの定理である．定理の主張を述べる前に若干の言葉の準備をする．可積分系の各積分の値を一定に定めた相空間の部分集合，すなわち $M_a = \{(q,p) \in R^{2N} \mid \Phi_j(q,p) = a_j, j = 1,\ldots,N\}$ は N 次元多様体であり，(a に関する) レベル多様体と呼ばれる．また，$T^N = (S^1)^N = (R/2\pi Z)^N$ を N 次元トーラスと呼び，その上の運動のうち閉じないものを準周期運動と呼ぶ．

定理 2 (Arnold–Jost) 可積分ハミルトン系のレベル多様体がコンパクトかつ連結であるとする．さらに，各積分の勾配ベクトル $\nabla\Phi_j$ がレベル多様体の各点で一次独立であるとする．このときレベル多様体は N 次元トーラス T^N のトポロジーをもち，軌道はそれに巻き付く周期運動または準周期運動になる．

このように，可積分ハミルトン系の相空間は極めて規則的である．上の仮定の一次独立性は，一般にはほとんど至るところで満たされるため，$2N$ 次元相空間は N 次元トーラスにより稠密に埋めつくされ，その中の軌道の振舞いは高々準周期運動である．図1を参照されたい．トーラス上の運動は，これから述べる作用・角変数による表現がわかりやすい．正確な定義は参考文献に譲ることとし，ここでは定性的な内容のみ述べる．すなわち，適当な正準変換 $(q,p) \mapsto (\theta, J)$ により，ハミルトニアンを作用変数 J のみの関数にすることができる．このとき $\theta \in T^N$ であり，J はトーラスの一般化された半径を，θ はその上での回転の位相を表現する．J で書き換えられたハミルトニアンを同じ記号を用いて $H(J)$ と書くと，運動方程式は

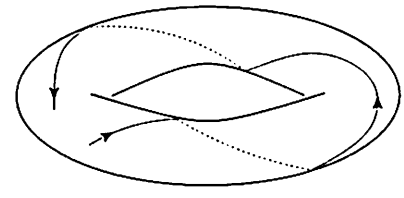

図 1: 2次元トーラス T^2 とそれに巻き付く軌道．

$$\frac{d\theta}{dt} = \frac{\partial H}{\partial J}, \quad \frac{dJ}{dt} = -\frac{\partial H}{\partial \theta} = 0 \tag{4}$$

となり，第2式は即座に積分され作用変数は第一積分，角変数は一様な回転を表すことがわかる．

定理2の最後にある，周期運動・準周期運動について少し触れておこう．運動方程式(4)に現れる $\partial H/\partial J$ を $\omega(J)$ と書き，回転数ベクトルと呼ぶ．$N = 2$ の場合，$\omega = (\omega_1, \omega_2)$ の各成分の比 ω_1/ω_2 が有理数である場合，トーラス上の任意の軌道は有限時間で閉じ，トーラスは周期軌道の1-パラメータファミリーを与える（図2左）．つまり，トーラス上の運動が可約である．このようなトーラスを共鳴トーラスと呼ぶ．対して $\omega_1/\omega_2 \in R\backslash Q$ であるとき，トーラス上の軌道は閉じず，トーラスを稠密に埋め尽くす無限周期の軌道を与える（図2右）．この軌道を準周期軌道と呼び，トーラスは非共鳴であるといわれる．これら共鳴トーラスと非共鳴トーラスは，摂動下での振舞いが大きく異なる．このことに関しては次小節で論じることにする．

以上のように，可積分ハミルトン系の相空間の構造は完全にわかっているといっても過言ではない．そこに摂動を加えた近可積分ハミルトン系の相空間はどうなっているのであろうか？ これがPoincaré曰く力学の基本問題[6]である．

2.3 近可積分系

N 自由度近可積分ハミルトン系を，ハミルトニアン

$$H = H^{(0)}(J) + \epsilon H^{(1)}(J,\theta) + \epsilon^2 H^{(2)}(J,\theta) + \cdots \tag{5}$$

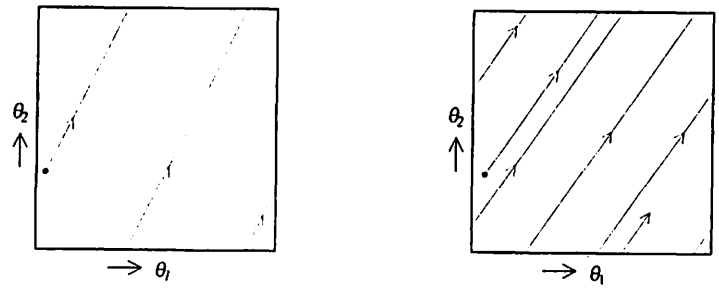

図 2: T^2 上の周期軌道（左）と準周期軌道（右）．T^2 を切り開き，長方形にして示す．

に対する運動方程式

$$\frac{d\theta}{dt} = \frac{\partial H}{\partial J}, \quad \frac{dJ}{dt} = -\frac{\partial H}{\partial \theta} \tag{6}$$

によって定義する．ここで $J \in D \subset R^N$, $\theta \in T^N = (R/2\pi Z)^N$, $0 < \epsilon \ll 1$ である．$\epsilon = 0$ のとき，ハミルトン系(6) は可積分ハミルトン系(4) に一致する．すなわち，可積分からの小さな摂動を考えていることになる．Poincaré は，ハミルトン系(6) は若干の仮定の下，ハミルトニアン以外に解析的第一積分が存在しないことを示した[8]．このように(5) 式の形のハミルトニアンを考えていれば，もし偶然ある特定の値 $\epsilon = \epsilon_0$ で可積分であっても，ϵ の値を少し動かしてやれば非可積分になるので，安心して近可積分系の解析ができるわけである．ただし，上で述べた「若干の仮定」というものが，現実に判定するのが難しいということを付け加えておく．我々は，ほとんどの摂動系がカオスになることを経験的に知って（感じて）いるので，ここではあまりこだわらないことにする．

摂動系の相空間の構造についての最初の結果は，1950 ~ 60 年代における**KAM 理論**[7] であろう．Kolmogorov と Arnold は解析的なハミルトニアンについて，Moser は有限階微分可能なハミルトニアンや写像系について，可積分系のトーラスの摂動下における安定性について論じた．3 人の頭文字をとって KAM である．

最も簡単な 2 自由度系に限って，KAM 理論の大筋を見てみよう．まず共鳴トーラスは，摂動下では一般に存在し得ないことが簡単に示される．KAM 理論ではフーリエ変換と正準変換を用いてハミルトニアンを作用変数のみの関数に変換するのであるが，その際に回転数ベクトル ω と整数ベクトル k の内積 $\omega \cdot k$ が分母に現れる．整数ベクトル k はフーリエ変換によって生じるため，$Z\backslash\{0\}$ をくまなく動く．よって共鳴トーラスでは，分母に 0 が現れることになり，変換が意味をもたない．これは，摂動により共鳴トーラスが壊れることを意味する．

一方，非共鳴トーラスでは $\omega \cdot k \neq 0$ であるが，k を選べば $\omega \cdot k$ は任意に小さくできる．これは**小分母の問題**と呼ばれる．小分母の存在は，摂動展開級数の収束性を著しく悪くするが，KAM の 3 人により，非共鳴トーラスの内の大部分[9]は壊れず生き残ることが示された．生き残りの条件は，回転数ベクトル ω の各成分の比 $\omega_1/\omega_2 (\in R\backslash Q)$ が有理数で近似しにくい無理数であること，すなわち Diophantine 数であることである．この結果は，トーラスの生き残りについては，摂動の詳細よりも可積分系における数論的な性質が重要であることを示唆しており，大変興味深い．

また，摂動で壊れた共鳴トーラス上の周期軌道の内，いくつかのものは線形安定な周期軌道として残り，同数の線形不安定な周期軌道が存在することも示される（**Poincaré–Birkhoff の定理**）．線形不安定な周期軌道の近傍においては，一般にホモ（ヘテロ）クリニックカオスが発生する．共

[8] J, θ, ϵ のすべての変数に対して解析性をもつ第一積分の非存在である．すなわち，特定の値 $\epsilon = \epsilon_0$ での可積分性を否定しない．

[9] Lebesgue の意味で測度有限．

鳴トーラスは近傍のトーラスを巻き込んで，いわゆるカオス層を形成するのである．共鳴はカオスの起源であり，これを調べることは重要な問題である．

このように，共鳴トーラスを調べることは近可積分系のカオスを調べる上で非常に重要であり，これを系統的に調べる手段として Birkhoff-Gustavson 標準形 [8] などが有名である．しかし，運動の詳細を知る，という意味では不十分である．共鳴近傍の運動を幾何学的に理解することが本稿，そして今後の我々の研究の大目標である．

2.4 多自由度系

2.2 節において，1 自由度ハミルトン系はいつも可積分であることを見た．よってカオスが生じるためには最低でも 2 自由度が必要であるが，自由度 2 と 3 の系では相空間の構造が大きく違うことを見ておく．

まず自由度 2 の場合，相空間の次元は 4 であるが，エネルギー積分の存在により軌道は 3 次元超曲面上に拘束される．一方 KAM トーラスは 2 次元であり，エネルギー超曲面に対し余次元 1 である．すなわち，トーラスはエネルギー曲面をその内側と外側に仕切る．よって 1 つのカオス軌道は，トーラスとトーラスに仕切られた領域しか動くことができない．

一般に自由度 N の場合，相空間は $2N$ 次元でありエネルギー曲面は $(2N-1)$ 次元，KAM トーラスは N 次元であるため，トーラスのエネルギー曲面に対する余次元は 2 以上である．よってトーラスは軌道の障壁とはなり得ない．つまり可能性でいえば，1 つの軌道はカオス層をつたって，相空間のあらゆる領域へ行くことができる．このようなことを踏まえ，我々は自由度 2 と 3 以上を分けて考えることが多い．今後多自由度系といった場合，自由度 3 以上の系のことを指す．

2.5 Poincaré 写像

ここで，本稿のもう 1 つのキーワードとなるPoincaré 写像について触れておく．ハミルトン系においてはカオスが生じるためには最低でも 2 自由度が必要であるが，その場合にさえも相空間の次元としては 4 次元ということになり，視覚に基づく理解は困難である．この困難を回避し，しかも本質を失なわず解析を行なうために用いられる手法が Poincaré 写像である．これは相空間の中に断面を用意し，軌道がその断面を一方から他方へと横切る点のみに注目するという方法である．以下に，N 自由度ハミルトン系における Poincaré 写像の作り方を簡単に説明する．

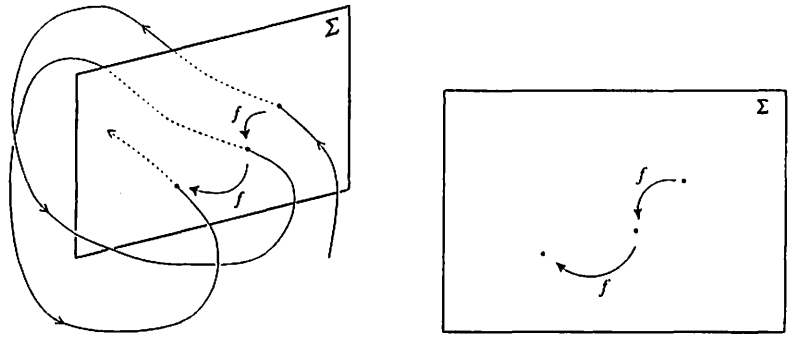

図 3: エネルギー超曲面内の軌道と Poincaré 断面 Σ（左）．Σ 上の Poincaré 写像 f（右）．

自励ハミルトン系の場合，エネルギー積分がいつも存在するため，軌道は $(2N-1)$ 次元超曲面

に拘束されることになる．この超曲面内に $(2N-2)$ 次元超平面を適当に選ぶ[10]．「適当に」の意味は，もちろん興味ある軌道と交差し，しかも横断的に交差するものを選ぶという意味である．この超平面は Poincaré 断面と呼ばれる．エネルギー曲面がコンパクトである場合，ほとんどの軌道はこの超平面と無限回交わり，ある交点から次の交点は一意的に定まる．つまり $(2N-2)$ 次元超平面上の離散力学系が構成されるわけである．この離散力学系を Poincaré 写像と呼ぶ（図 3 参照）．特に $N=2$ の場合，Poincaré 写像は 2 次元写像であり，視覚的に理解するのに都合がよい．

このとき重要であることは，得られた Poincaré 写像がシンプレクティック性を持った写像，いわゆるシンプレクティック写像になる，ということである．数学的に表現すれば，$q_N = \text{const.}, p_N > 0$ で定義された Poincaré 写像 $(q,p) \mapsto (q',p')$ に対して，

$$\sum_{i=1}^{N-1} dq_i' \wedge dp_i' = \sum_{i=1}^{N-1} dq_i \wedge dp_i \tag{7}$$

が成り立つ，ということである．ただし，$q=(q_1,\ldots,q_{N-1})$ 等とおいた．性質(7)（又は(3)）は直感的には理解しにくいが，$N=2$（(3) 式のようにハミルトン系の場合は $N=1$）に対しては，向きも含めた面積保存性（図 4）を表す．多次元の場合は，相空間の与えられた領域の各正準面（(q_i,p_i) 面）への射影面積の和が保存する．

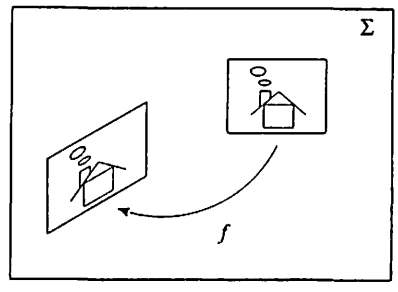

図 4: 向きも含めた面積保存性．

このように Poincaré 写像は相空間の次元を 2 つ落として，ハミルトン系の基本的な性質であるシンプレクティック性を損わない．これがハミルトン系の解析で Poincaré 写像がよく使われる理由である．$(2N-2)$ 次元シンプレクティック写像を N 自由度ハミルトン系と呼ぶ研究者もいるほどである．ただしこれには若干注意を要する．ハミルトン系とシンプレクティック写像の関係はそれほど自明でないのである．カオスが生じる最も簡単な 2 自由度系の場合，共鳴近傍の力学が，標準写像と呼ばれる 2 次元シンプレクティック写像（面積保存写像）

$$\begin{cases} I' &= I + K\sin\theta, \\ \theta' &= \theta + I' \end{cases} \tag{8}$$

に縮約されることはよく知られている．しかし $N \geq 3$ の場合，シンプレクティック写像を使うにおいての指導原理は（筆者の知る限り）与えられていない．これまでの論文の多くは多自由度系の Poincaré 写像のモデルとして，いくつかの面積保存写像を準備し，それを弱い結合で結び付けたものを用いている[11]．この仮定は実際のところ如何なものであろうか？ これが本稿の主題である．

3 セパラトリクス写像の構成

ここから本論に入る．近可積分多自由度ハミルトン系の非線形共鳴近傍において Chirikov の方法 [4] を用い，近似的な Poincaré 写像を構成する．まず取り扱うハミルトニアンとその仮定について述べ，共鳴を定義する．その後，共鳴近傍において正準変換を行い，速い運動と遅い運動を分離する．遅い運動を積分することにより近似 Poincaré 写像を構成し，自由度 3 の場合について具体的な例を示す．構成された近似 Poincaré 写像のことをセパラトリクス写像と呼ぶ．

[10] 従って，エネルギー値は固定されることに注意．

[11] 筆者もこれまでそのような論文を何本か書いてきた．言い訳ではあるが，そのようなものでないとなかなか手がつけられないのである．

3.1 ハミルトニアンと仮定

ハミルトニアン

$$H(J,\theta) = H^{(0)}(J) + \epsilon H^{(1)}(J,\theta), \quad J \in D \subset R^N_{\geq 0}, \theta \in T^N, \quad 0 < \epsilon \ll 1$$

によって定義されるハミルトン系

$$\frac{d\theta}{dt} = \frac{\partial H}{\partial J}, \quad \frac{dJ}{dt} = -\frac{\partial H}{\partial \theta}$$

を考えよう．$H^{(0)}, H^{(1)}$ はそれぞれ $D, D \times T^N$ で解析的であるとする．特に摂動ハミルトニアン $H^{(1)}$ は，θ についてフーリエ級数展開可能であり，$H^{(1)}(J,\theta) = \sum_m H_m(J) e^{im\cdot\theta}$ とおく．和はすべての $m \in Z^N$ についてとる．

また $H^{(0)}$ に対しては，任意の $J \in D$ についてねじれ条件

$$\left| \frac{\partial^2 H^{(0)}}{\partial J_i \partial J_j} \right| \neq 0 \tag{9}$$

が成り立つものとする．ここで $J = (J_1, \ldots, J_N)$ と書いた．$\partial H^{(0)}/\partial J$ が回転数ベクトルを与えることから，(9) は可積分系の各トーラスが違った回転数を持つことを意味する．すなわちこれからの議論では，可積分系として調和振動子を選んではならない．近可積分系の多くの議論には，このねじれ条件が課される．

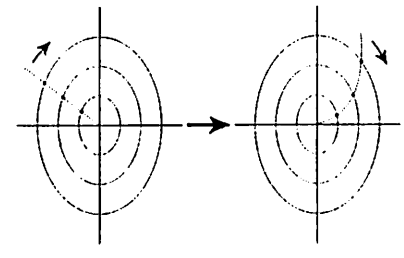

図 5: 2 自由度ハミルトン系の Poincaré 写像におけるねじれ条件．

3.2 共鳴

定義 2 (共鳴) $J^{(0)} \in D$ が共鳴であるとは，ある 0 でない $m \in Z^N$ が存在し，

$$m \cdot \omega(J^{(0)}) = 0 \tag{10}$$

が成り立つことである．

$N = 2$ の場合 $\omega = (\omega_1, \omega_2)$ として，(10) 式は $\omega_1/\omega_2 \in Q$ と同値である．すなわち，$J^{(0)}$ が 2.2 節で述べた周期軌道の 1-パラメータファミリーを表すトーラスを定めることになる．ねじれ条件(9)は，共鳴が存在し，かつ離散的であることを保証する．一般の N の場合，$\omega_1, \ldots, \omega_N$ のペアのうち，少なくとも 1 組が有理比であれば共鳴である．

$N = 2$ では共鳴するかしないかという区別しかないが，多自由度系において共鳴は，順番の入れ換えを除けば，分割数[12] $p(N)$ を用いて $(p(N) - 1)$ 個のタイプが考えられる．例えば $N = 3$ の場合 $p(3) = 3$ であり，

1. $\omega_1/\omega_2 \in R\backslash Q, \omega_2/\omega_3 \in Q$,
2. $\omega_1/\omega_2 \in Q, \omega_2/\omega_3 \in Q$

といった具合である．このうち本稿で我々が扱うものは上の 1 のタイプ，すなわち $i > j$ として，

$$\frac{\omega_i}{\omega_j} = \begin{cases} \dfrac{r}{s}, r, s \in Z, & \text{for } i = N-1 \text{ and } j = N \\ \alpha_{ij} \in R\backslash Q, & \text{otherwise} \end{cases} \tag{11}$$

[12] 自然数 N を N 以下のいくつかの自然数の和で表現する方法の数を分割数といい，$p(N)$ と書く．$p(N)$ は現在のところ，N の初等関数では表わされていない．

という，ある意味最も弱い共鳴である．この共鳴に限定する理由は，

- (11) 式のタイプの共鳴は，別のタイプに比べ圧倒的に多いこと，
- 別のタイプの解析は，これから使う方法では困難であること，

の 2 点である．また，ここでは技術的な問題で，$r = 1$ を仮定する．

3.3 正準変換

正準変換 $(J, \theta) \mapsto (\hat{J}, \hat{\theta})$ により，速い運動と遅い運動を分離しよう．正準母関数 $W(\hat{J}, \theta) = \sum_{j=1}^{N-1} \hat{J}_j \theta_j - (s\theta_{N-1} - \theta_N)\hat{J}_N$ を用いて，

$$J = \frac{\partial W}{\partial \theta}, \quad \hat{\theta} = \frac{\partial W}{\partial \hat{J}} \tag{12}$$

とする．このとき，

$$\dot{\hat{\theta}}_j = \dot{\theta}_j, \quad j = 1, \ldots, N-1,$$
$$\dot{\hat{\theta}}_N = \dot{\theta}_N - s\dot{\theta}_{N-1}$$

であり，$s\omega_{N-1} - \omega_N = \mathcal{O}(\epsilon)$ と $\dot{\theta}_j = \omega_j + \mathcal{O}(\epsilon)$ より，$\hat{\theta}_N$ は遅い回転を表すことがわかる．

また，変換(12) により摂動ハミルトニアン $H^{(1)}$ は，

$$H^{(1)} = \sum_m \hat{H}_m(\hat{J}) e^{im' \cdot \hat{\theta}}, \tag{13}$$

ここで，$m' = (m'_1, \ldots, m'_N) = (m_1, \ldots, m_{N-2}, m_{N-1} + sm_N, m_N)$ と変換される．さらに，$H^{(1)}$ は実関数であることから，$H^{(1)} = \hat{H}_0(\hat{J}) + \sum_{|m| \geq 1} \Lambda_m(\hat{J}) \cos(m' \cdot \hat{\theta})$ と書ける．ただし，$|m| = \sum_{j=1}^{N} m_j$．さらに，遅い変数 $\hat{\theta}_N$ を分離しておく：

$$\begin{aligned} H^{(1)} &= \hat{H}_0(\hat{J}) + \Lambda_{\tilde{m}_N} \cos\hat{\theta}_N + \sum_{\substack{|m| \geq 1 \\ m \neq \tilde{m}_N}} \Lambda_m(\hat{J}) \cos(m' \cdot \hat{\theta}) \\ &= \hat{H}_0(\hat{J}) + \Lambda_{\tilde{m}_N} \cos\hat{\theta}_N + \tilde{H}^{(1)}(\hat{J}, \hat{\theta}). \end{aligned}$$

ここで，$\tilde{m}_N = (0, \ldots, 0, -s, 1)$ である．非摂動ハミルトニアンも含めてまとめると，

$$H = \hat{H}^{(0)}(\hat{J}) + \epsilon \hat{H}_0(\hat{J}) + \epsilon \Lambda_{\tilde{m}_N} \cos\hat{\theta}_N + \epsilon \tilde{H}^{(1)}(\hat{J}, \hat{\theta}) \tag{14}$$

となり，$(\hat{J}_N, \hat{\theta}_N)$ は単振り子，残りのものは非線形回転子を表し，そこに摂動 $\tilde{H}^{(1)}$ が加わったものと見ることができる．

3.4 セパラトリクス写像の構成

ハミルトニアン(14) の中の単振り子が，セパラトリクス近傍において一回振動する周期を用いて Poincaré 写像を構成する．Poincaré 写像を $(\hat{J}, \hat{\theta}) \mapsto (\hat{J}', \hat{\theta}')$ と書く．作用変数の変化は $j = 1, \ldots, N-1$ に対し，

$$\Delta \hat{J}_j = \int_{-\infty}^{\infty} \frac{d\hat{J}_j}{dt} dt = -\int_{-\infty}^{\infty} \frac{\partial H}{\partial \hat{\theta}_j} dt = -\epsilon \int_{-\infty}^{\infty} \frac{\partial H^{(1)}}{\partial \hat{\theta}_j} dt \tag{15}$$

を計算する．ただし，$\Delta\hat{J}_j = \hat{J}'_j - \hat{J}_j$ とおいた．角変数の変化は，$\Delta\hat{\theta}_j = \hat{J}'_j$ とすればよい．

(15) 式において，積分を $-\infty$ から ∞ まで行なうのは近似である．実際には有限時間で回ってくれないと困るが，セパラトリクス近傍では一周期に非常に長い時間がかかる．そしてこのように有限時間の積分を広義積分に置き換えることにより，(15) 式が解析的に評価できるのである．また被積分関数は，$t \to \pm\infty$ に対し指数的に減衰するので，近似としても申し分ない．

(15) 式を積分する際，非線形回転子は回転数一定で回転しているものと仮定する（図 6 左参照）．すなわち

$$\hat{\theta}_j = \Omega_j t + \hat{\theta}_{j,n}, \quad j = 1, \ldots, N-1.$$

ここで $\hat{\theta}_{j,n}$ は実数の定数で，n 回目の Poincaré 写像の $\hat{\theta}_j$ の値である．一方，単振り子の方は，

$$\hat{\theta}_N = \phi_s(s) = 4\tan^{-1} e^s - \pi, \quad s = \omega_\phi t$$

とおく（図 6 右）．ω_ϕ は $\mathcal{O}(\sqrt{\epsilon})$ の定数である．

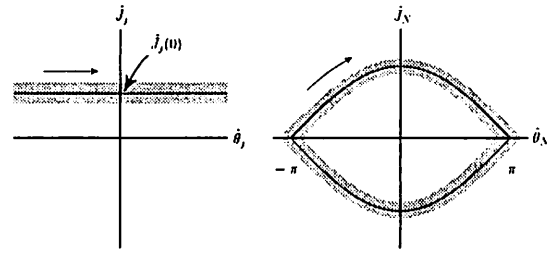

図 6: $\tilde{H}^{(1)} = 0$ であれば実線上の運動である．実際には $\tilde{H}^{(1)} \neq 0$ であるので，$\mathcal{O}(\epsilon)$ 程度のずれが生じる（図中影の部分）．

以上の準備により，作用変数の変化を見積ることができる．$Q_j = -\Omega_j/\omega_\phi (= \mathcal{O}(1/\sqrt{\epsilon}))$, $Q_{\tilde{m}} = \sum_{j=1}^{N-1} m'_j Q_j$, $\tilde{\theta}_{m,n} = \sum_{j=1}^{N-1} m'_j \hat{\theta}_{j,n}$ と置いて，

$$\Delta\hat{J}_j = \frac{\epsilon}{\omega_\phi} \sum_{\substack{|m|\geq 1 \\ m \neq \tilde{m}_N}} m'_j A_m \sin\tilde{\theta}_{m,n} \int_{-\infty}^{\infty} \cos[m_N\phi_s(s) - Q_{\tilde{m}}s]ds \tag{16}$$

なることが示される．

3.5 Melnikov-Type 積分

(16) 式の右辺の積分を，Melnikov-type 積分と呼ぶ．ホモクリニック交差の判定で有名な Melnikov 積分 [9] に現れる積分だからである．正確に定義しよう．

定義 3 (Melnikov-Type 積分) $k \in Z_+$ に対し，広義積分

$$\mathcal{A}_k(Q_0) = \int_{-\infty}^{\infty} \cos\left[\frac{k}{2}\phi_s(s) - Q_0 s\right] ds \tag{17}$$

を k 次の *Melnikov-type* 積分と呼ぶ．

重要な性質を，証明なしでまとめておく．

補題 1 *1.* $Q_0 < 0$ のとき

$$\mathcal{A}_k(Q_0) = (-1)^k \mathcal{A}_k(-Q_0)\exp(\pi Q_0), \tag{18}$$

2. $Q_0 > 0$ のとき

$$\mathcal{A}_1(Q_0) = \frac{2\pi\exp(\pi Q_0/2)}{\sinh \pi Q_0}, \tag{19a}$$

$$\mathcal{A}_2(Q_0) = 2Q_0\mathcal{A}_1(Q_0), \tag{19b}$$

$$\mathcal{A}_k(Q_0) = \frac{2Q_0\mathcal{A}_1(Q_0)}{k-1} - \mathcal{A}_{k-2}, \quad k \geq 2. \tag{19c}$$

3. $Q_0 \gg k$ の漸近形は，

$$\mathcal{A}_k(Q_0) \sim \frac{4\pi(2Q_0)^{k-1}\exp(-\pi Q_0/2)}{(k-1)!}, \quad Q_0 \to \infty. \tag{20}$$

(18)，(20) 式を用いれば，$Q > 0$ のとき，

$$\mathcal{A}_2(Q) = \frac{4\pi Q\exp(\pi Q/2)}{\sinh(\pi Q)} \sim 8\pi Q\exp\left(-\frac{\pi Q}{2}\right), \tag{21}$$

$$\mathcal{A}_2(-Q) = \frac{4\pi Q\exp(-\pi Q/2)}{\sinh(\pi Q)} \sim 8\pi Q\exp\left(-\frac{3\pi Q}{2}\right) \tag{22}$$

であり，引数が負であるものは，正であるものに比べ指数的に小さいことがわかる．

3.6 結果と具体例

これで ΔJ_j を見積る準備は整った．あとは興味あるハミルトニアンについて(16) 式を計算すればよい．ここでは具体的なハミルトニアンについての例を挙げるのはやめ，比較的一般的な議論をもう少し続ける．

まず $N = 3, s = 1$ とする．すなわち，3 自由度ハミルトン系の $1:1:\gamma(\in R\backslash Q)$ という共鳴を考える．また，$H^{(1)}$ は解析的であるとしたから，一般にそのフーリエ係数は $|m| \to \infty$ に対し指数的に減衰する．ここでは思いきって $|m| \le 2$ のみ取ることにする．$\hat{}$ を外して書けば，

$$\frac{\omega_\phi}{\epsilon}\Delta J_1 = \Lambda_{(1,0,1)}\mathcal{A}_2(Q_1+Q_2)\sin(\theta_1+\theta_2) - \Lambda_{(-1,0,1)}\mathcal{A}_2(-Q_1+Q_2)\sin(-\theta_1+\theta_2), \tag{23}$$

$$\begin{aligned}\frac{\omega_\phi}{\epsilon}\Delta J_2 = {} & \Lambda_{(0,0,1)}\mathcal{A}_2(Q_2)\sin\theta_2 + 2\big(\Lambda_{(0,1,1)}\mathcal{A}_2(2Q_2) - \Lambda_{(0,2,2)}\mathcal{A}_4(2Q_2)\big)\sin 2\theta_2 \\ & + \Lambda_{(1,0,1)}\mathcal{A}_2(Q_1+Q_2)\sin(\theta_1+\theta_2) + \Lambda_{(-1,0,1)}\mathcal{A}_2(-Q_1+Q_2)\sin(-\theta_1+\theta_2)\end{aligned} \tag{24}$$

が得られる．

これでもまだ繁雑過ぎてよくわからない．さらに仮定を入れよう．θ_1 と θ_2 は共鳴していないのだから $Q_1 \neq Q_2$ であるが，これらが同符号でその差は小さいとしよう．一般性を失わず，$Q_2 - Q_1 > 0$ としてよい．元々 $Q_1, Q_2 = \mathcal{O}(1/\sqrt{\epsilon})$ であるが，$Q_2 - Q_1 = Q = \mathcal{O}(\epsilon^\alpha)$, $\alpha \ge 0$ とすれば，(23), (24) 式は(18)-(21) 式を用いて寄与の小さい項を落として，

$$\begin{aligned}\frac{\omega_\phi}{\epsilon}\Delta J_1 &= -\Lambda_{(-1,0,1)}\mathcal{A}_2(Q)\sin(-\theta_1+\theta_2), \\ \frac{\omega_\phi}{\epsilon}\Delta J_2 &= \Lambda_{(0,0,1)}\mathcal{A}_2(Q_2)\sin\theta_2 + \Lambda_{(-1,0,1)}\mathcal{A}_2(Q)\sin(-\theta_1+\theta_2)\end{aligned}$$

となる．$\epsilon\Lambda_{(0,0,1)}\mathcal{A}_2(Q_2)/\omega_\phi = \epsilon_1$, $\epsilon\Lambda_{(-1,0,1)}\mathcal{A}_2(Q)/\omega_\phi = \epsilon_2$ とおいて写像の形で書けば，

$$\left\{\begin{array}{rcl} J_1' &=& J_1 - \epsilon_2\sin(-\theta_1+\theta_2), \\ \theta_1' &=& \theta_1 + J_1', \\ J_2' &=& J_2 + \epsilon_1\sin\theta_2 + \epsilon_2\sin(-\theta_1+\theta_2), \\ \theta_2' &=& \theta_2 + J_2' \end{array}\right. \tag{25}$$

となる．写像(25) は 4 次元シンプレクティック写像であり，可積分写像と標準写像が，ϵ_2 に比例した結合項で結びついたものと見ることができる．Froeschlé 写像(1) と大きく異なる点は，$\epsilon_2 = 0$ の場合の 2 つの面積保存写像が異なっている，というところである．単純な例であるが，Froeschlé 写像は 3 自由度ハミルトン系を代表しない，ということがわかる．

4 おわりに

多自由度ハミルトン系におけるセパラトリクス写像の構成について，少し駆け足で見てきた．ハミルトニアンと見たい共鳴を指定すれば，近似的なPoincaré写像が得られるわけである．Poincaré写像になってしまえば次元が2つ落ちるし，離散力学系なので数値計算のコストも稼げる．一度試してみては如何だろう？

今後の展開について述べたい．まずここで行なった多次元化では，真に多自由度的性質である高次の共鳴，例えば1:2:3の共鳴を調べることができない．これを調べるためには，Melnikov-Type積分(17)を多次元化しなくてはならない．この問題はすぐに，とは約束できないが，いつかは解いてみたい問題である．対して仮定$r=1$（(11)式参照）はそれほど本質的でないと考えている．この仮定は早急に外したい．

また我々のような力学系の研究者は，具体的に「このハミルトニアンを調べたい！」というものがあまりない．だからといって結果を書き連ねただけでは芸がなさすぎる．我々が現在考えている研究は，逆問題である．つまりこれまで扱われていたシンプレクティック写像（例えばFroeschlé写像(1)）に対応するハミルトン系を求め，写像系で得られた結果をハミルトン系に焼き直すのである．やっぱり最後はハミルトン系に戻りたいから．

もう1つだけ述べておこう．ハミルトン系はねじれ条件の下では多種多様な共鳴が存在する．共鳴近傍の縮約から得られたセパラトリクス写像を何らかの意味で分類することにより，共鳴近傍の力学を分類することができるだろう．あるものは低自由度系の直積のように見え，また別のあるものは真に多自由度的である，といった具合に．

セパラトリクス写像を通して共鳴を見る，これは案外近道かも知れない．

参考文献

[1] ハミルトン系の一般的な教科書としては，A. J. Lichtenberg and M. A. Lieberman: *Regular and Chaotic Dynamics* (Second Edition), Springer New York (1992); 斉藤信彦： カオスの物理（物理学最前線30)， 共立出版（1992)．また多少マニアックではあるが，大貫義郎・吉田春夫： 力学（岩波講座・現代の物理学1)，岩波書店(1994)の第II部など．

[2] V. I. Arnold: *Mathematical Methods of Classical Mechanics*, Springer New York (1978).

[3] R. S. MacKay and J. D. Meiss eds.: *Hamiltonian Dynamical Systems*, Adam-Hilger London (1987); R. S. MacKay: *Physica* **86D** (1995) 122.

[4] B. V. Chirikov: *Phys. Rep.* **52** (1979) 265.

[5] C. Froeschlé: *Astrophys. Space Sci.* **14** (1971) 110.

[6] H. Poincaré: *Méthodes Nouvelles de la Mécanique Célese*, Vol. 3, Gauthier-Villars (1899); 邦訳：福原満洲雄・浦太郎訳：常微分方程式，共立出版 (1970).

[7] A. N. Kolmogorov: *Dokl. Akad. Nauk. SSSR* **98** (1954) 527; V. I. Arnold: *Russ. Math. Surveys* **18** (1963) 85; J. Moser: *Nachr. Akad. Wiss. Göttingen. Math. Phys.* **1** (1962) 1.

[8] F. G. Gustavson: *Astro. J.* **71** (1966) 670.

[9] V. K. Melnikov: *Trans. Moscow Math. Soc.* **12** (1963) 1.

幾何学的方法による リアプノフスペクトルの考察

山口義幸*
606-8501 京都大学大学院情報学研究科力学系理論分野

概 要

リアプノフスペクトルは、サンプル軌道を横断する方向への軌道不安定性を計る指標であり、多自由度力学系でよく用いられる。しかし、リアプノフスペクトルで何がわかるのか、各リアプノフ指数がどのような運動を表しているのか、といったことは未だ明確になっていない。本稿では、軌道不安定性を考察するのにふさわしいと思われる幾何学的方法を紹介し、リーマン曲率テンソルとリアプノフスペクトルとの関係を調べる。

Lyapunov spectra with a geometrical method

YAMAGUCHI Y. Yoshiyuki
Department of Applied Mathematics and Physics,
Kyoto University, Kyoto, 606-8501, Japan

Abstract

The Lyapunov spectrum indicates instability of an orbit, and it is often used to analyse dynamical systems with many degrees of freedom. However, it has not been clarified what we can understand from Lyapunov spectra, and which motion each Lyapunov exponent picks up. In this paper we introduce a geometrical method which is suitable to consider the instability, and investigate the relation between Riemannian curvature tensor and Lyapunov spectra.

*yyama@amp.i.kyoto-u.ac.jp

1 はじめに

古典ハミルトン系は、古くて新しい話題であり、カオスの発見以来さまざまな問題を提示して来た。2自由度系については、低次元の特殊性を用いてある程度の理解が得られているが、3以上の多自由度系ではいまだ不明な点が多い。多自由度系における相空間の構造や運動の様子を知ることは、マクロな量の振舞の理解・予測を可能にすることから、特に重要な問題と言える。

リアプノフスペクトルは、相空間中の軌道不安定性を表す指標であり、多自由度力学系の解析によく用いられている。例えば、リアプノフスペクトルと相転移の臨界点との関係 [BC87, MB93] や、系のカオスの強さによるリアプノフスペクトルの普遍性 [LPRV87, Yam98] などが議論されてきた。これらは系の大まかな振舞や性質についての調査であり、より詳細な情報を得るためには、それぞれのリアプノフ指数がどのような運動を拾い上げているのかを考える必要がある。このためには幾何学的な方法が有効となるが、その理由を述べる前に従来の方法の問題点を考察して見よう。

次のハミルトン系を考える。

$$H(\boldsymbol{q},\boldsymbol{p}) = \frac{1}{2}\boldsymbol{p}^2 + V(\boldsymbol{q}).$$

この系においては、運動方程式

$$\frac{d^2\boldsymbol{q}}{dt^2} + \frac{\partial V}{\partial \boldsymbol{q}} = 0 \tag{1}$$

を線形化した

$$\frac{d^2(\delta q_i)}{dt^2} + \sum_{j=1}^{N} \frac{\partial^2 V}{\partial q_i \partial q_j}\delta q_j = 0 \tag{2}$$

からリアプノフスペクトルが計算されるため、ポテンシャル関数のヘッシアン $\frac{\partial^2 V}{\partial q_i \partial q_j}$ が不安定性を決めていることがわかる。軌道の指数的不安定性に対しては、主に2つの原因が考えられる：

1. ヘッシアンが負固有値を持つ。

2. 固有値はすべて正であるが、共鳴が起きている。

固有値を ν としよう。1番目の要因は、解が $q(t) \sim \exp(\pm\sqrt{-\nu})$ と書けることから容易に理解できる。2番目の要因は、例えば Mathieu 方程式

$$\frac{d^2x}{dt^2} + (a + b\cos 2t)x = 0, \quad (a > b > 0)$$

における不安定帯では指数的不安定性を示すことを思い起こせばよい。以上により、不安定性の出現にはヘッシアンの固有値の符号や時間変化が重要であること

がわかる。リアプノフスペクトルは軌道の進行方向に横断的な方向の指数的不安定性を計る指標であるため、ヘッシアンを進行方向と横断方向とに分離できることが望ましい。しかし一般には、

- 進行方向がポテンシャルヘッシアンの固有方向にはならない
- 固有方向になったとしても、固有値は時間変化する

であるため、線形化ニュートン運動方程式 (2) から横断方向に関連した情報のみを得ることは難しい。

これら2つの問題点は幾何学的方法を使えば解決できる。幾何学的方法 [Pet93] とは、ポテンシャルヘッシアンの代わりにリーマン曲率テンソルを不安定性を決定する要素として考える方法である。位置座標 $\boldsymbol{q}$ で張られた N 次元多様体 M にヤコビ計量

$$g_{ij} = 2W(q)\delta_{ij}, \qquad W(q) = E - V(q)$$

を入れると、運動方程式 (1) は M 上の測地線方程式

$$\nabla_{\boldsymbol{\xi}}\boldsymbol{\xi} = 0$$

として表される。ここに、$\boldsymbol{\xi}$ は測地線の接ベクトルである。また、線形化運動方程式 (2) は測地線の deviation 方程式である Jacobi 方程式

$$\nabla_{\boldsymbol{\xi}}\nabla_{\boldsymbol{\xi}}\boldsymbol{\eta} + \boldsymbol{R}(\boldsymbol{\eta},\boldsymbol{\xi})\boldsymbol{\xi} = 0. \tag{3}$$

で表され、サンプル軌道からの「ずれ」ベクトル $\boldsymbol{\eta}$ の時間発展はリーマン曲率テンソル $\boldsymbol{R}$ によって決定されていることがわかる。式 (3) では、$\boldsymbol{\eta} = \boldsymbol{\xi}$ として「ずれ」ベクトルを進行方向にとると、$\boldsymbol{R}$ の歪対称性のため $\boldsymbol{R}(\boldsymbol{\xi},\boldsymbol{\xi}) = 0$ となり、進行方向への指数的不安定性がないことが自明にわかる。

本稿では、幾何学的方法を3自由度ハミルトン系に対して適用し、リーマン曲率テンソルの静的・動的性質を調べる。

2 Model と観測量

リーマン曲率の意味での負曲率とポテンシャルの意味での負曲率を明確に区別するため、モデルとしてはいたる所で正曲率となるポテンシャル系を考える。

$$H(\boldsymbol{q},\boldsymbol{p}) = \sum_{j=1}^{3}\left[\frac{1}{2}\left(p_j^2 + (q^j)^2\right) + V_{HH}(q^j, q^{j+1})\right], \tag{4}$$

$$V_{HH}(x,y) = x^2 y - \frac{1}{3}y^3.$$

幾何学での慣例に従い、q の添字は上に、p の添字は下に付けた。このモデルを4次の Symplectic Integrator （時間幅 $\Delta t = 10^{-2}$）を用いて時間発展させる。

次に、どのような量を観測すればよいかを考察しよう。まず、平行移動する正規直行基底 $\{\boldsymbol{e}_1, \boldsymbol{e}_2, \boldsymbol{e}_3 = \boldsymbol{\xi}\}$, s.t. $\nabla_{\boldsymbol{\xi}} \boldsymbol{e}_i = 0$ を定めて Jacobi 方程式を成分表示する。すなわち、$\boldsymbol{\eta} = \sum_{i=1}^{3} \eta^i \boldsymbol{e}_i$ とすると、

$$\frac{d^2\eta^i}{ds^2} + \chi_{ij}\eta^j = 0, \qquad \chi_{ij} = \langle \boldsymbol{R}(\boldsymbol{e}_i, \boldsymbol{\xi})\boldsymbol{\xi}, \boldsymbol{e}_j \rangle .$$

ただし、s は $||\boldsymbol{\xi}|| = ||d\boldsymbol{q}/ds|| = 1$ を満たすようなパラメータである。このパラメータ s を $ds^2 = (2W)^2 dt^2$ なる関係を用いて実時間 t に変換すると、

$$\frac{d^2Y^i}{dt^2} + (Q_{ij} + \mu(t)\delta_{ij})Y^j = 0,$$

$$Q_{ij} = \langle \boldsymbol{R}(\boldsymbol{e}_i, \boldsymbol{p})\boldsymbol{p}, \boldsymbol{e}_j \rangle , \quad \mu(t) = -\frac{3}{4}\frac{\dot{W}^2}{W^2} + \frac{1}{2}\frac{\ddot{W}}{W}, \quad \eta^j = \sqrt{W}Y^j,$$

となる。行列 Q の中で、進行方向に関連する第 3 行や第 3 列の要素はリーマン曲率テンソル $\boldsymbol{R}$ の性質からすべて 0 になる。このことと、進行方向には指数的不安定性が発生しないことより、$\mu(t)$ は指数的不安定性を生じさせないと仮定して以後無視する。すなわち、軌道不安定性は行列 Q によって決定されているとする。第3節では、行列 Q の固有値に着目し、その静的・動的性質を調べて行く。

3 計算結果

第1節では不安定性の起源として、2つの可能性を挙げた。文献 [Pet93] では、FPU モデルや ϕ^4 モデルに対して負曲率による第1リアプノフ指数の見積もりを行っているが、我々の系 (4) に対してもこの見積もりが正しいかどうかを第3.1節で調べる。また、リーマン曲率テンソルの時系列の特徴を第3.2節で調べる。

3.1 リーマン曲率テンソルの負曲率による不安定性への寄与

ここでは、行列 Q の負の固有値による不安定性がどの程度寄与しているのかを調べよう。行列 Q の 3 つの固有値のうち一つは必ず 0 であり、固有ベクトルとして $\boldsymbol{\xi}$ (進行方向) を持つ。残りの 2 つのうち、大きい方を ν_ℓ 、小さい方を ν_s とすると、数値計算より $\nu_\ell > 0$ であることがわかった。よって、負となり得るのは ν_s のみである。そこで、時間変化する固有値 $\nu_s(t)$ が正である時間帯でのみ計算したリアプノフスペクトル $\{\lambda_1^+, \lambda_2^+\}$ と負である時間帯でのみ計算したリアプノフスペクトル $\{\lambda_1^-, \lambda_2^-\}$ との比較を行うことにより、負固有値による不安定性の寄与を見ることにする。具体的には、総計算時間を T として、

$$\lambda_1^{\pm} := \lim_{T\to\infty} \frac{1}{T} \sum_{\nu_s(t)\gtrless 0} \log \frac{||\boldsymbol{\eta}(t+\Delta t)||}{||\boldsymbol{\eta}(t)||}$$

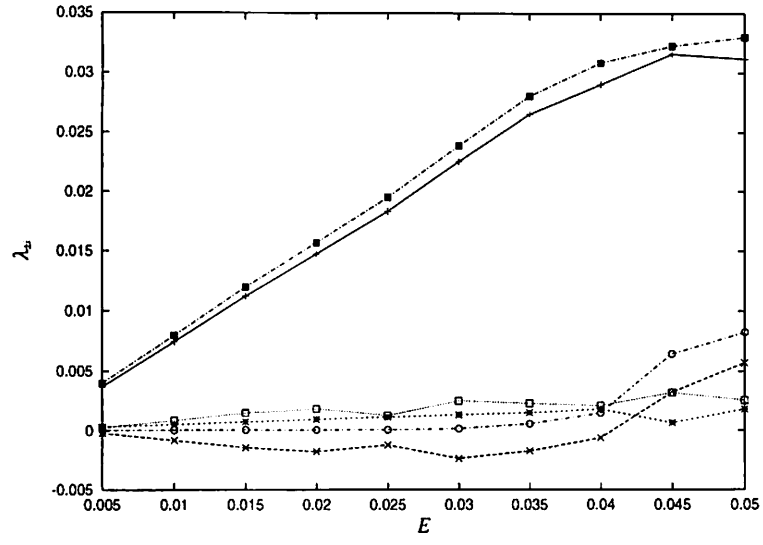

図 1: 不安定性に対する負固有値の寄与。横軸はエネルギー、縦軸はリアプノフ指数の値。$E = 0.05$ での値で上から順に $\lambda_1, \lambda_1^+, \lambda_2, \lambda_2^+, \lambda_2^-, \lambda_1^-$ を表す。

などと定義する。したがって、$\lambda_i = \lambda_i^+ + \lambda_i^-$ が成り立つ。

図 1 に結果を示す。まず、第 1 リアプノフ数に着目すると、λ_1^- による寄与もあるものの、ほとんどが λ_1^+ で支配されていることがわかる。また、第 2 リアプノフ数については、λ_2 がほとんどゼロである $E \leq 0.04$ で $\lambda_2^- > 0 > \lambda_2^+$ である一方で、λ_2 が λ_1 に比較しうるだけの値を持つ $E \geq 0.045$ では $\lambda_2^+ > \lambda_2^-$ となっている。さらに、エネルギー依存性をみても、λ_i^+ の方が λ_i^- よりも λ_i の関数形に近いことから、系 (4) においては、軌道不安定性には負曲率よりも正曲率の方がより重要であることが分かった。

3.2 リーマン曲率テンソルの時系列の性質

第 3.1 節によって、軌道不安定性にとっては負曲率よりも正曲率の時間変動の方が主要な要因であることがわかった。そこで、リーマン曲率テンソルから計算される行列 Q の固有値の時系列の特徴を調べる。固有値 ν_ℓ, ν_s は (q, p) を通して時間に依存する関数であり、ν_ℓ のパワースペクトルを計算したのが図 2 である。エネルギーが低い時 ($E \leq 0.04$) には高周波数領域での鋭いピークと低周波数領域でのローレンツィアンが観測でき、短時間では周期的な運動であるが長期的には相関が指数的に減少していることがわかる。このとき、相空間のほとんどが KAM トーラスで埋め尽くされていると考えられる。エネルギーを大きくする ($E \geq 0.045$) と高周波数領域でのピークがにぶり、低周波数領域では $1/f$ 型のスペクトルが見られる。$1/f$ 型スペクトルは相空間の自己相似構造を反映していると考えられており、エネルギーを上げると自己相似構造が観測できるほどに成長していることが

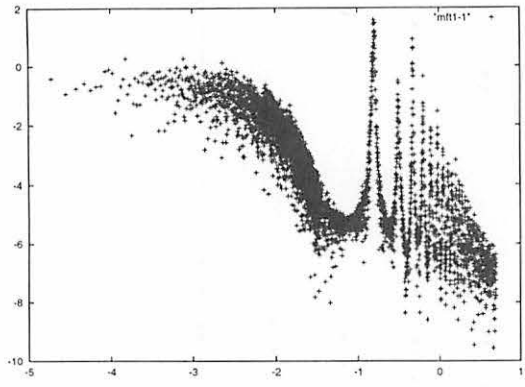

(a) $E = 0.01$

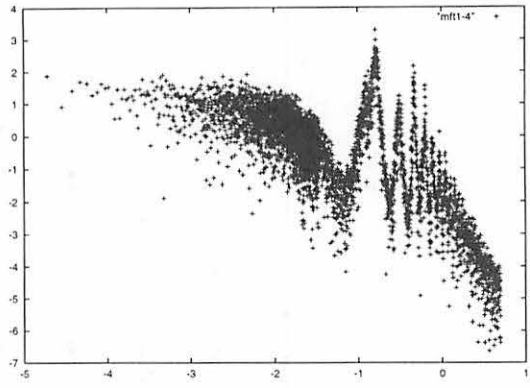

(b) $E = 0.04$

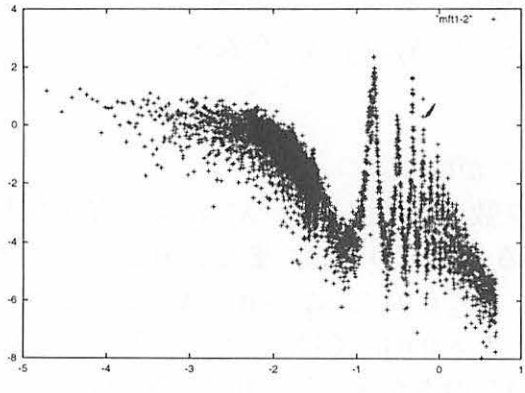

(c) $E = 0.02$

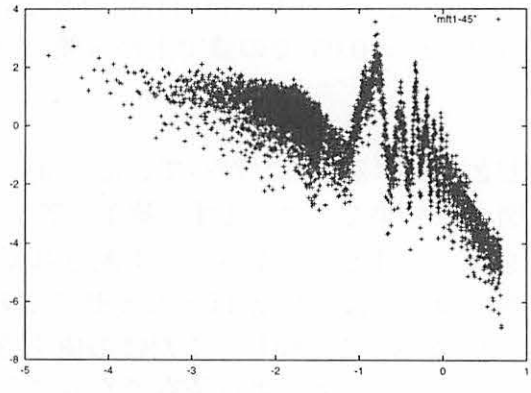

(d) $E = 0.045$

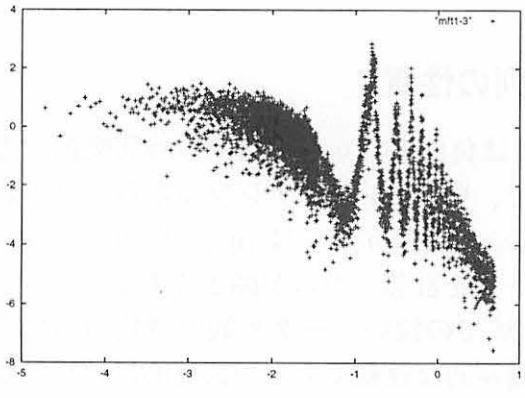

(e) $E = 0.03$

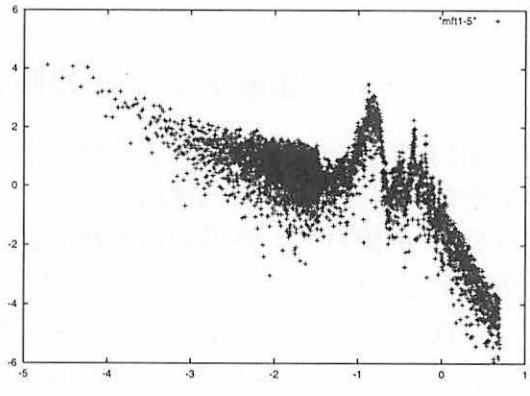

(f) $E = 0.05$

図 2: 行列 Q の固有値 ν_ℓ のパワースペクトル。

わかる。ν_s のスペクトルもほぼ同様である。しかし、$q^1(t), W(t)$ やポテンシャルヘッシアンの固有値のパワースペクトルではどのエネルギーでも $1/f$ スペクトルは観測されなかった。つまり、従来の方法では見えにくかったものが幾何学的方法ではよく捉えられていることがわかる。

4 まとめと議論と課題

本稿では、幾何学的方法を用いて古典ハミルトン系を解析する方法について調べ、次の結果を得た。

- 我々のモデル系では、負のリーマン曲率ではなく、正曲率の時間発展によって不安定性は支配されている。
- 従来の方法では観測しにくい $1/f$ 型スペクトルが、リーマン曲率を観測することにより観測できた。

$1/f$ 型スペクトルが現れるエネルギー領域と λ_2 が λ_1 に比して無視できないほどの大きさを持つエネルギー領域が一致していることから、λ_2 は $1/f$ 型スペクトルや自己相似階層構造と何らかの関係があるのではないかと予想される。

将来の課題としては、λ_2 と階層構造や階層間運動との関係を明らかにする、固有値のみではなく固有ベクトルの情報を用いる、一般の自由度系を考える、などが挙げられる。

参考文献

[BC87] P. Butera and G. Caravati. "Phase transitions and Lyapunov characteristic exponents". *Phys. Rev. A*, 36(2):962–4, 1987.

[LPRV87] R. Livi, A. Politi, S. Ruffo, and A. Vulpiani. "Liapunov exponents in high-dimensional symplectic dynamics". *J. Stat. Phys.*, 46:147–60, 1987.

[MB93] G. Mutschke and U. Bahr. "Kolmogorov-Sinai entropy and Lyapunov spectrum of a one-dimensional Φ^4-lattice model". *Physica D*, 69:302–8, 1993.

[Pet93] M. Pettini. "Geometrical hints for a nonperturbative approach to Hamiltonian dynamics". *Phys. Rev. E*, 47:828–50, 1993.

[Yam98] Y. Y. Yamaguchi. "New universality of Lyapunov spectra in Hamiltonian systems". *J. Phys. A*, 31:195–207, 1998.

Reduction of Round-Off Errors in Symplectic Integrators

Toshio Fukushima
National Astronomical Observatory
(E-mail) Toshio.Fukushima@nao.ac.jp

ABSTRACT

The double length addition routine (Dekker 1971) was incorporated to reduce round-off errors in symplectic integrators. The enhanced integrators provide a few digts more precise result at the cost of less than 25% increase of computational time. The full application of the double length library of the arithmetics and the square root operation to double precision variables realizes a quasi quadruple precision integration at the cost of 5.5-13.3 times increase of CPU time, which is still 3.8-22.6 times smaller than in the full quadruple precision computation. Also we confirmed that the accumulated round-off error in orbital integration by using the symplectic integrators grows in proportion to $T^{3/2}$ for the mean longitude, and $T^{1/2}$ for the semi-major axis and other Kepler elements.

Subject headings: Numerical integration—Orbital motion—Round-off error

1. Introduction

The symplectic integrator (See Sanz-Serna 1992 for its review) has become one of the most popular methods to investigate dynamical motions numerically. They, as well as the symmetric multistep methods (Lambert & Watson 1976, Quinlan & Tremaine 1990, Fukushima 1999, Evans & Tremaine 1999), are superior to the other integrators in the sense that (1) the truncation errors of action variables such as the total energy remain constant with time, and as a result, (2) the truncation errors of angle variables such as the longitude of orbital motion grow only linearly with respect to time. This is stated mathematically as

$$\Delta_{\mathrm{T}} J \sim C_J, \qquad \Delta_{\mathrm{T}} \theta \sim C_\theta T. \tag{1}$$

where J and θ denote the action and angle variables, respectively, and C_J and C_θ are the truncation error constants of the integrator used.

On the other hand, the round-off errors are predicted (Brouwer 1937) to grow in proportion to $T^{1/2}$ for action variables and to $T^{3/2}$ for angle variables;

$$\Delta_{\mathrm{R}} J \sim E_J N^{1/2}, \qquad \Delta_{\mathrm{R}} \theta \sim E_\theta N^{3/2}. \tag{2}$$

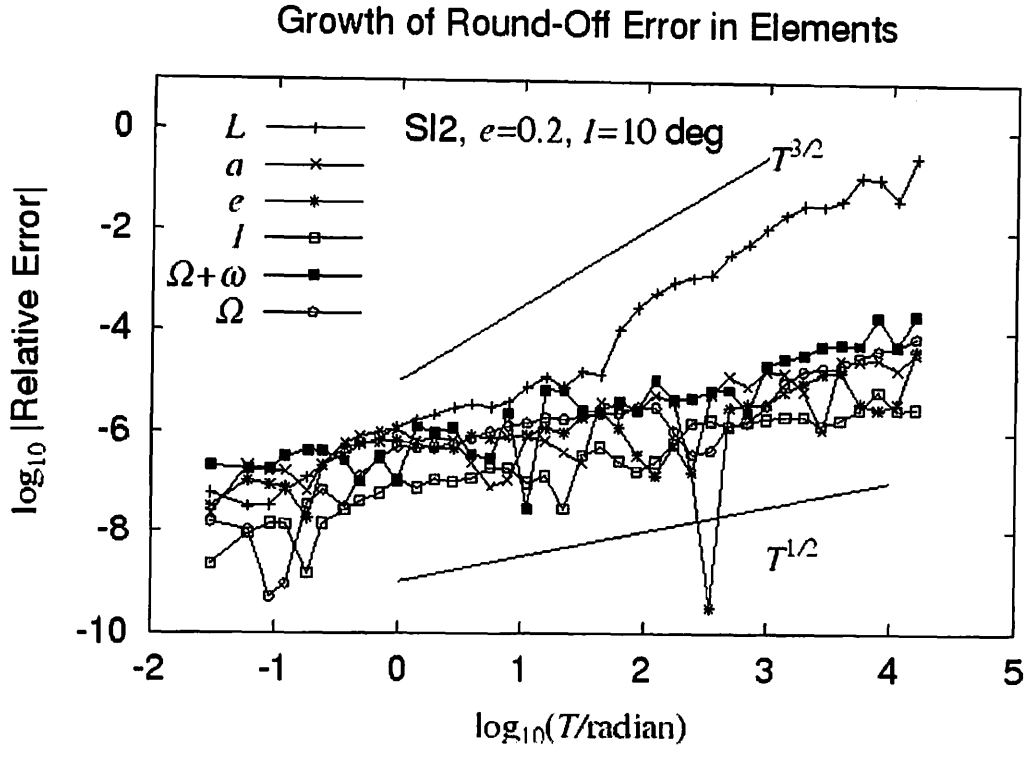

Fig. 1.— Growth of Round-Off Error in Elements
Shown are the round-off errors of an integrated Keplerian orbit. The integrator used was the second order symplectic integrator. The round-off errors were measured by comparison of the integrations in the single and double precision environments. The measured environment was a PC with Intel Pentium processor under the Windows 95 OS. The adopted compiler was the MS Fortran PowerStation ver.4.

where N is the number of steps and E_J and E_θ are some constants of the order of the machine epsilon. It has long been argued whether the actual error growth follows this rule or not (Milani and Nobili 1988, Section 6). For example, an error formula of N^2 type was given in Milani and Nobili (1988, Eq.(2.3)). This issue deeply relates to the internal rounding procedure of CPUs. While, there is an experimental evidence that the above Brouwer rule is valid (Quinlan 1994). We also confirmed this behaviour in Intel CPUs. See Figure 1. It is noteworthy that Figure 1 of Quinlan (1994) proved that this growth rate is independent on the order and type of integrators used.

Now, we note that the above error growth for an angle variable is the case when the rate of the angle variable has non-zero mean value. If the mean value is close to zero, then the round-off error of the angle variable grows only in proportion to $T^{1/2}$. The typical example is seen in the integration of a purely Keplerian orbit. Figure 1 shows that the round-off error of the mean longitude L grows in proportion to $T^{3/2}$ while those of the other two angles, the longitudes of

Table 1: Measured CPU Time of Basic Mathematical Operations

	Double Precision					Quadruple Precision	
Operation	i486	Pentium	PA-7000	μSparc2	Alpha	PA-7000	μSparc2
x = y	0.46	0.24	1.00	1.00	0.41	5.1	2.8
x = y + z	0.91	1.00	1.00	1.00	1.00	131	11.3
x = y * z	1.09	1.00	1.00	1.00	1.00	457	99.5
x = y / z	2.81	4.49	4.92	3.32	6.59	1100	168
x = sqrt(y)	12.0	19.6	4.95	24.4	38.5	1100	149
x = sin(y)	19.8	23.3	49.8	22.0	18.5	9510	1740
x = log(y)	20.2	23.9	47.8	31.9	22.0	5420	1240
x = atan(y)	19.8	27.3	46.3	37.3	23.5	5930	1270
x = tan(y)	18.0	28.3	63.2	30.0	35.1	8450	2040
x = exp(y)	24.9	32.7	42.0	19.0	23.2	6560	1370

Note: Shown is the relative CPU time of basic arithmetic operations and some mathematical functions for typical processors. The unit is DFLOPS, defined as a simple mean of addition ($x = y + z$) and the multiplication ($x = y * z$) in the double precision arithmetics.

the ascending node Ω and of the pericenter $\Omega + \omega$, do only in proportion to $T^{1/2}$ as well as the (equivalence of) action variables, the semi-major axis a, the eccentiricity e, and the orbital inclination I. This is because, the mean rates of Ω and ω are zeros in the purely Keplerian orbits.

Anyhow, from the comparison of the above expressions of error growth, it is clear that not the truncation but the round-off error is the main obstacle in conducting very long[1] integrations by the symplectic integrators and the symmetric multistep methods. Therefore, it is quite important to reduce the round-off errors as much as possible in utilizing these integrators. Of course, the ultimate approach to decrease the round-off is the introduction of higher precision computations. However, such remedy is not always possible. In fact, the quadruple precision computation is not availlable in ordinary PCs. Although it is availlable in some workstations, it costs quite a lot. See Tables 1 and 2. The ratio of CPU time increase from the double to the quadruple precisions ranges 27-275. This is because the quadruple precision computations are realized not by the hardware but by the software usually. Therefore we must seriously consider to decrease the round-off errors in a more active manner.

To do this, many techniques have been proposed (Milani and Nobili 1988; Quinn & Tremaine 1990; Quinlan 1994). A famous example is the Gauss-Jackson method (Jackson 1924) rewriting the integration of special second order ordinary differential equations in the summed forms. The usage of backward difference forms is another example (Quinlan 1994). For the multistep methods,

[1]The reader may refer Table 1 of Milani and Nobili (1988) for the examples of long integrations.

Table 2: Estimated CPU Times of N-body Routine

Precision	i486	Pentium	PA-7000	μSparc2	Alpha
Double	27	36	22	40	57
Double Length Double	360	282	268	284	311
Quadruple	—	—	6054	1070	—

Note: Shown is the relative CPU times of the core part of a routine to evaluate N-body interactions, $\sum_{J \neq K} (\mu_J / r_{JK}^3)\, \mathbf{r}_{JK}$. The unit is DFLOPS per perturber. The numbers were estimated from the data in in Tables 1 and 4 and the assumption that the ratios of basic operations used in the routine are; 5 additions/subtractions, 3 squares, 4 multiplications, 1 division, and 1 square root.

the introduction of a special ADD routine in evaluating the linear forms was proposed to reduce local round-off errors (Quinn & Tremaine 1990). It was used in computing the linear forms of integrals in the symmetric multistep methods (Quinlan & Tremaine 1990). For the extrapolation methods, we learned that the change of variables to their increments reduces the global round-off errors significantly with almost no extra increase of computational time (Fukushima 1996). For the symplectic integrators, the usage of integer arithmetics was proposed (Earn and Tremaine 1991). They reported the precision gain of a few digits. In this short note, we report that the introduction of double length routines (Dekker 1971) works quite well in reducing the round-off errors in the symplectic integrators.

2. Method

The symplectic integrators can be regarded as one of the fixed-step integrators to solve the initial value problem of an autonomous special second-order ordinary differential equations

$$\frac{\mathrm{d}^2 x}{\mathrm{dt}^2} = f(x), \qquad x(t_0) = x_0, \qquad v(t_0) \equiv \left(\frac{\mathrm{d}x}{\mathrm{dt}}\right)(t_0) = v_0. \tag{3}$$

Let us introduce two basic operators as

$$S_X(h):\ x_{n+1} := x_n + h v_n,\ v_{n+1} := v_n,$$

$$S_V(h):\ x_{n+1} := x_n,\ v_{n+1} := v_n + h f(x_n). \tag{4}$$

Then the single step formulas of the second and higher (even) order symplectic integrators are expressed as the symmetric products of these two basic operators (Yoshida 1990). See Appendix A also. In the below, we will examine the possible sources of round-off errors in the above basic

operations. Refer the similar discussions for the linear multistep methods (Quinlan & Tremaine 1990) and for the mid-point rule (Fukushima 1996).

In the floating-point arithmetics, the underflow is one of the major sources of round-off (Wilkinson 1960). The underflow appears in the sum of two quantities with a large difference between their magnitudes. Assume the usage of four-digits mantissa operation. Then a summation like $1.000 + 2.102 \times 10^{-3} \approx 1.002$ will lose the information of lower digits, 0.102×10^{-3}. Apart from the internal procedure to evaluate f, which we will discuss separately, the only candidate of the underflow in the formulas, Eq.(4), is the addition of the form $y := y + \Delta y$ where $y = x$ or $y = v$. If $|\Delta y|$ is considerably smaller than $|y|$, and this is almost always true when h is sufficiently small, an underflow will occur in this process. Therefore, the reduction of the number of additions leads to the reduction of round-off errors. A few primitive but effective techniques for the symplectic integrators are given in Appendix A although the expected gain is around 30% decrease at most.

Another source is the information loss in the multiplication. To express the full information of the multiplication of two quantities of m-digits mantissa, we need a mantissa of around $2m$-digits as $1.343 \times 2.103 = 2.824329$. Thus, if we store the product in a variable of the same m-digits mantissa as $1.343 \times 2.103 \approx 2.824$, we will lose the information of lower around m-digits, 0.000329. Note that this information loss is of no relation with the magnitudes, or the exponents if rigorously speaking, of the multiplicands. The exception occurs in the case the lower information is equal to 0. This happens when the sum of effective digits (or bits) is not greater than the number of mantissa as $1.343 \times 2.000 = 2.686$ or $1.300 \times 2.100 = 2.730$ for example. Especially, if one of the multiplicands is of the integral powers of 2, then no information loss occurs. In the above procedures, Eq.(4), the source of this type of information loss is the multiplications by h. Thus, if one can choose h as the power of 2 as $h = 2^{-k}$, this type of error is greatly reduced. This is feasible in the second order symplectic integrator, S_2. However, the step sizes in the higher order methods, say S_4 and S_6, are not commensurable with each other (See Appendix A). Therefore the information loss in multiplications is unavoidable in general.

Now consider to reduce these round-off errors. As stated earlier, the orthodox approach is to increase the mantissa of variables under consideration. To do this economically, we borrow the concept of *double length* computation of Dekker (1971). The idea is to assign two double precision floating point words, which we call a double length variable, to each variable and to realize their arithmetics and some basic mathematical operations such as `sqrt` in a quasi quadruple precision computation. The actual implementation consists of the exact addition and multiplication, Newton method, and other numerical techniques (Dekker 1971; Appendix B). When such a double length variable is represented as x, we label its components by indexing 1 or 2. Namely, we denote the single length variable, which is a double precision word, for the larger part by $x1$, and the other for the smaller part by $x2$. The sum of these two parts must represent the original double length variable exactly, $x = x1 + x2$. We assume that the smaller part is not greater than the larger one by the factor of the single length machine epislon ϵ as $|x2| \leq \epsilon |x1|$. When the condition is not satisfied, it is enforced *without loss of precision* by the f77 routine norm2 given in Appendix

B. The basic arithmetic operations of double length variables are realized by the f77 routines in the Appendix B, where the double precision of 53 bits mantissa is taken as the single length; the addition by add2, the subtraction by sub2, the multiplication by mul2, the division by div2, and the square root by sqrt2. By using these routines, we may replace the corresponding operations in the symplectic integrators, namely those given in Appendix A as Eqs (A3), (A5), (A7), (A11), or (A13). The resulting routines actually realize around 105 bits integration, which we confirmed by numerical experiments. Table 2 has already listed the estimate of the CPU times of double length routines to evaluate the N-body interactions for various processors. The ratio of the increase in CPU time from the double precision computation to the double length double precision one ranges from 5.5 of Alpha chip to 13.3 of i486. On the other hand, the ratio from the double length double to the quadruple environments spans 3.8 to 22.6. This is a significant speed up when considering the fact that a quasi quadruple precision (around 105 bits mantissa) computation is achieved.

3. Numerical Experiments

In order to measure the efficiencies of the introduction of double length arithmetics, we conducted a series of numerical integrations of a Keplerian motion of $e = 0.2$ and $I = 10°$. To emphasize the effects of round-off error clearly, we did the test integrations utilizing the double length routines in the single precision computations containing 24 bits mantissa and compared them with the results of the ordinary integrations in the double precision computations. The used routines for single precision computations are almost the same as those given in Appendix B. The only difference except the change in type declarations from REAL*8 to REAL*4 is the replacement of a numerical constant in mul2 and others to split the variable into quasi half length ones, namely $4097.0 \equiv 2^{12} + 1$ instead of $134217729.d0 \equiv 2^{27} + 1$.

In comparison, we prepared four kinds of options; (1) no reduction of round-off errors, (2) the usage of sum2, a variation of add2, in the summation procedures $x := x + (h/2) * v$ and $v := v + h * f$, (3) the usage of mul2 and sum2 in the above summation procedures, and (4) the full usage of double length operations both in the summation procedures and in the evaluation of two body accelerations, $f(x)$. Table 3 shows the relative CPU time of these four options actually measured by a PC of Intel Pentium processor. The measured value for the last option, 5.6-6.6, roughly confirms the previous estimate, 7.8, which can be deduced from Table 2. The difference is due to the effect of other minor operations as copying values and the overhead of calling subroutines.

Figure 2 shows the growths of accumulated round-off errors in the mean longitude, L, of these four options for the SI2 integrator. Here the step size was fixed as $1/(66\pi)$ of the orbital period. It is clear that the second and third options gave almost the identical results, which are around a few digits better than the case of no reduction. Since the third option costs more than the second one, we conclude that the second is better than the third. Of course, the last option resembles the double precision computations, and therefore achieved the precision gain of around 8 digits.

Table 3: Measured CPU Time of Options to Reduce Round-Off Errors

Option	Case A	Case B
No Reduction	1.00	1.00
sum2	1.22	1.00
sum2 & mul2	3.48	1.00
Full	5.64	6.56

Note: Shown is the relative CPU time of the options to reduce the round-off errors in orbital integration by the symplectic integrators. The measured environment was a PC with Intel Pentium processor under the Windows 95 OS. The adopted compiler was the MS Fortran PowerStation ver.4. The options compared are; (1) no extra care for the reduction, (2) the usage of double length summation routine `sum2` in the summations like $x_{n+1} := x_n + \Delta x_n$, (3) (2) plus the usage of double length multiplication routine, `mul2`, in the operations like $\Delta x_n := h * v_{n+1/2}$, and (4) the full usage of double length routines. The cases compared is (A) the pure two body problem, which is the case when the relative weight of the options (2) and (3) is the maximum, and (B) sufficiently large N-body problems, where the most of CPU time is consumed by the evaluation of mutual gravitational interaction containing `sqrt`.

All the round-off errors grow in proportion to $T^{3/2}$, which is well conformal with the prediction, Eq.(2). We obtained almost the same graphs for SI4 and SI6 integrators. The magnitude of errors are rather larger in the case of the higher order formulas. This is because the number of operations are larger than that of SI2 even after utilizing the reduction technique of number of operations described in Appendix A.

On the other hand, Figure 3 shows a similar error growth in the semi-major axis, a. As is easily conjectured from Figure 1, the effects of round-off error reductions for other Keplerian elements were almost the same as those for a.

4. Conclusion

The possible sources of round-off errors in the symplectic integrators were examined. Not so effective was the reduction of number of operations described in Appendix A. Rather the introduction of the double length addition routine of Dekker (1971) in the summation was turnd out to reduce the round-off errors by a few digits. The additional introduction of the double length multiplication routine gives practically no more gain in precision while costing significantly more. The full usage of double length routines not only in the integration formula but in the force evaluation realizes a quasi quadruple precision integration and achieves around 16 digits gain in precision. This is done at the cost of 5.5-13.3 times increase in CPU time. The ratio depends on the processor used and the problems applied. Note that this increased CPU time is significantly, say 3.8-22.6 times, smaller than that required in the fully quadruple precision computation. As

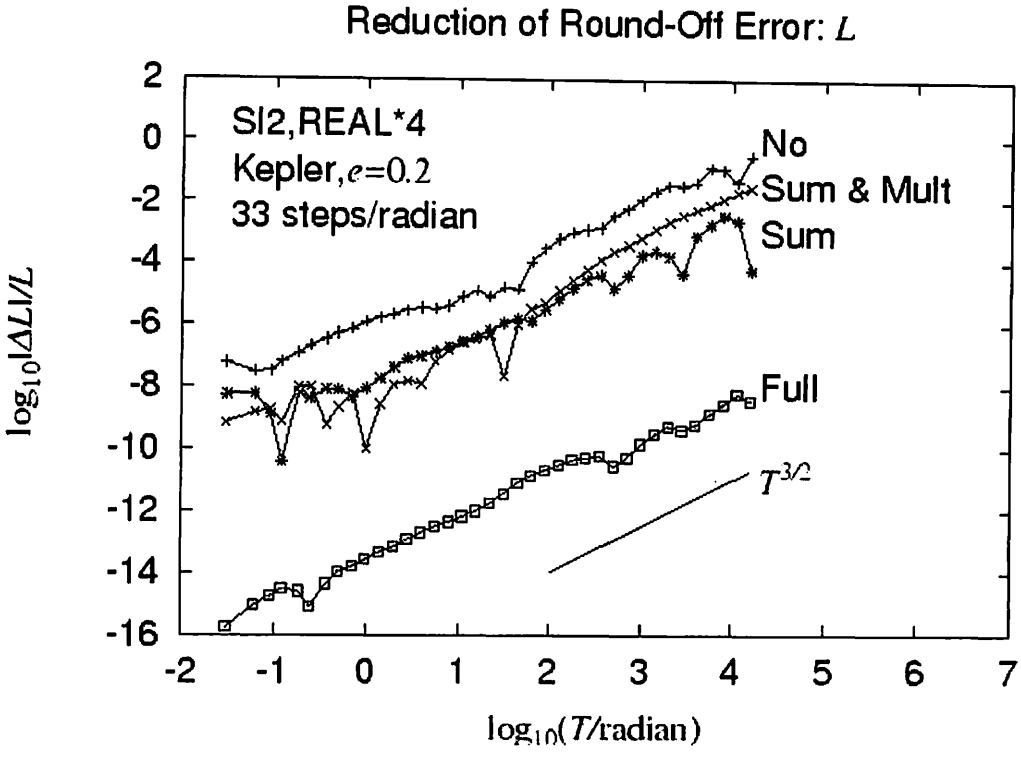

Fig. 2.— Reduction of Round-Off Error: L

a by-product, we confirmed that the accumulated round-off errors of orbital integration grow in proportion to $T^{3/2}$ for the mean longitude, and $T^{1/2}$ for the semi-major axis and other Kepler elements.

Unfortunately, the approach described here is not directly applicable to the mixed variable symplectic integrators, which require the trigonometric and exponential functions in double length environments. The issue will be resolved when these routines will be developed.

We also presented some basic f77 routines of double length double precision mathematical operations in Appendix B. The full package of these routines as well as the enhanced versions of symplectic integrators of orders of 2, 4, and 6 are availlable from the author on request.

REFERENCES

Brouwer, D. 1937, AJ, 46, 149

Dekker, T.J. 1971, Numerische Mathematik, 18, 224

Earn, D.J.D., and Tremaine, S. 1991, Physica D, 56, 1

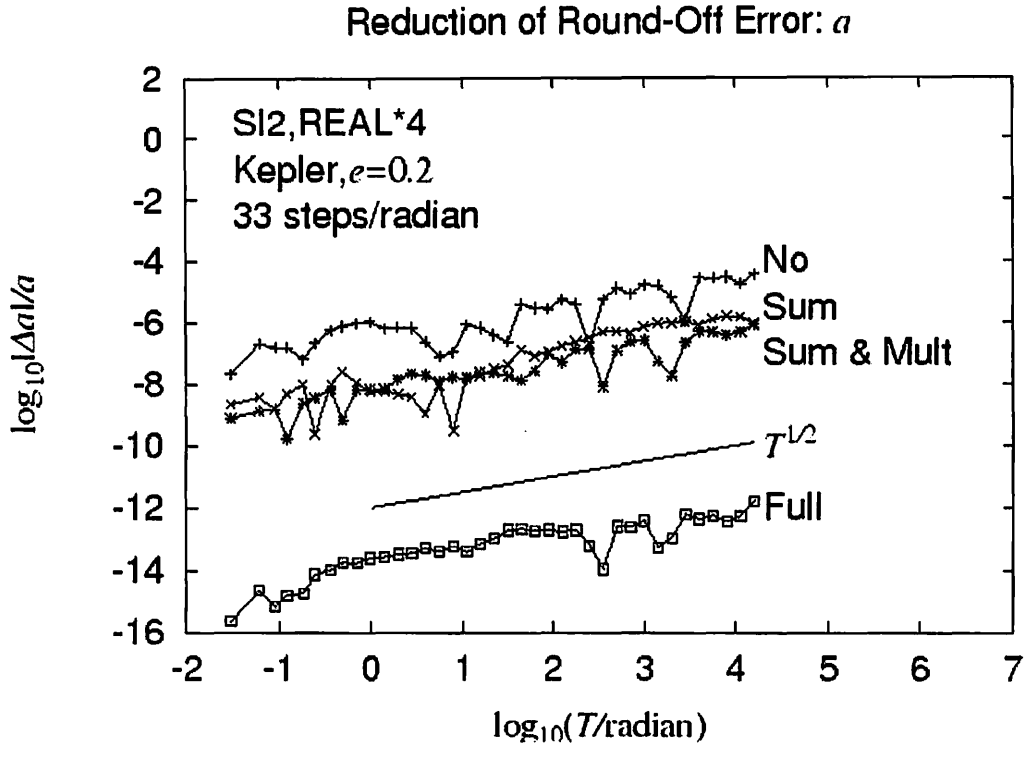

Fig. 3.— Reduction of Round-Off Error: a

Evans, N.W., and Tremaine, S. 1999, AJ, 118, 1888

Fukushima, T. 1996, AJ, 112, 1298

Fukushima, T. 1999, Proc. IAU Colloq. 173, 309

Hairer, E., Norsett, S.P., and Wanner, G. 1993, *Solving Ordinary Differential Equations I (2nd ed.)*, Springer-Verlag, Berlin

Jackson, J. 1924, MNRAS, 54, 602

Lambert, J.D., and Watson, I.A. 1976, J. Inst. Maths Applics, 18, 189

Milani, A., and Nobili, A. 1988, Celest. Mech., 43, 1

Quinlan, G.D. 1994, Celest. Mech. and Dyn. Astr., 58, 339

Quinlan, G.D., and Tremaine, S. 1990, AJ, 100, 1694

Quinn, T. R., and Tremaine, S. 1990, AJ, 99, 1016

Sanz-Serna, J.M. 1992, Acta Numer., 1, 243

Yoshida, H. 1990, Phys. Lett. A, 150, 262

Wilkinson, J.H. 1960, Numerische Mathematik, 2, 319

APPENDIX

A. Expressions of Symplectic Integrators Producing Less Round-Off Errors

As will be shown below, the round-off errors of the symplectic integrators can be reduced roughly 30% by rewriting the internal operations appropriately. Although this is a significant achievement, and we encourage strongly its full usage, its practical effect is far less than those obtained by the usage of double length arithmetics explained in the main text.

A.1. SI2

The symplectic integrator of the 'position-first' second order (SI2) is defined in terms of the first order symplectic operators Eq.(4) as

$$S_2(h) \equiv S_X\left(\frac{h}{2}\right) \circ S_V(h) \circ S_X\left(\frac{h}{2}\right) \tag{A1}$$

where h is the (fixed) step size. The actual procedure is explicitly written as the mapping

$$S_2(h) : (x_n, v_n) \to (x_{n+1}, v_{n+1}) \tag{A2}$$

where

$$x_{n+\frac{1}{2}} := x_n + \frac{h}{2} v_n, \qquad v_{n+1} := v_n + hf\left(x_{n+\frac{1}{2}}\right), \qquad x_{n+1} := x_{n+\frac{1}{2}} + \frac{h}{2} v_{n+1}. \tag{A3}$$

When this formula is repeatedly used while fixing the step size, as is usually done, the number of additions, the major sources of round-off, to transit from x_0 to x_n is $2n$. Here we ignored those in velocity computation since the round-off produced there was decreased by the factor h and therefore negligible. Now this number can be roughly halved by rewriting the above formula as

$$x_{n+\frac{1}{2}} := x_{n-\frac{1}{2}} + hv_n, \qquad v_{n+1} := v_n + hf\left(x_{n+\frac{1}{2}}\right), \qquad x_{n+1} := x_{n+\frac{1}{2}} + \frac{h}{2} v_{n+1}. \tag{A4}$$

This time the number of additions to reach x_n is only $n+1$. Thus, the accumulated round-off error is expected to reduce by $1 - \sqrt{1/2} \approx 29\%$ in the long run. Note that this rewriting requires no increase in the computational time.

This preprint was prepared with the AAS LaTeX macros v4.0.

A.2. SI4

The symplectic integrators of fourth and higher (even) orders are constructed from that of the second order (Yoshida 1990). In fact, the Ruth's fourth order formula (SI4) is expressed as

$$S_4(h) \equiv S_2(a_1 h) \circ S_2(a_2 h) \circ S_2(a_1 h) \tag{A5}$$

where

$$a_1 \equiv \frac{1}{2 - \sqrt[3]{2}} \approx 1.3512071919596576, \qquad a_2 \equiv 1 - 2a_1 \approx -1.7024143839193153. \tag{A6}$$

In order to reduce the round-off errors locally, it is better to rewrite these formulas in terms of basic operators directly as

$$S_4(h) = S_X(c_1 h) \circ S_V(a_1 h) \circ S_X(c_2 h) \circ S_V(a_2 h) \circ S_X(c_2 h) \circ S_V(a_1 h) \circ S_X(c_1 h) \tag{A7}$$

where

$$c_1 \equiv \frac{a_1}{2} \approx 0.67560359597982882,$$

$$c_2 \equiv \frac{a_1 + a_2}{2} = \frac{1}{2} - c_1 \approx -0.17560359597982882. \tag{A8}$$

The number of additions with respect to positions x, which are the main source of round-off errors, is reduced from 6 to 4 when compared with the naive combination of Eqs (A3) and (A5). Therefore, the effect of round-off errors is expected to reduce locally by the factor $1 - \sqrt{2/3} \sim 18\%$.

When this integrator is repeatedly used, we can reduce the number of additions with respect to x by one. This is done by combining the first S_X operation and the last S_X in the previous step as we did in the case of SI2. To illustrate this explicitly, we write down the above rewritten operation of SI4, Eq.(A7), explicitly as

$$\begin{aligned}
&x_{n+c_1} := x_n + c_1 h v_n, \qquad v_{n+a_1} := v_n + a_1 h f_{n+c_1}, \qquad x_{n+\frac{1}{2}} := x_{n+c_1} + c_2 h v_{n+a_1}, \\
&v_{n+1-a_1} := v_n + a_2 h f_{n+\frac{1}{2}}, \qquad x_{n+1-c_1} := x_{n+\frac{1}{2}} + c_2 h v_{n+1-a_1}, \\
&v_{n+1} := v_{n+1-a_1} + a_1 h f_{n+1-c_1}, \qquad x_{n+1} := x_{n+1-c_1} + c_1 h v_{n+1}.
\end{aligned} \tag{A9}$$

where we abbreviated $f(x_\nu)$ as f_ν. In the further rewriting, the first operation is replaced as

$$x_{n+c_1} := x_n + c_1 h v_n \qquad \Rightarrow \qquad x_{n+c_1} := x_{n-1-c_1} + 2c_1 h v_n. \tag{A10}$$

Therefore the number of additions finally reduces to 3, exactly the half of the naive combination. Namely, we can expect the accumulated round-off errors will reduce by the same factor as in SI2, $\sim 29\%$. Again there is no increase of CPU time by the introduction of this rewriting.

A.3. SI6

The sixth order formula is written in terms of S_2 as

$$S_6(h) \equiv S_2(b_1 h) \circ S_2(b_2 h) \circ S_2(b_3 h) \circ S_2(b_4 h) \circ S_2(b_3 h) \circ S_2(b_2 h) \circ S_2(b_1 h) \tag{A11}$$

where one of the Yoshida's three set of coefficients (SI6A) is

$$b_1 \approx 0.784513610477560, \qquad b_2 \approx 0.235573213359357, \qquad b_3 \approx -1.177679984178870,$$

$$b_4 \equiv 1 - 2(b_1 + b_2 + b_3) \approx 1.315186320683906; \tag{A12}$$

Similarly, the sixth order formula, Eq.(A11), is rewritten in terms of basic operations as

$$\begin{aligned} S_6(h) = {} & S_X(d_1 h) \circ S_V(b_1 h) \circ S_X(d_2 h) \circ S_V(b_2 h) \circ S_X(d_3 h) \circ S_V(b_3 h) \circ \\ & S_X(d_4 h) \circ S_V(b_4 h) \circ S_X(d_4 h) \circ S_V(b_3 h) \circ S_X(d_3 h) \circ S_V(b_2 h) \circ \\ & S_X(d_2 h) \circ S_V(b_1 h) \circ S_X(d_1 h), \end{aligned} \tag{A13}$$

where

$$d_1 \equiv \frac{b_1}{2} \approx 0.3922568052387800, \qquad d_2 \equiv \frac{b_1 + b_2}{2} \approx 0.5100434119184585,$$

$$d_3 \equiv \frac{b_2 + b_3}{2} \approx -0.4710533854097565, \qquad d_4 \equiv \frac{b_3 + b_4}{2} \approx 0.0687531682525180. \tag{A14}$$

This time, the number of additions with respect to x decreased from 14 to 8 when compared with the combination of Eqs (A3) and (A11). Therefore, the effect of local round-off errors is expected to reduce by the factor $1 - \sqrt{8/14} \sim 24\%$ in the long run. Again, in the repeat usage of this integrator, the factor can be made as the same as in the SI2 by combining the first S_X operation with the last S_X in the previous step.

B. Double Length Routines

The followings are the f77 adaptations of some basic routnies to realize double length arithmetics in the standard double precision environment (Dekker 1971). In the below, a magic number $134217729 \equiv 2^{26} + 1$ appears. This is used to pick up the upper 26 bits of double precision variables whose mantissa are of 53 bits length.

B.1. Normalization

```
subroutine norm2(x1,x2,z1,z2)
real*8 x1,x2,z1,z2
z1=x1+x2
z2=(x1-z1)+x2
return
end
```

B.2. Addition

```
subroutine add2(x1,x2,y1,y2,z1,z2)
real*8 x1,x2,y1,y2,z1,z2,v1,v2,w1,w2
w1=x1+y1
if(abs(x1).gt.abs(y1)) then
    w2=(((x1-w1)+y1)+y2)+x2
else
    w2=(((y1-w1)+x1)+x2)+y2
endif
z1=w1+w2
z2=(w1-z1)+w2
return
end
```

B.3. Subtraction

```
subroutine sub2(x1,x2,y1,y2,z1,z2)
real*8 x1,x2,y1,y2,z1,z2
call add2 (x1,x2,-y1,-y2,z1,z2)
return
end
```

B.4. Multiplication

```
subroutine mul2(x1,x2,y1,y2,z1,z2)
real*8 x1,x2,y1,y2,z1,z2,hx,tx,hy,ty,p,q,w1,w2
p=x1*134217729.d0
hx=(x1-p)+p
```

```
tx=x1-hx
p=y1*134217729.d0
hy=(y1-p)+p
ty=y1-hy
p=hx*hy
q=hx*ty+tx*hy
w1=p+q
w2=(((p-w1)+q)+tx*ty)+(x1*y2+x2*y1)
z1=w1+w2
z2=(w1-z1)+w2
return
end
```

B.5. Division

```
subroutine div2(x1,x2,y1,y2,z1,z2)
real*8 x1,x2,y1,y2,z1,z2,v1,v2,w1,w2,hw,tw,hy,ty,p,q
w1=x1/y1
p=w1*134217729.d0
hw=(w1-p)+p
tw=w1-hw
p=y1*134217729.d0
hy=(y1-p)+p
ty=y1-hy
p=hw*hy
q=hw*ty+tw*hy
v1=p+q
v2=((p-v1)+q)+tw*ty
w2=((((x1-v1)-v2)+x2)-w1*y2)/y1
z1=w1+w2
z2=(w1-z1)+w2
return
end
```

B.6. Square Root

```
subroutine sqrt2(x1,x2,z1,z2)
real*8 x1,x2,z1,z2,v1,v2,w1,w2,hw,tw,p,q
if(x1.le.0.d0) then
```

```
    w1=0.d0
    w2=0.d0
    return
endif
w1=sqrt(x1)
p=w1*134217729.d0
hw=(w1-p)+p
tw=w1-hw
p=hw*hw
q=2.d0*hw*tw
v1=p+q
v2=((p-v1)+q)+tw*tw
w2=(((x1-v1)-v2)+x2)/(2.d0*w1)
z1=w1+w2
z2=(w1-z1)+w2
return
end
```

B.7. Others

We developed some other routines which in theory can be derived by calling these basic routines but run a little faster. See Table 4. Their list is

- `add12(x1,y1,z)`: Evaluate the sum of two single length variables, `x1` and `y1`, and return the result in a double length one, `z`.
- `add21(x,y1,z)`: Evaluate the sum of a single length variable, `y1`, and a double length one, `x`, and return the result in another double length one, `z`.
- `sum21(x,y1)`: Add a single length variable, `y1`, to a double length one, `x`
- `sum2(x,y)`: Add a double length variable, `y`, to another double length one, `x`
- `mul12(x1,y1,z)`: Evaluate the product of two single length variables, `x1` and `y1`, and return the result in a double length one, `z`
- `sq12(x1,z)`: Square a single length variable, `x1`, and return the result in a double length one, `z`
- `sq2(x,z)`: Square a double length variable, `x`, and return the result in another double length one, `z`

Table 4: Number of Basic Mathematical Operations of Double Length Routines

	Number of Operation						CPU Times (unit:DFLOPS)				
Routine	±	*	if	abs	/	sqrt	i486	Pentium	PA-7000	μSparc2	Alpha
norm2	3	0	0	0	0	0	2.7		3.0		
add12	6	0	1	2	0	0	8.5		9.0		
add21	7	0	1	2	0	0	9.4		10.0		
add2	8	0	1	2	0	0	10.3		11.0		
sq12	10	5	0	0	0	0	14.6		15.0		
sq2	12	7	0	0	0	0	18.6		19.0		
mul12	14	6	0	0	0	0	19.3		20.0		
mul2	16	8	0	0	0	0	23.3		24.0		
inv2	17	7	0	0	2	0	28.7	28.5	28.9	27.3	37.2
div2	18	7	0	0	2	0	29.6	29.5	29.9	28.3	38.2
sqrt2	13	6	1	0	1	1	34.2	44.1	29.9	47.7	65.1

Note: Shown is the number of mathematical operations used in double length routines. Also given are the estimates of DFLOPS for typical three processors, which are computed from the data in Table 1 and the assumption that the averaged CPU times for `if` statement and `abs` function are 1.0 DFLOPS each. Note that the values for CPUs other than i486 are the same for the routines `norm2` through `mul2`.

- `inv2(x,z)`: Evaluate the inverse of a double length variable, `x`, and return the result in another double length one, `z`

B.8. CPU Time

The CPU times of the above routines are roughly estimated by counting the basic operations used. The results are shown in Table 4. The comparison with Table 1 reveals that the CPU times of the double length routines are of the same order of those of the typical mathematical libraries.

Fast Calculation of Hydrodynamic Interaction among Particles in the Stokes Flows

Kengo Ichiki (ichiki@kona.jinkan.kyoto-u.ac.jp)
Graduate School of Human and Environmental Studies, Kyoto University
Kyoto 606-8501, Japan

March 15-17, 2000

1 INTRODUCTION

The aim of this work is to present an efficient computational method of hydrodynamic interaction among spherical particles in low-Reynolds-number flows. Stokesian Dynamics [1] has two major difficulties: the heavy computational load scaled by $O(N^3)$, and no systematic way to improve approximation. These will overcome by multipole expansion, iterative scheme, and fast multipole method.

2 MULTIPOLE EXPANSION

We use simple derivatives in Cartesian coordinate rather than harmonic functions in spherical coordinate.

Let us consider the many-body problem in the Stokes flow:

$$U_i(\boldsymbol{x}^\alpha) = \sum_{\beta}^{N} M_{ij}(\boldsymbol{x}^\alpha - \boldsymbol{y}^\beta) \cdot F_j(\boldsymbol{y}^\beta), \tag{1}$$

where $\boldsymbol{U}(\boldsymbol{x}^\alpha)$ is the velocity of particle α, $\boldsymbol{F}(\boldsymbol{y}^\beta)$ is the force of particle β to the fluid, and $\mathsf{M}(\boldsymbol{r})$ is the mobility matrix. Greek letters in upper-case are label of particle $(1, 2, \cdots, N)$ and Roman letters in lower-case are index of Cartesian coordinate (x, y, z). From the Taylor expansion with $\boldsymbol{y}^\beta$ at $\boldsymbol{y}_0$,

$$U_i(\boldsymbol{x}^\alpha) = \sum_{m=0}^{p} \mathcal{M}^m_{ij,k\cdots}(\boldsymbol{x}^\alpha - \boldsymbol{y}_0) \cdot \mathcal{F}^m_{jk\cdots}(\boldsymbol{y}_0), \tag{2}$$

where $\mathcal{M}^m$ is m-th order derivative of mobility matrix

$$\mathcal{M}^m_{ij,k\cdots}(\boldsymbol{r}) = \frac{1}{m!} \left(\frac{\partial}{\partial \boldsymbol{r}}\right)^m_{k\cdots} M_{ij}, \tag{3}$$

and $\mathcal{F}^m$ is m-th order force moment

$$\mathcal{F}^m_{jk\ldots}(y_0) = \sum_\beta \{y_0 - y^\beta\}^m_{k\ldots} F_j(y^\beta). \tag{4}$$

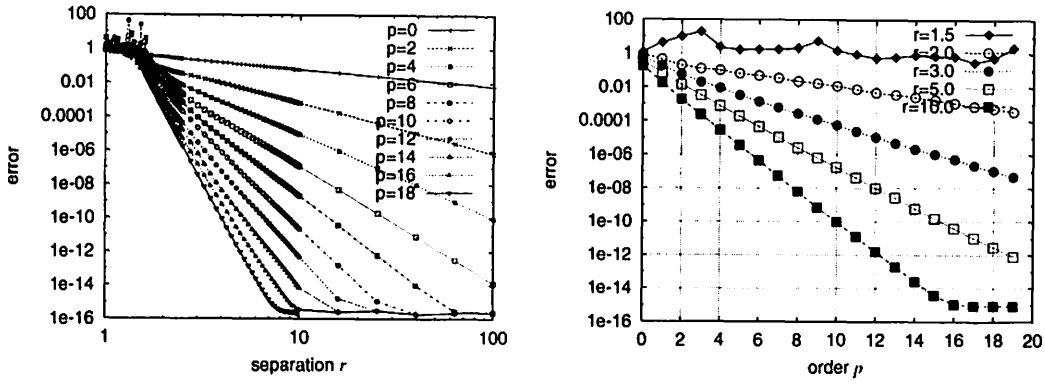

Figure 1: Error vs order p and separation r.

In Fig. 1, we consider two-body problems where particles are located at $\boldsymbol{x}$ and $\boldsymbol{y}$, under point-force approximation. The separation is defined by $r = |\boldsymbol{x}_0 - \boldsymbol{y}_0|$. The error $|\boldsymbol{U}_e - \boldsymbol{U}_d|/|\boldsymbol{U}_e|$ is averaged over 50 samples. $\boldsymbol{U}_d$ (direct) and $\boldsymbol{U}_e$ (expansion) are obtained by (1) and (2).

3 FAST CALCULATION

3.1 Iterative method

We need to calculate inverse in Stokesian Dynamics where resistance matrix R is approximated as

$$\mathsf{R} = \mathsf{M}^{-1} + \mathsf{L}. \tag{5}$$

where M is the mobility tensor with low order in expansion, and L is the lubrication tensor which contains contribution of higher order.

This inversion introduces many-body effect in way of method-of-reflections which is one of iterative method [2]. In turn, the application of iterative method which consists of the following matrix-vector product

$$\boldsymbol{U} = \mathsf{M} \cdot \boldsymbol{F} \tag{6}$$

is the first step to improve the calculation time which is scaled as $O(N^2)$.

3.2 Fast multipole expansion

Further improvement on speed is achieved on (6) in the iterative scheme by fast multipole method (FMM) [4]. The point of FMM is to expand not only with $\boldsymbol{y}$ but also with $\boldsymbol{x}$ in (1).

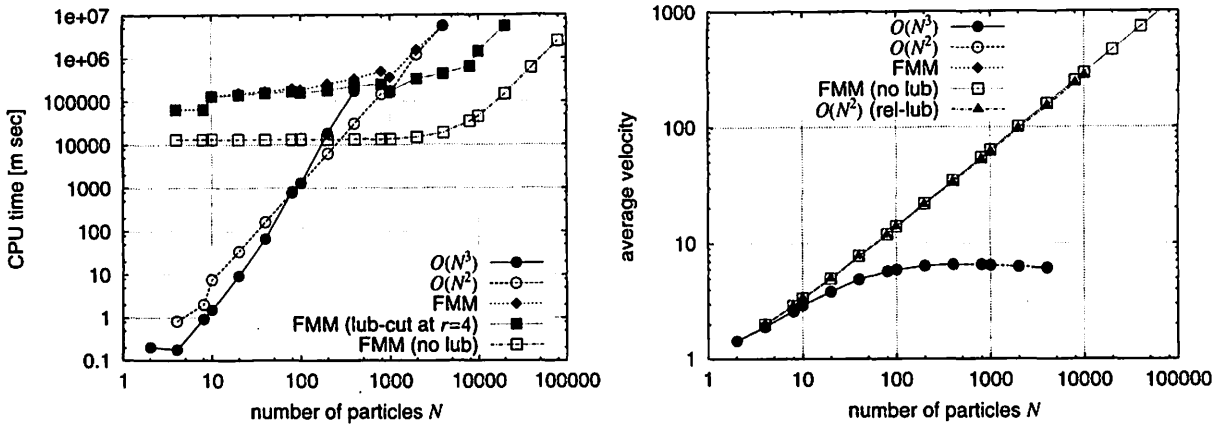

Figure 2: CPU time (left) and Average velocity (right).

Configuration of particles are regular array of simple-cubic lattice. In Fig. 2, $O(N^3)$ denots the original Stokesian Dynamics by (5), $O(N^2)$ denotes (5) using iterative method, FMM denotes (5) using iterative method with FMM, FMM(lub-cut) denotes FMM with cut-off in lubrication, FMM(no lub) denotes calculate without lubrication using FMM, and $O(N^2)$(rel-lub) denotes $O(N^2)$ using lubrication of relative motion. When $N < 100$, $O(N^3)$ is fastest, when $100 < N < 1000$, $O(N^2)$ is fastest, and when $1000 < N$, FMM(lub-cut) is fastest.

3.3 Systematic improvement of higher moments in Stokesian Dynamics

To improve accuracy, we need to improve base solution. For $\boldsymbol{x}_0 = \boldsymbol{y}_0$ (self-part),

$$\mathcal{U}^{(n)}_{i,l\cdots}(\boldsymbol{x}_0) = \sum_m \tilde{\mathcal{M}}^{(n,m)}_{i,l\cdots;j,k\cdots} \mathcal{F}^{(m)}_{j,k\cdots}(\boldsymbol{x}_0). \tag{7}$$

For $\boldsymbol{x}_0 \neq \boldsymbol{y}_0$,

$$\mathcal{V}^{(n)}_{i,l\cdots}(\boldsymbol{x}_0) = \sum_m \mathcal{M}^{(n,m)}_{i,l\cdots;j,k\cdots}(\boldsymbol{x}_0 - \boldsymbol{y}_0) \mathcal{F}^{(m)}_{j,k\cdots}(\boldsymbol{y}_0). \tag{8}$$

Relation between velocity derivatives and velocity moments are given by

$$\mathcal{U}^{(n)}_{i,l\cdots} = \sum_m \mathcal{V}^{(m)}_{i,k\cdots} \frac{1}{4\pi a^2} \int dS_r \; r^n_{l\cdots} r^m_{k\cdots} \tag{9}$$

Therefore, we get generalized grand mobility problem as

$$\begin{pmatrix} \boldsymbol{U} \\ \boldsymbol{\Omega} \\ \mathsf{E} \\ \hat{\mathcal{U}} \end{pmatrix} = \mathsf{M} \cdot \begin{pmatrix} \boldsymbol{F} \\ \boldsymbol{T} \\ \mathsf{S} \\ \hat{\mathcal{F}} \end{pmatrix}, \tag{10}$$

where $\boldsymbol{U}, \boldsymbol{\Omega}$ are translational and rotational velocity, E is asymmetric elements of first order (strain tensor), $\hat{\mathcal{U}}$ is irreducible velocity moments with higher moments, $\boldsymbol{F}, \boldsymbol{T}$ are force and torque, S is asymmetric elements of first order (stresslet tensor), and $\hat{\mathcal{F}}$ is irreducible force moments with higher moments.

We calculate mobility function of FTS versions – solving (10) under the condition of $\hat{\mathcal{U}} = 0$. (See Fig. 3.) FMM scheme of higher Stokesian Dynamics method Eq.(8), not Eq.(1), is also formulated.

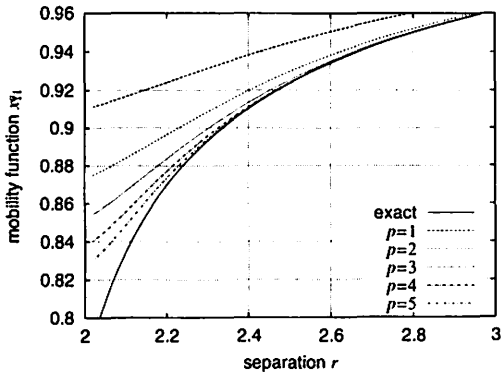

Figure 3: Mobility function x^a_{11}.

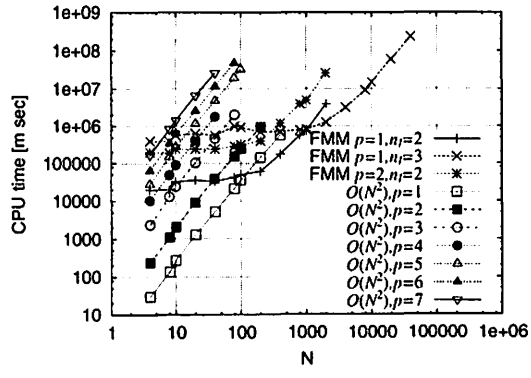

Figure 4: CPU time for higher SD method.

4 CONCLUSIONS

We established *FAST* and *ACCURATE* Stokesian Dynamics method. We have to give an explanation or proof for lubrication-correction, and formulate the case of periodic boundary condition.

Acknowledgment

The author would thank Prof. John F. Brady for his stay in California Institute of Technology and for fruitful discussions on the subject. This work is supported by Japan Society for the Promotion of Science.

References

[1] J. F. Brady & G. Bossis, Annu. Rev. Fluid Mech. **20**, 111 (1988).
[2] K. Ichiki & J. F. Brady, submitted to Phys. Fluids.
[3] R. Weiss, *Parameter-Free Iterative Linear Solvers* (Akademie Verlag, Berlin, 1996).
[4] L. Greengard and V. Rokhlin, J. Comput. Phys. **73**, 325 (1987).
[5] B. Cichocki, M.L. Ekiel-Jeżewska, & E.Wajnryb, J. Chem. Phys. **111**, 3265 (1999).

Long term integration error of KS regularized orbital motion

Hideyoshi Arakida

Department of Astronomical Science, Graduate University for Advanced Studies, 2-21-1, Osawa, Mitaka, Tokyo 181-8588 JAPAN

h.arakida@nao.ac.jp

Toshio Fukushima

National Astronomical Observatory of Japan, 2-21-1, Osawa, Mitaka, Tokyo 181-8588 JAPAN

Toshio.Fukushima@nao.ac.jp

ABSTRACT

We discovered that the growth of positional error of a perturbed harmonic oscillator is proportional to the physical time t. This feature does not depend on the integrator used, on the initial conditions, nor on the type of perturbations. As its application, we confirmed that the positional error of a perturbed two body problem expressed in the KS variable is proportional to the fictitious time s. This property is also independent on the integrator used, on the initial conditions including the nominal eccentricity, and on the type of perturbations. The error growth of the physical time evolution and the Kepler energy is proportional to s^2 if the equation of motion of the perturbed harmonic oscillator are integrated by the traditional integrators such as the Runge-Kutta, Adams, Störmer, or extrapolation methods and to s by the time symmetric integration formulae such as the leapfrog or the symmetric multistep method. In the case of general N-body problems, however, the positional error of a certain body grows in proportion to s^2 unless we take the fictitious time of the body as the independent variable of the system. As the best numerical integrator for the KS regularized equation of motions, we recommend the predictor formula of sufficiently high order symmetric multistep methods because (1) it runs fast, (2) its error constant is close to the minimum among the class of linear multistep methods, (3) its numerical error of the conserved quantities remain almost constant with time, and (4) it shows no step size resonance/instability which is seen in the unregularized cases. In conclusion the KS regularized equation of motion is useful to investigate the long term behavior of perturbed two body problems, namely those for studying the dynamics of comets, minor planets, the Moon, and other natural and artificial satellites.

Subject headings: celestial mechanics — equation of motion — KS regularization : method — numerical

1. Introduction

For the long term study of orbital motions, it is desirable to adopt a formulation producing small positional errors, especially those whose growth is proportional to time t. One effective direction is to search a numerical integrator leading to a small growth in the positional error. Unfortunately the traditional integrators, such as the Runge-Kutta, Adams, Störmer-Cowell, or extrapolation methods, are not suitable in the sense the positional error grows in proportion to t^2. This error growth has been the barrier for the long term integrations of dynamical system (Milani and Nobili 1988, Table 1). Recently, two new integrators are found to overcome this barrier; the symplectic integrator (see a review by Yoshida 1995) and the symmetric multistep method (Lambert and Watson 1976; Quinlan and Tremaine 1990; Fukushima 1999; Evans and Tremaine 1999). Both of them produce positional errors which are proportional to time.

On the other hand, the KS regularization (see the textbook by Stiefel and Scheifele 1971) has been used to treat the two body close approach properly. Especially it reduces the accumulation of numerical error in highly eccentric orbits of comets and minor planets (Yabushita and Tsuzii 1989; Shefer 1990; Zheng 1994) and of artificial satellite motion (Sharaf *et al* 1987). Also it has been an essential tool in studying general N-body problems and stellar dynamics (Asrseth and Zare 1974; Mikkola and Asrseth 1990,1993). So far the regularization has been regarded less effective in the case of circular and low eccentric orbits. The reason is that it cannot decrease the numerical error significantly while requires a significant increase in computational time and complexity.

However, is it the only advantage of the KS regularization to avoid the close approach of celestial bodies? Is not there another benefit in the fact that the KS regularization transforms a perturbed two body problem into a perturbed harmonic oscillator? In this paper, we will report that this fact greatly reduces the long term integration error of the orbital motion. First, in Section 2, we will study the numerical integration error of perturbed harmonic oscillators. Then, in Section 3, we will examine the application of the results obtained in Section 2 to the KS regularized equation of motion.

2. Perturbed Harmonic Oscillators

It is well known that the KS regularization transforms a perturbed Keplerian motion into a perturbed harmonic oscillator (Stiefel and Scheifele 1971, Chapter II, Eq. (52)). Then we will first consider to integrate a one-dimensional perturbed harmonic oscillator;

$$\frac{d^2x}{dt^2} + \omega^2 x = F\left(x, \frac{dx}{dt}, t\right) \tag{1}$$

where ω is the frequency of the oscillator and F is the perturbing acceleration. By using various numerical integrators, we conducted long term integrations of the equation for four types of perturbations; (1) no perturbation (denoted by N hereafter), (2) a shift of frequency (S), (3) a forced

oscillation (F), and (4) a resistive force causing a damping (D). Table 1 shows the explicit forms of the perturbing acceleration F and the exact solution $x(t)$, the perturbation parameters we adopted, and the conserved quantity.

Table 2 lists the eight kinds of integrators tested; (1) the fourth order Runge-Kutta method (RK4), (2) the eighth order Runge-Kutta-Fehlberg method (RKF8), (3) the n-th order Adams-Bashforth method[1] (ABn) for $n = 4$, 6, and 8, (4) the n-th order Störmer method [2] (Sn) for $n =$ 2, 4, 6, and 8, (5) the n-th order Gragg's extrapolation method using the polynomial extrapolation (EXn) for $n = 4$ and 6, (6) the n-th order symplectic integrator (SIn) for $n = 2$, 4, and 6, (7) the n-th order symmetric multistep method for the special second order ordinary differential equations (ODEs) (SMn) for $n = 2$, 4, 6, and 8, and (8) the fourth order zero-growth symmetric multistep method for the general first order ODEs of Evans and Tremaine (1999) (ET4) for $n = 4$. We adopted the predictor formula only for the multistep methods, namely the Adams-Bashforth, Störmer, and symmetric multistep methods. For the extrapolation method, we fixed not only the step size but the order by fixing the number of the extrapolation stages. For the sixth order symplectic integrator, we adopted the A type formula of Yoshida (Kinoshita,Yoshida and Nakai 1991). For the sixth order symmetric multistep method for the special second order ODEs (Lambert and Watson 1976, Method IV) we set the free parameter $a = 0$, and for the eighth order one, we adopted the coefficients given in Quinlan and Tremaine (1990). For the fourth order symmetric multistep method for the general first order ODEs (Evans and Tremaine 1999), we set the free parameter $u_2 = 0$. The starting values for the multistep methods were given by the analytical solution if it

Table 1. Tested Perturbations of Harmonic Oscillator

Type	F	$x(t)$	Parameters	Conserved Quantity
No Perturbation (N)	0	$A\cos(\omega t - \delta)$		$E = \frac{1}{2}(v^2 + \omega^2 x^2)$
Frequency Shift (S)	ϵx	$A\cos(\sqrt{\omega^2 - \epsilon}t - \delta)$	$\epsilon = 0.3$	$E = \frac{1}{2}(v^2 + (\omega^2 - \epsilon)x^2)$
Forced Oscillation (F)	$\varepsilon\sin(\omega' t + \theta)$	$A\cos(\omega t - \delta)$	$\omega' = 0.3$	
		$+\frac{\varepsilon\sin(\omega' t+\theta)}{\omega^2-\omega'^2}$	$\varepsilon = 0.03$	
			$\theta = 0$	
Damped Oscillation (D)	$-2\lambda v$	$Ae^{-\lambda t}\cos(\sqrt{\omega^2 - \lambda^2}t - \delta)$	$\lambda = 10^{-6}$	

Note. — The amplitude A, the frequency ω, and the initial phase δ of harmonic oscillators were commonly set as $A = 1$, $\omega = 1$, and $\delta = 0$.

[1]There are some typographical errors in the coefficients for the multistep methods listed in Stiefel and Scheifele (1971, p 133). The correct values are as follows; $\alpha_7 = \frac{5257}{17280}$, $\alpha_9 = \frac{25713}{89600}$, $\alpha_{10} = \frac{26842253}{94800320}$, and $\alpha_{11} = \frac{4777223}{17418240}$ for Adams-Bashforth method; $\alpha_5 = \frac{3}{160}$, $\alpha_7 = \frac{275}{24192}$, $\alpha_9 = \frac{8183}{1036800}$, and $\alpha_{11} = \frac{4671}{788480}$ for Adams-Moulton method.

[2]Note that the order, p of multistep method is equivalent to the number of steps k. However, in the case of the Störmer-Cowell linear multistep method, the order is usually defined by $p = k+1$. We adopted the definition of order of the linear multistep method as $p = k$ in all the case.

exists, and by using RK4 with a sufficiently small step size otherwise. However, in the calculation of Figure 15, which will be explained in section 4, the starting values were given by using the variable order extrapolation method where the error tolerance was set as 10^{-14}. Remark that the second order Störmer method (S2), the second order symplectic integrator (SI2), and the second order symmetric multistep method for the special second order ODEs (SM2) are equivalent with each other; the leapfrog method (LF). All the calculations were carried out in the double precision arithmetics (53 bit mantissa) by a PC with an Intel Pentium II 350MHz CPU under the Linux OS.

Let us present the results of numerical experiments. Figure 1 shows the perturbation type dependence of positional error growth. The errors shown here are the difference in x between the numerically integrated and the analytical solutions. Here the errors are plotted as functions of time while we fixed the integrator as the sixth order Adams-Bashforth method. Since the errors obtained were of almost the same magnitude, we multiplied constant factors to show their parallel nature clearly. On the other hand, Figure 2 does the integrator dependence where we fixed the perturbation as that of a shift of frequency. Here the step size was changed integrator by integrator so that the total number of function calls became the same. In both cases, it is clear that the growth of positional error is proportional to t. Since the error growth is the same for all the integrators, their efficiencies are measured by the magnitudes of the local integration error when the number of the function calls per unit time is the same. Table 3 shows the magnitudes of integration error for the integrators of each order. Remark that the relations among the those of different order depend on the step size adopted. For example, the line SI6A in Figure 2 is a little above the line of AB4. However this is reversed when the step size becomes smaller. Figure 3 illustrates the initial phase dependence of the positional errors after $10^3, 10^4$, and 10^5 steps. Here the integrator and the perturbation were fixed as the sixth order Adams-Bashforth method and the shift of frequency, respectively. Clearly the error is independent on the initial phase. Thus the feature of linear growth of the positional error does not depend on the type of perturbations, on the type of numerical integration methods, nor on the initial conditions.

Figures 4 and 5 show the integrator dependence of the energy error under the same situation as Figure 2. The energy error grows in proportion to t for the traditional integrators while stays almost constant for the symplectic and the symmetric ones. Table 4 lists the efficiencies measured by the magnitude of error after a sufficiently long time. The same phenomenon is seen in the case of no perturbation. In the case of traditional integrators, why is the positional error growth proportional to t even though the energy error grows linearly? This is because the frequency ω is independent on the energy integrated, and therefore the phase error being an integral of the frequency error is proportional to t. Figure 6 shows the step size dependence of the energy error after 1000 revolutions where we used as the integrator the n-th (n = 2, 4, 6, 8, 10, and 12) order symmetric multistep method for the special second order ODEs which shows an eminent step size resonance/instability in integrating a Kepler motion (Quinlan 1999; Fukushima 1999), and the fourth order symmetric multistep method for the general first order ODEs. See Figure 15 also. Apparently there appears no instability.

Table 2. Numerical Integrators Tested for Perturbed Harmonic Oscillator

Integrator	Perturbation Type N	S	F	D	Order	Number of function calls per step
Adams-Bashforth (ABn)	√	√	√	√	4, 6, 8	1
Extrapolation (EXn)	√	√	√	√	4, 6	6, 22
Fourth order Runge-Kutta (RK4)	√	√	√	√	4	4
Eighth order Runge-Kutta-Fehlberg (RKF8)	√	√	√	√	8	13
Symmetric Multistep for first order ODEs (ET4)	√	√	√	√	4	1
Störmer (Sn)	√	√	√	···	2, 4, 6, 8	1
Symmetric Multistep for second order ODEs (SMn)	√	√	√	···	2, 4, 6, 8	1
Symplectic (SIn)	√	√	···	···	2, 4, 6	1, 3, 7

Note. — The symplectic integrator is not applicable to the case of forced harmonic oscillator where the perturbation depends on the time explicitly. The Störmer, the symplectic, and the symmetric multistep method are not suitable to the case of damped oscillator since the perturbation depends on the velocity.

Table 3. Magunitude of Positional Error of Perturbed Harmonic Oscillator

Order of Integration	Small ⟵ Magunitude ⟶ Large
4th order	SM4 < S4 < ET4 < AB4 < RK4 < EX4 < SI4
6th order	SM6 < S6 < AB6 < EX6 < SI6A
8th order	SM8 < S8 < AB8 < RKF8

Note. — The magnitudes of positional error were compared with respect to the each order of integration when the number of the function calls are per unit time are the same.

Table 4. Magnitude of Error of Conserved Quantity of Perturbed Harmonic Oscillator

Order of Integration	Small ⟵ Magnitude ⟶ Large
4th order	SM4 < ET4 < SI4 ≪ S4 < AB4 < RK4 < EX4
6th order	SM6 < SI6A ≪ S6 < AB6 < EX6
8th order	SM8 ≪ S8 < AB8 < RKF8

Note. — Same as Table 3 but compared was the magnitudes of error of the conserved quantity.

From Figures 2, 4, 5, and 6 and Table 2, we conclude that a sufficiently high order symmetric multistep method for the special second order ODEs is the best integrator to solve the perturbed harmonic oscillator because of its high cost performance. Unfortunately it is not suitable when the perturbation depends on the velocity such as in the case of a damping oscillator. In that case, a sufficiently high order Adams-Bashforth method is recommended.

3. KS Regularized Orbital Motions

The main part of KS regularized equation of motion is written in the form of the four-dimensional perturbed harmonic oscillator (Stiefel and Scheifele 1971). Its independent variable is not the physical time but the fictitious time s which is a variation of eccentric anomaly. From the results in the previous section, it is expected that the positional error growth of KS regularized orbital motion is only proportional to s.

Before dealing with the orbital motions, let us examine the error growth of the physical time evolution first. This is because, in the KS regularization, the evolution of physical time must be obtained by numerical integration. From the discussion in Appendix A, the error of physical time, Δt, contains terms of both the odd and even powers of h in the case of the traditional integrators. While, only the terms of even powers of h appear in the cases of the time symmetric ones, such as the leapfrog, and the symmetric multistep methods. Therefore it is expected that the error of time evolution grows in proportion to s^2 for the traditional integrators and to s for the time symmetric integrators.

Now let us conduct numerical experiments on the KS regularized orbital motion. As the test problems, we adopted seven types of simple orbital motions; (1) the pure Keplerian problem (denoted by K hereafter), (2) the general relativistic one body problem in the post-Newtonian (PN) approximation (R), the orbital motion of the artificial satellite under the perturbations (3) by J_2 (J2), (4) by an air dragging force (A), and (5) by the solar radiation pressure (P), (6) the circular restricted three-dimensional three body problem (R3), and (7) the general three-dimensional three body problem (G3). For the relativistic one body problem, we adopted the following PN equation

Table 5. Adopted Initial Conditions for Three Body Problems

	a	e	I	Ω	ω	l
Asteroid	1 AU	0.05	20°	20°	20°	20°
Jupiter	5.2 AU	0.0	0°	0°	0°	0°

Note. — Elements shown are those referred to the Sun

of motion in the standard PN coordinate;

$$\boldsymbol{F}_{PN} = \frac{\mu}{c^2}\left[4\frac{\mu}{r^4}\boldsymbol{x} - \frac{\boldsymbol{v}^2}{r^3}\boldsymbol{x} + 4\frac{\boldsymbol{x}\cdot\boldsymbol{v}}{r^3}\boldsymbol{v}\right]. \tag{2}$$

See Soffel (1989, Eq. (4.2.1)) and Brumberg (1991, Eq. (3.1.46)). Here $\mu = GM$, c is the speed of light in vacuum, and we set all the PN parameters as those of Einstein's general theory of relativity. As for the air dragging force, we selected the following form (Vallado 1997, Eq. (7-24));

$$\boldsymbol{F}_A = \frac{-c_D A}{2m}\rho v^2 \frac{\boldsymbol{v}}{v}, \tag{3}$$

where c_D is the coefficient of drag, ρ is the atmospheric density, A and m are the cross sectional area and the mass of the artificial satellite, respectively. As for the solar radiation pressure, the force expression we used is;

$$\boldsymbol{F}_P = \frac{-c_R p A_\odot}{m}\frac{\boldsymbol{x}}{r}, \tag{4}$$

where c_R is the coefficient of reflectivity, p is the solar radiation pressure, and $A_\odot$ is the area of the artificial satellite exposed to the Sun (Vallado 1997, Eq. (7-39)). In the circular restricted- and the general three body problems, we named the bodies as Sun, Jupiter, and Asteroid. The adopted initial conditions of Jupiter and Asteroid are listed in Table 5. We regarded the mass of Sun as $M_\odot = 1$, that of Jupiter as $m_J = 10^{-3}M_\odot$, that of Asteroid as $m_A = 0$ (restricted) and $m_A = 10^{-7}M_\odot$ (general), respectively, while the gravitational constant was set as $G = 1$.

In the case of the general three body problem, not only the orbit of Asteroid but also that of Jupiter must be integrated. Since the fictitious time s is proper to each body, there exist N different fictitious times in general N-body problems. Thus one has to choose a specific s or a suitable function of them as the independent variable. As such, we adopted the fictitious time of Asteroid. In this case, the equation of motion of the KS variables of Jupiter differs from that of perturbed harmonic oscillator since the additional factor r_A/r_J appears and it varies with time.

The integrators used were listed in Table 6; (1) the fourth order Runge-Kutta method (RK4), (2) the eighth order Runge-Kutta-Fehlberg method (RKF8), (3) the n-th order Adams-Bashforth method (ABn), (4) the n-th order Gragg's extrapolation method (EXn), (5) the pair of the n-th order Störmer and Adams-Bashforth methods (Sn+ABn), (6) the pair of the n-th order symmetric multistep method for special second order ODEs (Quinlan and Tremaine 1990) and Adams-Bashforth methods (SMn+ABn), and (7) the similar pair of the symmetric multistep method for the general first order ODEs (Evans and Tremaine 1999) and Adams-Bashforth method (ET4+AB4). In the last three cases Sn+ABn, SMn+ABn, and ET4+AB4 mean that Sn, SMn, or ET4 were used for integrating the part of perturbed harmonic oscillators, namely the equation of motion for the KS variable $\boldsymbol{u}$, while ABn was used for integrating the rest part, i.e., the physical time t and the Keplerian energy h_k. When the ET4 was used for integrating the Kepler energy, we faced an instability. Then we always adopted the ABn for the rest part even when the part of perturbed harmonic oscillator was integrated by ET4. In preparing the initial condition of KS variables, we always set $u_4 = 0$.

We investigated the growth of positional errors for all the cases. We also did the error growth of some quantities such as the Jacobi integral, the total energy, and the total angular momentum when they were conserved. In the pure Kepler problem, we evaluated the error by the deviation from the analytical solution

$$\Delta X = X_{\text{numerical}} - X_{\text{analytical}}$$

where the analytical solution was that given in the explicit function of the fictitious time. In the other cases when the analytical solutions are not available easily, we conducted the numerical integrations by fixing step sizes and evaluated the error by a difference between two runs of numerical integrations with different step sizes as,

$$\Delta X = X_{h_1=h} - X_{h_2=\frac{h}{2}}.$$

Figure 7 shows the perturbation type dependence of the positional error growth while the integrator was fixed as the fourth order Adams-Bashforth method. The errors are plotted as functions of the independent variable s. Figure 8 shows the integrator dependence of the positional error growth while the perturbation was fixed as the restricted three body problem. In all the cases, the positional error growth is proportional to the fictitious time s. Table 7 shows the comparison of magnitudes of positional error among the same order of integrators while the number of the function calls was set the same for all the integrators.

Let us consider the eccentricity dependence in the KS transformation. In the KS regularization, the eccentricity appears as the initial phase of the corresponding harmonic oscillator. See Figure 9 for the eccentricity dependence of the positional error after 120 nominal revolutions where the integrator and problem are fixed as the eighth order symmetric multistep method (SM8) and the pure Kepler motion representatively. In the KS regularized case, the error hardly depends on the eccentricity. In the unregularized case, however, the error drastically increases according to the eccentricity, The situation is the same as we expected from the results in the previous section. In conclusion, this phenomenon that the positional error growth is proportional to s is independent on the perturbations, on the integration methods, and on the initial conditions including the nominal eccentricity.

Figures 10 and 11 show the integrator dependence of the error of time evolution of the pure Kepler problem. We obtained similar figures even when perturbations exist. Stiefel (1970) evaluated that the error of physical time propagates in proportion to s in the case of the fourth order Runge-Kutta method (RK4). However, as we considered at the beginning of this section, the error of time evolution grows in proportion to s^2 for the traditional integrators including RK4, and does in proportion to s for the symmetric multistep methods. As a result, if the traditional integrators were used in the restricted three body problem, the positional error of Asteroid grows only in proportion to s. While that of Jupiter, the perturber, does in proportional to s^2. This is because the position of Jupiter in evaluating perturbations is calculated by way of the integrated physical time. The situation is the same for the general three body problem. Figure 12 shows the comparison of error growths of the Keplerian energy h_k in the restricted three body problem between the pair of the

Table 6. Numerical Integrators Tested for Perturbed Two Body Problem

Integrator	Perturbation Type						
	K	J2	R3	P	A	R	G3
Adams-Bashforth (ABn)	√	√	√	√	√	√	√
Extrapolation (EXn)	√	√	√	√	√	√	···
Fourth order Runge-Kutta (RK4)	√	√	√	√	√	√	√
Eighth order Runge-Kutta-Fehlberg (RKF8)	√	√	√	√	√	√	···
Symmetric Multistep (Evans and Tremaine) and Adams-Bashforth (ET4+AB4)	√	√	√	√	√	√	···
Störmer and Adams-Bashforth (Sn+ABn)	√	√	√	√	···	···	···
Symmetric Multistep (Quinlan and Tremaine) and Adams-Bashforth (SMn+ABn)	√	√	√	√	···	···	···

Note. — The Störmer, and the symmetric multistep method (Quinlan and Tremaine 1990) are not suitable to the case of the general relativistic one body problem and the air dragging force since the perturbation depends on the velocity. Though the formula of Evans and Tremaine (1999) is for the general first order ODEs, it showed the instability when integrating the Kepler energy h_k. Therefore we adopted it only for integrating the part of perturbed harmonic oscillator.

Table 7. Magnitude of the Positional Error of Perturbed Two Body Problem

Order of Integration	Small ⟵ Magnitude ⟶ Large
4th order	SM4+AB4 < S4+AB4 < ET4+AB4 < AB4 < RK4 < EX4
6th order	SM6+AB6 < S6+AB6 < AB6 < EX6
8th order	SM8+AB6 < S8+AB8 < AB8 < RKF8

Note. — Same as Table 3, but compared was the magnitudes of positional error of perturbed two body problem.

Table 8. Magnitude of Error of Conserved Quantity of Perturbed Two Body Problem

Order of Integration	Small ⟵ Magnitude ⟶ Large
4th order	SM4+AB4 < ET4+AB4 $\ll$ S4+AB4 < AB4 < RK4 < EX4
6th order	SM6+AB6 $\ll$ S6+AB6 < AB6 < EX6
8th order	SM8+AB8 $\ll$ S8+AB8 < AB8 < RKF8

Note. — Same as Table 3 but compared was the magnitudes of error of the conserved quantity of perturbed two body problem.

fourth order symmetric and Adams-Bashforth method (SM4+AB4) and the similar pair of the fourth order Störmer and Adams-Bashforth methods (S4+AB4). Here the latter was chosen as the representative of the traditional integrators. In the case of the traditional integrators, the error of h_k is proportional to s^2. While the error grows linearly in the case of the pair of the symmetric multistep and Adams-Bashforth method. We also confirmed that the situation is unchanged if using the formula of Evans and Tremaine for the part of first order differential equation, such as t and h_k. This is natural since the origin of the quadratic error growth is not in the truncation error of the first order differential equations but in the non-zero averaged value of right hand side of the variational equations. Just as the same in the perturbed harmonic oscillators, the error growth of the conserved quantities are proportional to s for the traditional integrators and remain constant for the symmetric integrators. See Figures 13 and 14 for the case of Jacobi integral in the circular restricted three body problem. For the Keplerian energy, we saw the same result as Figures 4 and 5. This is because, in the KS regularization, solving a two body problem is equivalent to solving a pure harmonic oscillator. The same phenomenon was confirmed on the total angular momentum. Table 8 is the same as Table 7 but it compares the magnitude of errors in Jacobi integral. In the general three body problem, we must multiply a time-varying factor r_A/r_J with the equation of motion of Jupiter in order to obtain the same physical time evolution common to Asteroid and Jupiter. As a result, the equation of motion of Jupiter in the KS variable is no longer expressed in the form of a perturbed harmonic oscillator. This is the reason that the positional error growth of the perturber, Jupiter, is proportional to s^2 for the Runge-Kutta and Adams-Bashforth methods.

4. Conclusion

We investigated the long term behavior of the integration errors of the perturbed harmonic oscillators, first, and of the KS regularized orbital motions, next. The results showed that the KS regularized equation of motion is superior to the ordinary equation of motion in rectangular coordinates in the sense their numerical integrations lead to significantly smaller errors in position. This property hardly depends on the type of the perturbation considered, on the integrators used, and on the initial conditions adopted, especially on the value of nominal eccentricity.

The symmetric multistep method seems the most appropriate to integrate the KS regularized orbital motion because it achieved the highest cost performance among the integrators tested. Of course, it is known that the some symmetric multistep methods for the special second order ODEs have a curious instability with respect to the magnitude of step size in integrating orbital motions in the ordinary rectangular coordinates (Quinlan 1999; Fukushima 1999). However, we confirmed that this feature disappears in the perturbed harmonic oscillator, and therefore in the KS regularized orbital motions, too. See Figure 15, which shows the step size dependence of the error of Jacobi integral after 1000 nominal revolutions. Here we fixed the integrator as the eighth order symmetric multistep method of Quinlan and Tremaine (1990) both for the KS regularized and unregularized equations of motion. In the regularized case, the error decreases monotonically with respect to the

step size. While many spikes appear in the unregularized case.

In applying the KS regularization, the most practical concern would be the increase of the computational time. Figure 16 shows the comparison of CPU time of numerical integrations between the KS regularized and unregularized equations of motion plotted as a function of number of perturbing bodies. In the case of no perturbing bodies, the CPU time of the regularized case is about 40% larger than that of unregularized one. However, this difference almost reduces in the case of more than about six perturbing bodies. Therefore, although the KS regularization requires the integration of 10 variables instead of 6 ones in the rectangular coordinates, the actual increase of CPU time is not significant if the force computation is sufficiently complicated, say more than that of six perturbers in the case of asteroid integration, or more than that of gravitational potential of Earth of three degree and higher in the case of artificial satellite.

In conclusion, the KS regularization is useful not only because it properly deals close approaches among the celestial bodies (see Figure 9 for example) but because the positional error growth is only proportional to the fictitious time s. The regularization also stabilizes the numerical integration by the symmetric multistep method for the special second order ODEs, which turned out to be the most efficient integrator. However, this good property fails in the general N-body ($N \geq 3$) problem because the fictitious time is proper to each body. Therefore, the KS regularization is effective to study the long term behavior of perturbed two body problems; especially the dynamics of comets, minor planets, the Moon, and natural/artificial satellites including LAGEOS and GPS/NAVSTAR.

Appendix

A. Error growth of the physical time evolution

In the KS regularization, the physical time evolution is obtained by numerical integration. Let us consider its error growth. To simplify the situation, we restrict ourselves to its two-dimensional subset, the Levi-Civita transformation. Without losing a generality, we assume the transformed equation of motion is written as;

$$\frac{d^2 u_k}{ds^2} + u_k = 0, \quad (k = 1,\ 2) \tag{A1}$$

under the initial condition

$$u_1(0) = 1, u_2(0) = 0, \frac{du_1(0)}{ds} = 0, \frac{du_2(0)}{ds} = 1$$

where u_k were the new variables connecting to the position vector (x, y) as $x = u_1^2 - u_2^2$, and $y = 2u_1 u_2$. The analytical solution of Eq. (A1) is expressed as

$$u_1 = \cos s, \quad u_2 = \sin s. \tag{A2}$$

Consider the truncation error of the numerical integration. According to Henrici (1962), the differential equation of error, Δu_k is given as;

$$\frac{d\Delta u_k^2}{ds^2} + \Delta u_k = \sum_{j=p}^{\infty} C_j h^p \left(\frac{d}{ds}\right)^p u_k, \ (k = 1, \ 2) \tag{A3}$$

This is rewritten as;

$$\frac{d^2}{ds^2}\begin{pmatrix} \Delta u_1 \\ \Delta u_2 \end{pmatrix} + \begin{pmatrix} \Delta u_1 \\ \Delta u_2 \end{pmatrix} = \begin{pmatrix} C_{even} & C_{odd} \\ -C_{odd} & C_{even} \end{pmatrix}\begin{pmatrix} \cos s \\ \sin s \end{pmatrix} \tag{A4}$$

where

$$C_{even} = \sum_{i=[p/2]}^{\infty} C_{2i} h^{2i}(-1)^i, \quad C_{odd} = \sum_{i=[p/2]}^{\infty} C_{2i-1} h^{2i-1}(-1)^i, \tag{A5}$$

where C_j are the error constants proper to the integrator. In generally, if the initial conditions are given by,

$$\begin{pmatrix} \Delta u_1 & \frac{d\Delta u_1}{ds} \\ \Delta u_2 & \frac{d\Delta u_2}{ds} \end{pmatrix} = \begin{pmatrix} a_1 & b_1 \\ a_2 & b_2 \end{pmatrix}, \quad (s = 0) \tag{A6}$$

the solutions of Eq. (A4) become,

$$\begin{pmatrix} \Delta u_1 \\ \Delta u_2 \end{pmatrix} = \frac{1}{2}\begin{pmatrix} C_{even} & C_{odd} \\ -C_{odd} & C_{even} \end{pmatrix}\begin{pmatrix} s\sin s \\ \sin s - s\cos s \end{pmatrix} + \begin{pmatrix} a_1 & b_1 \\ a_2 & b_2 \end{pmatrix}\begin{pmatrix} \cos s \\ \sin s \end{pmatrix} \tag{A7}$$

The differential equation describing the time evolution is written as

$$\frac{dt}{ds} = r = u_1^2 + u_2^2, \tag{A8}$$

where the variational equation becomes

$$\frac{d\Delta t}{ds} = 2(u_1\Delta u_1 + u_2\Delta u_2) \tag{A9}$$

which is explicitly integrated as

$$\begin{aligned} \Delta t \ = \ & C_{even}\left(\frac{s}{2} - \frac{\sin 2s}{4}\right) - C_{odd}\left(\frac{s^2}{2} + \frac{\cos 2s}{4}\right) \\ & +2\left\{(a_1 + b_2)\frac{s}{2} - (b_2 + a_1)\frac{\cos 2s}{2} + (a_1 - b_2)\frac{\sin 2s}{4}\right\} \end{aligned} \tag{A10}$$

In general, there appear error terms of both odd and even powers of h. Thus Δt grows in proportion to s^2. However, in the case of the time symmetric integrators, Δu_k contains only the even powers of h. Therefore the error Δt only grows linearly. Even if there are errors corresponding to the initial values, its contribution only appears as the linear growth.

REFERENCES

Aarseth, S. J., and Zare, K., 1974, Celest. Mech., 10, 185

Brumberg, V. A., 1991, Essential Relativistic Celestial Mechanics, Adam-Hilger, Bristol

Brumberg, V. A., 1995, Analytical Techniques of Celestial Mechanics, Springer-Verlag, Berlin

Evans N. W., and Tremaine, S., 1999, AJ, 118, 1888

Fukushima, T., 1999, Proc. IAU Coll. 173, 304, eds: Svoreñ, J., Pittich, E.M., and Rickman, H., Astron. Inst, Slovak. Acad. Sci., Tatranskä Lomnica

Hairer, H., Nørsett, S. P., and Wanner, G., 1987, Solving Ordinary Differential Equation I, Springer-Verlag, Berlin

Henrici, P., 1962, Discrete Variable Methods in Ordinary Differential Equations, Wiley & Sons, Inc., New York

Kinoshita, H., Yoshida, H., and Nakai, H., 1991, Celest. Mech., 50, 59

Lambert, J. D., and Watson, I. A., 1976, J. Inst. Math. Applic., 18, 189

Mikkola, S., and Aarseth, S. J., 1990, Celest. Mech. Dyn. Astr., 47, 375

Mikkola, S., and Aarseth, S. J., 1993, Celest. Mech. Dyn. Astr., 57, 439

Milani, A., and Nobili, A. M., 1988, Celest Mech., 43, 1

Quinlan, G. D., and Tremaine, S., 1990, AJ, 100, 1694

Quinlan, G .D., 1999, astro-ph/9901136

Sharaf, M. A., Awad, M. E., and Banaja, M. A., 1987, Ap&SS, 133, 339

Shefer, V. A., 1990, Celest. Mech. Dyn. Astr., 49, 197

Soffel, M. H., 1989, Relativity in Astrometry, Celestial Mechanics and Geodesy, Springer-Verlag, Berlin

Stiefel, E. L., 1970, Celest. Mech., 2, 274

Stiefel, E. L., and Scheifele, G., 1971, Linear and Regular Celestial Mechanics, Springer-Verlag, Berlin

Vallado, D. A., 1997, Fundamentals of Astrodynamics and Application, McGraw-Hill, New York

Yabushita, S., and Tsuzii, T., 1989, MNRAS, 241, 59

Yoshida, H., 1993, Celest. Mech. Dyn. Astr., 56, 27

Zheng, Jia-Quin, 1994, Astr. ApJS, 108, 253

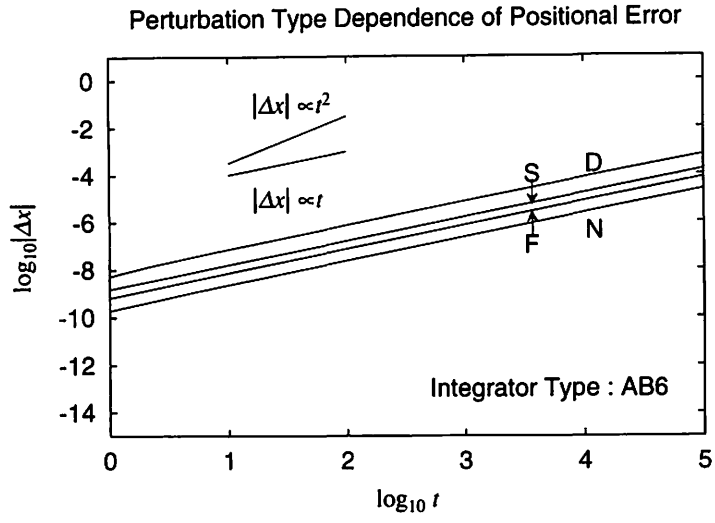

Fig. 1.— Perturbation Type Dependence of Positional Error Growth of Perturbed Harmonic Oscillator

Note: Plotted are the perturbation type dependence of the positional error of the perturbed harmonic oscillator as a function of time t. We adopted the sixth order Adams-Bashforth method as the integrator. The step size was fixed as $h = 0.03$ where the nominal oscillation period is 2π. See Table 1. In order to show their similarity more clearly, the errors were plotted after multiplying by $10^{0.5}$ for the forced oscillator, by 10^{1} for the shift of frequency, and by $10^{1.5}$ for the damped oscillator.

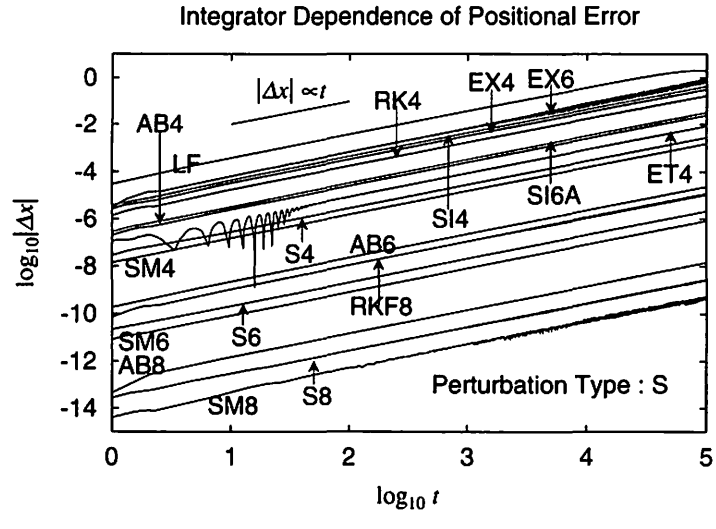

Fig. 2.— Integrator Dependence of Positional Error Growth of Perturbed Harmonic Oscillator

Note: Same as Figure 1 but the integrator were changed (See Table 2) while the perturbation type was fixed as the shift of frequency. The step size was adjusted so that the number of function calls per unit time become the same.

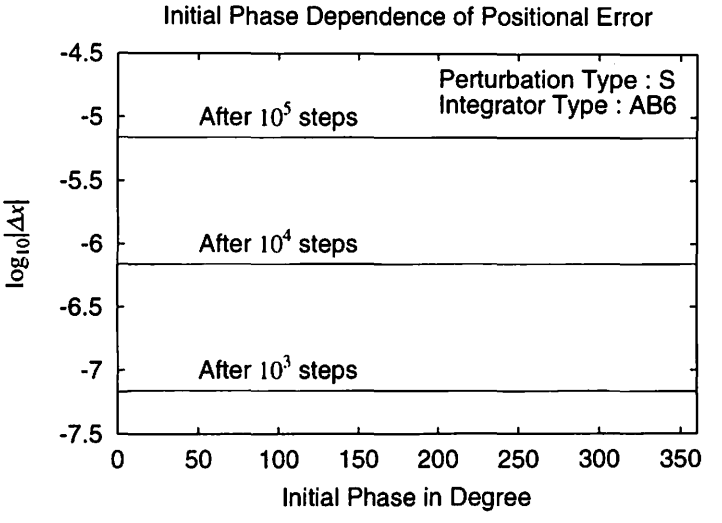

Fig. 3.— Initial Phase Dependence of Positional Error

Note: Same as Figure 2 but the errors after $10^3, 10^4,$ and10^5 steps were plotted as a function of the initial phase. Here we fixed the sixth order Adams-Bashforth method as the integrator

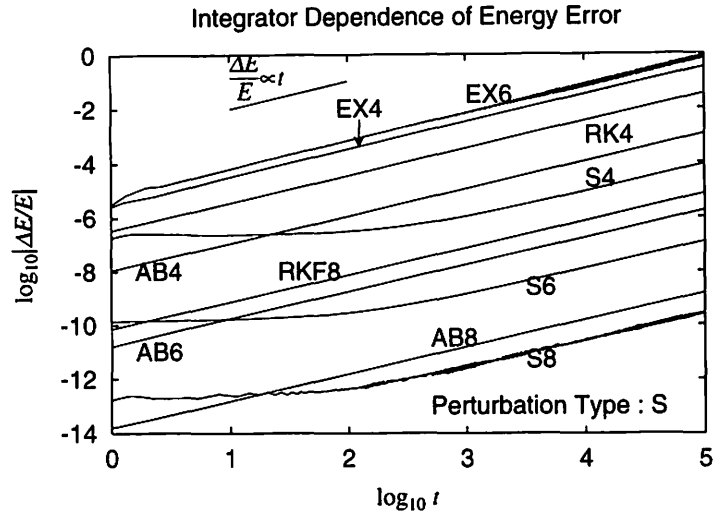

Fig. 4.— Integrator Dependence of Energy Error Growth of Perturbed Harmonic Oscillator

Note: Same as Figure 2 but plotted were the relative error of energy calculated by using the traditional integrators. We fixed the shift of frequency as the perturbation type.

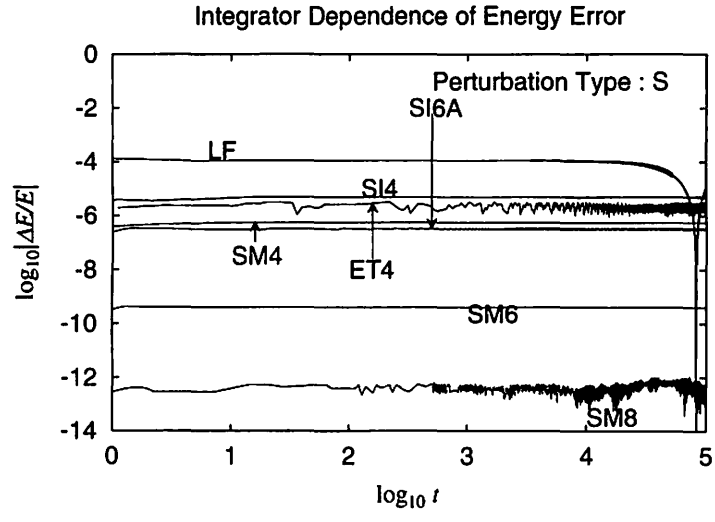

Fig. 5.— Integrator Dependence of Energy Error Growth of Perturbed Harmonic Oscillator

Note: Same as Figure 4 but plotted were the result calculated by using the time symmetric integrators.

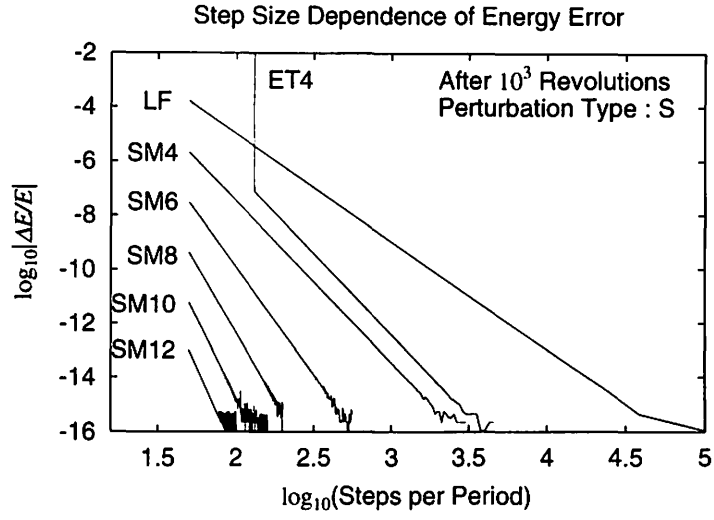

Fig. 6.— Step Size Dependence of Energy Error of Perturbed Harmonic Oscillator.

Note: Illustrated is the relative energy error after 1000 nominal revolutions as a function of steps per period. The integrators adopted are the symmetric multistep method. We denote by LF by the leapfrog, by SM4 the method IV of Lambert and Watson (1976), SM6 is the method VI of Lambert and Watson (1976) where the free parameter a was set as $a = 0$, by SM8, SM10, and SM12 the 8th, 10th, and 12th order formulas of Quinlan and Tremaine (1990), and by ET4 the 4th order formula of Evans and Tremaine (1999) where the free parameter was put as $u_2 = 0$, respectively.

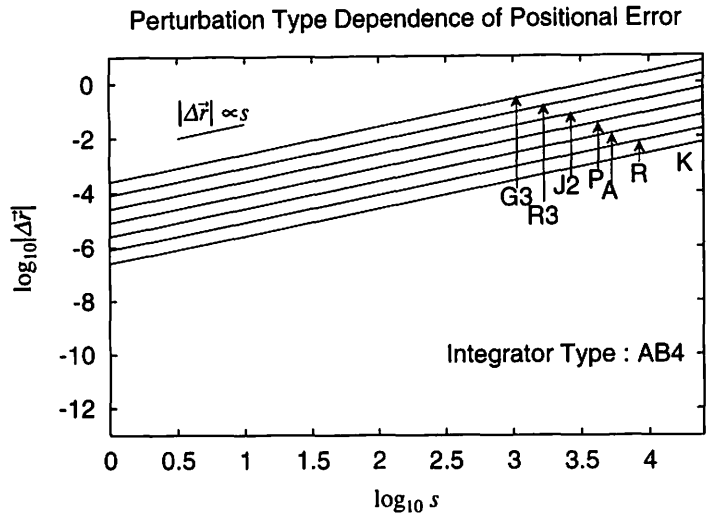

Fig. 7.— Perturbation Type Dependence of Positional Error Growth of KS Regularized Perturbed Two Body Problem

Note: We adopted the fourth order Adams-Bashforth method (AB4) as the integrator. The step size was fixed as $h = 0.06$ where the nominal orbital period is 2π. Just as the same as in Figure 1, the errors were plotted after multiplying the constant factors to make the difference clearly; $10^{0.5}$ for the relativistic one body problem (R), 10^{1} for the air drag (A), $10^{1.5}$ for the solar radiation pressure (P), 10^{2} for the J_2 perturbation (J2), $10^{2.5}$ for the restricted three body problem (R3), and 10^{3} for the general three body problem (G3).

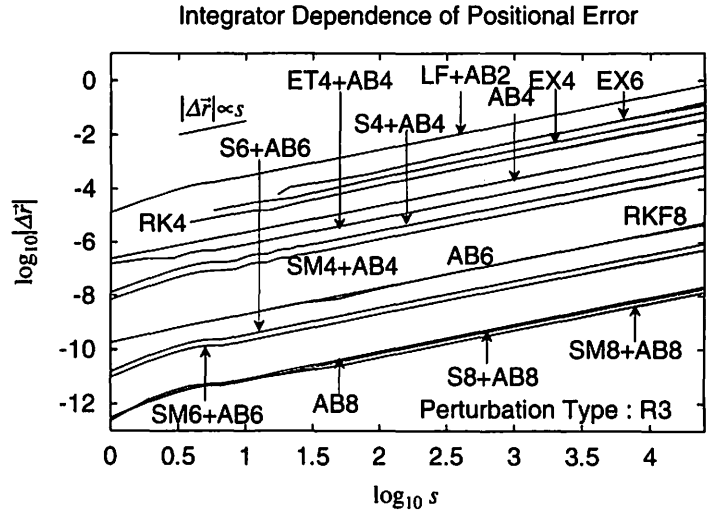

Fig. 8.— Integrator Dependence of Positional Error Growth of KS Regularized Perturbed Two Body Problem

Note: Same as Figure 7 but the integrator for the main KS variables was changed while the integrator for the other variables t and h_k was still fixed as the AB4. The perturbation type was fixed as the circular restricted three body problem. The line AB6 is almost the same as the line of RKF8 so that the difference is hardly seen in the figure.

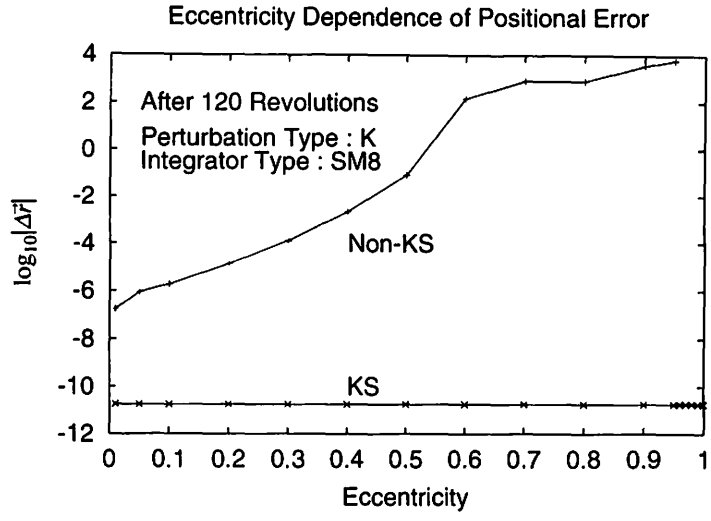

Fig. 9.— Eccentricity Dependence of Positional Error

Note: The eccentricity dependence was compared between the KS regularized and unregularized approaches. The problem was fixed as the pure Kepler problem. The errors after 120 revolutions were plotted as a function of the eccentricity. The integrator was fixed as the 8th order symmetric multistep method of Quinlan and Tramaine (1990).

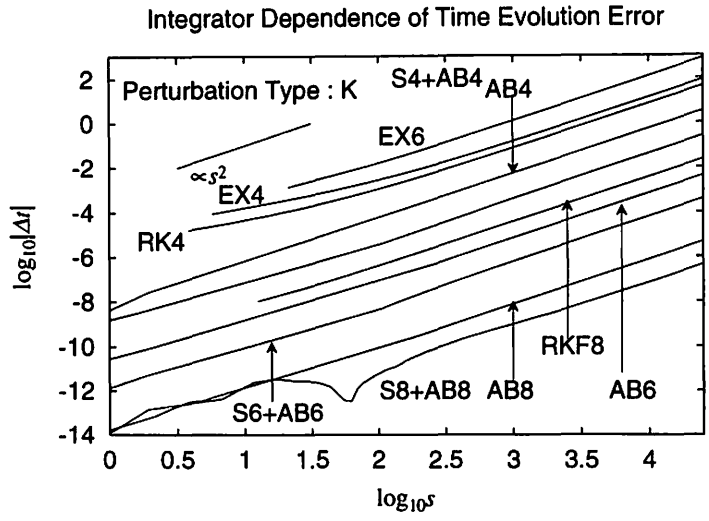

Fig. 10.— Integrator Dependence of Error Growth of Time Evolution

Note: Same as Figure 8 but for the error growth of physical time t integrating the part of perturbed harmonic oscillator by using the traditional integrators. The problem was fixed as the pure Kepler problem.

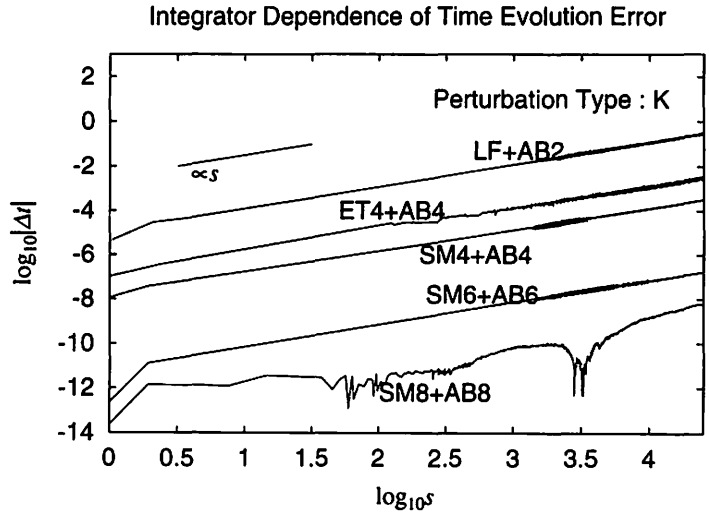

Fig. 11.— Integrator Dependence of Error Growth of Time Evolution

Note: Same as Figure 10 but the result using the time symmetric integrators.

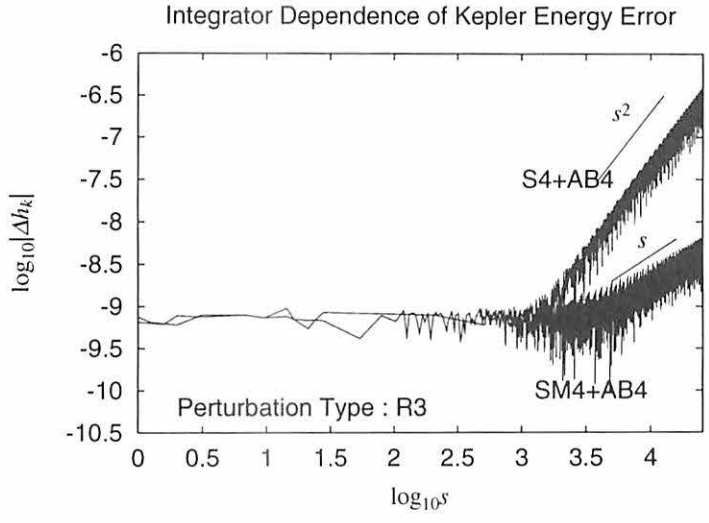

Fig. 12.— Integrator Dependence of Error Growth of Kepler Energy

Note: Same as Figure 7 but for the error growth of Kepler energy, h_k. As the integrators to be compared, we adopted the pair of the fourth order Störmer and Adams-Bashforth methods (S4+AB4), and the similar pair of the fourth order symmetric and Adams-Bashforth methods (SM4+AB4).

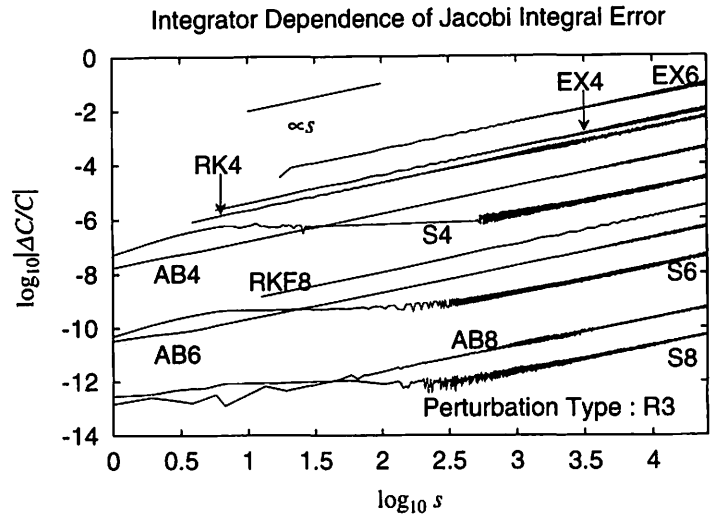

Fig. 13.— Integrator Dependence of Error Growth of Jacobi Integral

Note: Same sa Figure 8 but plotted were the error of Jacobi integral. In this calculation, we adopted the traditional integrators for integrating the part of perturbed harmonic oscillator.

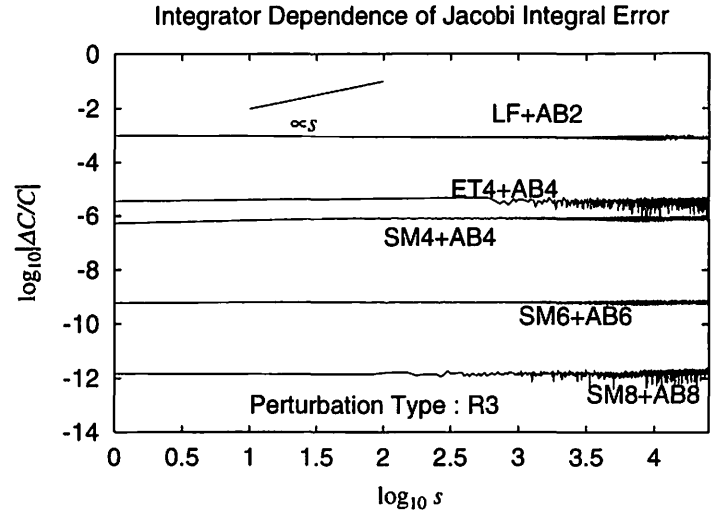

Fig. 14.— Integrator Dependence of Error Growth of Jacobi Integral

Note: Same as Figure 13 but adopted integrators were the time symmetric ones. In this figure, the maximum error were plotted because the errors themselves contain a large oscillating part.

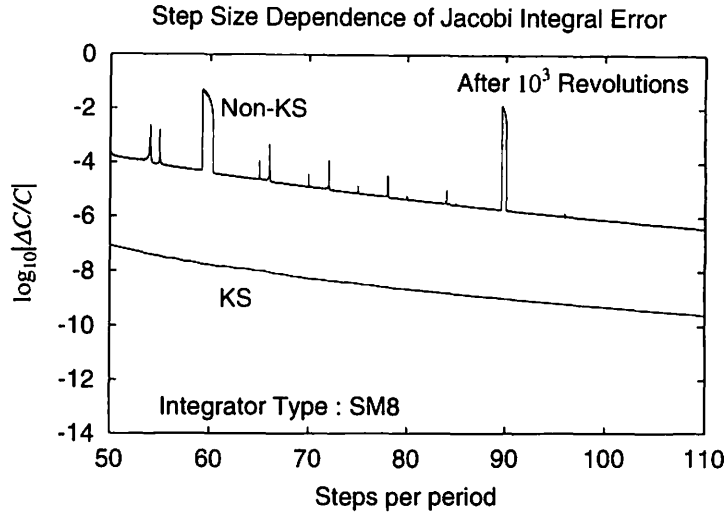

Fig. 15.— Step Size Dependence of Error of Jacobi Integral

Note: Same as Figure 8 but the errors after 10^3 nominal revolutions were plotted as functions of the step size. As the integrator, we adopted the eighth order symmetric multistep method of Quinlan and Tremaine (1990). Calculations were done for both the KS regularized and unregularized equations of motion. The initial eccentricity was fixed as $e = 0.2$.

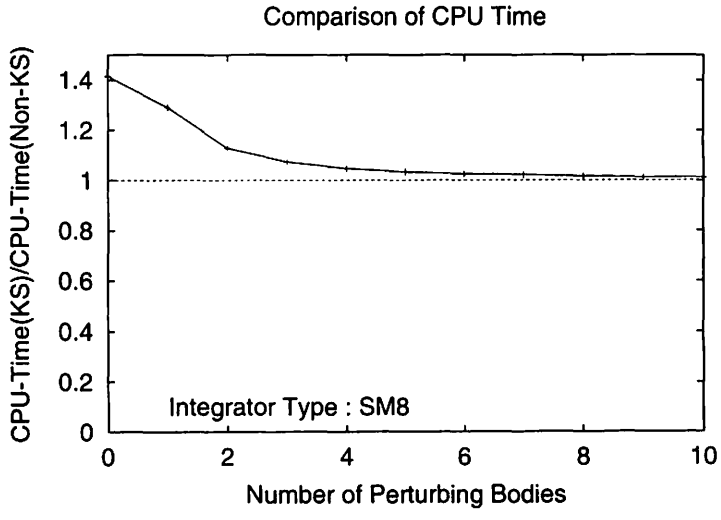

Fig. 16.— Comparison of CPU Time

Note: Illustrated are the ratio of CPU times of numerical integration of one step between the KS regularized and non-regularized equations of motion. The CPU times are plotted as function of the number of perturbing bodies.

天体力学N体力学研究会プログラム

第1日 15日(水)

午後

13:20-13:30	世話人挨拶
【惑星科学他】	座長：牧野淳一郎(前半)/関口昌由(後半)
13:30-14:15	長沢真樹子(東工大)
	永年共鳴の移動に伴うカイパーベルト天体の軌道進化
14:15-15:00	木下宙(国立天文台)
	ネレイド(海王星衛星)の運動理論
15:00-15:20	ポスター短発表I
15:20-15:40	休憩
15:40-16:25	Saad Abdel-naby Saad(総研大)
	The Theory of Motion of Nereid II. Non-planar motion
16:25-17:10	谷川清隆(国立天文台)
	一次元自由落下四体問題
17:10-17:30	ポスター短発表II
16:30-18:30	ポスターセッション
19;00-21:00	懇親会(湘南国際村センター)

第2日 16日(木)

午前

7;30-	朝食
9;00-10;00	ポスターセッション
【重力系計算】	座長：台坂博
10:00-10:45	牧野淳一郎(東大)
	1次元自己重力系における熱力学的緩和について
10:45-11:30	福島登志夫(国立天文台)
	倍長精度計算ライブラリ開発と軌道計算への応用
11:30-13:30	ポスターセッション、昼食

第2日 16日(木)

午後

【力学系理論】	座長：山口義幸(前半)/篠原晋(後半)
13:30-14:15	吉田春夫(国立天文台)
	微分ガロア理論にもとづくハミルトニアン系の可積分性の必要条件
14:15-15:00	中川克也(総研大)
	運動量について4次の多項式第一積分を持つ2次元同次多項式ポテンシャル系
15:00-15:30	休憩
15:30-16:15	平田吉博(名大)
	多自由度ハミルトン系における共鳴近傍の力学
16:15-17:00	山口喜博(帝京平成大)
	Homoclinic intersection in C^2 standard-like mappings
17:00-18;30	ポスターセッション
18;30-	夕食

第3日 17日(金)

午前

7;30-	朝食
9;00-10;00	ポスターセッション
【各種】	座長：伊藤孝士
10:45-11:30	山本一登(京都産業大)
	Schwarzschild 問題の中間軌道による解
11:30-12:15	井上猛(京都産業大)
	水星近日点前進の問題 Newcomb の場合
12:15-12:25	世話人挨拶

ポスター発表

【惑星科学他】

1　古屋泉 (神戸大)　ダスト層の自己重力不安定による微惑星形成
2　森島龍司 (名大)　巨大衝突後の地球と月の共成長進化；Lunar Impact Ejecta の脱出による角運動量の減少
3　武田隆顕 (東工大)　巨大衝突説に基づく原始月円盤の進化
4　台坂博 (東工大)　Viscosity in dense, self-gravitating particle systems induced by gravitational instability
5　岩崎一典 (東工大)　原始惑星系の安定性に対するガス抵抗の効果について
6　白井俊道 (東大)　非剛体地球の章動理論の改良
7　谷川清隆 (国立天文台)　生命の寿命と環境変化
8　伊藤孝士 (国立天文台)　惑星運動の長期安定性
9　小林浩 (東工大)　他の恒星の接近が原始惑星系円盤にもたらす影響

【系外惑星】

10　伊藤孝士 (国立天文台)　Upsilon Andromedae 惑星系の安定性
11　中井宏 (国立天文台)　Upsilon Andromedae 惑星系の安定性

【天体観測】

12　河合雅司 (富山商船高専)　衛星軌道解析における対流圏電波伝搬補正モデル
13　谷川清隆 (国立天文台)　Space Occultation
14　布施哲治 (国立天文台ハワイ)　すばる望遠鏡よる観測と天体力学の融合（仮題）

【重力系計算】

15　市來健吾 (京大)　粘性流体中の多粒子系の高速計算法
16　荒木田英禎 (総研大)　Long term integration error of KS regularized orbital motion

【多体系】

17　関口昌由 (木更津高専)　対称型 1 次元 4 体問題の数値計算（4 体衝突軌道の初期値探索）
18　石井雅治 (椙山女学園大)　力学系における第一積分の非退化性の証明と特異点解析
19　後藤振一郎 (名大)　離散時間力学系における不安定 (安定) 多様体の漸近展開
20　山口義幸 (京大)　幾何学的方法によるリアプノフスペクトルの考察
21　山口喜博 (帝京平成大)　Standard mapping における KAM の崩壊と Non-Birkhoff 軌道
22　篠原晋 (早大)　Kicked Harper Map における Last KAM 曲線の崩壊

【物性多体系】

23　小林泰三 (立命館大)　自発的合金化に於ける熱浴効果 II
24　曽田康秀 (お茶大)　自己重力リングモデルにおける相転移現象とフラクタル
25　関根忍 (都立大)　ハミルトン系における内部自由度間の遅いエネルギー緩和

Author Index and Participants List

(氏名 50 音順、ページは筆頭著者のみ)

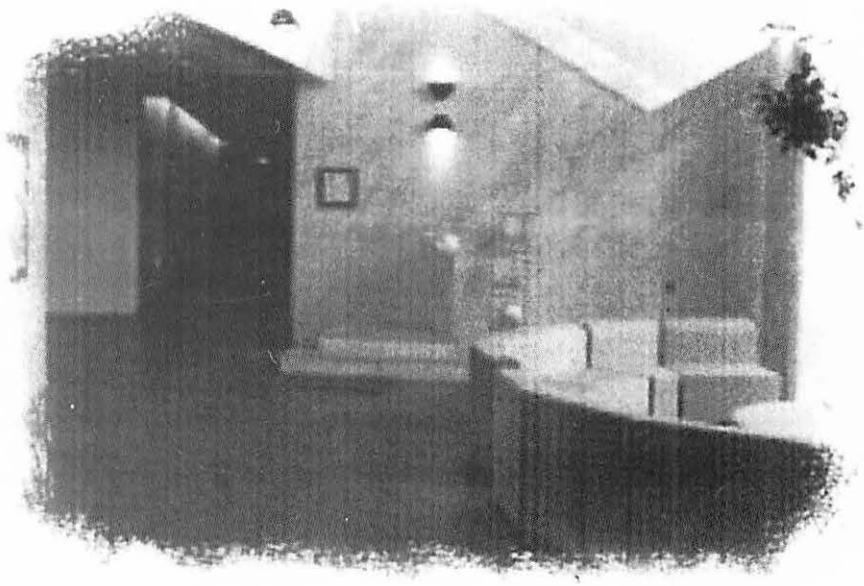

The Graduate University for Advanced Studies

(in Shonan Village, Hayama, Kanagawa)